Transactions of the ASME®

Technical Editor, **T. H. OKIISHI (1998)**
Associate Technical Editors
Aeromechanical Interaction
R. E. KIELB (1996)
Gas Turbine
C. J. RUSSO (1995)
Heat Transfer
M. G. DUNN (1996)
Nuclear Engineering
H. H. CHUNG (1996)
Power
P. H. GILSON (1996)
Turbomachinery
R. A. DELANEY (1998)
N. A. CUMPSTY (1996)

BOARD ON COMMUNICATIONS
Chairman and Vice-President
R. MATES

Members-at-Large
T. BARLOW, N. H. CHAO, A. ERDMAN, G. JOHNSON, L. KEER, E. M. PATTON, S. PATULSKI, S. ROHDE, R. SHAH, F. WHITE, J. WHITEHEAD, K. T. YANG
OFFICERS OF THE ASME
President, **D. T. KOENIG**
Executive Director
D. L. BELDEN
Treasurer
R. A. BENNETT

PUBLISHING STAFF
Managing Director, Engineering
CHARLES W. BEARDSLEY
Director, Technical Publishing
JANET M. WEINRIB
Managing Editor, Technical Publishing
CYNTHIA B. CLARK
Managing Editor, Transactions
CORNELIA MONAHAN
Senior Production Editor,
VALERIE WINTERS
Production Assistant,
MARISOL ANDINO

Transactions of the ASME, Journal of Turbomachinery (ISSN 0889-504X) is published quarterly (Jan., Apr., July, Oct.) for $150.00 per year by The American Society of Mechanical Engineers, 345 East 47th Street, New York, NY 10017. Second class postage paid at New York, NY and additional mailing offices. POSTMASTER: Send address changes to Transactions of the ASME, Journal of Turbomachinery, c/o THE AMERICAN SOCIETY OF MECHANICAL ENGINEERS, 22 Law Drive, Box 2300. Fairfield, NJ 07007-2300.
CHANGES OF ADDRESS must be received at Society headquarters seven weeks before they are to be effective. Please send old label and new address.
PRICES: To members, $40.00, annually; to nonmembers, $150.00.
Add $24.00 for postage to countries outside the United States and Canada.
STATEMENT from By-Laws. The Society shall not be responsible for statements or opinions advanced in papers or . . . printed in its publications (B7.1, Par. 3).

COPYRIGHT © 1996 by The American Society of Mechanical Engineers. Authorization to photocopy material for internal or personal use under circumstances not falling within the fair use provisions of the Copyright Act is granted by ASME to libraries and other users registered with the Copyright Clearance Center (CCC) Transactional Reporting Service provided that the base fee of $3.00 per article is paid directly to CCC, 222 Rosewood Dr., Danvers, MA 01923. Request for special permission or bulk copying should be addressed to Reprints/Permission Department.

INDEXED by Applied Mechanics Reviews and Engineering Information, Inc.
Canadian Goods & Services Tax Registration #126148048

Journal of Turbomachinery

Published Quarterly by The American Society of Mechanical Engineers

VOLUME 118 • NUMBER 2 • APRIL 1996

TECHNICAL PAPERS

181 **Effects of Rotating Inlet Distortion on Multistage Compressor Stability** (94-GT-220)
J. P. Longley, H.-W. Shin, R. E. Plumley, P. D. Silkowski, I. J. Day, E. M. Greitzer, C. S. Tan, and D. C. Wisler

189 **Rotating Stall in a Single-Stage Axial Flow Compressor** (94-GT-210)
C. A. Poensgen and H. E. Gallus

197 **Numerical Investigation of Stall Flutter** (94-GT-206)
J. A. Ekaterinaris and M. F. Platzer

204 **Off-Design Transition and Separation Behavior of a CDA Cascade** (94-GT-214)
W. Steinert and H. Starken

211 **Measurement of Tip-Clearance Flow in a Multistage, Axial Flow Compressor** (94-GT-431)
A. C. Foley and P. C. Ivey

218 **Experimental and Computational Investigation of the Tip Clearance Flow in a Transonic Axial Compressor Rotor** (94-GT-365)
K. L. Suder and M. L. Celestina

230 **The Effect of Tip Clearance on a Swept Transonic Compressor Rotor** (94-GT-363)
W. W. Copenhaver, E. R. Mayhew, C. Hah, and A. R. Wadia

240 **Flow Analyses in a Single-Stage Propulsion Pump** (94-GT-139)
Y. T. Lee, C. Hah, and J. Loellbach

250 **Computational Modeling of Three-Dimensional Endwall Flow Through a Turbine Rotor Cascade With Strong Secondary Flows** (94-GT-136)
Y.-H. Ho and B. Lakshminarayana

262 **Radial Mixing in an Axial Turbine** (94-GT-137)
R. P. Dring

268 **Numerical Analysis of Three-Dimensional Unsteady Hot Streak Migration and Shock Interaction in a Turbine Stage** (94-GT-76)
A. P. Saxer and H. M. Felici

278 **Film Cooling of the Gas Turbine Endwall by Discrete-Hole Injection** (94-GT-67)
M. Y. Jabbari, K. C. Marston, E. R. G. Eckert, and R. J. Goldstein

285 **Detailed Measurements of Local Heat Transfer Coefficient in the Entrance to Normal and Inclined Film Cooling Holes** (94-GT-1)
D. R. H. Gillespie, A. R. Byerley, P. T. Ireland, Z. Wang, T. V. Jones, and S. T. Kohler

291 **Investigation of the Flow Field Downstream of a Turbine Trailing Edge Cooled Nozzle Guide Vane** (94-GT-209)
C. H. Sieverding, T. Arts, R. Dénos, and F. Martelli

301 **Simulation of Cooling Systems in Gas Turbines** (94-GT-49)
G. Ebenhoch and T. M. Speer

307 **Transition Modeling Effects on Turbine Rotor Blade Heat Transfer Predictions** (94-GT-22)
A. A. Ameri and A. Arnone

314 **Flow and Heat Transfer Behavior in Transitional Boundary Layers With Streamwise Acceleration** (94-GT-24)
F. J. Keller and T. Wang

327 **Unsteady Boundary Layers on a Flat Plate Disturbed by Periodic Wakes: Part I—Measurement of Wake-Affected Heat Transfer and Wake-Induced Transition Model** (94-GT-429)
K. Funazaki

337 **Unsteady Boundary Layers on a Flat Plate Disturbed by Periodic Wakes: Part II—Measurements of Unsteady Boundary Layers and Discussion** (94-GT-430)
K. Funazaki

347 **The Influence of Blade Wakes on the Performance of Interturbine Diffusers** (94-GT-207)
R. G. Dominy and D. A. Kirkham

353 **A Design Study of Radial Inflow Turbines With Splitter Blades in Three-Dimensional Flow** (94-GT-36)
W. D. Tjokroaminata, C. S. Tan, and W. R. Hawthorne

362 **Design and Test of a Small, High Pressure Ratio Turbine** (94-GT-135)
A. C. Jones

(Contents continued on page 249)

Downloaded 01 Jun 2010 to 171.66.16.52. Redistribution subject to ASME license or copyright; see http://www.asme.org/terms/Terms_Use.cfm

(Contents continued)

371 An Experimental and Computational Investigation of Flow in a Radial Inlet of an Industrial Pipeline Centrifugal Compressor (94-GT-134)
M. B. Flathers, G. E. Bache, and R. Rainsberger

385 Inverse Design of Centrifugal Compressor Vaned Diffusers in a Inlet Shear Flows (94-GT-144)
M. Zangeneh

394 Detailed Stress Tensor Measurements in a Centrifugal Compressor Vaneless Diffuser (94-GT-227)
A. Pinarbasi and M. W. Johnson

400 Experimental and Numerical Study of Orifice Discharge Coefficients in High-Speed Rotating Disks (94-GT-142)
S. Wittig, S. Kim, R. Jakoby, and I. Weißert

408 Turbulent Flow Between Two Disks Contrarotating at Different Speeds (94-GT-54)
M. Kilic, X. Gan, and J. M. Owen

414 Windage Heating of Air Passing Through Labyrinth Seals (94-GT-56)
J. A. Millward and M. F. Edwards

ANNOUNCEMENTS

203 Change of address form for subscribers

420 Information for authors

Downloaded 01 Jun 2010 to 171.66.16.52. Redistribution subject to ASME license or copyright; see http://www.asme.org/terms/Terms_Use.cfm

J. P. Longley
Whittle Laboratory,
Cambridge University,
Cambridge, United Kingdom

H.-W. Shin
Aerodynamics Research Lab.,
GE Aircraft Engines,
Cincinnati, OH 44135

R. E. Plumley

P. D. Silkowski

Gas Turbine Laboratory,
Massachusetts Institute of Technology,
Cambridge, MA 02139

I. J. Day
Whittle Laboratory,
Cambridge University,
Cambridge, United Kingdom

E. M. Greitzer

C. S. Tan

Gas Turbine Laboratory,
Massachusetts Institute of Technology,
Cambridge, MA 02139

D. C. Wisler
Aerodynamics Research Lab.,
GE Aircraft Engines,
Cincinnati, OH 44135

Effects of Rotating Inlet Distortion on Multistage Compressor Stability

In multispool engines, rotating stall in an upstream compressor will impose a rotating distortion on the downstream compressor, thereby affecting its stability margin. In this paper experiments are described in which this effect was simulated by a rotating screen upstream of several multistage low-speed compressors. The measurements are complemented by, and compared with, a theoretical model of multistage compressor response to speed and direction of rotation of an inlet distortion. For corotating distortions (i.e., distortions rotating in the same direction as rotor rotation), experiments show that the compressors exhibited significant loss in stability margin and that they could be divided into two groups according to their response. The first group exhibited a single peak in stall margin degradation when the distortion speed corresponded to roughly 50 percent of rotor speed. The second group showed two peaks in stall margin degradation corresponding to distortion speeds of approximately 25–35 percent and 70–75 percent of rotor speed. These new results demonstrate that multistage compressors can have more than a single resonant response. Detailed measurements suggest that the two types of behavior are linked to differences between the stall inception processes observed for the two groups of compressors and that a direct connection thus exists between the observed forced response and the unsteady flow phenomena at stall onset. For counterrotational distortions, all the compressors tested showed minimal loss of stability margin. The results imply that counterrotation of the fan and core compressor, or LP and HP compressors, could be a worthwhile design choice. Calculations based on the two-dimensional theoretical model show excellent agreement for the compressors, which had a single peak for stall margin degradation. We take this first-of-a-kind comparison as showing that the model, though simplified, captures the essential fluid dynamic features of the phenomena. Agreement is not good for compressors that had two peaks in the curve of stall margin shift versus distortion rotation speed. The discrepancy is attributed to the three-dimensional and short length scale nature of the stall inception process in these machines; this includes phenomena that have not yet been addressed in any model.

1.0 Scope and Objectives

Inlet distortion can modify the flow rate at which rotating stall occurs in an aeroengine compressor, degrading the range over which stable operation is possible. This paper addresses the relationship between the speed and direction at which the inlet distortion pattern rotates around the compressor annulus and the severity of the degradation in stability margin. Imposition of a rotating distortion can also be thought of as a type of forced response experiment to probe the compressor dynamic behavior. Although not originally envisaged, the results from these forced response experiments appear to be relevant to the types of instability phenomena that occur in undistorted operation as well.

The loss of stability margin associated with a rotating, and hence locally time-dependent, inlet distortion is directly relevant to multispool aeroengines. When the upstream compressor or fan is in rotating stall, the downstream compressor operates with an inlet flow nonuniformity that rotates around the compressor annulus. This form of nonsteady compressor interaction has been known for some time but has not been treated in any rigorous manner for multistage machines. Investigating the magnitude of the effect in a representative configuration was thus one initial objective of the experimental work.

Another equally important objective was to provide a diagnostic tool for evaluating new theories that describe the response of a compressor to nonsteady and nonuniform flow. Although the forms of the predicted response in these instances can be complex, the modeling techniques employ rather rudimentary models for the nonsteady flow within the compressor. Detailed data of the type obtained are of considerable utility in evaluating the theory. An additional benefit of the experiments, only recognized once the results had been obtained, is that measurements of forced compressor response can also be interpreted to give information about the general problem of compressor stall onset in uniform as well as nonuniform flows.

2.0 Background to the Problem

2.1 Compressor Response to Rotating Inlet Distortion. There are few detailed data concerning the degradation in stability margin when compressors are subjected to a rotating inlet distortion. The industry standard document on distortion (SAE

Contributed by the International Gas Turbine Institute and presented at the 39th International Gas Turbine and Aeroengine Congress and Exposition, The Hague, The Netherlands, June 13–16, 1994. Manuscript received by the International Gas Turbine Institute February 18, 1994. Paper No. 94-GT-220. Associate Technical Editor: E. M. Greitzer.

Copyright © 1996 by ASME

Downloaded 01 Jun 2010 to 171.66.16.53. Redistribution subject to ASME license or copyright; see http://www.asme.org/terms/Terms_Use.cfm

AIR 1419) contains no discussion of the effects of corotating versus counterrotating distortion on gas turbine engines. Experiments carried out by Ludwig et al. (1973) for an isolated rotor show clearly that the rotation speed of the distortion has a major influence on the stability margin of the compressor. Distortions that rotate in the same direction as the compressor (corotating distortions) have a larger effect than counterrotating distortions, with the greatest loss of stability occurring at distortion speeds close to the speed at which a rotating stall cell would propagate. Kozarev and Fedorov (1983) investigated the forced response of a two-stage compressor with similar results.

No relevant theoretical analysis accompanied either of these investigations, but such an analysis was subsequently carried out by Chue et al. (1989). They linked this phenomenon to the resonant response of the compressor, i.e., to a correspondence between the forcing (distortion speed) and the natural eigenmodes of the compression system. (Note that the response at issue is a nonlinear one; from a linearized analysis there is no effect of forcing on stability.) The experiments and theoretical analysis described in the present paper advance the understanding of stability degradation obtained by previous researchers in three ways: (1) quantifying the degradation in stability, (2) demonstrating, for the first time, that a compressor can have more than one natural, or characteristic, speed, and (3) suggesting the link between the type of behavior observed with rotating distortion and the unsteady phenomena at stall onset.

2.2 Stall in Multistage Axial Compressors. To establish the connection between the results of the screen rotation rate tests and the fluid dynamic events at stall onset, it is useful to summarize the stall inception phenomena that occur in the natural situation, i.e., without forcing. This will be seen to be important in the interpretation of the forced response data. Day (1993a) demonstrated that there are at least two routes by which rotating stall can develop, referred to here as "modal-wave" and "spike" types. The first, modal-wave stall inception, is characterized by a small-amplitude propagating disturbance (typically detected at 1–2 percent of mean flow velocity) that affects the entire flow-field, with a characteristic circumferential wavelength, which is comparable to the circumference of the compressor. Observations are that at inception, these modal-waves propagate at approximately 20–45 percent of rotor speed, increasing to 40–60 percent rotor speed as they grow to fully developed rotating stall. The behavior of these types of flowfield disturbances has been well modeled using a two-dimensional stability analysis (Longley, 1994), which is based on the length scale of the disturbance being much larger than a blade pitch.

The other type of stall inception, spikes, is a much more localized flow disturbance. The spikes initially occupy only a few blade passages and are concentrated at the tips of the rotor blades. Observations so far are that these disturbances have only been found on the first rotor in multistage compressors (Day, 1993c). Typically they propagate at a higher speed of 70–80 percent rotor speed and can travel only once or twice around the compressor annulus before growing into rotating stall. Little is known quantitatively about the evolution of spike-type disturbances other than that as they grow their propagation speed decreases to that of fully developed rotating stall. It is evident from the data that spikes are a three-dimensional, short-length-scale, flow feature. As yet, however, the basic fluid dynamics associated with their appearance, propagation, and growth is not understood and they have not been satisfactorily modeled.

Some compressors have been found to exhibit both types of unsteady disturbances. Even in these circumstances, in any particular configuration, one can still point to one or the other (modes or spikes) as being the dominant phenomenon in the process of transition to rotating stall.

2.3 Theoretical Model. In this research there are strong links between the experimental work and the theoretical modeling. The model was used to guide both the planning and the interpretation of the experimental work, while the measurements were used to assess the conditions under which the model is reliable. It is thus useful to describe briefly the model, and, more importantly, the prediction of the flowfield that arises from it.

The model is an extension of that developed by Hynes and Greitzer (1987). It addresses the behavior of two-dimensional flowfield disturbances that have a circumferential length scale that is an appreciable fraction of the compressor circumference (and hence much longer than a blade pitch). The analysis is therefore *strictly* applicable only to cases where the flow through the compressor may be considered as radially uniform.

While such *purely* two-dimensional flow disturbance are not observed in practice, there are many situations in which the disturbances are predominantly two dimensional, and the usefulness of the theory has been born out in a number of cases. These include analysis of the nonlinear evolution of small amplitude disturbances into rotating stall (Garnier, 1991), predictions of the existence of modal waves (McDougall et al., 1990), calculations of the effects of active control in axial compressors (Paduano et al., 1993; Haynes et al., 1994) and design and demonstration of the suppression of rotating stall using aeromechanical feedback (Gysling, 1993). For compressors operating with inlet distortion, the model shows overall trends with distortion parameters that are well in line with experimental results such as the loss of compressor stability margin with distortion parameters (Hynes and Greitzer, 1987). Further, the predictions of spatial growth and decay of circumferentially propagating disturbances when a distortion was present have also been verified experimentally (Longley, 1990). In summary there are a variety of situations in which the model has been a useful conceptual tool, and the extent of its applicability in the present instance is of interest.

3.0 Overall Approach

The approach adopted was to rotate a distortion screen upstream of several low-speed multistage compressors. The experimental facility used allowed the distortion screen to be rotated in either direction (co- or counterrotational) at various fractions of rotor speed. Both time-mean and time-resolved measurements were recorded for four different compressors with the data analyzed in terms of the insight they gave into the forced and unforced compressor response. Comparisons were also made with calculations using the theoretical model.

Anticipating the results to be presented, we note that the compressors tested exhibited two qualitatively different types of behavior as far as stability margin degradation with screen speed. Two showed a single resonant response peak as a function of distortion propagation speed while the others exhibited a double peaked response. As a framework for organizing the experimental and theoretical information, we first present the results for the two compressors that showed a single peak. These compressors, which will be referred to as "dromedary," appear to respond in a two-dimensional long-length-scale manner (i.e., long compared to a blade pitch), in accord with the assumptions on which the analysis is based. The results for the compressors that showed two peaks will then be presented. These compressors, which will be referred to as "bactrian," do not appear to respond in a two-dimensional manner. Comments on the behavior of the two bactrian compressors will then be given, along with discussion of the broader implications of this work.

4.0 Experimental Facility and Instrumentation

The experimental measurements were made in the four-stage research compressor at the General Electric Aerodynamics Research Laboratory. A schematic of the facility is shown in Fig. 1 and a detailed description is given by Wisler (1985). The facility is a large-scale (1.52 m tip diameter) low-speed research

Downloaded 01 Jun 2010 to 171.66.16.53. Redistribution subject to ASME license or copyright; see http://www.asme.org/terms/Terms_Use.cfm

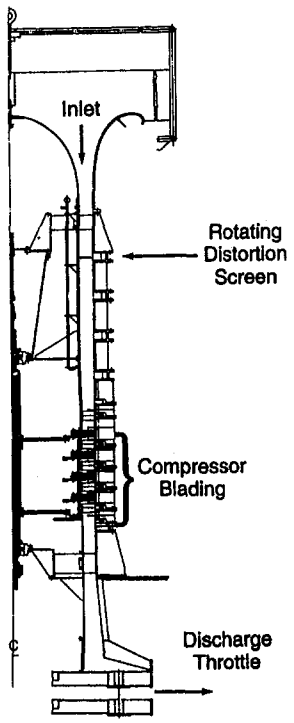


Fig. 1 Low-speed research compressor showing location of rotating distortion screen relative to blading

compressor well suited for obtaining detailed measurements of steady and unsteady compressor flowfield phenomena. The rotor tip speed in the experiments to be described was 40 m/s (at 500 rpm) so the flow can be considered incompressible. All the compressors tested had inlet guide vanes and four stages of blading. The hub/tip radius ratio of the present configurations was 0.85.

Four different blade geometries were used, denoted as compressors A to D. They are low Mach number equivalents of current state-of-the-art aeroengine compressor designs. The total-to-static pressure rise characteristics measured for the four compressors when operating with undistorted inlet conditions are shown in Fig. 2. Compressor C has a stage loading representative of current commercial as well as military high-pressure cores, while compressors A, B, and D, are targeted at very aggressive stage loadings.

4.1 Inlet Distortion Characteristics. For the distortion experiments the facility was equipped with a drive mechanism that can rotate a wire mesh screen at speeds between zero and 100 percent of the design rotor speed in either direction. The advantage of a screen-generated distortion, rather than one generated by another compressor in rotating stall, is that it allows independent control of the severity of the distortion, the rotation direction, and the speed.

The screen was located 1.5 radii upstream of the IGVs, as shown in Fig. 1. This is far enough upstream so that there is negligible potential field interaction between the distortion generator and the compressor. The screen produced a roughly square-wave total pressure distortion of 120 deg circumferential extent, with amplitude corresponding to 1.2 dynamic heads based on the mean inlet velocity. This total pressure nonuniformity was chosen to be representative of realistic inlet distortion conditions (DC(60 deg) $\approx$ 0.8) and to give a large change in the compressor stability margin for the case where the screen was stationary (based on calculations using the model).

4.2 Instrumentation. Time-mean and fast-response instrumentation were used during the series of tests, which spanned a four-year period. In all cases the overall pressure rise and mass flow were measured using the same time-mean instrumentation. The fast response instrumentation was changed between experiments according to which flow aspects were of concern. For the initial experiments (which were in fact carried out on compressor D) the fast-response measuring probes (a circumferential array of eight equally spaced single element hot-film velocity sensors at midspan) were placed 0.7 radii upstream of the IGVs where they could detect the presence of modal-waves (McDougall et al., 1990).

For compressor C the fast-response instrumentation included up to 20 velocity and 10 casing static pressure transducers, which were concentrated around the first rotor. Here we will only discuss the casing static pressure measurements at 0.2 chords upstream of the first rotor. In light of the discovery and definition of the spike-type route to rotating stall, which took place between the initial tests and those for compressors A and B, the later configuration included sixteen equally spaced velocity sensors placed 0.2 chords upstream of the first rotor at 30 percent immersion. These velocity sensors were used both as an array of eight equally spaced transducers and as an array of sixteen. The sensors were placed close to the first rotor in order to be able to detect both long and short-length-scale flowfield disturbances (Day, 1993a).

4.3 Data Analysis for Long Length Scale Disturbances (Modal Waves). The presence of small-amplitude long circumferential-length-scale flowfield disturbances (modal-waves) was investigated by conducting a spatial–temporal Fourier analysis of the data. This process makes use of a two-dimensional Fourier decomposition. The coefficient of the $e^{in\theta+ivt}$ component of the velocity flowfield is calculated from the spatial and temporal data. Using sixteen sensors equally spaced around the circumference, one can analyze up to the seventh circumferential harmonic. The temporal resolution depends upon the sampling rate. The spatial–temporal decomposition was done in two steps. First, at each instant in time, the sixteen signals can be spatially Fourier analyzed to yield the phase and amplitude for each of the resolved circumferential harmonics. This information, represented as a complex number, is a function of time, and can therefore be Fourier analyzed to yield the temporal spectra of any of the required spatial modes, usually the first.

5.0 Experimental Results: Compressors With a Single Resonant Peak (Dromedary Type)

5.1 Forced Response to a Rotating Distortion. The measured mean flow coefficients at stall inception as a function of screen rotational speed, nondimensionalized by rotor rotation

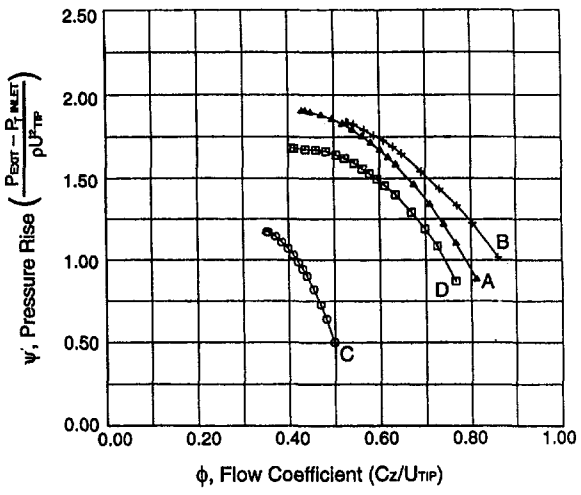


Fig. 2 Overall pressure rise for the four-stage compressors tested

Downloaded 01 Jun 2010 to 171.66.16.53. Redistribution subject to ASME license or copyright; see http://www.asme.org/terms/Terms_Use.cfm

speed, for the dromedary compressors A and B are presented in Figs. 3 and 4. The calculations from the theory are shown in the figures as the solid lines. The stall flow coefficients with no distortion and the design flow coefficients are also indicated in the figure. Negative screen speeds correspond to distortion rotating in the direction opposite to the rotor rotation (counterrotation). For both compressors some tests were carried out at reduced compressor speeds to allow higher screen-to-compressor speed ratios; the agreement in the portions of the data that overlap indicates minimal Reynolds number effects.

Several observations can be made concerning these data. The most evident is that the speed at which the inlet distortion rotates has a major effect on the stability point, with corotation of the screen having a much larger impact than counterrotation. The change in the stall flow coefficient with corotation is a substantial fraction of the difference between the stall flow coefficient at zero distortion screen speed and the design flow; this gives an indication of how much the stability margin is degraded by corotating distortion. Further, the degradation of compressor stability margin is largest near a certain screen corotation speed, 45 percent for compressor A and 55 percent for compressor B. The screen speeds about which these peaks are centered and the percent loss in stability margin are listed in Table 1. In the case of compressor B, the reduction in stability is a much as 90 percent of the margin which would exist for a steady distortion.

Counterrotating distortions have much less deleterious effect, as seen in Table 1 and Figs. 3 and 4. There are no peaks in the response curve, as there were for corotation. The flow range for some cases is larger then with uniform flow.

Finally, for both of these compressors the calculations of stability degradation are in good agreement with the measurements, implying that the stability margin degradation is governed by two-dimensional long circumferential-length-scale phenomena.

5.2 Natural Stall Inception. Compressor A had hot wires located 0.2 chords upstream of the first rotor. Time-resolved measurements of the velocity at each of the eight equally spaced sensors at 30 percent immersion are shown in Fig. 5. No short-length-scale disturbances (spikes) could be detected at this location close to the rotor. From the data we conclude that the route to rotating stall was via the growth of a long length scale small amplitude disturbance (modal-wave).

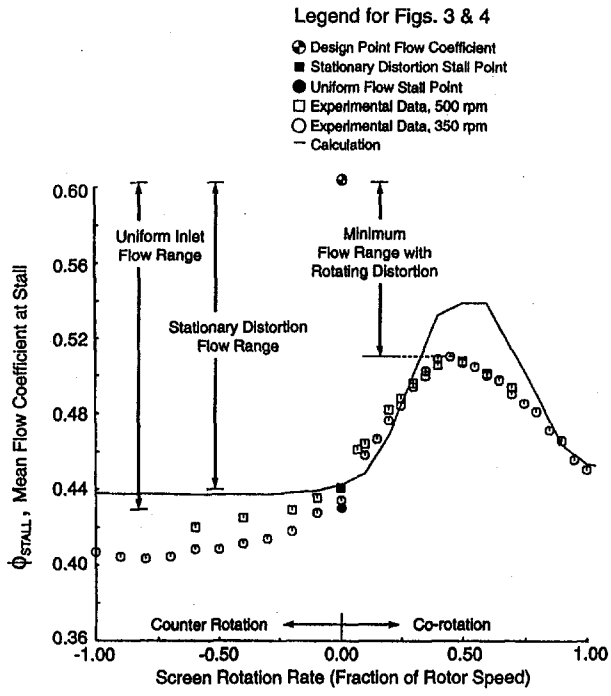


Fig. 3 Flow coefficient at stall versus distortion rotation rate for compressor A; uniform flow stall point and design point are also shown

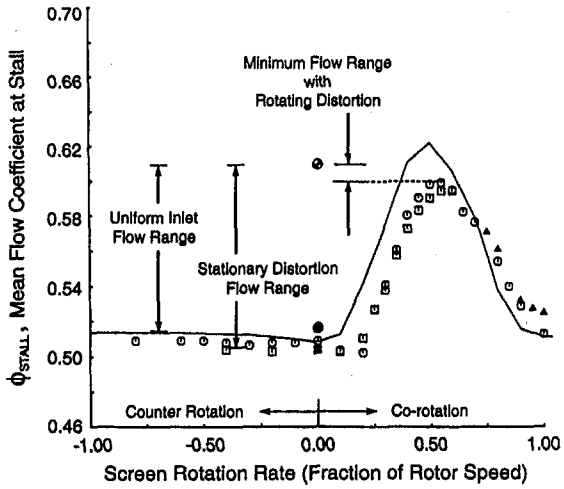


Fig. 4 Flow coefficient at stall versus distortion rotation rate for compressor B; uniform flow stall point and design point are also shown

The presence of a first harmonic modal-wave prior to stall was confirmed by a spatial–temporal Fourier analysis. The spectra of the first spatial harmonic of the velocity flowfield recorded by sixteen sensors are shown in Fig. 6. The data were taken 20 rotor revolutions prior to stall for a slow throttle closure. (The height of the peaks in the spectra is dependent on the throttle range over which the data were acquired, so that the ordinate should be used as a relative measurement only.) The smaller of the two peaks in the spectrum corresponds to a once-per-revolution disturbance associated with a slight rotor asymmetry. The taller peak indicates a modal-wave traveling at 33 percent of rotor speed; the measured amplitude was 1.4 percent of the mean axial velocity. The fully developed stall cell propagated at 46 percent of rotor speed.

Data for compressor B were similarly analyzed to determine the stall inception process. Figure 7 shows the velocities recorded ahead of the first rotor. A modal-wave-type stall inception is seen with the fully developed stall cell propagating at 46 percent of rotor speed. The lines of constant phase, calculated using spatial–temporal analysis, drawn on the figure show that the modal disturbance initially travels at 53 percent of rotor speed and slows as it grows into rotating stall. Spatial–temporal analysis of the output from sixteen sensors measured at fixed throttle close to the stall point identifies a first spatial harmonic modal-wave traveling at 53 percent of rotor speed, as shown in Fig. 8. The average amplitude of the wave at this throttle position was 0.4 percent of mean flow velocity.

The measurements of stall inception in these two compressors indicate that the natural (unforced) behavior is a two-dimensional, long-length-scale, modal-wave. The measured wave and stall cell speeds are summarized in Table 1. For compressor A the peak stall margin degradation occurs when the distortion is rotated at the stall cell speed while for compressor B it occurs at the modal-wave speed.

5.3 Velocity Distribution at the Compressor. The velocity variation due to the distortion is also of interest as another means of assessing the capabilities of the theory. This flowfield, which is steady in a screen fixed coordinate system, provides the background conditions for the growth or decay of traveling small perturbations that propagate at the mode speed. For compressor B the flowfield nonuniformity was measured at the compressor face since this could be compared with that calculated by the model. For the compressor operating at fixed throttle

Downloaded 01 Jun 2010 to 171.66.16.53. Redistribution subject to ASME license or copyright; see http://www.asme.org/terms/Terms_Use.cfm

Table 1 Overall mean flow and unsteady flow results for the four compressors

Compressor	A	B	C	D
Mean Flow				
Flow range: uniform inlet $\phi_{design} - \phi_{stall\ uniform\ flow}$	0.174	0.093	0.068	0.163
Flow range: stationary distortion $\phi_{design} - \phi_{stall\ stationary\ distortion}$	0.162 (93%)	0.105 (113%)	0.068 (100%)	0.117 (72%)
Minimum flow range: co–rotating distortion $\phi_{design} - \phi_{stall\ rotating\ distortion}$	0.093 (53%)	0.010 (11%)	0.046 (68%)	0.060 (35%)
Flow range: counter–rotating distortion –50% $\phi_{design} - \phi_{stall\ -50\%\ rotating\ distortion}$	0.194 (111%)	0.103 (111%)	0.083 (122%)	0.140 (86%)
Unsteady Flow				
Screen speed of first peak	45%	55%	20%	30%
Screen speed of second peak	-	-	72%	70%
Spike propagation speed	-	-	70%	–
Stall cell speed	46%	46%	45%	44%
Modal–wave speed (measured)	33%	53%	10%	18%
Modal–wave speed (calculated)	35%	33%	33%	27%

setting close to the stability boundary, each velocity sensor measures the entire circumferential flowfield variation as the screen rotates. The resulting velocity distribution as a function of time, or rather screen position, can be ensemble averaged for each sensor to give eight independent measurements. The stagnation pressure distribution far upstream, which had been measured for the stationary screen in earlier experiments, was used as input. In carrying out the computations it was assumed that the screen produced a similar distortion profile at all rotation speeds.

The measured and calculated circumferential distribution of axial velocity at three different screen speeds are compared in Fig. 9. The measurements represent the average of eight hot wires. The comparisons show that the model captures the asymmetry and the difference in flow between the plateau and trough of the velocity distribution. Note that the largest velocity nonuniformity measured between plateau and trough occurs at 35 percent screen speed. For this compressor, the greatest stability margin degradation occurred at 55 percent screen speed. The measured velocity distribution at 55 percent screen speed, however, shows an appreciably smaller flow coefficient nonuniformity than that at 35 percent speed. The implication is that loss of stability margin is not just a function of the degree of velocity nonuniformity but is also crucially dependent on the propagation speed of the distortion.

6.0 Experimental Results: Compressors With Two Resonant Peaks (Bactrian Type)

In the previous section we discussed two compressors that responded in a two-dimensional manner. The main features of this response were well captured using a theoretical model based on a two-dimensional, long-length-scale approach. In this section we present results for two other four-stage compressors, which responded quite differently to the rotating distortion. Specifically, these compressors exhibited two peaks in the curves of stalling flow versus screen rotation rate; the shape of the curves is not captured by calculations using the model.

6.1 Forced Response to a Rotating Distortion. Measured and calculated mean flow coefficients at stall inception are shown as a function of screen rotation rate for bactrian compressors C and D, in Figs. 10 and 11, respectively. Both of these two compressors show two peaks in stability margin degradation as a function of distortion rotation rate. The first peak is at 20 percent for compressor B and 30 percent for

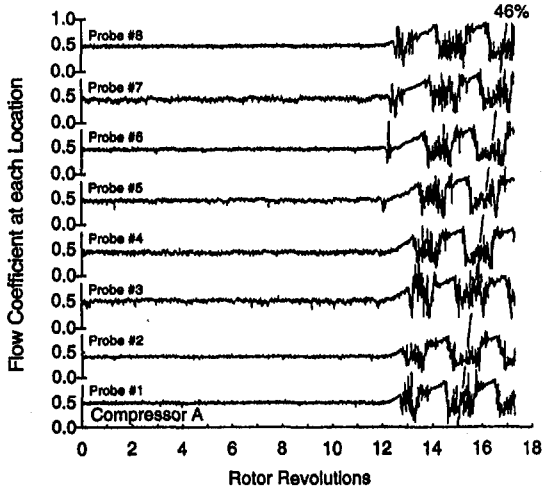


Fig. 5 Inlet hot-wire measurement of axial velocity in front of compressor A during slow throttle closing to stall showing modal-type stall inception process: uniform flow, eight wires equally spaced around the circumference, 30 percent immersion, 0.2 chords upstream of the first rotor

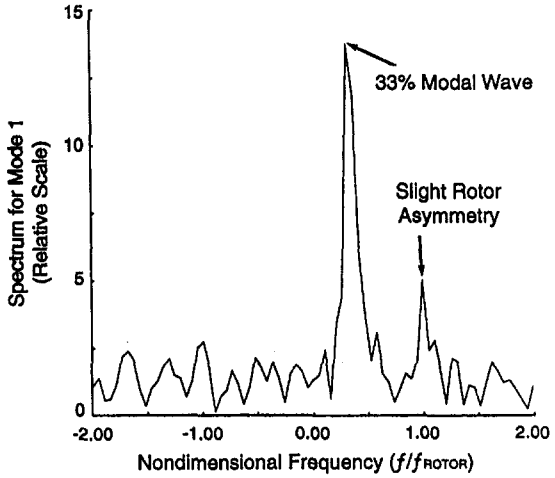


Fig. 6 Temporal spectrum of first spatial harmonic of hot wire measurements for compressor A: slow throttle closing, 20 revolutions prior to stall; uniform flow, instrumentation as in Fig. 5

Downloaded 01 Jun 2010 to 171.66.16.53. Redistribution subject to ASME license or copyright; see http://www.asme.org/terms/Terms_Use.cfm

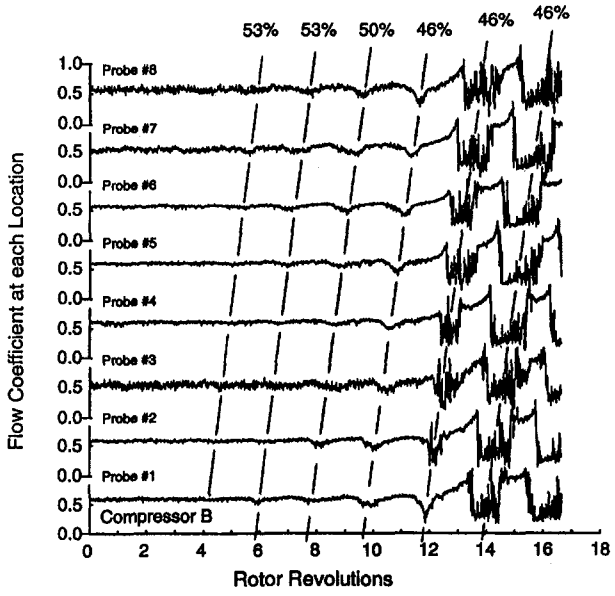


Fig. 7 Inlet hot-wire measurement of axial velocity in front of compressor B during slow throttle closing to stall showing modal-type stall inception process: uniform flow, eight wires equally spaced around the circumference, 30 percent immersion, 0.2 chords upstream of the first rotor

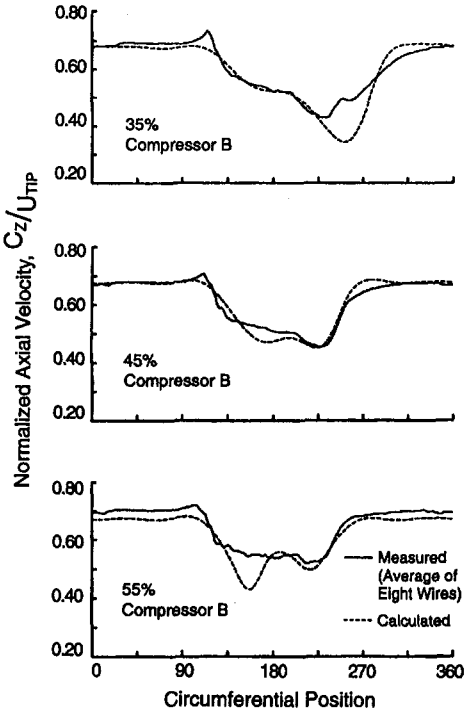


Fig. 9 Comparison of computed and measured axial velocity profiles at IGV inlet for three distortion rotation speeds: Measurements are averages of eight hot wires around the circumference

compressor C. The second peak, which is much narrower, occurs at 72 and 70 percent respectively. The stability computations, on the other hand, yield curves with a single peak, and the maximum loss of stability is calculated to occur in the range of 40–60 percent of rotor speed.

6.2 Natural Stall Inception. As a clue to the forced response behavior, we now describe the natural (unforced) stall inception process for compressor C. This has been determined by Silkowski (1992) as part of a detailed investigation of unsteady flow behavior in multistage compressors. As a representative data set, static pressure measurements recorded at the casing just ahead of the first rotor are reproduced in Fig. 12. The spike-type process of stall inception occurs in this case. The line marked on the figure indicates that the propagation speed of the spike is 70 percent of rotor speed. Within several revolutions around the compressor annulus the local spike evolves into a fully developed, full-span rotating stall that travels at 45 percent of rotor speed. Spatial–temporal analysis of these eight casing pressure signals shows a broad-band response for the first spatial mode at 10 percent of the rotor speed with amplitude $\Delta P/\varrho U_{tip}^2 = 0.6 \times 10^{-3}$. This compressor, therefore, exhibits only a weak modal-wave behavior (in many signals this response could not be detected).

For compressor D limited information is available concerning the stall inception process because the time resolved measurements were recorded 0.7 radii upstream of the IGVs (Plumley, 1990). In the absence of instrumentation placed closer to the compressor face, the presence of spikes cannot be decided. The data of compressor D are useful, however, in showing that the two-peaked behavior in the curve of stall flow coefficient versus

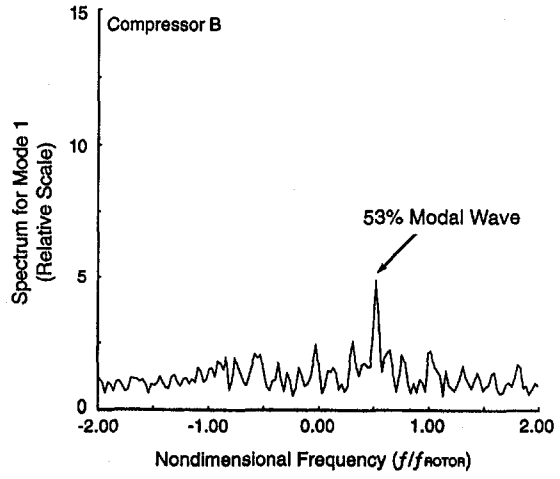


Fig. 8 Temporal spectrum of first spatial harmonic of hot-wire measurements for compressor B: fixed throttle near to stall; uniform flow, instrumentation as in Fig. 7

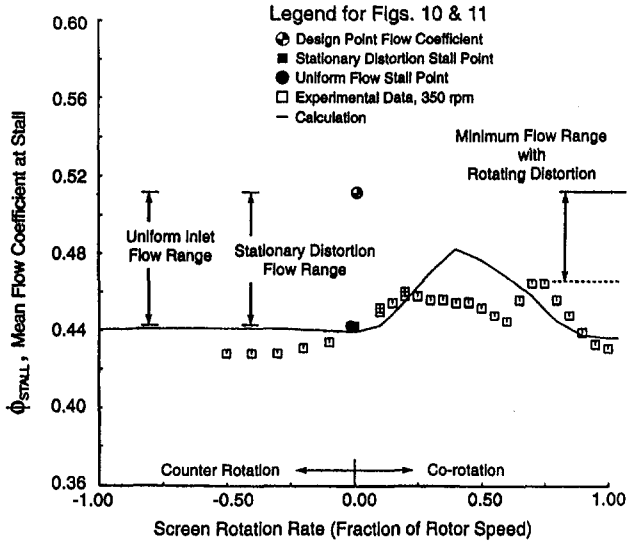


Fig. 10 Flow coefficient at stall versus distortion rotation rate for compressor C; uniform flow stall point and design point are also shown

Downloaded 01 Jun 2010 to 171.66.16.53. Redistribution subject to ASME license or copyright; see http://www.asme.org/terms/Terms_Use.cfm

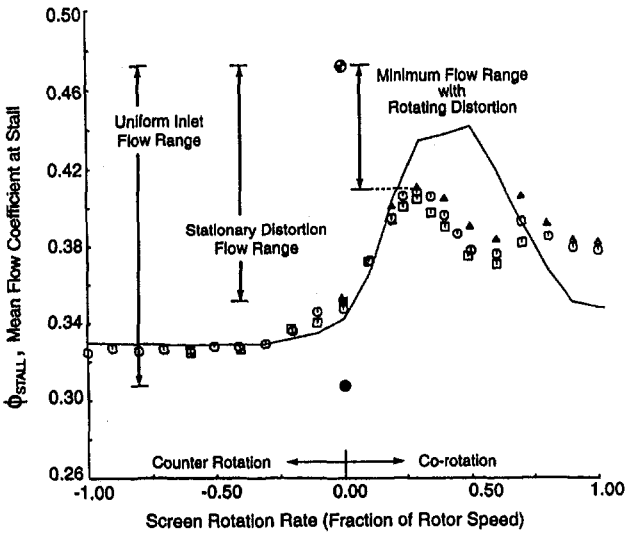


Fig. 11 Flow coefficient at stall versus distortion rotation rate for compressor D; uniform flow stall point and design point are also shown

distortion speed is not simply tied to loading or stage work coefficient. Compressor D was from the same family of designs, and had comparable constant speed line shapes as compressors A and B.

6.3 Summary of the Different Measured and Calculated Propagation Speeds. Table 1 shows a comparison of the mean flow coefficients at design and at stall points and the different disturbance propagation and screen speeds. For the two compressors just described, the first peak does not coincide with either the measured stall cell speed or the modal-wave speed. The speed at which the second peak appears for both compressors matches the measured spike propagation speed for compressor C. This aspect will be discussed further in the next section.

6.4 A Suggestion Concerning the Connection Between Forced Response and the Natural Stall Onset Behaviors. The interpretation of the results for the two single humped (dromedary) compressors seems clear. The disturbances that characterize the unsteady response are predominantly two dimensional, long circumferential length scale. For the compressors that exhibit the two-humped behavior, however, the dynamic response is less well understood. In this and the next sections an attempt is made to provide an interpretation of this behavior that may be useful as a basis for further work.

It is suggested that the two peaks on the degradation of compressor stability margin with screen speed are related to the two types of stall inception processes. The first peak on these curves is associated with the long circumferential length scale, primarily two-dimensional, response of the flowfield. The second peak is associated with short length scale, probably three-dimensional, flowfield response and occurs at a distortion speed corresponding to the spike propagation speed. These results suggest that compressors are susceptible to both types of stall inception; in some cases one type may be dominant, in other cases the other, but there also may be cases in which both types have the capability to cause stall.

6.5 Interpretation of the Second Peak. For both of the bactrian compressors (C and D), the second peak occurs at a screen speed (72 and 70 percent) that is similar to the spike propagation rate. For the dromedary compressors (A and B) there is no measurable second peak and spikes could not be detected prior to stall. It is therefore likely that the occurrence of the second peak is associated with the inlet distortion exciting the creation of a (three-dimensional) spike that then develops into rotating stall. The second peak is relatively narrow and this is consistent with an interaction between two distinct types of flowfield phenomena (i.e., spike and modal-wave). Interaction can only occur over a very narrow range of speeds since any mismatch in speed allows the two phenomena to behave independently.

From another point of view, since the spike is a short-length-scale event, a spike may be expected to behave and propagate according to the local flow environment only. Consider a compressor that exhibits a spike-type stall inception in undistorted flow. When operating with distorted inflow, spikes are likely to be created whenever a sufficiently large portion (a few blade passages) of the flowfield has reached a flow level that is below the uniform-flow stall point. Once created, the spike propagates round the annulus. If it enters a high-flow region, it is likely to be suppressed. For an inlet distortion traveling at the spike propagation speed, the spikes do not leave the local low-flow region until they have grown enough so that their speed has changed. This condition would seem likely to promote the growth of the spike into rotating stall. The consequence of such a sequence of events would be, as seen in the experiments, a degradation of stall margin centered about a rotation speed corresponding to the spike propagation rate. This is no more than a hypothesis at present, but it is one that seems useful to pursue.

6.6 Calculating Bactrian Compressor Stability Margin Degradation. The theoretical model is for long-length-scale two-dimensional flowfield disturbances. Therefore, it is unable to capture the spike phenomena. However, the model does not accurately capture the first hump for the bactrian compressors, which is hypothesized to be a primarily two-dimensional response. A possible explanation is that three-dimensional flow within bactrian compressors affects the speed of the long-length-scale resonance, which appears to be between the modal-wave speed and the fully developed stall cell speed.

7.0 Additional Comments on Compressor Response to Rotating Inlet Distortion

Aside from the insight that the results given above give into the fluid dynamic response of compressor flowfields, there are practical implications of direct interest to the aeroengine designer. For example, in a fan and core compressor combination, the speed of the fan stall cell is, generally speaking, about one half of fan speed and the fan speed itself is about one half of core compressor speed. Consequently for a corotational fan and

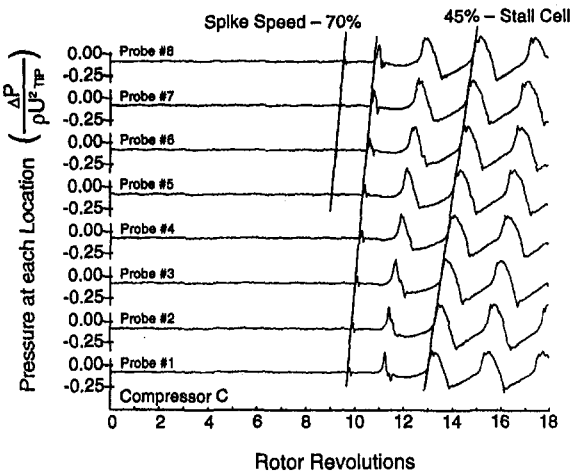


Fig. 12 Wall static pressure measurements during slow throttle closing to stall showing spike type of stall inception process: uniform flow, eight equally spaced pressure transducers, 0.2 chords upstream of the first rotor

Downloaded 01 Jun 2010 to 171.66.16.53. Redistribution subject to ASME license or copyright; see http://www.asme.org/terms/Terms_Use.cfm

core compressor, the speed of the rotating disturbance generated by a fan stall cell would be approximately 25 percent of the core compressor speed. Reference to Figs. 3, 4, 10, and 11 for the four compressors tested in this paper shows that most would suffer a severe stability margin degradation with rotating distortion. However, for counterrotation of the fan and core compressor, all would actually show beneficial results.

Finally, we note that the four compressors can be ranked according to the stability boundary range, measured in terms of flow coefficient, between the most and least favorable screen speeds; see Table 1. Compressor C (bactrian) has the smallest range, while compressors A and B (both dromedary) have the largest. This ranking correlates with the stacking of the pressure rise characteristics given in Fig. 2 and shows the effect of stage pressure rise in determining the unsteady compressor response. It is a topic of current research interest into what aspect of compressor design determines the spike or modal response.

8.0 Conclusions

1 The change in compressor stability margin when a rotating inlet distortion is present depends strongly on the speed at which the flow nonuniformity travels around the annulus. If the distortion speed matches a characteristic speed of the compressor flowfield, a resonant response can result, with the consequence of a severe degradation in stability margin.

2 For multistage compressors that exhibit modal-type stall behavior, the response to inlet distortion appears to be well described by the present theoretical model. The disturbance structure is in accord with the assumptions of the theory, which yields good predictions of the changes in compressor stability margin with distortion rotation speed. Machines of this class have a single peak in the curve of loss in stability margin versus distortion rotation speed.

3 Compressors that exhibit a spike type stall inception process have a second characteristic disturbance speed at which there is a stall margin degradation. The speed corresponds closely with the spike propagation rate. The theory does not describe the phenomena associated with this situation.

4 In the first of these circumstances (i.e., for the conditions corresponding to (2)), the disturbances appear to have wavelengths that are long compared to the blade pitch and to be essentially two dimensional in nature. In the second (conditions corresponding to (3)), the disturbances are much more local, with a length scale that is on the order of one to several blade pitches, and are strongly three dimensional.

5 All the compressors tested would benefit from counterrotation of fan and core compressor as a means of decoupling the nonsteady flowfield interaction between successive compressors.

6 While many of the two-dimensional aspects of stall onset appear to be yielding to theoretical investigation, there is no corresponding description of the three-dimensional aspects. These have been shown to be the observed route to instability in a number of compressors and seem a fruitful area to address.

Acknowledgments

This work has been supported by the Air Force Office of Scientific Research, under grants No. F4960-93-1-0015 and AFOSR-90-0035, Major D. B. Fant, Program Manager. This support is gratefully acknowledged. Support for P. Silkowski and R. Plumley was provided under the Air Force Research in Aero Propulsion Technology (AFRAPT) Program; this assistance is also appreciated. The authors would like to thank General Electric Aircraft Engines Division, especially Dr. L. H. Smith and Mr. C. C. Koch, for support and for permission to publish the results. Finally we are pleased to acknowledge the contributions of Prof. N. A. Cumpsty throughout this work.

References

Chue, R., Hynes, T. P., Greitzer, E. M., Tan, C. S., and Longley, J. P., 1989, "Calculations of Inlet Distortion Induced Compressor Flowfield Instability," *Int. J. Heat Fluid Flow,* Vol. 10, No. 3,

Day, I. J., 1993a, "Stall Inception in Axial Flow Compressors," ASME JOURNAL OF TURBOMACHINERY, Vol. 115, pp. 1–9.

Day, I. J., 1993b, "Active Suppression of Rotating Stall and Surge in Axial Compressors," ASME JOURNAL OF TURBOMACHINERY, Vol. 115, pp. 40–47.

Day, I. J., 1993c, Private communication.

Emmons, H. W., Pearson, C. E., and Grant, H. P., 1955, "Compressor Surge and Stall Propagation," *Transactions of the ASME,* Vol. 77, pp. 455–469.

Garnier, V. H., Epstein, A. H., and Greitzer, E. M., 1991, "Rotating Waves as a Stall Inception Indication in Axial Compressors," ASME JOURNAL OF TURBOMACHINERY, Vol. 113, pp. 290–301.

Gysling, D. L., 1993, "Dynamic Control of Rotating Stall in Axial Flow Compressors Using Aeromechanical Feedback," MIT Gas Turbine Laboratory Report No. 219, Aug.

Haynes, J. M., Hendricks, G. J., and Epstein, A. H., 1994, "Active Stabilization of Rotating Stall in a Three-Stage Axial Compressor," ASME JOURNAL OF TURBOMACHINERY, Vol. 116, pp. 226–239.

Hynes, T. P., and Greitzer, E. M., 1987, "A Method for Assessing Effects of Inlet Flow Distortion on Compressor Stability," ASME JOURNAL OF TURBOMACHINERY, Vol. 109, pp. 371–379.

Kozarev, L. A., and Federov, R. M., 1983, "Aspects of the Appearance and Elimination of Breakdown in an Axial-Flow Compressor in the Presence of a Rotating Non-uniformity at the Inlet," *Izevstiya vuz Aviatsionnaya Tekhnika,* Vol. 26(1), pp. 33–37 (translated).

Longley, J. P., "Measured and Predicted Effects of Inlet Distortion on Axial Compressors," ASME Paper No. 90-GT-214.

Longley, J. P., 1994, "A Review of Nonsteady Flow Models for Compressor Stability," ASME JOURNAL OF TURBOMACHINERY, Vol. 116, pp. 202–215.

Longley, J. P., and Hynes, T. P., 1990, "Stability of Flow Through Multistage Axial Compressors," ASME JOURNAL OF TURBOMACHINERY, Vol. 112, pp. 126–132.

Ludwig, G. R., Nenni, J. P., and Arendt, R. H., 1973, "Investigation of Rotating Stall in Axial Flow Compressors and the Development of a Prototype Stall Control System," Technical Report USAF-APL-TR-73-45.

McDougall, N. M., Cumpsty, N. A., and Hynes, T. P., 1990, "Stall Inception in Axial Compressors," ASME JOURNAL OF TURBOMACHINERY, Vol. 112, pp. 116–125.

Nagano, S., Machida, Y., and Takata, H., 1971, "Dynamic Performance of Stalled Blade Rows," Japan Society of Mechanical Engineering, Paper #11, presented at Tokyo Joint International Gas Turbine Conference, Tokyo, Japan, Oct.

Paduano, J., Epstein, A. H., Valavani, L., Longley, J. P., Greitzer, E. M., and Guenette, G. R., 1993, "Active Control of Rotating Stall in a Low Speed Axial Compressor," ASME JOURNAL OF TURBOMACHINERY, Vol. 115, pp. 48–56.

Plumley, R. E., 1990, "Unsteady Compressor Distortion Response and Compressor Instability," MSc Thesis, Massachusetts Institute of Technology, Feb.

SAE Aerospace Information Report, 1983, AIR 1419 Section 7.2.3.1 and 7.2.3.2, Publisher's Choice Book Mfg. Co., Mars PA 16046.

Silkowski, P. D., 1992, "Unsteady Phenomena and Flow Field Instabilities in Multistage Axial Compressors," internal Gas Turbine Laboratory Report, Massachusetts Institute of Technology, Aug.

Wisler, D. C., 1985, "Loss Reduction in Axial-Flow Compressors Through Low-Speed Model Testing," ASME *Journal of Engineering for Gas Turbines and Power,* Vol. 107, pp. 354–363.

Downloaded 01 Jun 2010 to 171.66.16.53. Redistribution subject to ASME license or copyright; see http://www.asme.org/terms/Terms_Use.cfm

Rotating Stall in a Single-Stage Axial Flow Compressor

C. A. Poensgen

H. E. Gallus

Institut für Strahlantriebe und Turboarbeitsmaschinen, RWTH, Aachen, Federal Republic of Germany

This paper describes the results on an experimental investigation of rotating stall flow inside a single-stage axial flow compressor. Tests were carried out in two steps. First, measurements were taken to investigate the transition process into rotating stall. The compressor starts into rotating stall via the "modal route" with a single rotating stall cell. Further throttling yields to a two-cell shape followed by a significant outlet pressure drop. Both transition processes are discussed in detail. Results from the Moore–Greitzer theory are compared with measured data. In a second step, measurements were taken to determine the three-dimensional unsteady structure of a fully developed rotating-stall cell. Based on unsteady total pressure and three-dimensional hot-wire data, the structure of a rotating stall cell could be resolved in detail upstream and downstream of the rotor. A typical part-span stall was found. By inserting the measured data into the Euler equations, convective and unsteady effects on the pressure fluctuations can be isolated. A dependence between the radial flow inside the stall cell and the unsteady flow accelerations was found.

Introduction

Compressor performance is limited by many factors, e.g., system instabilities, rotating stall, and surge. Although rotating stall was first observed by the group developing centrifugal compressors for the Whittle turbojet in 1938 (see Chesire, 1945), it is yet not fully understood. In the past a rotating-stall cell was assumed to consist of a region of very low or zero throughflow velocity surrounded on both sides by streamlines of unstalled flow (Emmons et al., 1955). Day (1976) took a remarkable step toward a better understanding of a rotating-stall cell by describing the stall cell to be in mass exchange with the surrounding flow.

Within the last 20 years there have been many experimental investigations on stalled compressors (Tanaka and Murata, 1975; Day and Cumpsty, 1978; Breugelmans et al., 1983; Giannissis et al., 1989). The results indicate that the structure of the rotating-stall cell has many different appearances. Rotating stall is classified in part-span and full-span stall. Both types of rotating stall vary over a wide range according to the compressor used for the investigations.

The research groups concentrated their main effort on the detection of stall precursor events. They want to build up an active control system (Day, 1993; Paduano et al., 1991) or a long-term monitoring system to avoid rotating stall (Hönen and Gallus, 1995). Nevertheless, there is a need to understand the basic effects taking place inside a rotating stall cell.

The experimental investigations described in this paper were carried out in a single-stage axial flow research compressor. The compressor shows a typical part-span rotating stall. One purpose of this work is to study the mechanisms leading to rotating stall. Another purpose is the investigation of the detailed structure of a fully developed stall cell. Detailed measurements were taken upstream and downstream of the rotor (see plane 1 to 3 in Fig. 2). With the acquired data it is possible to describe the structure of a part-span rotating stall cell.

Experimental Facility and Techniques of Measurement. Ambient air enters the inlet pipe of the research compressor 9.5 m ahead of the rotor (Fig. 1). A venturi nozzle, which is located 1.5 m upstream of the test section, measures the mass flow. A 500 kW motor with speed control drives the rotor. The tests were performed from 2000 to 6000 rpm. Figure 2 gives additional information on the compressor. The observed effects are similar within the adjusted speeds. Results obtained at 3000 rpm are shown and discussed in this paper. Table 1 shows a summary of the operating points. More data are available on request from the authors.

Single hot-wire, triple hot-wire, and unsteady pneumatic pressure probes were used. An eight-channel transient recorder linked to the processing computer digitized and sampled the data. Accuracy obtained is estimated to be about 2 percent in the unstalled flow and about 5 percent inside a stall cell.

Three problems had to be solved for a successful data acquisition and data evaluation. First it is not possible to operate the compressor for a longer time in the rotating stall regime. To perform a measurement, the compressor had to be driven into rotating stall. The throttle was closed continuously. To acquire one data set took about five seconds. Afterward the compressor was set to unstalled stable flow to avoid blade damage. As a stall-cell signal is not clear enough to serve as a high-quality trigger signal (phase errors of about 10 percent and more) the data were acquired without any trigger. The starting phase angle of a stall-cell signal is therefore arbitrary. A single hot-wire sensor was fixed near the casing at rotor inlet. This sensor gave a reference signal for all measurements taken within this investigation. The second problem is the flow angle variation at the boundaries of a stall cell. It is about three times larger than the range of the calibration of the hot-wire probes used. The flanks of the stall-cell signal are not regular. They have a small variation with time, which causes the third problem. The stall cell interacts with the rotor blades. The interaction between stall cell and rotor blade is large if the number of rotor blades is small. The different relative positions of rotor blades and stall cell cause a variable stall-cell size when a stall cell passes a stationary sensor. All problems could be solved by modifying the ensemble average method. Because of the complexity of this method we do not report it here.

Stall Inception. Figure 3 shows the compressor pressure rise characteristic at 3000 rpm. At the inception point of rotating stall the characteristic is of flat-top type. When passing the compressor stability line, the stalling events can be classified into five different periods. The upper left time trace in Fig. 3 was taken by a triple hot wire, located at 10 percent span down-

Contributed by the International Gas Turbine Institute and presented at the 39th International Gas Turbine and Aeroengine Congress and Exposition, The Hague, The Netherlands, June 13–16, 1994. Manuscript received by the International Gas Turbine Institute February 25, 1994. Paper No. 94-GT-210. Associate Technical Editor: E. M. Greitzer.

Copyright © 1996 by ASME

Downloaded 01 Jun 2010 to 171.66.16.53. Redistribution subject to ASME license or copyright; see http://www.asme.org/terms/Terms_Use.cfm

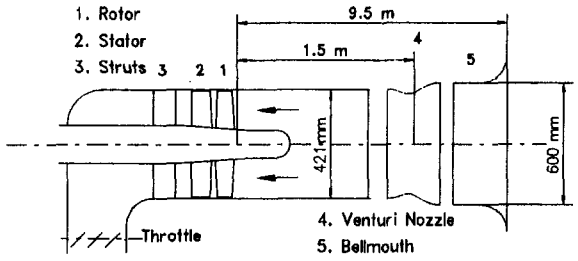
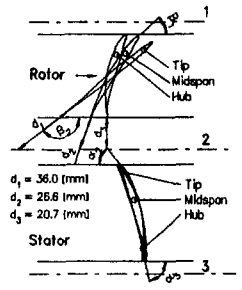


Fig. 1 Test compressor



Outer Diameter	421.8 [mm]
Inner Diameter at Inlet	160.0 [mm]
Inner Diameter at Exit	192.2 [mm]
Profile	NACA - 65
Reaction	ϱ_h = 0.80 at Tip ϱ_h = 0.55 at Hub
Total Pressure Rise	π = 1.11
RPM at Design	n = 9500 1/min
Flow Rate	φ = 0.80
Hub to Tip Ratio at Rotor Exit	ν = 0.37
Number of Rotor Blades	16
Number of Stator Blades	14
Rotor Tip Gap	0.35 [mm]
Stator Tip Gap	0.65 [mm]
Stator Hub Gap	0.55 [mm]

Fig. 2 Cross section through the blading

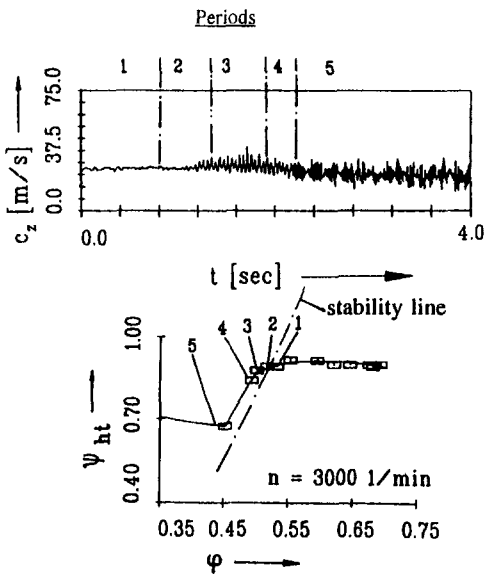


Fig. 3 Inception of rotating stall

Table 1 Operating points and corresponding stall cell configurations

rpm/min	2000	3000	4000	5000	6000
φ stable flow	0.53	0.54	0.54	0.54	0.55
φ	0.46	0.50	0.51	0.51	0.53
numbers of cells	1	1	1	1	1
cell speed [Hz]	16.0	24.1	32.0	40.4	48.5
φ	0.40	0.48	0.49	0.50	0.51
numbers of cells	2	2	2	2	2
cell speed [Hz]	20.0	30.6	41.5	52.2	61.0

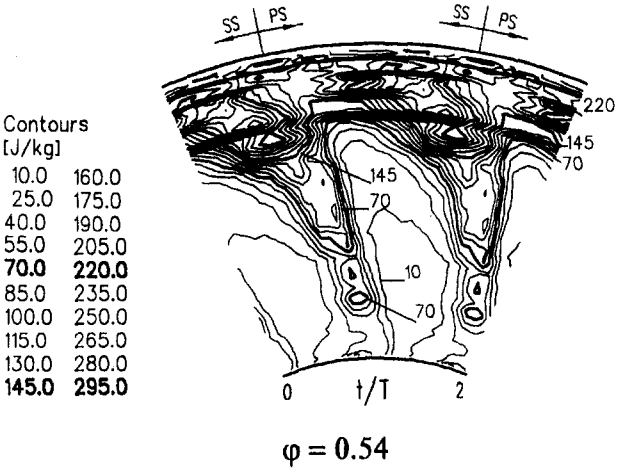


Fig. 4 Turbulent kinetic energy near stall

stream of the rotor. On the right the same signal is shown. The specific events are enlarged.

First the operating point of the highly throttled compressor is stable. The rotor blades are severely stalled at the tip. Close to the hub the flow is attached. For this case Fig. 4 shows the turbulent kinetic energy downstream of the rotor. A tip leakage vortex cannot be seen. At all other operating points with higher flow rate the tip leakage vortex was visible. The contours in Fig. 4 indicate a typical blade stall. Reducing the mass flow rate, the flow becomes unstable (period 2 in Fig. 3). Small periodic waves appear. They are amplified for about 20 revolutions. Finally a stable single-cell rotating stall is established (period 3, $\Psi_{ht} = 0.9$). The single-cell stall collapses when the flow rate φ is equal to 0.51 (period 4). A two-cell rotating stall appears. The pressure ratio is reduced and the compressor operates on its rotating stall characteristic (period 5, $\Psi_{ht} = 0.7$).

To determine the number of stall cells, three hot-wire sensors were placed around circumference. From the measured phase difference of the traveling stall cells, the number of stall cells is evaluated.

Detailed hot-wire measurements upstream and downstream of the rotor were performed to detect the spatial location of the

Nomenclature

c_r = radial velocity
c_φ = circumferential velocity
c_z = axial velocity
p = static pressure
p_t = total pressure
r = radius
t = time
U_m = mean rotor speed at midspan
U_{HW} = hot-wire anemometer output voltage
ρ = density
φ = mass flow rate = c_z/U
Ψ_{ht} = total pressure coefficient = $2\Delta p_t/\rho u^2$
ω = vortex vector
LE = leading edge of the stall cell
TE = trailing edge of the stall cell

Superscript

* = dimensionless value

Downloaded 01 Jun 2010 to 171.66.16.53. Redistribution subject to ASME license or copyright; see http://www.asme.org/terms/Terms_Use.cfm

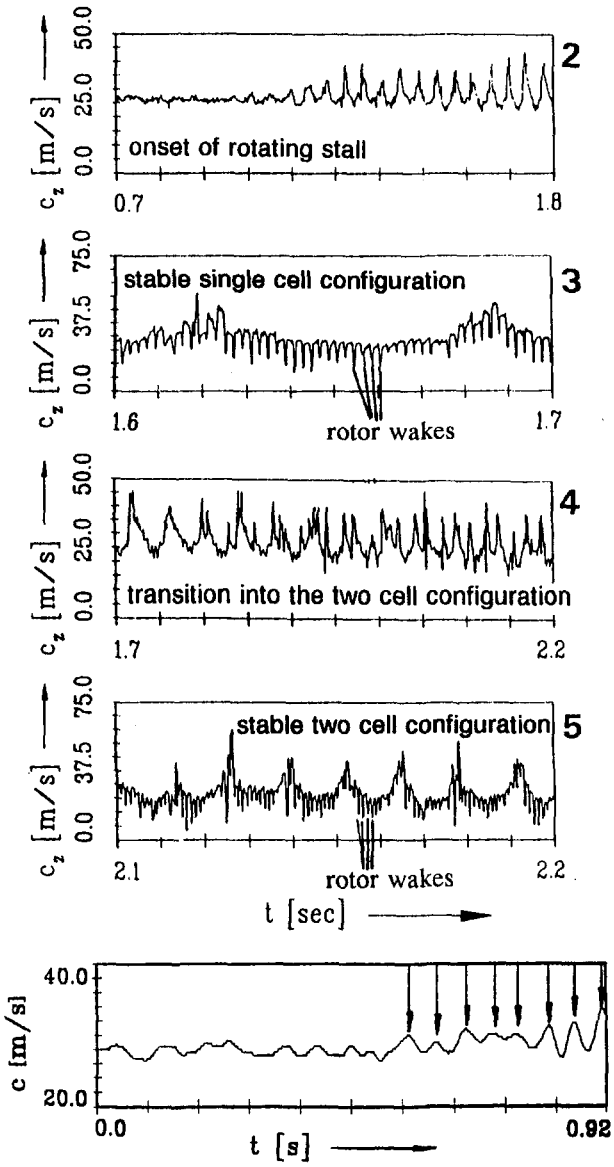


Fig. 5 Filtered time trace of the inception of a single-cell stall (prewave)

stall inception. All sensors recorded simultaneously the onset of the periodic velocity fluctuations (period 2 in Fig. 3). No spatial location of the preferred stall inception was found. A periodic velocity perturbation is observed, as it is predicted by the theory of Moore and Greitzer (1986). When the compressor operates on its stability line, this perturbation grows without any changes in phase and frequency.

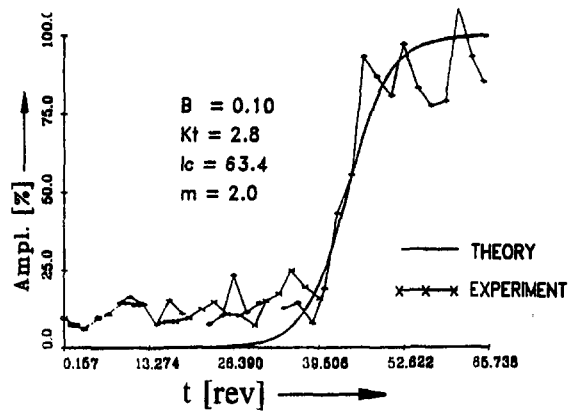


Fig. 6 Stall cell growth, comparison of experiment and theory

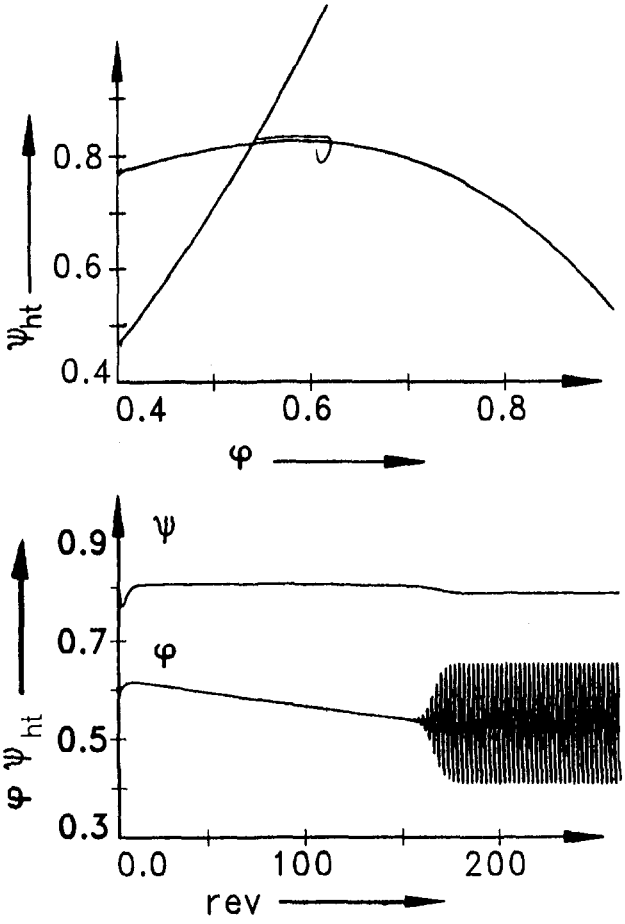


Fig. 7 Prediction of the onset of rotating stall (Moore–Greitzer theory)

The tests of the stall inception have been repeated. It is possible to estimate the process of a stall cell from the measured real-time traces (Fig. 5) (see also Garnier et al., 1991). Figure 6 shows a set of experimental results in comparison with a calculation based on the Moore–Greitzer theory. The nondimensionalized amplitude of a stall cell is plotted versus time. Experiment and theory are in good accordance. Figure 7 displays results from the application of the theory. The onset of stall could be modeled quite well. The calculated stall cell frequency fits the measured frequency within a range of 10 percent. The parameters used for this calculation are listed in Fig. 6. The theory gave results for the one-cell configuration only. It was not possible to obtain reasonable results from the calculation for the two-cell rotating stall configuration.

The single-cell rotating stall is stable in a small range of compressor operation. If the mass flow rate is further decreased, a stable two-cell rotating stall is formed. Figure 8 shows a characteristic time trace of two seconds. The corresponding enlargement is shown in the bottom half of the figure. The dashed pointed box in the upper figure marks the time of transition. At both sides of this box either the single-cell or the two-cell form is stable. At the top of the figure the arrows mark the location of the peaks belonging to a single-cell form. The dashed lines mark the events of the two-cell stall. With time the circumferential size of the single-cell rotating stall is damped. The emerging cell of the two-cell stall is visible as a sharp peak. About two and a half cell rotations later a complementary stall cell appears. The growing process of both cells takes about seven to ten cell revolutions.

Downloaded 01 Jun 2010 to 171.66.16.53. Redistribution subject to ASME license or copyright; see http://www.asme.org/terms/Terms_Use.cfm

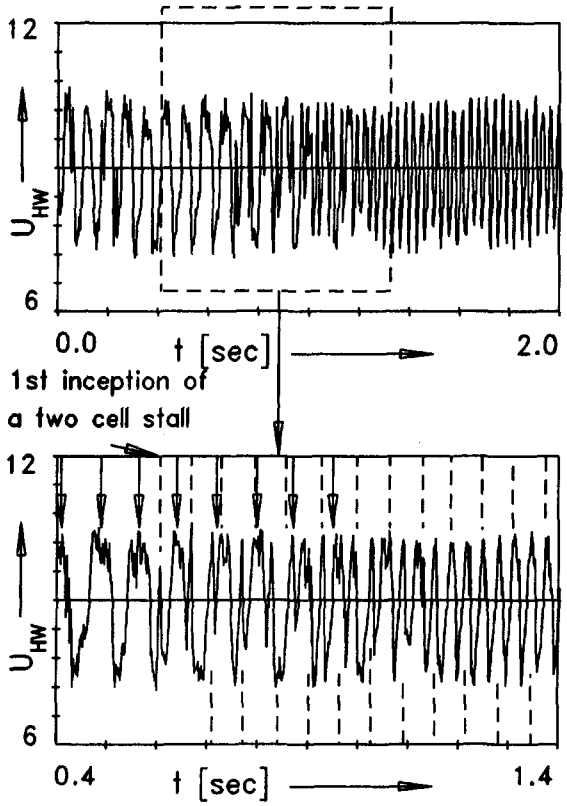


Fig. 8 Inception of the two-cell rotating stall

A stable single-cell rotating stall can only be achieved in a small range of compressor operation. Stall events were recorded at 25 spanwise radial positions. It was not possible to set the operating point with the necessary repeating accuracy for all radial positions. If the stability point of the single-cell rotating stall was not found correctly the stall cells are unstable. We observed by detailed real-time data analysis a phase shift in the single-cell signal. Due to an unknown distortion a two-cell stall is formed and damps the single-cell rotating stall (Fig. 9). The two-cell type is not stable. A new single-cell rotating stall appears. The phase difference between the old and the new single-cell stalls was found to be arbitrary. This procedure takes place within 10 to 30 rotor revolutions. The arrows indicate the position of the peaks of the single-cell stall signals (Fig. 9). They are traced from the left for the old stall cell. For the new stall cell the arrows are traced back from the right where the new stall cell is stable. Above the arrows a cross marks whether

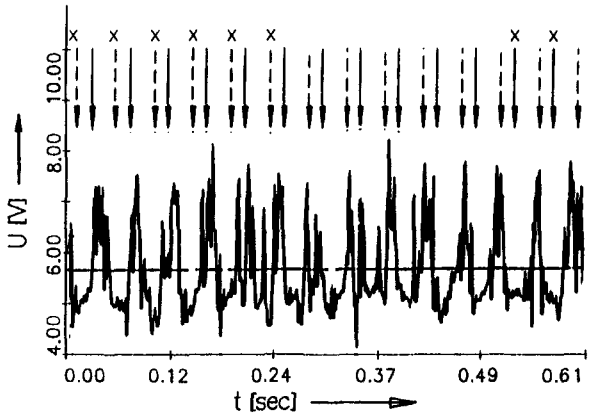


Fig. 9 Phase shift of the one-cell rotating stall

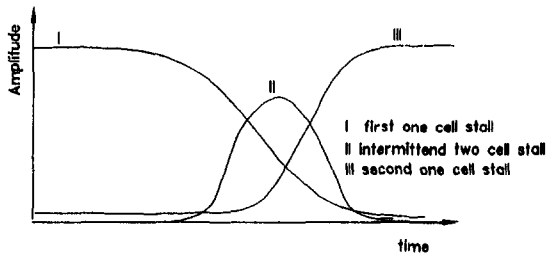


Fig. 10 Simple model of a one-cell/two-cell stall cycle

a cell was found. The position of the arrows relative to each other shows the phase shift. Inside the transition region an intermittent two-cell rotating stall is formed. The data shown here indicate on the left and on the right hand of the time window stable single-cell rotating stall. In the transition region the amplitudes of both single-stall cells were recorded. They coexist for this time. A simple model shown in Fig. 10 illustrates this process.

The time trace in Fig. 9 was selected to demonstrate the phase shift of the single cell shape. The transition zone is quite small and noisy. Nevertheless, the two-cell shape could be stable for a longer term. Then this signal triggers an oscilloscope. Figure 11 shows a series of FFT spectra. The FFT data originate from one single time trace (digitized into 32768 data words). Thus it is possible to calculate 32 instantaneous FFT spectra with a length of 512 frequency points each. This corresponds to 1024 points in the time domain. The lower spectrum displays the corresponding 32-average FFT spectrum. Both frequencies, one-cell and two-cell rotating stall, are detected. The upper

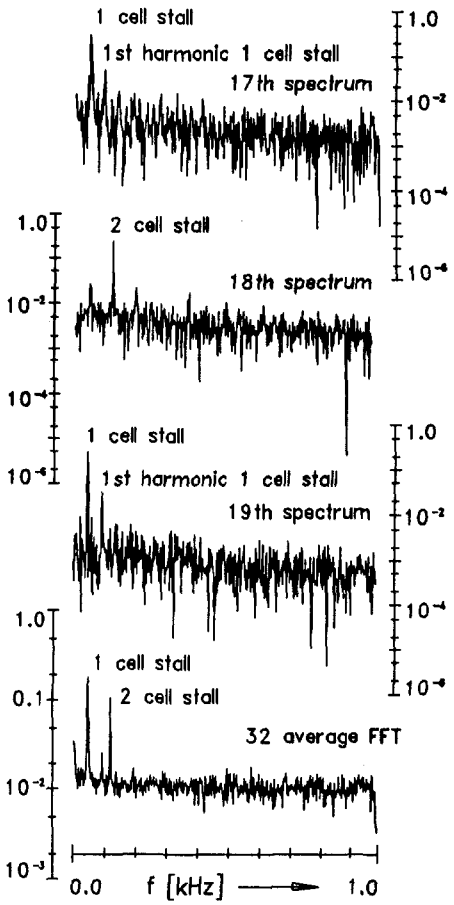


Fig. 11 Fourier spectra of the one-cell/two-cell stall cycle

Downloaded 01 Jun 2010 to 171.66.16.53. Redistribution subject to ASME license or copyright; see http://www.asme.org/terms/Terms_Use.cfm

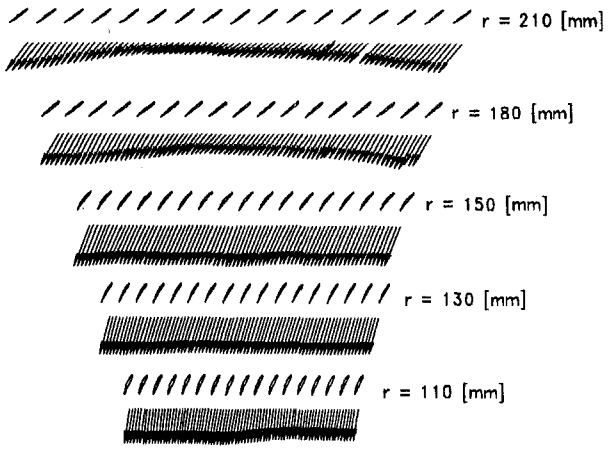


Fig. 12 Relative flow vectors downstream of the rotor (single-cell stall)

spectra are instantaneous FFT spectras. The reason for the presence of both frequencies in the averaged spectrum becomes obvious. The one-cell stall frequency is the dominant frequency in the 17th and 19th spectra. The 18th spectrum indicates the existence of a two-cell rotating stall while the one-cell shape is less pronounced.

Structure of a Stall Cell. To investigate the detailed structure of the different rotating stall patterns, radial measurements were carried out upstream and downstream of the rotor. The relative velocity vectors for both stall cell types are shown at five spanwise locations in Figs. 12 and 13, respectively. The profiles represent the complete blade row. In Fig. 12 the wavy nature of the single-cell stall is clearly visible. The length of the relative velocity vectors is harmonic with circumference at the tip. No flow angle variations take place. At midspan only a minor flow unsteadiness was measured. Near the hub there is a slight increase of the velocity fluctuations. Figure 13 emphasizes the flow inside a two-cell configuration. Inside a stall cell the flow close to the rotor tip is reversed. At the trailing edge of the stall cell the flow recovers. The axial velocity rises but the velocity vectors are overturned. The recovery process is finished when the outlet flow angle reaches design angle. Then the flow decelerates continuously until flow reversal takes place inside the next stall cell. This mechanism can be followed from tip to midspan. At the hub the flow accelerates inside the stall cell. Between two stall cells the velocity becomes very small.

When the rotor operates stably at $\varphi \gtrsim 0.53$ a strong secondary flow vortex exists close to the hub. This vortex rolls up in the corner between rotor blade suction side and rotor hub. Therefore, no corner separation is observed, but strong flow diffusion

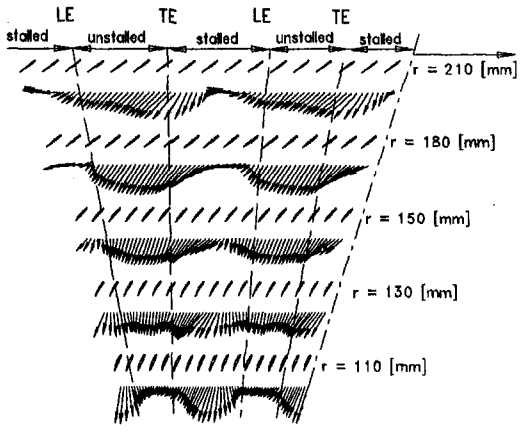


Fig. 13 Relative flow vectors downstream of the rotor (two-cell stall)

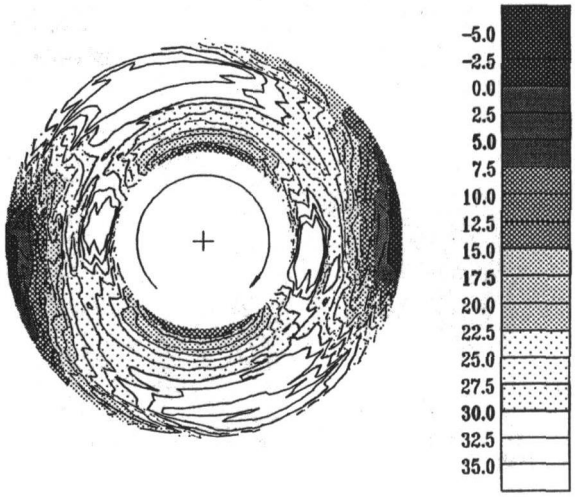


Fig. 14 Axial velocity [m/s] downstream of the rotor (two-cell stall)

takes place (Poensgen, 1991). This effect explains the low throughflow near the hub between two stall events.

Figure 14 shows the axial velocity distribution downstream of the rotor. Shown here is a view from downstream. In the absolute frame of reference the stall cells rotate in a clockwise direction. To give an orientation the circumferential locations are labeled like a compass. Reversed flow occurs near the casing (east and west direction) while the throughflow rate at the hub is larger than design. Figure 15 displays for the same stall cells the distribution of the circumferential velocity. Comparing both figures the shape of the stall cell is different. The axial velocity distribution shows part-span stall, but the circumferential velocity distribution indicates "full-span" stall. The trailing edges of both stall cells are located horizontally (west–east axis). Starting north and following the contours in the rotational sense, the circumferential velocities are increasing. This indicates a large blade loading. Inside the stall cell there is a drop of the circumferential velocity, which signifies the collapse of the profile flow.

Figure 16 summarizes the effects downstream of the rotor. The stall cell leading edge is not a sharp line, as observed in compressors operating at full-span stall. The axial flow in the annulus can be classified as fully reversed, partially reversed, unstalled, accelerated, and re-entered flow. The reversed flow

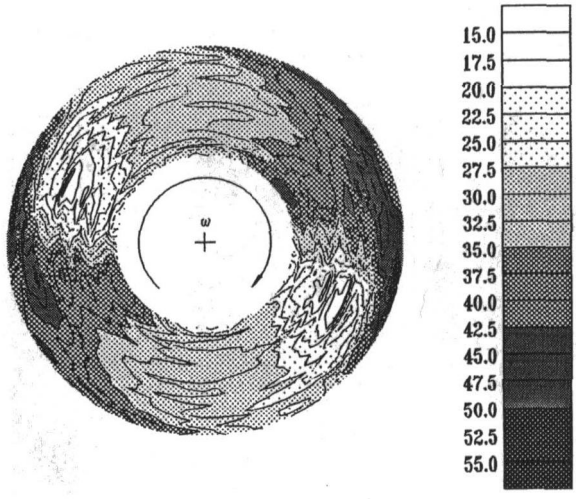


Fig. 15 Circumferential velocity [m/s] downstream of the rotor (two-cell stall)

Downloaded 01 Jun 2010 to 171.66.16.53. Redistribution subject to ASME license or copyright; see http://www.asme.org/terms/Terms_Use.cfm

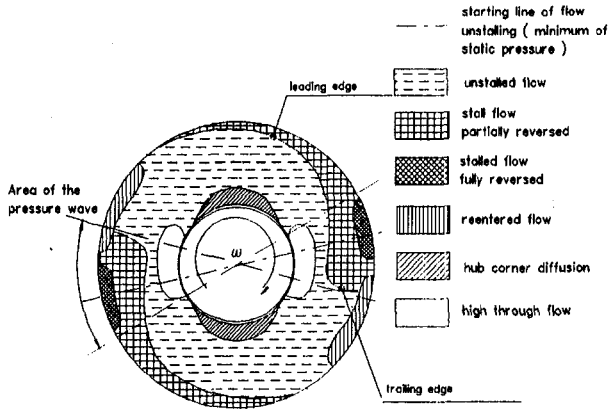


Fig. 16 Sketch of the structure of the two-cell part-span stall downstream of the rotor

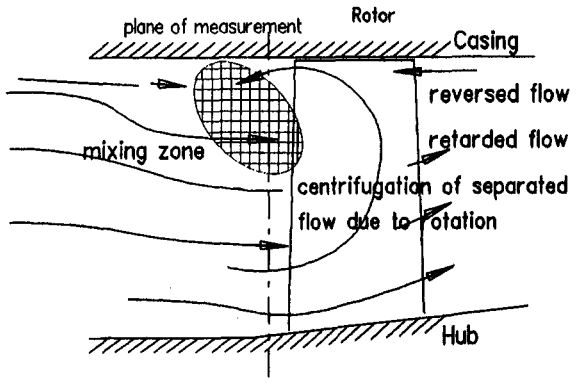


Fig. 18 Meridional flow structure inside the stall cell (view on a rotor blade suction side)

inside the stall cell leaves the rotor at the front. Here the circumferential velocity of the reversed flow is larger than the speed of blade rotation. Therefore, the stalled flow re-enters the blade passage at the stall cell's trailing edge.

Figure 17 illustrates the contours of the total pressure upstream of the rotor in the absolute frame of reference. The areas of reversed flow are located near the casing. Here the absolute circumferential velocity is larger than blade speed. These large circumferential velocities produce high total pressures. Near midspan a total pressure drop is observed. This pressure loss is produced when the reversed axial velocity and the incoming velocity are dissipated to 100 percent near the casing. Figure 18 outlines this process. The area of the mixing process is cut by the plane of probe traversing. Due to the blockage of the reversed flow the incoming flow is forced toward the hub. The low-momentum flow is transported along the radial shifted streamlines into the plane of measurement. Therefore, the measured total pressure drop results from transport of low-momentum fluid. Figure 19 shows the total pressure contours upstream of the rotor in the stall cell frame of reference. Two areas of low total pressure exist inside the stall cell. They are marked by the shadowed areas. Flow reversal takes place in the outer area. The low total pressures near midspan are caused by flow mixing. If the flow upstream of the rotor is assumed to be irrotational, then the total pressure relative to the stall cell is constant. As Fig. 19 indicates, the flow upstream of the rotor

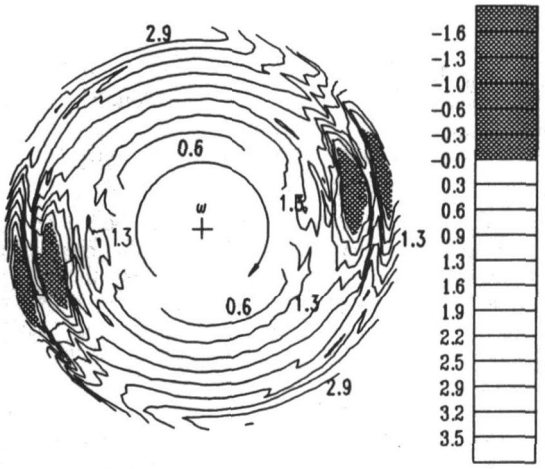


Fig. 19 Unsteady total pressure upstream of the rotor (stall cell frame of reference)

is not irrotational because the plane of measurement is not far enough upstream. It cuts the zone of flow mixing.

Figure 20 shows the circumferential velocities enlarged upstream of the rotor inside the stall cell. The corresponding secondary flow vectors are superimposed. In this case secondary flow is defined to be the deviation from the axial inlet flow. These vectors denote a strong vortex whose vector is normal to the blade suction side. Its center is near midspan. This vortex can be divided into its circumferential and axial components. The influence of its circumferential component is sketched in

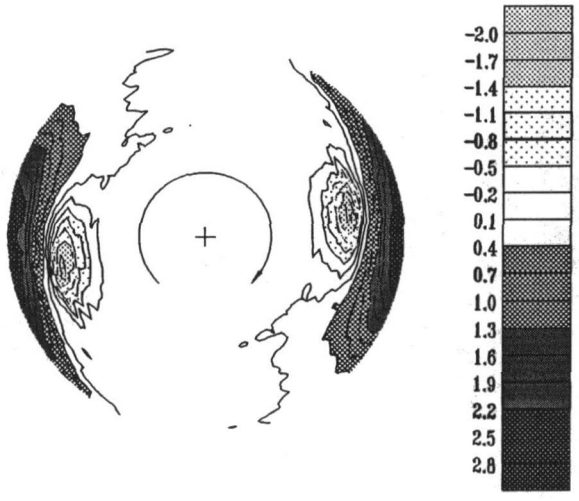


Fig. 17 Unsteady total pressure upstream of the rotor (absolute frame of reference)

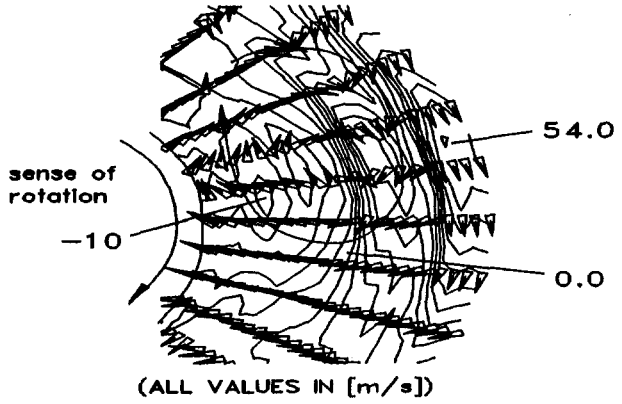


Fig. 20 Circumferential velocities inside the stall cell upstream of the rotor and secondary flow

Downloaded 01 Jun 2010 to 171.66.16.53. Redistribution subject to ASME license or copyright; see http://www.asme.org/terms/Terms_Use.cfm

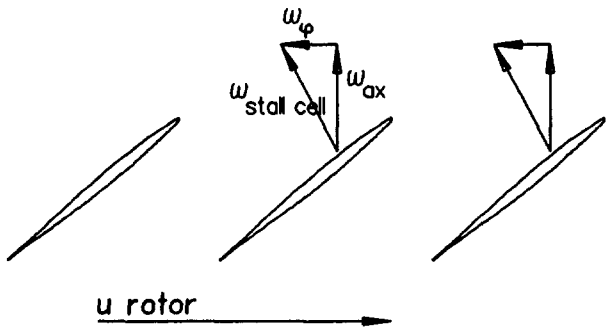


Fig. 21 Rotating stall vortex on the rotor blade suction side

Fig. 21. Inside the rotor blade passage the flow separates. This separated flow is centrifuged and forced to the leading edge by the adverse pressure gradient. The incoming flow is blocked at the casing. It moves farther toward the hub. The influence of the axial component of the vortex vector yields to high circumferential velocities of the reversed flow. Near the hub the flow enters the rotor blade passage with a positive incidence (Fig. 22). Strong radial flow was detected. The radial velocities are within a range from −40 percent to 40 percent of the axial velocity.

Evaluating the unsteady pressure measurements upstream (also downstream) of the rotor, the radial equilibrium is satisfied in the undisturbed regions between the two stall cells. The meridional streamline curvature was neglected in this estimate. Inside a stall cell the simplified radial equilibrium was not fulfilled either downstream or upstream of the rotor. This indicates unsteady flow due to violation of the radial pressure balance.

To get a better understanding of the balancing forces inside the stall cell, the circumferential component of the Euler equation was evaluated:

$$\frac{\partial c_\varphi}{\partial t} + c_r \frac{\partial c_\varphi}{\partial r} + c_\varphi \frac{\partial c_\varphi}{r\partial \psi} + c_z \frac{\partial c_\varphi}{\partial z} + \frac{c_\varphi c_r}{r} = -\frac{\partial p}{\rho r \partial \psi}$$

Except for the axial derivation of the circumferential velocity, all terms can be calculated from the measurements. In a first and rough estimation this term is neglected. Assuming the measured data to be homogeneous with circumference, the unsteady term $\partial c_\varphi/\partial t$ can be calculated because all the other terms are known. The momentum equation is nondimensionalized by the mean radius r and the rotational speed u at midspan. Results of this calculation are shown in Figs. 23 and 24. The contours of the unsteady velocity distribution $(\partial c/\partial t)^*$ and the radial convected momentum $(c_r \partial c_\varphi/\partial r)$ are shown. Both contours are nearly identical. To estimate the influence of these terms, the maximum and minimum values are listed in Table 2. Each term of Eq. (1) fluctuates between these limiting values. According to Table 2, the highest flow accelerations occur due to the term $c_r \partial c_\varphi/\partial r$, which is practically balanced by $\partial c/\partial t$ in front of the rotor. The influence of the circumferential pressure gradient is

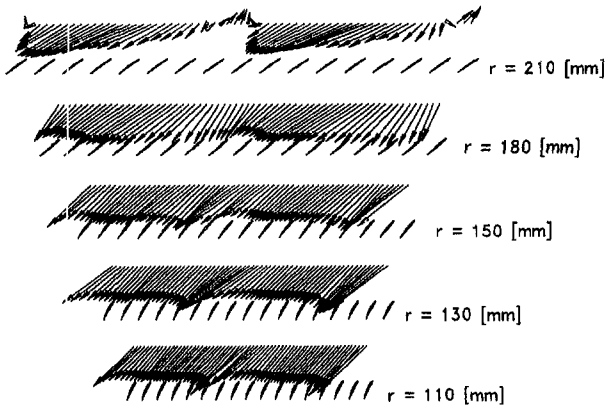


Fig. 22 Relative flow vectors upstream of the rotor (two-cell rotating stall)

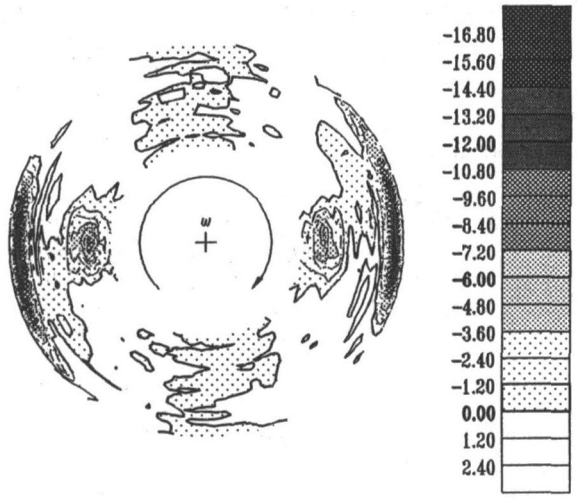


Fig. 23 Flow acceleration $\partial c_\psi/\partial t$

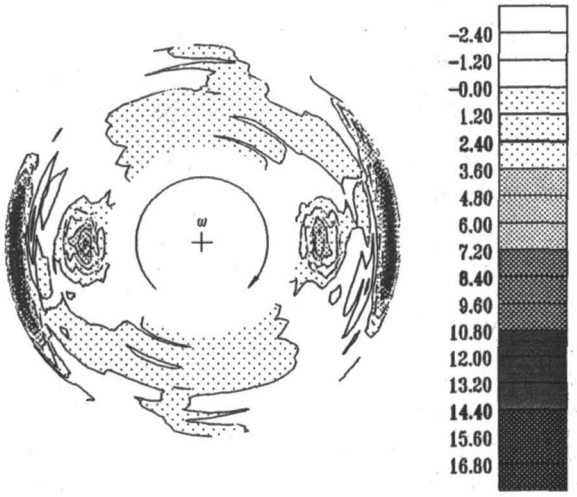


Fig. 24 Flow acceleration $c_r \partial c_\varphi/\partial r$

Table 2 Nondimensional peak values of the terms of Eq. (1)

value	upstream		downstream	
	minimal	maximal	minimal	maximal
$\frac{\partial c_\varphi}{\partial t}$	−16.8	3.6	−2.4	1.2
$c_r \frac{\partial c_\varphi}{\partial r}$	−3.6	16.8	−2.4	1.5
$c_\varphi \frac{\partial c_\varphi}{r \partial \varphi}$	−1.1	1.1	−0.9	1.1
$\frac{c_r c_\varphi}{r}$	−0.24	0.20	−1.8	0.07
$\frac{\partial p}{\rho r \partial \varphi}$	−4.0	2.5	−1.5	1.1

Downloaded 01 Jun 2010 to 171.66.16.53. Redistribution subject to ASME license or copyright; see http://www.asme.org/terms/Terms_Use.cfm

smaller by a factor of four. The convective acceleration in the circumferential direction $c_\varphi \partial c_\varphi / r \partial \varphi$ is about 15 times smaller than the unsteady term. $c_r c_\varphi / r$ can be neglected upstream and downstream of the rotor.

Discussion and Conclusions

- The transition into rotating stall occurs within two steps. The first stall configuration originates from a global perturbation. Further throttling yields to a stable two-cell-stall shape. The two corresponding transients, from undisturbed flow into the single-cell form and the transition into a two-cell rotating stall, are physically different. In the first process the compressor stall comes up via the "modal route" (long length scale disturbance). A global small velocity perturbation is amplified. It forms a stable single-cell-stall configuration. The transition into the two-cell shape follows the short length scale model (Emmons et al., 1955; Day, 1993). Small and sharp stall cells are detected. With time they grow in amplitude and circumferential size. Both types of flow disturbance (small and long-scale disturbances) exist together for a short time.
- As the relative velocity vectors demonstrate in Figs. 12 and 13 the compressor has two different types of stall cell. The single-cell configuration is of periodic wave type. No severe flow reversal is observed. The losses produced by the stall cell are low. The compressor still operates near peak pressure. When the compressor operates in two-cell rotating stall regime, large flow reversal is observed near the rotor tip. At the rotor inlet, the reversed axial velocities reach up to -20 m/s, which is about half the undisturbed inlet velocity. The reversed flow produces a large area of mixing upstream of the rotor generating high mixing losses. This leads to a lower total pressure as measured at the rotor inlet. The compressor operates at its stall characteristic with a lower pressure ratio.
- Real-time analysis of the single-cell stall data showed an intermittent stalling behavior of the compressor. In a period of 10 to 100 rotor revolutions, the single-cell configuration collapses and a two-cell stall is formed. This configuration is not stable and another single-cell stall is generated. All configurations coexist over a short time. But the difference in the phase between both stall cells was found to be arbitrary. It can be concluded that several waves may initially coexist traveling around the annulus. In the compressor investigated only one of them is amplified and yields to a fully developed rotating stall. In some data sets of stall inception this effect was also observed to occur in the prestall wave.
- The highest values of the time-dependent flow acceleration are detected in front of the rotor. The unsteady term of the inviscid circumferential momentum equation is practically balanced by the second term on the left side of Eq. (1). This indicates that the major flow unsteadiness occurs where radial flow is present in combination with a gradient of the circumferential velocity in the radial direction. This effect can also be observed downstream of the rotor. The flow unsteadiness is lower there.
- It was not possible to evaluate the radial component of the inviscid momentum vector. The radial velocity could not be measured with the accuracy needed to form the term $c_r \partial c_r / \partial r$. The magnitude of the radial velocities was found to be very sensitive with the point of compressor operation. The circumferential derivatives of the velocity and the radial gradient of the circumferential velocity are much less sensitive. Only values obtained from the circumferential component of the Euler equation gave useful results.

Acknowledgments

The authors are indebted to Dipl.-Ing. Werner Jahnen and Dipl.-Ing. Andreas Zimmer for their large effort in calculation and the reduction of the measured data. Dipl.-Ing. Ralf E. Walraevens is gratefully acknowledged for his contribution to this paper.

References

Breugelmans, F. A. E., Mathioudakis, K., and Casasalini, F., 1983, "Flow in Rotating Stall Cells of a Low Speed Axial-Flow Compressor," *Proc. ISABE,* Paris, pp. 623–631.

Chesire, L. J., 1945, "The Design and Development of Centrifugal Compressors for Aircraft Gas Turbines," *Proc. IMechE,* Vol. 153.

Day, I. J., 1976, "Axial Compressor Stall," PhD Dissertation, University of Cambridge, Cambridge, United Kingdom.

Day, I. J., and Cumpsty, N. A., 1978, "The Measurement and Interpretation of Flow Within Rotating Stall Cells in Axial Compressors," *J. Mech. Eng. Sci.,* Vol. 20, No. 2.

Day, I. J., 1993, "Active Suppression of Rotating Stall and Surge in Axial Compressors," ASME JOURNAL OF TURBOMACHINERY, Vol. 115, pp. 40–47.

Emmons, H. W., Pearson, C. E., and Grant, H. P., 1955, "Compressor Surge and Stall Propagation," *Trans. ASME,* Vol. 77, p. 455.

Garnier, V. H., Epstein, A. H., and Greitzer, E. M., 1991, "Rotating Waves as a Stall Inception Indication in Axial Compressors," ASME JOURNAL OF TURBOMACHINERY, Vol. 113, pp. 290–302.

Giannissis, G. L., McKenzie, A. B., and Elder, R. L., 1989, "Experimental Investigation of Rotating Stall in a Mismatched Three-Stage Axial Flow Compressor," ASME JOURNAL OF TURBOMACHINERY, Vol. 111, pp. 418–425.

Greitzer, E. M., and Moore, F. K., 1986, "A Theory of Post-Stall Transients in Axial Compression Systems: Part II—Application," ASME *Journal of Engineering for Gas Turbines and Power,* Vol. 108, pp. 231–239.

Hönen, H., and Gallus, H. E., 1995, "Monitoring of Aerodynamic Load and Detection of Stall in Multistage Axial Compressors," ASME JOURNAL OF TURBOMACHINERY, Vol. 117, pp. 81–87.

Moore, F. K., and Greitzer, E. M., 1986, "A Theory of Post-Stall Transients in Axial Compression Systems: Part I—Development of Equations," ASME *Journal of Engineering for Gas Turbines and Power,* Vol. 108, pp. 68–76.

Paduano, J., Epstein, A. H., Valavani, L., Longley, J. P., Greitzer, E. M., and Guenette, G. R., 1991, "Active Control of Rotating Stall in a Low-Speed Axial Compressor," ASME JOURNAL OF TURBOMACHINERY, Vol. 115, pp. 48–56.

Poensgen, C. A., 1991, "Experimentelle Untersuchung der Strömung in einer Unterschall-Axialverdichterstufe bei hoher Drosselung und im Rotating Stall," PhD Dissertation, RWTH Aachen, Federal Republic of Germany.

Tanaka, S., and Murata, S., 1975, "On the Partial Flow Rate Performance of Axial-Flow Compressor and Rotating Stall: 1st Report—Influences of Hub–Tip Ratio and Stators; 2nd Report—Influences of Impeller Load and a Study of Mechanism of Unstable Performances," *Bulletin of the JSME,* Vol. 18, No. 117, Mar.

Downloaded 01 Jun 2010 to 171.66.16.53. Redistribution subject to ASME license or copyright; see http://www.asme.org/terms/Terms_Use.cfm

Numerical Investigation of Stall Flutter

J. A. Ekaterinaris
Navy–NASA Joint Institute of Aeronautics,
NASA Ames Research Center,
Moffett Field, CA 94035

M. F. Platzer
Department of Aeronautics
and Astronautics,
Naval Postgraduate School,
Monterey, CA 93943

Unsteady, separated, high Reynolds number flow over an airfoil undergoing oscillatory motion is investigated numerically. The compressible form of the Reynolds-averaged governing equations is solved using a high-order, upwind biased numerical scheme. The turbulent flow region is computed using a one-equation turbulence model. The computed results show that the key to the accurate prediction of the unsteady loads at stall flutter conditions is the modeling of the transitional flow region at the leading edge. A simplified criterion for the transition onset is used. The transitional flow region is computed with a modified form of the turbulence model. The computed solution, where the transitional flow region is included, shows that the small laminar/transitional separation bubble forming during the pitch-up motion has a decisive effect on the near-wall flow and the development of the unsteady loads. Detailed comparisons of computed fully turbulent and transitional flow solutions with experimental data are presented.

Introduction

The prediction of stall flutter of propellers and turbomachinery blades continues to be an important problem in the design and development of modern propulsion systems. Carta and Lorber [1] recently performed an experimental study of the aerodynamics of incipient torsional stall flutter of propeller blades and found that small-amplitude oscillations near stall may be extremely unstable. Sisto [2] presented a rather comprehensive review of the stall flutter phenomena occurring in axial-flow turbomachines. He noted that no purely analytical method of description has yet evolved and that experimental correlations are used as design criteria, followed by a development phase in which observed deficiencies are corrected.

There exists, therefore, a need to develop "rational" prediction methods so that expensive and time consuming development testing can be minimized. There are broadly two different approaches available to achieve this goal, i.e., viscous–inviscid interaction methods and Navier–Stokes methods. The former method couples inviscid flows with boundary layer flows (Abdel-Rahim et al. [3], Jang et al. [4], Cebeci et al. [5]), whereas the latter relies on the solution of the full viscous flow equations.

In a previous investigation [6], we attempted the analysis of airfoil stall flutter by applying a Navier–Stokes flow solver to the problem of low subsonic flow, $M_\infty = 0.3$, over an oscillating NACA-0012 airfoil in the light stall regime. The flow was assumed to be fully turbulent, and the Baldwin–Lomax [7], the algebraic RNG-based model [8], and the half-equation Johnson–King [9] turbulence models were used. It was found that none of these models was capable of reproducing the hysteresis loops measured by McCroskey [10].

As is well known, modeling of the turbulent flow behavior is an important issue in computational aerodynamics. The flow over an oscillating blade is often massively separated and involves multiple length scales. For the computation of these flows, application of algebraic turbulence models, such as the Cebeci–Smith [11], the Baldwin–Lomax [7], or the Johnson–King [9] model, becomes very complicated and often ambiguous. The source of ambiguity comes from the difficulty in defining characteristic length scales, such as boundary layer thickness. An extensive investigation of the ability of these simple models as well as the recently developed Baldwin–Barth [12] and Spalart–Almaras [13] one-equation models to predict unsteady separated flows has been conducted in [14]. The one-equation models have shown superior behavior compared to algebraic models. Therefore, here the one-equation Baldwin–Barth model, which is "sufficiently" accurate for the present type of application, is used. In addition, this model is numerically robust, computationally efficient, and it does not have strong dependency on ambiguous quantities such as specified model parameters. It can be used for the computation of the entire flowfield, in contrast to the algebraic models, which have to be complemented with a wake model.

Two-equation models, such as the $k-\epsilon$ [15] and the $k-\omega$ [16] models, have been also used to compute steady and unsteady airfoil flows [17]. It appears that the $k-\omega$ model provides some improvements over the one equation models. The $k-\epsilon$ model, on the other hand, does not predict well the adverse pressure gradient separated flow regions. Because the Baldwin–Barth model requires only about half the time compared to the two-equation models, and because the focal point of this paper is to show the effect of transitional region on the development of the unsteady flow field, only this model is used.

Initially, fully turbulent flow over an oscillating blade using the Baldwin–Barth model was computed. The solution showed disappointing disagreement with the measured loads, especially for the downstroke where not even qualitative agreement with the pitching moment and drag coefficients was obtained. Note that similar observations were made [6] where only algebraic and half equation models have been used. The computations of [6] were performed at a slightly larger amplitude of oscillation than the experiment. Larger amplitude of oscillation was also used in [18]. In these investigations the larger oscillation amplitude was employed in order to force the flow to separate enough and to obtain a hysteresis loop. Numerical experiments [17] have also demonstrated that certain turbulence models may reproduce closely enough the lift and pitching moment hysteresis loops when the amplitude of the oscillation is increased. However, the drag hysteresis does not agree with the experiment, and the surface pressure distributions during the downstroke have large deviations from the experimental values.

Experimental [19] and numerical [20] investigations of airfoil flows for a range of Reynolds number from 0.5×10^6 to 1.0×10^6 were recently conducted. It was shown that the effect

Contributed by the International Gas Turbine Institute and presented at the 39th International Gas Turbine and Aeroengine Congress and Exposition, The Hague, The Netherlands, June 13–16, 1994. Manuscript received by the International Gas Turbine Institute February 25, 1994. Paper No. 94-GT-206. Associate Technical Editor: E. M. Greitzer.

Copyright © 1996 by ASME

Downloaded 01 Jun 2010 to 171.66.16.53. Redistribution subject to ASME license or copyright; see http://www.asme.org/terms/Terms_Use.cfm

of the leading edge transitional flow region is of primary importance to the overall development of the suction side viscous flow region. Laminar/transitional separation bubbles form near the airfoil leading edge for angles of incidence as low as 6 deg and significantly alter the suction side pressure distribution and the boundary layer formation. These observations of the low Reynolds number flow behavior stimulated our interest to investigate the effect of transitional flow on dynamic stall at a higher Reynolds number of $\mathrm{Re}_c = 4.0 \times 10^6$.

The main objective of the present investigation, therefore, is to show that it is important to take into account the leading edge transitional flow not only for the lower Reynolds number regime but also for the high Reynolds number in order to predict stall flutter. For the high Reynolds number regime, transition is expected to occur very close to the leading edge after the adverse pressure gradient region is encountered. The extent of the transition region and the separation bubble is also expected to be very small. In practice, turbomachinery flows occur at a low Reynolds number in the range of 0.1×10^6 to 1.0×10^6. Experimental investigations [21] have shown that for these Reynolds numbers transition occurs downstream from the leading edge suction peak sometimes in the vicinity of the midchord or close to the trailing edge depending on the airfoil shape and the Reynolds number. Reliable prediction of the transition location onset for these cases requires more sophisticated analysis, which is still in the development stage, even for steady flows. Modeling of the transitional flow region for these cases presents a difficult problem because the transitional region is large. On the other hand, predictions of the transitional region for complex geometries with Navier–Stokes methods requires enormous computational effort. Application of the recently developed Parabolized Stability Method [22, 23] is more promising for these cases. Therefore, here the high Reynolds number case was chosen to demonstrate the effect of transition on the prediction of stall flutter.

For the numerical implementation, a simplified criterion for the onset of transitional region is used. Furthermore, an effective eddy viscosity for the transitional flow region is obtained from the same turbulence model used for the computation of the turbulent flow region. The computed results for an oscillating airfoil show that modeling of the transitional flow near the leading edge decisively changes the character of the pitching moment hysteresis loop. Whereas the fully turbulent calculations produce only counterclockwise loops, the transitional calculations produce clockwise loops. As is well known from the literature, e.g., Carta [1], single-degree-of-freedom stall flutter in pitch occurs as soon as the area enclosed by the clockwise loop exceeds the area enclosed by the counterclockwise loop. The computation shows that the initial part of the downstroke is in close agreement with the experiment for the lift, pitching moment, and drag hysteresis loops. The prediction of the development of the flow during the remainder of the downstroke still shows substantial deviations from the experiments. These results as well as the basic approach are described in the following sections.

Numerical Implementation

The strong conservation-law form of the thin-layer, compressible Navier–Stokes equations for a curvilinear coordinate system (ξ, η) along the axial and normal direction, respectively, is as follows:

$$\partial_t \hat{\mathbf{Q}} + \partial_\xi \hat{\mathbf{F}} + \partial_\eta \hat{\mathbf{G}} = \mathrm{Re}^{-1}\, \partial_\eta \hat{\mathbf{S}} \tag{1}$$

Here, $\hat{\mathbf{Q}}$ is the conservative variable vector, $\hat{\mathbf{F}}$ and $\hat{\mathbf{G}}$ are the inviscid flux vectors, and $\hat{\mathbf{S}}$ represents the viscous terms in the normal direction. The conservative variable vector $\hat{\mathbf{Q}}$ is

$$\hat{\mathbf{Q}} = \frac{1}{J}\begin{pmatrix} \rho \\ \rho u \\ \rho v \\ e \end{pmatrix}$$

Here $J = 1/(x_\xi y_\eta - x_\eta y_\xi) = \xi_x \eta_y - \xi_y \eta_x$ is the Jacobian of the transformation, and $\hat{\mathbf{F}}$, $\hat{\mathbf{G}}$ are the inviscid fluxes given by

$$\hat{\mathbf{F}} = \frac{1}{J}\begin{pmatrix} \rho U \\ \rho u U + \xi_x p \\ \rho v U + \xi_y p \\ (e + p)U - \xi_t p \end{pmatrix} \quad \hat{\mathbf{G}} = \frac{1}{J}\begin{pmatrix} \rho V \\ \rho u V + \eta_x p \\ \rho V V + \eta_y p \\ (e + p)V - \eta_t p \end{pmatrix}$$

The viscous term, when the thin-layer approximation is applied, and assuming that $\lambda = -2/3\mu$, is given by

$$\hat{\mathbf{S}} = \frac{1}{J}\begin{pmatrix} 0 \\ \mu m_1 u_\eta + (\mu/3) m_2 \eta_x \\ \mu m_1 v_\eta + (\mu/3) m_2 \eta_y \\ \mu m_1 m_3 + (\mu/3) m_2 m_4 \end{pmatrix}$$

Here,

$$m_1 = \eta_x^2 + \eta_y^2$$

$$m_2 = \eta_x u_\eta + \eta_y v_\eta$$

$$m_3 = \frac{\partial}{\partial \eta}(u^2 + v^2)/2 + \kappa\, \mathrm{Pr}^{-1}\left(\frac{\partial a^2}{\partial \eta}\right)$$

$$m_4 = (\eta_x u + \eta_y v)$$

where a is the local speed of sound, κ is the thermal conductivity, Pr is the Prandtl number, and U, V are the contravariant velocity components given by

$$U = u\xi_x + v\xi_y + \xi_t$$

$$V = u\eta_x + v\eta_y + \eta_t$$

In Eq. (1), all geometric dimensions are normalized with the airfoil root-chord length; the density is normalized with the free-stream density ρ_∞; the velocity components are normalized with the free-stream speed of sound, a_∞; the total energy per unit volume is normalized with $\rho_\infty a_\infty^2$; and the pressure is related to density and total energy through the equation of state for an ideal gas, $p = (\gamma - 1)[e - \rho(u^2 + v^2)/2]$.

The numerical integration is performed using an upwind-biased, factorized, iterative, implicit numerical scheme given by

$$\begin{aligned}[I + h_\xi(\nabla_\xi^b \tilde{A}_{i,k}^+ + \Delta_\xi^f \tilde{A}_{i,k}^-)]^p \times [I + h_\eta(\nabla_\eta^b \tilde{B}_{i,k}^+ \\ + \Delta_\eta^f \tilde{B}_{i,k}^- - \mathrm{Re}^{-1}\, \delta_\eta \tilde{M}_{i,k})]^p \times (\tilde{Q}_{i,k}^{p+1} - \tilde{Q}_{i,k}^p) \\ = -[(\tilde{Q}_{i,k}^p - Q_{i,k}^n) + h_\xi(\hat{F}_{i+1/2,k}^p - \hat{F}_{i-1/2,k}^p) \\ + h_\eta(\hat{G}_{i,k+1/2}^p - \hat{G}_{i,k-1/2}^p) \\ - \mathrm{Re}^{-1}\, h_\eta(\hat{S}_{i,k+1/2}^p - \hat{S}_{i,k-1/2}^p)]\end{aligned} \tag{2}$$

In Eq. (2), $h_\xi = \Delta\tau/\Delta\xi$, etc., $\tilde{A}^\pm = (\partial \tilde{F}/\partial \tilde{Q})$, $\tilde{B}^\pm$, $\tilde{\mathrm{M}}$ are flux Jacobian matrices. The quantities $\hat{F}_{i+1/2,k}$, $\hat{G}_{i,k+1/2}$, and $\hat{S}_{i,k+1/2}$ are numerical fluxes.

Time accuracy of the implicit numerical solution is obtained by performing Newton iteration to convergence within each time step. The approximation to $\tilde{Q}^{n+1}$ at each subiteration is the quantity $\tilde{Q}^p$. When $p \geq 2$, during a given subiteration, $\tilde{Q}^p = \tilde{Q}^{n+1}$, but when $p = 1$ and no subiterations are performed, then $\tilde{Q}^p = \tilde{Q}^n$, and $\tilde{Q}^{p+1} = \tilde{Q}^{n+1}$. By subiterating to convergence, linearization and factorization errors are minimized, because the left-hand side of Eq. (2) can be driven to zero at each time step. The inviscid fluxes $\hat{F}$ and $\hat{G}$ are evaluated using Osher's [24, 25] upwinding.

The numerical fluxes for a third-order accurate upwind-biased scheme are given by

Downloaded 01 Jun 2010 to 171.66.16.53. Redistribution subject to ASME license or copyright; see http://www.asme.org/terms/Terms_Use.cfm

$$\hat{F}_{i+1/2,k} = \tilde{F}_{i+1/2,k} + \tfrac{1}{6}[\Delta F^{+}_{i-1/2,k} + 2\Delta F^{+}_{i+1/2,k}] - \tfrac{1}{6}[\Delta F^{-}_{i+3/2,k} + 2\Delta F^{-}_{i+1/2,k}]$$
$$= \tilde{F}(Q_{i,k}, Q_{i+1,k}) + \tfrac{1}{6}[\Delta F^{+}(Q_{i+1,k}, Q_{i,k}) + 2\Delta F^{+}(Q_{i,k}, Q_{i+1,k})] - \tfrac{1}{6}[\Delta F^{-}(Q_{i,k}, Q_{i+1,k}) + 2\Delta F^{-}(Q_{i+1,k}, Q_{i,k})] \quad (3)$$

where $\tilde{F}$ is the first-order accurate numerical flux for Osher's scheme given by

$$\tilde{F}_{i+1/2,k} = \frac{1}{2}\left[F_{i,k} + F_{i+1,k} - \int_{Q_i}^{Q_{i+1}} \{F_q^{+} - F_q^{-}\}\, dQ\right] \quad (4)$$

where $F_q = F_q^{+} + F_q^{-}$, $F_q^{\pm} = (\partial F/\partial Q)^{\pm}$, and $\Delta F^{\pm}$ are the corrections to obtain high-order accuracy. The Osher scheme evaluates the flux assuming a shock tube solution where F_q is piecewise continuous, and yields good predictions of the flux. For the linearization of the left-hand side of Eq. (2), the flux Jacobian matrices $\tilde{A}$, $\tilde{B}$ are evaluated by the Steger–Warming [26] flux-vector splitting.

The viscous fluxes $\hat{S}_{i,k+1/2}$ are computed with central differences as follows:

$$\hat{S}_{i,k+1/2} = S[Q_{i,k+1/2}, (Q_\eta)_{i,k+1/2}, \eta_{i,k+1/2}]$$
$$Q_{i,k+1/2} = \tfrac{1}{2}(Q_{i,k} + Q_{i+1,k})$$
$$(Q_\eta)_{i,k+1/2} = Q_{i,k+1} - Q_{i,k} \quad (5)$$

The accuracy of the present method has been demonstrated before for various steady and unsteady flow problems [17, 27, 28]. Good agreement with experimental surface loads and velocity profiles was obtained. Also the Navier–Stokes solutions [28] were in excellent agreement with viscous–inviscid computations.

Boundary Conditions

On the blade surface the density and pressure are obtained from the interior by simple extrapolation. For unsteady solutions the surface velocity is set equal to the airfoil speed obtained by the prescribed airfoil motion as follows:

$$u = \frac{1}{J}(\eta_t \xi_y - \xi_t \eta_y), \quad v = \frac{1}{J}(\xi_t \eta_x - \eta_t \xi_x) \quad (6)$$

Solutions are computed for subsonic speeds. For subsonic inflow/outflow boundaries the flow variables are evaluated using one-dimensional Riemann invariant extrapolation. At the inflow boundary there are three incoming and one outgoing characteristic. Therefore, three primitive variables, the density ρ, the normal velocity v, and the pressure p, are specified and the fourth variable, the axial velocity u, is extrapolated from the interior. At the outflow boundary there are one incoming and three outgoing characteristics. Therefore, only one quantity, the pressure, is specified, while the others are extrapolated from the interior. For the density and normal velocity, simple first-order extrapolation is used, and the axial out-flow velocity is obtained from the zero-order outgoing Riemann invariant.

Turbulence Model

The Baldwin–Barth [12] model has been derived from the $k-\epsilon$ model equations by introducing some simplifying assumptions. An advantage of this model compared to the algebraic [7, 8, 11] and half-equation models [9] is that it does not require evaluation of ambiguous length scales, and it describes more accurately the physics of the turbulent flow. It requires numerical solution of only one partial differential equation. Therefore, it is less computationally intensive compared to two-equation models. It solves the following partial differential equation:

$$\frac{D(\nu\tilde{R}_T)}{Dt} = (c_{\epsilon_2} f_2 - c_{\epsilon_1})\sqrt{\nu\tilde{R}_T P} + \left(\nu + \frac{\nu_t}{\sigma_\epsilon}\right)\nabla^2(\nu\tilde{R}_T) - \frac{1}{\sigma_\epsilon}(\nabla\nu_t)\cdot\nabla(\nu\tilde{R}_T) \quad (7)$$

This is a partial differential equation for the field quantity $\tilde{R}_T$ or the modified turbulent Reynolds number $\nu\tilde{R}_T$ which is related to the $k-\epsilon$ quantities by $R_T = k^2/\nu\epsilon = \tilde{R}_T f_3(\tilde{R}_T)$. The quantity R_T, named turbulent Reynolds number, is related to the eddy viscosity as

$$\nu_t = \nu c_\mu f_\mu R_T = \nu c_\mu f_\mu f_3 \tilde{R}_T \quad (8)$$

where

$$\frac{1}{\sigma_\epsilon} = (c_{\epsilon_2} - c_{\epsilon_1})\sqrt{c_\mu}/\kappa^2$$
$$\nu_t = c_\mu(\nu\tilde{R}_T) D_1 D_2$$
$$\mu_t = \rho\nu_t$$
$$f_\mu = D_1 D_2$$
$$D_1 = 1 - \exp(-y^+/A^+)$$
$$D_2 = 1 - \exp(-y^+/A_2^+)$$
$$f_3 = D_1 D_2/f_\mu$$
$$P = \nu_t\left(\frac{\partial U_i}{\partial x_j} + \frac{\partial U_j}{\partial x_i}\right)\frac{\partial U_i}{\partial x_j} - \frac{2}{3}\nu_t\left(\frac{\partial U_i}{\partial x_j}\right)$$

$$f_2(y^+) = \frac{c_{\epsilon_1}}{c_{\epsilon_2}} + \left(1 - \frac{c_{\epsilon_1}}{c_{\epsilon_2}}\right)\left(\frac{1}{\kappa y^+} + D_1 D_2\right) \times \left\{\sqrt{D_1 D_2} + \frac{y^+}{\sqrt{D_1 D_2}}\left(\frac{1}{A^+}\exp(-y^+/A^+)D_2 + \frac{1}{A_2^+}\exp(-y^+/A_2^+)D_1\right)\right\}$$

Here $y^+ = u_\tau y/\nu$ and u_τ is the skin friction velocity. The constants used for the Baldwin–Barth model are the same as in the original paper [12] and are given by:

$$\kappa = 0.41, \quad c_{\epsilon_1} = 1.2, \quad c_{\epsilon_2} = 2.0$$
$$c_\mu = 0.09, \quad A^+ = 26., \quad A_2^+ = 10.$$

For the fully turbulent flow case the model is applied to the entire flow field, including the wake to compute the eddy viscosity.

The transitional flow behavior is modeled as follows. The transition onset is specified downstream from the maximum pressure gradient location on both the suction and the pressure sides. The flow in the region between the lower and upper transition onset points is computed as laminar. An effective eddy viscosity in the transitional region is computed from Eq. (7) by imposing zero production at the transition onset as boundary value.

The computed eddy viscosity for the transitional flow region starts from a zero value and increases gradually and smoothly to the fully turbulent value as shown in Fig. 1. The values of the effective eddy viscosity in the vicinity of the transitional flow region are shown in Fig. 1(*a*). In Fig. 1(*b*) two eddy viscosity profiles, one in the transitional flow region and another one in the fully turbulent flow region, are shown.

Results and Discussion

A solution was first obtained for a NACA-0012 airfoil, which executes a harmonic motion $\alpha(t) = 9$ deg + 5 deg sin (ωt) around the quarter chord pivot point with a reduced frequency $k = 2\pi fc/2U_\infty = 0.1$, at a free-stream compressible flow $M_\infty =$

Downloaded 01 Jun 2010 to 171.66.16.53. Redistribution subject to ASME license or copyright; see http://www.asme.org/terms/Terms_Use.cfm

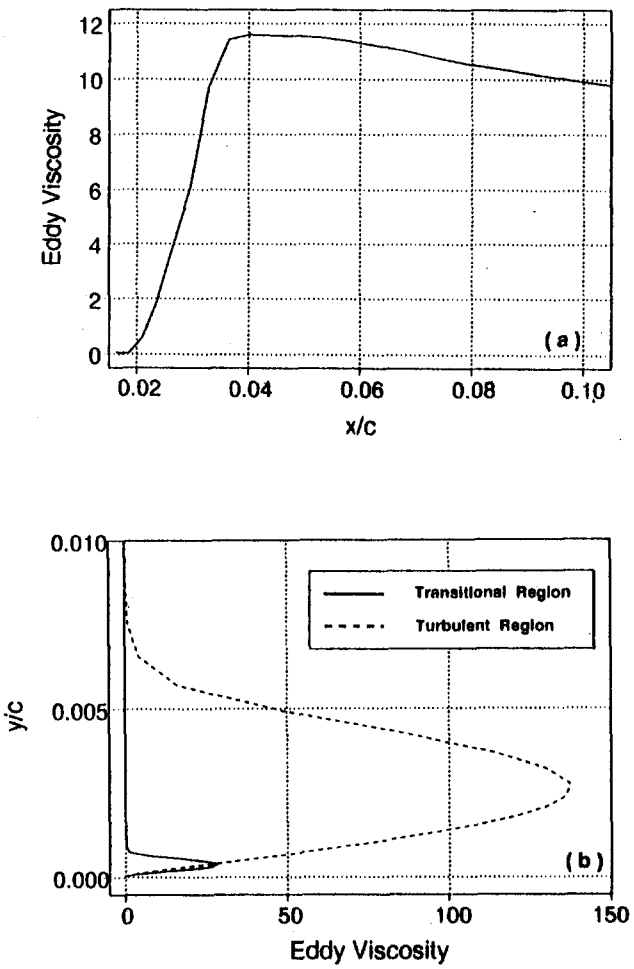


Fig. 1 Computed eddy viscosity along the axial and normal directions

0.3 and a Reynolds number $Re_c = 4.0 \times 10^6$. Detailed experimental measurements in the form of integrated aerodynamic loads (C_l, C_d, C_m) and unsteady surface pressure coefficients have been obtained for this flow condition [10]. A 311 × 91 point grid was used for the computation. The first grid point away from the surface was located at a distance $dy = 0.00001c$. This grid spacing yields a y^+ value of approximately two, which is adequate to capture the high Reynolds number turbulent flow behavior. The entire oscillatory cycle was computed in 20,000 time steps, which corresponds to a nondimensional time step $\Delta t \approx 0.005$ and a CFL ≈ 650, even though numerical stability could be obtained for $\Delta t = 0.01$. Two oscillatory cycles only were computed because the third cycle coincided with the second. The CPU time required on a Cray YMP was about one hour for one oscillation cycle.

The fully turbulent flow solution is compared with the measured unsteady loads in Fig. 2. Fair agreement with the experiment is obtained for the pitch-up part of the oscillation. However, almost no hysteresis loop is obtained for the downstroke. Also, the computed drag and pitching moment coefficients disagree with the experiment. In particular, the pitching moment hysteresis loop is counterclockwise, whereas the experimental loop shows the "figure eight" loop behavior indicative of single-degree-of-freedom flutter.

The laminar/transitional/turbulent flow solution is compared with the experiment in Fig. 3. It is seen that the lift hysteresis loop shows good qualitative agreement. There is some overprediction of the lift drop during part of the downstroke. Similar trends are shown for the drag and pitching moment. It appears that the computed solution predicts a more rapid reattachment of the flow. The source of this disagreement will be pointed out in the next paragraph where the computed surface pressure coefficients are compared with the experiment. However, there is good agreement with the measured nose-down pitching moment and drag increase caused by the massively separated flow during the initial part of the downstroke. It is significant that the extreme values of the drag and pitching moment are closely predicted.

The surface pressure coefficient distributions at three angles of attack during the upstroke $\alpha = 13.0$ deg, $\alpha = 13.5$ deg, and $\alpha = 14.0$ deg obtained from the fully turbulent and the transitional computations are compared with the measured values [10] in Fig. 4. As expected, both computed solutions are in good agreement with the measured values because all the computed integrated loads are in agreement with the experiment during the upstroke. Note, however, that the fully turbulent solution at the peak of the cycle $\alpha = 14.0$ deg already overpredicts the suction peak. The computed solution for the downstroke at the angles $\alpha = 13.0$ deg, $\alpha = 12.0$ deg, and $\alpha = 11.0$ deg are compared with the experiment in Fig. 5. At $\alpha = 13.0$ deg (Fig. 5(*a*)) the solution with transition is in good agreement with the experiment for the region near the leading edge. The secondary suction peak, indicating the trace of the dynamic stall vortex,

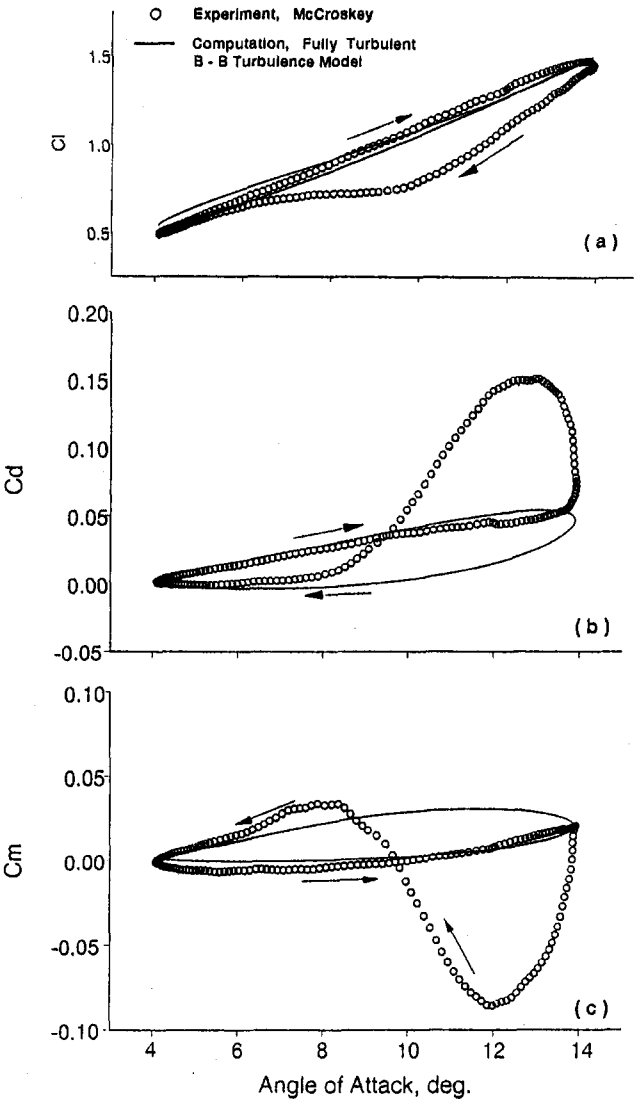


Fig. 2 Comparison of the computed and measured lift, drag and pitching moment coefficients: $\alpha(t) = 9$ deg + 5 sin (ωt), for the NACA-0012 airfoil; experiment [10]; M = 0.3, $k = 0.1$, Re = 4×10^6 (fully turbulent)

Downloaded 01 Jun 2010 to 171.66.16.53. Redistribution subject to ASME license or copyright; see http://www.asme.org/terms/Terms_Use.cfm

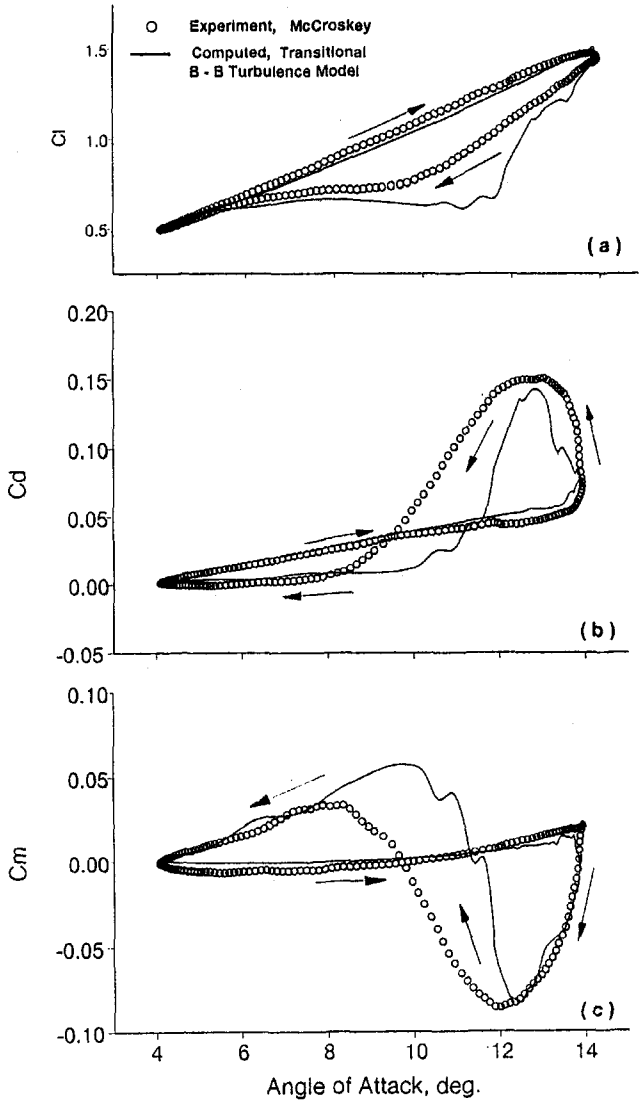


Fig. 3 Comparison of the computed and measured lift, drag and pitching moment coefficients: $\alpha(t) = 9$ deg + 5 sin (ωt), for the NACA-0012 airfoil; experiment [10]; M = 0.3, $k = 0.1$, Re = 4×10^6 (transitional)

lags the one shown by the experiment. The fully turbulent solution, on the other hand, does not show any significant separation or vortex formation and the computed suction peak considerably overshoots the experimental value. Visualization of the computed velocity fields shows that only trailing edge separation was obtained for the fully turbulent computation. In contrast, the transitional solution properly captures the physical mechanism observed in the experiment and shows development of a leading edge, vortical, dynamic-stall-like structure as the computed surface pressure coefficient during downstroke demonstrates. At lower angles of incidence $\alpha = 12$ deg and $\alpha = 11$ deg during the down-stroke (Figs. 5(b, c)) the fully turbulent solution does not predict any significant separation. The transitional solution is again in good agreement with the experiment near the leading edge region, but the lag obtained in the vortex formation causes discrepancies with the measured values.

In turbomachinery applications lower oscillation amplitudes are of interest. Therefore, one of the few low amplitude cases measured [10] was investigated next. It involves a Sikorsky SC-1095 airfoil oscillating around the quarter chord point about a mean angle of 14 deg and an amplitude of 2 deg. The reduced frequency is $k = 0.198$, the free-stream Mach number is $M_\infty = 0.3$ and the Reynolds number $Re_c = 3.85 \times 10^6$. The increase of the mean angle causes stall to occur prior to the reversal of the motion. In addition, changes of the airfoil section and reduced frequency produce a leading edge dynamic stall vortex prior to the maximum angle of attack. Figure 6 shows the lift, drag, and pitching moment hysteresis loops obtained from a fully turbulent and a transitional solution. Again the agreement between the predicted and measured values is seen to be excellent for most of the upstroke for both solutions. However, the fully turbulent flow solution delays the development of the leading edge dynamic stall vortex. As a result very substantial discrepancies ensue over the remainder of the cycle. The transitional solution, on the other hand, is again seen to capture the main physics of the unsteady flow. Note that incorporation of transition is essential to obtain drag rise and pitching moment decrease at the correct phase during the upstroke. Visualization of the computed solutions during the downstroke showed that along with the dynamic stall vortex, a trailing edge vortex appears. This trailing edge vortex is responsible for the oscillatory behavior of the computed loads observed in both solutions.

It was found that the transitional solution is sensitive to the suction side transition location. Here the transition onset is specified based on the computed extremum of the pressure gradient.

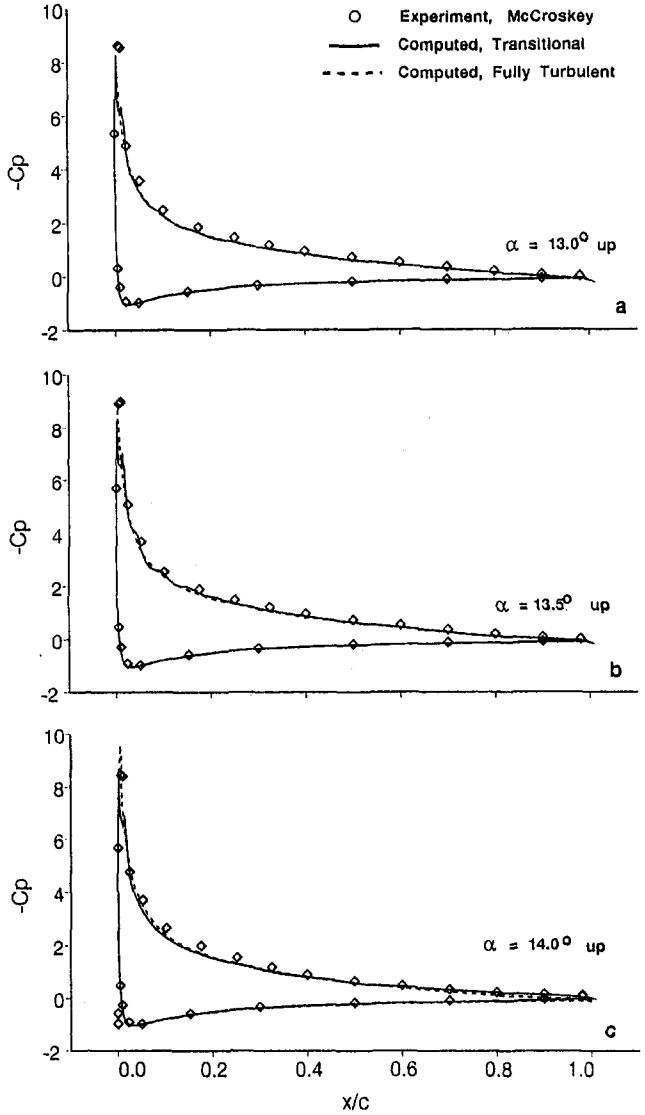


Fig. 4 Comparison of the turbulent and transitional computed surface pressure coefficients during upstroke, $\alpha = 13.0$ deg and $\alpha = 13.5$ deg: $\alpha(t) = 9$ deg + 5 sin (ωt), for the NACA-0012 airfoil; experiment [10]; M = 0.3, $k = 0.1$, Re = 4×10^6

Downloaded 01 Jun 2010 to 171.66.16.53. Redistribution subject to ASME license or copyright; see http://www.asme.org/terms/Terms_Use.cfm

Accurate prediction of the transition location for unsteady adverse pressure gradient flow is difficult. Empirical criteria [29] developed for steady low Reynolds number flows at small adverse pressure gradient have been applied but they predicted transition very close to stagnation. For the present experiment, unsteadiness, free-stream turbulence, and other disturbances, as well as significant compressibility at the leading edge region make the problem of determining the transition onset very difficult. It appears that the well-known e^N method, appropriate for flight conditions, would not be accurate here due to free-stream turbulence and significant wall effects. The main objective of our work is to demonstrate that inclusion of transition is the key to the successful prediction of stall flutter and dynamic stall at high Reynolds numbers. While the need for the inclusion of transition modeling in the lower Reynolds number range is beginning to be appreciated more and more, the fact that transition is also important at the high Reynolds number range, as our results demonstrate, is more surprising.

Conclusions

Unsteady high Reynolds number flow over an oscillating blade at stall flutter conditions has been computed. It was found that the leading edge transitional flow is of primary importance to the overall development of the unsteady flow field. Laminar/transitional leading-edge separation bubbles developing during the pitch-up motion produce a dynamic-stall-like vortical structure. During the downstroke, this vortical structure is convected downstream and causes massive separation manifested by significant hysteresis effects, which are not obtained in a fully turbulent situation. A critical issue for accurate computations is the reliable prediction of the transition onset. For high Reynolds number flow, the transitional region is small and it appears that computation with an effective eddy viscosity obtained from a turbulence model does not significantly degrade the accuracy of the solution. Further work is needed to develop reliable criteria for transition onset under unsteady adverse pressure gradient conditions.

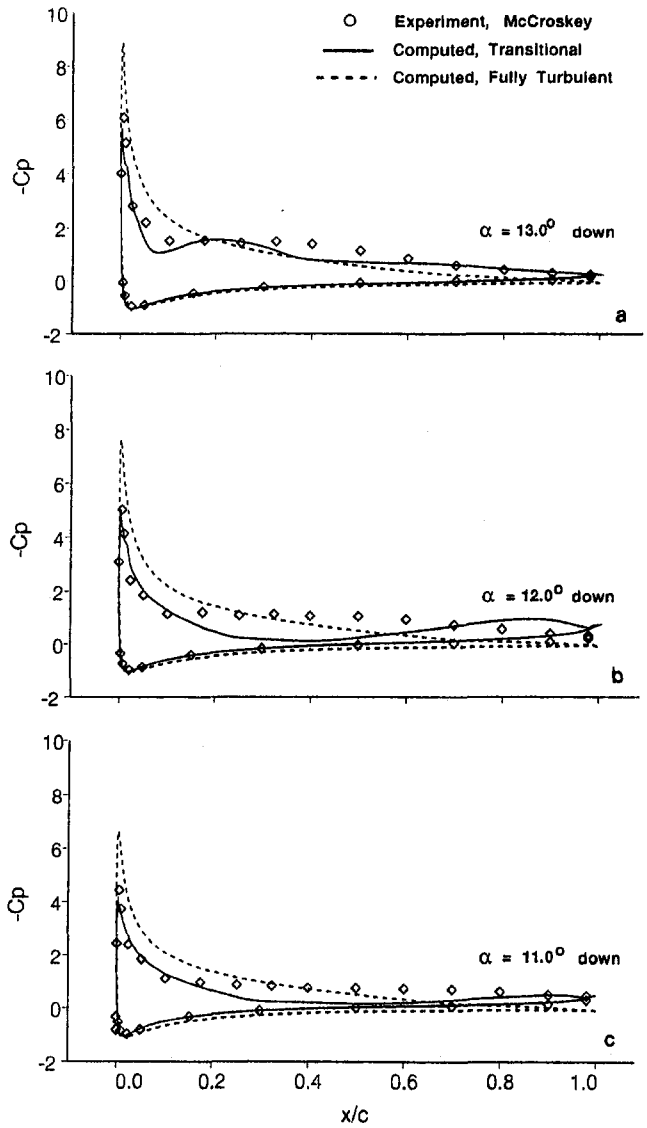


Fig. 5 Comparison of the turbulent and transitional computed surface pressure coefficients during downstroke, α = 13.0 deg, 12.0 deg, and α = 11.0 deg: $\alpha(t)$ = 9 deg + 5 sin (ωt), for the NACA-0012 airfoil; experiment [10]; M = 0.3, k = 0.1, Re = 4 × 10^6

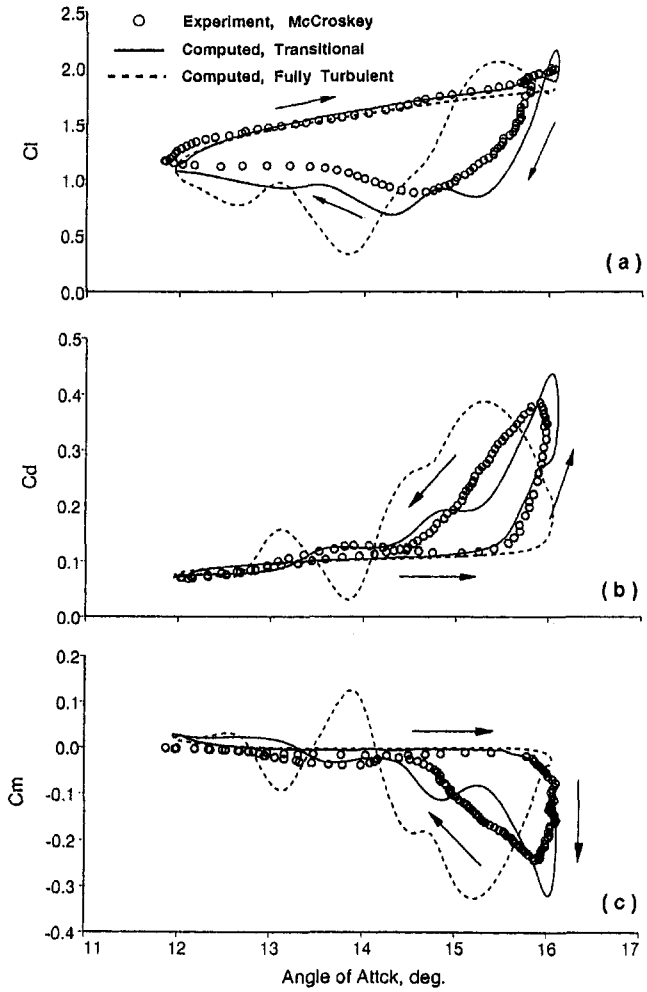


Fig. 6 Comparison of the computed and measured drag and pitching moment coefficients for the SC-1095 airfoil: $\alpha(t)$ = 14 deg + 2 sin (ωt), experiment [10]; M = 0.3, k = 0.2, Re = 4 × 10^6

Acknowledgments

This investigation was supported by the Naval Warfare Center, Weapons Division, China Lake CA, and the Naval Postgraduate School Internal Research Program.

References

1 Carta, F. O., and Lorber, P. F., "Experimental Study of the Aerodynamics of Incipient Tortional Stall Flutter," *Journal of Propulsion,* Vol. 3, No. 2, 1987, pp. 164–170.

2 Sisto, F., "Stall Flutter," *AGARD Manual on Aeroelasticity in Axial-Flow Turbomachines,* Vol. 1, AGARD-AG-298, Mar. 1987, Chap. 7.

Downloaded 01 Jun 2010 to 171.66.16.53. Redistribution subject to ASME license or copyright; see http://www.asme.org/terms/Terms_Use.cfm

3 Abdel-Rahim, A., Sisto, F., and Thangam, S., "Computational Study of Stall Flutter in Linear Cascades," ASME JOURNAL OF TURBOMACHINERY, Vol. 115, 1993, pp. 157–166.

4 Jang, H. M., Ekaterinaris, J. A., Platzer, M. F., and Cebeci, T., "Essential Ingredients for the Computation of Steady and Unsteady Boundary Layers," ASME JOURNAL OF TURBOMACHINERY, Vol. 113, 1991, pp. 608–616.

5 Cebeci, T., Platzer, M. F., Jang, H. M., and Chen, H. H., "An Inviscid–Viscous Interaction Approach to the Calculation of Dynamic Stall Initiation on Airfoils," ASME JOURNAL OF TURBOMACHINERY, Vol. 115, 1993, pp. 714–723.

6 Clarkson, J. D., Ekaterinaris, J. A., and Platzer, M. F., "Computational Investigation of Airfoil Stall Flutter," *Unsteady Aerodynamics, Aeroacoustics and Aeroelasticity of Turbomachines and Propellers,* H. M. Atassi, ed., Springer-Verlag, New York, 1993, pp. 415–432.

7 Baldwin, B. S., and Lomax, H., "Thin Layer Approximation and Algebraic Model for Separated Turbulent Flows," AIAA Paper No. 78-257, Jan. 1978.

8 Yakhot, V., and Orzag, S. A., "Renormalization Group Analysis of Turbulence. 1—Basic Theory," *Journal of Scientific Computing,* Vol. 1, 1986.

9 Johnson, D. A., and King, L. S., "A Mathematically Simple Turbulence Closure Model for Attached and Separated Turbulent Boundary Layers," *AIAA Journal,* Vol. 23, 1985, pp. 1684–1692.

10 McCroskey, W. J., "The Phenomenon of Dynamic Stall," NASA TM-81264, Mar. 1981.

11 Cebeci, T., and Smith, A. M., *Analysis of Turbulent Boundary Layers,* Academic Press, New York, 1974.

12 Baldwin, B. S., and Barth, T. J., "A One-Equation Turbulence Transport Model for High Reynolds Number Wall-Bounded Flows," NASA TM 102847, 1990.

13 Spalart, P. R., and Allmaras, S. R., "A One-Equation Turbulence Model for Aerodynamic Flows," AIAA Paper No. 92-0439, Jan. 1992.

14 Srinivasan, G. R., Ekaterinaris, J. A., and McCroskey, W. J., "Dynamic Stall of an Oscillating Wing, Part 1: Evaluation of Turbulence Models," AIAA Paper No. 93-3403, Aug. 1993.

15 Jones, W. P., and Launder, B. E., "The Calculation of Low-Reynolds-Number-Phenomena With a Two-Equation Model of Turbulence," *International Journal of Heat and Mass Transfer,* Vol. 16, 1973, pp. 1119–1130.

16 Wilcox, D. C., "Reassessment of the Scale-Determining Equation for Advanced Turbulence Models," *AIAA Journal,* Vol. 26, 1988, pp. 1299–1310.

17 Ekaterinaris, J. A., and Menter, F. R., "Computation of Separated and Unsteady Flows with One and Two Equation Turbulence Models," AIAA Paper No. 94-0190, Jan. 1994.

18 Dindar, M., and Kaynak, U., "Effect of Turbulence Modeling on Dynamic Stall of a NACA-0012 Airfoil," AIAA Paper No. 92-0027, Jan. 1992.

19 Wilder, M. C., Chandrasekhara, M. S., and Carr, L. W., "Transition Effects on Compressible Dynamic Stall of Transiently Pitching Airfoils," AIAA Paper No. 93-2978, July 1993.

20 Ekaterinaris, J. A., Chandrasekhara, M. S., and Platzer, M. F., "Analysis of Low Reynolds Number Airfoils," AIAA Paper No. 94-0534, Jan. 1994.

21 Hoheisel, H., "A Comparison of Laser Doppler Anemometry and Probe Measurements Within the Boundary Layer of an Airfoil in Subsonic Flow," *Proc. Laser-Doppler Anemometry in Fluid Mechanics,* Second International Symposium on Applications of Laser Anemometry to Fluid Mechanics, Lisbon, Portugal, July 1984, pp. 143–157.

22 Herbert, Th., "Boundary Layer Transition Analysis and Prediction Revisited," AIAA Paper No. 91-0737, Jan. 1991.

23 Bertolotti, F. P., "Compressible Boundary Layer Stability Analyzed With the PSE Equations," AIAA Paper No. 91-1637, June 1991.

24 Osher, S., and Solomon, F., "Upwind Difference Schemes for Hyperbolic Systems of Conservation Laws," *Mathematics of Computation,* Vol. 38, No. 158, 1982, pp. 339–374.

25 Osher, S., and Chakravarthy, S. R., "Upwind Schemes and Boundary Conditions With Applications to Euler Equations in General Geometries," *Journal of Computational Physics,* Vol. 50, 1983, pp. 447–481.

26 Steger, J. L., and Warming, R. F., "Flux Vector Splitting of the Inviscid Gas Dynamic Equations With Applications to Finite-Difference Methods," *Journal of Computational Physics,* Vol. 40, 1981, pp. 263–293.

27 Ekaterinaris, J. A., Cricelli, A. S., and Platzer, M. F., "A Zonal Method for Unsteady, Viscous, Compressible Airfoil Flows," *Journal of Fluids and Structures,* Vol. 8, Jan. 1994.

28 Tuncer, I., Ekaterinaris, J. A., and Platzer, M. F., "A Viscous-Inviscid Interaction Method for 2-D Unsteady, Compressible Flows," AIAA Paper No. 93-3019, Jul. 1993.

29 Chen, K. K., and Thyson, N. A., "Extension of Emmons' Spot Theory to Flows of Blunt Bodies," *AIAA Journal,* Vol. 9, 1971, pp. 821–825.

Downloaded 01 Jun 2010 to 171.66.16.53. Redistribution subject to ASME license or copyright; see http://www.asme.org/terms/Terms_Use.cfm

Off-Design Transition and Separation Behavior of a CDA Cascade

W. Steinert

H. Starken

Institut für Antriebstechnik,
DLR,
Köln, Federal Republic of Germany

The design of modern axial flow compressor blade sections as well as the code validation require experimental information about the transition and separation behavior of blade surface boundary layers. The experience has shown in the past that such information has to be obtained on the whole surface and not only by point measurements because both transition and separation may be of a three-dimensional nature even in a straight cascade. Therefore, a new visualization technique based on Liquid Crystals (LC), showing the adiabatic wall temperature, has been developed. With this method, transition, local separation, and complete separation can be detected. Design and off-design data of a subsonic (M_1 = 0.62) Controlled Diffusion Airfoil (CDA) compressor cascade measured in a wind tunnel are presented. The LC results are supplemented by ink-injection tests and overall performance data.

Introduction

In 1989 a subsonic CDA compressor cascade was tested extensively in the DLR transonic cascade wind tunnel. The cascade was designed by the company MAN GHH and is representative of the rotor hub section of an industrial axial flow compressor. The cascade design as well as the measurements were presented at the IGTI conference in 1990 (Steinert et al., 1991). The design data for the blade section were as follows:

$$M_1 = 0.62 \quad M_2 = 0.45 \quad \beta_s = 120.0 \text{ deg}$$

$$\beta_1 = 137 \text{ deg} \quad \beta_2 = 110.6 \text{ deg}$$

$$t/c = 0.68 \quad \Omega = 1.1$$

The definitions of these data are presented in Fig. 1. In order to get experimental information about the transition and separation behavior of blade surface boundary layers, flow visualization was performed. Besides ink-injection tests, a new Liquid Crystal measurement technique was applied (Starken and Steinert, 1992).

Liquid crystal coatings have been used in the past to detect transition by making use of the different heat transfer rates of laminar and turbulent boundary layers (Holmes and Obara, 1987; Mee et al., 1991). In the present work, however, compressor blade sections were thermally insulated by a plastic film or made completely out of carbon fiber composite and then covered by liquid crystals. By accurate adjustment of the upstream total temperature within the color band of the liquid crystals, a near-adiabatic wall temperature could be visualized. Whereas with the heat transfer method only transition and, of course, cooled or heated blade surfaces can be visualized, the present method does provide additional information about the flow properties along the blade surfaces.

Test Arrangement

Seven blades with 70 mm chord length were installed in the test section of the cascade wind tunnel. The fourth blade had 10 pressure taps on the suction side and the sixth blade had 10 taps on the pressure side. The intermediate blade was the thermally insulated one covered with liquid crystals. The test procedure and the conventional measuring technique are described by Steinert et al. (1991). Also the profile coordinates are published there. Ahead of and behind the cascade, several holes were provided in one side wall (Fig. 1) to enter borescopes, which were equipped with video cameras. With this instrumentation, the dynamic behavior of the color play of the liquid crystals as well as the flow path of ink, released through blade surface pressure taps at midspan, could be recorded.

The LC coating used was the "Licritherm general purpose coating" (TCS) of BDH Limited. The standard type TCS 1006 has a color range from 29 to 35°C with a temperature response curve as shown in Fig. 2. The curve shows that the highest sensitivity exists at the low-temperature side with red to yellow and green colors providing a temperature resolution of about 1.0°C. The transparent coating has to be sprayed on black surfaces, which were established by black paint. A comprehensive description of thermochromic liquid crystals is available from BDH Limited (Sage and Archer, 1989).

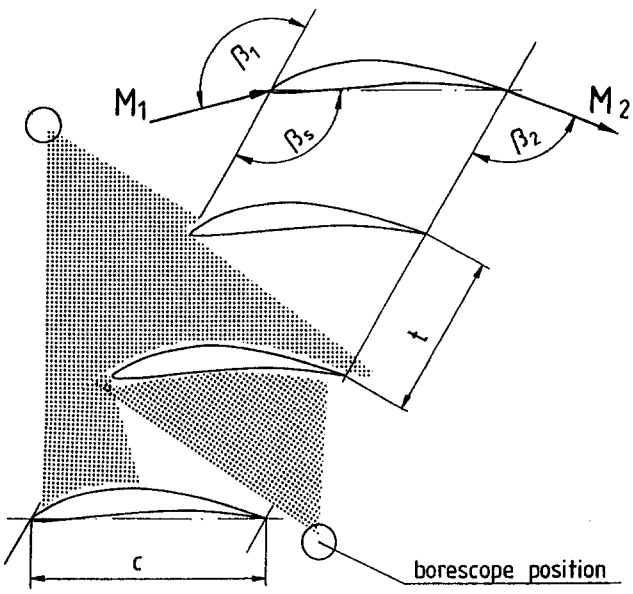


Fig. 1 Borescope position in cascade side wall and definition of cascade inlet and exit flow

Contributed by the International Gas Turbine Institute and presented at the 39th International Gas Turbine and Aeroengine Congress and Exposition, The Hague, The Netherlands, June 13–16, 1994. Manuscript received by the International Gas Turbine Institute February 26, 1994. Paper No. 94-GT-214. Associate Technical Editor: E. M. Greitzer.

Copyright © 1996 by ASME

Downloaded 01 Jun 2010 to 171.66.16.53. Redistribution subject to ASME license or copyright; see http://www.asme.org/terms/Terms_Use.cfm

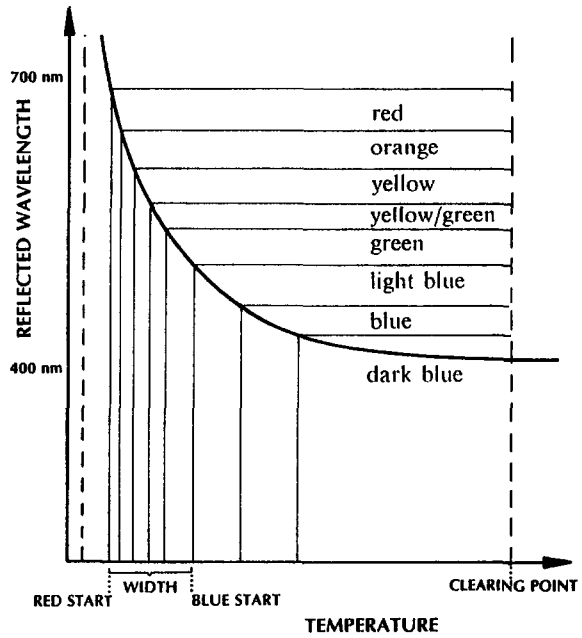


Fig. 2 Typical pitch versus temperature response curve of a thermochromic liquid crystal mixture

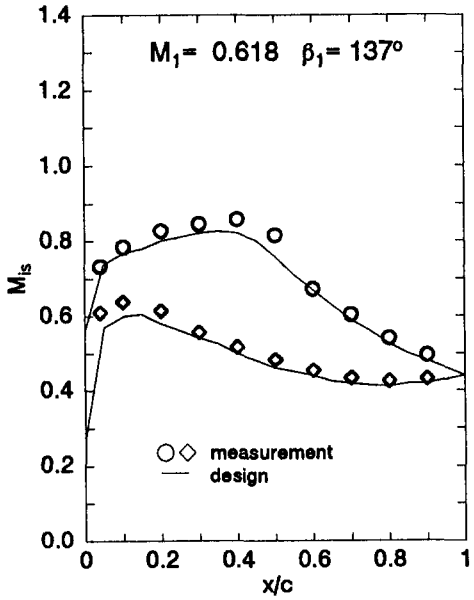


Fig. 3 Design and measured surface Mach numbers

Application of the LC Technique

The application of the LC measuring technique is described for the design point with an inlet Mach number of 0.62. Figure 3 shows the calculated design and measured surface Mach number distribution. Along the suction surface the flow is accelerated until 40 percent of chord and then decelerated to an exit Mach number of 0.45. Therefore, laminar boundary layer conditions can be expected in the front and turbulent ones in the rear part, probably with a laminar separation bubble in between.

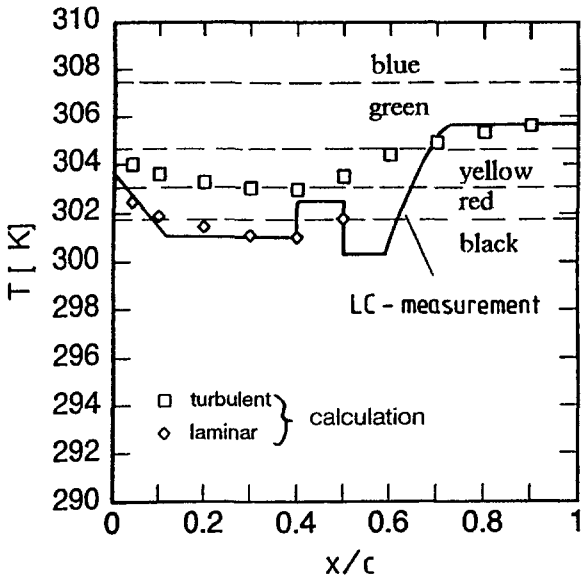


Fig. 4 Calculated and measured adiabatic wall temperature

The corresponding adiabatic wall temperature levels calculated from the measured surface velocities are shown in Fig. 4. Between laminar and turbulent boundary layers about 2°C difference of wall temperature exists, which should be detectable by the liquid crystals used in the tests. The experimental results verified this as shown in Fig. 20. Near black, that means cold areas, are visible in the laminar front part of the blades and green, which means warm areas, are visible in the turbulent rear part. Additionally clear yellow turbulent wedges, starting at the leading edges can be observed.

These are caused by surface roughnesses due to the LC coating or by dust particles of the incoming flow. During the tests new wedges appeared and also disappeared sometimes. Between the wedges, a yellow band, that means higher temperatures, can be observed between 40 and 50 percent of chord. Additional tests by releasing ink out of the pressure taps showed that the yellow band corresponds to a laminar separation bubble. A local separation bubble is therefore characterized by a wall temperature higher than in the laminar boundary layer region. The following cold region between about 50 to 60 percent of chord is probably caused by longitudinal "Görtler vortices." This assumption is mainly based upon the streaky temperature structure in this region, which was especially clear at negative incidences (see also Fig. 21). Only due to this cold "transitional vortex region," it is possible to see also the end of the separation bubble. In Fig. 4, the approximate development of the surface

Nomenclature

AVDR, Ω = axial velocity density ratio between inlet and outlet of cascade
c = blade chord
M = Mach number
M_{is} = isentropic Mach number = $f(p/p_{t1})$
p = static pressure
p_t = total pressure
t/c = pitch-to-chord ratio
T = adiabatic wall temperature
x = coordinate in chordwise direction
β = flow angle with reference to circumferential direction
β_s = stagger angle with reference to circumferential direction
Θ = flow turning = $\beta_1 - \beta_2$
η = coordinate in circumferential direction
ω = total pressure loss coefficient = $(p_{t1} - p_{t2})/(p_{t1} - p_1)$

Subscripts

1 = inlet plane
2 = outlet plane

Downloaded 01 Jun 2010 to 171.66.16.53. Redistribution subject to ASME license or copyright; see http://www.asme.org/terms/Terms_Use.cfm

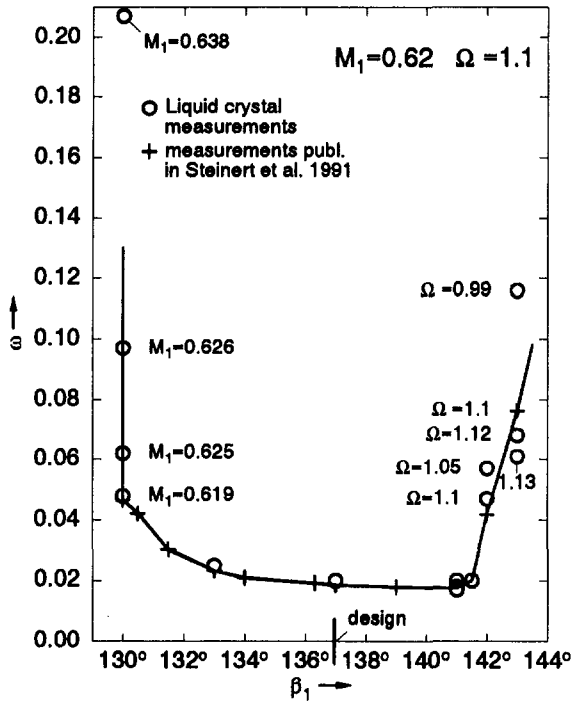


Fig. 5 Loss development with inlet flow angle

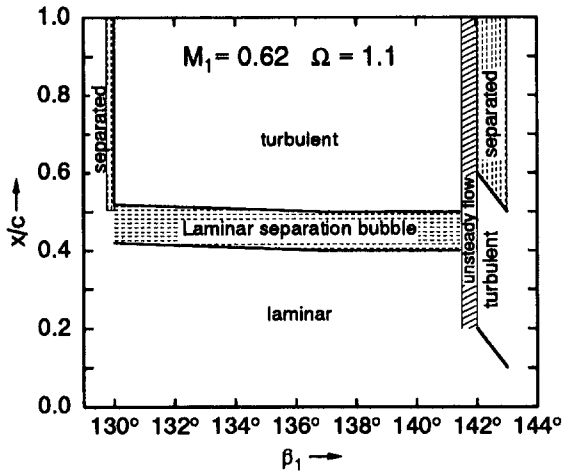


Fig. 6 Development of transition and separation on the suction surface at different inlet flow angles

temperature, as derived from the liquid crystal picture, is compared to the calculated adiabatic wall temperatures at design conditions. The experimental curve was derived by engineering judgment of the observed colors and the related temperature bands. It must be noted, however, that the absolute temperature level depends essentially on the viewing and incident light angle and is therefore less accurate than the relative temperature variations. These results confirm that really the adiabatic wall temperature is shown by the liquid crystals.

It can also be derived that within a laminar separation bubble, a recovery factor may be defined that is near or equal to that one of a turbulent boundary layer. In the reattachment region behind a separation bubble, however, a recovery factor lower than that of the laminar boundary layer has to be used to predict the adiabatic wall temperature there.

The reason for this, which may be the three-dimensional nature of the flow in these regions, needs to be investigated in special tests with larger models.

Test Results

In addition to the design point, the loss rises due to incidence and inlet Mach number variations were investigated. Figure 5 shows the loss coefficient at a constant inlet Mach number of 0.62 as function of the inlet flow angle. The diagram includes the former test results as well as the new ones obtained during the LC tests. The chord Reynolds number for the design conditions was 840,000 and the turbulence level 2.5 percent. The latter was derived from Laser Two-Focus measurements and is low compared to most applications in turbomachines. About the influence of the turbulence level, see, for instance, Kiock (1972).

In Figs. 6 and 7 the corresponding results of the LC and ink tests are summarized showing the boundary layer transition and separation position with varying inlet flow angle on suction and pressure side. In the inlet flow angle range between $\beta_1 = 130$ to $\beta_1 = 141.5$ deg the boundary layer behavior on the suction surface (Fig. 6) was nearly identical. Only the laminar separation bubble moved slightly downstream at negative incidences. Around $\beta_1 \approx 130$ deg the cascade choked when the Mach number was increased somewhat, as shown in Fig. 5, resulting in a loss rise due to flow separation just behind the suction surface separation bubble.

At positive incidence a nonstable region was detected between $\beta_1 = 141.5$ and $\beta_1 = 142$ deg where the transition point moved randomly upstream to about 22 percent of chord. Thereby the laminar separation bubble vanished and unsteady separation occurred around 60 percent of chord. At $\beta_1 = 142$ deg the transition stabilized at 22 percent and also the separation at 60 percent of chord. A further increase of the incidence by one degree caused the transition to move to 10 percent and the separation to 50–55 percent of chord.

On the pressure side (Fig. 7) only a very small separation bubble was observed around 3 percent of chord at $\beta_1 = 130$ deg caused by a shock wave due to the high flow expansion around the leading edge. The transition region was nearly constant between $\beta_1 = 133$ and 143 deg of inlet flow angle and observed around 20 to 23 percent of chord.

In Fig. 8, the dependency of the measured loss coefficient on the inlet Mach number is presented for two different inlet flow angles. Calculations revealed that the cascade chokes at $M_1 = 0.625$ for $\beta_1 = 130$ deg and $\Omega = 1.06$. This confirms the former test results where choking was observed at $M_1 = 0.63$ for $\beta_1 = 130$ deg. The highest loss value included in this curve obtained at $M_1 = 0.638$ was only possible at a reduced Ω value

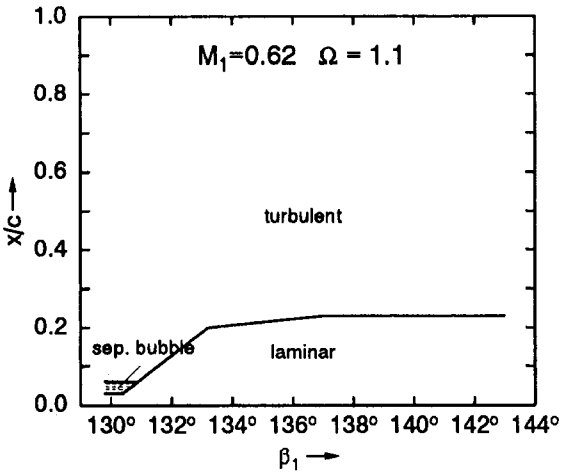


Fig. 7 Development of transition and separation on the pressure surface at different inlet flow angles

Downloaded 01 Jun 2010 to 171.66.16.53. Redistribution subject to ASME license or copyright; see http://www.asme.org/terms/Terms_Use.cfm

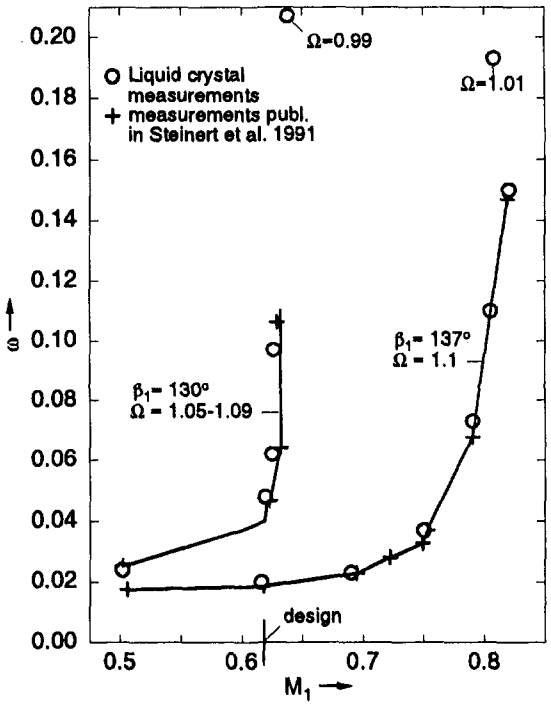


Fig. 8 Loss coefficient as function of inlet Mach number

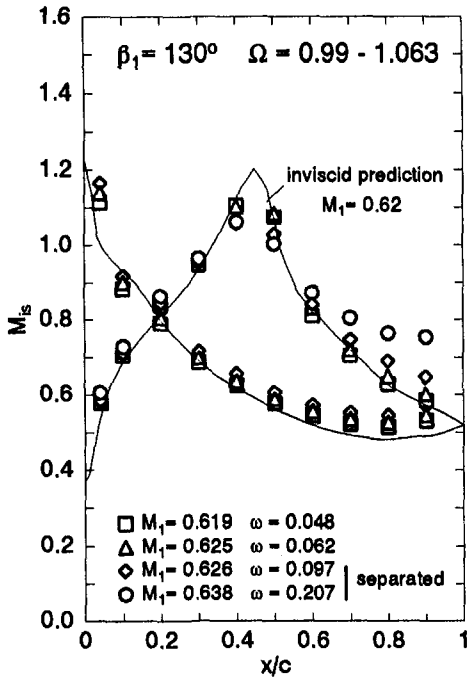


Fig. 10 Measured surface Mach numbers at −7 deg of incidence

($\Omega = 0.99$). At the design inlet flow angle the cascade choked between $M_1 = 0.8$ and 0.82 depending on Ω.

The separation and transition behavior on the suction surface as function of the inlet Mach number is shown in Fig. 9. The laminar separation bubble, to be seen between 40 and 50 percent of chord at low Mach numbers, decreases with rising inlet Mach number. Beyond $M_1 = 0.75$ an increased shock–boundary layer interaction causes the bubble to extend farther upstream.

Selected Test Points

In the following chapter some test points are described in more detail.

Tests at Negative Incidence. In Fig. 10 four different surface Mach number distributions measured at the smallest inlet flow angle ($\beta_1 = 130$ deg) but varying inlet Mach number are plotted. The axial velocity density ratio (AVDR) decreased from $\Omega = 1.07$ to 1.05 with M_1 rising from 0.619 to 0.626. The highest Mach number with $M_1 = 0.638$ was measured, as already mentioned, at $\Omega = 0.99$. At this point only the suction surface distribution was measured because the instrumented pressure side blade was covered with liquid crystals. All four distributions exceeded sonic velocities on the suction and pressure sides and shock waves were probably generated there. Corresponding ink traces on the pressure surface showing the leading edge separation bubble are provided in Fig. 11.

The liquid crystals on the suction side showed that the test points with $M_1 = 0.619$ and $M_1 = 0.625$ (Figs. 5 and 10) were only locally separated, although the loss values were up to 0.048 and 0.062. These results were confirmed by ink tests. The corresponding LC picture (Fig. 21) is very similar to that for the design condition (Fig. 20). Only the separation bubble is shifted slightly to the rear. The black streaky reattachment region between 52 and 60 percent of chord and the rear green attached turbulent region are clearly visible.

These results, however, indicate that the conclusion in the previous paper about separation at $M_1 = 0.623$ ($\omega = 0.047$) was not correct. Complete separation was detected first at $M_1 = 0.626$ with a loss coefficient as high as 0.097. Ink released

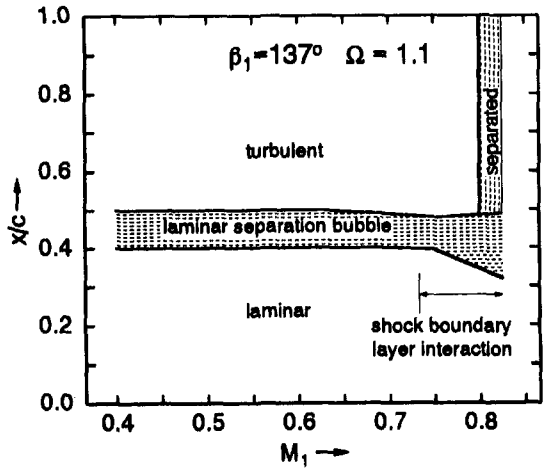


Fig. 9 Development of transition and separation on the suction surface at different inlet Mach numbers

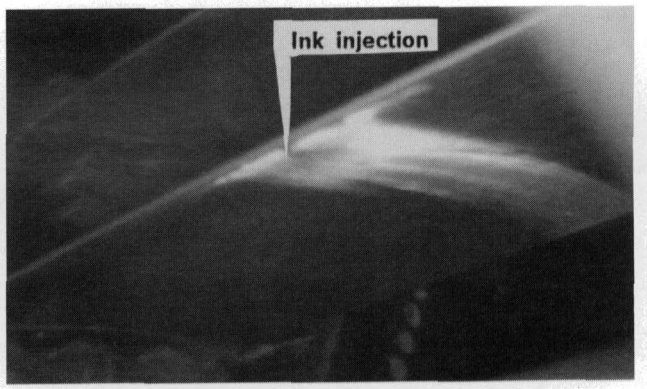


Fig. 11 Leading edge separation on pressure side indicated by ink traces; $\beta_1 = 130$ deg, $M_1 = 0.625$, $\Omega = 1.06$, $\omega = 0.062$

Downloaded 01 Jun 2010 to 171.66.16.53. Redistribution subject to ASME license or copyright; see http://www.asme.org/terms/Terms_Use.cfm

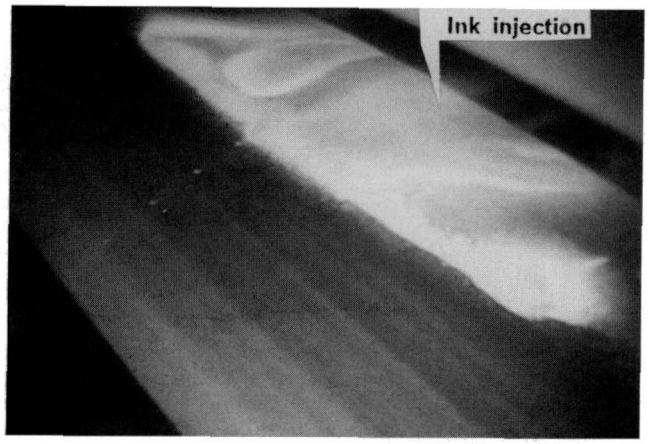


Fig. 12 Ink traces of laminar separation bubble followed by complete separation on suction surface β_1 = 130 deg, M_1 = 0.626, Ω = 1.05, ω = 0.097

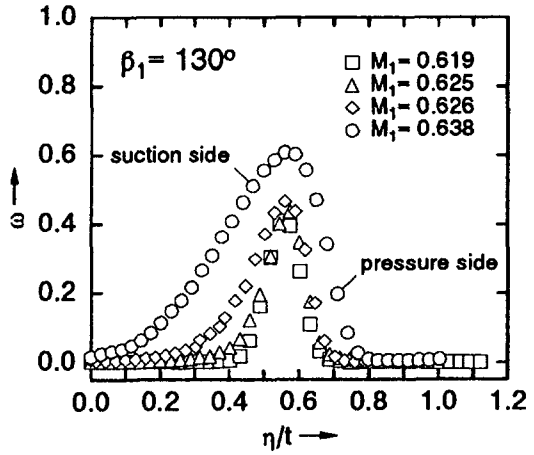


Fig. 14 Total pressure loss coefficient for negative incidence measured behind the cascade

at 80 percent of chord moved straight upstream (Fig. 12) and entered the still existing closed separation bubble where it was distributed in the spanwise direction and then sprayed back in the rear separated shear layer starting at 50 percent of chord. This surprising flow behavior may be due to a lambda shock system and therefore a shock boundary layer interaction phenomenon, which is sketched in Fig. 13. The LC tests shown in Fig. 22 confirm this effect where at M_1 = 0.638 a closed separation bubble exists between about 40 to 48 percent of chord followed by complete separation. Also the wake shapes reflect the suction side separation of the two higher inlet Mach numbers (Fig. 14). In the diagram of Fig. 14 the maximum loss value has been plotted at the same circumferential position because the exit flow angle varied from β_2 = 111.7 to 112.5, 113.7, and 116.2 deg at increasing Mach number.

Tests at Positive Incidence. In Fig. 15 three isentropic surface Mach number distributions at increasing inlet flow angle but constant inlet Mach number (M_1 = 0.62) and AVDR (Ω = 1.1) are plotted. At β_1 = 141 deg minimum losses (ω = 0.018) were measured. But by increasing the inlet flow angle by only one degree, severe separation was observed. The ink injection (at 80 percent of chord) visualizes the separation at 60 percent chord at β_1 = 142 deg as shown in Fig. 16. Whereas at β_1 = 141 deg a laminar separation bubble between 40 and 50 percent occurred, at β_1 = 142 deg natural transition around 20 percent of chord could be observed. An example of natural transition on the suction side is presented in Fig. 23 at β_1 = 143 deg and M_1 = 0.62.

Natural transition as shown in this figure around 10 percent of chord gives a streaky stable structure. The same figure shows also a sudden temperature drop around 55 percent of chord visualized by a color change from green to yellow. This is caused by complete separation, which can therefore also be detected by this method. The recovery factor in the totally separated areas seems to be of the order of that of the laminar boundary layer or even lower.

As already mentioned before, the AVDR has a considerable influence on the loss rise around stall. The dependency of loss and turning from AVDR at β_1 = 143 deg is shown in Fig. 17. It shows the typical loss decrease and turning increase with rising AVDR. The same strong dependency also exists around β_1 = 141 to 141.5 deg. If the AVDR is reduced below 1.04, the boundary layer also becomes unstable and unsteady separation can be observed as at the test points for Ω = 1.1 and β_1 = 141.5–142 deg, where the losses just start to increase (see Fig. 5).

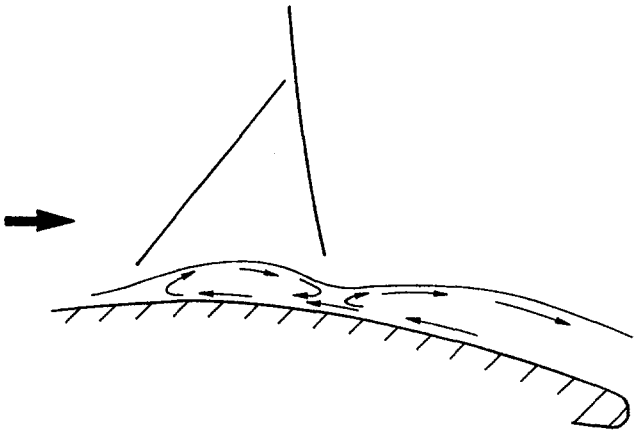


Fig. 13 Principle sketch of laminar shock boundary layer interaction with rear separation

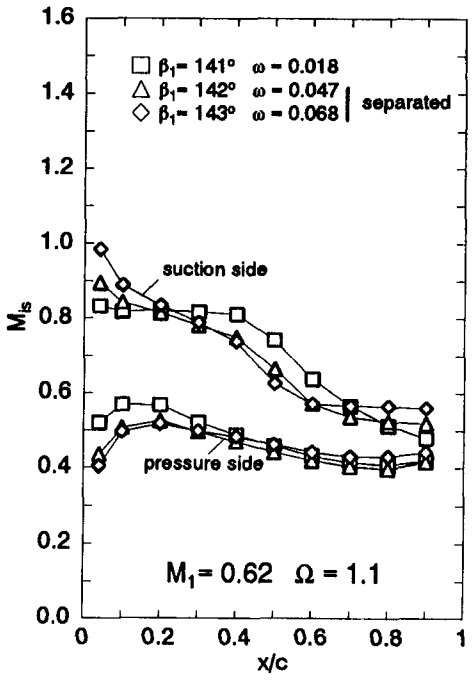


Fig. 15 Measured surface Mach numbers at positive incidence

Downloaded 01 Jun 2010 to 171.66.16.53. Redistribution subject to ASME license or copyright; see http://www.asme.org/terms/Terms_Use.cfm



Fig. 16 Ink injection on suction surface (9th pressure tap) indicating separation near 60 percent of chord; β_1 = 142 deg, M_1 = 0.61, Ω = 1.05, ω = 0.057

Inlet Mach Number Effect. The influence of M_1 on the blade surface Mach number distribution is provided in Fig. 18 for the design incidence. LC and ink tests showed that there was no rear separation (Fig. 24) up to an inlet Mach number of M_1 = 0.79. Beyond this Mach number the boundary layer separates at 48 to 50 percent of chord. Thereby the LC picture (Fig. 25) as well as the ink tests (injection at 80 percent Fig. 19) demonstrate again the side-by-side existence of a laminar separation bubble (between 35 and 50 percent of chord) and complete turbulent rear separation as sketched in Fig. 13.

Conclusions

In order to detect transition, local separation, and complete separation, a new technique based on Liquid Crystals (LC) has been developed for visualizing the adiabatic wall temperature. It has been successfully applied to a subsonic CDA compressor cascade. Some interesting flow phenomena could be observed:

- Turbulent reattachment behind a laminar separation bubble is characterized by a low adiabatic wall temperature probably caused by "Görtler vortices."
- At supersonic surface Mach numbers a closed laminar separation bubble sometimes directly followed by complete turbulent separation did exist in the shock boundary layer interaction region.
- The steep high incidence loss rise is indicated by an unstable upstream movement of the boundary layer transition.

The LC results are supplemented by ink traces along the blade surface and overall performance data at design and off-design conditions and are useful to validate boundary layer calculations.

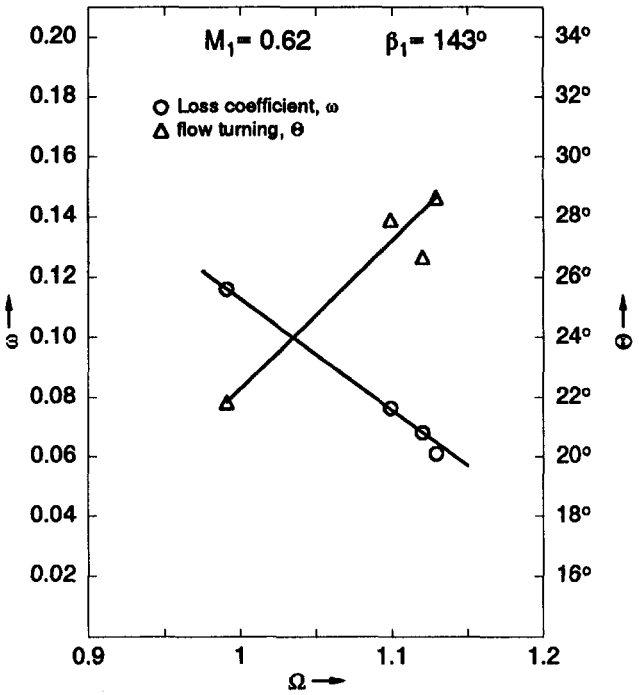


Fig. 17 Loss and turning development with axial velocity density ratio at positive incidence

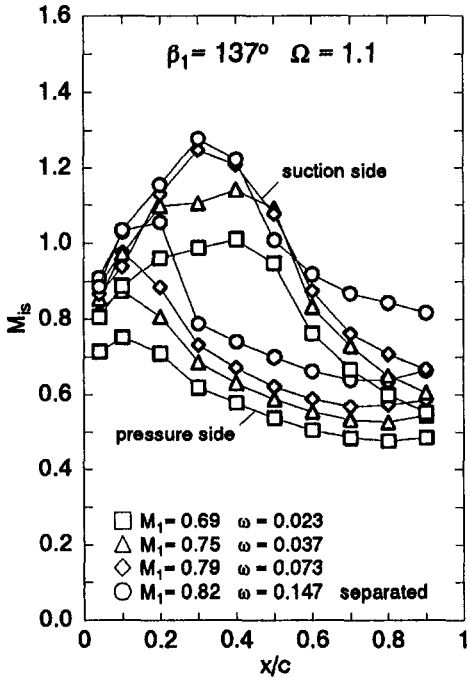


Fig. 18 Measured surface Mach numbers at design incidence and rising inlet Mach number

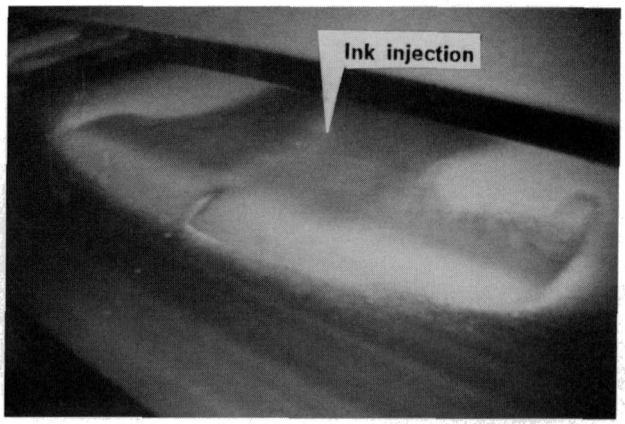


Fig. 19 Ink injection on suction surface (9th pressure tap) β_1 = 137 deg, M_1 = 0.808, Ω = 1.1, ω = 0.11

Downloaded 01 Jun 2010 to 171.66.16.53. Redistribution subject to ASME license or copyright; see http://www.asme.org/terms/Terms_Use.cfm

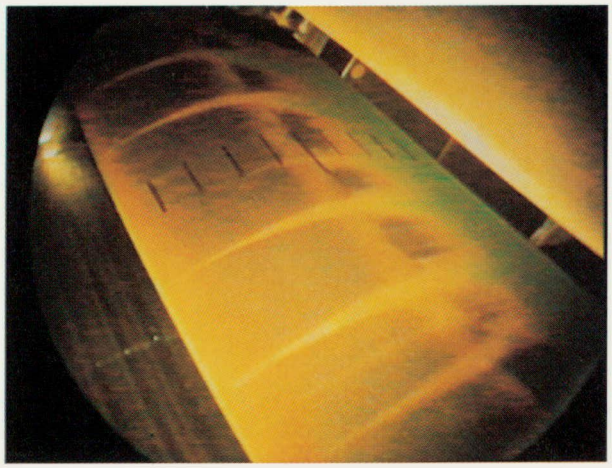


Fig. 20 Laminar separation bubble at design condition β_1 = 137 deg, M_1 = 0.62, Ω = 1.1

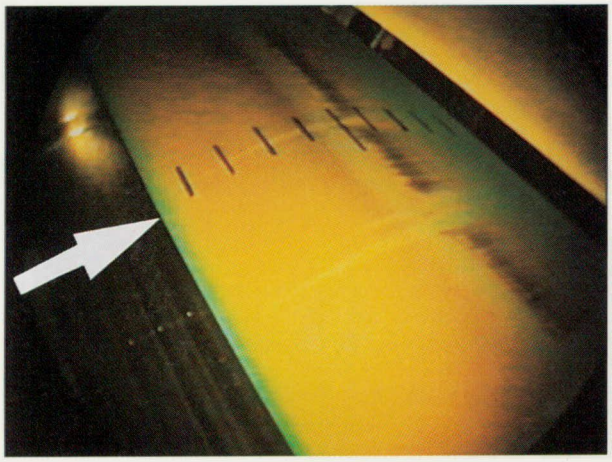


Fig. 21 Laminar separation bubble at negative incidence β_1 = 130 deg, M_1 = 0.619, Ω = 1.07



Fig. 22 Laminar separation bubble with rear separation at negative incidence β_1 = 130 deg, M_1 = 0.638, Ω = 0.99

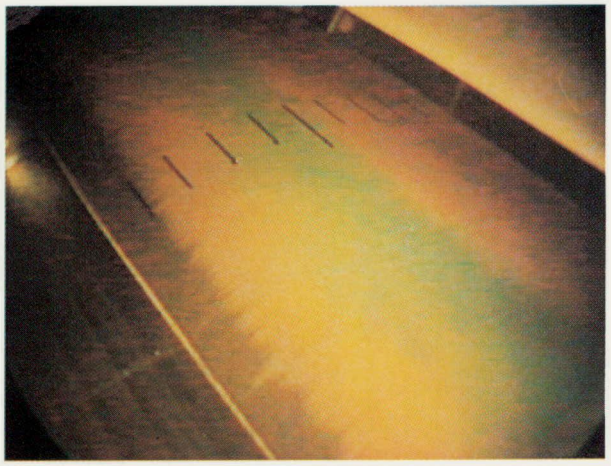


Fig. 23 Natural transition and rear separation at positive incidence β_1 = 143 deg, M_1 = 0.62, Ω = 0.99



Fig. 24 Laminar separation bubble at design incidence and increased inlet Mach number β_1 = 137 deg, M_1 = 0.79, Ω = 1.1

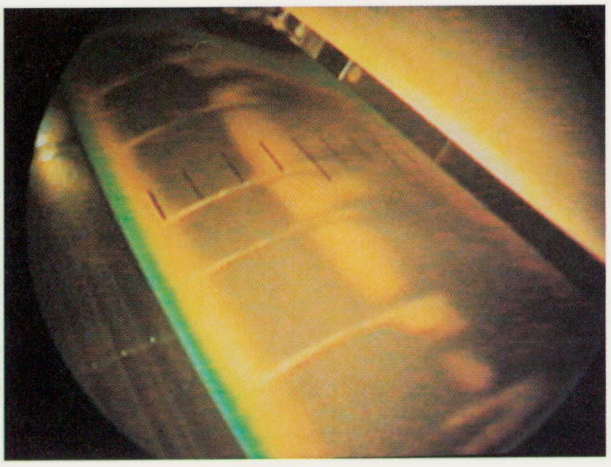


Fig. 25 Laminar separation bubble with rear separation at increased inlet Mach number β_1 = 137 deg, M_1 = 0.808, Ω = 1.01

References

Holmes, B. J., and Obara, C. J., 1987, "Advances in Flow Visualization Using Liquid-Crystal Coatings," SAE Technical Paper Series 871017.

Kiock, R., 1972, "Influence of the Degree of Turbulence on the Aerodynamic Coefficients of Cascades," in: *Boundary Layers in Turbomachines,* AGARDograph 164, J. Surugue, ed., Paper 1–4, pp. 73–88.

Mee, D. J., Walton, T. W., Harrison, S. B., and Jones, T. V., 1991, "A Comparison of Liquid Crystal Techniques for Transition Detection," AIAA Paper No. 91-0062.

Sage, I. C., and Archer, K. G., 1989, *Thermochromic Liquid Crystals,* 2nd ed., BDH Licritherm.

Starken, H., and Steinert, W., 1992, "Boundary Layer Separation and Transition Visualized by Liquid Crystal Coating," *Proceedings of the 11th Symposium on Measuring Techniques for Transonic and Supersonic Flow in Cascades and Turbomachines,* L. Fottner, ed., Universität der Bundeswehr München, Germany.

Steinert, W., Eisenberg, B., and Starken, H., 1991, "Design and Testing of a Controlled Diffusion Airfoil Cascade for Industrial Axial Flow Compressor Application," ASME *Journal of Turbomachinery,* Vol. 113, No 4.

Downloaded 01 Jun 2010 to 171.66.16.53. Redistribution subject to ASME license or copyright; see http://www.asme.org/terms/Terms_Use.cfm

Measurement of Tip-Clearance Flow in a Multistage, Axial Flow Compressor

A. C. Foley

P. C. Ivey

School of Mechanical Engineering,
Cranfield University,
Bedfordshire, United Kingdom

Detailed measurements using pneumatic probe traverses, blade static pressure tappings, and laser anemometry are made in the third stage of a large-scale, low-speed, four-stage, axial flow, research compressor. Inlet conditions show well-ordered "two-dimensional" flow from approximately 40 to 85 percent annulus span. Outside of this region, reduced total pressure due to upstream leakage losses and endwall effects results in high incidence to the following blade row. As a result, peak suction surface static pressure moves forward along the blade chord for both the hub and tip of stators and rotors. At the blade tip, however, the peak suction pressure is maintained with chord due to radial flow on the suction surface being entrained into the tip leakage jet. The extent of rotor chord for which this "entrainment" occurs increases with increasing rotor tip clearance gap. The leakage jet from both stators and rotors is seen to "roll up" into a vortex downstream of their respective blade rows.

1 Introduction

Numerous and extensive studies have been conducted to investigate the effects of rotor tip clearance flow on the performance of axial compressors, and to examine the structure of the flow itself. These studies have encompassed cascades, isolated rotors, and complete compressor stages: Measurements have been obtained in both the stationary and rotating frame of reference, using conventional pneumatic probes, hot-wire, and laser anemometry.

Predictions using either simple models of the flow structure, or complex Navier–Stokes and Euler solvers, are becoming more detailed (see Lymberopoulos et al., 1993, and Nikolos et al., 1993). As a consequence the need to validate models requires detailed measurements, particularly in multistage machines. The description of tip leakage flows in particular, and secondary flows in general, despite a number of numerical and experimental studies, still remains one of the least understood areas in turbomachinery. What is clear, however, is the importance of these flows in contributing to the few remaining losses that designers believe can be eliminated.

An early study of the secondary losses in a three-stage axial water pump was carried out by Rains (1954), who conducted ingenious flow visualization experiments using both cavitation and oil injection to identify tip leakage vortices. Rains detailed the tip leakage flow and identified differences between the stationary and rotating blade leakage characteristics. The importance of the tip gap to blade thickness ratio for potential flow assumptions and classical secondary flow was also revealed. Rains formulated an early model of the leakage flow, which has been extensively revised. (See Vavra, 1960; Hesselgreaves, 1969; Storer and Barton, 1991.)

To expand further, it is convenient to consider only a few of the more recent studies. Storer and Cumpsty (1991) examined tip clearance flow in a linear cascade. Using flow visualization, static pressure measurements on the blade surface and endwall, and a flattened Pitot tube in the clearance region. Tip clearances (t/c) of 0, 2, and 4 percent were examined for incompressible flow at a blade Reynolds number of 5×10^5. Measurements showed intense shearing between tip clearance and core flows. Suction side static pressures, measured at 2 percent chord from the tip, were effected by the presence of a discrete tip clearance vortex formed by the clearance flow "rolling up." However, from the evidence available, these authors were not able to clarify for clearances (t/c) less than 1 percent, that "the establishment of a leakage vortex was an inevitable consequence of tip-clearance."

A further study was reported by Lakshminarayana et al. (1991). In this single-stage compressor measurements were obtained using a rotating five-hole pneumatic probe. Three orthogonal velocity components were measured at the exit from both rotor and stator. The study addressed the issue of whether a discrete vortex always developed with tip clearance flows. From measurements at a Reynolds number (Re_c) of 5×10^5 and a clearance (t/c) of 2.3 percent, it was concluded that the structure of tip-clearance flow in cascades and rotors was substantially different and further, that isolated rotors and embedded stages also induced such differences; for this single-stage compressor no evidence was obtained upon which the presence of a discrete vortex could be inferred.

Stauter (1993) reported laser anemometry experiments in a two-stage axial compressor. The measurements were obtained in the tip clearance region of a second-stage rotor at various axial stations both within the blade passage and downstream of the rotor. Using a two-color five-beam LDV system, three orthogonal components of velocity were measured. Results were reported for axial locations of 42 to 130 percent chord, at radial locations typically from 83 to 98.4 percent annulus height, and at 64 discrete circumferential locations across the rotor passage.

For a rotor tip clearance (t/c) of 1.25 percent and the compressor operating at its design flow coefficient of $\Phi = 0.51$, examination of the measured vectors showed a discrete vortex in the blade passage adjacent to the suction surface. Roll-up of the tip leakage flow was reported at 42, 63, and 115 percent chord from the leading edge. The vortex was shown to develop into the passage between 42 and 63 percent chord; at 115 percent chord the center of the vortex was located approximately midway between upstream blade surfaces. Unexpectedly, using identical analysis methods, no vector pattern that would suggest a discrete vortex was obtainable at 90 or 130 percent chord. Stauter concluded that the tip clearance vortex was subject to both decay and generation throughout the passage and down-

Contributed by the International Gas Turbine Institute and presented at the 39th International Gas Turbine and Aeroengine Congress and Exposition, The Hague, The Netherlands, June 13–16, 1994. Manuscript received by the International Gas Turbine Institute March 12, 1994. Paper No. 94-GT-431. Associate Technical Editor: E. M. Greitzer.

Copyright © 1996 by ASME

Downloaded 01 Jun 2010 to 171.66.16.53. Redistribution subject to ASME license or copyright; see http://www.asme.org/terms/Terms_Use.cfm

stream of the rotor. Stauter also measured the static-pressure distribution on the rotor at 95.8 percent annulus height. The suction side distribution showed none of the disturbance, reported by Storer and Cumpsty (1991), caused by the presence of a tip-leakage vortex.

An unambiguous model for the structure of tip-clearance flow is not readily apparent from a review of these studies, nor do other well-documented studies reconcile the differences. Generation of a tip-clearance vortex in cascades is accepted, although this may not be the case for small tip clearances. Isolated rotors and compressor stages are reported to have different tip-clearance flow structures with isolated rotors having similar characteristics to cascades; see Inoue et al. (1986). Preliminary analysis of important data from a multistage compressor presents the tip-clearance vortex appearing distinct and then difficult to locate alternatively throughout the passage.

This paper presents measurements from a large-scale, four-stage, low-speed, axial flow, research compressor using controlled diffusion blading for two values of rotor tip clearance. Static pressure distributions near the rotor tip are used together with interblade laser anemometry to examine the effect of tip leakage flow on the chordwise distribution of static pressure. The intention was to contribute to the tip clearance flow information base, with particular regard to the detailed effects on an embedded stage. Section 2 describes the experimental facility, section 3 presents results, which are discussed in section 4. Section 5 concludes the paper.

2 Experimental Facility

2.1 Large-Scale, Low-Speed, Axial Flow, Research Compressor. Low-speed compressors have long been used to model many of the characteristics of high-speed compressors. Large-scale, low-speed research compressors can be used to augment high-speed compressor development and offer a potential, using simpler hardware and at a lower cost, of more detailed and systematic measurement of many intractable turbomachinery problems. The low-speed research compressor at Cranfield has been used extensively for the systematic examination of various high-speed designs (see Robinson et al., 1989), the validation of design/analysis methods, and to gain an understanding of subsonic aerodynamics. An operational review of this Cranfield facility is given by Robinson (1991). The validity of this approach is established and the interested reader is referred to Wisler (1985).

Figure 1 shows a general arrangement of the compressor facility. Air flow is shown from right to left. A so-called working section (low-speed compressor) is supported independently from a drive section; these sections are coupled together at a central flange. Overall dimensions are a height and length of approximately 2.5 m and 7.5 m, respectively.

Air passes through an inlet filter and a calibrated bell mouth before entering the working section. The area presented to the flow initially contracts by some 5 percent (thereby thinning the boundary layer); subsequently a parallel annulus having an outer diameter of 1.21 m is formed. The working section comprises a row of 72 inlet guide vanes, followed by 4 identical stages each having 79 rotors and 72 cantilevered stators, and finally an exit row of 72 outlet guide vanes. The compressor has a hub/tip ratio of 0.85 (which is an average value for a midstage of a modern high-pressure compressor).

At exit from the compressor, the air is ducted through an annulus; the flow through the facility is completely symmetric. A drive section (housed inside the exit annulus) comprises a 120 kW thyristor-controlled variable-speed DC motor, a 5.71:1 ratio epicyclic reduction gearbox, and a strain gage torquemeter. Control of the mass flow rate through the compressor is maintained by a conical valve located at the exhaust exit.

2.2 Pneumatic Probes. The third stage is the study stage reported in this paper. Area traverses using cobra-type three-hole pneumatic probes were obtained at inlet and exit for both rotor and stator. These probes were calibrated for the effect of flow incidence, and absolute air angles then resolved using this calibration. For geometric details of the probes, see Howard et al. (1994).

The probes are mounted on the outside of a so-called "traversing ring," which moves circumferentially relative to stationary rings supporting the stators. Radial and yaw movements of the probes, together with the circumferential movement, are all achieved using computer-controlled stepper motors. Further detail on the pneumatic traversing mechanisms is given by Robinson (1991).

2.3 Aerofoils. The compressor was assembled with modern, controlled-diffusion aerofoils. Table 1 details design parameters for rotors and stators.

Both rotors and stators are instrumented on pressure and suction surfaces with static-pressure tappings. At nominal "root," "mid," and "tip" locations, the pressure and suction surfaces had 14 and 12 tappings, respectively, placed equispaced along the surface from leading to trailing edge. Cross referencing between aerofoils was necessary as both suction surface and pressure surface tappings were not possible on one aerofoil alone. This was provided by lone "reference" tapping on the opposite side of the blade to the full set of tappings.

Static pressure measurement in the rotating frame of reference was achieved by a rotating scannivalve, which output to data-acquisition equipment via slip-rings.

2.4 Laser Time of Flight. The laser time of flight (LTF) technique requires that two equal intensity parallel laser beams be directed into a flow. These beams are focused so that their diameter reduces to a minimum of approximately 10 μm. The intensity of the laser at this minimum is such that sufficient light can be reflected from particles passing through the beam to enable sensing by photomultiplier tubes. For this study the beam's reduced diameter results in an "effective" length of approximately 300 μm. The separation of the two beams making up this "measurement volume" was set at 450 μm. If an oil particle seeded into the flow crosses both beams, then the resulting time lapse between crossings is cross-correlated and a velocity is resolved. The strength of the correlation is dependent upon the orientation of these beams with the flow; a maximum strength occurs when the beams are aligned precisely with the mean flow angle. Hence rotating the laser beams through a

Nomenclature

c = chord
IGV = Inlet Guide Vane
LDV = Laser-Doppler Velocimetry
LTF = Laser Time of Flight
p = pitch
P_l = local static pressure coefficient
P_t = local total pressure coefficient
Re = Reynolds number using blade chord
t = tip gap
λ = tip gap/max blade thickness
U = absolute velocity, blade speed (mid)
Φ = flow coefficient (axial velocity/mid blade speed)
ρ = density of air
Ω = angular velocity

Definitions

$P_l = ((P_{\text{local static}} - P_{\text{inlet total}})/\frac{1}{2}\rho U^2)$
$P_t = ((P_{\text{local total}} - P_{\text{inlet total}})/\frac{1}{2}\rho U^2)$

Downloaded 01 Jun 2010 to 171.66.16.53. Redistribution subject to ASME license or copyright; see http://www.asme.org/terms/Terms_Use.cfm

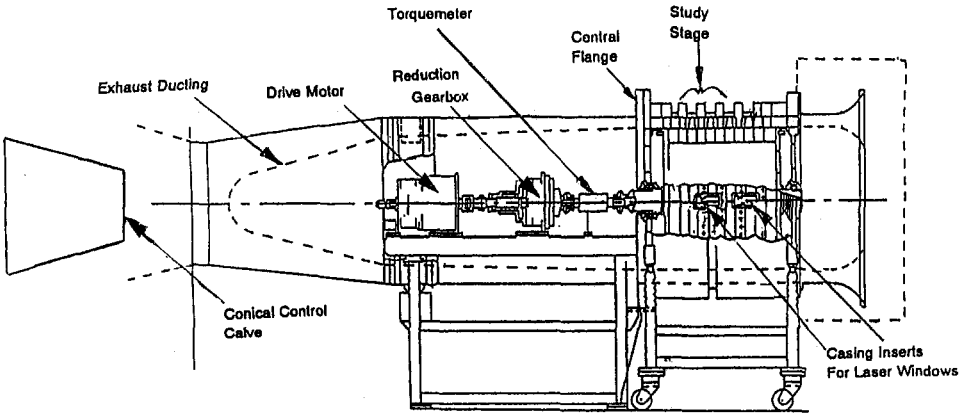


Fig. 1 *The Cranfield four-stage low-speed axial flow research compressor*

range of angles while recording correlations, it is possible to detect the mean flow angle.

The anemometry equipment used combined a Lexel Model 95 2-Watt Argon-Ion laser, with a Malvern Instruments beam splitter, transmission, and receiving optics. Measurements were processed using a Malvern Instruments 10 ηs correlator with data store. The anemometer was aligned radially normal to the compressor casing and traversed in a radial and an axial direction. The LTF system used measured velocities in two dimensions orthogonal to the beams: If a strong third-dimensional component was present, or the flow is highly turbulent, cross correlation is not possible. However, this technique is well established for two-dimensional measurements in turbomachinery and experience in its use at Cranfield suggests that mean flow angles can be resolved to ± 1 deg and velocities to 1 m/s. Similar values of accuracy have been found by other authors (e.g., Ross, 1980).

The blade passing time interval is recorded by an optical pickup, which is triggered by the passing rotor blade. This interval is subdivided into 10 discrete time slots; 9 of these are masked electronically while measurements are made for the remaining slot. Once the mean flow angle and corresponding velocity are resolved this slot is masked, another is exposed, and the process repeated. A complete vector map is built up for velocities measured in the stationary frame of reference. Translation to a rotating frame is performed by subtraction of the local blade velocity (Ωr) from each vector.

3 Results

3.1 Overall Characteristics. Figure 2 shows the effect of rotor tip clearance on the measured efficiency of the low-speed compressor. Efficiency was calculated from the obtained static pressure rise through the compressor compared to the ideal based on torque and angular velocity measurements. The peak efficiency occurred at a flow coefficient of approximately $\Phi = 0.63$; the precise point is difficult to determine as the characteristic is almost flat to the point of rotating stall. Increasing the rotor casing clearance from 1.2 to 3 percent (t/c) reduces the measured efficiency at $\Phi = 0.63$ by approximately 0.6 percent. The range of flow coefficient where the efficiency remains fairly constant is also reduced, the higher clearance dropping into rotating stall earlier than the smaller clearance. Rains (1954) noted that for a value of $\lambda < 0.167$, where λ is the ratio of clearance to maximum blade thickness, viscous effects became significant and the potential flow model for tip leakage flow breaks down. The clearances tested here effectively fall either side of Rains' critical value with $\lambda = 0.11$ and 0.28 for 1.2 and 3 percent (t/c), respectively.

Table 1 Design parameters for rotor and stator

	ROTOR	STATOR
Tip clearance (t/c)	*1.2 % & 3%*	*2.4%*
Mid Span Pitch/Chord (p/c)	*0.76*	*0.85*
Max Blade Thickness/Chord	*0.11*	*0.097*
Aspect Ratio (h/c)	*1.54*	*1.59*
Chord (mm) (tip)	*59.2*	*57.7*
Stagger (deg) (mid)	*28.2*	*30.2°*
Camber (deg)	*29*	*30*
Number of Blades	*79*	*72*
Axial Gap/Chord	*0.44*	*0.45*
Reynolds Number (Re_c)	*$2x10^5$*	

3.2 Pneumatic Traverses

Rotor Inlet. Figures 3(a) and 3(b) show the normalized total pressure and derived flow angle, respectively, downstream of stator 2 (inlet to the third-stage rotor) for a rotor tip clearance of 1.2 percent (t/c). The ordered two-dimensional region of the flow extends from approximately 40 to 85 percent annulus span; regions adjacent to the outer casing and the inner hub have reduced total pressure due to upstream leakage jet losses and three-dimensional endwall effects. In the lower part of the passage the pressure is seen reducing from 40 percent annulus span to the hub. There is a distinctive reduced pressure core at approximately 75 percent pitch close to the hub; this is the effect of the upstream stator leakage vortex. Confirmation of this is given in Fig. 3(b), which shows a marked variation in

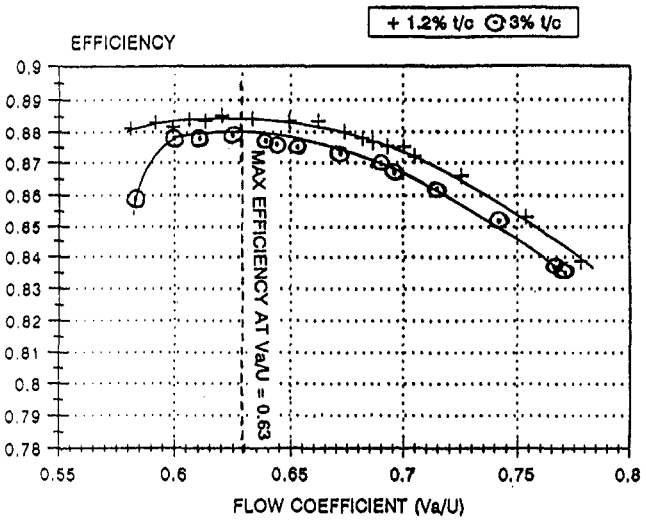


Fig. 2 Efficiency characteristic

Downloaded 01 Jun 2010 to 171.66.16.53. Redistribution subject to ASME license or copyright; see http://www.asme.org/terms/Terms_Use.cfm

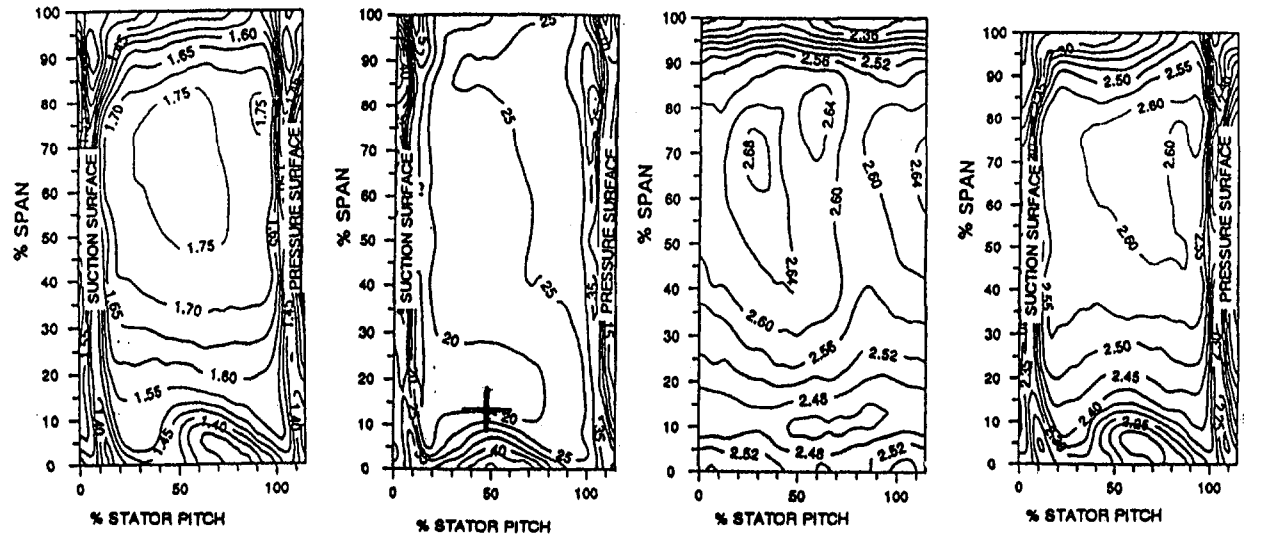


Fig. 3(*a*) Total pressure upstream of rotor 3

Fig. 3(*b*) Flow angle upstream of rotor 3

Fig. 3(*c*) Total pressure downstream of rotor 3

Fig. 3(*d*) Total pressure downstream of stator 3

Fig. 3 Area contour plots around stage three at design flow point

isocline values in this region. The isoclines are instructive: Work by Lakshminarayana (1970) and more recently by Krain (1988) has shown that vortices can be inferred from the analysis of the isocline pattern. Concentric ellipses either side of parallel lines mark a free vortex surrounding a forced vortex. The center of the combined vortex is always located in the middle of these parallel isoclines and is indicated by a cross in Fig. 3(*b*).

Rotor Exit. Figure 3(*c*) shows the normalized total pressure contours at exit from the third-stage rotor having 1.2 percent (t/c) casing clearance. Although the measurements were obtained in the stationary frame of reference, this figure is instructive. Adjacent to the casing (above 90 percent annulus span) the contours are generally pitchwise uniform due to the developing wall layer and the mixed-out effects of the upstream rotor tip-leakage flows. Toward the center of the passage and at approximately 75 percent pitch from the suction surface, the diffused effects of a stator wake are apparent with reduced pressures at exit from the rotor. Smith (1966) discusses the mechanism by which such wakes are attenuated through a rotating blade row. Adjacent to the hub (at approximately 10 percent span) a high-pressure region at midpitch is bracketed by reduced pressure regions, which may be the remains of the stator-hub-leakage vortex identified in Fig. 3(*b*).

Stator Exit. Figure 3(*d*) shows the normalized total pressure at exit from the third-stage stator and as would be expected, given a repeating stage assumption, this figure is similar to that shown in Fig. 3(*a*). Once again an ordered two-dimensional region is clearly evident with upstream leakage jet losses and three-dimensional end-wall effects adjacent to casing and hub. Of particular note is the further development into the passage of the reduced pressure region adjacent to the stator suction surface and between 84 percent span and the outer casing.

3.3 Aerofoil Static Pressure Distributions

Rotor. Figure 4(*a*) shows the chordwise distribution of static pressure measured on the rotor suction and pressure surfaces at the nominal hub, mid, and casing locations for 1.2 percent (t/c) rotor casing clearance and $\Phi = 0.63$. Lower total pressure at the rotor hub than at mid is indicated by Fig. 3(*a*) and a consequence of this is reduced absolute velocity and hence an increase in incidence in the relative frame. This results in the peak pressure difference moving forward from 30 percent chord as indicated at the mid location to approximately 20 percent chord at the hub.

Similarly, at the rotor tip the reduced total pressure, and hence reduced absolute velocity, increases the relative incidence. The suction peak pressure therefore also moves forward of the mid; however, unlike the hub, at the casing the pressure then remains relatively constant for the first 30 percent of chord. Figure 4(*b*) shows the region of constant suction surface static pressure increasing by approximately 10 percent chord with the increase in clearance from 1.2 to 3 percent t/c.

Stator. Figure 4(*c*) shows a similar plot to that of Fig. 4(*a*) but for the stator. Apart from the first 35 percent of chord, the stator suction surface is shown to have a similar pressure distribution profile at each spanwise position, the rise in the absolute static pressure toward the hub being due to radial equilibrium. In a similar manner to that observed in the rotor, increased incidence results in the peak suction pressure point moving forward along the chord for both the hub and casing when compared to the distribution at midspan. At the casing location the pressure decreases from this peak as at midspan. However, at the hub clearance, as in the rotor casing clearance, there is a region of approximately constant suction surface static pressure (10–30 percent chord).

For a comparison of static pressures with design intentions and further information on blade design the reader is referred to the paper by Howard et al. (1994).

3.4 Interblade Anemometry. Table 2 details measurements obtained both in the blade-to-blade region and downstream of the third-stage rotor. Gaps in the matrix at 66 percent chord for 97 and 99 percent height indicate positions at which measurements proved unobtainable (probably due to radial flows making the two-dimensional system ineffective). The matrix encompasses axial locations of 4 to 125 percent chord from the leading edge, annulus span of 80 to 99 percent, and up to eight discrete blade-to-blade locations (two time slots being occupied by the rotor itself).

Figure 5(*a*) shows the rotor relative velocity vectors measured at five axial locations at 80 percent height. The flow appears well ordered: On the suction side fluid is accelerated and the magnitude of the velocity decreases toward the pressure side. There is underturning relative to the local blade angle throughout the passage with a perceptible deviation at rotor exit.

Downloaded 01 Jun 2010 to 171.66.16.53. Redistribution subject to ASME license or copyright; see http://www.asme.org/terms/Terms_Use.cfm

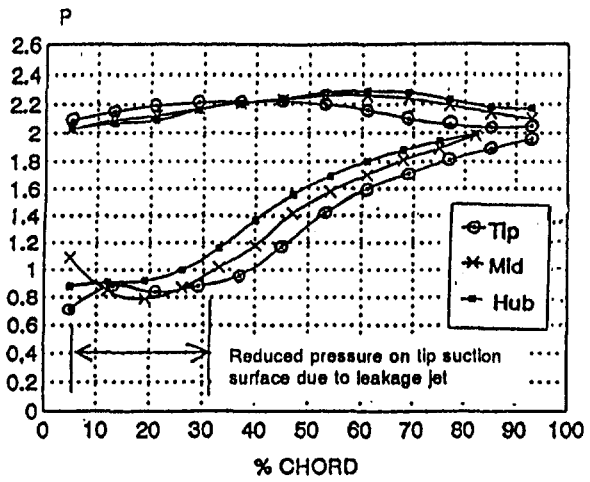


Fig. 4(*a*) Rotor 3 normalized blade surface pressure distribution variation with span; 1.2 percent rotor clearance at design flow point

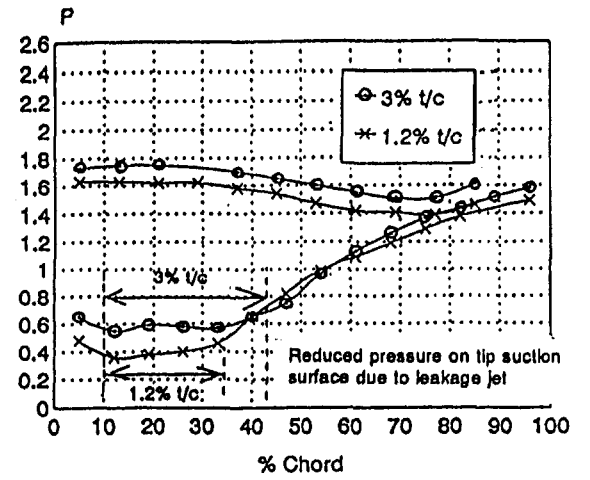


Fig. 4(*b*) Rotor 3 normalized blade surface pressure distribution variation with tip clearance; 1.2 and 3 percent rotor clearance at design flow point

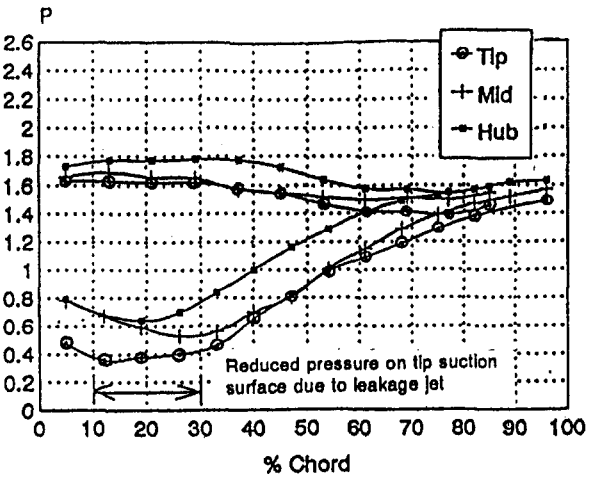


Fig. 4(*c*) Stator 3 normalized blade surface pressure distribution variation with span; 2.4 percent stator clearance at design flow point (rotor clearance 3 percent)

Figure 5(*b*) shows the velocity vectors at 99 percent height. At this height the measurement volume is in the casing clearance gap and consequently the blade profiles shown are for reference purposes only. In this figure there is significant underturning at all locations within the passage (although no measurements were possible at 66 percent chord). Also clearly shown is fluid close to the rotor pressure surface at 33 percent chord flowing across the rotor tip and into the adjacent passage, resulting in significant underturning adjacent to the suction surface.

Table 2 Laser anemometry measurement matrix

	% Axial Chord from rotor leading edge					
	0	33	66	96	125	
% Annulus Height	99	99		99		
					98	
	97	97		97	97	
					96	
	95	95	95	95	95	
	93	93	93	93	93	
	90	90	90	90	90	
	88	88	88	88		
	85	85	85	85	85	
	83	83	83	83	83	
	80	80	80	80	80	

4 Discussion

This section discusses the results presented in section 3 and will in effect follow the flow through the "study" stage. Rotor inlet is measured at 25 percent chord downstream of stator 2. Rotor and stator outlet conditions are measured at the same distance downstream of rotor 3 and stator 3, respectively. The results will highlight multistage inlet conditions and the effect of clearance flows measured in the stationary frame and presented in both the stationary and rotor relative frame of reference.

Inlet conditions to stage 3 are shown by a complete area traverse of flow angle and normalized total pressure between stator 2 and rotor 3 (Figs. 3(*a*) and 3(*b*)). At approximately 15 percent annulus height and 70 percent blade pitch, a leakage vortex is indicated quite clearly from isocline patterns (see Fig. 3(*b*)). The vortex is distinct as it has yet to pass through a rotating blade row. The previous stationary blade row hub leakage vortices (i.e., IGV and stator 1), having been diffused by their axial passage and "chopped" by rotating blade rows, are believed to contribute to the "background" reduction in pressure extending from 0 to 40 percent span.

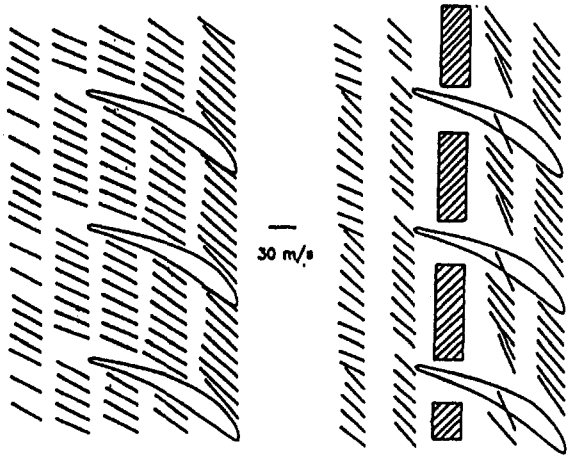


Fig. 5(*a*) Velocity vectors @ 80 percent span

Fig. 5(*b*) Velocity vectors @ 99 percent span

Downloaded 01 Jun 2010 to 171.66.16.53. Redistribution subject to ASME license or copyright; see http://www.asme.org/terms/Terms_Use.cfm

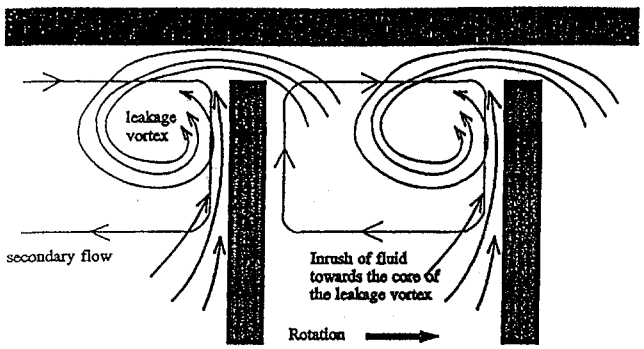


Fig. 6 Fluid entrainment into leakage jet (from Lakshminarayana and Horlock, 1965)

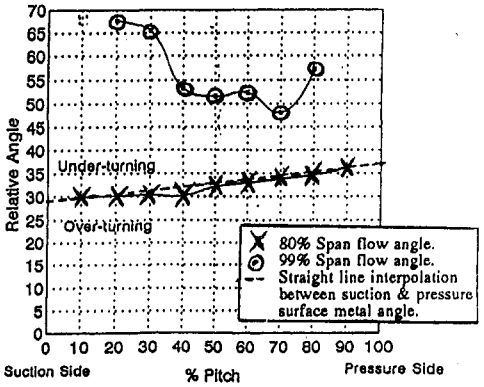


Fig. 7 Rotor relative flow angles

In the top 15 percent of the annulus, the total pressure is seen to decrease toward the outer casing. The main cause of this is believed to be the effect of upstream rotor tip leakage losses passing through the stator blade row; however, other influences such as wall "boundary layers" and stator-casing corner stall will also contribute. The pneumatic probes measure in the stationary frame and hence "circumferentially" average the flow. The reduced pressure is therefore seen spread across the passage and unlike the stator vortex and wakes, no discrete rotor-induced flow structures are visible.

The effect of the reduced total pressures in the hub and casing regions described downstream of stator 2 is reduced absolute flow velocities and as a result, high incidence flow angles relative to rotor 3. In the rotor blade row surface static pressure tappings at midspan are compared with those at the casing and hub. The hub receives highly skewed inlet flow and the peak suction pressure is measured at 20 percent chord as opposed to 30 percent chord for the midspan location: Note that maximum blade thickness occurs at approximately 30 percent chord. The casing, where the flow also has increased incidence, similar to the hub, also shows a peak suction pressure point closer to the leading edge than that at the mid location. However, this peak is then maintained from about 10 to 30 percent chord (Fig. $4(a)$). This observation is consistent with the findings of Dean's (1954) investigation of a rectilinear cascade with four different values of tip clearance. The continuation of this reduced suction pressure with chord is caused by radial flow of fluid on the suction surface entraining into the tip leakage jet. Figure 6 from Lakshminarayana and Horlock (1965) illustrates the flow field in this region. Increasing the rotor clearance from 1.2 percent t/c to 3 percent t/c results in this region extending approximately 10 percent further along the chord (Fig. $4(b)$).

Interblade rotor tip leakage flow is investigated further with laser anemometry. The well-ordered two-dimensional flow at 80 percent annulus height is compared to that found at 99 percent where velocity vectors clearly show the leakage jet at 33 percent chord (Figs. $5(a)$ and $5(b)$). The variation of measured flow angle with rotor pitch at these heights is seen more clearly in Fig. 7. Also shown is a simple (and somewhat arbitrary) straight line interpolation between the suction and pressure surface metal angles at 33 percent chord (shown at pitchwise locations of 0 and 100 percent pitch, respectively). The figure shows quite clearly how at 80 percent span and 33 percent chord the flow follows the blade metal angles faithfully. At 99 percent annulus span, however, there is large underturning on the suction side due to the casing tip leakage jet progressing across the passage to about 30 percent pitch. For 40 to 70 percent pitch the reduced value of underturning is a result of highly skewed flow at inlet to the blade row. From 70 percent pitch the underturning increases due to fluid flowing into the clearance gap on the pressure side of the blade.

Downstream of the rotor the attenuated stator wakes are indicated by reduced pressures at 40 to 85 percent annulus height and 75 to 95 percent pitch (Fig. $3(c)$). Similarly reduced pressure cores at 15 percent annulus height and 5 and 100 percent pitch indicate the remains of the previous stator blade row leakage vortices. The effect of the rotor leakage, although circumferentially averaged, is also seen in rapidly reducing total pressure in the upper 15 percent of the annulus. Further analysis of the rotor exit is provided by the laser results, which are presented as contour maps of relative flow angle and axial velocity at 125 percent chord in Fig. $8(a)$ and $8(b)$. These show isoclines of rotor relative flow angles at radial heights between 80 and 100 percent annulus span (the outer casing). The measurements were simply repeated for adjacent passages and a relative boundary condition imposed at the casing. Considering Fig. $8(a)$: At a circumferential location of 12 and at a radial height of approximately 90 percent span the isocline pattern shown is

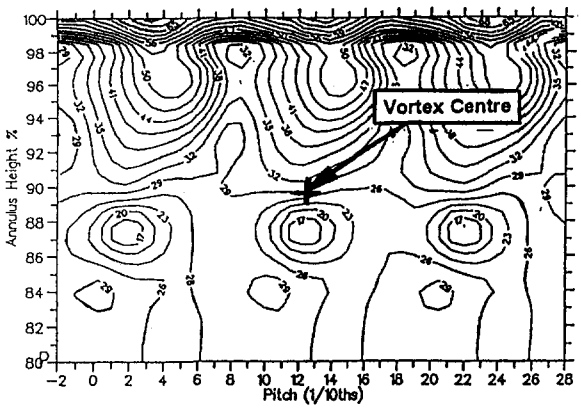


Fig. 8(*a*) Relative flow angle at exit from rotor three at design

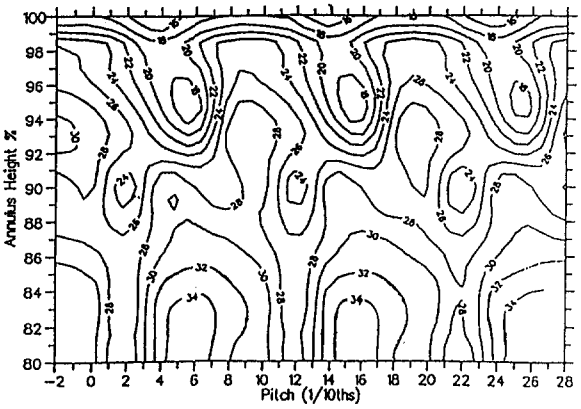


Fig. 8(*b*) Axial velocity at exit from rotor three at design

Downloaded 01 Jun 2010 to 171.66.16.53. Redistribution subject to ASME license or copyright; see http://www.asme.org/terms/Terms_Use.cfm

similar to that both predicted and measured, downstream of a linear cascade, by Lakshminarayana (1970). Lakshminarayana deduced from this pattern the presence of a strong vortex. Further, Inoue et al. (1986), using Lakshminarayana's model, generated similar patterns, downstream of a rotor, which were in good agreement with patterns derived from measurements of the tip leakage vortex. Analysis of the isoclines shown in Fig. 8(a), as viewed from upstream, suggests a clockwise rotating vortex (which is consistent with the tip clearance jet rolling up). The mean flow angle of the vortex is approximately 30 deg and its circumferential location after traversing the passage is coincident with that of the rotor wake. Goto (1992) also found a vortex coincident with the wake in his single-stage rotor at 130 percent chord. Figure 8(b) shows contour plots of axial velocity at the same axial location. A loss core of reduced velocity is clearly shown coincident with the vortex center.

Reduced pressure in the hub and tip region at exit to rotor 3 (Fig. 3(c)) results in highly skewed flow in the endwall regions at the inlet to this blade row. In the blade passage, examination of static pressure measurements shows the hub peak suction surface static pressure moving to less than 10 percent chord compared to the 28 percent chord position shown at mid. This is a similar effect to that seen in the upstream rotor. For the stator tip the peak pressure also moves forward of the position seen at mid. As in the rotor, this reduced suction pressure is then maintained due to fluid entrainment into the clearance gap. The stator vortex, unlike the rotor vortex, however, is seen at midpitch.

For the regions adjacent to the casing and rotor drum that are affected by rotor and stator tip clearance flows, it is possible to visualize a possible flow structure generated in the blade passage and downstream of the blade row. Fluid enters the blade row with significant skew, caused in the main by losses from upstream leakage jets. This inlet skew causes peak suction pressures to occur closer to the blade leading edge. Unlike the blade root location, where there is no clearance, at the tip this reduced pressure is then maintained by the radial flow of fluid going through the clearance gap. As the clearance is increased, in the case of the rotor from 1.2 percent t/c to 3 percent t/c, the length of chord in which the static pressure peak is maintained also increases. The implication is that more fluid enters the leakage jet and more energy is therefore dissipated by the eventual decay of the tip leakage vortex. At the design flow point, in this compressor configuration an increase in the rotor tip clearance from 1.2 percent to 3 percent t/c resulted in a 0.6 percent reduction in the overall compressor efficiency.

5 Conclusions

Detailed pneumatic area traverses have been carried out at inlet and outlet of both rotor and stator in the third stage of a large-scale, low-speed, four-stage, axial flow, research compressor. In addition, chordwise static pressure distributions for both rotor and stator at three radial heights and at two values of rotor tip clearance have been presented. Laser measurements in the tip region of the rotor show rotor relative flows in, and downstream of, the rotor passage.

Measurements throughout the third stage show a region of low loss, "two-dimensional," ordered flow for approximately 40 to 85 percent annulus span. Outside of this region lower values of total pressure are measured. These are due to upstream stator and rotor tip leakage losses as well as other endwall effects. These low pressures result in high incidence to the following blade rows. As a consequence, the rotor peak suction pressure point at the blade root occurs at 20 percent chord as opposed to 30 percent chord measured at midspan. At the tip, the peak suction pressure point also occurs nearer the leading edge at approximately 12 percent chord, but then remains fairly constant with chord. This is believed to be caused by fluid traveling radially up the suction surface as it is entrained into the leakage jet. The length of chord where this entrainment occurs is seen to increase by approximately 10 percent when the rotor clearance is increased from 1.2 to 3 percent t/c. The rotor leakage jet is measured at 33 percent chord and its "roll up" into a vortex is indicated by isocline patterns at 125 percent chord. The rotor vortex is shown coincident with the blade wakes.

Inlet conditions to the stator show increased incidence at the root and tip. At the tip location a suction surface entrainment length, in which static pressure does not vary with chord, is produced in a similar manner to that measured on the rotor. The stator vortex is also shown at 125 percent chord, but unlike the rotor it is situated at midpitch and not coincident with the blade wakes.

Acknowledgments

The project was funded by the European Community, Rolls-Royce, Snecma, and Turbomeca as BRITE/EURAM Program No. AERO-0021-C. The project officer was Dr. R. Dunker.

References

Dean, R. C., 1954, "The Influence of Tip Clearance on Boundary Layer Flow in a Rectilinear Cascade," Massachusetts Institute of Technology, Report No. 27-4, Dec.

Goto, A., 1992, "Three-Dimensional Flow and Mixing in an Axial Flow Compressor With Different Rotor Tip Clearances," ASME JOURNAL OF TURBOMACHINERY, Vol. 114, pp. 675–685.

Hesselgreaves, J. E., 1969, "A Correlation of Tip Clearance/Efficiency Measurements on Mixed Flow and Axial Turbomachines," presented at the 3rd NEL Conference on Hydraulics and Hydraulic Machinery, Budapest.

Howard, M. C., Ivey, P. C., Barton, J. P., and Young, K. F., 1994, "Endwall Effects at Two Tip Clearances in a Multistage Axial Flow Compressor With Controlled Diffusion Blading," ASME JOURNAL OF TURBOMACHINERY, Vol. 116, pp. 635–647.

Inoue, M., Kuroumaru, M., and Fukuhara, M., 1986, "Behavior of Tip Leakage Flow Behind an Axial Compressor Rotor," ASME *Journal of Engineering for Gas Turbines and Power,* Vol. 108, pp. 7–14.

Krain, H., 1988, "Swirling Impeller Flow," ASME JOURNAL OF TURBOMACHINERY, Vol. 108, pp. 122–128.

Lakshminarayana, B., and Horlock, J. H., 1965, "Leakage and Secondary Flows in Compressor Cascades," A. R. C. 3486, Mar.

Lakshminarayana, B., 1970, "Methods of Predicting the Tip Clearance Effects in Axial Flow Turbomachinery," ASME *Journal of Basic Engineering,* Vol. 92, p. 467.

Lakshminarayana, B., Zaccaria, M., and Marathe, B., 1991, "Structure of Tip Clearance Flow in Axial Flow Compressors," ISABE Paper No. 91-7144.

Lymberopoulos, N., Giannakoglou, K., Nikolaou, I., Papailiou, K., Tourlidakis, A., and Elder, R., 1993, "Modeling of Tip Clearance Flows Through an Improved Three-Dimensional Pressure Correction Navier–Stokes Solver," ASME Paper No. 93-GT-374.

Nikolos, I., Couvikas, D., and Papailiou, K., 1993, "A Method for the Calculation of the Tip Clearance Flow Effects in Axial Flow Compressors: Part 1—Description of Basic Models; Part 2—Calculation Procedure," ASME Papers No. 93-GT-150 and 93-GT-151.

Rains, D. A., 1954, "Tip Clearance Flows in Axial Compressors and Pumps," PhD Thesis, California Institute of Technology, Pasadena, CA.

Robinson, C. J., Northall, J. D., and Mcfarlane, C. W. R., 1989, "Measurement and Calculation of the Three-Dimensional Flow in Axial Compressor Stators With and Without End-Bends," ASME Paper No. 89-GT-6.

Robinson, C. J., 1991, "End-Wall Flows and Blading Design for Axial Flow Compressors," PhD Thesis, Cranfield Institute of Technology, United Kingdom.

Ross, M. M., 1980, "Transit Laser Anemometry Data Reduction for Flow in Industrial Turbomachinery," *Optica Acta,* Vol. 27, No. 4, pp. 511–528.

Smith, L. H., Jr., 1966, "Wake Dispersion in Turbomachines," *Transactions of the ASME,* Vol. 88, pp. 688–690.

Stauter, R. C., 1993, "Measurements of the Three-Dimensional Tip Region Flow Field in an Axial Compressor," ASME JOURNAL OF TURBOMACHINERY, Vol. 115, pp. 468–476.

Storer, J. A., and Cumpsty, N. A., 1991, "Tip Leakage Flow in Axial Compressors," ASME JOURNAL OF TURBOMACHINERY, Vol. 113, pp. 252–259.

Storer, J. A., and Barton, J. P., 1991, "An Investigation of the Flow Within the Clearance Space of a Compressor Blade Tip," ISABE Paper No. 91-7013.

Vavra, M. H., 1960, *Aerothermodynamics and Flow in Turbomachines,* Wiley, New York.

Wisler, D. C., 1985, "Loss Reduction in Axial-Flow Compressors Through Low-Speed Model Testing," ASME *Journal of Engineering for Gas Turbines and Power,* Vol. 107, pp. 354–363.

Downloaded 01 Jun 2010 to 171.66.16.53. Redistribution subject to ASME license or copyright; see http://www.asme.org/terms/Terms_Use.cfm

Experimental and Computational Investigation of the Tip Clearance Flow in a Transonic Axial Compressor Rotor

K. L. Suder
NASA-Lewis Research Center,
Cleveland, OH 44135

M. L. Celestina
Sverdrup Technology Inc.,
Lewis Research Center Group,
Cleveland, OH 44135

Experimental and computational techniques are used to investigate tip clearance flows in a transonic axial compressor rotor at design and part-speed conditions. Laser anemometer data acquired in the endwall region are presented for operating conditions near peak efficiency and near stall at 100 percent design speed and at near peak efficiency at 60 percent design speed. The role of the passage shock/leakage vortex interaction in generating endwall blockage is discussed. As a result of the shock/vortex interaction at design speed, the radial influence of the tip clearance flow extends to 20 times the physical tip clearance height. At part speed, in the absence of the shock, the radial extent is only five times the tip clearance height. Both measurements and analysis indicate that under part-speed operating conditions a second vortex, which does not originate from the tip leakage flow, forms in the end-wall region within the blade passage and exits the passage near midpitch. Mixing of the leakage vortex with the primary flow downstream of the rotor at both design and part-speed conditions is also discussed.

Introduction

Endwall flow fields continue to be the focus of many research efforts because of their impact on compressor stability and performance. For example, Wisler (1985) reports that an increase in tip clearance from 1.4 to 2.8 percent of blade height in a low-speed multistage compressor resulted in a 1.5 point efficiency penalty, an 11 percent reduction in flow range, and a 10 percent reduction in peak pressure rise. The accumulation of low-momentum fluid near the blade tip and the vortical structure of the flow downstream of low-speed compressors has been documented by Inoue et al. (1986), Inoue and Kuroumaru (1989), McDougall (1990), Stauter (1993), and others. Inoue and Kuroumaru (1989) have also provided data concerning the endwall flow field within the compressor blade passage in a low-speed compressor. Although these investigations have shed light on the endwall flow in low-speed machines, there is much less information concerning the endwall flow fields within the blade passage in high-speed compressors. Measurements reported have been primarily limited to high-response static pressure data over the rotor tip, for example those of Copenhaver et al. (1993).

Our understanding of the endwall flow has been enhanced by models of the tip clearance flow developed from detailed measurements in the endwall region of low speed compressors. For example, Storer and Cumpsty (1994) have shown that the losses due to the tip leakage flow are primarily associated with the mixing process that takes place between the leakage flow and the throughflow, and that these losses can be predicted from the angle formed between the clearance flow and the throughflow. In addition, Chen et al. (1991) developed a model to describe the trajectory of the leakage vortex. These modeling efforts have yielded reasonable agreement with data available from low-speed compressors.

Due to the limited availability of detailed measurements, our understanding of the endwall flow in high-speed compressors has been largely obtained from numerical simulations. In high-speed compressors, the endwall flow is further complicated by the interaction between the rotor passage shock and the tip leakage flow. Adamczyk et al. (1993) and Copenhaver et al. (1993) have used three-dimensional Navier–Stokes solvers to study this shock/vortex interaction. Adamczyk studied the effect of variations in tip clearance on the performance of a transonic rotor, and showed that the shock/vortex interaction plays a major role in determining the compressor flow range. Although such efforts have improved our understanding of the endwall flow over the last 5–10 years, we continue to have difficulty in accurately predicting the blockage in the endwall region, especially in multistage compressors. It is clear that there is a need for detailed experimental data within high-speed compressors to assess numerical simulations and models, and to enhance our understanding of the shock/vortex interaction and its affect on blockage.

The objectives of this investigation are (1) to study the shock/vortex interaction in a high-speed compressor and its impact on the endwall blockage, and (2) to study the development of the tip leakage vortex within and downstream of the compressor rotor with and without the presence of a rotor passage shock. In order to achieve these objectives, the present effort couples experimental measurements with three-dimensional Navier–Stokes numerical simulations of the endwall flow within a highly loaded transonic axial compressor rotor. Measurements and numerical simulations are presented for both transonic and subsonic operating conditions. The numerical simulations are presented to illustrate the interaction between the tip leakage flow and the rotor passage shock and the generation of blockage that results from this interaction. Laser anemometer measurements acquired at design speed for operating conditions near peak efficiency and near stall are presented to show the effect of varying the rotor back pressure on the shock/vortex interaction and endwall blockage. Additional measurements acquired within and downstream of the blade row are presented to illustrate the mixing of the leakage vortex with the primary flow.

Contributed by the International Gas Turbine Institute and presented at the 39th International Gas Turbine and Aeroengine Congress and Exposition, The Hague, The Netherlands, June 13–16, 1994. Manuscript received by the International Gas Turbine Institute March 4, 1994. Paper No. 94-GT-365. Associate Technical Editor: E. M. Greitzer.

Copyright © 1996 by ASME

Downloaded 01 Jun 2010 to 171.66.16.53. Redistribution subject to ASME license or copyright; see http://www.asme.org/terms/Terms_Use.cfm

Test Facility

The experiment was performed in the single-stage transonic compressor facility at the NASA Lewis Research Center. This is an open loop facility with atmospheric inlet and exit conditions. The mass flow rate is measured by an orifice plate located far upstream of the compressor and a downstream throttle valve is used to backpressure the rotor. A detailed description of the facility is given by Urasek and Janetzke (1972).

The test compressor was designed as an inlet stage for a core compressor and is designated as NASA Stage 37. For this experiment the rotor was tested in isolation to avoid the interaction effects generated by the presence of an upstream inlet guide vane or downstream stator blade row. The rotor design pressure ratio is 2.106 at a mass flow of 20.19 kg/s. The inlet relative Mach number is 1.13 at the hub and 1.48 at the tip at the design speed of 454 m/s. The rotor aspect ratio is 1.19 and the hub/tip radius ratio is 0.70. Details of the rotor aerodynamic design were reported by Reid and Moore (1978). Overall aerodynamic performance of the stage was reported by Moore and Reid (1980).

The rotor tip clearance was measured using both a Rotodata touch probe and rub probes. The uncertainty in the touch probe and rub probe clearance measurements is estimated to be 0.05 mm (0.002 in.). Touch probe measurements were obtained at 10, 50, and 90 percent of rotor chord at one circumferential location on the compressor casing and indicated a design speed tip clearance of 0.330 mm with a variance of 0.005 mm. The rub probes were located in three different regions around the circumference and indicated an average tip clearance of 0.320 mm with a variance of 0.120 mm. Both the touch probe and the rub probes measure the longest blade and therefore yield a conservative measure of the tip clearance. An inspection of the rotor wheel assembly at the conclusion of testing revealed that the variance in tip radius was ±0.075 mm. Therefore, 0.075 mm was added to the average clearance probe measurement of 0.325 mm to arrive at an estimated clearance of 0.400 mm (0.016 in.), which corresponds to 0.5 percent of blade span and 0.7 percent of rotor tip chord.

Laser Anemometer System

Detailed flow field measurements are acquired with a two-color fringe-type laser anemometer system. The two anemometer channels are configured to acquire the tangential and axial velocity components simultaneously. One of the laser beams in each of the two channels is frequency shifted to enable detection of flow reversals. The effective length of the measurement volume is reduced by using a short focal length f2 focusing lens and by using optical masks in the collection optics. The measurement volume is 60 μm in diameter and has an effective length of 0.5 mm, which corresponds to less than 1 percent of the blade span. The uncertainties in the laser anemometer velocity and flow angle measurements are estimated as 1 percent and 0.5 deg, respectively.

Polystyrene latex spheres are injected into the facility ducting far upstream of the compressor rotor and serve as the seed material for the laser anemometer system. The seed particles are manufactured at NASA-Lewis using the procedure developed by Nichols (1987). Scanning electron microscope inspections of the seed particles within a given batch indicate that they are spherical in shape and uniform in size. However, the mean particle diameter varies from batch-to-batch over a range of 0.7–0.9 μm. Laser anemometer measurements acquired under identical operating conditions with particles manufactured in different batches indicate that there are no differences in the measurements attributable to particle size variations within this range.

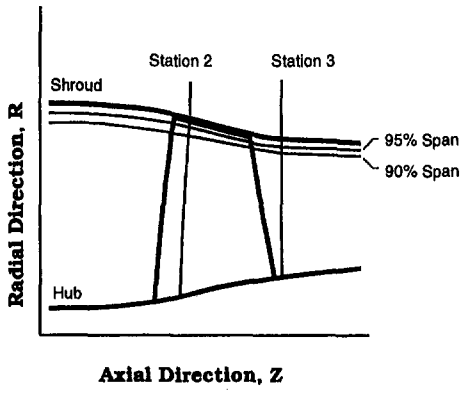


Fig. 1 Laser anemometer survey planes

A 2.54-mm-thick alumina silica window, which is contoured in both the axial and circumferential directions to conform to the rotor flowpath, provides optical access to the flow field. The window extends more than one rotor chord upstream and three rotor chords downstream, providing continuous access throughout the rotor flow field.

Laser anemometer measurements are acquired upstream, within, and downstream of the rotor along the 90 and 95 percent span stream-surfaces shown in Fig. 1 at axial intervals of approximately 5 percent rotor chord. The measurements are synchronized to the rotor circumferential position using a high-frequency clock and supporting electronics as described in Hathaway et al. (1993). At each axial location, data are acquired across all blade passages at a circumferential resolution of 184 points across a blade pitch. The flow field is also surveyed along cross-channel planes such as stations 2 and 3 shown in Fig. 1, nominally over the outer 20 percent of span in radial increments of 2 percent span. Measurements were made as close as 1 mm (0.040 in.) from the shroud, which corresponds to 2.5 times the clearance gap.

All laser anemometer results presented are based on the velocity distribution across an averaged blade passage, which is calculated by ensemble-averaging the measurements acquired in each individual blade passage. The relative Mach number is calculated from the relative velocity and the local speed of sound at each point in the flow field using the procedure discussed by Strazisar et al. (1989). The radial velocity component, which is not measured by the laser anemometer, is ignored in the calculation of the measured relative Mach number. Using the predicted flow fields generated by the three-dimensional Navier–Stokes simulations described below, we calculated the Mach number distributions throughout the flow field with and without the radial velocity component included and found that ignoring the radial velocity component resulted in a maximum error of only 2 percent. All measured Mach number distributions presented below do not include the radial velocity component,

Nomenclature

M_{rel} = relative Mach number
P_{ref} = standard day total pressure = 101,325 n/m^2
ps = denotes pressure surface
q_{rel} = relative dynamic head normalized by P_{ref}
R = radial direction
ss = denotes suction surface
Z = axial direction
θ = circumferential direction

Downloaded 01 Jun 2010 to 171.66.16.53. Redistribution subject to ASME license or copyright; see http://www.asme.org/terms/Terms_Use.cfm

while all predicted Mach number distributions do include the radial velocity component.

Computational Procedure

The analysis code used in the present study solves the Reynolds-averaged form of the Navier–Stokes equations. Details of the code can be found from Adamczyk et al. (1989). The flow in the clearance gap was simulated using a model suggested by Kirtley et al. (1990), which treats the clearance flow as an orifice flow with no loss in mass, momentum, or energy. The effect of the vena contracta, which occurs in orifice flows, is accounted for by using a discharge coefficient, which makes the effective tip clearance gap smaller than the actual clearance. A discharge coefficient of 0.5 is used for all results presented herein.

The grid used in the simulations had 51 cells in the radial direction, 41 cells in the circumferential direction, and 132 cells were placed between the inlet and exit boundaries, of which 41 were along the blade chord line. The clearance gap was spanned by two cells in the radial direction. The grid in the clearance gap region above the rotor tip is constructed by simply extending the grid below the tip to the shroud while maintaining the tangential distance across the blade passage fixed to its value at the rotor tip. The number of grid points spanning the gap in the radial direction would be too few if one were interested in resolving the details of the flow entering and exiting the gap, as done by Crook (1989). In the present study, however, we are interested mainly in the clearance flow interaction with the primary throughflow in the blade passage. Several studies have shown that reasonable estimates of this interaction can be obtained without a detailed description of the flow exiting the gap if one has a good estimate of the gap mass flow. This can be accomplished in a numerical simulation with as few as one grid cell spanning the radial direction if one accounts for the blockage introduced by the vena contracta.

Results and Discussion

Design Speed Computational Results. Computational results generated for operating conditions near peak efficiency and near stall are presented first in order to identify key features associated with the tip clearance flow and to aid in the interpretation of experimental results. Flow field predictions were generated for a clearance of 0.356 mm (0.014 in.) as well as a larger clearance of 0.584 mm (0.023 in.) or 0.6 and 1.0 percent of rotor tip chord, respectively. The results indicated that there were no significant qualitative differences in the vortex trajectory or relative Mach number distribution between the predicted endwall flow fields for these two levels of clearance. All numerical results presented below are therefore based on a tip clearance of 0.356 mm (0.014 in.). Computational results are presented in terms of (1) relative Mach number and relative dynamic head on a blade-to-blade stream surface at a radius below the blade tip, and (2) pathlines of particles released in the clearance gap. Relative Mach number contours are used to provide a direct comparison with the experimental data, while contours of the relative dynamic head depict the blockage in the blade passage. Pathlines of particles released in the clearance gap are shown to illustrate the formation and trajectory of the leakage vortex. The numerical results indicate that the key flow features associated with the clearance flow occupy the outer 3 percent of blade span, and the results are therefore presented on a blade-to-blade stream surface at 98 percent of blade span, which passes through the approximate center of this region.

Predicted relative Mach number contours are shown in Fig. 2(*a*). The Mach number contours are drawn in increments of 0.1 and the same color bar is used for both peak efficiency and near stall. At near-peak efficiency the passage shock is oblique and is attached to the leading edge, while at near stall the shock is nearly normal and is detached from the leading edge. The near-stall results indicate a distortion of the passage shock near midpitch and there is evidence of a similar but weaker distortion in the shock front at the near-peak efficiency condition. At both operating conditions a region of low Mach number fluid originates near midpitch just downstream of the shock and migrates toward the pressure surface of the blade. At the near-peak efficiency condition the fluid in this region merges with the wake downstream of the blade.

Distributions of the relative dynamic head at 98 percent span, normalized by inlet total pressure, are presented in Fig. 2(*b*) to illustrate the correlation between the flow features described above and flow blockage within the blade passage. At the near-stall condition, a region of low dynamic head originates at the leading edge of the blade, crosses through the shock near midpitch, and continues downstream near the pressure surface. The dynamic head just downstream of the shock is extremely low, and corresponds to only 20 percent of the upstream dynamic head. This represents a severe flow blockage within the center of the blade passage. Similar features are evident at the near-peak efficiency condition, although the loss in dynamic head is less severe than at near stall. A comparison of the relative Mach number to the relative dynamic head contours in Fig. 2 indicates that a region of low Mach number coincides with a region of low dynamic head. Therefore, regions of low Mach number are also indicative of blockage.

The origin of the fluid located in the regions of low dynamic head was determined by tracking the pathlines of fluid particles which pass through the rotor tip clearance gap. These pathlines are illustrated in Fig. 2(*c*). Note that the pathlines are not constrained radially (in other words the radius changes along a pathline), and that Fig. 2(*c*) is simply a view of the pathlines as seen by an observer looking radially inward toward the hub. Also shown in Fig. 2(*c*) is the location of the shock front, which is depicted by the relative Mach number contour level of 1.4 and a shaded region representing the relative dynamic head contour level of ≤ 0.5 from the computational results at 98 percent span. The pathlines are shown only for those particles that pass through the clearance gap in the first 20 percent of blade chord, since inspection of the pathlines of particles that pass through the clearance gap downstream of 20 percent chord indicates that these particles do not contribute substantially to the formation of the clearance vortex. The results in Fig. 2(*c*) illustrate that fluid that passes through the clearance gap in the first 20 percent of chord rolls into a vortex and that the path of this vortex coincides with the shock front distortion and the region of low dynamic head downstream of the shock. A comparison of the pathlines and Mach number distributions further shows that the vortex path between the leading edge and the shock front can be inferred from the distortion of the Mach contour lines in this region. Using the relative dynamic head contour of 0.5 to identify the blockage region, we see that the blockage region is larger and is located further upstream for the near stall compared to the near peak efficiency operating condition. Also, note that the leakage vortex penetrates closer to the blade pressure surface at near-peak efficiency than at near stall condition. Upstream of the shock the vortex trajectory is nearly identical for the two operating conditions. As the vortex crosses the shock, it is diffused by the pressure gradient and is more readily turned by the throughflow. Since the pressure gradient across the shock is greater at the near-stall than at the near-peak efficiency operating condition, the vortex experiences a greater diffusion and is turned more by the throughflow at the near-stall as compared to the near-peak efficiency operating condition.

In summary, the computational results indicate that the clearance flow over the front portion of the rotor chord forms a well-defined vortex, which moves toward the pressure side of the blade passage. A distortion of the passage shock arises from the interaction between this vortex and the shock. The severe pressure rise across the shock causes a substantial diffusion of the vortex, resulting in

Downloaded 01 Jun 2010 to 171.66.16.53. Redistribution subject to ASME license or copyright; see http://www.asme.org/terms/Terms_Use.cfm

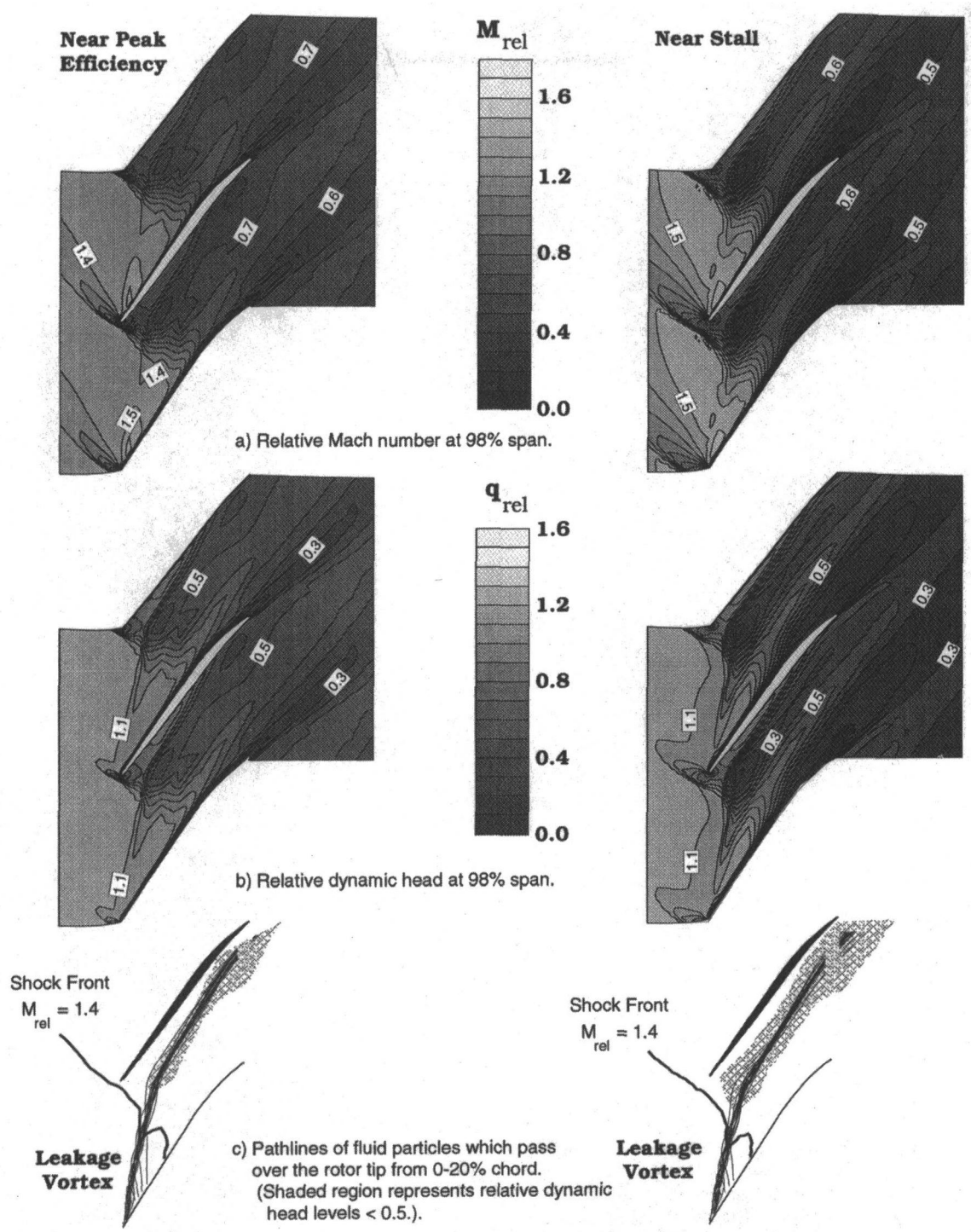


Fig. 2 Computational results at design speed for near-peak efficiency (left column) and near-stall (right column) operating conditions

a region of very low dynamic head, which occupies almost half of the blade pitch downstream of the shock. (A more quantitative examination of the vortex diffusion will be presented in the experimental results discussion.) In addition, these features of the vortex are depicted in the relative Mach number distribution, which is important in light of the fact that the relative Mach number is a quantity that can be determined from laser anemometer surveys of the rotor flow field.

Design Speed Experimental Results. Due to reflections from the window surface and blade tips, 95 percent span is the closest approach to the shroud at which laser anemometer measurements were successfully acquired within the rotor. In the previous section the computational results were presented at 98 percent span. However, the tip clearance flow features, such as the distortion of the passage shock and the development of regions of low relative dynamic head, identified from the computational results presented at 98 percent span, were representative of those throughout the region of influence of the tip clearance flow (over the outer 3 percent of span). Comparisons of the computations to the experiment, though not shown herein, have revealed that the computations predict the correct structure of the leakage vortex but underpredict the radial extent of influence of the tip leakage flow. However, we are only concerned

Downloaded 01 Jun 2010 to 171.66.16.53. Redistribution subject to ASME license or copyright; see http://www.asme.org/terms/Terms_Use.cfm

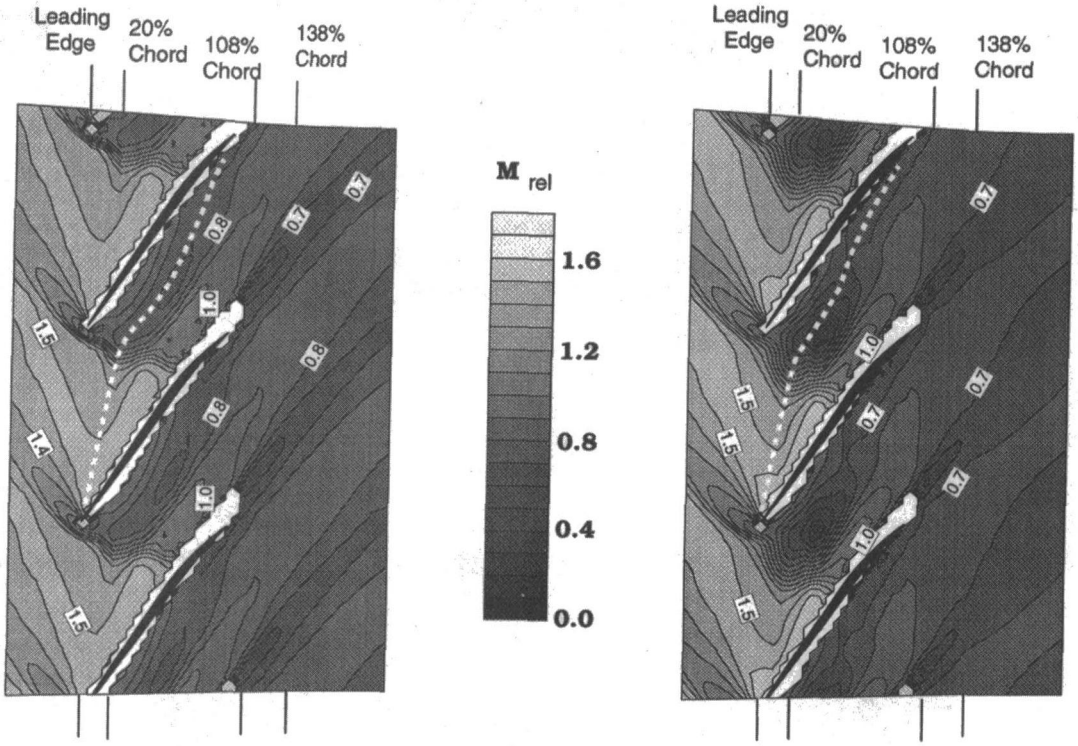


Fig. 3 Measured relative Mach number contours at 95 percent span for near-peak efficiency and near-stall operating conditions at design speed [. . . estimated clearance vortex path]

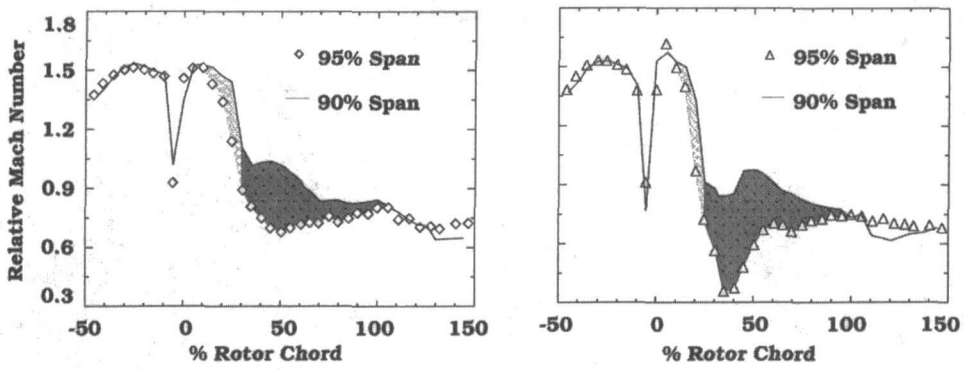
with using the computations to identify the structure of the leakage vortex in this paper. Therefore, the conclusions drawn from the computations at 98 percent span are used to interpret the data at 95 percent span.

Clearance Vortex Path. Relative Mach number distributions measured on the 95 percent span stream surface at the near-peak efficiency and near-stall operating points are shown in Fig. 3, plotted to the same color scale as that used for the numerical results in Fig. 2(*a*). The location of cross-channel planes at 20, 108, and 138 percent chord, which will be discussed below, is also shown. The white areas in each plot indicate regions in which laser anemometer measurements could not be made due to reflections from the blades and optical blockage of the laser beam paths by the blades. The clearance vortex path upstream of the shock can be inferred from the deflections of the Mach contour lines, and is shown by a broken line. The vortex path is in good agreement with the path predicted by the numerical analysis. The experimental results also confirm the predicted distortion of the shock front. The presence of the blockage region in the pressure surface half of the blade passage downstream of the shock is also confirmed by the low relative Mach numbers measured in this region. The data indicate that the fluid within the clearance vortex downstream of the shock migrates toward the pressure surface more rapidly than predicted by the numerical analysis, and impacts on the blade pressure surface before reaching the blade trailing edge. The vortex fluid then appears to merge with the rotor wake fluid for both the peak efficiency and the near-stall operating conditions. Using the location of lowest Mach number to indicate the "heart" of the blockage region and the level to represent the severity, the data confirm the computational results in that the blockage becomes more severe and is located further upstream as the rotor back pressure is increased from near-peak efficiency to near-stall operating conditions.

Clearance Vortex Blockage. Comparison of the blade-to-blade Mach number distributions discussed above to similar results obtained at 90 percent span, which are not shown here, indicates that the upstream relative Mach number and blade incidence angle is virtually identical at 90 and 95 percent span. (The inlet relative Mach number differs by only 0.01 and the blade incidence angle differs by only 0.5 between 90 and 95 percent span results.) We can therefore assume that differences in the 90 and 95 percent span flow fields within the blade row are due to the influence of the tip clearance flow. We can use this assumption to illustrate the strength of the blockage resulting from the clearance flow by comparing measurements obtained at these two immersions. Figure 4 is a comparison of the relative Mach number distributions measured along the vortex trajectories shown in Fig. 3 by the dashed lines. The symbols represent the data acquired at 95 percent span and the solid line represents the data acquired at 90 percent span. The lightly shaded region represents the influence of the leakage vortex on the Mach number distribution upstream of the shock/vortex interaction and the darker shaded region represents the influence of the leakage vortex downstream of the shock/vortex interaction. The Mach number distributions are identical upstream of the leading edge and nearly identical within the blade passage upstream of the shock/vortex interaction, which occurs at approximately 20 percent chord, indicating that the vortex has very little influence at 95 percent span upstream of the shock. However, the most striking feature shown in Fig. 4 is the Mach number difference in the region between the shock and the trailing edge, which is evidence of the blockage generated when the clearance vortex crosses the shock.

Clearance Vortex Impact on Tip Stall. McDougall et al. (1990) have suggested that flow spillage forward of the blade passage triggers the onset of stall. Adamczyk et al. (1993) performed numerical simulations similar to those used herein,

Downloaded 01 Jun 2010 to 171.66.16.53. Redistribution subject to ASME license or copyright; see http://www.asme.org/terms/Terms_Use.cfm



a) Near Peak Efficiency

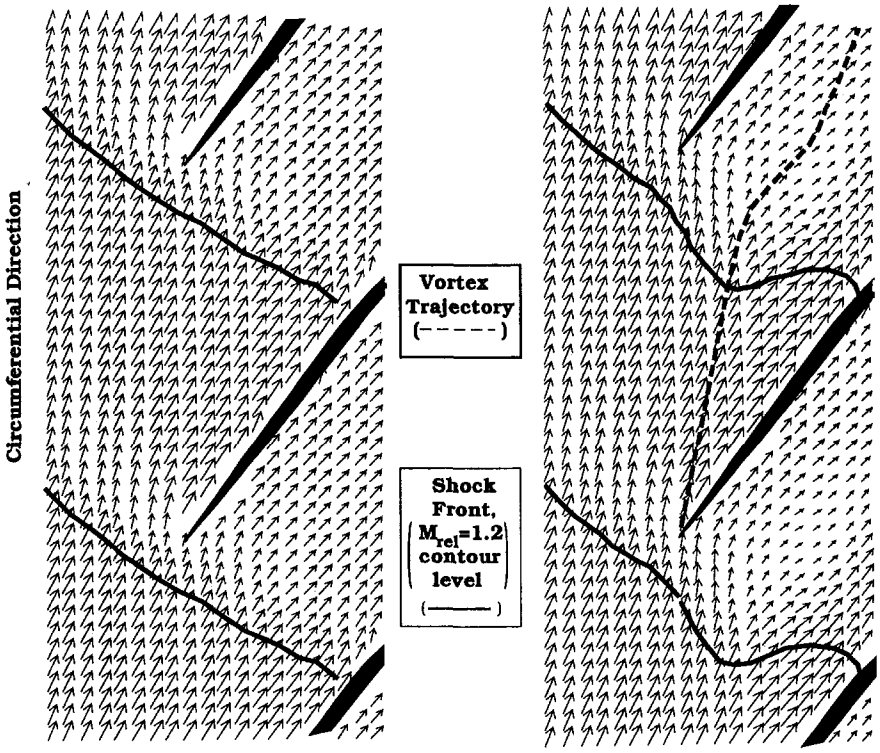
b) Near Stall

Fig. 4 Measured relative Mach number distributions along the vortex trajectory indicating the blockage generated by the shock/vortex interaction

which indicate that at a near-stall operating point, spillage of low-energy fluid in the clearance flow drives the shock further forward, altering the upstream wave pattern, reducing the mass flow rate, and increasing the blade incidence angle. This process resulted in a steady reduction in mass flow rate as the simulation time proceeded, and ultimately lead to numerical stall. While it is not clear whether spillage and high incidence cause stall, it does appear that there is a strong link between the presence of these flow features and the onset of stall. The present experimental results are therefore investigated in more detail for evidence of these flow features at the near-stall operating condition.

Relative velocity vectors measured at 90 and 95 percent span for the near-stall flow point are shown in Fig. 5 along with the shock front location as depicted by the relative Mach number contour level of 1.2. The vectors are presented at every 5 percent chord in the axial direction. For the sake of clarity, vectors are plotted for every eighth circumferential location at which data was acquired. The length of each vector indicates the magnitude of the relative velocity normalized by the maximum velocity in each respective plot.

At 90 percent span, which is relatively free from tip clearance flow effects, the flow just downstream of the shock is turned toward the pressure surface, resulting in a slight increase in incidence angle at the nose of the blade. In contrast, at 95 percent span the interaction of the leakage vortex and the passage shock results in a large region of high relative flow angle downstream of the shock. The relative flow in this region is nearly tangential, indicating that the axial velocity is near zero



a) 90% Span

b) 95% Span

Fig. 5 Measured relative velocity vectors at 90 and 95 percent span for the near-stall operating condition at design speed

Downloaded 01 Jun 2010 to 171.66.16.53. Redistribution subject to ASME license or copyright; see http://www.asme.org/terms/Terms_Use.cfm

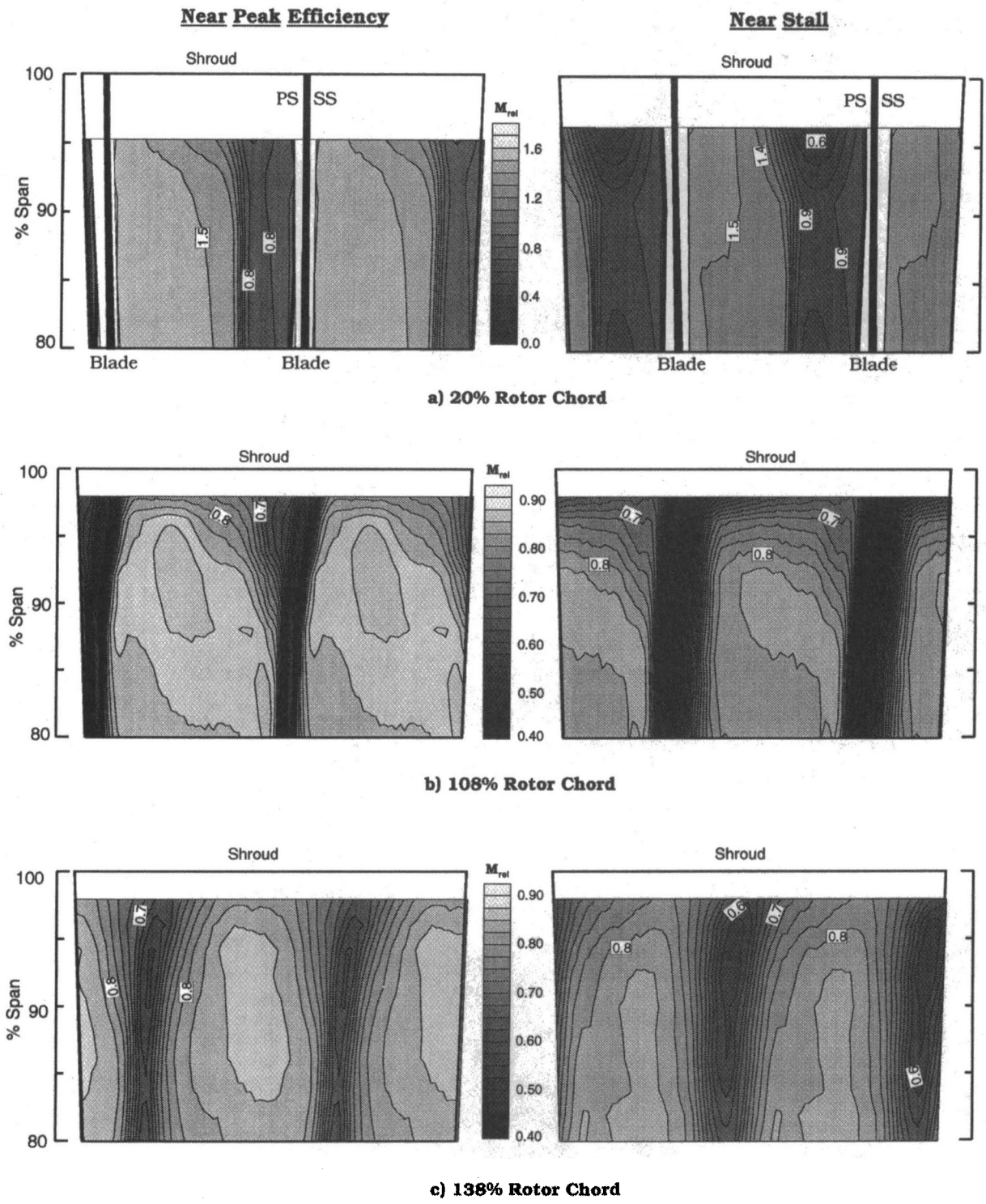


Fig. 6 Measured cross-channel Mach number distributions at design speed for near-peak efficiency (left column) and near-stall (right column) operating condition

in this region. The fluid in this region is moving toward the pressure surface, contributing to a high incidence angle at the nose of the blade. It seems plausible that any further increase in rotor backpressure will lead to a stall of the blade section at 95 percent span.

In summary, the experimental results shown in Fig. 5 suggest that flow blockage caused by the shock/vortex interaction results in axial velocities that are nearly zero in the interaction region. This in turn generates high relative flow angles near the nose of the blade. These results suggest that an alleviation of the blockage generated by the shock/vortex interaction by using casing treatment or alternate blade tip designs could result in an increase in stable operating range by reducing the incidence angle at the blade tip.

Radial Extent of the Clearance Flow. Thus far we have examined the flow along a blade-to-blade streamsurface. We will now consider the radial extent of the shock/vortex interaction by presenting measured Mach number distributions on cross-channel $(R-\theta)$ planes at the axial stations shown in Fig.

Downloaded 01 Jun 2010 to 171.66.16.53. Redistribution subject to ASME license or copyright; see http://www.asme.org/terms/Terms_Use.cfm

3. The first axial location to be discussed is 20 percent chord, which corresponds to the approximate location of the shock/vortex interaction. The second axial plane is located just downstream of the blade at 108 percent rotor chord, where the impact of the clearance vortex on the rotor wake structure is evident. The final axial location to be presented is located at 138 percent rotor chord and coincides with the location of the stator leading edge plane if the stator was installed. Comparison of the results obtained at 108 and 138 percent chord will be used to illustrate the mixing of the clearance flow downstream of the rotor.

The cross-channel Mach number distributions at 20 percent chord are presented in Fig. 6(a). The white regions adjacent to the blade surfaces denote areas in which measurements could not be acquired due to optical blockage. The Mach number contours are incremented by 0.1. The distortion of the rotor shock, as depicted by the Mach contours bending toward the blade suction surface near the endwall, is seen for both operating conditions. Both the circumferential and radial extent of the blockage region are larger near stall. The shock distortion that results from the shock/vortex interaction penetrates to approximately 93 percent span for the near-peak efficiency case and to 90 percent span for the near-stall case. Recall that the measured tip clearance is approximately 0.5 percent of span. Therefore, the influence of the clearance flow can be seen over a radial extent that is approximately 20 times the physical clearance in this transonic compressor.

Mixing Downstream of the Rotor. The cross-channel Mach number distributions at 108 percent of rotor chord are presented in Fig. 6(b) in order to study the behavior of the clearance flow downstream of the rotor. Note the color bar has been changed from that of Fig. 6(a), and that the Mach number contours are now incremented by 0.025. The peak efficiency results clearly indicate that the rotor wake is asymmetric outboard of about 90 percent span due to the presence of low Mach number fluid (with Mach numbers in the range 0.55–0.75) in the pressure surface/shroud corner of the flow field. Recall that the measured blade-to-blade Mach number distributions indicated that the low Mach number region downstream of the shock/vortex interaction migrates to the blade pressure surface and impacts on the surface before reaching the blade trailing edge. It therefore seems plausible that the low Mach number fluid in the pressure surface/shroud corner represents the remnants of the clearance vortex as it exits the blade passage. Turning to the near-stall case, we see that the wake is also asymmetric in the outer 10 percent of blade span. However, in the near-stall case, it appears that the low Mach number fluid occupies the entire blade pitch outboard of 95 percent span.

The cross-channel Mach number distributions at 138 percent chord are shown in Fig. 6(c). Note that this is the stator leading edge plane, although the stator was not installed during this investigation. At this location the rotor wakes are nearly symmetric about their centerline. The rotor wakes begin to widen at about 85 and 80 percent of span for the peak efficiency and near-stall conditions, respectively. However, it is not clear that the increased wake width near the shroud is due solely to the continued mixing of the clearance vortex. The radial-outward migration of fluid within the blade wakes also contributes to wake widening near the shroud. The results shown in Fig. 6(b) and 6(c) indicate that the mixing process downstream of the rotor is complex and is still in progress by the time the flow would reach the stator leading edge.

A final observation on the results shown in Fig. 6 concerns the concept of an "endwall boundary layer" downstream of the rotor. Consider the radial gradient in Mach number at midpitch in the peak efficiency results at 108 and 138 percent chord. The radial gradient is quite small at immersions below 97 percent span, indicating that the endwall boundary layer thickness at midpitch is only about 3 percent of span. However, a pitchwise average of the flow field would indicate a considerably thicker endwall boundary layer, since the average will be weighted by the presence of the low Mach number levels within the widened wakes that result from the merging of the clearance vortex fluid with the blade wake fluid. Low-response instrumentation such as total pressure probes, which cannot respond to flow fluctuations at the blade passing frequency, yield such a pitchwise average of the flow field. To illustrate this point the Mach number distribution at 138 percent rotor chord for the near-peak efficiency operating condition was area-averaged in the pitchwise direction at each radial location and is compared to the relative Mach number at midpitch between the blade wakes in Fig. 7. The area-averaged results indicate a roll-off in relative Mach number at 86 percent span compared to 94 percent span for the midpitch results. Since the midpitch results are more indicative of the casing boundary layer, care must be exercised when using low-response instrumentation to measure the endwall boundary layer.

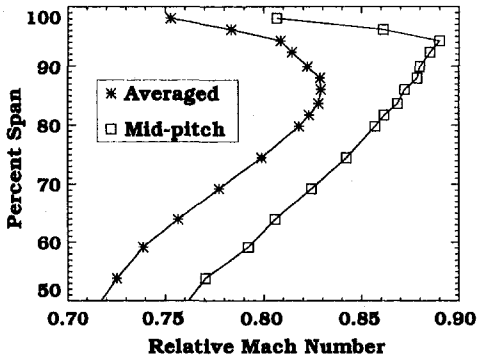


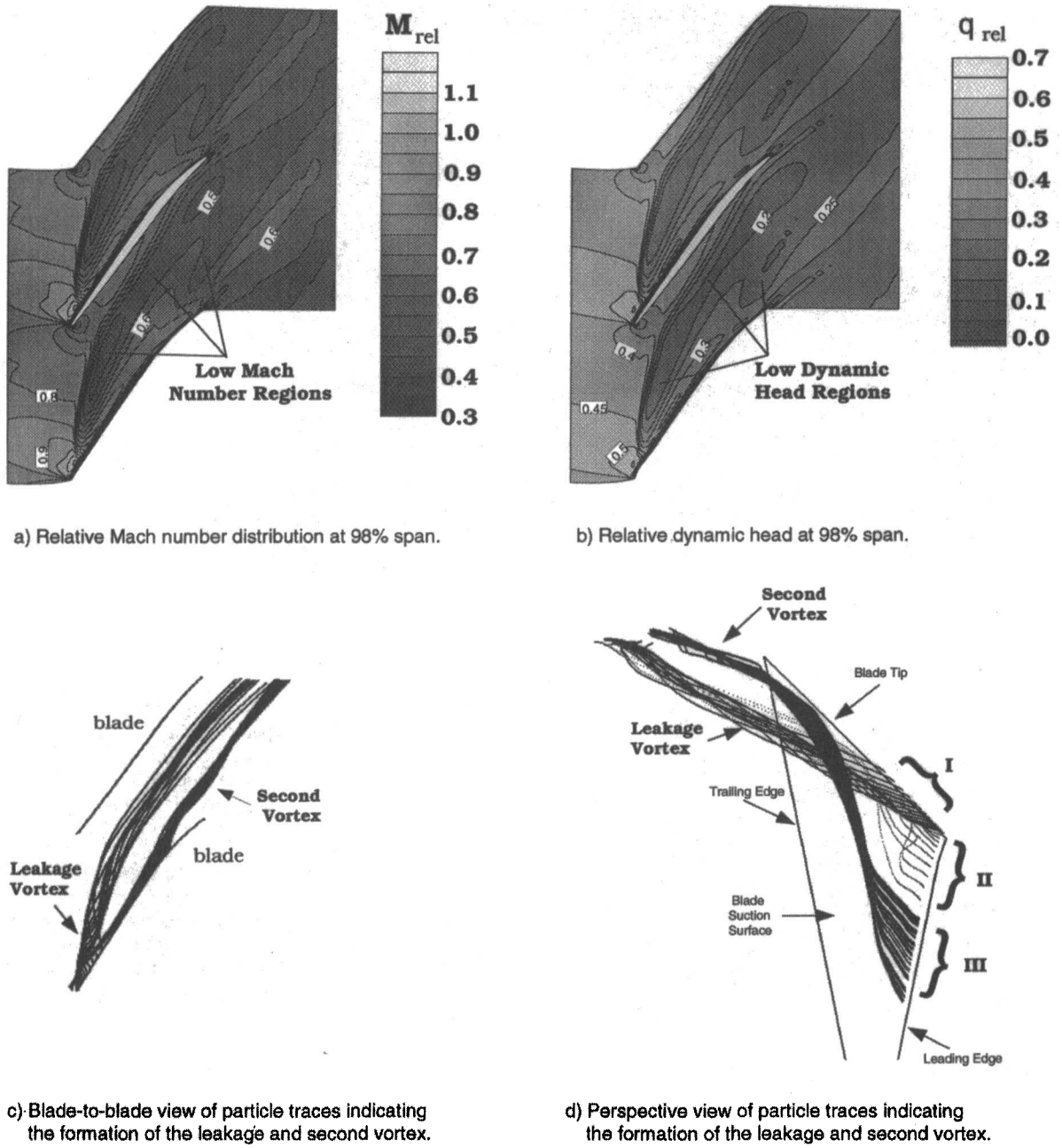
Fig. 7 A comparison of the area-averaged and midpitch values of the measured relative Mach number at 138 percent rotor chord for the peak efficiency operating condition

In summary, at design speed the interaction between the rotor passage shock and the tip leakage vortex generates a blockage in the passage. This blockage moves forward and becomes larger in both the circumferential and radial directions with increased rotor back pressure. At near-stall operating conditions, the blockage associated with the shock/vortex interaction leads to high incidence angles near the blade tip and spillage of flow around the nose of the blade. Within the rotor blade passage, the clearance flow effects extend over the outer 10 percent of blade span. Remnants of the clearance vortex exit the rotor in the pressure surface/shroud corner of the flow field and mix into the rotor wake.

Part-Speed Computational Results. To investigate the tip leakage flow in the absence of the passage shock, the compressor was operated at 60 percent of design speed at the same flow coefficient as the near-peak efficiency case at design speed. Analogous to the design speed case, computational results are presented first in order to identify key features associated with the tip clearance flow and to aid in the interpretation of the experimental results. At 60 percent speed the centrifugal force on the rotor blade is only 36 percent of that at design speed, resulting in a larger tip clearance and a change in blade untwist of approximately 0.5 deg. The computations to be presented for 60 percent speed utilized the same blade geometry as that used at design speed and therefore did not account for the change in blade twist. The 60 percent speed tip clearance was measured to be 0.584 mm (0.023 in.) or 1 percent of rotor tip chord and the computations presented herein do account for this increase in clearance relative to the design speed condition.

The predicted relative Mach number contours and normalized relative dynamic head contours are shown in Fig. 8(a) and 8(b), respectively. These contours are drawn in increments of 0.05 for the blade-to-blade streamsurface at 98 percent span. The regions of low Mach number and low relative dynamic

Downloaded 01 Jun 2010 to 171.66.16.53. Redistribution subject to ASME license or copyright; see http://www.asme.org/terms/Terms_Use.cfm



a) Relative Mach number distribution at 98% span.

b) Relative dynamic head at 98% span.

c) Blade-to-blade view of particle traces indicating the formation of the leakage and second vortex.

d) Perspective view of particle traces indicating the formation of the leakage and second vortex.

Fig. 8 Computational results at 60 percent speed

head coincide and indicate the path of the tip leakage vortex and the location of the blockage associated with the vortex. The trajectory of the tip leakage vortex at 60 percent design speed is similar to that predicted at design speed. However, there is a second region of low Mach number that first appears near the trailing edge of the blade at about 15 percent pitch from the suction surface. An island of low relative dynamic head in this region confirms that there is an additional source of blockage. Particle pathlines were studied in order to determine the source of this second region of low Mach number and low relative dynamic head.

The formation of the tip leakage vortex emanating from the blade leading edge is depicted by the pathlines of particles which pass through the clearance gap and is shown in Fig. 8(c). Note that Fig. 8(c) is a view of the pathlines as seen by an observer looking radially inward toward the hub. Particles released in the clearance gap over the first 35–40 percent of rotor chord are entrained in the leakage vortex. However, for clarity, the fluid particles released over only the first 20 percent of rotor chord are shown. Particles that pass through the clearance gap in the front portion of the blade roll up into a vortex whose trajectory is coincident with the regions of low Mach number and low relative dynamic head that start at the leading edge and cross the passage toward the pressure surface. The pathlines of fluid particles that pass through the clearance gap over the last 60 percent of rotor chord (not shown) do not indicate a roll-up into a vortex. Furthermore, the trajectory of these pathlines does not coincide with the low Mach number region that emanates near the blade trailing edge. To determine the origin of the fluid in this second low Mach number region, particles were released within the region and traced backwards in time. The resulting pathlines are shown in Fig. 8(c) and are denoted as the "second vortex." It is important to note that the fluid forming the second vortex does not pass through the rotor tip clearance gap.

Why does this second vortex form at part speed and not at design speed? For the 60 percent speed near peak efficiency

Downloaded 01 Jun 2010 to 171.66.16.53. Redistribution subject to ASME license or copyright; see http://www.asme.org/terms/Terms_Use.cfm

operating condition, the blade incidence is positive and results in a small region of supersonic flow at the suction surface near the leading edge as indicated in Fig. 8(*a*). This supersonic region at the leading edge extends over the outer 70 percent span. At the downstream edge of the supersonic region, the flow encounters an adverse pressure gradient, which results in a radial migration of fluid along the blade suction surface. The fluid climbing up the suction surface encounters the leakage fluid at the blade tip and rolls up into a vortex. These flow features are depicted by particle pathlines in Fig. 8(*d*), which is a perspective view of approximately the outer 15 percent of blade span. The pathlines of particles released in the clearance gap over the first 20 percent chord, indicated by group "I" in Fig. 8(*d*), illustrate the formation of the leakage vortex. Particles released near the suction surface, indicated by groups "II" and "III," turn radially upward within the first 10 percent rotor chord. This radial migration occurs at the trailing edge of the supersonic region, where the flow encounters the adverse pressure gradient. Particles released along the suction surface from 96–99 percent span (group II) are entrained in the leakage vortex. Therefore, the leakage vortex not only consists of fluid that has passed over the rotor tip, but also includes fluid from the suction surface boundary layer. The second vortex develops from particles originating at 90–95 percent span near the suction surface leading edge (group III). Though not evident from the perspective illustrated in Fig. 8(*d*), the second vortex lies entirely below the tip clearance region. The radial migration of the fluid along the suction surface is the key to the formation of the second vortex. At design speed the flow along the suction surface is expanding behind the shock in a favorable pressure gradient. Particle traces at design speed indicate virtually no radial migration upstream of the shock and downstream of the shock the radial migration is small. In addition, a computation was performed at 60 percent speed using the same tip clearance as that at design speed, which represents a 40 percent reduction in clearance. The second vortex still developed and the radial migration of fluid near the suction surface still occurred. Therefore, the formation of the second vortex is not related to the strength of the clearance flow but rather is due to the secondary flows along the blade suction surface that result from operating at an off-design condition. Laser anemometer data acquired at both 60 percent speed (discussed below) and 80 percent speed (not discussed herein) confirm the presence of this second vortex. It seems plausible that the formation of the second vortex is not specific to this machine, but could exist on many transonic blades operated at off-design conditions.

Part-Speed Experimental Results. Laser anemometer measurements were acquired along the 95 percent span stream surface for the 60 percent design speed case at near-peak efficiency. The experimental results are presented in terms of relative Mach number in Fig. 9. The Mach number contours and color bar are identical to those used for the computational results presented in Fig. 8(*a*). The white areas in Fig. 9 indicate regions in which laser anemometer measurements could not be made due to reflections from the blades and optical blockage of the laser beam paths by the blades. The measured Mach number distribution confirms the numerically predicted region of supersonic flow near the leading edge. Based on the deflections of the Mach number contours, the paths of the leakage and second vortex were estimated and are shown by the dashed lines in Fig. 9. Within the blade passage, the trajectory of the tip leakage vortex that originates at the leading edge is similar to that observed at 100 percent speed in that it migrates across the blade passage and intersects the pressure surface near the blade trailing edge. The path of the second vortex is reflected in the measured Mach number distribution and is in qualitative agreement with the predicted path shown in Fig. 8(*c*).

Radial Extent and Downstream Mixing. The Mach number distributions determined from laser anemometer surveys in a cross-channel plane are presented at four axial locations in Fig. 10 to illustrate the radial extent and the mixing process for both vortices. The scale of all four plots is held constant; however, the radial extent of each plot may vary somewhat because each axial location was surveyed over slightly different areas. The Mach number contours are incremented by 0.025 and the color scale is identical for all four plots. The white regions adjacent to the blade surfaces in the 30 percent chord plot are the regions in which measurements could not be acquired due to optical blockage.

The leakage vortex emanating from the leading edge of the blade will be referred to as Vortex A and that formed in the rear half of the blade near the suction surface will be referred to as Vortex B. Tip leakage Vortex A is shown in Fig. 10(*a*) at the 30 percent chord location. The leakage vortex is located near midpitch and exhibits a radial penetration of about 5 percent of span and a circumferential extent of about 50 percent of blade pitch. Note that even though the tip clearance at part speed is double that of design speed, the radial extent of the leakage flow is about half of that at design speed at this axial location. This difference in radial extent is due to the enlargement of the tip leakage vortex when it encounters the shock at design speed.

As shown in the blade-to-blade Mach number distribution in Fig. 9, Vortex A moves across the passage and impacts on the pressure surface before reaching the blade trailing edge. Therefore, in the Mach number distribution measured at 108 percent chord, Fig. 10(*b*), Vortex A accounts for the low Mach number fluid in the pressure surface/shroud corner of the flow field. This behavior is similar to that of the leakage vortex at design speed. The region of low Mach number fluid at midpitch above 94 percent span corresponds to Vortex B. At 138 percent chord, shown in Fig. 10(*c*), Vortex A has mixed with the rotor wake and is no longer detectable while Vortex B has undergone very little mixing. In fact Vortex B has not mixed out by 225 percent chord as shown in Fig. 10(*d*). Furthermore, the Mach number deficit in the vortex is comparable to that of the blade wake. Therefore, the vortex that forms from suction surface boundary layer fluid and emanates from the rear half of the

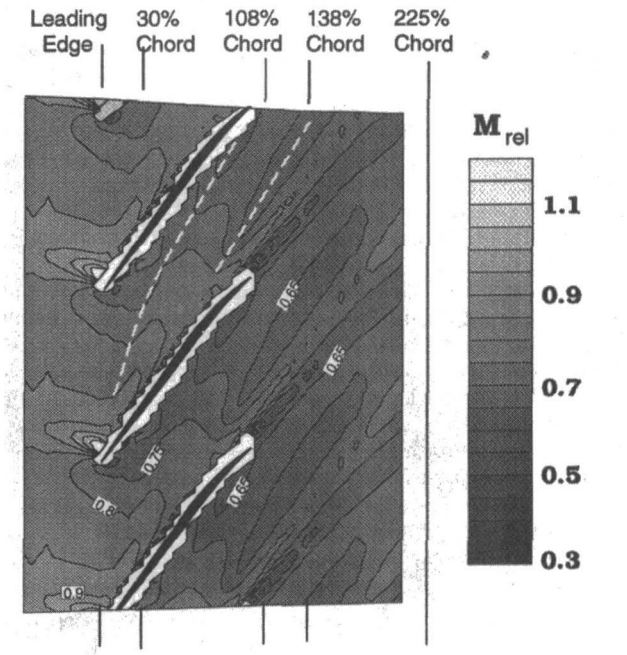


Fig. 9 Measured relative Mach number contours at 95 percent span [. . . estimated clearance vortex path]

Downloaded 01 Jun 2010 to 171.66.16.53. Redistribution subject to ASME license or copyright; see http://www.asme.org/terms/Terms_Use.cfm

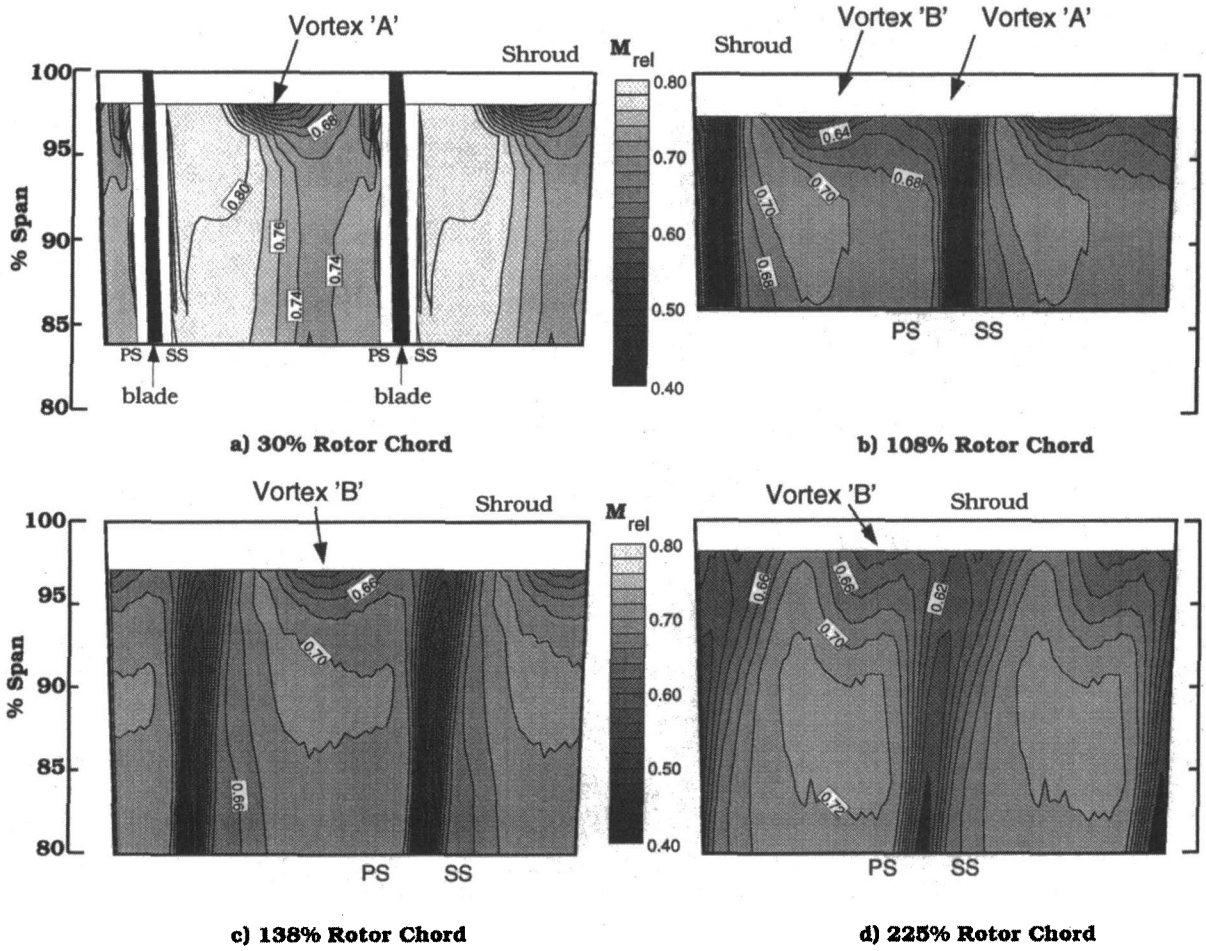


Fig. 10 Measured cross-channel Mach number distributions at 60 percent speed operating at near-peak efficiency

blade diffuses very slowly downstream of the blade. In the present compressor Vortex B would reach the stator leading edge, located at 138 percent chord, intact. The impact of the blade wake and Vortex B on the stator performance is a topic of future research. However, one point that has emerged is that at design speed, where the vortex and wake fluid have intermixed, the stator will be exposed to an unsteady flow field generated at the rotor blade passing frequency, whereas at part speed the stator will be exposed to an unsteady flow field generated by the rotor blade wakes plus Vortex B in the endwall region.

In summary, at 60 percent speed operating conditions the leakage flow over the front portion of the rotor rolls into a vortex, which moves across the blade passage, impacts on the pressure surface before reaching the trailing edge, and merges with the rotor wake downstream of the blade. A second vortex is formed by fluid that migrates radially outward along the suction surface and rolls up into a vortex when it encounters the tip leakage flow in the rear half of the blade. The second vortex exits the blade passage near midpitch and persists for more than one rotor chord downstream. At stations far downstream of the rotor this vortex exhibits a Mach number deficit comparable to that of the wake.

Conclusions

Experimental and computational techniques are used to investigate the flow physics of the endwall region within and downstream of a transonic compressor rotor. The rotor is operated at 100 and 60 percent of design speed, which provides an inlet relative Mach number at the rotor tip of 1.5 and 0.9, respectively.

The conclusions of this investigation at design speed are:

1 The strong interaction between the rotor passage shock and the tip leakage vortex generates a region of high blockage in the passage, which moves forward and becomes larger in both the circumferential and radial directions as the rotor loading is increased.
2 The shock/vortex interaction and ensuing blockage leads to high incidence angles at the blade tip, which may play a role in triggering tip stall.
3 The influence of the shock/vortex interaction extends over the outer 10 percent of span, which is a distance equal to 20 times the tip clearance gap.
4 The mixing process of the tip clearance flow with the primary flow is complex and is still in progress by the time the flow would reach the stator leading edge plane in this closely coupled compressor stage (interblade gap equal to 40 percent rotor chord at the tip).

The conclusions of this investigation at part speed, in the absence of the shock, are:

1 A second vortex forms along the suction surface near the blade trailing edge as fluid within the suction surface boundary layer migrates outward and encounters the tip clearance flow over the rear half of the blade. This second vortex develops as a result of operating at an off-design condition and does not exist at design speed.
2 The second vortex persists for more than one rotor chord downstream and exhibits a relative Mach number deficit comparable to that of the blade wake.
3 Although the rotor tip clearance at part speed is double that at design speed, the radial extent of the leakage flow

Downloaded 01 Jun 2010 to 171.66.16.53. Redistribution subject to ASME license or copyright; see http://www.asme.org/terms/Terms_Use.cfm

within the blade passage at part speed is about half of that at design speed. This difference in radial extent is caused by the enlargement of the leakage vortex when it encounters the rotor passage shock present under design speed conditions.

Acknowledgements

The authors wish to acknowledge the efforts of Dr. Tony Strazisar of NASA Lewis Research Center for his guidance not only in the writing of this paper, but also in acquiring and analyzing the experimental data. We are also grateful to Dr. John Adamczyk of NASA Lewis Research Center and Dr. Ed Greitzer of Massachusetts Institute of Technology for their helpful comments and suggestions.

References

Adamczyk, J. J., Celestina, M. L., Beach, T. A., and Barnett, M., 1989, "Simulation of Three-Dimensional Viscous Flow Within a Multi-stage Turbine," ASME JOURNAL OF TURBOMACHINERY, Vol. 112, pp. 370–376.

Adamczyk, J. J., Celestina, M. L., and Greitzer, E. M., 1993, "The Role of Tip Clearance in High-Speed Fan Stall," ASME JOURNAL OF TURBOMACHINERY, Vol. 115, pp. 28–38.

Chen, G. T., Greitzer, E. M., Tan, C. S., and Marble, F. E., 1991, "Similarity Analysis of Tip Clearance Flow Structure," ASME JOURNAL OF TURBOMACHINERY, Vol. 113, pp. 260–271.

Copenhaver, W. W., Hah, C., and Puterbaugh, S. L., 1993, "Three-Dimensional Flow Phenomena in a Transonic, High-Throughflow, Axial-Flow Compressor Stage," ASME JOURNAL OF TURBOMACHINERY, Vol. 115, pp. 240–248.

Crook, A., 1989, "Numerical Investigation of Endwall/Casing Treatment Flow Phenomena," M.S. Thesis, MIT, Cambridge, MA.

Hathaway, M. D., Chriss, R. M., Wood, J. R., and Strazisar, A. J., 1993, "Experimental and Computational Investigation of the NASA Low-Speed Centrifugal Compressor Flow Field," ASME JOURNAL OF TURBOMACHINERY, Vol. 115, pp. 527–542.

Inoue, M., Kuroumaru, M., and Fukuhara, M., 1986, "Behavior of Tip Leakage Flow Behind an Axial Compressor Rotor," ASME *Journal of Engineering for Gas Turbines and Power*, Vol. 108, pp. 7–13.

Inoue, M., and Kuroumaru, M., 1989, "Structure of Tip Clearance Flow in an Isolated Axial Compressor Rotor," ASME JOURNAL OF TURBOMACHINERY, Vol. 111, pp. 250–256.

Kirtley, K. R., Beach, T. A., and Adamczyk, J. J., 1990, "Numerical Analysis of Secondary Flow in a Two-Stage Turbine," Paper No. AIAA-90-2356.

McDougall, N. M., Cumpsty, N. A., and Hynes, T. P., 1990, "Stall Inception in Axial Compressors," ASME JOURNAL OF TURBOMACHINERY, Vol. 112, pp. 116–125.

McDougall, N. M., 1990, "A Comparison Between the Design Point and Near Stall Performance of an Axial Compressor," ASME JOURNAL OF TURBOMACHINERY, Vol. 112, pp. 109–115.

Moore, R. D., and Reid, L., 1980, "Performance of Single-Stage Axial-Flow Transonic Compressor With Rotor and Stator Aspect Ratios of 1.19 and 1.26, Respectively, and With Design Pressure Ratio of 2.05," NASA TP 1659.

Nichols, C. E., Jr., 1987, "Preparation of Polystyrene Microspheres for Laser Velocimetry in Wind Tunnels," NASA TM 89163.

Reid, L., and Moore, R. D., 1978, "Design and Overall Performance of Four Highly Loaded, High-Speed Inlet Stages for an Advanced High-Pressure Ratio Core Compressor," NASA TP 1337.

Stauter, R. C., 1993, "Measurement of the Three-Dimensional Tip Region Flow Field in an Axial Compressor," ASME JOURNAL OF TURBOMACHINERY, Vol. 115, pp. 468–476.

Storer, J. A., and Cumpsty, N. A., 1994, "An Approximate Analysis and Prediction Method for Tip Clearance Loss in Axial Compressors," ASME JOURNAL OF TURBOMACHINERY, Vol. 116, pp. 648–656.

Strazisar, A. J., Wood, J. R., Hathaway, M. D., and Suder, K. L., 1989, "Laser Anemometer Measurements in a Transonic Axial-Flow Fan Rotor," NASA TP 2879.

Urasek, D. C., and Janetzke, D. C., 1972, "Performance of Tandem-Bladed Transonic Compressor Rotor With Rotor Tip Speed of 1375 Feet per Second," NASA TM X-2484.

Wisler, D. C., 1985, "Loss Reduction in Axial-Flow Compressors Through Low-Speed Model Testing," ASME JOURNAL OF TURBOMACHINERY, Vol. 107, pp. 354–363.

Downloaded 01 Jun 2010 to 171.66.16.53. Redistribution subject to ASME license or copyright; see http://www.asme.org/terms/Terms_Use.cfm

The Effect of Tip Clearance on a Swept Transonic Compressor Rotor

W. W. Copenhaver

E. R. Mayhew

Wright Laboratory,
Wright Patterson AFB, OH 45433

C. Hah
NASA Lewis Research Center,
Cleveland, OH 44135

A. R. Wadia
GE Aircraft Engines,
Cincinnati, OH 45215

An experimental and numerical investigation of detailed tip clearance flow structures and their effects on the aerodynamic performance of a modern low-aspect-ratio, high-throughflow, axial transonic fan is presented. Rotor flow fields were investigated at two clearance levels experimentally, at tip clearance to tip blade chord ratios of 0.27 and 1.87 percent, and at four clearance levels numerically, at ratios of zero, 0.27, 1.0, and 1.87 percent. The numerical method seems to calculate the rotor aerodynamics well, with some disagreement in loss calculation, which might be improved with improved turbulence modeling and a further refined grid. Both the experimental and the numerical results indicate that the performance of this class of rotors is dominated by the tip clearance flows. Rotor efficiency drops six points when the tip clearance is increased from 0.27 to 1.87 percent, and flow range decreases about 30 percent. No optimum clearance size for the present rotor was indicated. Most of the efficiency change occurs near the tip section, with the interaction between the tip clearance flow and the passage shock becoming much stronger when the tip clearance is increased. In all cases, the shock structure was three dimensional and swept, with the shock becoming normal to the endwall near the shroud.

Introduction

Flight maneuvers for military aircraft place significant demands on the engines that power them. In many instances the turbine engine compressors are driven into transients that, either temporarily or permanently, increase tip clearance levels. Therefore, compressor designs must be insensitive to variations in tip clearance levels if they are to meet the demands of future propulsion systems. Tip flow fields of current design high-speed, low-aspect-ratio compressors dominate performance levels and, in many cases, are highly sensitive to tip clearance levels, making them less desirable from an operability standpoint. Design system clearance models require improvements if this trend is to be reversed.

Axisymmetric streamline curvature design methods are the backbone of today's design systems. These codes currently have minimal tools for accounting for loss production and blockage due to changes in the tip clearance levels. Therefore, a study of the impact of clearance in such rotors is critical to improvements to design systems, improvements that will allow for the inclusion of clearance effects. Further experimental and numerical studies are necessary to understand detailed flow phenomena in the tip clearance area and to build a simpler tip clearance model for the current compressor design system.

Many previous numerical studies for the tip clearance flow in a high-speed compressor used rather simple models to describe the tip clearance geometry. Actual blade tip geometries were not modeled and a wedge-shaped tip was assumed at the blade tip for simplicity of analysis. This rather crude approximation was based on the assumption that the tip clearance flow acts like an inviscid jet flow and the net effect on the main flow field can be sufficiently represented with such a simple model. However, recent studies on modern transonic compressor stages indicate that the aerodynamic performance depends directly on the details of the flow structure in this area.

The purpose of the current study is to investigate detailed flow structures in the tip clearance region and their effects on the aerodynamic characteristics of a modern low-aspect-ratio, high-throughflow, axial transonic fan. Sellin et al. (1993) explored the tip flow structures for three different blade designs with loading levels, tip speeds, and clearances similar to the fan in this study. They concluded that the casing static pressure distributions were not affected by blade design and that sweep, throat margin, and suction surface shape have little effect on the casing static pressure. It may therefore be inferred, although not conclusively, that the results from the swept fan stage tested here may be generally valid for this class of transonic rotor.

The swept fan stage in this study was tested for two different clearance sizes. For the numerical study, the actual tip geometry is accurately modeled and the rotor flow field is calculated across the rotor speed line with four different clearance sizes. The numerical results are compared with the available measurement and analyzed to understand the flow structure and the role of the tip clearance flow on the fan performance.

Background

Extensive experimental and analytical studies have been carried out by various researchers. L. H. Smith (1970) found from subsonic test data that a 5 percent loss in peak pressure rise would be expected from a one percent increase in clearance to chord ratio. Adamczyk et al. (1993) also found this ratio to be valid. Adamczyk performed a numerical experiment on three rotors with tip chord ratios of zero, 0.25, 0.75, and 1.25 percent. He found that a zero clearance resulted in an increase in flow range compared to results with clearance and also that the low clearance near the leading edge was critical to increased stable operating range. J. Denton's (1993) theory predicts that the rate of change of efficiency with tip clearance over span ratio is in the range of 2.0–3.0, increasing with increasing stage loading and with reduced flow coefficients. R. D. Moore (1982) looked at four different tip clearances between 0.2 and 1.2 percent of leading edge blade height for a 1.75 pressure ratio, 2.4 aspect ratio rotor. For a change of 1 percent of clearance to blade height, efficiency varied 6.7 percent at 100 percent speed. This also resulted in a 15 percent loss in stall margin. He also noted

Contributed by the International Gas Turbine Institute and presented at the 39th International Gas Turbine and Aeroengine Congress and Exposition, The Hague, The Netherlands, June 13–16, 1994. Manuscript received by the International Gas Turbine Institute March 4, 1994. Paper No. 94-GT-363. Associate Technical Editor: E. M. Greitzer.

Copyright © 1996 by ASME

Downloaded 01 Jun 2010 to 171.66.16.53. Redistribution subject to ASME license or copyright; see http://www.asme.org/terms/Terms_Use.cfm

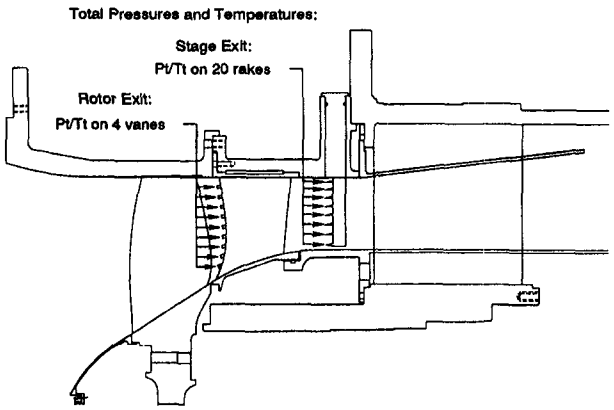


Fig. 1 Single-stage transonic test vehicle

that the effect of tip clearance was not confined to the rotor tip region; instead it affected the region from the tip to about 70 percent span.

Over the last decade, computational methods for turbomachinery aerodynamics have significantly advanced from two-dimensional inviscid analysis to fully three-dimensional Navier–Stokes methods. In recent years, significant progress has been reported in applying various numerical methods based on the Reynolds-averaged Navier–Stokes equations to the investigation of detailed flow physics inside turbomachinery (Davis et al., 1987; Dawes, 1986; Denton, 1986; Giles, 1988; Hah, 1986; Moore and Moore, 1985; Rao and Delaney, 1990; etc.).

Although numerical methods based on the steady Reynolds-averaged Navier-Stokes equations are widely used for many design applications, further improvements in numerical as well as physical models are necessary to obtain more accurate predictions with less empiricism. Recent studies for the development of low-aspect-ratio, high-throughflow, transonic axial fan stages have shown that detailed flow structures near the casing and in the tip clearance region dominate the aerodynamic efficiency and the stall margin. Many studies have been reported to investigate tip clearance flow in a compressor (Hah, 1986; Storer, 1991; Kang and Hirsch, 1994; Adamczyk et al., 1993).

Experiment

The tests were conducted in the Wright Laboratory Compressor Aero Research Lab. This test facility is configured for closed-loop testing of high specific flow fans and compressors with a 1.49 MW (2000 hp) maximum power requirement. The test configuration and instrumentation, shown schematically in Fig. 1, were designed to define overall steady-state performance of the stage and time-resolved rotor tip static pressures. Details of the test facility and steady-state instrumentation are provided by Law and Wadia (1993) and Copenhaver et al. (1993).

The test rig consisted of a rotor-stator combination. The rotor used for this study is a backward swept design, with the primary means of sweep obtained through lean in the direction opposite to rotation. It is one of a series of rotors tested as part of the swept rotor study carried out at Wright Laboratory's Compressor Aero Research Lab. The rotor salient design features are:

Design pressure ratio	2.06
Specific flow rate	212.77 kg/s/m^2 (43.6 lbm/s/ft^2)
Tip speed	457.2 m/s (1500 ft/sec)
Inlet tip relative Mach number	1.55
Mean aspect ratio	1.32
Inlet radius ratio	0.311
Rotor leading edge height	148.66 mm (5.85 in.)
Rotor shroud radius	215.9 mm (8.5 in.)
Number of blades	20

The stator configuration was designed through a computational fluid dynamics (CFD) technique as was reported by Copenhaver et al. (1993).

The experimental data are presented in two forms, steady-state and time-resolved ensemble average. Although the experiment was performed with a rotor/stator combination, the test

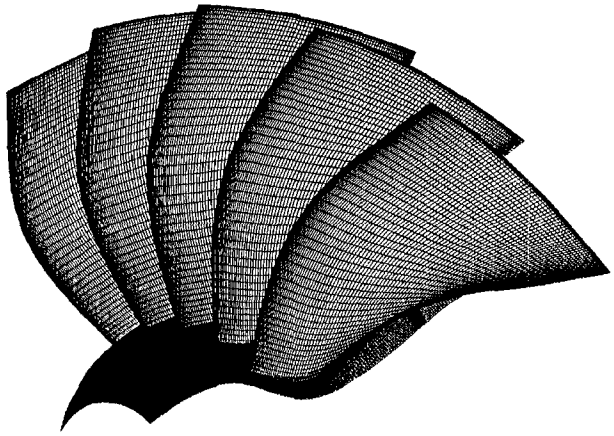


Fig. 3(*a*) Computational grid for rotor

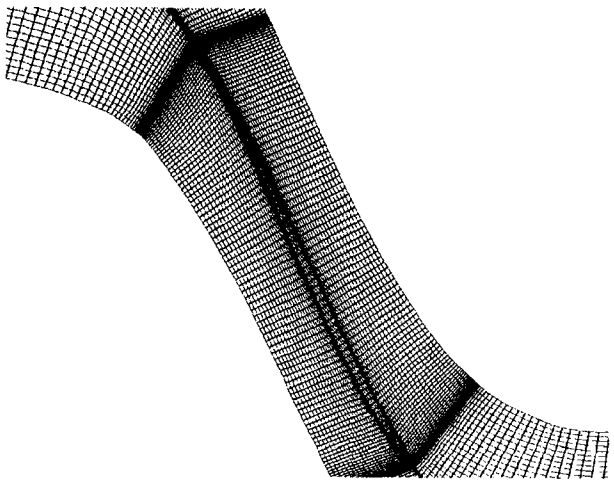


Fig. 3(*b*) Computational grid inside tip clearance

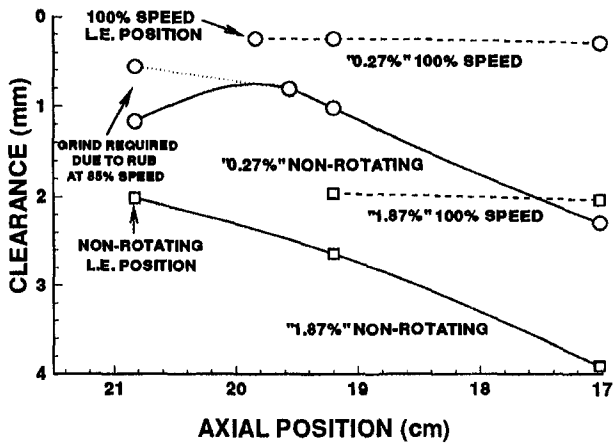


Fig. 2 Tip clearance description

Downloaded 01 Jun 2010 to 171.66.16.53. Redistribution subject to ASME license or copyright; see http://www.asme.org/terms/Terms_Use.cfm

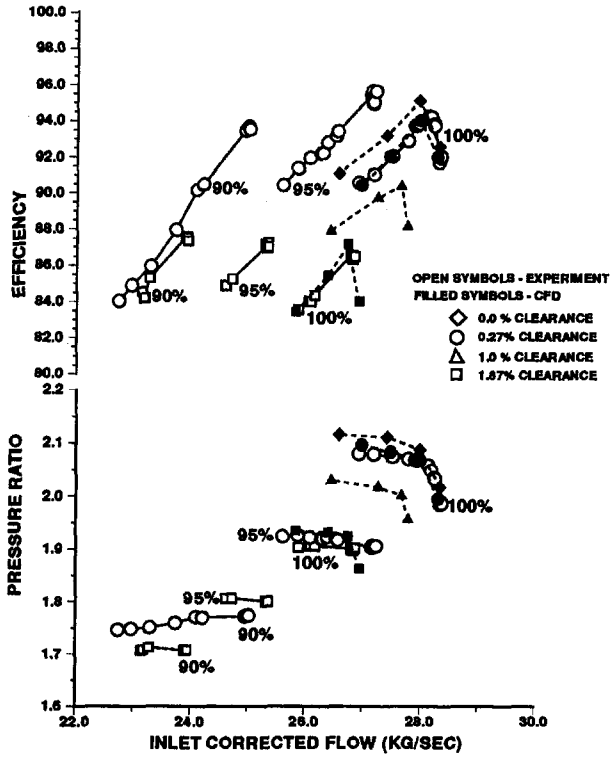


Fig. 4 Comparison of rotor performance

results presented here are for the rotor only, which was determined from stator leading edge instrumentation distributed on four different stator vanes. Tip static pressure fields were determined from ten dynamic and ten steady pressure measurements axially spaced on the casing over the rotor tip. The data were ensemble averaged to remove randomness. In a study of this type, where data comparisons are made between two configurations tested within the same facility, precision errors are of the greatest importance. At design speed data comparisons can be resolved within the following range at a 95 percent confidence level:

Steady temperature measurements	at 37.7°C (100°F) ± 0.22°C (0.4°F)
Steady pressure measurements	± 82.7 pa (.012 psi)
Dynamic pressure	± 965 pa (.14 psi)
Flow rate	± 0.2 percent
Overall pressure ratio	± 0.001
Overall efficiency	± 0.25 points
Clearance	± 0.076 mm (0.003 in.)

The lean and twist of the blades resulted in unusual blade growth characteristics. It was predicted that no growth would occur at the leading edge, and about 3.05 mm (120 mils) would occur at the trailing edge. To account for this, the blade tip was angled to give an even leading to trailing edge clearance under running conditions. Running clearance data were taken with four clearance probes, two located circumferentially at each of two nonrotating chordwise locations, 28.4 and 66.6 percent of cold chord. An additional clearance probe was located at the blade leading edge, but the reading was lost as the blade's leading edge migrated aft with speed. For the high clearance condition, the minimum measured running clearance was 1.96 mm (77 mils), at the 28.4 percent chord position as shown in Fig. 2. Based on this clearance level, the clearance to chord ratio is 1.87. Results related to this operating condition are defined as "1.87 percent clearance." Extrapolating from the 28.4 and 66.6 percent chord clearance measurements, it appeared that almost no blade growth occurred at the leading edge, and close to the expected amount occurred at the trailing edge. With the leading edge migrating aft from the leading edge probe location, the actual change in leading edge clearance could not be determined.

To obtain a reduced clearance configuration, about 1.65 mm (65 mils) of material was welded to the blade tips, for a design intent of 0.25 to 0.38 mm (10 to 15 mils) running clearance. However, at only 85 percent speed, a 0.076 mm (3 mil) rub occurred 9.9 mm (0.39 in.) aft of the nonrotating leading edge position, with 0.38 mm (15 mils) of clearance still showing at the 28.4 percent chord probe. Apparently, as the leading edge moved aft, it also grew in a nonlinear fashion. At 100 percent speed, it was now predicted that a 0.23 mm (9 mil) rub would occur, 11.18 mm (0.44 in.) aft of the nonrotating leading edge position.

To continue testing, it was necessary to grind the blade leading edge. Keying off of the blade that was the longest under running conditions, a small wedge of nominally 0.61 mm (24 mils) of material was ground off at a small angle from the blade leading edges, yielding the "0.27 percent clearance" configuration as shown in Fig. 2. At 100 percent speed, all the clearance readings were 0.25 to 0.30 mm (10 to 12 mils) resulting in a clearance to chord ratio of 0.27 percent.

Numerical Methods

Although significant progress has been made in numerical techniques during the last decade, obtaining an accurate numerical solution of the flow field inside a transonic compressor remains one of the more difficult problems. The development of three-dimensional boundary layers on the blade surface and endwalls, as well as shock-boundary layer interaction, and the

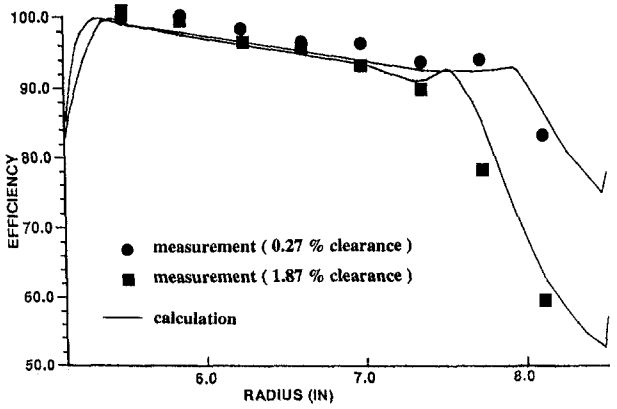


Fig. 5(*a*) Comparison of blade section efficiency (near peak efficiency)

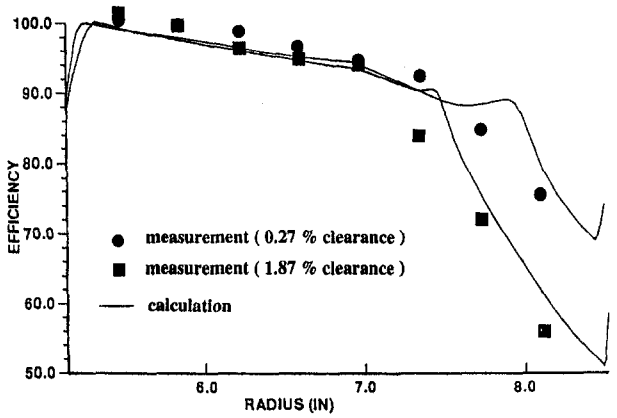


Fig. 5(*b*) Comparison of blade section efficiency (near stall)

Downloaded 01 Jun 2010 to 171.66.16.53. Redistribution subject to ASME license or copyright; see http://www.asme.org/terms/Terms_Use.cfm

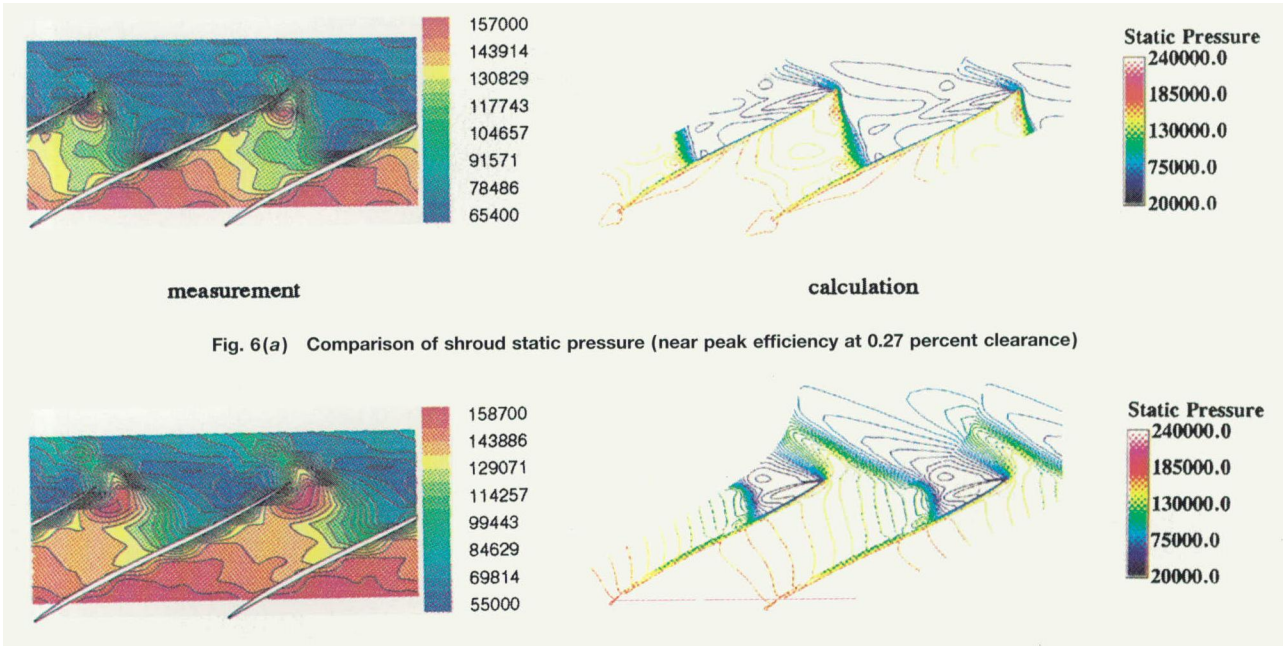


Fig. 6(*a*) Comparison of shroud static pressure (near peak efficiency at 0.27 percent clearance)

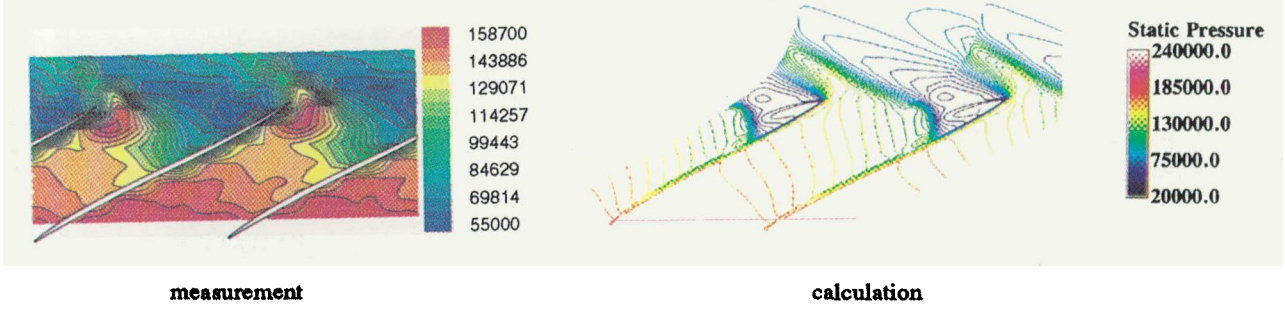


Fig. 6(*b*) Comparison of shroud static pressure (near stall at 0.27 percent clearance)

tip clearance flow, should all be accurately calculated to capture the overall flow field correctly.

For the current study, the governing equations are solved with a pressure-based implicit relaxation method using a fully conservative control volume approach. For the current study, a standard two-equation model is modified to include the low Reynolds number effects following the studies of Chien (1982). A third-order accurate interpolation scheme is used for the discretization of the convection terms and central differencing is used for the diffusion terms. The method is of second-order accuracy with smoothly varying grids. Previous studies using the current numerical code indicate that the aerodynamic loss in a typical transonic compressor is predicted well enough for design application. Also, the qualitative stall range is reasonably well calculated with the numerical code. Details of the current method and applications to transonic flows are given by Hah and Wennerstrom (1991).

The computational grid used for the current study is shown in Fig. 3. The current computational grid was generated to give an orthogonal grid near the leading edge and near the blade

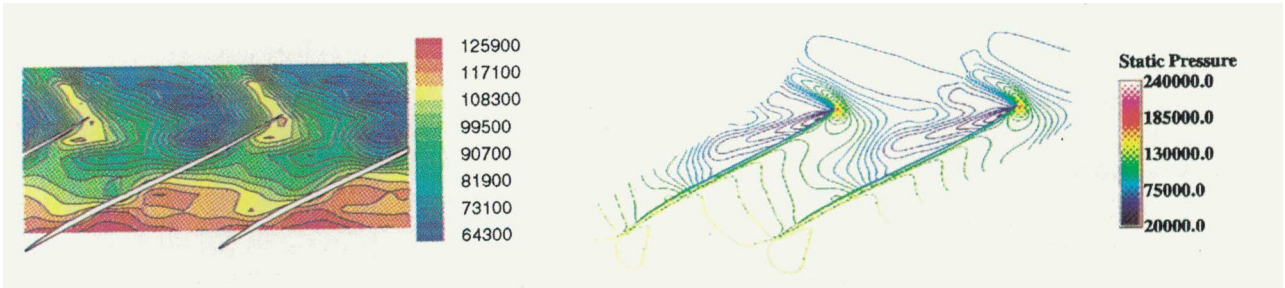


Fig. 7(*a*) Comparison of shroud static pressure (near peak efficiency at 1.87 percent clearance)

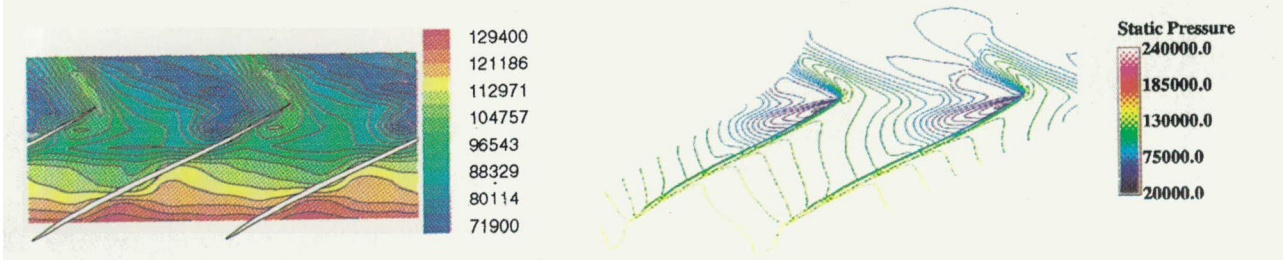


Fig. 7(*b*) Comparison of shroud static pressure (near stall at 1.87 percent clearance)

Downloaded 01 Jun 2010 to 171.66.16.53. Redistribution subject to ASME license or copyright; see http://www.asme.org/terms/Terms_Use.cfm

surface where the most important flow phenomena (passage shock, shock-boundary layer interaction, etc.) occur. With this grid, spatial periodicity at the periodic surfaces is not enforced for the grid, so the physical periodicity condition is handled inside the code using an interpolation function. The grid consists of 61 nodes in the blade-to-blade direction, 56 nodes in the spanwise direction, and 162 nodes in the streamwise direction. As shown in Fig. 3, ten computational nodes are actually distributed on the blade tip to describe the blade tip geometry and ten nodes are located between the blade tip and the shroud. As a very small change in the size of the tip clearance changes the flow structures significantly, the precise geometry of the blade tip was correctly modeled for the current study. The standard boundary conditions for the transonic flow in a compressor are used (Hah and Wennerstrom, 1991). Residuals of each finite difference equation are integrated over the entire domain. When the integrated residuals of all the equations are reduced by four orders of magnitude from their initial value, the solution is considered to be converged. About three Cray YMP single-processor CPU hours are required to get a fully converged solution for each operating condition.

Results and Discussion

The primary objective of the current study is to investigate the detailed flow structure of the tip clearance flow and its effects on the aerodynamic performance of a modern low-aspect-ratio, high-throughflow, axial transonic fan. The overall performance and shock structure near the casing at two clearance levels were studied experimentally. To understand detailed flow features, four clearance levels were also investigated numerically. The ratios of the tip clearance to the tip blade chord were 0 percent, 0.27 percent, 1.0 percent, and 1.87 percent, and data were taken at 0.27 percent and 1.87 percent. For numerical calculations, a blade stress analysis was performed to obtain true running deflected geometry of the rotor. This running rotor geometry was used for calculations at various tip clearances.

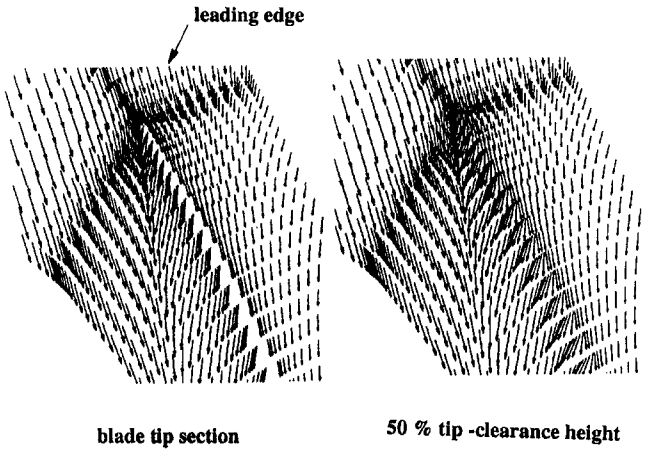


Fig. 8(*a*) Calculated velocity vectors near blade tip (near peak efficiency at 0.27 percent clearance)

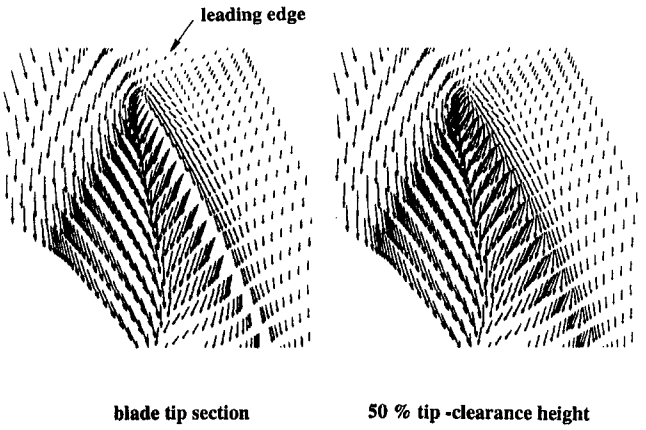


Fig. 8(*b*) Calculated velocity vectors near blade tip (near stall at 0.27 percent clearance)

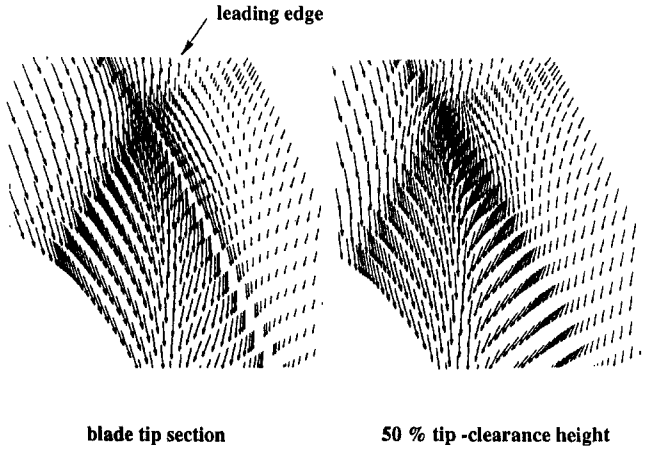


Fig. 9(*a*) Calculated velocity vectors near blade tip (near peak efficiency at 1.87 percent clearance)

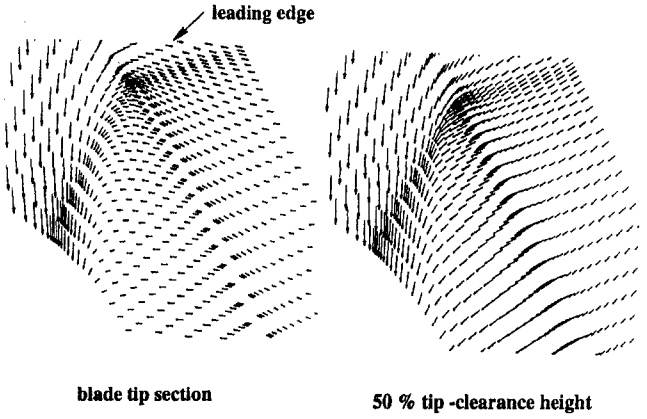


Fig. 9(*b*) Calculated velocity vectors near blade tip (near stall at 1.87 percent clearance)

Overall Performance. Measured and calculated performance maps of the fan at different clearance levels are presented in Fig. 4. The clearance sizes were chosen to perform a parametric study on the effects of tip clearance size on the fan performance. The data suggest that significant performance reductions result from increased clearance levels. At 100 percent speed an 8.5 percent loss in peak pressure rise occurs with the 1.6 percent increase in clearance to chord ratio. This is very close to the findings of L. H. Smith (1970) of 5 percent loss for 1 percent increase in clearance to chord ratio. The peak efficiency operating conditions for the open clearance case could not be experimentally established due to facility constraints. Based on the highest efficiency achieved in the test, a 7.7 percent loss in peak efficiency occurs with the increase in clearance. Using the correlation of R. D. Moore (1982), a 7.5 percent drop in efficiency would be predicted.

Figure 4 also indicates that calculated rotor efficiency is somewhat lower than the measured value at 0.27 percent clearance. However, the decrease in the rotor performance due to the increase in the tip clearance is well calculated. A 30 percent loss in flow range was measured with the 1.6 percent increase in clearance (near stall operation described by lowest flow con-

Downloaded 01 Jun 2010 to 171.66.16.53. Redistribution subject to ASME license or copyright; see http://www.asme.org/terms/Terms_Use.cfm

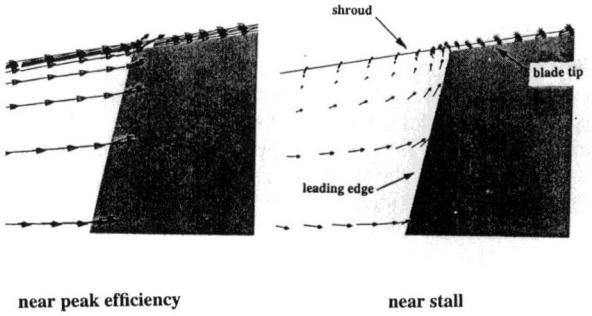


Fig. 10(*a*) Calculated velocity vectors near leading edge (0.27 percent clearance)

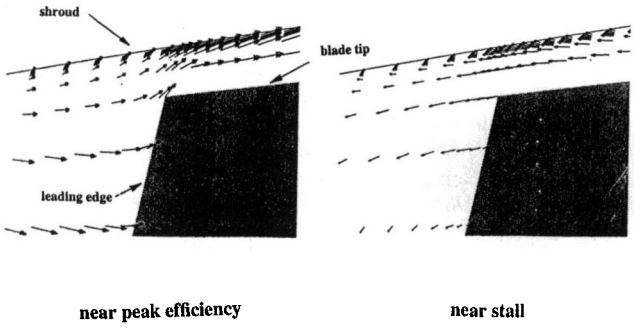


Fig. 10(*b*) Calculated velocity vectors near leading edge (1.87 percent clearance)

ditions shown on Fig. 4 for a given speed). The numerical solution predicts a slightly higher pressure rise than the measured value at both clearance ratios. The numerical results at zero clearance indicate that both the efficiency and the pressure

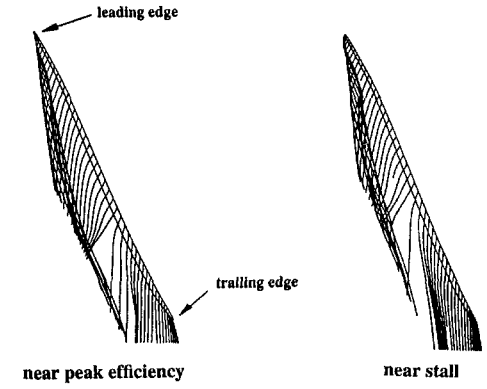


Fig. 11(*a*) Particle traces on blade tip (0.27 percent clearance)

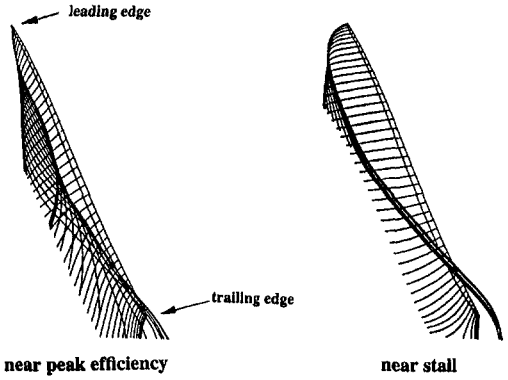


Fig. 11(*b*) Particle traces on blade tip (1.87 percent clearance)

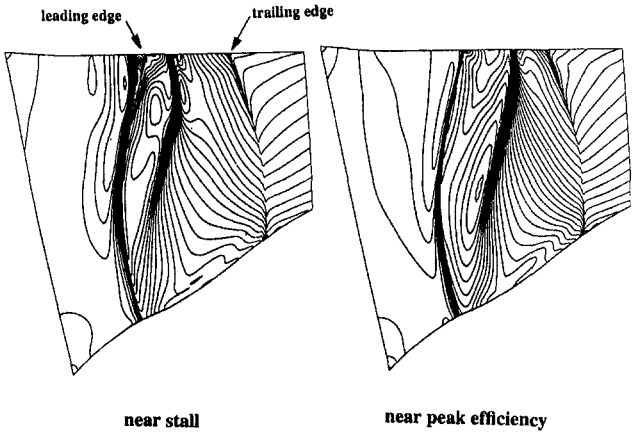


Fig. 12(*a*) Blade suction surface static pressure distribution (0.27 percent clearance)

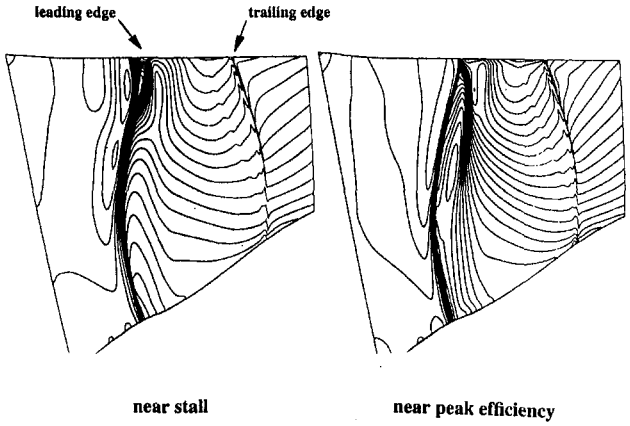


Fig. 12(*b*) Blade pressure surface static pressure distribution (0.27 percent clearance)

ratio increase compared to the 0.27 percent clearance ratio. It should be pointed out that the zero clearance configuration was run with a stationary case. The zero clearance configuration was also analyzed with rotating shroud motion. However, with rotating shroud motion, the efficiency and stall margin were lower than those with the 0.27 percent clearance. The relative wall motion energizes low-momentum flow very near the shroud and prevents massive flow separation.

The results reported in Fig. 4 do not indicate the existence of optimum clearance for the operating range studied if relative shroud motion is allowed. Current results indicate that the aerodynamic efficiency drops about a point for each increase of quarter percent of tip clearance. The change is almost linear from zero clearance to 1.87 percent clearance. The numerical results indicate that the flow range is reduced almost 40 percent when the tip clearance is increased from zero to 1.87 percent.

Spanwise distribution of the blade section efficiency at 100 percent speed is compared in Fig. 5. The profiles indicate that the major losses in efficiency occur in the outermost 30 percent of the blade span and little if any impact is noted at 50 percent span and below. This is somewhat less than the findings of R. D. Moore (1982) of 70 percent span effected by the increases in clearance. The agreement between the measurement and the calculation is quite good considering the complexity of the flow field. Although the absolute value of the aerodynamic loss is not calculated exactly, the differences in the efficiency at different flow conditions are well calculated. Overall, the difference in aerodynamic efficiency of the fan across the speed line is mostly due to the change of the blade section efficiency near the tip.

Downloaded 01 Jun 2010 to 171.66.16.53. Redistribution subject to ASME license or copyright; see http://www.asme.org/terms/Terms_Use.cfm

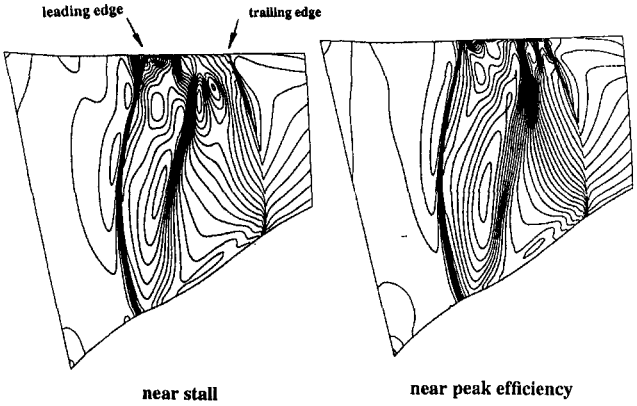


Fig. 13(*a*) Blade suction surface static pressure distribution (1.87 percent clearance)

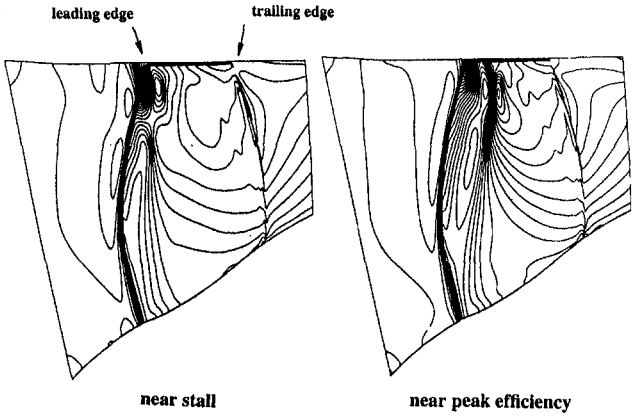


Fig. 13(*b*) Blade pressure surface static pressure distribution (1.87 percent clearance)

The results in Figs. 4 and 5 demonstrate the importance of the optimum design and flow control near the rotor tip for maximum efficiency as well as for the compressor stall margin.

Flow Structure Near the Casing. In Figs. 6 and 7, time-averaged static pressure contours on the casing are compared between the numerical solution and the measurement for clearances of 0.27 percent and 1.87 percent. Figure 6(*a*) indicates that for both the computation and measurement the shock system is attached to the blade leading edge and near normal to the flow. Also, little influence of the tip vortex is seen near the suction surface. At the near-stall condition (Fig. 6(*b*)), both the measured data and the calculation show that the passage shock near the endwall is located ahead of the blade passage. Also, the leading edge shock is not normal to the incoming relative flow angle. The numerical results indicate that the tip-leakage vortex interacts strongly with the passage shock. The passage shock is deflected farther downstream near the suction surface due to this interaction. The measured results also show this interaction, but the weaker pressure gradients at the suction surface suggest the shock is much more diffuse than in the computation. Perhaps the shock vortex interaction is greater than the computation predicts. This may be the result of high levels of shock unsteadiness that exist at the near-stall condition. The computation is steady in nature, and the measurements are ensemble averaged. Averaging of an unsteady shock system would result in the weak static pressure gradient shown in the measurements.

At the larger clearance (Fig. 7), pressure contours on the shroud show that the shock has been greatly diffused across the clearance gap. The figures suggest that the shock system remained detached from the blade leading edge for all operating conditions achieved in the test. Near the suction surface leading edge, a large region of low pressure exists, which extends back to about 50 percent chord. This may indicate that the tip vortex has a significant influence on the casing flow fields when clearance is increased.

The comparisons in Figs. 6 and 7 show that the numerical solutions do calculate the shock structure correctly at different flow conditions, although some details may be lost due to the steady nature of the calculation. The computation and the experiment show that the interaction between the passage shock and the tip-leakage vortex becomes stronger when the flow rate is reduced. When the clearance is increased, the shock diffuses across the clearance gap significantly and the pressure on the casing indicates that the tip vortex deflects the shock leg near the suction surface further.

Calculated velocity vectors at the tip plane and at the middle of the tip clearance are given in Fig. 8 for the 0.27 percent clearance case. The figure shows that the tip clearance flow mixes with the main flow near the suction side and forms a strong vortex line. At the near-stall point, this tip vortex follows a curved path, which indicates strong interaction with the passage shock near the suction surface. The flow pattern for the larger clearance, which is shown in Fig. 9, indicates that the interaction is stronger than for the tight clearance case. The vortex line shows some curvature even at the near-peak efficiency point.

The velocity vectors in front of the leading edge near the casing are shown in Fig. 10. A reversed flow field is formed near the casing when the flow rate is reduced. This reversed flow region is further increased and moves toward the inlet when the tip clearance is increased. The current numerical investigation is based on the numerical integration of the Reyn-

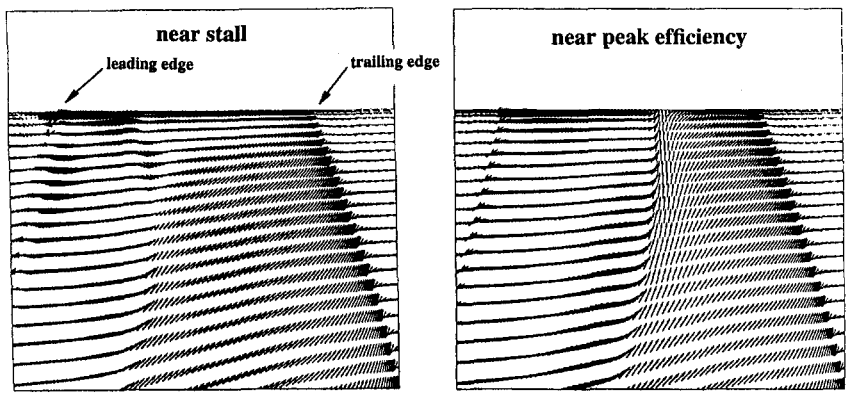


Fig. 14 Velocity vectors near blade suction surface (0.27 percent clearance)

Downloaded 01 Jun 2010 to 171.66.16.53. Redistribution subject to ASME license or copyright; see http://www.asme.org/terms/Terms_Use.cfm

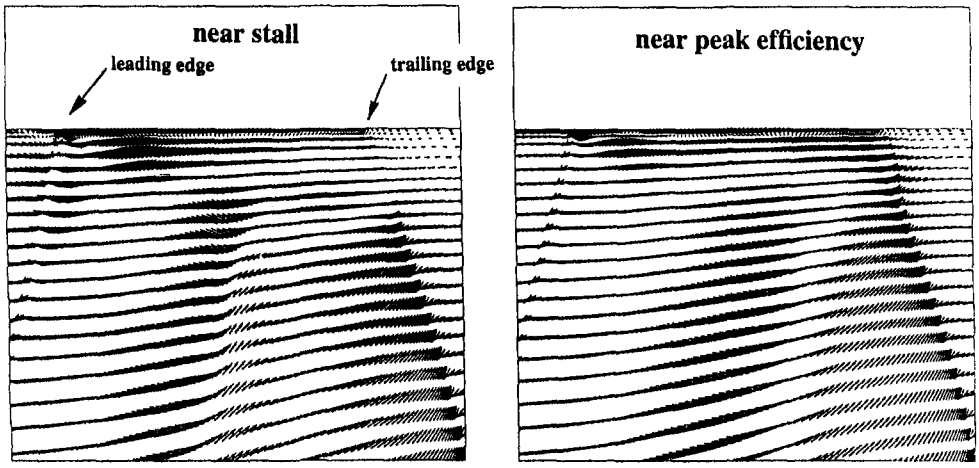


Fig. 15 Velocity vectors near blade suction surface (1.87 percent clearance)

olds-averaged Navier-Stokes equations. When the flow rate is reduced beyond a certain point by increasing the back pressure, the numerical solution does not converge to a finite mass flow and the mass flow rate continues to decrease. At these conditions, the recirculation zone shown in Figs. 9 and 10 extends farther upstream and eventually the numerical integration fails. These operating conditions are assumed to be beyond the fan operating range for the numerical analysis. The measured and the calculated fan operating ranges shown in Fig. 4 demonstrate some resemblance to each other. However, further studies are necessary to identify the numerical instabilities near the stall line and their relationship to the real fan stall phenomena.

In Fig. 11, particle traces across the tip section are presented for two clearance ratios. Again, the formation of the tip clearance vortex and the influence of the flow rate and the size of the tip clearance are clearly illustrated. Figure 11(a) shows the particles moving from the pressure surface of the blade across the blade tip in a slightly downstream direction. The particles are entrained into a vortex by the passage flow. Particles emanating from about midchord, behind where the shock intersects the suction surface, travel in a more downstream direction. This is most likely due to their reduced tangential velocity caused by the lower across-blade pressure ratio. At the near-stall condition this phenomenon is even more evident. Figure 11(b) for the 1.87 percent clearance case shows little evidence of the shock at the suction surface. The figure also indicates that the particles move across the blade tip in an upstream direction and then are entrained into a large vortex by the throughflow stream much farther across the passage than for the 0.27 percent clearance case.

These results suggest that the across blade flows are in an upstream direction and are of the same magnitude as the through blade flows.

Flow Structure Across the Span. Calculated static pressure contours on the blade surfaces at two clearances are shown in Figs. 12 and 13. Figure 12 shows changes in the shock structure for the near-stall and peak efficiency operating points at 0.27 percent clearance. At all operating conditions, the shock shape is three dimensional with the shock quite oblique in the spanwise direction away from the endwall. However, the shock becomes normal to the endwall near the casing due to the physical constraint. The shock impingement point moves forward on the suction surface of the blade from peak efficiency to the near-stall condition and the sweep of the shock structure is stronger near the peak efficiency. Figure 13, for the 1.87 percent clearance, indicates minimal movement of the shock position between these two operating points. Instead, the shock becomes offset in the tip region at the near stall operating condition. The structures for the near-stall 0.27 percent clearance (Fig. 12) and for peak efficiency 1.87 percent clearance (Fig. 13) are very similar except that the shock is slightly farther back in the passage for the more open clearance. The flow rates for these two conditions are nearly identical (Fig. 4). Figures 12 and 13 also indicate that most changes in flow structure due to the change in mass flow rate happen between the casing and 50 percent span.

The swept structure of the shock is diminished near the casing when the tip clearance is increased. These results suggest that at lower flows (off-design operation) the shocks become more normal in the spanwise direction, thereby reducing the benefits of swept airfoils.

Relative velocity vectors inside the suction surface boundary layer are shown in Figs. 14 and 15. Velocity vectors follow the conventional stream surfaces before the passage shock. However, strong radial flow develops immediately after the shock. This strong radially outward flow inside transonic compressors was previously observed and discussed (Kerrebrock, 1980; Kotidis and Epstein, 1990; Hah and Wennerstrom, 1991). The radially outward flow is due to the shock-boundary layer interaction near the casing (above 40 percent of the span) while traditional secondary flow phenomena cause the radial flow near the hub.

Figure 4 demonstrates the dramatic impact tip clearance has on efficiency. Therefore, it is important to determine where losses increase when clearance is increased. For this purpose and since entropy is a better quantity for loss analysis than total pressure in rotating system, generation and migration of entropy inside the blade passage is presented in Figs. 16 and 17. Figure 16 shows distributions of entropy at three cross planes (20, 50, and 80 percent chord) with 0.27 percent clearance at two operating conditions. The aerodynamic losses are much larger on the suction surface than the pressure surface due to the shock-boundary layer interaction. There also is a large loss region immediately below the casing, which is associated with the tip clearance vortex. Near the leading edge, a high loss region is formed near the corner of the blade suction side and the casing due to the interaction between the tip clearance vortex and the passage shock. This high loss region migrates toward the pressure side following the direction of the tip clearance vortex. This high loss region moves nearer to the pressure side of the blade when the mass flow rate is reduced. As the compressor is throttled to near stall the throughflow velocity is reduced.

During this throttle change the clearance flow velocity undergoes little change. The net result is that the vortex is forced farther out into the passage toward the pressure surface by the

Downloaded 01 Jun 2010 to 171.66.16.53. Redistribution subject to ASME license or copyright; see http://www.asme.org/terms/Terms_Use.cfm

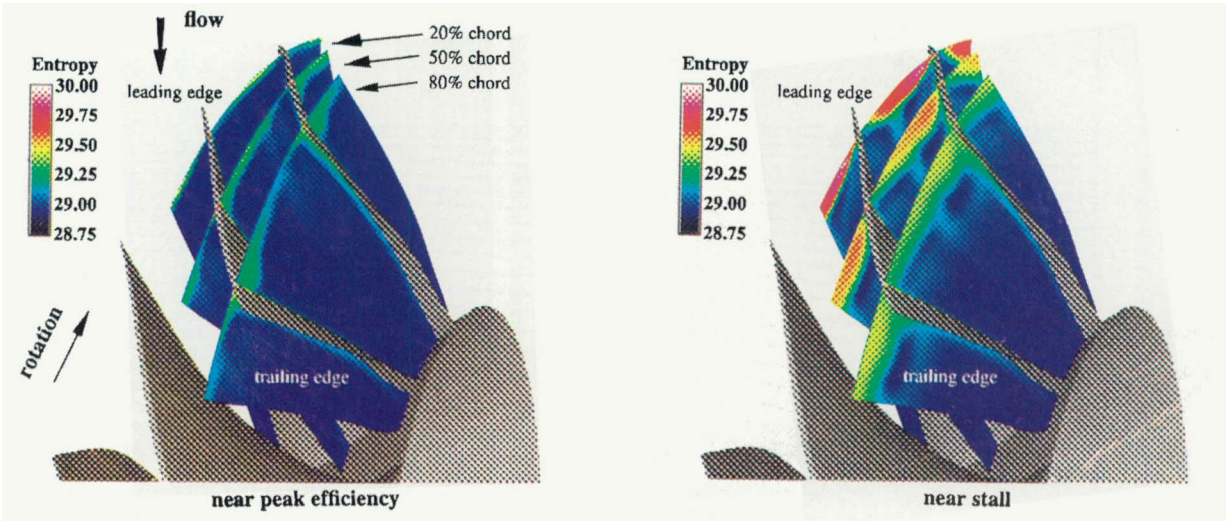


Fig. 16 Generation of entropy inside blade passage (0.27 percent clearance)

momentum of the clearance flow. The entropy contours in Fig. 17 for the 1.87 percent clearance case show the same trends as for the 0.27 percent case. But the region of high loss extends much farther down the span and the impact of the vortex is much more pronounced.

Concluding Remarks

This paper describes an experimental and numerical study to investigate the detailed flow structure inside the tip clearance of a modern, low-aspect-ratio, high-throughflow, transonic axial fan and the effects of varying clearance on the aerodynamic performance. The rotor flow fields at four different clearance gap sizes were investigated. For the numerical analysis, a relatively fine computational mesh was used to describe the actual blade tip. The currently applied numerical method, along with the turbulence model, seems to calculate the aerodynamic behavior of the rotor at different clearance size and mass flow rates well. Some disagreement in aerodynamic loss calculation, especially near the tip region, might be improved if a more realistic turbulence model and a further refined grid are used.

For the rotor investigated, the rotor efficiency drops about six points when the tip clearance is increased from 0.27 percent of the tip chord to 1.87 percent. In addition, the flow range decreases about 30 percent. The correlations for pressure and efficiency loss with increased clearance developed by cited authors were found to apply for this class of compressor.

The numerical results do not indicate the existence of any optimum clearance size for the present rotor. Details of the flow structure across tip clearance indicate that the interaction between the tip clearance flow and the passage shock becomes much stronger when the tip clearance is increased. With the tip clearance at 1.87 percent chord, regions of reverse flow were found near the tip. In general for all cases investigated the passage shock system shows a three-dimensional swept structure. The shock becomes normal to the endwall near the casing. At larger tip clearances, the shock system shows a less swept structure.

The study indicates that the clearance flows impact primarily the outer 30 percent of the blade span. In this region on transonic fans, the shock system governs the obtainable pressure rise. Vortices formed by the clearance flow interact negatively with the swept shock system and severely reduce pressure rise capability and efficiency. Therefore, the key to higher efficiency and clearance insensitive designs is better management of the clearance flows; specifically in the tip clearance vortex/shock interaction region.

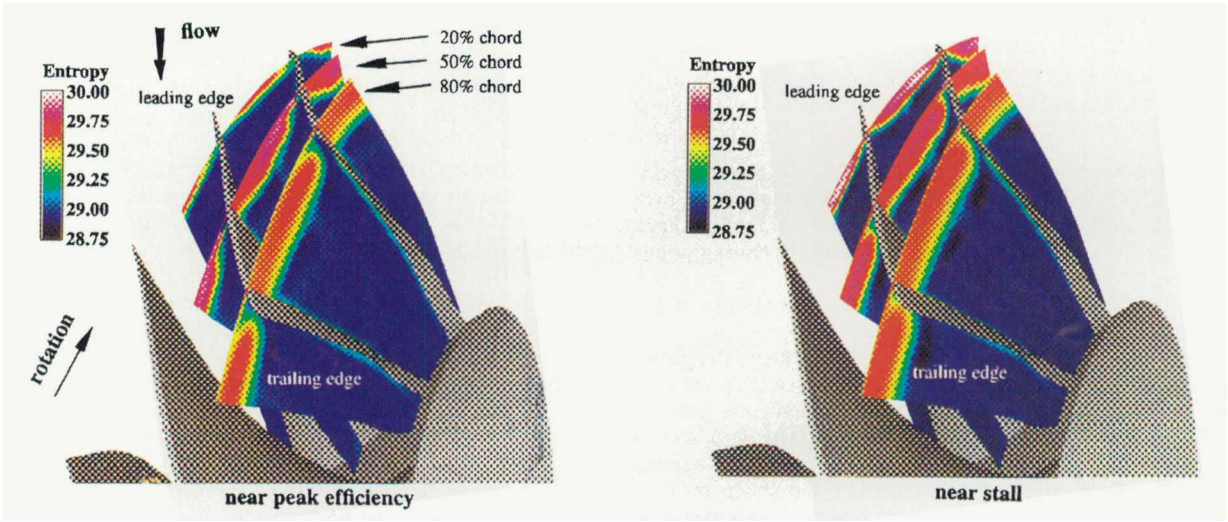


Fig. 17 Generation of entropy inside blade passage (1.87 percent clearance)

Downloaded 01 Jun 2010 to 171.66.16.53. Redistribution subject to ASME license or copyright; see http://www.asme.org/terms/Terms_Use.cfm

Acknowledgments

The authors would like to acknowledge the Compressor Aero Research Lab staff for their excellent support in obtaining the data presented here. We also thank the management at GE, Wright Lab, and NASA for allowing us to present this work.

References

Adamczyk, J. J., Celestina, M. L., and Greitzer, E. M., 1993, "The Role of Tip Clearance in High-Speed Fan Stall," ASME JOURNAL OF TURBOMACHINERY, Vol. 115, No. 1, pp. 28–39.

Chien, K. Y., 1982, "Prediction of Channel and Boundary-Layer Flows With a Low Reynolds Number Turbulence Model," *AIAA Journal,* Vol. 20, No. 1, pp. 33–38.

Copenhaver, W. W., Hah, C., and Puterbaugh, S. L., 1993, "Three-Dimensional Flow Phenomena in a Transonic, High-Throughflow, Axial-Flow Compressor Stage," ASME JOURNAL OF TURBOMACHINERY, Vol. 115, No. 2, pp. 240–248.

Davis, R. L., Hobbs, D. E., and Weingold, H. D., 1988, "Prediction of Compressor Cascade Performance Using a Navier–Stokes Technique," ASME JOURNAL OF TURBOMACHINERY, Vol. 110, No. 4, pp. 520–531.

Dawes, W. N., 1986, "Development of a 3D Navier–Stokes Solver for Application to All Types of Turbomachinery," ASME Paper No. 86-GT-70.

Denton, J. D., 1986, "The Use of a Distributed Body Force to Simulate Viscous Flow in 3D Flow Calculations," ASME Paper No. 86-GT-144.

Denton, J. D., 1993, "Loss Mechanisms in Turbomachines," ASME JOURNAL OF TURBOMACHINERY, Vol. 115, No. 4, pp. 621–656.

Giles, M. B., 1988, "Stator/Rotor Interaction in a Transonic Turbine," AIAA Paper No. 88-3093.

Hah, C., 1986, "A Numerical Modeling of Endwall and Tip Clearance Flow of an Isolated Compressor," ASME *Journal of Engineering for Gas Turbines and Power,* Vol. 108, No. 1, pp. 15–21.

Hah, C., 1987, "Calculation of Three-Dimensional Viscous Flows in Turbomachinery With an Implicit Relaxation Method," AIAA *Journal of Propulsion and Power,* Vol. 3, No. 5, pp. 415–422.

Hah, C., and Wennerstrom, A. J., 1991, "Three-Dimensional Flowfields Inside a Transonic Compressor With Swept Blades," ASME JOURNAL OF TURBOMACHINERY, Vol. 113, No. 1, pp. 241–251.

Kang, S., and Hirsch, Ch., 1994, "Tip Leakage Flow in a Linear Compressor Cascade," ASME JOURNAL OF TURBOMACHINERY, Vol. 116, pp. 657–664.

Kerrebrock, J. L., 1980, "Flow in Transonic Compressors," *AIAA Journal,* Vol. 19, No. 4.

Kotidis, P. A., and Epstein, A. H., 1990, "Unsteady Radial Transport in a Transonic Compressor Stage," ASME Paper No. 90-GT-133.

Law, C. H., and Wadia, A. R., 1993, "Low Aspect Ratio Transonic Rotors: Part 1—Baseline Design and Performance," ASME JOURNAL OF TURBOMACHINERY, Vol. 115, No. 2, pp. 218–225.

Moore, J., and Moore, J. E., 1985, "Performance Evaluation of Linear Turbine Cascade Using Three-Dimensional Viscous Flow Calculations," ASME *Journal of Engineering for Gas Turbines and Power,* Vol. 17, No. 1, pp. 969–975.

Moore, R. D., 1982, "Rotor Tip Clearance Effects on Overall and Blade-Element Performance of Axial-Flow Transonic Fan Stage," NASA TP-2049.

Rao, K., and Delaney, R., 1990, "Investigation of Unsteady Flow Through Transonic Turbine Stage," AIAA Paper No. 90-2408.

Sellin, D. S., Puterbaugh, S. L., and Copenhaver, W. W., 1993, "Tip Shock Structures in Transonic Compressor Rotors," AIAA Paper No. 93-1869.

Smith, L. H., Jr., 1970, "Casing Boundary Layers in Multistage Axial-Flow Compressors," *Flow Research on Blading,* L. S. Dzung, ed., Elsevier Publishing, Amsterdam, Netherlands.

Storer, J. A., 1991, "Tip Clearance Flow in Axial Compressors," Ph.D. thesis, Cambridge University, United Kingdom.

Downloaded 01 Jun 2010 to 171.66.16.53. Redistribution subject to ASME license or copyright; see http://www.asme.org/terms/Terms_Use.cfm

Flow Analyses in a Single-Stage Propulsion Pump

Y. T. Lee
David Taylor Model Basin,
Bethesda, MD 20084

C. Hah

J. Loellbach

NASA and ICOMP/NASA-Lewis
Research Center,
Cleveland, OH 44135

Steady-state analyses of the incompressible flow past a single-stage stator/rotor propulsion pump are presented and compared to experimental data. The purpose of the current study is to validate a numerical method for the design application of a typical propulsion pump and for the acoustic analysis based on predicted flowfields. A steady multiple-blade-row approach is used to calculate the flowfields of the stator and the rotor. The numerical method is based on a fully conservative control-volume technique. The Reynolds-averaged Navier–Stokes equations are solved along with the standard two-equation $k-\epsilon$ turbulence model. Numerical results for both mean flow and acoustic properties compare well with measurements in the wake of each blade row. The rotor blade has a thick boundary layer in the last quarter of the chord and the flow separates near the trailing edge. These features invalidate many Euler prediction results. Due to the dramatic reduction of the turbulent eddy viscosity in the thick boundary layer, the standard $k-\epsilon$ model cannot predict the correct local flow characteristics near the rotor trailing edge and in its near wake. Thus, a modification of the turbulence length scale in the turbulence model is applied in the thick boundary layer in response to the reduction of the turbulent eddy viscosity.

Introduction

A great deal of CFD (computational-fluid-dynamics) effort has been spent in the past decade on solving the compressible steady and unsteady Navier–Stokes equations for turbomachinery (for example, Chen (1988), Dawes (1988), Giles (1988), Jorgenson and Chima (1989), Rai (1985), Rao and Delaney (1990), etc.). Recently, solutions for incompressible flows in turbomachinery have emerged from more mature computational technologies for compressible flows. Stanier (1992), for instance, extended Dawes' (1988) viscous approach for marine open-water propeller calculations. NASA Marshall Space Flight Center (MSFC) formed a consortium (Garcia et al., 1992a, b) to investigate the liquid fuel characteristics in rocket engines. Both pressure-based methods (Chen, 1989; Chen et al., 1992; Hah et al., 1988) and pseudocompressibility methods (Kiris et al., 1993) have been used for pump inducer calculations. As indicated by Walker and Dawes (1990), the choice of a suitable acoustic speed is still on ad hoc grounds for the pseudocompressibility method using time-marching algorithms. Although the pressure-based method uses a more complex algorithm, the extension of the method to the unsteady problem is quite straightforward.

In the present study, a pressure-correction numerical method based on the steady-state Reynolds-averaged Navier–Stokes equations is applied to investigate the flowfield inside the subject pump stage. A relatively simple numerical procedure is employed to handle the full-stage computation. The method utilizes a mixing plane to transmit information between blade rows. This simple method does not attempt to model any unsteady effects on the steady flowfield.

This paper presents an incompressible flow solution for a representative single-stage stator/rotor propulsion pump and compares results with measurements of detailed wake structures after each blade row. The present numerical procedure uses a pressure-based approach. The turbulence closure is the standard $k-\epsilon$ model with a low-Reynolds-number modification near the wall. The rotor blade profile has a thick trailing edge, which invalidates Euler solutions, but also causes problems for viscous solutions using the conventional standard $k-\epsilon$ models. This latter phenomenon has also been observed by Deng et al. (1993) in their ship stern flow computations. Therefore results based on a simple modification of the standard $k-\epsilon$ model are also addressed.

Experimental Data

The propulsion pump, shown in Fig. 1(*a*), was tested in water. The pump consists of a 13-blade inlet guide vane (IGV) and a 7-blade backward swept rotor. The IGV blades are lightly loaded and have a constant spanwise chord of 0.572 ft. The rotor trailing edge is modified to prevent it from singing and has a special thick trailing-edge section and a flow recirculating region in its near wake. The blade rows of the IGV and the rotor are separated at the tip by nearly 130 percent of the IGV chord. Although the IGV wake exists and was measured, the large spacing between the IGV and the rotor minimizes the effect of the IGV wake on the rotor tip flow and its wake.

The present propulsion pump tested in the HIREP facility (Farrell et al., 1987) has a constant hub diameter of 21 in. and a constant casing diameter of 42 in. The pump operates at an inlet velocity of 35 fps and an inlet pressure of 43.2 psia. The rotor rotates at 260 rpm with a flow coefficient of 1.36 and a tip speed of 47.6 fps. The tested Reynolds number based on the chord of the IGV blade is 2.3×10^6.

The measured quantities include blade surface pressures, total pressures, inlet and wake velocities, and turbulence quantities. The axisymmetric pump inlet velocities were surveyed using a five-hole probe at 37 percent IGV chord upstream of the IGV leading edge. Five-hole probe surveys were also performed at 49.7 percent chord downstream of the IGV. These surveys provide three-component time-averaged velocities at eleven radial locations and cover 360 deg circumference with 0.373 deg angular resolution. LDV velocity surveys were conducted at four axial stations located at 43.5 percent IGV chord upstream of the rotor tip leading edge and at 7.3, 32.6, and 49 percent IGV chord downstream of the rotor tip trailing edge. The data include axial and tangential mean velocities and root-mean-square values of the turbulent fluctuating velocities. LDV surveys were also performed axially at $r/r_{tip} = 0.881$ (or 76.2 percent span) and from 45 percent IGV chord upstream of the rotor tip leading

Contributed by the International Gas Turbine Institute and presented at the 39th International Gas Turbine and Aeroengine Congress and Exposition, The Hague, The Netherlands, June 13–16, 1994. Manuscript received by the International Gas Turbine Institute February 9, 1994. Paper No. 94-GT-139. Associate Technical Editor: E. M. Greitzer.

Copyright © 1996 by ASME

Downloaded 01 Jun 2010 to 171.66.16.53. Redistribution subject to ASME license or copyright; see http://www.asme.org/terms/Terms_Use.cfm

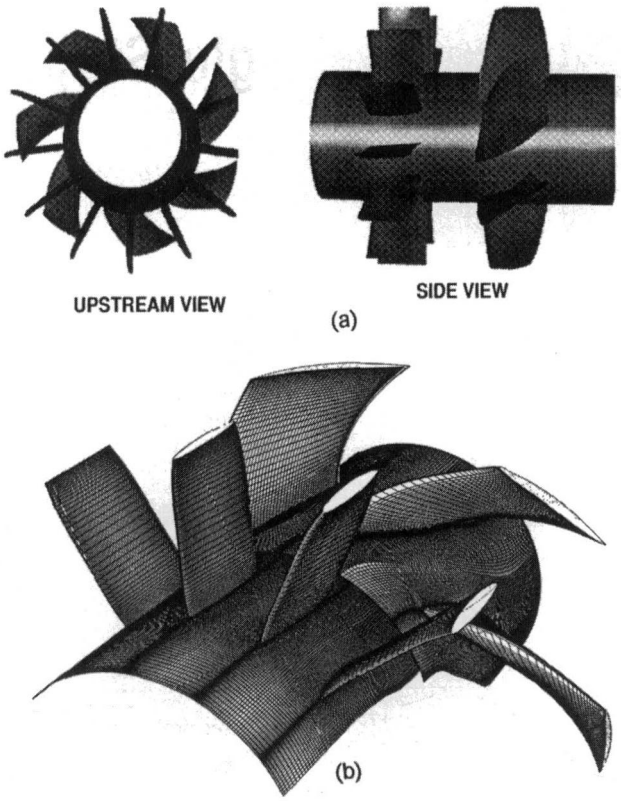


Fig. 1 Single-stage IGV/rotor propulsion pump: (*a*) geometry; (*b*) computational grid

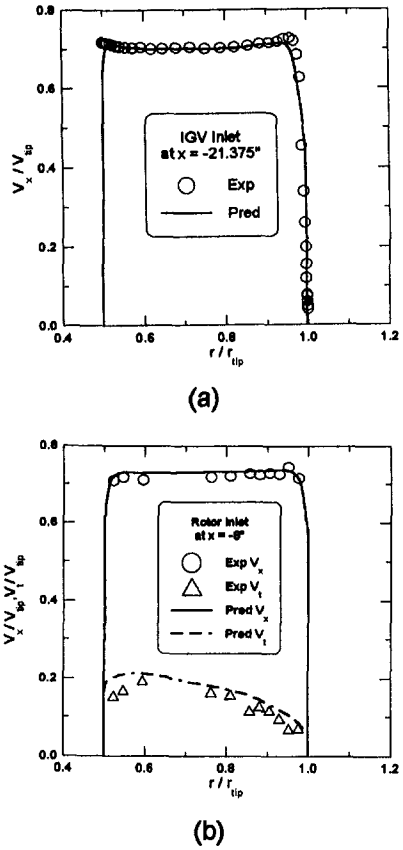


Fig. 2 Inlet conditions for the IGV and the rotor

edge to 49 percent downstream of the rotor tip trailing edge. These surveys map the range of the rotor influence upstream of the rotor and the continuous wake formation downstream of the rotor. The details of the measurement matrix and measuring techniques are given by Zierke et al. (1993).

Prediction Method

The steady incompressible Reynolds-averaged Navier–Stokes equations are solved for the flow past the current pump, i.e.,

$$\frac{\partial U_i}{\partial x_i} = 0$$

$$\frac{\partial}{\partial x_j}(U_i U_j) + 2\epsilon_{ijk}\Omega_j U_k = -\frac{1}{\rho}\frac{\partial p}{\partial x_i} + \frac{\partial}{\partial x_j}\left[\nu_{\text{eff}}\left(\frac{\partial U_i}{\partial x_j} + \frac{\partial U_j}{\partial x_i} - \frac{2}{3}\frac{\partial U_k}{\partial x_k}\delta_{ij} - \overline{u_i u_j}\right)\right] \quad (1)$$

where U_i and u_i are mean and fluctuating velocities, Ω_i is the angular velocity, and $\nu_{\text{eff}} = \nu_{\text{lam}} + \nu_{\text{tur}}$.

To close the system of equations, a closure model for the turbulence stress should be applied. Currently many turbulence models are available for large-scale three-dimensional flow calculations. Although none of the existing closure models represent all of the salient flow features accurately, major differences between the flowfields of different aerodynamic designs can be calculated with the existing models.

It is well known that neither the conventional mixing length type turbulence model nor any standard two-equation type turbulence model describes the turbulence stresses properly in the separated flow regions. Previous studies (Hah, 1985) indicate that significant improvement can be achieved when the standard two-equation model is modified to include the low-Reynolds-number effects for the laminar sublayer region. For the current study, a standard two-equation model is modified to include the low Reynolds number

Nomenclature

C_1, C_2, C_3, C_4, C_μ = constants used in turbulence closure models
C_n = Fourier coefficients
C_p = pressure coefficient, normalized by rotor tip speed
c = chord length
f = function defined in Eq. (4)
k = turbulent kinetic energy
l = characteristic length
PS = pressure side
p = static pressure
r = radial
SS = suction side
t = tangential
U_i = mean velocity components used in Eqs. (1) and (2)
u_i = fluctuating velocity components
u_* = shear velocity
V = mean velocity components
$x_i(x, y, z)$ = Cartesian coordinates
δ_{ij} = Krönecker delta
ϵ = turbulence dissipation rate
ν_{eff} = effective kinematic viscosity
ρ = density
σ_k, σ_ϵ = constants used in turbulence closure models
Ω_i = angular velocity of rotor

Downloaded 01 Jun 2010 to 171.66.16.53. Redistribution subject to ASME license or copyright; see http://www.asme.org/terms/Terms_Use.cfm

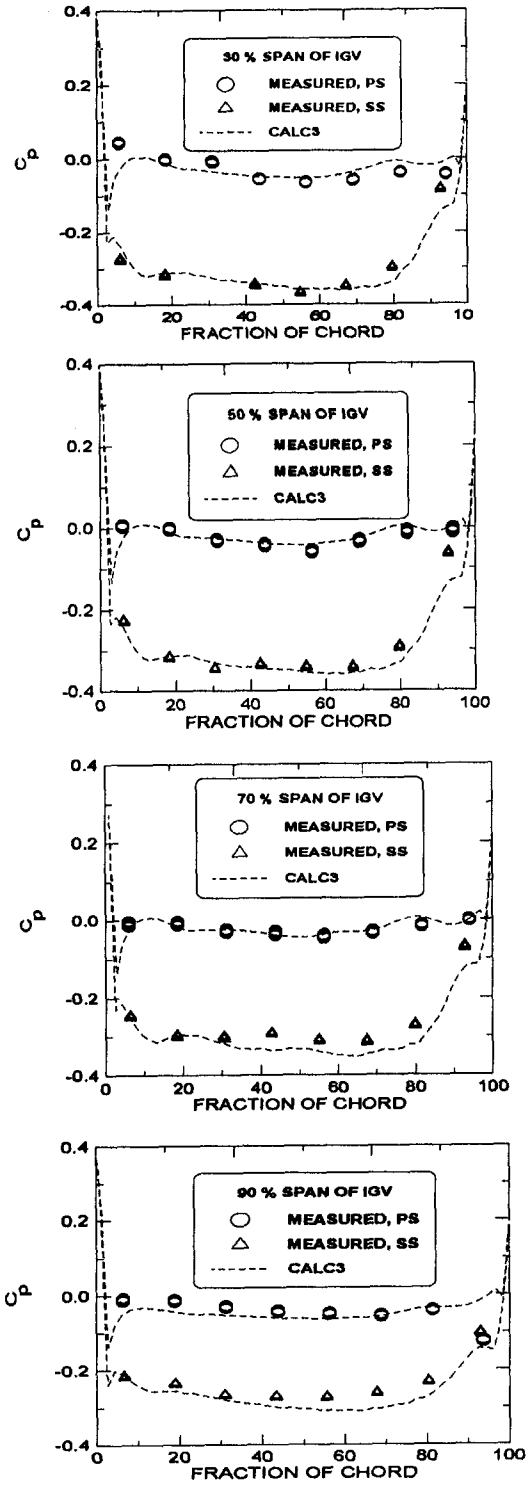


Fig. 3 Pressure distribution on IGV blades

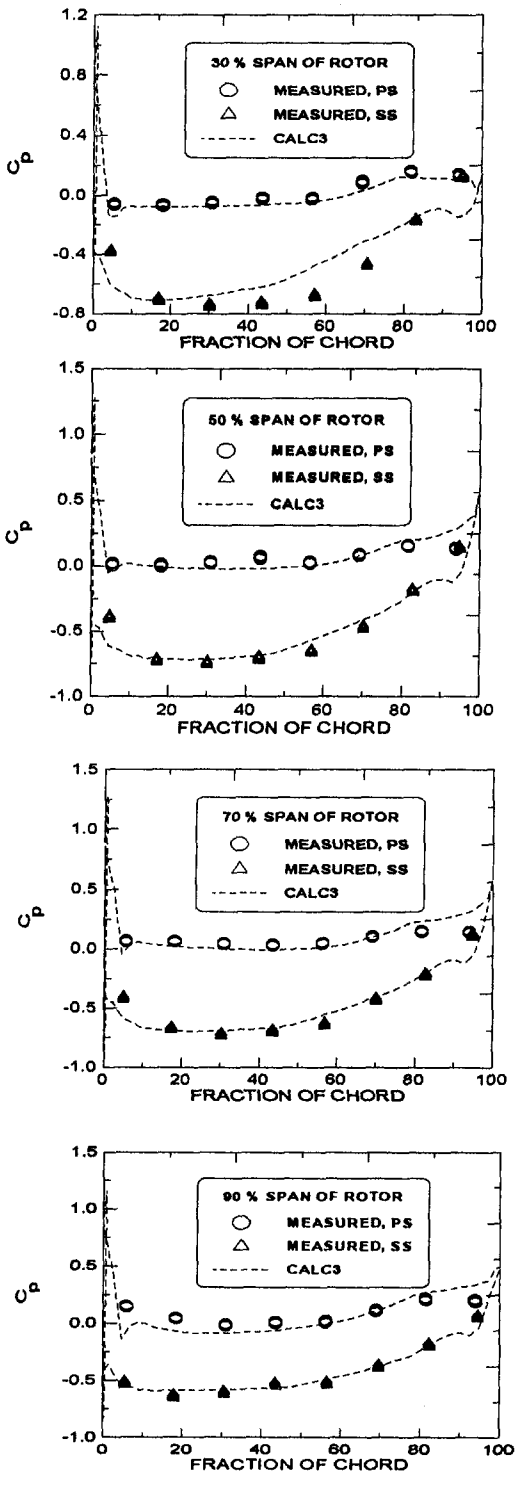


Fig. 4 Pressure distribution on rotor blades

effects following the studies of Chien (1982). The following transport equations are solved for the turbulent shear stresses:

$$U_i \frac{\partial k}{\partial x_i} = \frac{\partial}{\partial x_i}\left(\frac{\nu_{\text{eff}}}{\sigma_k}\frac{\partial k}{\partial x_i}\right) - \overline{u_i u_j} U_{ij} - \epsilon - \frac{2\nu_{\text{lam}} k}{l^2}$$

$$U_i \frac{\partial \epsilon}{\partial x_i} = \frac{\partial}{\partial x_i}\left(\frac{\nu_{\text{eff}}}{\sigma_\epsilon}\frac{\partial \epsilon}{\partial x_i}\right) - C_1 \frac{\epsilon}{k}\overline{u_i u_j} U_{ij} - \frac{\epsilon}{k}\left[C_2 f \epsilon + \frac{2\nu_{\text{lam}} k e^{-C_4 u_* l/\nu_{\text{lam}}}}{l^2}\right] \quad (2)$$

where

$$\nu_{\text{eff}} = \nu_{\text{lam}} + \frac{C_\mu}{\rho}\frac{k^2}{\epsilon}\left[1 - e^{-C_3 u_* l/\nu_{\text{lam}}}\right] \quad (3)$$

and

$$f = 1 - \frac{0.4}{1.8} e^{-(k^2/6\nu_{\text{lam}}\epsilon)^2} \quad (4)$$

The constants used in these equations are:

Downloaded 01 Jun 2010 to 171.66.16.53. Redistribution subject to ASME license or copyright; see http://www.asme.org/terms/Terms_Use.cfm

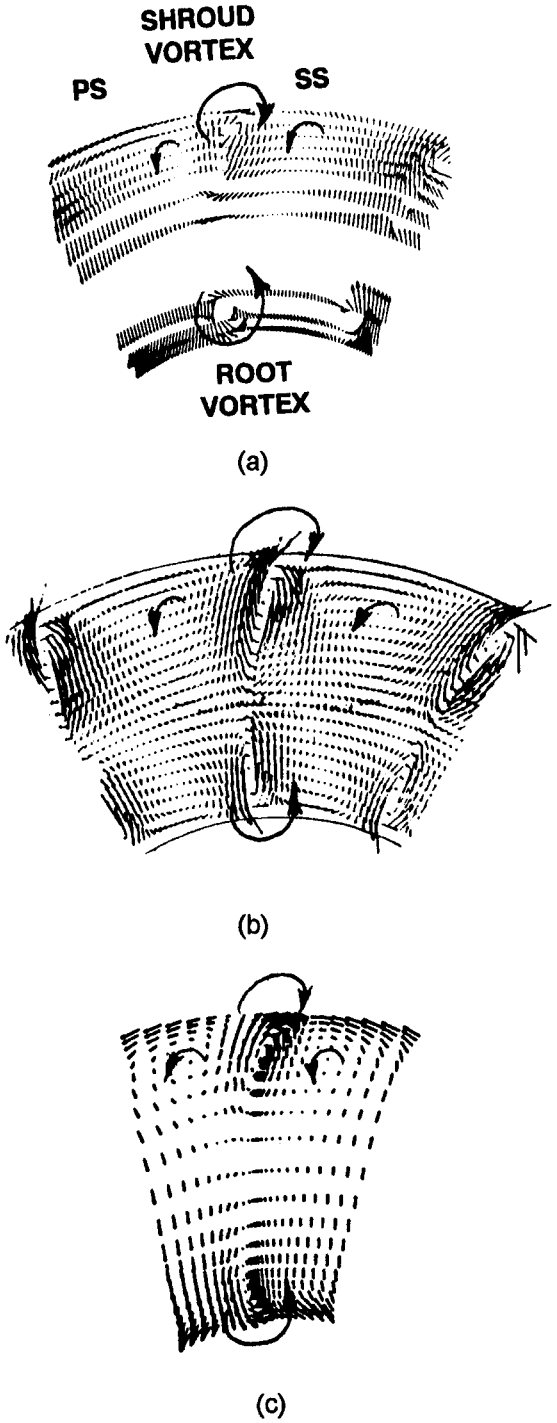


Fig. 5 Secondary flow structures of the IGV wake: (*a*) measurement; (*b*) lifting-surface prediction; (*c*) present prediction

$$C_\mu = 0.09, \quad C_1 = 1.35, \quad C_2 = 1.8, \quad \sigma_k = 1.0$$

$$\sigma_\epsilon = 1.3, \quad C_3 = 0.00115, \quad C_4 = 0.5 \qquad (5)$$

No attempt was made to optimize these constants in this study.

The current turbulence model performs better in predicting separated flows compared to a standard two-equation model coupled with a wall function treatment near the solid wall. About 20 percent of the total computational work is used to solve the transport equations for the turbulence. The low-Reynolds-number modification for the turbulence model requires less than 1 percent of the total CPU used.

These governing equations are solved with a pressure-based implicit relaxation method using a fully conservative control volume approach described by Hah (1987) for isolated rotor configurations. A third-order accurate interpolation scheme is used for the discretization of the convection terms and central differencing is used for the diffusion terms. Details of the current method are given by Copenhaver et al. (1992).

The current computational method has been validated against many flowfields to examine the accuracy and grid-dependency of numerical results. One example of the validation studies was made by Leylek and Wisler (1991) for flow over a cylinder at a Reynolds number of 30. With 12,000 computational nodes,

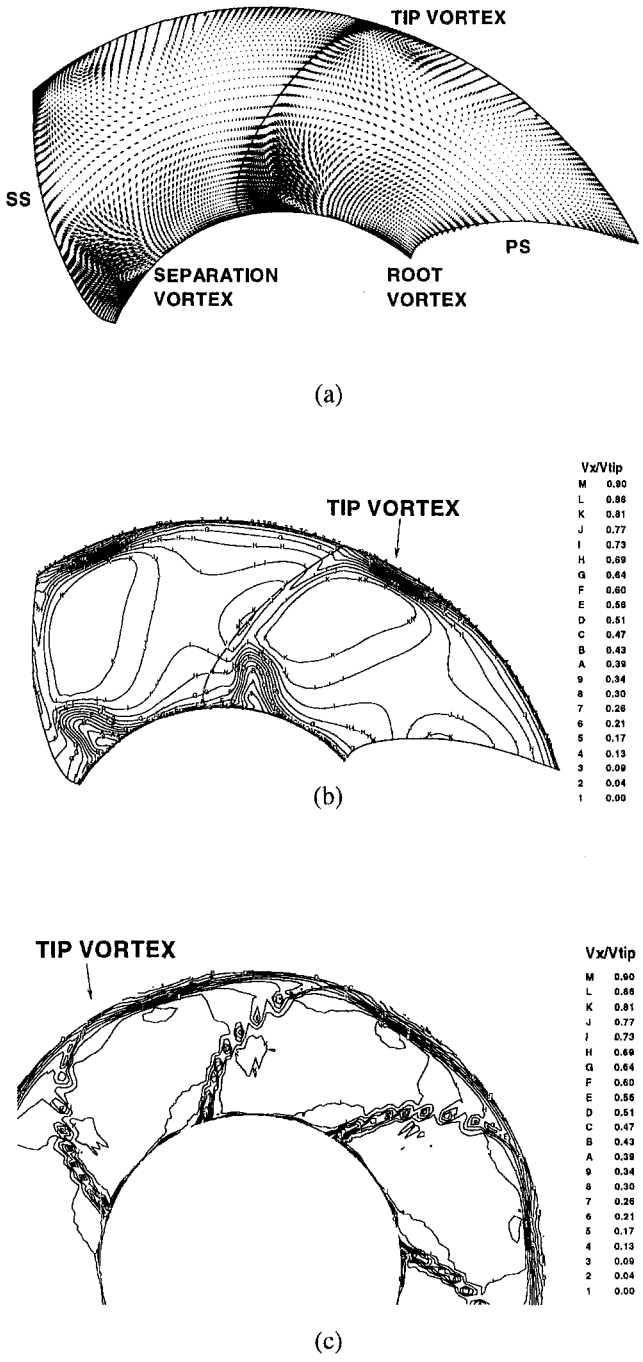


Fig. 6 Wake flow structures of the rotor: (*a*) predicted secondary flow; (*b*) predicted contours of axial velocity; (*c*) measured contours of axial velocity

Downloaded 01 Jun 2010 to 171.66.16.53. Redistribution subject to ASME license or copyright; see http://www.asme.org/terms/Terms_Use.cfm

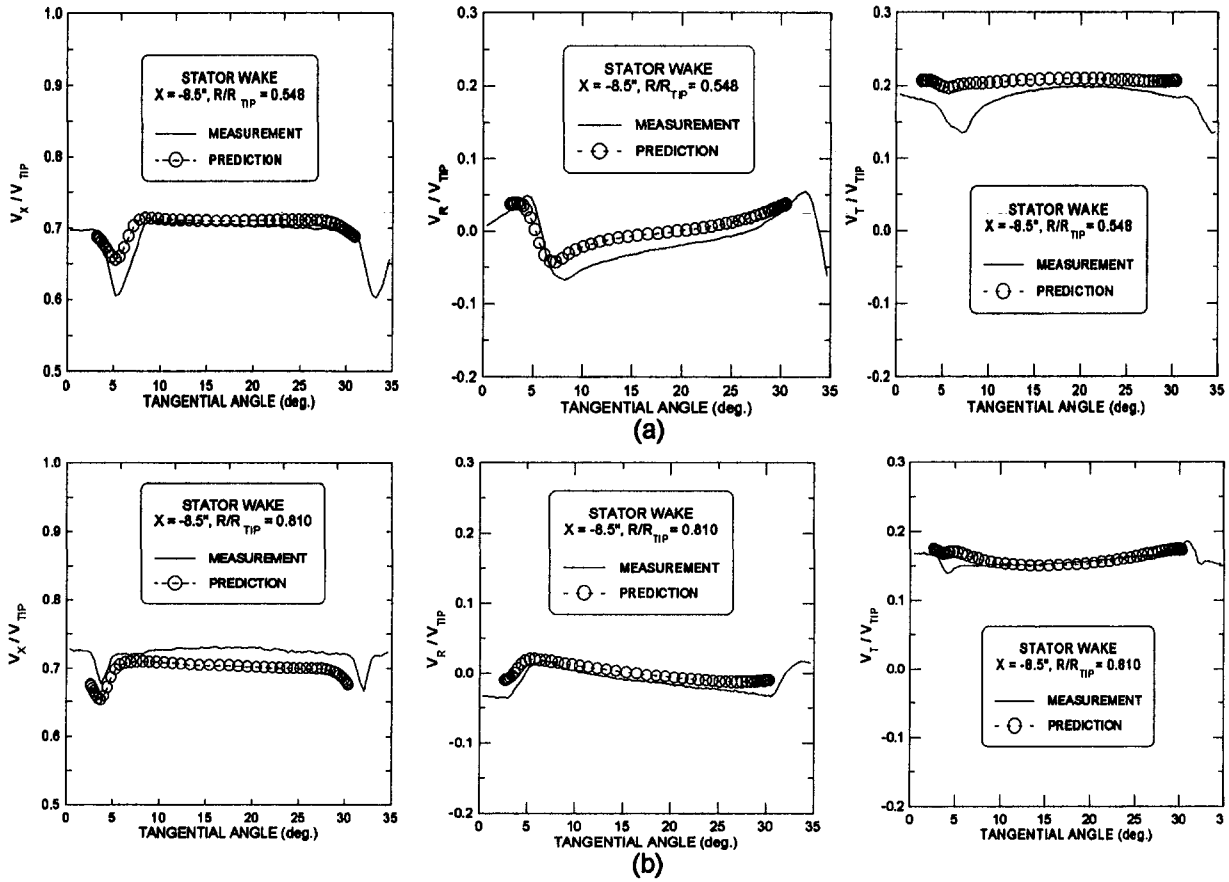


Fig. 7 Velocity comparisons in IGV wake at 49.7 percent IGV chord downstream of IGV trailing edge

the flow separation on the cylinder was predicted within 0.5 percent error compared to the measured separation length and drag. In their study of grid dependency on general gas turbine components, Hah and Leylek (1987) concluded that 700,000 nodes for two-blade-row calculation are necessary to get grid-independent solutions for the current type of flow prediction.

In this study, the numerical procedure is expanded to handle a stage configuration. As the spacing between the IGV and the rotor is relatively large, a mixing plane is established approximately centered between the two blade rows. The computational grid of the pump stage is shown in Fig. 1(b). With the current steady-state multiple-blade-row calculations, the flowfields of the IGV and the rotor are computed iteratively.

For the IGV, the radial distribution of the static pressure at the exit of the computational domain is obtained from the rotor flowfield. At this plane, all of the other flow variables are extrapolated from the IGV interior solution.

For the rotor, radial distributions of all the flow variables at the inlet of the computational domain are obtained from the IGV solution. At this mixing plane, a classical mixing analysis is performed at each radial location to obtain circumferentially uniform values of velocity. The mixing analysis, which is based on the work of Dring and Spear (1991), is necessary to obtain a steady inlet condition for the rotor flowfield. The overall mass flow rate across the stage is determined by the specified velocity components at the inlet of the IGV. This calculation can also be performed by running two separate isolated blade row solutions. However, some human intervention during the solution process can be eliminated with the current procedure. For a grid system of 700,000 grid points used for two-blade-row calculation, about 4 hours CPU time on Cray YMP single processor are required for a fully converged solution.

Results and Discussion

The current prediction method was applied to the propulsion pump described previously. The intent was to evaluate the capability of the numerical method in predicting the detailed wake structure of each blade row. The pump was operating at the design flow rate of 15,200 ft^3/min.

The computational grid, as shown in Fig. 1(b), was generated to give an orthogonal grid near the blade surfaces, particularly near the blade leading and trailing edges. Two different grid densities were used for the present calculations. The coarser grid is 102 × 39 × 29 (axial, blade-to-blade, spanwise) for the IGV and 102 × 39 × 35 for the rotor. The corresponding finer grids are 122 × 49 × 45 and 122 × 69 × 50. There are 6 (coarser grid) and 10 (finer grid) grid nodes used to describe the tip-clearance region. Inside the tip gap, the grid is closed in the blade-to-blade direction and the periodicity condition is applied. Only minor variations, as shown in the following figures, are observed between the solutions obtained with the coarser and the finer grids. All the following results are presented using the finer grid solutions.

Figure 2 shows the inlet conditions for each blade row as compared with the measured profiles. The experimental inlet axial-velocity profile for the IGV is located 37 percent chord upstream of the IGV blade. However, the computational inlet, located at 107 percent chord upstream, is prescribed by a $\frac{1}{7}$-th power boundary-layer profile. The comparison shown in Fig. 2(a) indicates that the measured boundary layer thicknesses at both the hub and casing walls are slightly thinner than the predicted ones. The rotor inlet condition was defined using the mixing analysis mentioned previously. Both the axial and the tangential velocities are compared in Fig. 2(b) at 43.5 percent

Downloaded 01 Jun 2010 to 171.66.16.53. Redistribution subject to ASME license or copyright; see http://www.asme.org/terms/Terms_Use.cfm

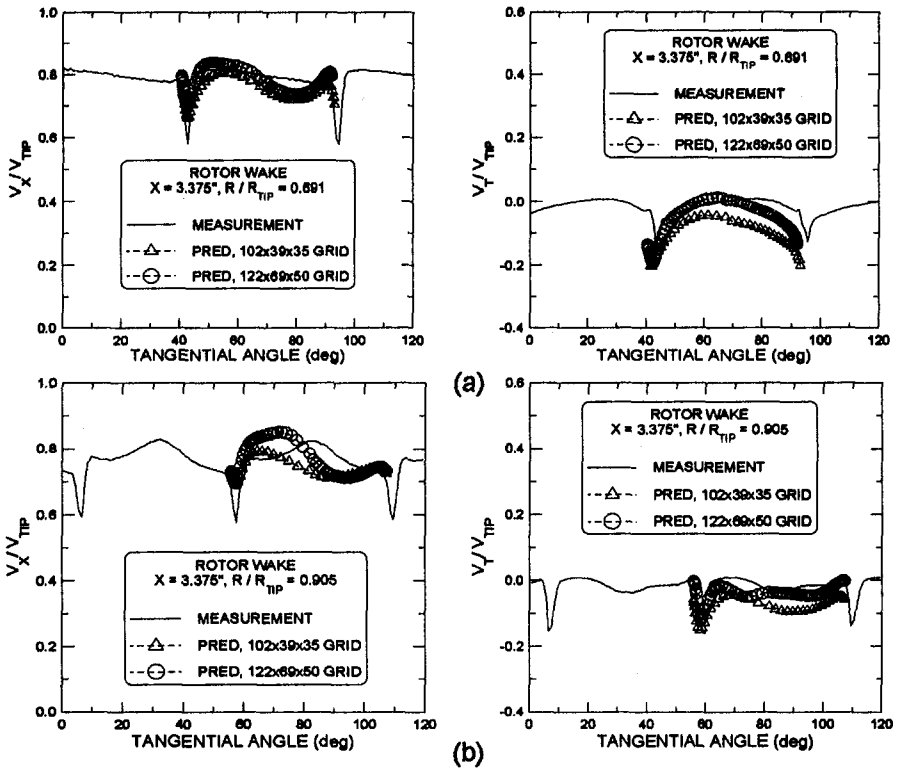


Fig. 8 Velocity comparisons in the rotor wake at 49 percent IGV chord downstream of rotor trailing edge

IGV chord upstream of the rotor tip leading edge. Although the tangential component is slightly overpredicted, the comparison implies that the flowfield out of the IGV is correctly simulated by the present steady mixing analysis.

Figures 3 and 4 provide comparisons of the blade surface pressure on each blade row at four different spanwise locations. The loading on the IGV blade is about half of that on the rotor blade (note the difference in scales used for ordinates in Figs. 3 and 4). The loading decreases along the span toward the tip for both blades. This also suggests the three dimensionality of the flowfield. Nevertheless, the blade surface pressure is well predicted.

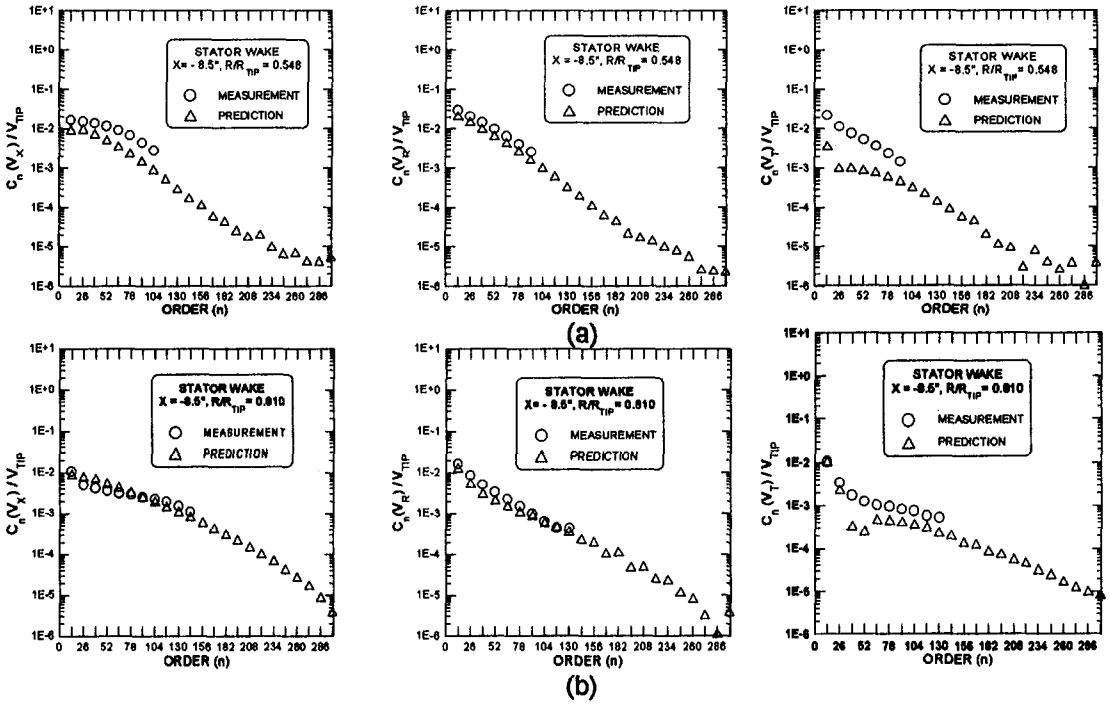


Fig. 9 Harmonic components of IGV wake velocities

Downloaded 01 Jun 2010 to 171.66.16.53. Redistribution subject to ASME license or copyright; see http://www.asme.org/terms/Terms_Use.cfm

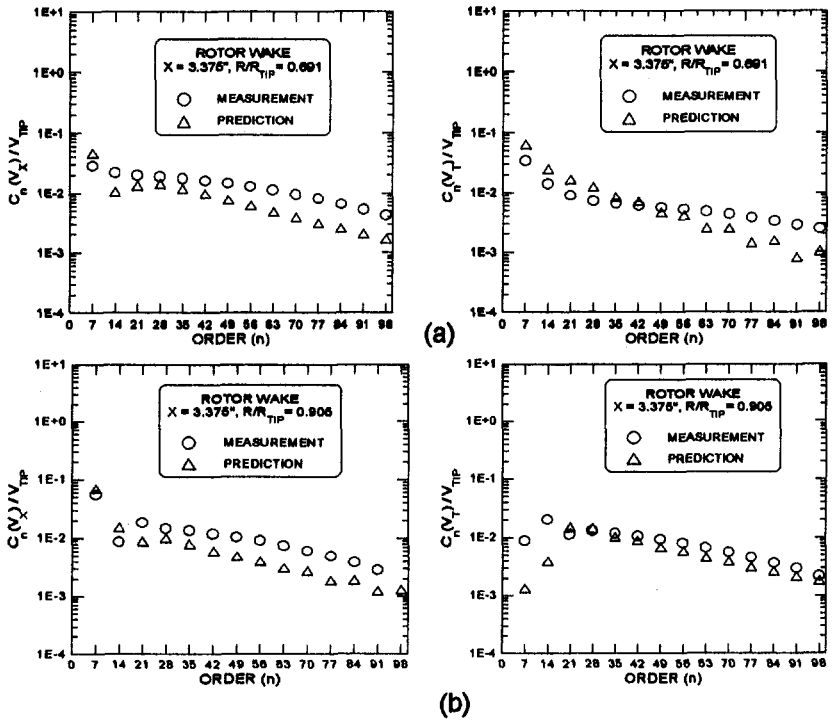


Fig. 10 Harmonic components of rotor wake velocities

Secondary-flow patterns after each blade row are presented in Figs. 5 and 6. The plotted secondary flows were obtained by subtracting mean circumferential velocities from the total crossflow velocity at each grid point or measurement location. Figure 5 shows the IGV-wake patterns obtained from measurement (Fig. 5(*a*)), a lifting-surface calculation (Fig. 5(*b*)), and the present prediction (Fig. 5(*c*)) at 49.7 percent chord downstream of the IGV. Figure 5(*b*) was reproduced from Zierke et al. (1993). The measurement and the lifting-surface solution are presented for two blade passages, but the present prediction is plotted only for one blade passage. The main shroud and root vortices appear in all three plots. The lifting-surface solution, however, predicts much larger vortices due to the lack of viscous damping effect. The present viscous solution slightly underestimates the size of the shroud vortex along the radial direction. Nevertheless, the general IGV wake vorticity structure was simulated well by the present prediction method.

The rotor wake flow is quite different from the IGV wake. Since the radial velocity in the rotor wake was not measured, Fig. 6(*a*) shows only the predicted wake flowfield of the rotor at 49 percent IGV chord downstream of the rotor tip trailing edge. Although the data are compared at roughly the same distance behind the IGV and the rotor trailing edges, the root vortex of the rotor has traveled to the midpitch region due to Corriolis acceleration. The rotor shroud vortex has mingled with the tip-clearance vortex and shows up very weakly in the velocity vector plot. However, the radial expansion of the tip-clearance vortex is underpredicted, as seen in the contour plots of the axial velocity in Figs. 6(*b*) and 6(*c*). In addition, a very strong vortex due to the flow separation on the blade suction side occurs near the hub (also shown in Fig. 11). This separation-induced vortex does not exist in the measurement.

Detailed quantitative velocity comparisons after each blade row are given in Figs. 7 and 8. Figure 7 shows three-component velocity distributions in the IGV wake at two representative radii. The predicted results are plotted using symbols to indicate the grid resolution at the comparing section. The predictions generally agree well with the measurements. The blade wake in the predicted axial velocity could be improved with a better-aligned grid along the wake developing direction. Figure 8 compares predicted and measured velocity components for the rotor wake, also at two representative radii. Predicted solutions from two different grids are shown to assess the effect of grid density. The axial-velocity comparison in the rotor wake at $r/r_{tip} = 0.905$ again shows the effect of the underpredicted size of the

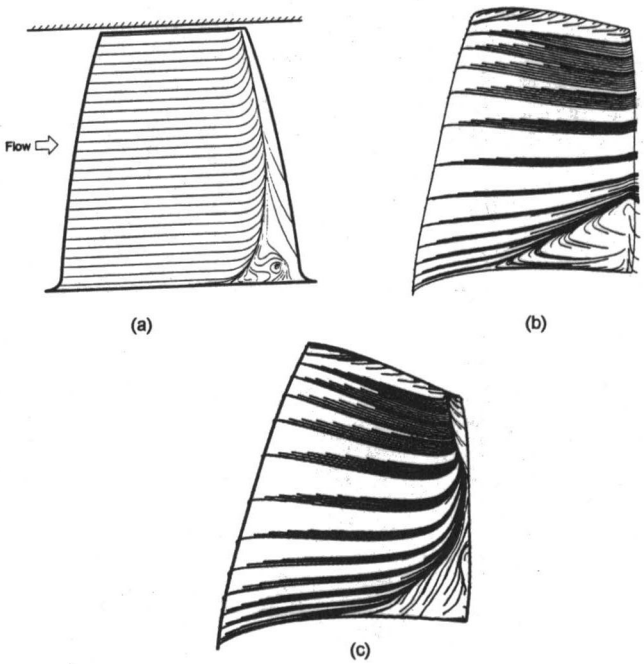


Fig. 11 Particle traces on the suction side of the rotor: (*a*) experimental observation; (*b*) prediction with standard k–ϵ model; (*c*) prediction with modified k–ϵ model

Downloaded 01 Jun 2010 to 171.66.16.53. Redistribution subject to ASME license or copyright; see http://www.asme.org/terms/Terms_Use.cfm

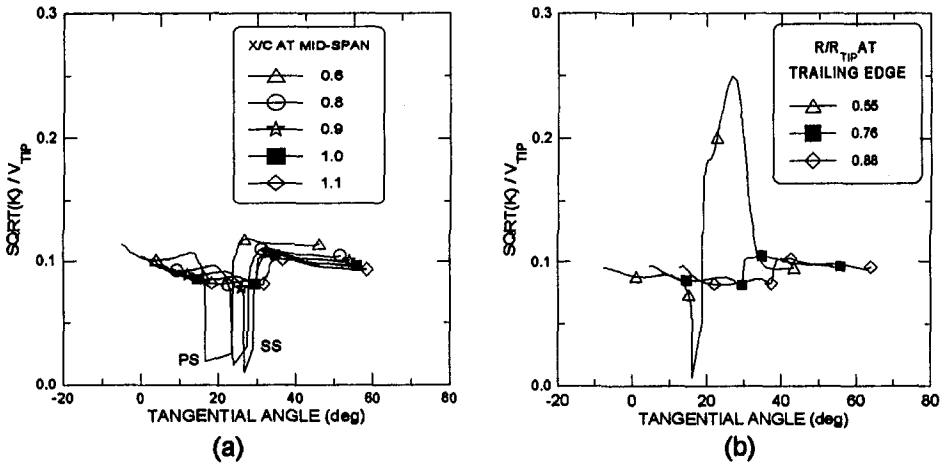


Fig. 12 Distributions of rotor turbulent kinetic energy: (*a*) along the chord; (*b*) along the span

shroud vortex. The predicted maximum velocity occurs closer to the blade suction side instead of at the midpitch shown in the experimental data. The midpitch activity in the measurement is associated with the larger swirling effect of the tip-clearance vortex.

Figures 9 and 10 show the harmonic components of the measured and predicted velocities at two different radii. The measured velocities were taken to cover 360 deg of the wake at each radius. Since these data reflect the variation between blade passages, significant noise exists in the experimental harmonic components. A simple constant-value filtering process was therefore used to eliminate those high harmonic components whose magnitude are less than or equal to the noise levels. The scales for the abscissas in Figs. 9 and 10 use multiples of 13 and 7, reflecting the numbers of blades for the IGV and the rotor. Again, the agreement between the measurements and the predictions is better for the IGV than for the rotor. However, it is worth noting that the initial fall-off of the harmonic components of the tangential velocity in the rotor wake at $r/r_{\text{tip}} = 0.905$, shown in Fig. 10(b), exists both in the measurement and in the prediction. The general agreement between the prediction and the measurement indicates that the present solution method can provide useful acoustic predictions for this type of problem.

Figure 11(a) shows the experimentally observed oil-paint tracing on the suction side of the tested rotor blade. It indicates a strong recirculating region at the hub near the trailing edge. This flow reversal at the hub is carried radially by the rotor's centrifugal motion all the way up to the rotor tip. Figure 11(b) shows the predicted particle tracing near the rotor blade suction surface. Although it contains the hub separation, the strong radial flow at the trailing edge toward the tip is not present.

Figure 12 shows distributions of the turbulent kinetic energy, k, for different chordwise locations at the midspan and for different spanwise locations at the trailing edge. It indicates that k is significantly larger in the separated region than anywhere else. This result implies that the standard $k-\epsilon$ model may have difficulty predicting the flow separation from the midspan to the tip near the trailing edge. Therefore, a simple modification of the standard $k-\epsilon$ model was made as follows. Since the experiment was performed in the water tunnel, the characteristic length scale of the incoming turbulence might be much larger than the length scale based on the IGV blade dimension. To examine this possibility, the inlet length scale was increased to 100 times the original turbulence length scale in the two-equation turbulence model. This indeed produces the particle trace as shown in Fig. 11(c) with a locally separated flow all the way up to the tip. Although this solution does not predict the complete flow features correctly, it links the thick-trailing-edge flow to a required modification of the standard $k-\epsilon$ model.

Conclusions

Steady-state Reynolds-averaged Navier–Stokes solutions for the incompressible flow past a single-stage stator (IGV)/rotor propulsion pump are presented. The prediction method uses a pressure-based scheme and a standard $k-\epsilon$ model with low-Reynolds-number approach near the wall for the turbulence closure. The steady multiple-blade-row calculation, which uses a simple mixing plane, works well for the present two-blade-row calculations. The solution compares well with the experiment in terms of stator and rotor loadings and stator wake structures, which include qualitative wake vortex patterns and quantitative velocity comparisons. Although the vorticity characteristics of the IGV wake are primarily inviscid in nature, the present viscous solution predicts more localized root and shroud vortices, in agreement with the measurement, than those obtained from the inviscid solution. Since the measurements of all the velocity components in the rotor wake were not completed, limited comparisons can be made for the rotor. However, the thick trailing edge of the rotor blade with locally separated flow clearly challenges the standard $k-\epsilon$ turbulence model. Although the rotor wake velocity distributions were predicted with reasonable accuracy, detailed assessment of the effects of the tip-clearance vortex, turbulence model, and thick trailing-edge flows require further in-depth study. The harmonic analyses of the stator and the rotor wake components enhance the ability to identify strong acoustical sources during design.

Acknowledgments

This work was partially supported by the Applied Hydrodynamics Research Program (AHR) and the Submarine Block Program for Hydrodynamics and Hydroacoustics of Internal Flow. The program monitor is Dr. L. P. Purtel. Computer resources were provided by Numerical Aerodynamic Simulation (NAS) facility at NASA Ames Research Center. The authors are indebted to Messrs. W. C. Zierke, W. A. Straka, P. D. Taylor, and J. J. Dreyer for providing the test data and pump geometry.

References

Chen, W. C., Pruger, G., Chen, D., and Eastland, A., 1992, "On the Use of a Three-Dimensional Navier–Stokes Solver for Rocket Pump Impeller Design," AIAA Paper No. 92-3223.

Chen, Y. S., 1988, "3-D Stator–Rotor Interaction of the SSME," AIAA Paper No. 88-3095.

Downloaded 01 Jun 2010 to 171.66.16.53. Redistribution subject to ASME license or copyright; see http://www.asme.org/terms/Terms_Use.cfm

Chen, Y. S., 1989, "Compressible and Incompressible Flow Computations With a Pressure Based Method," AIAA Paper No. 89-0286.

Chien, K. Y., 1982, "Predictions of Channel and Boundary-Layer Flows With a Low-Reynolds-Number Turbulence Model," *AIAA Journal,* Vol. 20, No. 1, pp. 33–38.

Copenhaver, W. W., Hah, C., and Puterbauch, S. L., 1992, "Three-Dimensional Flow Phenomena in a Transonic, High-Through-Flow Compressor Stage," ASME JOURNAL OF TURBOMACHINERY, Vol. 115, pp. 240–248.

Dawes, W. N., 1988, "Development of a 3D Navier–Stokes Solver for Application to all Types of Turbomachinery," ASME Paper No. 88-GT-70.

Deng, G. B., Queutey, P., and Visonneau, M., 1993, "Navier–Stokes Computations of Ship Stern Flows: A Detailed Comparative Study of Turbulence Models and Discretization Schemes," presented at the 6th International Conference on Numerical Ship Hydrodynamics, Iowa City, IA.

Dring, R. P., and Spear, D. A., 1991, "The Effects of Wake Mixing on Compressor Aerodynamics," ASME JOURNAL OF TURBOMACHINERY, Vol. 113, pp. 600–607.

Farrell, K. J., McBride, M. W., and Billet, M. L., 1987, "High Reynolds Number Pump Facility for Cavitation Research," The Pennsylvania State University/ARL Technical Report No. TR 87-011.

Garcia, R., Jacson, E. D., and Schutzenhofer, L. A., 1992a, "A Summary of the Activities of the NASA/MSFC Pump Stage Technology Team," *Proceedings of the Fourth International Symposium on Transport Phenomena and Dynamics of Rotating Machinery,* Honolulu, HI.

Garcia, R., McConnaughey, P., and Eastland, A., 1992b, "Activities of MSFC Pump Stage Technology Team," AIAA Paper No. 92-3232.

Giles, M. B., 1988, "Stator/Rotor Interaction in a Transonic Turbine," AIAA Paper No. 88-3093.

Hah, C., 1985, "Modeling of Turbulent Flow Fields Through Cascade of Airfoils at Stall Condition," *AIAA Journal,* Vol. 23, pp. 1411–1417.

Hah, C., 1987, "Calculation of Three-Dimensional Viscous Flows in Turbomachinery With an Implicit Relaxation Method," *AIAA Journal of Propulsion and Power,* Vol. 3, No. 5, pp. 415–422.

Hah, C., and Leylek, J. H., 1987, "Numerical Solution of Three-Dimensional Turbulent Flows for Modern Gas Turbine Components," ASME Paper No. 87-GT-84.

Hah, C., Brayns, A. C., Moussa, Z., and Tomsho, M. E., 1988, "Application of Viscous Flow Computations for Aerodynamic Performance of a Backswept Impeller at Viscous Operating Conditions," ASME JOURNAL OF TURBOMACHINERY, Vol. 110, pp. 303–311.

Jorgenson, P. C. E., and Chima, R. V., 1988, "An Explicit Runge–Kutta Method for Unsteady Rotor/Stator Interaction," AIAA Paper No. 88-0049.

Kiris, C., Chang, L., Kwak, D., and Rogers, S., 1993, "Incompressible Navier–Stokes Computations of Rotating Flows," AIAA Paper No. 93-0678.

Leylek, J. H., and Wisler, D. C., 1991, "Mixing in Axial-Flow Compressors: Conclusions Drawn From Three-Dimensional Navier–Stokes Analysis and Experiment," ASME JOURNAL OF TURBOMACHINERY, Vol. 113, pp. 139–160.

Rai, M. M., 1985, "Navier–Stokes Simulations of Rotor–Stator Interaction Using Patched and Overlaid Grids," AIAA Paper No. 85-1519.

Rao, K., and Delaney, R., 1990, "Investigation of Unsteady Flow Through Transonic Turbine Stage," AIAA Paper No. 90-2408.

Stanier, M. J., 1992, "Design and Devaluation of New Propeller Blade Section," presented at the Int. Sym. on Propulsors and Cavitation, Hamburg, June 22–25.

Walker, P. J., and Dawes, W. N., 1990, "The Extension and Application of Three-Dimensional Time-Marching Analysis to Incompressible Turbomachinery Flows," ASME JOURNAL OF TURBOMACHINERY, Vol. 112, pp. 385–390.

Zierke, W. C., Straka, W. A., and Taylor, P. D., 1993, "The High Reynolds Number Flow Through an Axial-Flow Pump," The Pennsylvania State University/ARL Technical Report No. TR93-12, Nov.

DISCUSSION

W. C. Zierke[1]

As an experimentalist, I am pleased to see engineers compare my data with their numerical computations. This particular data set offers measurements of a very complex flow field to those attempting to compute the incompressible flow through a turbomachine. The authors should be commended for attempting to use their code in such a severe test case.

First, I would like to clear up a few discrepancies between the authors' paper and the experimental report of Zierke et al. (1993). The authors' description of the rotor blade thickness and camber distributions is incorrect, although I am sure that they did in fact use the correct blade coordinates for their computations. Also, the experimental data used in the inlet axial-velocity profile of Fig. 2(a) must have been some preliminary data, since these data do not correspond to data from the experimental report. Finally, the computations in Fig. 5(b) were performed with lifting surface theory, not lifting line theory.

Next, I would like to address some of the comparisons between the experimental and computational results. First, the authors stated that the secondary velocity vectors predicted in Figs. 5(c) and 6(a) came from single blade passages; and yet, the radial components do not seem to show periodicity. Is the entire passage shown in each of these figures? Then, for the predicted axial-velocity contours of Fig. 6(b), the authors predict a "separation induced vortex" not shown in the measurements. Lee et al. feel that this vortex is damped out quicker in the measurements than in the prediction. And yet, Zierke et al. (1993) report additional data measured much closer to the trailing edge near the rotor blade root and these data also show no sign of this vortex. Therefore, our laser-Doppler velocimeter measurements do not detect a significant vortex in this region—in contrast to the computations. Finally, the velocities predicted downstream of each blade row are fair, although the tangential velocities predicted downstream of the inlet guide vanes are poor and this leads to a poorly predicted harmonic content. Downstream of the rotor blades, the mismatch in the comparisons does not necessarily mean that the measured and computed strengths of the tip leakage vortex are different. The plots in Fig. 8 are simply two-dimensional cuts through a complex, three-dimensional flow field. The computed vortex strength could be very good—but simply computed to be in the wrong location.

Finally, I would like to comment on statements made by the Lee et al.—in particular, those concerning the flow patterns near the rotor blade suction surface. Contrary to their statement, the flow reversal in the corner separation does not produce the strong radial flow in the experimental flow visualization. Centrifugal effects cause this radial migration. By altering characteristics of the rotor blade design (such as the blade lean), one could design a blade with a flow reversal in the corner separation without having a strong radial migration. Later, in their alternate computation with a variation in their turbulence model, Lee et al. stated that our water tunnel experiment could produce a characteristic length scale of the incoming turbulence that might be much larger than the length scale based on the IGV dimension. Using this reasoning, they increased the inlet length scale to 100 times their original length scale. I have a very difficult time following this argument. As stated by Zierke et al. (1993), the water tunnel turbulence is controlled using a honeycomb. This honeycomb will establish an inlet turbulent length scale that is much smaller than the IGV dimensions. Even without a honeycomb, the inlet turbulent length scale cannot be larger than the IGV dimensions. If the authors need to change their length scale so dramatically—and change it in the wrong direction—one should question both the sensitivity and the utility of using their turbulence model for this type of flow field.

In summary, I feel that the comparison of these computations with our experimental data show just how difficult it is to compute the flow through a turbomachine. This type of complex, unsteady, three-dimensional flow field places a large burden on the numerical analyst. Issues with the numerical algorithms, the turbulence models, and the computational grids must all be addressed in order to improve the predictions of this and similar turbomachinery flow fields. Again, the authors should be commended for testing their code by performing these computations.

Authors' Closure

As the computational analysts, we are delighted to see the experimentalist providing his view about our computational results.

First of all, these computational results were obtained almost two and half years ago. We were the first group attempting to

[1] Applied Research Laboratory, The Pennsylvania State University, State College, PA 16804.

Downloaded 01 Jun 2010 to 171.66.16.53. Redistribution subject to ASME license or copyright; see http://www.asme.org/terms/Terms_Use.cfm

Chen, Y. S., 1989, "Compressible and Incompressible Flow Computations With a Pressure Based Method," AIAA Paper No. 89-0286.

Chien, K. Y., 1982, "Predictions of Channel and Boundary-Layer Flows With a Low-Reynolds-Number Turbulence Model," *AIAA Journal,* Vol. 20, No. 1, pp. 33–38.

Copenhaver, W. W., Hah, C., and Puterbauch, S. L., 1992, "Three-Dimensional Flow Phenomena in a Transonic, High-Through-Flow Compressor Stage," ASME JOURNAL OF TURBOMACHINERY, Vol. 115, pp. 240–248.

Dawes, W. N., 1988, "Development of a 3D Navier–Stokes Solver for Application to all Types of Turbomachinery," ASME Paper No. 88-GT-70.

Deng, G. B., Queutey, P., and Visonneau, M., 1993, "Navier–Stokes Computations of Ship Stern Flows: A Detailed Comparative Study of Turbulence Models and Discretization Schemes," presented at the 6th International Conference on Numerical Ship Hydrodynamics, Iowa City, IA.

Dring, R. P., and Spear, D. A., 1991, "The Effects of Wake Mixing on Compressor Aerodynamics," ASME JOURNAL OF TURBOMACHINERY, Vol. 113, pp. 600–607.

Farrell, K. J., McBride, M. W., and Billet, M. L., 1987, "High Reynolds Number Pump Facility for Cavitation Research," The Pennsylvania State University/ARL Technical Report No. TR 87-011.

Garcia, R., Jacson, E. D., and Schutzenhofer, L. A., 1992a, "A Summary of the Activities of the NASA/MSFC Pump Stage Technology Team," *Proceedings of the Fourth International Symposium on Transport Phenomena and Dynamics of Rotating Machinery,* Honolulu, HI.

Garcia, R., McConnaughey, P., and Eastland, A., 1992b, "Activities of MSFC Pump Stage Technology Team," AIAA Paper No. 92-3232.

Giles, M. B., 1988, "Stator/Rotor Interaction in a Transonic Turbine," AIAA Paper No. 88-3093.

Hah, C., 1985, "Modeling of Turbulent Flow Fields Through Cascade of Airfoils at Stall Condition," *AIAA Journal,* Vol. 23, pp. 1411–1417.

Hah, C., 1987, "Calculation of Three-Dimensional Viscous Flows in Turbomachinery With an Implicit Relaxation Method," *AIAA Journal of Propulsion and Power,* Vol. 3, No. 5, pp. 415–422.

Hah, C., and Leylek, J. H., 1987, "Numerical Solution of Three-Dimensional Turbulent Flows for Modern Gas Turbine Components," ASME Paper No. 87-GT-84.

Hah, C., Brayns, A. C., Moussa, Z., and Tomsho, M. E., 1988, "Application of Viscous Flow Computations for Aerodynamic Performance of a Backswept Impeller at Viscous Operating Conditions," ASME JOURNAL OF TURBOMACHINERY, Vol. 110, pp. 303–311.

Jorgenson, P. C. E., and Chima, R. V., 1988, "An Explicit Runge–Kutta Method for Unsteady Rotor/Stator Interaction," AIAA Paper No. 88-0049.

Kiris, C., Chang, L., Kwak, D., and Rogers, S., 1993, "Incompressible Navier–Stokes Computations of Rotating Flows," AIAA Paper No. 93-0678.

Leylek, J. H., and Wisler, D. C., 1991, "Mixing in Axial-Flow Compressors: Conclusions Drawn From Three-Dimensional Navier–Stokes Analysis and Experiment," ASME JOURNAL OF TURBOMACHINERY, Vol. 113, pp. 139–160.

Rai, M. M., 1985, "Navier–Stokes Simulations of Rotor–Stator Interaction Using Patched and Overlaid Grids," AIAA Paper No. 85-1519.

Rao, K., and Delaney, R., 1990, "Investigation of Unsteady Flow Through Transonic Turbine Stage," AIAA Paper No. 90-2408.

Stanier, M. J., 1992, "Design and Devaluation of New Propeller Blade Section," presented at the Int. Sym. on Propulsors and Cavitation, Hamburg, June 22–25.

Walker, P. J., and Dawes, W. N., 1990, "The Extension and Application of Three-Dimensional Time-Marching Analysis to Incompressible Turbomachinery Flows," ASME JOURNAL OF TURBOMACHINERY, Vol. 112, pp. 385–390.

Zierke, W. C., Straka, W. A., and Taylor, P. D., 1993, "The High Reynolds Number Flow Through an Axial-Flow Pump," The Pennsylvania State University/ARL Technical Report No. TR93-12, Nov.

DISCUSSION

W. C. Zierke[1]

As an experimentalist, I am pleased to see engineers compare my data with their numerical computations. This particular data set offers measurements of a very complex flow field to those attempting to compute the incompressible flow through a turbomachine. The authors should be commended for attempting to use their code in such a severe test case.

First, I would like to clear up a few discrepancies between the authors' paper and the experimental report of Zierke et al. (1993). The authors' description of the rotor blade thickness and camber distributions is incorrect, although I am sure that they did in fact use the correct blade coordinates for their computations. Also, the experimental data used in the inlet axial-velocity profile of Fig. 2(a) must have been some preliminary data, since these data do not correspond to data from the experimental report. Finally, the computations in Fig. 5(b) were performed with lifting surface theory, not lifting line theory.

Next, I would like to address some of the comparisons between the experimental and computational results. First, the authors stated that the secondary velocity vectors predicted in Figs. 5(c) and 6(a) came from single blade passages; and yet, the radial components do not seem to show periodicity. Is the entire passage shown in each of these figures? Then, for the predicted axial-velocity contours of Fig. 6(b), the authors predict a "separation induced vortex" not shown in the measurements. Lee et al. feel that this vortex is damped out quicker in the measurements than in the prediction. And yet, Zierke et al. (1993) report additional data measured much closer to the trailing edge near the rotor blade root and these data also show no sign of this vortex. Therefore, our laser-Doppler velocimeter measurements do not detect a significant vortex in this region—in contrast to the computations. Finally, the velocities predicted downstream of each blade row are fair, although the tangential velocities predicted downstream of the inlet guide vanes are poor and this leads to a poorly predicted harmonic content. Downstream of the rotor blades, the mismatch in the comparisons does not necessarily mean that the measured and computed strengths of the tip leakage vortex are different. The plots in Fig. 8 are simply two-dimensional cuts through a complex, three-dimensional flow field. The computed vortex strength could be very good—but simply computed to be in the wrong location.

Finally, I would like to comment on statements made by the Lee et al.—in particular, those concerning the flow patterns near the rotor blade suction surface. Contrary to their statement, the flow reversal in the corner separation does not produce the strong radial flow in the experimental flow visualization. Centrifugal effects cause this radial migration. By altering characteristics of the rotor blade design (such as the blade lean), one could design a blade with a flow reversal in the corner separation without having a strong radial migration. Later, in their alternate computation with a variation in their turbulence model, Lee et al. stated that our water tunnel experiment could produce a characteristic length scale of the incoming turbulence that might be much larger than the length scale based on the IGV dimension. Using this reasoning, they increased the inlet length scale to 100 times their original length scale. I have a very difficult time following this argument. As stated by Zierke et al. (1993), the water tunnel turbulence is controlled using a honeycomb. This honeycomb will establish an inlet turbulent length scale that is much smaller than the IGV dimensions. Even without a honeycomb, the inlet turbulent length scale cannot be larger than the IGV dimensions. If the authors need to change their length scale so dramatically—and change it in the wrong direction—one should question both the sensitivity and the utility of using their turbulence model for this type of flow field.

In summary, I feel that the comparison of these computations with our experimental data show just how difficult it is to compute the flow through a turbomachine. This type of complex, unsteady, three-dimensional flow field places a large burden on the numerical analyst. Issues with the numerical algorithms, the turbulence models, and the computational grids must all be addressed in order to improve the predictions of this and similar turbomachinery flow fields. Again, the authors should be commended for testing their code by performing these computations.

Authors' Closure

As the computational analysts, we are delighted to see the experimentalist providing his view about our computational results.

First of all, these computational results were obtained almost two and half years ago. We were the first group attempting to

[1] Applied Research Laboratory, The Pennsylvania State University, State College, PA 16804.

Copyright © 1996 by ASME

Downloaded 01 Jun 2010 to 171.66.16.53. Redistribution subject to ASME license or copyright; see http://www.asme.org/terms/Terms_Use.cfm

Computational Modeling of Three-Dimensional Endwall Flow Through a Turbine Rotor Cascade With Strong Secondary Flows

Y.-H. Ho

B. Lakshminarayana

Center for Gas Turbines and Power,
Department of Aerospace Engineering,
Pennsylvania State University,
University Park, PA

A steady, three-dimensional Navier–Stokes solver that utilizes a pressure-based technique for incompressible flows is used to simulate the three-dimensional flow field in a turbine cascade. A new feature of the numerical scheme is the implementation of a second-order plus fourth-order artificial dissipation formulation, which provides a precise control of the numerical dissipation. A low-Reynolds-number form of a two-equation turbulence model is used to account for the turbulence effects. Comparison between the numerical predictions and the experimental data indicates that the numerical model is able to capture most of the complex flow phenomena in the endwall region of a turbine cascade, except the high gradient region in the secondary vortex core. The effects of inlet turbulence intensity and turbulence length scale on secondary vortices, total pressure loss, and turbulence kinetic energy inside the passage are presented and interpreted. It is found that higher turbulence intensity energizes the vortical motions and tends to move the passage vortex away from the endwall. With a larger turbulence length scale, the secondary flow inside the passage is reduced. However, the total pressure loss increases due to higher turbulence kinetic energy production.

Introduction

The flow field in the endwall region of a turbine is complex and three dimensional, with horseshoe vortices, secondary vortices, and large flow turning, resulting in substantial deviation from the midspan flow and increased losses. The flow mechanisms inside axial turbines are reasonably understood, but the loss-generating mechanisms and their dependency on some important parameters have not been resolved. Many investigators have tried to isolate these sources. Walsh and Gregory-Smith (1990) studied the effects of inlet boundary layer skew on the development of the secondary flow and losses. Moore and Adhye (1985) investigated the mixing process and the loss mechanism downstream of a turbine cascade. The effects of incidence angle and pitch-chord ratios on secondary flows were investigated by Perdichizzi and Dossena (1993). The effects of different levels of inlet turbulence were studied by Adjlout and Dixon (1992). Sharma and Butler (1987) developed a secondary loss correlation to account for the effects of inlet boundary layer and turbine geometric variables.

The ability to model and simulate complex flow phenomena inside turbomachinery passages with good accuracy can provide reliable guidance for the design of the next generation turbines, and provide confidence on the role of CFD codes in the turbine design process. Accurate computation of three-dimensional turbomachinery flow fields is now feasible due to advances in high-speed computers. The numerical predictions by Hah (1984) and Moore and Moore (1985) are typical examples of viscous turbine flow computations. Cleak and Gregory-Smith (1992) computed the flow field inside an annual turbine cascade with different turbulence models. A better agreement of the mean flow with the experimental data (Gregory Smith et al., 1988) was achieved through the use of a mixing length model and specifying a block of laminar flow up to 80 percent axial chord and 10 percent span away from the endwall. A review of the computational techniques is given by Lakshminarayana (1991).

In this paper, a Navier–Stokes procedure that utilizes a pressure-based method is used to simulate the same turbine flow field investigated by Cleak and Gregory-Smith (1992). A low-Reynolds-number form of the two-equation turbulence model is used to simulate the turbulence effects without special treatment of the near-wall flow field. The effects of the high inlet turbulence intensity and differing turbulence length scales, encountered in practical turbine applications, are simulated, and their effects on the secondary flows and losses are studied.

Governing Equations and Numerical Technique

Details of the equations, formulation, and numerical procedure can be found in Basson and Lakshminarayana (1994). Only a brief summary is given here. The momentum equations and the two-equation turbulence model (Chien, 1982) can be treated as special cases of the following general convection-diffusion transport equation, which is used in the formulation of the solution procedure:

$$\frac{\partial(\rho J G_1 \phi)}{\partial \xi} + \frac{\partial(\rho J G_2 \phi)}{\partial \eta} + \frac{\partial(\rho J G_3 \phi)}{\partial \zeta} = \frac{\partial}{\partial \xi}\left(\Gamma \alpha J \frac{\partial \phi}{\partial \xi} + \Gamma \theta_1 J \frac{\partial \phi}{\partial \eta} + \Gamma \theta_2 J \frac{\partial \phi}{\partial \zeta}\right) + \frac{\partial}{\partial \eta}\left(\Gamma \beta J \frac{\partial \phi}{\partial \eta} + \Gamma \theta_1 J \frac{\partial \phi}{\partial \xi} + \Gamma \theta_3 J \frac{\partial \phi}{\partial \zeta}\right) + \frac{\partial}{\partial \zeta}\left(\Gamma \gamma J \frac{\partial \phi}{\partial \zeta} + \Gamma \theta_2 J \frac{\partial \phi}{\partial \xi} + \Gamma \theta_3 J \frac{\partial \phi}{\partial \eta}\right) + JS \quad (1)$$

Contributed by the International Gas Turbine Institute and presented at the 39th International Gas Turbine and Aeroengine Congress and Exposition, The Hague, The Netherlands, June 13–16, 1994. Manuscript received by the International Gas Turbine Institute February 11, 1994. Paper No. 94-GT-136. Associate Technical Editor: E. M. Greitzer.

Copyright © 1996 by ASME

Downloaded 01 Jun 2010 to 171.66.16.53. Redistribution subject to ASME license or copyright; see http://www.asme.org/terms/Terms_Use.cfm

A second-order central difference approximation is used for all the derivatives in the momentum equations. The following second and fourth-order artificial dissipation terms are added to the right-hand side to maintain the numerical stability:

$$+\frac{1}{2}\epsilon_2\left[\frac{\partial}{\partial\xi}\left(|\rho JG_1|\frac{\partial\phi}{\partial\xi}\right)+\frac{\partial}{\partial\eta}\left(|\rho JG_2|\frac{\partial\phi}{\partial\eta}\right)+\frac{\partial}{\partial\zeta}\left(|\rho JG_3|\frac{\partial\phi}{\partial\zeta}\right)\right]-\frac{1}{8}\epsilon_4\left[\frac{\partial}{\partial\xi}\left(|\rho JG_1|\frac{\partial^3\phi}{\partial\xi^3}\right)+\frac{\partial}{\partial\eta}\left(|\rho JG_2|\frac{\partial^3\phi}{\partial\eta^3}\right)+\frac{\partial}{\partial\zeta}\left(|\rho JG_3|\frac{\partial^3\phi}{\partial\zeta^3}\right)\right] \quad (2)$$

The first derivative terms, and the second derivative terms that do not contain cross derivatives, are treated implicitly. The fourth-order artificial dissipation terms are split into implicitly treated and explicitly treated parts. The remaining terms are treated explicitly. The *E*-factor underrelaxation scheme due to Van Doormaal and Raithby (1984) is implemented in the present formulation.

In the Navier–Stokes code, the momentum, turbulent kinetic energy, and turbulence dissipation rate conservation equations are solved subsequently using the formulation for the general convection-diffusion equation. The artificial dissipation scheme described above is applied to the momentum equations. The power-law scheme is used for the k and ϵ equations, where stronger dissipation terms are necessary to maintain numerical stability.

A periodic boundary condition is used for all velocity components, pressure, and turbulent kinetic energy, and turbulence dissipation rate at the blade to blade interface. The velocity components and turbulent kinetic energy are prescribed at the inlet for the convection-diffusion equations. The turbulence dissipation rate at the inlet is derived from the following formulation:

$$\epsilon_1 = \rho_1 C_\mu \frac{k_1^2}{\mu_t} \quad (3)$$

where $C_\mu = 0.09$, μ_t is the turbulent viscosity, and the subscript 1 represents the inlet condition. This viscosity ratio controls the inlet turbulence length scale. At the exit, all variables in the scalar-transport equations are calculated directly from the convection-diffusion equations without using any assumptions. Velocities and turbulent kinetic energy are set to zero on all solid surfaces. For the two-equation turbulence model employed in this code, the gradient of turbulence dissipation rate is set to zero. For the pressure correction equation, the Neumann boundary condition is applied to the inlet and all solid surfaces and a constant pressure is prescribed at the exit plane for the cascade case studied in this paper. The difference equations for the convection-diffusion and pressure correction equations are solved by an ADI solution scheme.

Description of the Test Case and the Numerical Model

The case chosen to demonstrate the ability of the Navier–Stokes code to predict the complex three-dimensional flow field inside a turbine passage is the experimental investigation carried out by Gregory-Smith and Cleak (1990) and Gregory-Smith (1993). The characteristics of the turbine cascade are as follows: inlet flow angle, 42.75 deg; blade exit angle, −68.7 deg; blade chord, 224 mm; blade pitch, 191 mm; blade half-span, 200 mm; Reynolds number (based on the axial chord and exit velocity), 4.0×10^5. The corresponding free-stream velocity is 19.1 m/s. The inlet boundary layer can be well represented by a power law profile, with thickness of 41 mm and an exponent of 0.10 (Gregory-Smith, 1993). The inlet turbulence intensity is set to 4 percent and length scale at 0.5 mm.

An **H**-type grid is used to discretize the flow domain. The flow is assumed to be symmetric about the midspan plane. The value of y^+ of the first grid point from the solid surface is chosen to be less than 1. The grid has $165 \times 61 \times 45$ points in the streamwise, pitchwise, and spanwise directions, respectively. Most of the grid points are located in the secondary flow/vortex region, which spans from the endwall to about one quarter of the span away from the endwall. Only 10 grid points are distributed from 125 mm to the midspan (200 mm) in the spanwise direction.

The stability limits of the numerical scheme restrict the choice of the artificial dissipation parameters. It is known from prior experience (Basson and Lakshminarayana, 1994) and the traditional time-marching techniques, that the second-order numerical dissipation is too dissipative and should be set to zero if possible. However, it is necessary to have a certain amount of second-order numerical dissipation at the initial stage of

Nomenclature

B = axial chord length
C_f = skin friction coefficient = τ_w/Q_1
C_p = static pressure coefficient = $(p - p_1)/Q_1$
G_1 = contravariant velocity in ξ direction = $\xi_x u + \xi_y v + \xi_z w$
G_2 = contravariant velocity in η direction = $\eta_x u + \eta_y v + \eta_z w$
G_3 = contravariant velocity in ζ direction = $\zeta_x u + \zeta_y v + \zeta_z w$
J = Jacobian of coordinate transformation = $x_\xi(y_\eta z_\zeta - y_\zeta z_\eta) + x_\eta(y_\zeta z_\xi - y_\xi z_\zeta) + x_\zeta(y_\xi z_\eta - y_\eta z_\xi)$
k = turbulent kinetic energy (normalized by U_1^2)
P_0 = total pressure
p = static pressure
Q_1 = inlet dynamic head
S = source term in finite difference equation/blade spacing
S_{ke} = secondary kinetic energy coefficient) = V_{se}^2/U_1^2
T_u = inlet turbulence intensity
U = streamwise velocity
U_c = maximum velocity defect in wake
V = total velocity
V_{se} = total secondary velocity
u, v, w = Cartesian velocity components
x, y, z = Cartesian coordinates
X = distance in the axial direction measured from the leading edge
Y = distance in the pitchwise direction
$y^+ = \rho\sqrt{\tau_w/\rho}(y/\mu)$
Z = Distance in the spanwise direction
$\alpha, \beta, \gamma = \nabla\xi\cdot\nabla\xi, \nabla\eta\cdot\nabla\eta, \nabla\zeta\cdot\nabla\zeta$
Γ = diffusion coefficient
ϵ = turbulence dissipation rate
ϵ_2, ϵ_4 = coefficient for second-order and fourth-order artificial dissipation
λ = inlet turbulence length scale
$\theta_1, \theta_2, \theta_3 = \nabla\xi\cdot\nabla\eta, \nabla\xi\cdot\nabla\zeta, \nabla\eta\cdot\nabla\zeta$
ϕ = general scalar dependent variable
μ = viscosity
ρ = density
τ_w = shear stress on the surface
ξ, η, ζ = generalized coordinates (unit increments in computational domain)
ζ = total pressure loss coefficient = $(P_{01} - P_0)/Q_1$

Subscripts

1 = condition at the inlet
e = local edge velocity
l = laminar

Superscripts

− = pitch-averaged
= = mass-averaged

Downloaded 01 Jun 2010 to 171.66.16.53. Redistribution subject to ASME license or copyright; see http://www.asme.org/terms/Terms_Use.cfm

computation to damp out the high frequency error. The second-order artificial dissipation is reduced every 200 iterations, bringing it to zero toward the end of 2000 iterations. The coefficient of fourth-order artificial dissipation is set to 0.5 and the numerical dissipation for the pressure equation is set to 0.3. The under-relaxation factor is set to 0.3 for the momentum and the turbulence equations. The error in mass flow is less than 0.2 percent of the inlet mass flow rate after 3000 iterations and the pressure residual has been reduced three orders of magnitude. The residuals of transport equations are reduced to at least two order of magnitude.

Comparison Between Prediction and Data

For all the contour plots shown in this section, the viewpoint will be looking at the upstream direction from the downstream location, with the suction surface on the left-hand side and the pressure surface on the right-hand side. A comparison between the numerical prediction and the experimental data is presented at 51 percent axial chord downstream of the turbine.

Blade Static Pressure Distribution. The chordwise distribution of the blade static pressure coefficient at various spanwise locations is shown in Fig. 1. The agreement between the prediction and the experimental data (Gregory-Smith, 1993) is excellent except at the 3.4 percent spanwise location away from the endwall. The blade pressure distributions are found to be almost identical from midspan to 13.4 percent span from the endwall. Therefore, the two-dimensional flow is still dominant in this region. At 8.4 percent span, the influence of the passage vortex on the blade static pressure becomes significant as indicated by a sudden pressure drop beyond 55 percent of the axial chord on the suction surface, while the effect of the passage vortex can be seen near the 35 percent axial chord location at 3.4 percent span from the wall. However, the pressure distribution on the pressure surface remains unchanged along the entire span. This indicates that for this particular turbine cascade the passage vortex remains much closer to the suction surface throughout the passage.

Comparison of the Local Flow Properties. The development of the secondary flow at 51 percent downstream of the turbine cascade is shown in Fig. 2. The secondary flow is defined as the resultant of the velocity component perpendicular (principal normal direction) to the mean velocity at the midspan plane and the spanwise velocity component. The agreement between the experimental data and the numerical results is good. The location of the passage vortex is off by 10 mm and 20 mm in the spanwise and the pitchwise directions, respectively. The predicted magnitude of the secondary flow is slightly smaller than the measured values. Inaccuracies arise due to not enough grid resolution in the high gradient region. In a previous study (not shown here) using a coarser grid ($121 \times 51 \times 31$), the results for both the location of the passage vortex and the magnitude of the secondary flow were found to be markedly poorer. Because of the limitations on memory on the supercomputer used, only five or six grid points are located inside the vortex core. Nevertheless, it is encouraging that the numerical model is able to simulate the development of a passage vortex accurately.

As the passage vortex travels toward the trailing edge, it moves away from the endwall and grows in its size due to the interaction of the secondary flow, the main flow, and the wall. At 51 percent axial chord downstream of the turbine blade, the core of the passage vortex has moved farther away from the endwall and is located at about 65 mm from the endwall. The magnitude of the secondary flow has decreased due to mixing and dissipation phenomena. It is interesting to note, from both the prediction and the experimental data, the formation of an auxiliary vortex adjoining the passage vortex in the wake region. A counterclockwise vortex motion is initiated at the edge of the passage vortex due to interaction between the wake (which

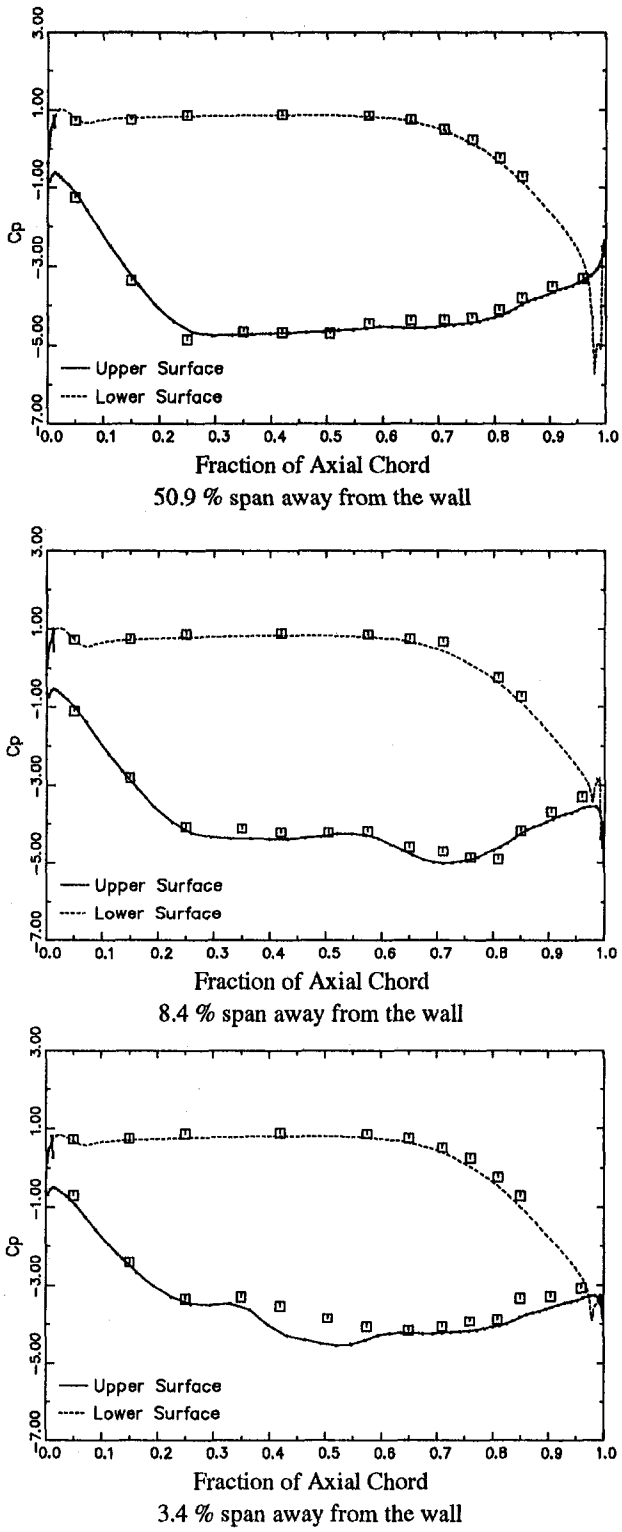
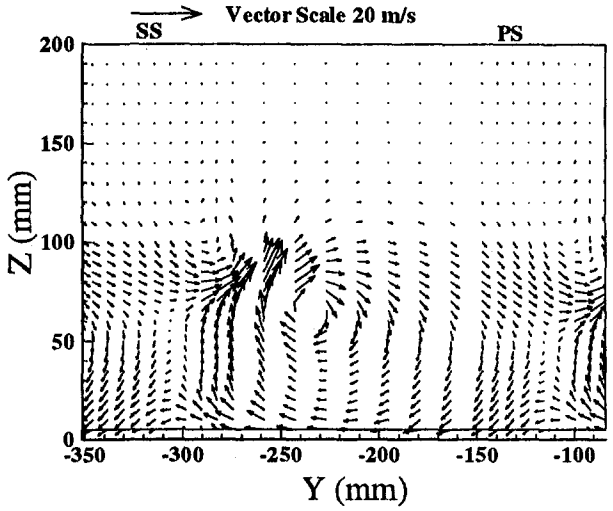


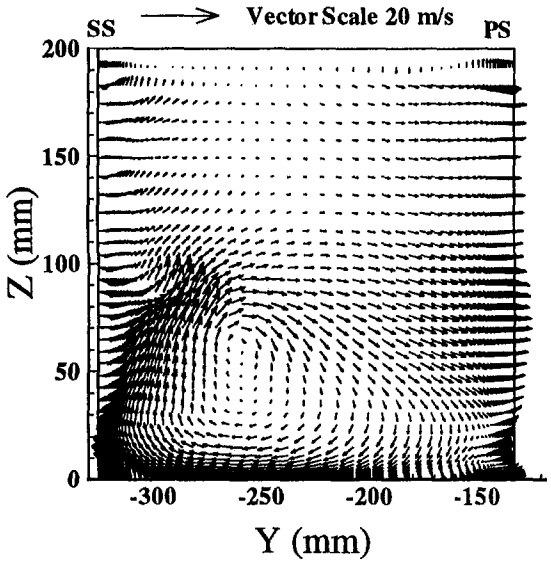
Fig. 1 Static pressure distributions at different spanwise locations on the turbine blade; square symbol: experimental data (Gregory-Smith, 1993)

is transported downstream) and the passage vortex. The wake merges with the secondary vortex as it travels downstream as indicated later in the discussion of the wake structure. Computation shows that secondary flow velocities are small away from the vortex region, except near the midspan. The presence of the secondary flow near the midspan maybe due to very coarse grid used in this region. Only 10 grid points are used in the region from 120 mm to 200 mm span from the endwall.

Downloaded 01 Jun 2010 to 171.66.16.53. Redistribution subject to ASME license or copyright; see http://www.asme.org/terms/Terms_Use.cfm



Experimental Data (Gregory-Smith and Cleak, 1990)



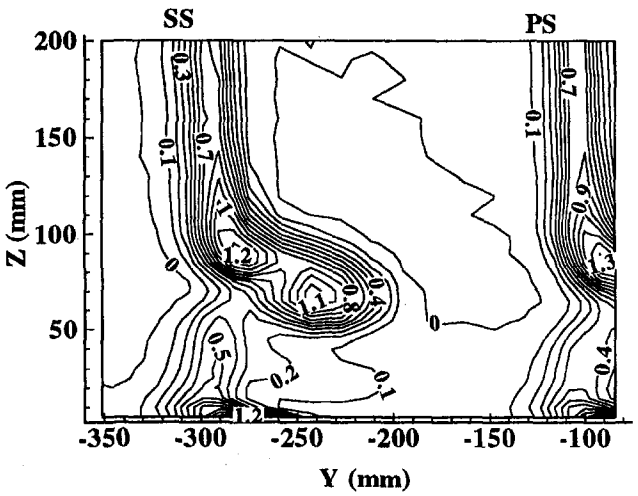
Numerical Prediction

Fig. 2 Secondary flow velocity distribution at 51 percent axial chord downstream of the trailing edge

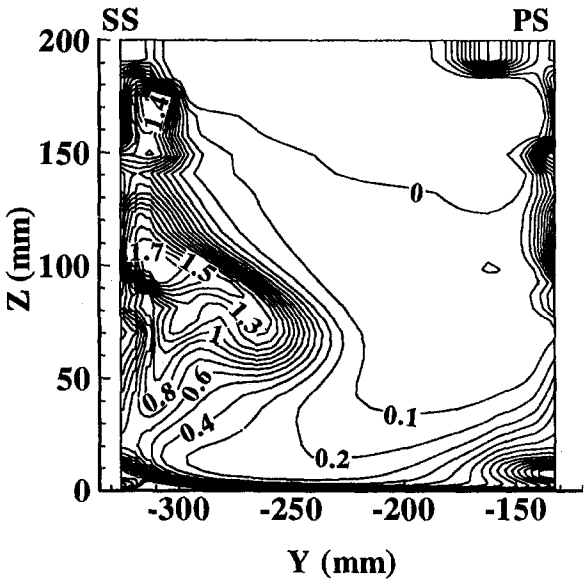
The contour of total pressure loss coefficient (ζ) at 51 percent of the axial chord downstream of the turbine cascade is shown in Fig. 3. The ability of the code to predict the total pressure loss coefficient provides good validation of the numerical scheme and the turbulence model. All the major features of the total pressure loss contours are captured by the numerical scheme. The two vortex cores, which correspond to the passage vortex and the interaction between the passage vortex and the wake, are captured. However, higher total pressure loss is predicted in the core region for both cases. The maximum values of the measured total pressure loss coefficients are 1.1 and 1.2 at those two vortex cores, while the predicted values are 1.3 and 1.7, respectively. The higher loss prediction in the core could have been caused by insufficient grid points. A computation with a coarser grid, mentioned earlier, was incapable of capturing the magnitude of the passage vortex and the loss cores associated with the passage vortex and the wake interaction. Increased grid resolution provided much better prediction, as shown in Fig. 3. Once again, higher loss prediction near midspan is probably caused by insufficient grid resolution in this region.

Yaw angle (blade-to-blade flow angle) distribution is shown in Fig. 4. This plot clearly indicates the exact spanwise location of the core of the passage vortex, i.e., the location of the largest yaw angle, which is at about $Y = -250$ mm. The overall distribution is in very good agreement with the experimental data, except in the vortex core region. Lack of sufficient spatial resolution at this location is the most likely cause for the inability of the numerical model to capture the peak values in yaw angle (This is also the cause for the redundant contours appearing near the midspan region.) Even within these limitations, the numerical model succeeds in capturing the spanwise location and extent of the passage vortex and predicts overturning and underturning angles very accurately. Similar good agreement is obtained for pitch angle (or spanwise flow), as shown in Fig. 5. The distribution is captured accurately, with the exception of peak values on either side of the vortex core. Thus, the code is able to capture the magnitude of secondary flows, losses, outlet angle, and pitch angle accurately.

Figure 6 shows the distribution of the turbulent kinetic energy at 51 percent axial chord downstream of the turbine cascade.



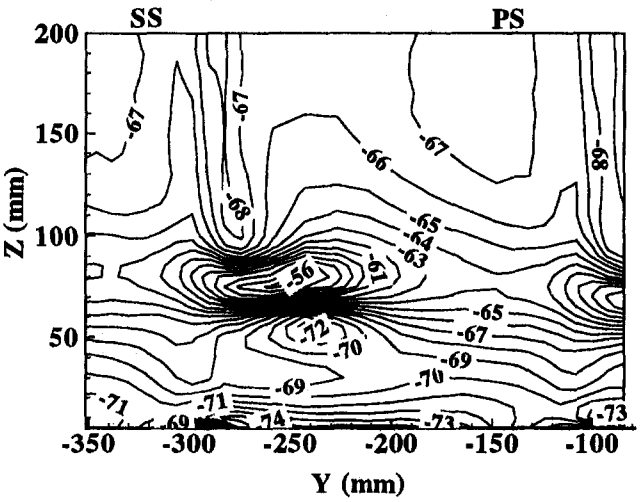
Experimental Data (Gregory-Smith and Cleak, 1990)



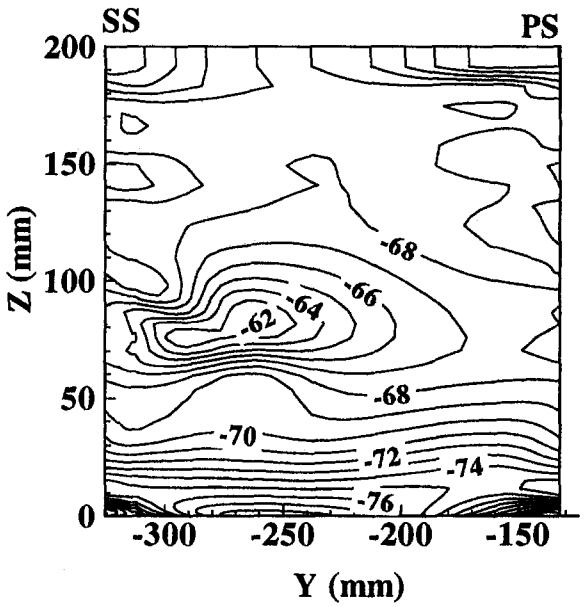
Numerical Prediction

Fig. 3 Total pressure loss coefficient (ζ) at 51 percent axial chord downstream of the trailing edge

Downloaded 01 Jun 2010 to 171.66.16.53. Redistribution subject to ASME license or copyright; see http://www.asme.org/terms/Terms_Use.cfm



Experimental Data (Gregory-Smith and Cleak, 1990)



Numerical Prediction

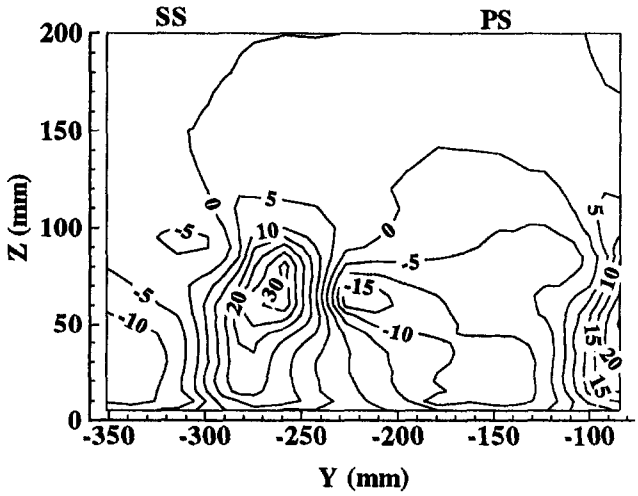
Fig. 4 Distribution of yaw angle (in deg) at 51 percent axial chord downstream of the trailing edge

The turbulent kinetic energy, k, is normalized by the inlet velocity and compared with Gregory-Smith (1993) and Gregory-Smith and Cleak's (1989) data. In the numerical simulation, the inlet turbulence length scale is chosen such that the predicted turbulent kinetic energy profile "matches" the measured values at the first measuring station. It is very difficult to match the turbulent kinetic energy profile with the experimental data very accurately. A small error in the inlet turbulent kinetic energy profile leads to amplification of the error in the predictions of k at downstream locations. Near the passage vortex core, the predicted maximum value is 0.08 while the measured value is 0.16. Nevertheless, the location of the maximum turbulence kinetic energy and the extent of the vortex are captured well.

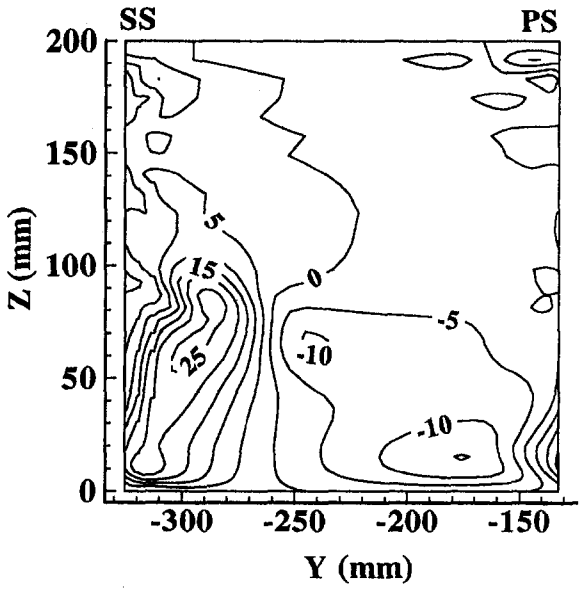
Additional Simulation

After achieving confidence in the code, the numerical technique, the turbulence model, and the grid, additional simulations are carried out to understand the physics of flow development in the endwall region. These include: wake development in the presence of the passage vortex, development and trajectory of the passage vortex and the leading edge vortex, nature of flow structure near blade surfaces and wake, and effects of inlet turbulence intensity and length scale on the endwall flow.

Flow Features on the Endwall and Blade Surfaces. One of the most striking features in a turbine flow field is the separation and saddle point on the endwall near the leading edge. Although the flow visualization conducted by Gregory-Smith et al. (1988) did not extend sufficiently far upstream to detect the location of the saddle point near the leading edge, they did observe a flow pattern similar to those reported by Langston et al. (1977) downstream of the leading edge. The predicted flow pattern near the leading edge of the turbine, shown in Fig. 7, clearly reveals the existence of the saddle point. Two attachment lines, S_{a1} and S_{a2}, and two separation lines, S_{s1} and S_{s2}, can be identified from the velocity vectors. The separation lines correspond to the two legs of the horseshoe vortex formed near the leading edge. The separation line S_{s1} moves around the



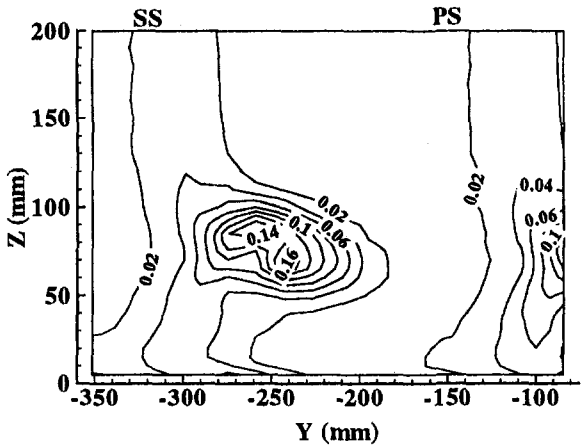
Experimental Data (Gregory-Smith and Cleak, 1990)



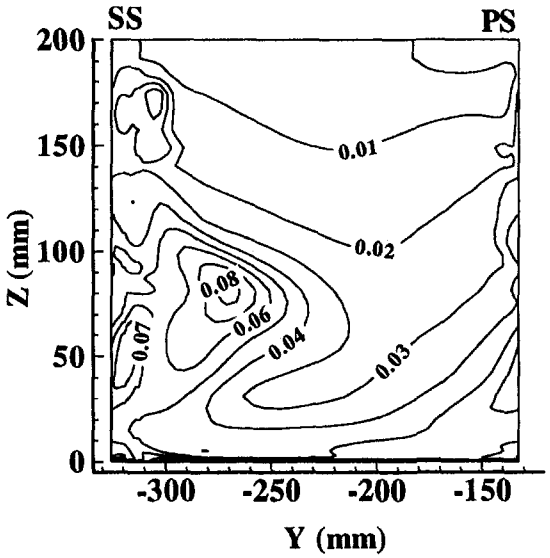
Numerical Prediction

Fig. 5 Distribution of pitch or spanwise angle (in degrees) at 51 percent axial chord downstream of the trailing edge

Downloaded 01 Jun 2010 to 171.66.16.53. Redistribution subject to ASME license or copyright; see http://www.asme.org/terms/Terms_Use.cfm



Experimental Data (Gregory-Smith and Cleak, 1990)



Numerical Prediction

Fig. 6 Distribution of turbulence kinetic energy (k) at 51 percent axial chord downstream of the trailing edge

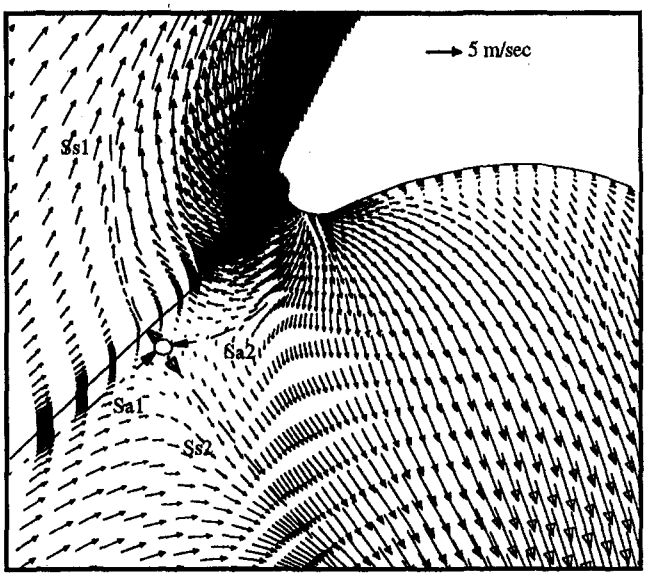


Fig. 7 Velocity vectors at the leading edge of the turbine cascade (2 percent span from the end wall)

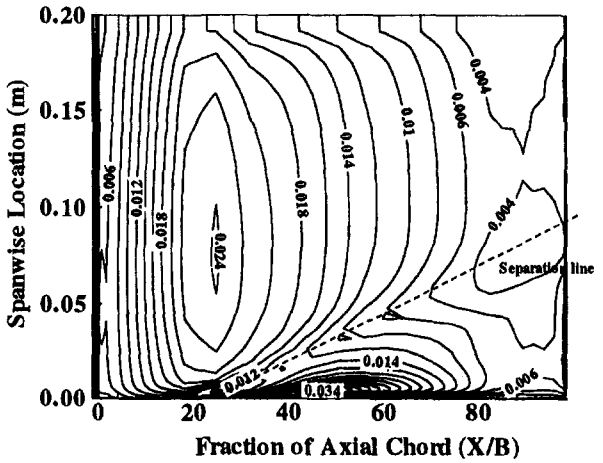


Fig. 8 Skin friction coefficient C_f on the suction surface of the axial turbine cascade

leading edge and merges with the fluid coming from the free-stream direction to form the suction-side leg of the horseshoe vortex. The second separation line S_{s2} is pushed away from the leading edge and merges into the passage or secondary vortex.

The inception and transport of the passage vortex and its impact on the surface boundary layers can be seen from the distribution of the skin friction coefficient and the static pressure coefficient on the suction surface, shown in Figs. 8 and 9, respectively. A decrease in C_f indicates a tendency for the boundary layer to separates on the blade surface. Furthermore, the chordwise and spanwise gradient in C_p in this region should be small. This is clear from Figs. 8 and 9 where the possible location of the boundary layer separation line is marked. The radial and chordwise gradient in C_p along the separation line is small. The inception of the passage vortex is around 25 percent of the axial chord, in the corner formed by the suction surface and the endwall. The vortex grows continuously to about 20 percent span at the exit. In addition, the trajectory of the vortex core, indicated by the suction peak can be seen in Fig. 9. The vortex tends to move away from the suction surface beyond about 80 percent of the axial chord. Its influence on the suction surface C_p and C_f reduces substantially downstream of 80 percent of the axial chord, confirming the movement of the passage vortex in the pitchwise direction. An additional feature revealed by the plot is the corner flow separation. The C_p and C_f distributions indicate that flow is separated in the corner at the inner

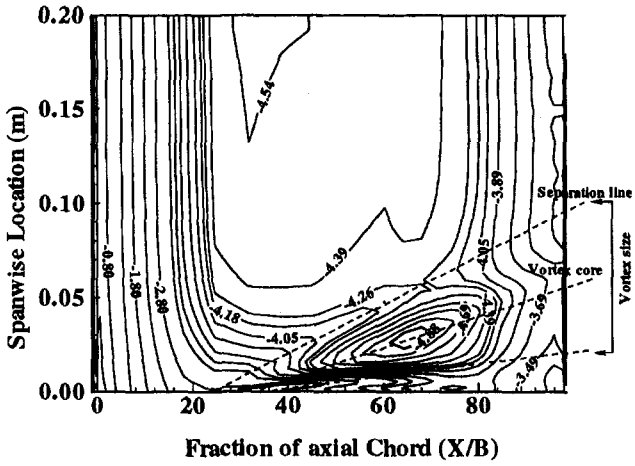


Fig. 9 Static pressure coefficient C_p on the suction surface of the axial turbine cascade

Downloaded 01 Jun 2010 to 171.66.16.53. Redistribution subject to ASME license or copyright; see http://www.asme.org/terms/Terms_Use.cfm

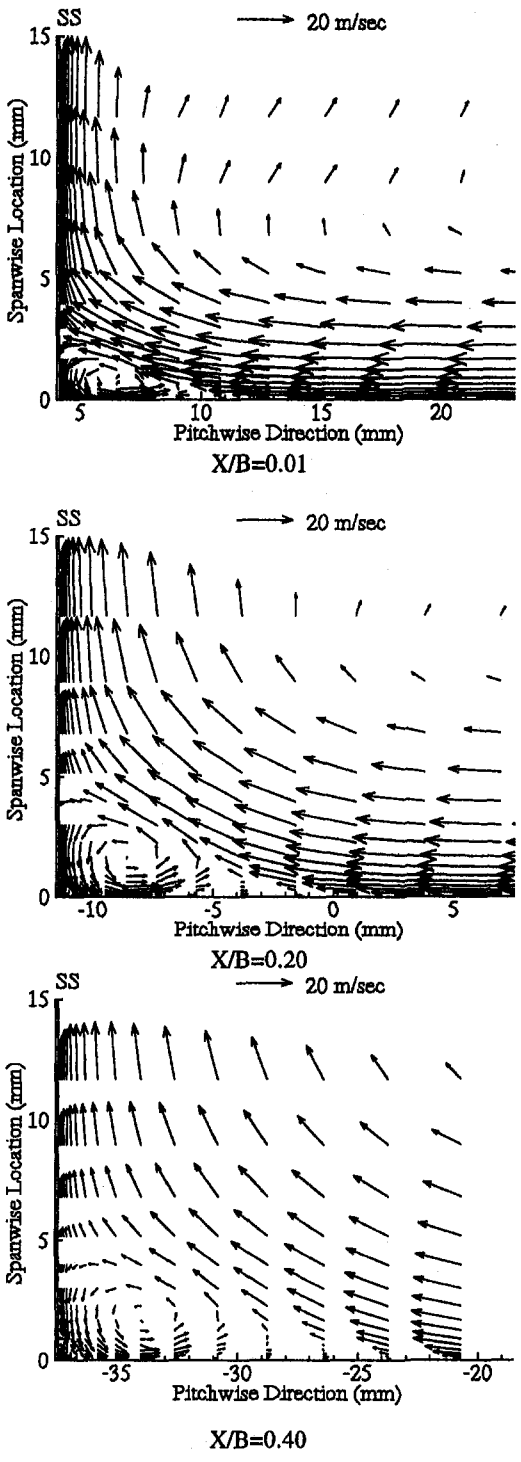


Fig. 10 The development of the suction-side leg of the leading edge vortex (secondary velocity vectors)

edge of the vortex. Once again, its influence reduces beyond about 80 percent of the axial chord, indicating flow reattachment beyond this location.

Leading Edge Vortex Formation. The leading edge vortices arise due to large flow turning in the endwall boundary layers and the presence of a thick leading edge. Since the location of the leading edge vortex (horseshoe vortex) is so close to the endwall, it is very difficult to measure the location and the strength of the horseshoe vortex along the passage in an experiment. The secondary velocity plots, shown in Fig. 10, can be used to identify the development and decay of the suction-side leg of the leading edge (horseshoe) vortex along the blade passage. The region near the vortex is magnified for clarity. The inception of the pressure-side leg of the leading edge vortex is shown to be along S_{s2} in Fig. 7. However, the pressure-side leg of the leading edge vortex either mixes up with the secondary flow or decays rapidly, and no traces of this were seen inside the passage in this simulation study. But, the suction-side leg of the leading edge vortex persists for a long time and can be clearly seen in Fig. 10. At the leading edge (X/B = 0.01), the vortex is small and has counterclockwise rotation. It is located very close to the corner and the passage secondary flow observed outside the corner is already stronger than the secondary flow due to the horseshoe vortex at the leading edge. The suction-side leg of the leading edge vortex grows in size and strength until X/B = 0.4. Its extent covers about 5 mm (1.25 percent of span) along the spanwise direction and 15 mm (about 8 percent of the blade pitch) along blade pitch. The vortex starts to decay at X/B = 0.6 and completely disappears at X/B = 0.8. Contrary to many hypotheses, this vortex does not merge with the passage vortex. High turbulence intensity and viscous effects combined with the passage secondary flow tend to dissipate and diffuse the vortex, and this can be clearly seen at the location of X/B = 0.8.

All of these important flow features were summarized and reviewed by Sieverding (1985). The numerical flow visualization proves that the numerical scheme is able to capture all the important features of the endwall and surface flows.

Wake Development Downstream of the Turbine Cascade. The flow phenomena inside the turbine cascade have received much more attention than the flow phenomena downstream of

Downloaded 01 Jun 2010 to 171.66.16.53. Redistribution subject to ASME license or copyright; see http://www.asme.org/terms/Terms_Use.cfm

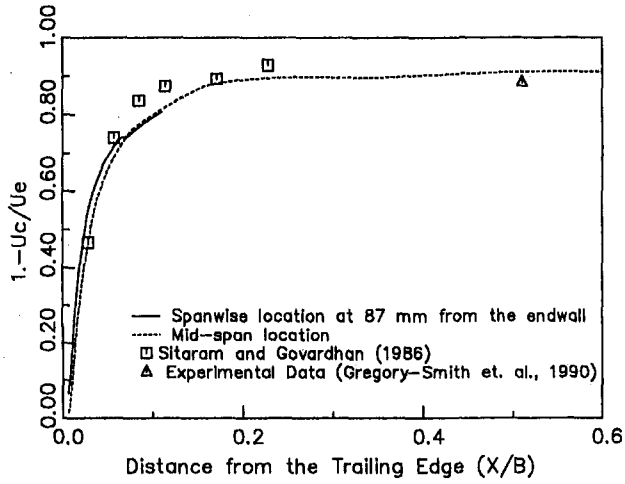


Fig. 11 The distribution of the velocity defect downstream of the turbine cascade

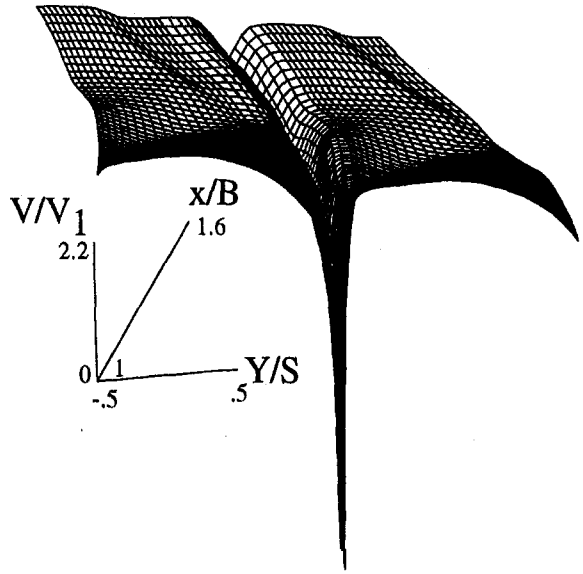


Fig. 12 The wake development at the midspan location downstream of a turbine cascade (trailing edge to 60 percent axial chord downstream)

the turbine blade. An understanding of the development of the passage vortex and its interaction with the wake is of vital importance in the study of the unsteady flow in the subsequent blade row (rotor–stator interaction). The purpose of this section is to assess the wake decay in a turbine and the effect of the passage vortex on the wake decay.

In Fig. 11, the decay of the maximum velocity defect in the wake is shown and compared with the experimental data at the midspan location and at 87 mm from the endwall, where the effect of the passage vortex is strong. The wake decays faster in a turbine cascade compared to those of a compressor cascade. In the turbine cascade investigation, the maximum velocity defect is reduced to 20 percent of the free-stream velocity at 10 percent axial chord downstream of the trailing edge. Since the only available data from Gregory-Smith (1993) are at 51 percent axial chord downstream, the experimental data obtained by Sitaram and Govardhan (1986) on a turbine cascade with a similar flow turning (120 deg) are shown. The comparison between the computational results and two sets of experimental data is good. The wake decay at 87 mm away from the endwall is also presented in Fig. 11. The prediction is shown only up to 10 percent axial chord, beyond which the wake and the passage vortex tend to merge, as described later, and these two are not clearly distinguishable.

The structure of the wake and its decay at both the midspan and 87 mm away from the endwall, is shown in Figs. 12 and 13, respectively. The wakes are well behaved at the midspan and, as shown in Fig. 12, the decay is rapid. Strong influence of the passage vortex on the wake decay can be seen in Fig. 13. When the flow just leaves the blade surface, the wake and the adjacent passage vortex are separate and distinct. As the flow travels farther downstream, the interaction between the passage vortex and the wake becomes very significant and a distinctive feature is the appearance of a small peak in the velocity distribution within the wake as seen at $X/B = 1.06$ and 1.20. As the flow continues to travel downstream, the passage vortex and the wake interact with each other and finally merge together and become indistinguishable.

When the wake development at 87 mm from the end wall (approximate spanwise location of the passage vortex) is compared with that at the midspan, the interaction between the vortex and the wake seems to decay the wake faster up to about 6 percent of the axial chord (Fig. 11). After that, the secondary flow starts to "overshadow" the wake, as revealed in Fig. 13. The interaction between the wake and the vortex results in a thicker shear layer in this region. Reduction of the secondary flow will not only reduce the secondary loss but also will have

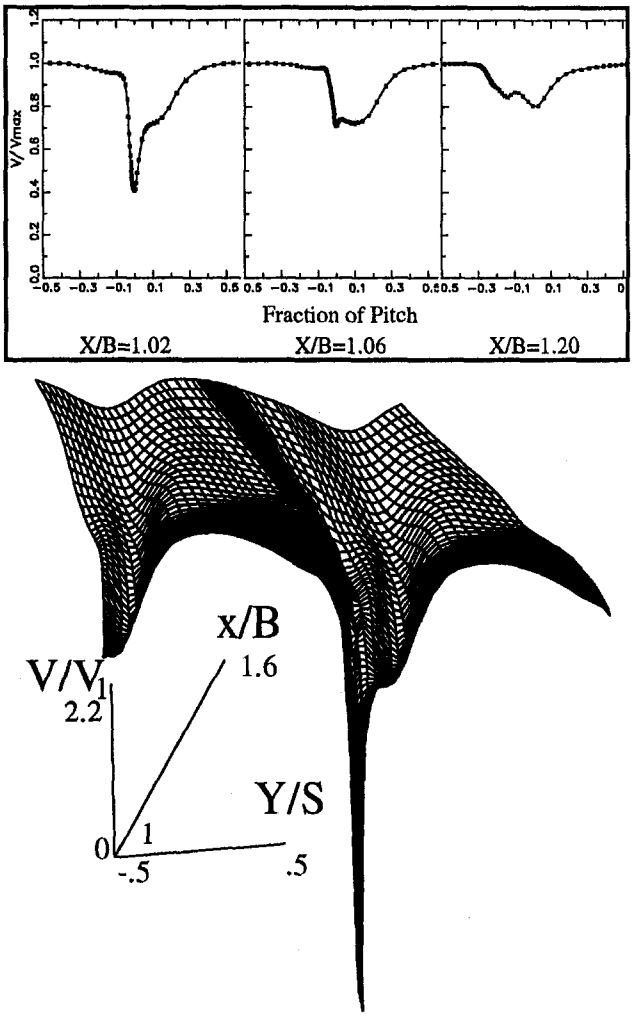


Fig. 13 The wake development at 87 mm away from the endwall downstream of a turbine cascade (trailing edge to 60 percent axial chord downstream)

Downloaded 01 Jun 2010 to 171.66.16.53. Redistribution subject to ASME license or copyright; see http://www.asme.org/terms/Terms_Use.cfm

a significant effect in reducing the profile and the wake mixing losses.

Passage-Averaged Profiles and Simulation of the Effects of Turbulence Intensity and Length Scale. Detailed comparison between the numerical simulation and the experimental data were presented earlier. The numerical model is able to capture most of the phenomena inside the turbine cascade with the exception of the extreme values inside the passage vortex core. The effect of high turbulence intensity and large inlet turbulence length scale on the endwall flow is simulated and their effects will be discussed in this section. In addition, the predicted pitch-averaged values of the flow properties are compared with the experimental data (Gregory-Smith, 1993). The inlet turbulence intensity is increased from 4 to 12 percent. This value represents a more realistic inflow condition encountered in aircraft engine turbines. To study the effects of larger inlet turbulence length scale, the turbulence length scale is increased to 1.0 mm, which is 2 times larger than the one used for the computation of the test case. The prediction of Cleak and Gregory-Smith (1992) is also shown for comparison.

Figure 14 shows the comparison of the predicted pitch-averaged yaw angle distribution with different inflow turbulence, numerical results of Cleak and Gregory-Smith, and the experimental data, at 51 percent axial chord downstream of the trailing edge. The pitch-averaged yaw angles are predicted accurately except in the region where the vortex is located. It is clear that the effect of higher turbulence intensity is confined only to the vortex core region. The prediction of the maximum yaw angle near the vortex core is improved by about 2 deg. One surprising result is the effect of the larger inlet turbulence length scale. An increase in the turbulence length scale results in smaller underturning and overturning. This indicates that the secondary flow inside the turbine cascade and the strength of the secondary vorticity are reduced by strong turbulence production inside the passage.

The secondary kinetic energy S_{ke} distributions with various inflows at 51 percent axial chord downstream of the trailing edge are presented in Fig. 15. The numerical simulation captures most of the features except those near the vortex core. Higher turbulence intensity does not affect the magnitude of the secondary flow inside the vortex core. However, the magnitude of the secondary kinetic energy near the endwall increases, and the peak values near the wall are almost twice as much as the data and the prediction with 4 percent turbulence intensity. The second peak near the wall probably corresponds to a countervortex that is sustained when the turbulence intensity is increased. Even though the computation of Cleak and Gregory-Smith (1992) also shows a high peak near the endwall similar to that of the high turbulence intensity case, one would suspect that laminar vortices were predicted in their computations. A contour plot of the turbulent kinetic energy from their paper shows that no turbulent kinetic energy was predicted at this location and this confirms the argument that laminar vortices were predicted by their results. When the inlet turbulence length is increased by a factor of 2, strong turbulence is developed and this dominates the entire flow field. The secondary flow in this case is reduced by the strong turbulence.

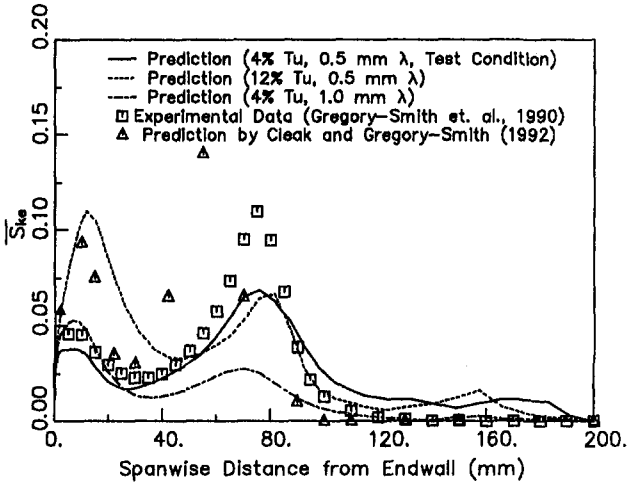


Fig. 15 Distribution of pitch-averaged secondary kinetic energy at 51 percent axial chord downstream of the trailing edge

Figure 16 shows the distribution of pitch-averaged total pressure loss coefficient at 51 percent axial chord downstream of the trailing edge. The overall trend in the total pressure loss distribution is captured by the prediction, but the predicted loss is about 20 percent higher than the measured values inside the vortex core. With a higher turbulence intensity at the inlet, the loss core tends to move away from the endwall and the results yield better prediction for the region between the endwall and the passage vortex. This region is dominated by the high level of turbulence as shown by the turbulent kinetic energy contour plot in Fig. 6.

As mentioned in previous paragraphs, large turbulence length scale can reduce the secondary flow and losses inside the passage. However, a much stronger turbulence effect could be introduced through an increase of the turbulence length scale,

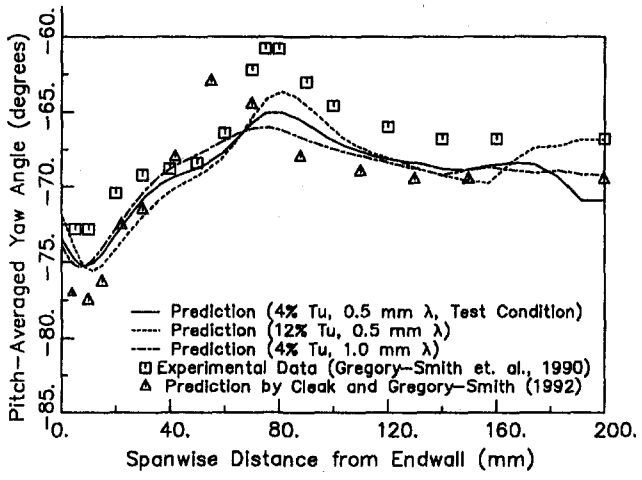


Fig. 14 Distribution of pitch-averaged yaw angle at 51 percent axial chord downstream of the trailing edge

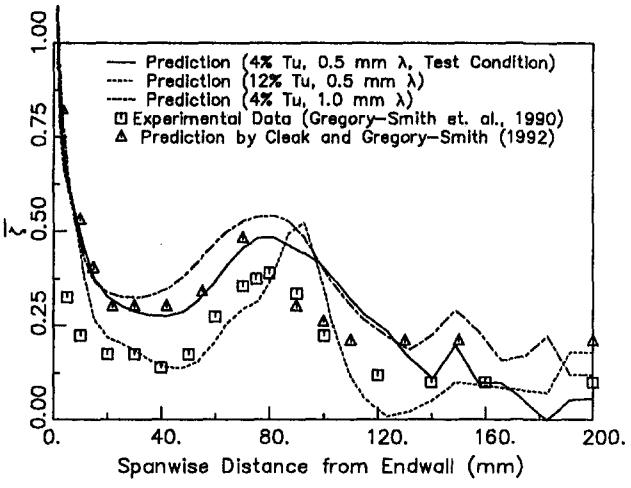


Fig. 16 Distribution of pitch-averaged total pressure loss coefficient at 51 percent axial chord downstream of the trailing edge

Downloaded 01 Jun 2010 to 171.66.16.53. Redistribution subject to ASME license or copyright; see http://www.asme.org/terms/Terms_Use.cfm

such that the loss becomes higher than the flow field with the strong secondary flows. This effect is demonstrated in Fig. 16. In this case, the loss is increased substantially near the wall up to 60 mm when the length scale is increased by a factor of 2.

In Fig. 17, the distribution of pitch-averaged turbulent kinetic energy for two different inflow turbulence intensities are compared with the experimental data at 51 percent axial chord downstream of the trailing edge. The effect of high turbulence intensity is not significant on the magnitude of the turbulent kinetic energy. In fact, a slight improvement is achieved in the region between the endwall and the passage vortex. When the inlet turbulence intensity is increased by three times, the corresponding turbulence dissipation rate at the inlet is calculated using the following relation:

$$\epsilon = C_\mu k^{3/2}/\lambda \tag{4}$$

The turbulence dissipation rate is increased by almost 5.2 times compared to the computation with 4 percent turbulence intensity, if the turbulence length scale is kept constant. The higher turbulence dissipation rate results in insignificant change observed in Fig. 17. The turbulent kinetic energy increases rapidly across the entire span when the length scale is increased to 1.0 mm. This high turbulent kinetic energy accounts for the high total pressure loss and the reduction of the secondary flow observed in Fig. 15 and 16.

The pitch-averaged total velocity profiles along the spanwise direction are shown in Fig. 18. As can be seen from Figs. 18(*a*) and 18(*b*), the turbulence intensity and the length scale do not have any significant influence on the pitch-averaged axial and tangential velocity components. The agreement between the experimental data and the prediction is good for most of the locations. The flow overturning near the endwall is also captured well. The discrepancy between the measured and predicted velocity distribution at 55 percent of the axial chord is most likely due to the fact that the streamwise velocity gradient is very high in this region and a small error in the axial coordinate will result in a large deviation in the magnitude of the velocity components. This may also explain the smaller discrepancy that exists at 97 percent axial chord location. The trace of the passage vortex can be seen clearly at 80 mm from the endwall downstream of the cascade. The effects of higher turbulence intensity and larger turbulence length scale are more pronounced on the spanwise velocity, as shown in Fig. 18(*c*). Again, the higher turbulence intensity tends to increase the magnitude of the secondary flow and the higher turbulence length scale reduces the secondary flow.

The mass-averaged (across the entire passage) total pressure loss coefficient and turbulent kinetic energy coefficient through the turbine passage are presented in Figs. 19 and 20, respec-

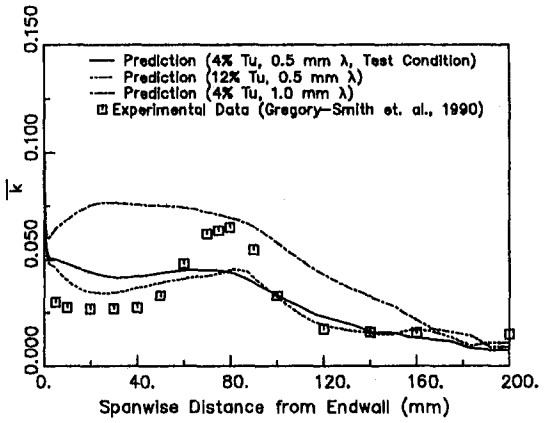


Fig. 17 Distribution of pitch-averaged turbulence kinetic energy at 51 percent axial chord downstream of the trailing edge

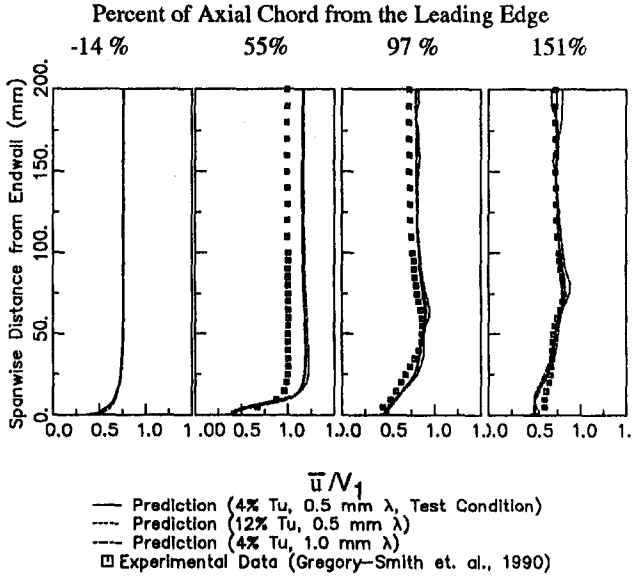


Fig. 18(*a*) Pitch-averaged axial velocity profiles at different axial locations of the turbine cascade

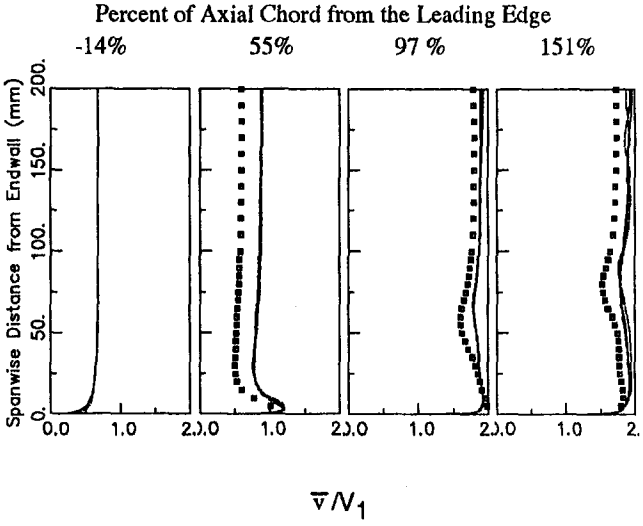


Fig. 18(*b*) Pitch-averaged tangential velocity profiles at different axial locations of the turbine cascade (see Fig. 18(*a*) for legend)

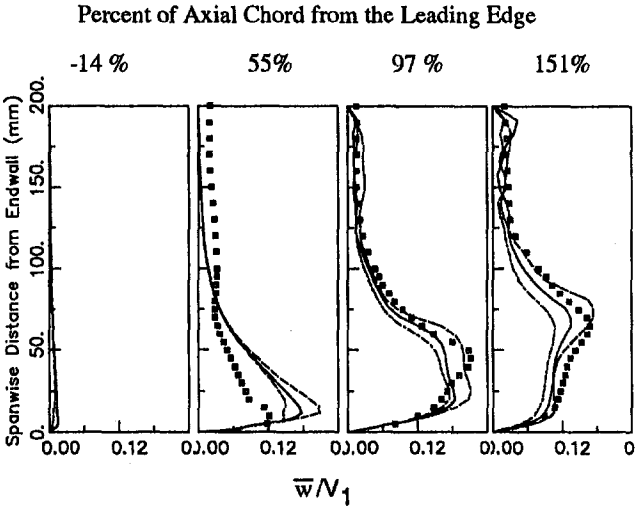


Fig. 18(*c*) Pitch-averaged radial velocity profiles at different axial locations of the turbine cascade (see Fig. 18(*a*) for legend)

Downloaded 01 Jun 2010 to 171.66.16.53. Redistribution subject to ASME license or copyright; see http://www.asme.org/terms/Terms_Use.cfm

tively. The trend is as expected from the comparison described earlier. One interesting feature that can be seen from Fig. 19 is that the predicted total pressure loss decreases from the trailing edge to about 130 percent of the axial chord and then increases again. This is in agreement with data reported by Gregory-Smith et al. (1988). They attributed this phenomenon to the lack of spatial resolution across the wake. However, the separation zone and its eventual reattachment near the trailing edge may also account for the higher loss. At larger turbulence length scale case, the prediction of higher turbulence inside the passage reduces the separation zone near the trailing edge, resulting in the observed trend. Therefore, the decrease in total pressure is limited only to the trailing edge.

The mass-averaged turbulent kinetic energy distribution, shown in Fig. 20, also reveals some interesting features. At higher turbulence intensity, a reduction in kinetic energy is observed from far upstream to the leading edge location. The turbulence then increases toward the trailing edge. For the larger length scale case, the turbulent kinetic energy increases slightly before entering the passage with much faster increases inside the passage. The turbulent kinetic energy is increased by almost three times as compared to the test condition.

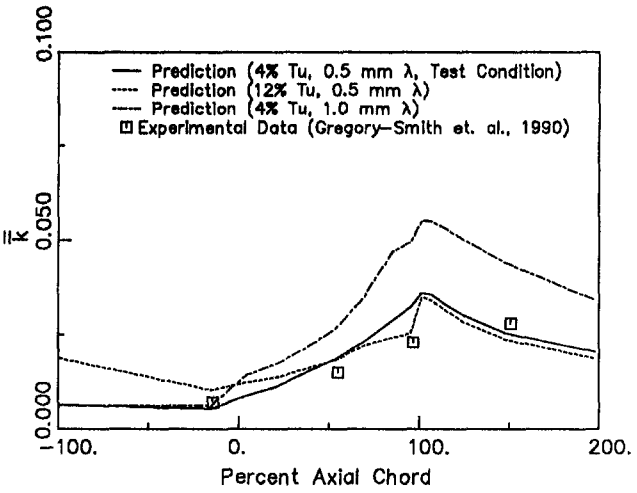


Fig. 20 Mass-averaged turbulence kinetic energy coefficient across an axial turbine passage

Concluding Remarks

A comparison of the numerical prediction, based on the pressure-based method, and the experimental data indicates that the numerical model is able to capture most of the complex flow phenomena in the endwall region of a turbine cascade. Insufficient grid resolution may be the cause for the discrepancies between the numerical prediction and the experimental results near the vortex core. It is found that:

- At 4 percent inlet turbulence intensity, the suction-side leg of the leading vortex grows to its maximum size and strength at about 40 percent of the axial chord and is dissipated quickly, leaving no traces near 80 percent axial chord location.
- The pressure-side leg of the leading edge vortex cannot be found in the turbine passage. The vortex may have merged quickly with the passage secondary flow or been dissipated by the viscous effects.
- The passage vortex has a strong effect on the decay of the wake downstream of the turbine. The passage vortex tends to decay the wake faster compared to the wake decay at the midspan. However, it merges with the wake as it travels downstream and becomes indistinguishable from the shear layer generated by the secondary vortex.

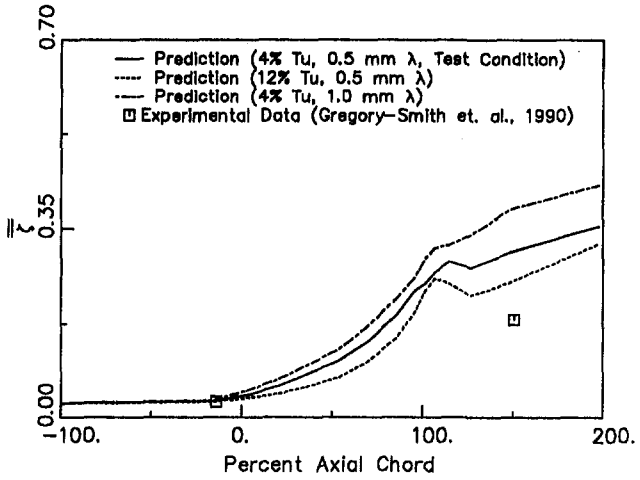


Fig. 19 Mass-averaged total pressure loss coefficient across an axial turbine passage

Simulations of the effects of higher turbulence intensity and turbulence length scale are performed on the same turbine configuration. The simulations demonstrate that:

- Higher turbulence intensity tends to energize the vortical motions and moves the passage vortex away from the endwall. It also tends to reduce the total pressure loss in the turbulence dominated regions near the endwall.
- Higher inlet turbulence intensity has no significant effect on the magnitude of turbulent kinetic energy.
- Increase in the turbulence length scale tends to decrease the secondary flow inside the flow passage. However, the associated high turbulent kinetic energy in the flow causes the total pressure loss to increase.
- An increase in the turbulence intensity and length scale do not have any significant effect on the axial and tangential velocity profiles. Higher turbulence intensity tends to increase the spanwise velocity and larger length scale tends to reduce the spanwise velocity.

Acknowledgments

This work is supported by the Office of Naval Research through Contract No. N00014-90-J1182 with J. Fein as the contract monitor. The authors would like to thank Dr. P. J. Morris and Dr. D. E. Thompson for their helpful suggestions and Dr. D. G. Gregory-Smith for providing the experimental data. The authors also wish to acknowledge NASA for providing the supercomputing resources at the National Aerodynamic Simulation Facility at NASA Ames Research Center and at the NASA Lewis Research Center.

References

Adjlout, L., and Dixon, S. L., 1992, "Endwall Losses and Flow Unsteadiness in a Turbine Blade Cascade," ASME JOURNAL OF TURBOMACHINERY, Vol. 114, pp. 191–197.

Basson, A. H., and Lakshminarayana, B., 1994, "An Artificial Dissipation Formulation for Semi-implicit Pressure Based Solution Scheme for Viscous and Inviscid Flows," *Int. J. Comp. Fluid Dynamics,* Vol. 2, pp. 253–282.

Chien, K.-Y., 1982, "Predictions of Channel and Boundary-Layer Flows With a Low-Reynolds-Number Turbulence Model," *AIAA Journal,* Vol. 20, No. 1, pp. 33–38.

Cleak, J. G. E., and Gregory-Smith, D. G., 1992, "Turbulence Modeling for Secondary Flow Prediction in a Turbine Cascade," ASME JOURNAL OF TURBOMACHINERY, Vol. 114, pp. 590–598.

Gregory-Smith, D. G., Graves, C. P., and Walsh, J. A., 1988, "Growth of Secondary Losses and Vorticity in an Axial Turbine Cascade," ASME JOURNAL OF TURBOMACHINERY, Vol. 110, No. 1, pp. 1–8.

Gregory-Smith, D. G., and Cleak, J. G. E., 1990, "Secondary Flow Measurements in a Turbine Cascade With High Inlet Turbulence," ASME Paper No. 90-GT-20.

Downloaded 01 Jun 2010 to 171.66.16.53. Redistribution subject to ASME license or copyright; see http://www.asme.org/terms/Terms_Use.cfm

Gregory-Smith, D. G., 1993, private communication.

Hah, C., 1984, "A Navier–Stokes Analysis of Three-Dimensional Turbulent Flows Inside Turbine Blade Rows at Design and Off-Design Conditions," ASME *Journal of Engineering for Gas Turbines and Power,* Vol. 106, pp. 421–429.

Lakshminarayana, B., 1991, "An Assessment of Computational Fluid Dynamic Techniques in the Analysis and Design of Turbomachinery—The 1990 Freeman Scholar Lecture," ASME *Journal of Fluids Engineering,* Vol. 113, pp. 315–352.

Langston, L. S., Nice, M. L., and Hooper, R. M., 1977, "Three-Dimensional Flow Within a Turbine Cascade Passage," ASME *Journal of Engineering for Power,* Vol. 99, pp. 21–28.

Moore, J., and Adhye, R. Y., 1985, "Secondary Flows and Losses Downstream of a Turbine Cascade," ASME *Journal of Engineering for Gas Turbines and Power,* Vol. 107, pp. 961–968.

Moore, J., and Moore, J. G., 1985, "Performance Evaluation of Linear Turbine Cascades Using Three-Dimensional Viscous Flow Calculations," ASME *Journal of Engineering for Gas Turbines and Power,* Vol. 107, pp. 969–975.

Perdichizzi, A., and Dossena, V., 1993, "Incidence Angle and Pitch-Chord Effects on Secondary Flows Downstream of a Turbine Cascade," ASME JOURNAL OF TURBOMACHINERY, Vol. 115, pp. 383–391.

Sharma, O. P., and Butler, T. L., 1987, "Predictions of Endwall Losses and Secondary Flows in Axial Flow Turbine Cascade," ASME JOURNAL OF TURBOMACHINERY, Vol. 109, pp. 229–236.

Sieverding, C. H., 1985, "Recent Progress in the Understanding of Basic Aspects of Secondary Flows in Turbine Blade Passages," ASME *Journal of Engineering for Gas Turbines and Power,* Vol. 107, pp. 248–252.

Sitaram, N., and Govardhan, M., 1986, "Effect of Incidence Angle on Wake Characteristics of High Deflection Turbine Rotor Linear Cascade," presented at 9th Australasian Fluid Mechanics Conference, Auckland, Dec.

Van Doormaal, J. P., and Raithby, G. D., 1984, "Enhancements of the SIMPLE Method for Predicting Incompressible Fluid Flows," *Numerical Heat Transfer,* Vol. 7, pp. 147–163.

Walsh, J. A., and Gregory-Smith, D. G., 1990, "Inlet Skew and the Growth of Secondary Losses and Vorticity in a Turbine Cascade," ASME JOURNAL OF TURBOMACHINERY, Vol. 112, pp. 633–642.

Downloaded 01 Jun 2010 to 171.66.16.53. Redistribution subject to ASME license or copyright; see http://www.asme.org/terms/Terms_Use.cfm

Radial Mixing in an Axial Turbine

R. P. Dring
United Technologies Research Center,
East Hartford, CT 06108

The objective of this work was to examine radial mixing in an axial turbine from a number of different perspectives. These include: (1) its impact on the spanwise distributions of the force on the airfoils and the change in the fluid momentum as it passed between them, (2) the mixing coefficient distribution based on measured secondary flow velocities, and (3) comparisons of measured and calculated profile redistribution for an axisymmetric inlet profile and for profiles generated by introducing hot and cold streaks upstream of the turbine. It was seen that a simple diffusive transport model could give a good prediction of most of the measured results.

Introduction

The design of a high-pressure turbine involves an intimate coupling of the aerodynamic performance as well as the local heat loads to the airfoil and end-wall surfaces. Without an accurate prediction of the full-span aerodynamics, the efficiency of the turbine will suffer due to mismatches in local incidence across the span of the airfoils. Without an accurate prediction of the spanwise distribution of gas temperature, turbine durability will suffer due to mismatches between the local gas path heat flux and the heat flux capability on the coolant side of the airfoil or endwall.

This need for accurate local information is further aggravated by the fact that although the flow leaving the combustor and entering the turbine is of a relatively uniform total pressure, it typically has strong radial and circumferential gradients in total temperature. The flow near the hub and tip may be close to compressor discharge temperature while the flow in the midspan region may be hotter by 2000°F. The inability to predict the attenuation of this temperature profile due to work extraction and radial mixing can result in mismatches in both local airfoil incidence and heat flux. The first-principles nature of the work extraction process allows it to be predicted accurately. The prediction of radial mixing, however, is more difficult and is the subject of the present work.

The computational community is energetically pursuing the goal of fully three-dimensional design but it is likely that the historical quasi-two-dimensional design approach (i.e., throughflow and airfoil-to-airfoil analysis) will be in use for some time to come, albeit with better modeling of the three-dimensional features of the flow. Throughflow analysis is at the heart of this design process. It is an essentially axisymmetric model of the flow in a turbine (or compressor). It is used to predict the spanwise distributions of the flow parameters within and between the airfoil rows. Most importantly, it defines the velocity triangles for which the airfoil contour at each span location must be designed.

Throughflow analysis normally does not account for flow crossing the meridional stream surfaces. These radial transport effects arise from both deterministic, three-dimensional secondary flows, and from turbulent diffusion. With the inclusion of these effects, throughflow analysis can, to some degree, account for the impact that radial transport has on velocity triangles and on airfoil design.

Adkins and Smith (1982) devised a method to estimate radial mixing in compressors due to deterministic convection caused by mainstream non-free-vortex flow, endwall boundary layers, airfoil end clearances, airfoil end shrouding, and airfoil boundary layer and wake centrifugation. The mixing phenomenon was modeled as a diffusion process with the mixing coefficient related to the estimated radial velocities.

Gallimore and Cumpsty (1986) took a different view of the mechanism causing radial mixing in compressors, namely that it was dominated by turbulent diffusion and not by deterministic secondary flows. This view was supported by their measurements of trace gas diffusion. Like Adkins and Smith, they also modeled the mixing phenomenon as a diffusion process; however, their mixing coefficient was based on turbulent transport.

Since the publication of these two papers, there has been considerable effort expended examining the two approaches to radial mixing in compressors. Wisler et al. (1987) acquired trace gas and hot-wire data indicating that "both secondary flows and turbulent diffusion play important roles depending on (spanwise, circumferential and axial) location . . . and loading level." Leylek and Wisler (1991) used extensive numerical modeling (three-dimensional Navier–Stokes solutions) at design and off-design conditions, compared it with trace gas data, and showed that both secondary flow and turbulent diffusion play important roles.

Radial mixing in a turbine was studied experimentally by Joslyn and Dring (1989, 1992). They measured radial-circumferential distributions of the flow downstream of each of the three airfoil rows in a 1.5 stage turbine. The measurements were in the stationary frame for the stators and in the rotating frame for the rotor. The aerodynamic measurements included the total and static pressures and the three components of velocity. This work also documented the attenuation of an inlet trace gas profile (simulating an axisymmetric combustor exit temperature profile) at the same locations.

Additional measurements of radial mixing in turbines were obtained by Lewis (1993a). Trace gas data were obtained to estimate the contributions of secondary flow and turbulent diffusion to radial mixing in multistage turbines. Two scaling expressions were derived to estimate the total mixing coefficient and the results were applied in a throughflow analysis. It was demonstrated that "modeling of spanwise transport is . . . crucial in predicting the attenuation of a temperature profile through a turbine."

In brief, the present paper examines: (1) the spanwise distributions of airfoil force and momentum exchange to determine whether radial transport has the same large impact that it has on compressor airfoils, (2) the spanwise distribution of the mixing coefficient due to secondary flows, and (3) the ability of a simple diffusive mixing model to predict the measured profile attenuation. These results will be seen to quantify the degree to which radial mixing affects the flows within and

Contributed by the International Gas Turbine Institute and presented at the 39th International Gas Turbine and Aeroengine Congress and Exposition, The Hague, The Netherlands, June 13–16, 1994. Manuscript received by the International Gas Turbine Institute February 15, 1994. Paper No. 94-GT-137. Associate Technical Editor: E. M. Greitzer.

Copyright © 1996 by ASME

Downloaded 01 Jun 2010 to 171.66.16.53. Redistribution subject to ASME license or copyright; see http://www.asme.org/terms/Terms_Use.cfm

between airfoil rows, and the degree to which the detailed radial distribution of the mixing coefficient needs to be modeled.

Background

All of the work to be reported on here was carried out in the 1.5 stage turbine model in the UTRC Large Scale Rotating Rig (Fig. 1). This model has an outer diameter of 5 ft (1.524 meters) and a hub/tip ratio of 0.8. The axial chord of all three airfoils is approximately 6 in. and their aspect ratios are approximately one. In all of the work reported on here the turbine model was operated at its nominal design flow coefficient (C_x/U_m) of 0.78. At the test shaft speed of 410 rpm, this corresponds to a nominal airfoil Reynolds numbers (based on exit speed and axial chord) of 6×10^5, a value typical of altitude cruise conditions. The rotor tip clearance was 1 percent of its axial chord.

The nature of the aerodynamics of this turbine is presented in detail by Joslyn and Dring (1989, 1992). Of particular relevance to the present work is the fact that the data include sufficient information to calculate the spanwise distributions of all of the circumferential area and mass averages needed in the following sections. The radial-circumferential traverse data were acquired at the following axial locations: (*a*) at the turbine inlet, Station #1, 100 percent of axial chord upstream of stator #1, (*b*) at stator #1 exit, Station #2, 17 percent aft of the stator, (*c*) at the rotor exit, Station #3, 36 percent aft of the rotor, and (*d*) at stator #2 exit, Station #4, 14 percent aft of the stator. The available data also include documentation of the attenuation of an inlet trace gas profile, which simulates an inlet temperature profile. A study of the rectification of combustor-generated hot and cold streaks was also carried out in this turbine by Roback and Dring (1993). These data will also be used in the assessment of the radial mixing calculation.

Airfoil Force and Flow Momentum Change

It was demonstrated by Dring (1993) that radial transport in compressors could cause large differences between the force on an airfoil and the change in the fluid momentum across the airfoil at the same radius. Differences of 100 percent were demonstrated. This imbalance occurred most strongly when the compressor was operating at near-stall conditions where hub corner separation had grown to cover much of the airfoil suction surface. The imbalance was also strong close to the rotor tip when the clearance was large, $(cl/B) = 0.04$. Both of these situations produce strong radial flows in the immediate vicinity of the airfoil and hence a strong radial redistribution of momentum. The first question to be addressed is whether such large imbalances occur in turbines.

When the hub and tip radii are constant, the force vector on each airfoil must equal the vector for the change in fluid momentum across the airfoil. The momentum components at any plane in the turbine are given by the following:

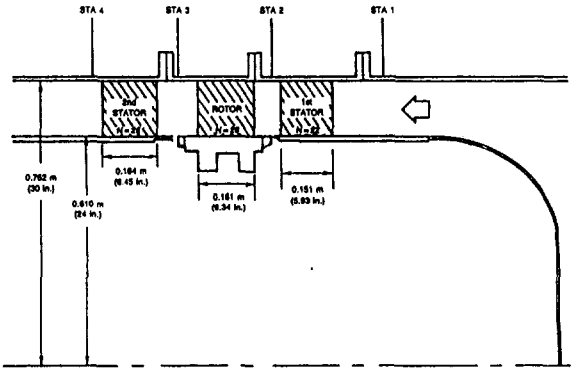


Fig. 1 1.5-stage turbine model

$$M_x = \int_{r_h}^{r_t} \tau_m \left(\frac{r}{r_m}\right)(\bar{P}^a + \rho \overline{C_x}^a \overline{C_x}^m) dr \quad (1)$$

$$M_\theta = \int_{r_h}^{r_t} \tau_m \left(\frac{r}{r_m}\right)(\rho \overline{C_x}^a \overline{C_\theta}^m) r dr \quad (2)$$

Each of the averaged quantities in these expressions could be determined from the radial-circumferential arrays of data acquired by Joslyn and Dring (1992). The spanwise distributions of the components of force on the airfoils could also be determined from the measured airfoil pressure distributions. The small contributions of skin friction to the force on the airfoils and on the end-walls were neglected.

The axial and tangential components of the force and the change in momentum across each airfoil are shown in Fig. 2. The thick lines with solid symbols indicate the pressure force components measured at seven spanwise locations on the stator and rotor airfoils. The thin lines with the hollow symbols indicate the measured changes in flow momentum occurring between the traverse planes up- and downstream of each airfoil. The axial component of momentum is the dimensionless form of the integrand in Eq. (1). The tangential component is the dimensionless form of the integrand in Eq. (2) without the final factor of "r". It represents the tangential force, not torque. When integrated from hub to tip according to Eqs. (1) and (2) the force and momentum changes across each airfoil must agree. Any differences are due to measurement error (and a small contribution due to skin friction). If there is no radial transport, the force on the airfoil must be equal to the momentum change across it locally from hub to tip.

The results in Fig. 2 are comparable to those for the compressor (Dring, 1993) operating at its lowest loading condition (wide-open throttle) and at a small rotor tip clearance ($cl/B = 0.01$). However, these results are very different from those observed for the compressor operating at its nominal design and near-stall conditions. At these conditions the hub corner

Nomenclature

C = absolute flow speed
C_x/U_m = flow coefficient
E = dimensionless mixing coefficient = $\epsilon/C_x^* L_s$
f = a function
L_s = axial stage length
M = momentum, Eqs. (1) and (2)
P = pressure
Q_{Um} = dynamic pressure based on U_m
r = radial coordinate
U_m = wheel speed at midspan
ϵ = dimensional mixing coefficient
θ = angular coordinate
ρ = density
τ = airfoil pitch

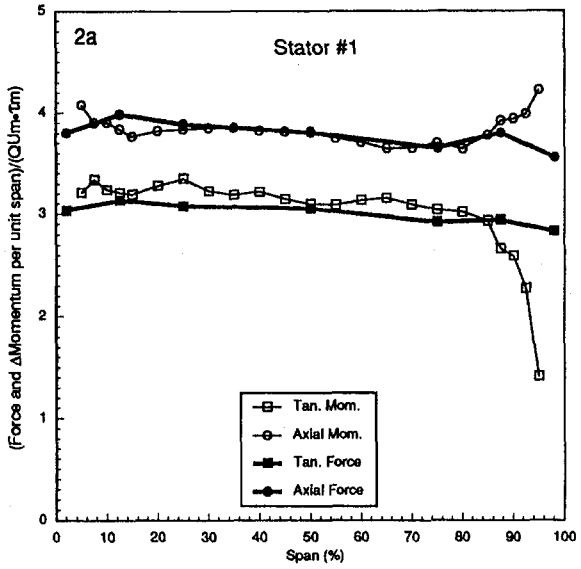
Subscripts

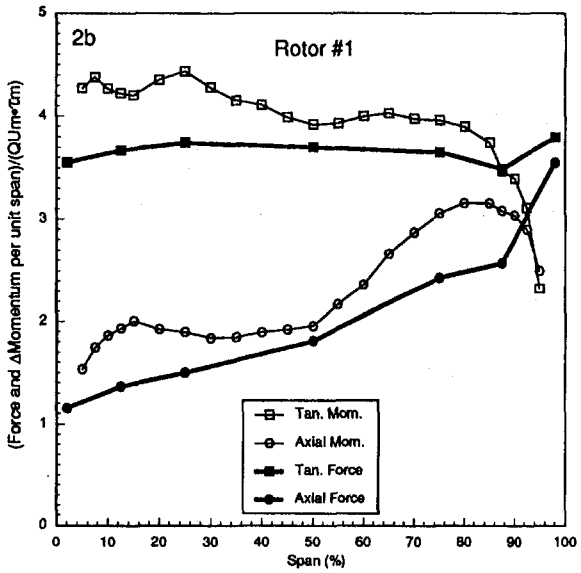
h = hub
m = midspan
mc = midchord
r = radial component
t = tip
x = axial component
θ = tangential component

Superscripts

$-a$ = pitchwise area average; $\bar{f}^a = \int_0^\tau f d\theta / \int_0^\tau d\theta$
$-m$ = pitchwise mass average: $\bar{f}^m = \overline{\rho C_x f}^a / \overline{\rho C_x}^a$

Downloaded 01 Jun 2010 to 171.66.16.53. Redistribution subject to ASME license or copyright; see http://www.asme.org/terms/Terms_Use.cfm





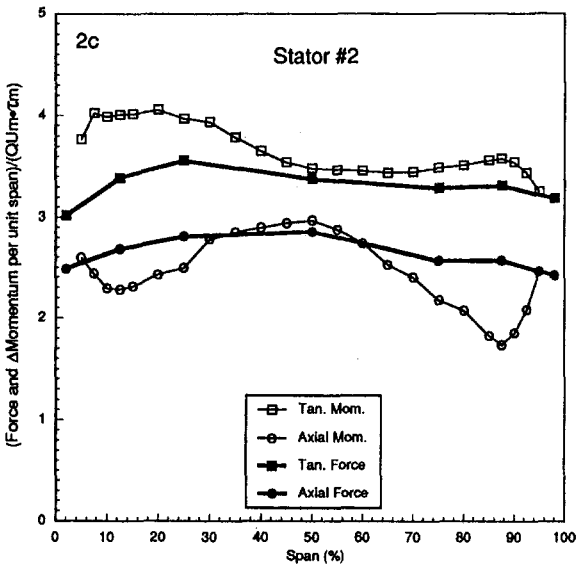


Fig. 2 Airfoil force and flow momentum change

separations on the compressor airfoils were far more severe and local differences in the force-momentum balance of 100 percent were observed.

From these results one can conclude that the hub and tip secondary flows in the turbine have a much weaker impact on the force-momentum balance than does the hub corner separation in the compressor. For this reason, it should be expected that radial mixing within turbine airfoil passages will be weaker than that within the passages of compressor airfoils with significant corner separation. However, these observations about radial mixing within airfoil passages should not be used to infer the rate of radial mixing in the region between adjacent airfoil rows. This will depend on the magnitude and the rate of decay of the radial velocities produced by corner separation in the compressor and by secondary flow vortices in the turbine. This will be examined in the following section.

Mixing Coefficient

The spanwise distributions of the mixing coefficient due to secondary flow were calculated from the radial-circumferential arrays of velocity component data that were available downstream of each of the three airfoils. This calculation was based on the deterministic secondary flow model proposed by Adkins and Smith (1982), but with some modifications described by Dring (1993). The expression used to calculate the mixing coefficient from the traverse data was as follows:

$$E = \left(\frac{x - x_{mc}}{L_s}\right)\overline{\left(\frac{C_r}{C_x}\right)^2}^m \tag{3}$$

The results of this calculation for the traverse planes downstream of each airfoil row are shown in Fig. 3 as the solid lines and symbols. The regions of high mixing coefficient correspond to regions of large secondary flow. The regions of low mixing coefficient correspond to regions of nearly two-dimensional wake flow. For comparison, similar data are shown in Fig. 4 for the second-stage rotor and stator of the compressor operating at nominal design and near-stall conditions (Dring, 1993). These compressor results are for planes 24 percent of axial chord aft of the rotor and 18 percent aft of the stator.

It was mentioned above that at these conditions the compressor airfoils had a much stronger imbalance between the local airfoil force and the momentum change than did the turbine. However, Figs. 3 and 4 indicate that the turbine generally has a higher level of mixing coefficient than does the compressor. The explanation for this is that the force-momentum imbalance for the compressor occurs due to radial flows within the airfoil passage due to the hub corner separation. Some evidence for this can be seen in the high level of the mixing coefficient near the stator hub at the near-stall condition in Fig. 4. Downstream of the airfoils, however, the radial flows in the compressor decay relatively quickly. In the turbine, on the other hand, the radial flows are produced by secondary flow vortices, which do not have a strong impact on the force-momentum balance but which do persist for a long time in the flow downstream of each airfoil, giving rise to the high levels of the mixing coefficient.

Figures 3 and 4 also show the values of the mixing coefficient from the correlation by Lewis (1993a and 1993b) for the total diffusion (turbulent plus secondary flow) for the turbine and from the Gallimore and Cumpsty (1986) correlation for turbulent diffusion for the compressor. The correlation for the compressor is high relative to the measurements, especially at the nominal design conditions. The correlation for the turbine is of comparable magnitude to the data, but the variation through the turbine bears little similarity to the data. Recall that the data represent only the secondary flow contribution (Eq. (3)) whereas the correlation includes the contributions of both secondary flow and turbulent diffusion.

Downloaded 01 Jun 2010 to 171.66.16.53. Redistribution subject to ASME license or copyright; see http://www.asme.org/terms/Terms_Use.cfm

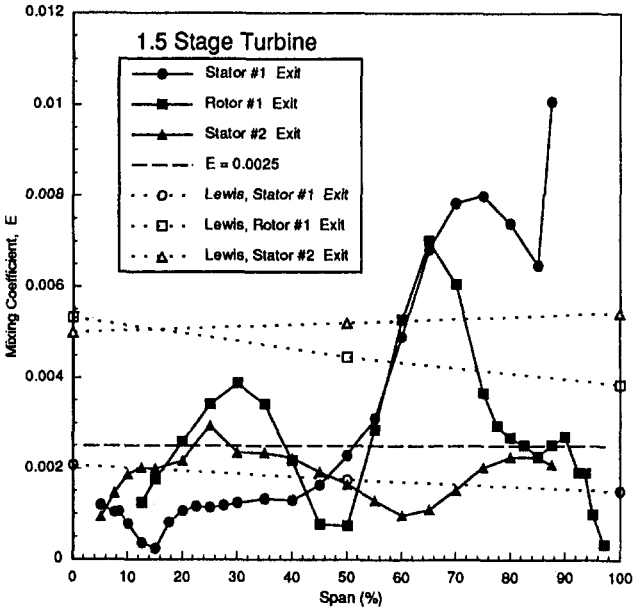


Fig. 3 Dimensionless mixing coefficient for the 1.5 stage turbine at the exit of each airfoil row

The conclusion from this section is that radial mixing in turbines is dominated by the secondary flow vortices, which persist down-stream of the airfoil rows.

Throughflow Modeling

The throughflow analysis used was the finite element analysis of Habashi (1980) and Habashi and Youngson (1983). The aerodynamic input to the analysis consisted of spanwise distributions of total pressure loss and exit flow angle for each of the three rows of turbine airfoils. These data came directly from the measurements made in this turbine by Joslyn and Dring (1992). These measurements indicated that blockage (Dring, 1984) was approximately 1 percent and hence it was neglected.

The mixing process for a parameter "f" was modeled as follows:

$$C_x\left(\frac{\partial f}{\partial x}\right) = \epsilon\left(\frac{\partial^2 f}{\partial r^2}\right) \tag{4}$$

For a specified value of the dimensionless mixing coefficient "E" this mixing equation was solved such that: (1) the mixed quantities (absolute total enthalpy, absolute total pressure, and angular momentum) were conserved on a full-span mass-averaged basis, and (2) they had zero normal derivatives at the hub and tip.

The calculation contained the option of choosing which of the three quantities (absolute total enthalpy, absolute total pressure, and angular momentum) were to be mixed. The argument might be made that since the total pressure loss and exit angle profiles for each row were taken from the measured data, they should not be further mixed. It was demonstrated, however, that the mixing of the temperature field was very insensitive to whether the total pressure and/or angular momentum were being mixed.

The mixing calculation was compared with data taken from two experiments carried out in the turbine model. The first comparison was with the full-span profile attenuation measurements of the simulated combustor-generated inlet profile of Joslyn and Dring (1992). The second comparison was with the hot and cold streak data of Roback and Dring (1993).

Profile Attenuation Comparisons

The total temperature profile at the turbine inlet in the calculation, one chord length upstream of the first stator leading edge (Fig. 1) was set equal to the axisymmetric inlet trace gas profile measured at that location, Fig. 5 (Joslyn and Dring, 1992). Since the inlet temperature of the flow in the experiment was uniform, the magnitude of the temperature profile in the calculation was kept very small (10°F). Several calculations were carried out varying the magnitude of the mixing coefficient until an overall best match was obtained between the measured and calculated profiles at the measurement planes downstream of the first stator, the rotor, and the second stator.

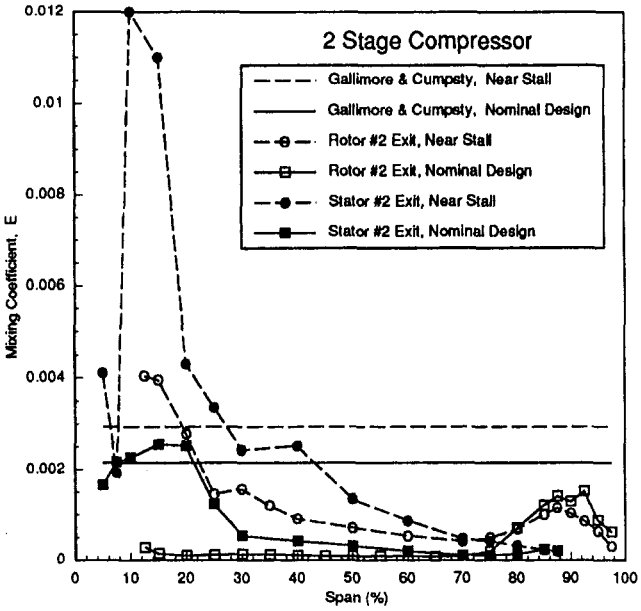


Fig. 4 Dimensionless mixing coefficient for the two-stage compressor at the exit of each airfoil row, at nominal design and near-stall flow conditions

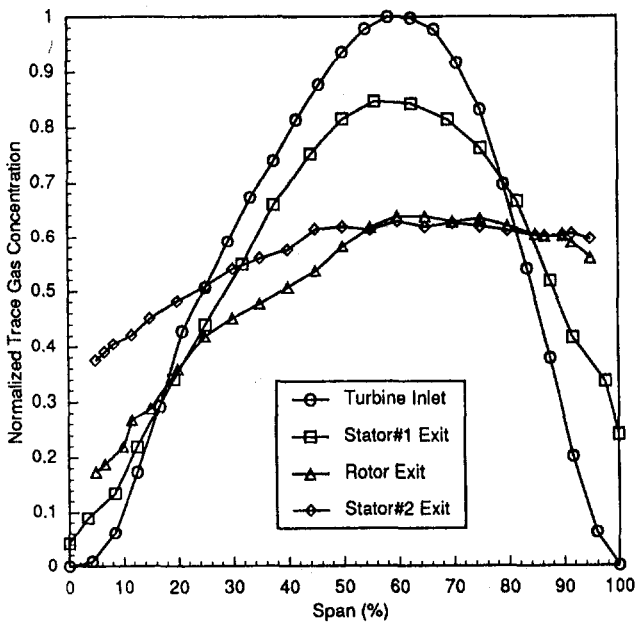


Fig. 5 Measured profile attenuation

Downloaded 01 Jun 2010 to 171.66.16.53. Redistribution subject to ASME license or copyright; see http://www.asme.org/terms/Terms_Use.cfm

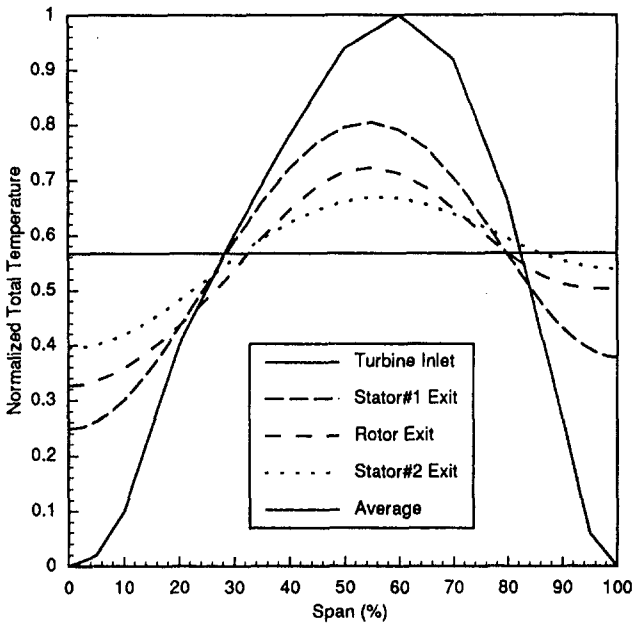


Fig. 6 Calculated profile attenuation with $E = 0.0025$

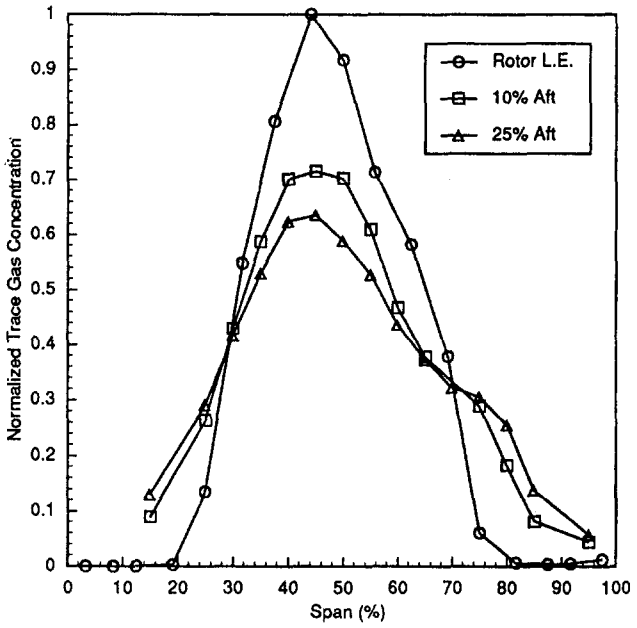


Fig. 7 Measured cold streak attenuation

The measured and calculated results are shown in Figs. 5 and 6. The measured results were normalized with the maximum and minimum trace gas concentrations at the turbine inlet plane. The computed results were similarly normalized with the maximum and minimum total temperature at the turbine inlet plane, and in addition they were adjusted to account for the temperature drop due to work extraction. The results in Fig. 6 were achieved with E equal to 0.0025. This value is plotted in Fig. 3, where it is seen to be in the midst of the range of the mixing coefficient computed from the measured secondary flow using Eq. 3, and also in the range of the values from the correlation by Lewis (1993a, 1993b) for total (turbulent plus secondary flow) diffusion.

The predicted mixing across the first stator is somewhat stronger than measured. This is particularly evident near the hub where very little mixing has occurred in the data, and to a lesser degree between 50 and 80 percent span. At the rotor exit the predicted mixing in the hub region is somewhat stronger than measured and near the tip it is somewhat weaker than measured. These differences are due in part to the relative eddy (Dring and Joslyn, 1983), which causes a large-scale radial redistribution of the flow inside the rotor airfoil-to-airfoil passage. Downstream of the second stator the measured and computed results are in relatively good agreement. A prediction for these measurements by Lewis (1993a) produced similar results, the major difference being somewhat lower mixing across the first stator. This was to be expected due to his lower mixing coefficient for this stator (Fig. 3).

It is apparent from these results that it is not necessary to model the strong spanwise variations in mixing coefficient that exist in the flow (Fig. 3) to get a reasonably accurate prediction.

Hot and Cold Streak Comparisons

The throughflow calculation with radial mixing was also used to model data acquired for the radial mixing of simulated combustor-generated hot and cold streaks by Roback and Dring (1993). The streaks were nominally 2 in. in diameter and they were injected into the flow at Station 1, one chord length upstream of the first stator. The hot streak had a density half that of the surrounding fluid and the cold streak density was 1.5 times that of the surrounding fluid. No attempt was made to model the streak density in the calculation.

The experimental results documented the attenuation of the streaks between the rotor leading edge plane and traverse planes 10 and 25 percent aft of the rotor. The calculation was done in the same manner as for the radial profile attenuation study described above. The streak profile was input to the calculation to be the same as the measured profile at the rotor leading edge. The mixing process was initiated at the rotor leading edge and the mixing coefficient was the same as that used above, $E = 0.0025$. The measured and calculated results were normalized in the same manner as in the profile attenuation study described above except that the normalization was based on conditions at the rotor leading edge.

The measured results are shown in Fig. 7 for the cold streak and in Fig. 8 for the hot streak. Since the leading edge profiles are nearly the same for the two cases, the calculated results in

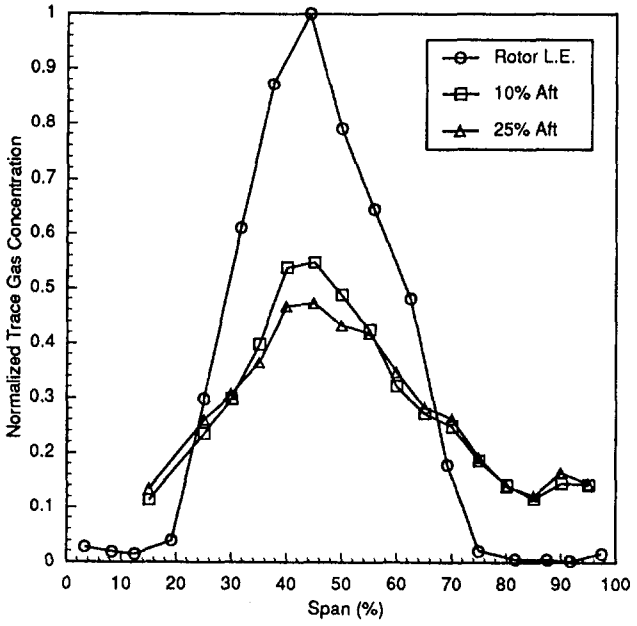


Fig. 8 Measured hot streak attenuation

Downloaded 01 Jun 2010 to 171.66.16.53. Redistribution subject to ASME license or copyright; see http://www.asme.org/terms/Terms_Use.cfm

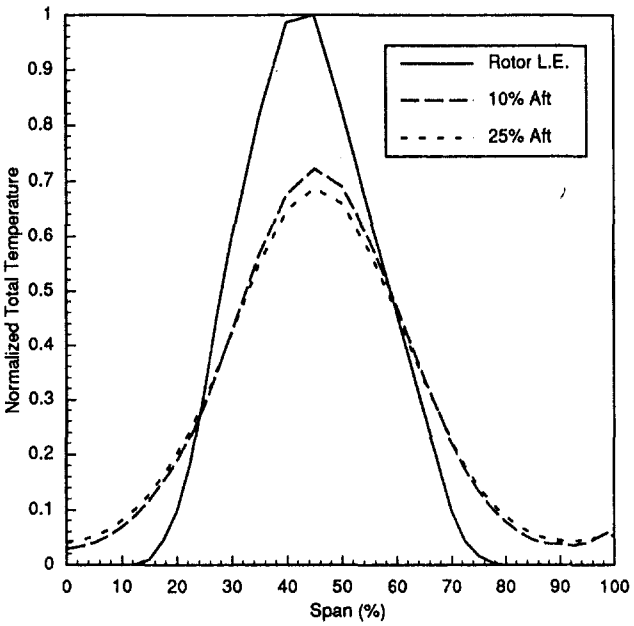


Fig. 9 Calculated streak attenuation with $E = 0.0025$

Fig. 9 will be compared with both sets of data. There is good agreement between the calculation and the cold streak data in that the profile maximum has decreased to about 65 percent of its leading edge value. However, for the hot streak data the maximum has decreased to about 50 percent of its leading edge value. It was demonstrated by Roback and Dring (1993) that hot streaks experience a stronger rectification process within rotor passages than do cold streaks. This was caused by a stronger density-driven secondary flow. This secondary flow was much weaker for the cold streak and it was nonexistent for the profile attenuation study above. Hence, it is not unreasonable that the same diffusion coefficient that predicted the trace gas radial profile mixing (Figs. 5 and 6) and the cold streak mixing (Figs. 7 and 9), $E = 0.0025$, underpredicts the mixing of the hot streak (Figs. 8 and 9).

Conclusions

The objective of this work was to examine radial mixing in axial turbines from three perspectives: (1) the spanwise distributions of airfoil force and momentum exchange to determine whether radial transport has the same large impact it has on compressor airfoils, (2) the spanwise distribution of the mixing coefficient due to secondary flows, and (3) the ability of a simple diffusive mixing model to predict measured radial profile mixing for full span profile attenuation and for hot and cold streaks. From the results the following conclusions can be drawn:

- The hub and tip secondary flows in a turbine have a much weaker impact on the force-momentum balance than does hub corner separation in a compressor.
- It can be expected that radial mixing within turbine airfoil passages will be weaker than that within the passages of compressor airfoils with significant corner separation.
- It can also be expected that mixing downstream of turbine airfoils will be strong due to the strong secondary flow vortices that persist in the flow.
- The correlation of Lewis (1993a) generally gave a level of total mixing (secondary flow plus turbulent) comparable to that of the secondary flow model of Adkins and Smith (1982) when the latter was based on measured radial velocities (Eq. (3)).
- The simple radial diffusion model gave a reasonably accurate prediction of the mixing of the simulated turbine inlet temperature profile at the various locations through the turbine.
- The radial diffusion model also gave a reasonably accurate prediction of the mixing of a cold streak profile.
- When mixing was caused by a strong density driven secondary flow, as in the case of hot streaks, it was faster than the model predicted.

References

Adkins, G. G., Jr., and Smith, L. H., Jr., 1982, "Spanwise Mixing in Axial-Flow Turbomachines," ASME JOURNAL OF ENGINEERING FOR POWER, Vol. 104, pp. 97–110.

Dring, R. P., 1984, "Blockage in Axial Compressors," ASME *Journal of Engineering for Gas Turbines and Power*, Vol. 106, pp. 712–714.

Dring, R. P., 1993, "Radial Transport and Momentum Exchange in an Axial Compressor," ASME JOURNAL OF TURBOMACHINERY, Vol. 115, pp. 477–486.

Dring, R. P., and Joslyn, H. D., 1983, "The Relative Eddy in Axial Turbine Rotor Passages," ASME Paper No. 83-GT-22.

Gallimore, S. J., and Cumpsty, N. A., 1986, "Spanwise Mixing in Multistage Axial Flow Compressors: Part I—Experimental Investigations; Part II—Throughflow Calculations Including Mixing," ASME JOURNAL OF TURBOMACHINERY, Vol. 108, pp. 2–16.

Habashi, W. G., 1980, "Numerical Methods for Turbomachinery," in: *Recent Advances in Numerical Methods in Fluids*, C. Taylor and K. Morgan, eds., Pineridge Press, United Kingdom, Chap. 8.

Habashi, W. G., and Youngson, G. C., 1983, "A Transonic Quasi-3D Analysis for Gas Turbine Engines Including Split-Flow Capability for Turbofans," *Int. J. Num. Meth. in Fluids*, Vol. 3, pp. 1–21.

Joslyn, H. D., and Dring, R. P., 1989, "Three-Dimensional Flow and Temperature Profile Attenuation in an Axial Turbine," Final Report, AFOSR Contract No. F49620-86-C-0020.

Joslyn, H. D., and Dring, R. P., 1992, "Three-Dimensional Flow in an Axial Turbine: Part I—Aerodynamic Mechanisms; Part II—Profile Attenuation," ASME JOURNAL OF TURBOMACHINERY, Vol. 114, pp. 61–78.

Lewis, K. L., 1993a, "Spanwise Transport in Axial-Flow Turbines; Part I—The Multistage Environment; Part II—Throughflow Calculations Including Spanwise Transport," ASME Paper Nos. 93-GT-289 and -290.

Lewis, K. L., 1993b, private communication.

Leylek, J. H., and Wisler, D. C., 1991, "Mixing in Axial-Flow Compressors: Conclusions Drawn From Three-Dimensional Navier–Stokes Analysis and Experiments," ASME JOURNAL OF TURBOMACHINERY, Vol. 113, pp. 161–174.

Roback, R. J., and Dring, R. P., 1993, "Hot Streaks and Phantom Cooling in a Turbine Rotor: Part I—Separate Effects; Part II—Combined Effects and Analytical Modeling," ASME JOURNAL OF TURBOMACHINERY, Vol. 115, pp. 657–674.

Wisler, D. C., Bauer, R. C., and Okiishi, T. H., 1987, "Secondary Flow, Turbulent Diffusion, and Mixing in Axial-Flow Compressors," ASME JOURNAL OF TURBOMACHINERY, Vol. 109, pp. 455–482.

Downloaded 01 Jun 2010 to 171.66.16.53. Redistribution subject to ASME license or copyright; see http://www.asme.org/terms/Terms_Use.cfm

Numerical Analysis of Three-Dimensional Unsteady Hot Streak Migration and Shock Interaction in a Turbine Stage

A. P. Saxer

H. M. Felici

Turbomachinery Laboratory,
Institute of Energy Technology,
Swiss Federal Institute of Technology,
Zürich, Switzerland

A three-dimensional unsteady flow computation has been performed for a transonic first turbine stage under the influence of streaks of hot gas exiting the combustion chamber. Realistic flow conditions are obtained by using an unequal stator-to-rotor pitch, a single-streak/multistator channel configuration, and periodic boundary conditions. The resulting unsteady shock wave system and the hot streak migration as well as the shock wave/streak interaction are presented and discussed. In addition, the time average of the periodic unsteady solution is analyzed and compared with a steady-state computation. The steady-state solution matches the time-averaged one in terms of the pressure field and the maximum stagnation temperature on the rotor blade surface. However, the rotor blade temperature patterns are different with a stronger radial secondary flow present in the time-averaged solution due to the retention of the circumferential streak variations at the stator/rotor interface.

1 Introduction

The accurate prediction of the heat loads encountered by the first turbine stage of a gas turbine is of primary importance for the design of an efficient cooling system. By construction, a modern first turbine stage has to operate under circumferential and radial nonuniform inlet temperature conditions produced by the combustor, as well as transonic flow conditions. This, and the inherent unsteadiness of a stator/rotor configuration, creates a highly complex three-dimensional environment for the turbine designer.

In this paper a three-dimensional, inviscid, periodic unsteady solution is presented for the flow in a generic industrial transonic axial turbine stage. This flow includes nonuniform inlet conditions produced by streaks of hot gas discharged from the combustion chamber. A realistic periodic configuration comprising a stator-to-rotor pitch ratio of 5:3 and a streak count different from the stator blade count has been chosen. This is important as the time-averaged rotor blade surface temperature is directly dependent on the streak count and residence time in the passage. The problem of temperature redistribution in an axial flow turbine stage has been analyzed by several authors; see for instance Butler et al. (1986), Krouthén and Giles (1988), Ni and Sharma (1990), Harasgama (1990), Dorney et al. (1990), and Takahashi and Ni (1990). In particular, the numerical studies of Ni and Sharma, and Dorney et al. tend to reproduce the migration of one midspan, circular hot streak of fluid, experimentally investigated by Butler et al. Notice that in contrast to the present analysis, the above-mentioned studies report on a turbine operating under subsonic flow conditions, where the level of unsteadiness is much lower than for the transonic cases. It has been experimentally observed that the periodic unsteady interaction between a shock wave and a turbine airfoil can cause considerable effects in terms of blade loading and heat transfer; see for instance Doorly and Oldfield (1985), Johnson et al. (1990), and Collie et al. (1993). As they occur simultaneously in a transonic first turbine stage and as they both are primarily driven by inviscid mechanisms, it appears quite natural to simulate streak migration and unsteady shock wave interaction in a single unsteady inviscid computation.

The numerical procedure is briefly described in Section 2, together with the boundary condition formulation. In Section 3, the unsteady results are presented. The identification of the different phases of the basic stator trailing edge shock wave impinging on the moving downstream rotor is performed in Section 3.1. The migration of the hot streak as it is chopped by the moving rotor blades is discussed in Section 3.2. The interaction between the shock waves and the hot streaks is treated in Section 3.3. Although the unsteady solution is necessary to get the knowledge of the maximum temperature, the time-averaged flow solution is important, as the turbine designer has to rely on mean flow values. Hence, the time average of the periodic unsteady solution is presented in Section 4. This allows us to assess the mean effect of the shock and the streak unsteadiness. The comparison of the time-averaged and the steady-state solutions on the rotor blade surfaces allows us to assess the importance of the circumferential streak variations (not retained in the steady-state mode) on the rotor flow field. A summary and the essential conclusions are given in Section 5.

2 Numerical Procedure

The time-dependent Euler equations are solved using a node-based, explicit Ni–Lax–Wendroff scheme (Ni, 1981). The extension of this procedure to three dimensions on unstructured meshes with hexahedral cells has been reported previously by the first author (Saxer, 1992). The mesh is found by solving Poisson equations with source terms calibrated to control spacing and orthogonality at the blade/hub/tip surfaces. A combined second and fourth-difference numerical smoothing acting on the state vector is added to the algorithm to prevent high-frequency oscillations in the solution as well as to capture shocks. The fourth-difference smoothing, an extension to three dimensions of the method of Holmes and Connell (1989), exploits the advantages of a pseudo-Laplacian to ensure second-order accuracy in shock-free regions even on distorted grids. This is a desired feature to study inlet distortion effects or to compare different solutions without spurious distortions due to numerical

Contributed by the International Gas Turbine Institute and presented at the 39th International Gas Turbine and Aeroengine Congress and Exposition, The Hague, The Netherlands, June 13–16, 1994. Manuscript received by the International Gas Turbine Institute February 11, 1994. Paper No. 94-GT-76. Associate Technical Editor: E. M. Greitzer.

Copyright © 1996 by ASME

Downloaded 01 Jun 2010 to 171.66.16.53. Redistribution subject to ASME license or copyright; see http://www.asme.org/terms/Terms_Use.cfm

smoothing. A nonlinear second-difference operator is used to capture shocks with an artificial bulk viscosity parameter tailored by the local flow divergence and the Mach number. This avoids large shock overshoots, and does not alter the global accuracy of the scheme in smooth flow regions. In each blade row, relative flow variables are used.

2.1 Boundary Conditions. Numerical and physical boundary conditions have to be applied at the stator inlet, stator/rotor interface, and rotor exit as well as on solid and periodic surfaces. The stator and most of the rotor flow is choked at the throat, indicating that the periodic unsteadiness created by the relative motion between the stator and the rotor blades does not reach the rotor exit and the stator inlet. Hence, steady-state boundary conditions are applied at both the stator inlet and the rotor exit. At the stator inlet, the one-dimensional characteristics theory is used to prescribe the stagnation enthalpy, the radial and tangential flow angles as well as the entropy (or stagnation pressure). At the rotor exit, the quasi-three-dimensional nonreflecting boundary conditions formulation developed by Saxer and Giles (1993) is used together with the requirement that the outflow be in radial equilibrium. This avoids spurious reflections of the rotor trailing edge shock wave off the exit of the computational domain.

For time-accurate calculations of stator/rotor flow fields, the changes required by the Lax–Wendroff algorithm from a time level to the next one at the stator outflow and at the rotor inflow are set to eliminate the following characteristic jumps, taking note of the direction of propagation of each characteristic:

$$\begin{pmatrix} \Delta\phi_1 \\ \Delta\phi_2 \\ \Delta\phi_3 \\ \Delta\phi_4 \\ \Delta\phi_5 \end{pmatrix} = \begin{pmatrix} -c^2 & 0 & 0 & 0 & 1 \\ 0 & 0 & \rho c & 0 & 0 \\ 0 & 0 & 0 & \rho c & 0 \\ 0 & \rho c & 0 & 0 & 1 \\ 0 & -\rho c & 0 & 0 & 1 \end{pmatrix} \begin{pmatrix} \rho_s - \rho_r \\ u_{xs} - u_{xr} \\ u_{\theta s} - u_{\theta r} - \Omega R \\ u_{Rs} - u_{Rr} \\ p_s - p_r \end{pmatrix}, \quad (1)$$

where ρ, u_x, u_θ, u_R, and p represent the values of density, axial, circumferential and radial velocity components, and pressure, respectively. Note that because of the use of relative flow variables, the rotor wheel speed ΩR has to be introduced into the condition of matching circumferential velocities. The outgoing characteristics changes are calculated by the Lax–Wendroff algorithm. The combined five characteristic changes on both sides of the interface are then converted back to primitive and finally conservation variables before the flow field is updated.

In a steady-state calculation of a stator/rotor interaction, the quasi-three-dimensional nonreflecting boundary conditions mentioned above are used together with a circumferential stream-thrust flux-averaging technique in order to conserve mass, momentum, and energy across the mixing plane between a stator and a rotor row. Hence, radial variations are automatically accounted for and the stator and the rotor flow fields are matched at the interface (Saxer, 1992).

In addition to these boundary conditions, a no-mass-flux condition is enforced at the hub and the tip endwalls as well as on the stator and the rotor blades. Also, periodic boundary conditions along the outer boundaries of the H-type grid are enforced in the tangential direction.

3 Unsteady Solution

The numerical procedure discussed above is applied to the computation of the unsteady shock wave/hot streak interaction occurring in the transonic first turbine stage represented in Fig. 1. The design of this stage with a 4:1 pressure ratio was performed by Rolls-Royce as part of the Advanced Core Engine program (ACE). It is representative of a high-pressure, cooled aircraft turbine operating in the transonic regime. The flow simulation uses a 3-to-5 stator-to-rotor blade count ratio and periodic boundary conditions, which corresponds very closely to the actual configuration of (36 stators)/(61 rotors). $56 \times 36 \times 21$ nodes are used in each of the three stator channels, and $56 \times 22 \times 21$ in each of the five rotor passages. Starting from the steady-state solution, the unsteady computation took 12 stator periods (or 20 rotor periods) to converge to a periodic solution, using 1300 iterations/cycle. A CPU time of 241×10^{-6} seconds/iteration/grid point was required on a Silicon Graphics Indigo R4000 workstation.

The stator inlet conditions are set by specifying a radial and a tangential flow angle, a stagnation pressure, and a total temperature distribution in the form of a streak of hot gas. The streak is placed midway between Stator S1 and Stator S2 at 60 percent span, see Figs. 3 and 9 (top, left). Due to periodicity this means that a hot streak is introduced in one out of every three stator passages. Relative to the surrounding free stream, the streak peak stagnation temperature ratio is 1.97. The total pressure is assumed to be uniform over the entire inlet section, which means that the streak-to-free stream stagnation temperature ratio is the reciprocal of the streak-to-free stream total density ratio. The assumption of constancy of the inlet total pressure is motivated by the low Mach number at the exit of the combustion chamber considered as a plenum, and the neglect of viscous effects.

The transonic nature of the flow field and the introduction of the hot streak produce two distinct unsteady stator/rotor interaction phenomena. For supersonic vane exit conditions, a system of oblique shock waves is generated at the trailing edge of the stator. For small axial gaps, the suction side trailing edge shock extends to the downstream rotor and impinges on the suction side. This produces reflected waves on both the adjacent rotor and on the upstream stator causing unsteady blade loading. This is discussed in Section 3.1. The unsteady temperature migration in the rotor passages due to the periodic chopping of the streak of hot gas exiting the vane by the rotors is analyzed in Section 3.2. The unsteady shock wave/hot streak interaction is discussed in Section 3.3.

3.1 Unsteady Shock Motion. Figure 2 shows the instantaneous static pressure contours at a constant radius set at 60 percent span (thus corresponding to a cut through the core of the streak at the inlet), at eight intervals during one periodic cycle. Note that a cycle, starting at $t = 0$, is defined here as the time for one rotor

Nomenclature

c = speed of sound
h_t = stagnation enthalpy
p = static pressure
p_t = stagnation pressure
R = radius = $\sqrt{y^2 + z^2}$
t = time (nondimensionalized with period)
T_t = stagnation temperature
u_x, u_θ, u_R = cylindrical velocity components in (x, θ, R)
V = absolute velocity (stator)
W = relative velocity (rotor)
γ = ratio of specific heats
ρ = static density
ϕ = characteristic variable
Ω = angular speed
ω = vorticity
$(\ )_\infty$ = inlet undisturbed flow (no streak)
$(\ )_{r,s}$ = rotor, stator

Downloaded 01 Jun 2010 to 171.66.16.53. Redistribution subject to ASME license or copyright; see http://www.asme.org/terms/Terms_Use.cfm

passage to rotate by an amount of five rotor pitches to $t = 1$, which by periodicity also corresponds to $t = 0$. As opposed to the three-stator period for the hot streak migration, the stator/rotor shock interaction occurs during one stator period. Hence, a complete view of the unsteady shock motion in one rotor passage would have been required to store many more time-dependent solutions. However, this can be circumvented by noting that a basic phenomenon occurring in a given rotor passage at a given instant can also be seen in another passage at another time. This implicitly assumes that the hot streak has only a weak effect on the basic stator/rotor shock mechanism and that only the relative position between stator and rotor is of importance. As the results will show, this seems to be a valid assumption.

Examining the pressure contours at the beginning of the cycle at $t = 0$, at the bottom of the figure the oblique shock extending downstream from the trailing edge of Stator S1 is just about to impact on the suction side of Rotor R1. The actual impact on the crown of the rotor is seen at time $t = 0.750$ between Stator S2 and Rotor R4, where also a weak reflection is noticeable. As the rotor blade moves upward, the location of the shock wave impingement moves forward toward the leading edge; see for example Rotor R1 at $t = 0.375$. As this occurs, the reflection is also growing stronger; see Rotor R4 at $t = 0.125$.

At $t = 0.250$ for Rotor R2, the primary reflection point has reached the rotor leading edge, and a primary reflected wave is clearly visible. The leading edge shock wave impact is also noticeable for Rotor R3 at $t = 0.375$ and R5 at $t = 0.625$. In addition to this primary reflection, the portion of the reflected wave that moves toward the pressure surface of the adjacent rotor is reflecting a second time and is moving back toward the original rotor; see R5 at $t = 0$.

As the rotor continues to move, the primary reflection passes the leading edge; see R2 at $t = 0.250$, for example. From now on the stator oblique shock no longer impacts on the rotor. The curved diffracting part of the shock wave (see for example R5 at $t = 0.000$ and R4 at $t = 0.875$) is weak and is continuing to weaken. However, the length of its straight portion is increased (due to a velocity component approximately $\sqrt{V^2 - c^2}$ along the shock front). Compare for example the stator trailing edge shock wave S1 at $t = 0.750$ with S3 at $t = 0.250$.

While the original stator shock no longer impacts on the rotor surface, the primary reflected wave has left the rotor and is propagating upstream toward the stator suction surface; see interaction S2 with R4 at $t = 0.875$, and the middle of the figure at $t = 0.625$ (bowed pressure contours between R2, R3 and S1). Also seen in the passage between Rotors R4 and R5 is the crossing back of the secondary reflected shock from the pressure side of R5 towards the suction side of R4. As it crosses back from a low Mach number to a larger Mach number region, toward the original rotor, the secondary reflection gets stronger; see for example R4 at $t = 0.875$, R2 at $t = 0.625$ and R1 at $t = 0.500$.

At $t = 0.875$ the primary reflected wave from Rotor R1 has just struck the suction side of Stator S1 in a region close to the trailing edge, and moves back to the adjacent rotor. However, this reflection is not very visible on the contour plots. As the rotor moves away from the stator primary oblique shock, the latter regains its maximum strength—see S2 at $t = 0.125$—until it strikes the next rotor, and the basic shock mechanism starts again.

For the case examined here, the unsteady stator/rotor shock interaction is essentially a two-dimensional process driven by the oblique shock leaving the stator trailing edge and impinging on the moving rotor blade. This unsteady shock interaction is similar in nature to the result presented by Giles (1990) in a two-dimensional time-accurate numerical simulation, which included quasi-three-dimensional source terms. However, some differences appear due to the hot streak interaction and three-dimensional effects.

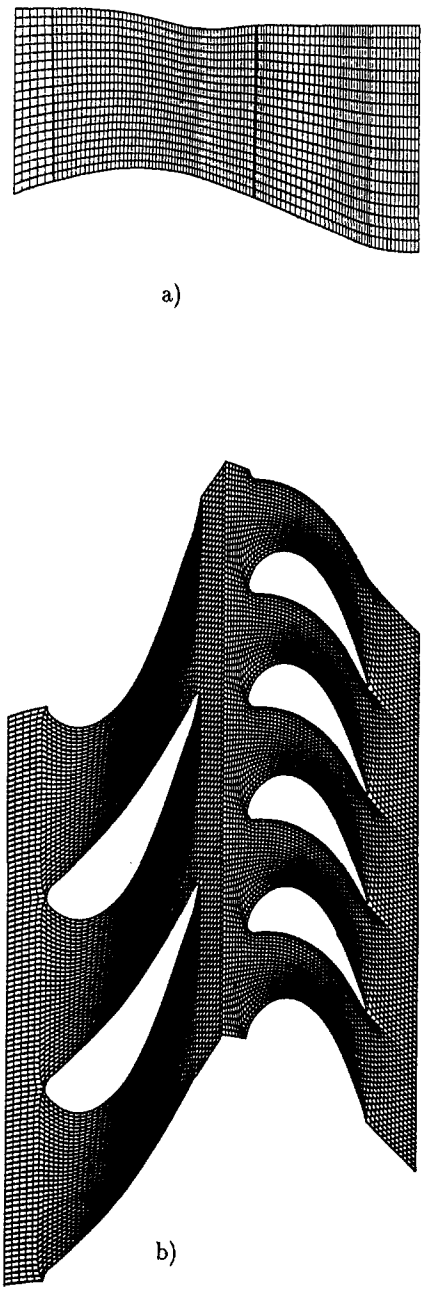


Fig. 1 (*a*) **Side view of the transonic first turbine stage with stator pressure and rotor suction sides, and** (*b*) **mesh on the hub surface (stator: 56 × 36 × 21, rotor: 56 × 22 × 21 nodes)**

3.2 Unsteady Temperature Migration. The objective of this section is to analyze the migration of the hot streak introduced at the inlet of the transonic turbine stage of Fig. 1. Figure 3, showing the time-dependent stagnation temperature contours at 60 percent span, is the pendant of Fig. 2. A uniform flow of the same mass-averaged stagnation temperature as the one imposed here at the stator inlet is used as reference. Notice that the absolute stagnation temperature is plotted in the stator while the rotor-relative total temperature is represented in the moving frame. This explains the mismatch of the temperature contours across the stator/rotor interface. In Fig. 3, the lower temperature levels as well as the higher ones (streak core) have been filtered out. The hot streaks are between the bands of isoclines representing the transition between hot and cold gas.

Due to the absence of secondary flow, no significant temperature redistribution occurs in the stator during the entire cycle.

Downloaded 01 Jun 2010 to 171.66.16.53. Redistribution subject to ASME license or copyright; see http://www.asme.org/terms/Terms_Use.cfm

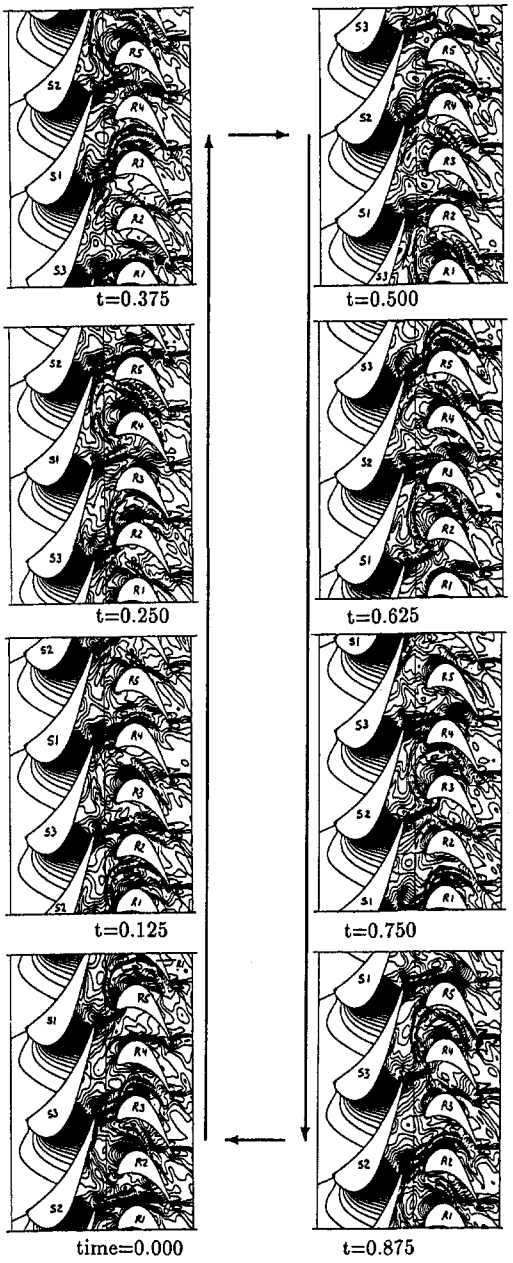


Fig. 2 Unsteady static pressure contours at 60 percent span ($\Delta p/p_{t_\infty}$ = 0.02)

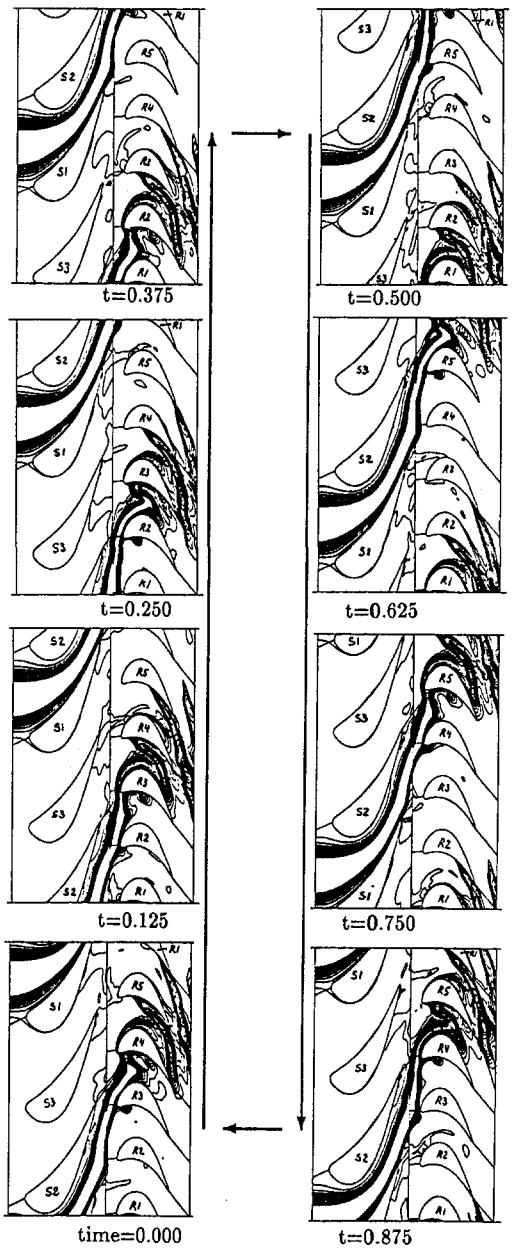


Fig. 3 Unsteady stagnation temperature contours at 60 percent span ($\Delta T_t/T_{t_\infty}$ = 0.03, except in streak core) (stator: absolute T_t/T_{t_∞}, rotor: relative T_t/T_{t_∞})

At the stator inlet in the streak region, the boundary conditions produce a radial as well as a tangential sheared velocity field, hence vorticity. However, under the invariance of the inlet stagnation pressure and by using the Munk and Prim substitution principle (Munk and Prim, 1947), it can be shown that no three-dimensional secondary flow associated with the temperature gradient occurs in the vane (Saxer, 1992). Indeed, the Munk and Prim principle states that if a steady isentropic flow field without body forces is determined for a specific geometry and a total pressure distribution, then the streamline pattern, the Mach number, and static pressure fields remain unchanged for any other stagnation temperature distribution. Another way of checking this statement is to use secondary flow theory (Hawthorne, 1974; Johnson, 1978; Horlock and Lakshminarayana, 1973). It can be shown that in the absolute frame of reference the growth of the absolute streamwise vorticity is dependent upon the gradient of stagnation pressure, which is set to zero at the inlet, i.e., the vortex lines introduced at the inlet have to remain perpendicular to the flow in the vane. In fact, the secondary flow developed by the turning of the inlet normal vorticity is exactly balanced by the secondary flow introduced by the temperature gradient. These arguments are valid up to the vane choked throat. Downstream of this area, the unsteady pressure waves resulting from the stator/rotor shock and potential interaction discussed in Section 3.1 reach the aft part of the stator suction surface. This affects the streak path and width.

Examining the interaction between the rotor blade and the streak during one cycle, five different phases of the streak redistribution can be identified. The first phase consists of the hot streak crossing the interface and being convected toward the blade row (t = 0, middle of the figure). The second phase is when the hot streak impinges on the leading edge and starts to separate into the suction and pressure side legs, as seen for R3 at t = 0, R2 at t = 0.125, or R4 at t = 0.750. In the stagnation point region on the pressure side hot fluid seems to attach to the blade, while cooler surrounding gas wraps around it forming

Downloaded 01 Jun 2010 to 171.66.16.53. Redistribution subject to ASME license or copyright; see http://www.asme.org/terms/Terms_Use.cfm

a "socket" of hot fluid slowly convecting along the pressure surface, see for example R2 at $t = 0.250$, R3 at $t = 0$, and R1 at $t = 0.500$. Meanwhile on the suction side part of the leading edge, the streak width tightens under the local acceleration of the flow.

The next phase is the bowing of the streak into a V-shape in the blade passage, due to the acceleration gradient in the high-speed region between the pressure and the suction surface of two consecutive blades. The V-shape distortion is accentuated as the streak convects down the interblade channel. This effect is clearly seen at all times for different blade passages.

Phase four is the merging of the pressure and suction side legs of the streak in the second part of the blade channel and in the exit region. Finally, the remainder of the chopped streak convects outside of the domain.

Figure 4 represents the rotor-relative stagnation temperature distribution on eleven axial cuts at time $t = 0$ during the streak/rotor interaction. This allows us to identify the extent of the streak radial migration, as well as the mixing of the suction and the pressure side leg of the hot gas in the five computed rotor passages. As in Fig. 3, the lower and upper temperature levels have been filtered out to see the streak migration better.

The unsteady rotor-relative stagnation temperature contours and static pressure contours on the pressure surface of Rotor R3 are plotted in Fig. 5. Figure 6 shows these same quantities on the suction surface of Rotor R3. Clearly the pattern of the streak migration from the leading edge toward the trailing edge is different on these two surfaces, with a significant secondary flow in the radial direction on the pressure surface. This forces hot midspan fluid toward the hub and the tip endwalls. Also,

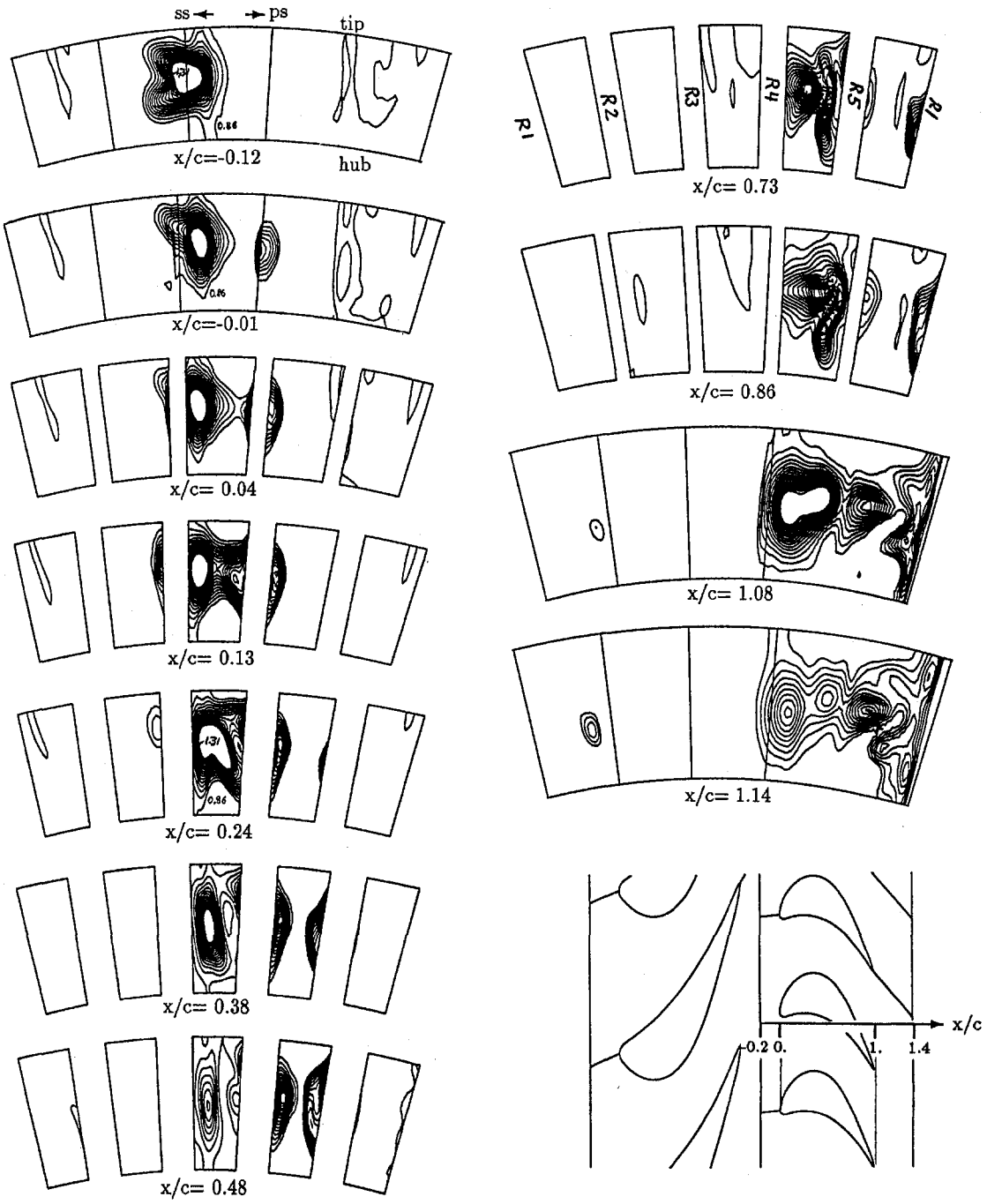


Fig. 4 Rotor-relative stagnation temperature contours on axial cuts at time $t = 0.0$, ($\Delta T_t/T_{t_\infty} = 0.03$, ss: suction side, ps: pressure side)

Downloaded 01 Jun 2010 to 171.66.16.53. Redistribution subject to ASME license or copyright; see http://www.asme.org/terms/Terms_Use.cfm

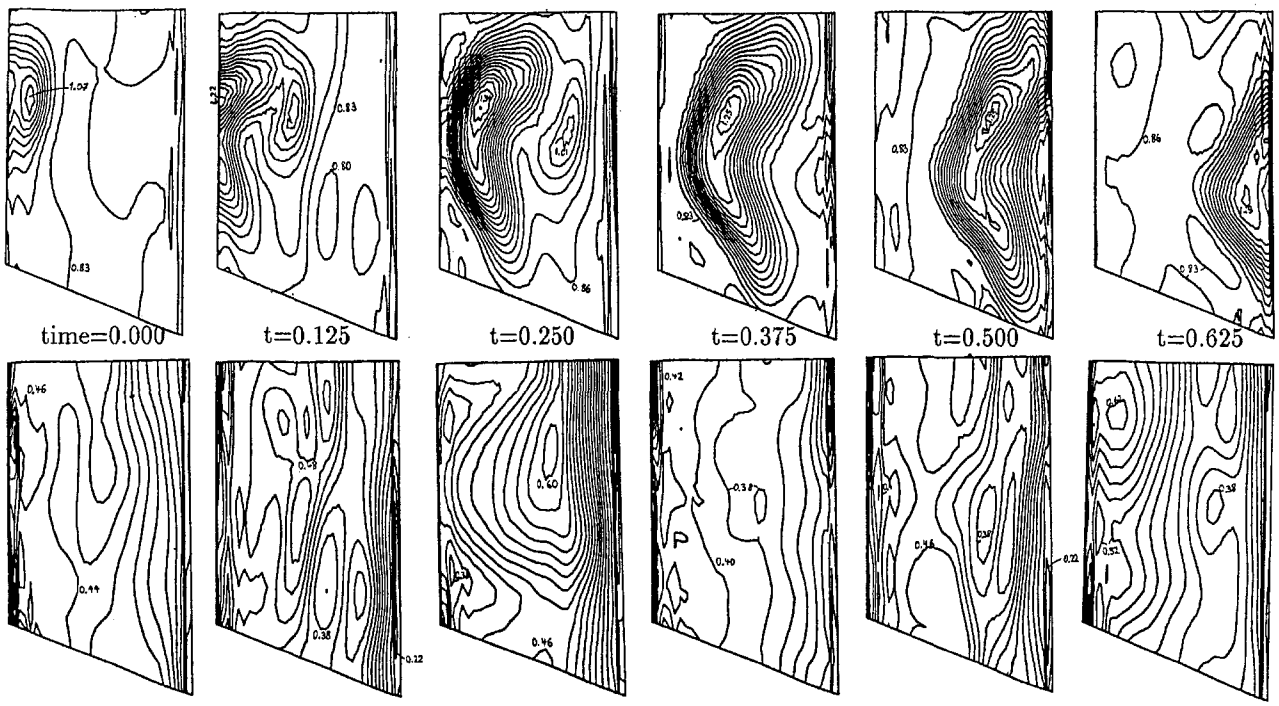


Fig. 5 Unsteady rotor-relative stagnation temperature (top) and static pressure (bottom) on pressure surface of rotor R3 (see Figs. 2 & 3) ($\Delta T_t/T_{t_\infty}$ = 0.03, $\Delta p/p_{t_\infty}$ = 0.02)

the "residence" time of the hot streak is smaller on the suction surface than on the pressure side, due to the generally lower convection speed on the pressure side. On the rotor pressure surface the streak "residence" time corresponds approximately to $\frac{3}{4}$ of a cycle period, i.e., roughly four rotor periods, whereas only two rotor periods are needed for the streak to transit on the suction surface.

3.3 Unsteady Shock Wave/Hot Streak Interaction. The unsteady pressure waves distribution discussed in Section 3.1 will influence both the path and the strength of the hot streak as it migrates in the rotor row. Fluid particles crossing a compression wave, such as the one detaching from the rotor leading edge (primary reflection) and moving back toward the stator, will have their trajectories slightly deviated, see for ex-

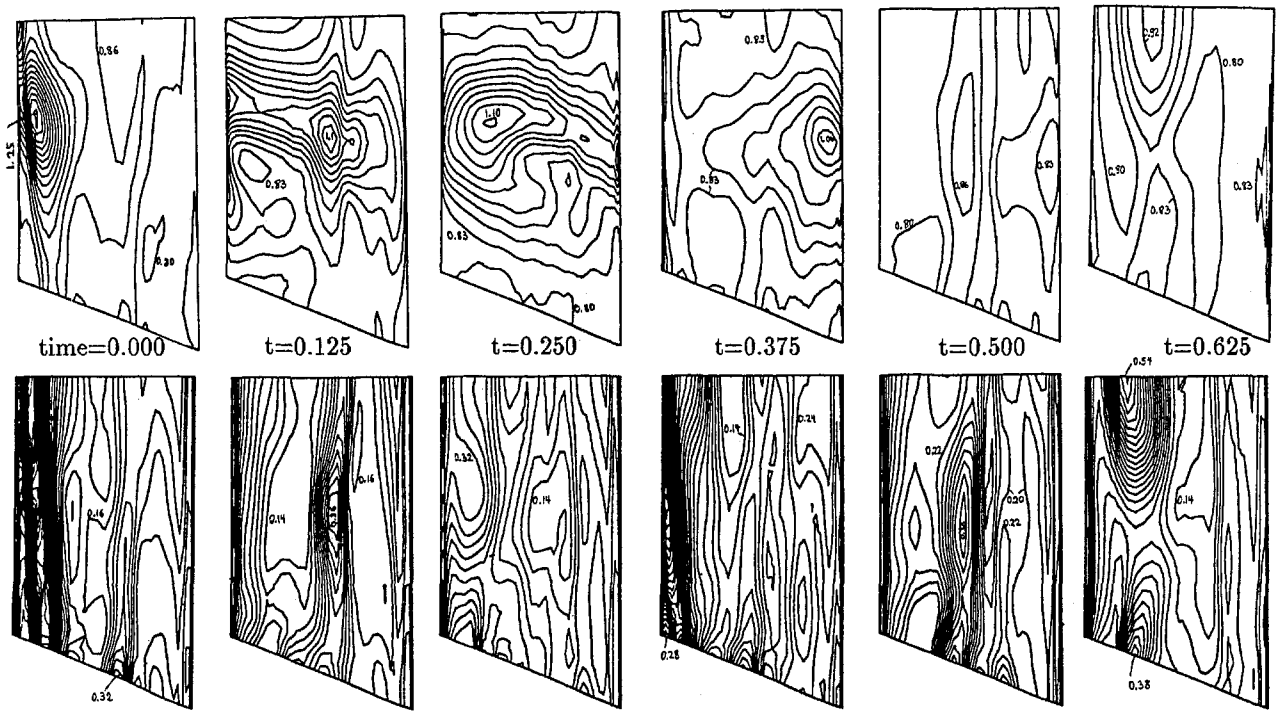


Fig. 6 Unsteady rotor-relative stagnation temperature (top) and static pressure (bottom) on suction surface of rotor R3 (see Figs. 2 and 3) ($\Delta T_t/T_{t_\infty}$ = 0.03, $\Delta p/p_{t_\infty}$ = 0.02)

Downloaded 01 Jun 2010 to 171.66.16.53. Redistribution subject to ASME license or copyright; see http://www.asme.org/terms/Terms_Use.cfm

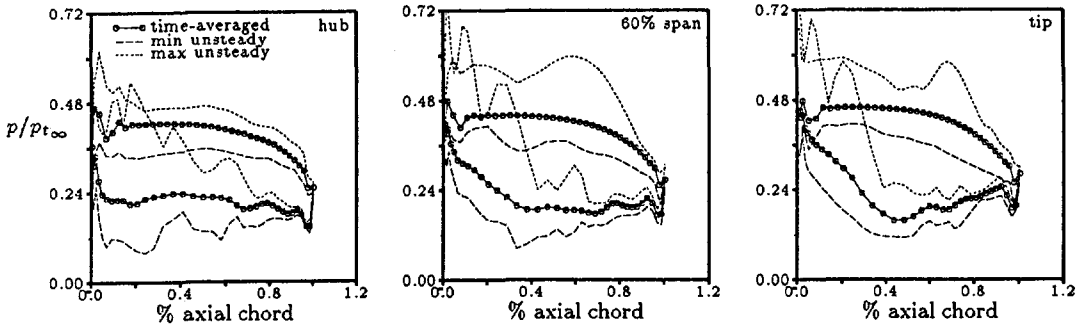


Fig. 7 Time-averaged and unsteady static pressure on rotor blade

ample Figs. 2 and 3 at $t = 0.750$. Also, according to the energy equation written in the rotating frame of reference,

$$\frac{DI}{Dt} = \frac{1}{\rho}\frac{\partial p}{\partial t}, \tag{2}$$

the shock wave increases the local rotor-relative stagnation enthalpy, hence total temperature. In Eq. (2) D/Dt represents the material derivative, whereas $I = (h_t)_r - 0.5(\Omega R)^2$ is the rothalpy. For example, this effect can be seen on the suction surface as the stator trailing edge shock wave impinges on the blade (R3 at $t = 0$, see Figs. 2, 3, and 6). Also, as the secondary reflection off the adjacent rotor strengthens into a shock near the rotor crown (R3 at $t = 0.125$, see Figs. 2, 3, and 6), it increases the local blade surface temperature. By recording the streak peak stagnation temperature at the rotor inlet during one cycle, one can estimate the effect of the shock waves interaction on the temperature distribution. Compared to the rotor inlet time-averaged maximum value (i.e., time-averaged value of the streak core), variations as much as 12 percent are observed.

Figures 7 and 8 present the static pressure and the relative stagnation temperature distributions on the rotor blade surface, respectively. The difference between the maximum and minimum values on both the pressure and the suction sides, i.e., the envelopes of unsteadiness, provide an estimate of the overall effect of unsteadiness during one cycle. These values were extracted from eight unsteady snapshots during the final blade-passing cycle. Thus, a certain amount of discreteness is observed in those quantities. Notice, however, that the time-averaged solution also presented in Figs. 7 and 8 has been computed during the blade-passing period from all the time-steps. Examining the static pressure envelopes of Fig. 7 at three spanwise locations, one notices that unsteadiness is particularly intense on the forward portion of the blade due to the primary reflection off the suction surface, with peak-to-peak variations in the order of half the (stator) inlet reference stagnation pressure. The level of unsteadiness is generally lower on the pressure side than on the suction side, except near the area of impact of the secondary shock reflection on the pressure side in the second portion of the blade.

As seen on Fig. 8, the unsteady rotor-relative stagnation temperature fluctuations are larger at 60 percent span than at the hub and the tip, which is a clear indication of the transit of the hot streak. On the pressure side, these midspan variations account for more than half the (stator) inlet reference total temperature. Also, at 60 percent span the maxima in T_t are larger on the pressure side than on the suction side. The effect of the streak pressure side radial migration is visible through the increase in total temperature near the trailing edge at the tip. Since the streak doesn't quite extend to the root of the blade (recall Figs. 5 and 6), the variation in relative stagnation temperature in the absence of streak transit can be assessed by considering the root unsteady total temperature envelope. For the case presented here, this accounts for 15 percent T_{t_∞}, which is 3.5 times less than at midspan (streak crossing).

On the stator blade surface, the unsteady (absolute) total temperature variation accounts for 10 percent of the inlet distortion, whereas the unsteady static pressure envelope represents about 25 percent of p_{t_∞} (due to choked flow conditions, the unsteadiness is restricted to the end portion of the suction side).

4 Time-Averaged and Steady-State Results

As mentioned in the introductory section, the turbine blade designer has to rely upon mean flow quantities. The objective of this section is to assess the mean effect of the shock and the streak unsteadiness in the first turbine stage. The flow conditions for the steady-state and for the time-averaged periodic unsteady computations are listed in Table 1. To provide a basis for comparison, the steady-state computation was performed with uniform inlet conditions (i.e., $p_{t_\infty} = cst$, $T_{t_\infty} = cst$, no streak), but with identical mass flow. On a time-averaged basis, the crossing of the hot streak produces an increase in the rotor blade surface total temperature (near streak radius) representing about 10 percent of the (stator) inlet temperature distortion; see Fig. 8. In Fig. 9, time-averaged stagnation temperature isoclines are

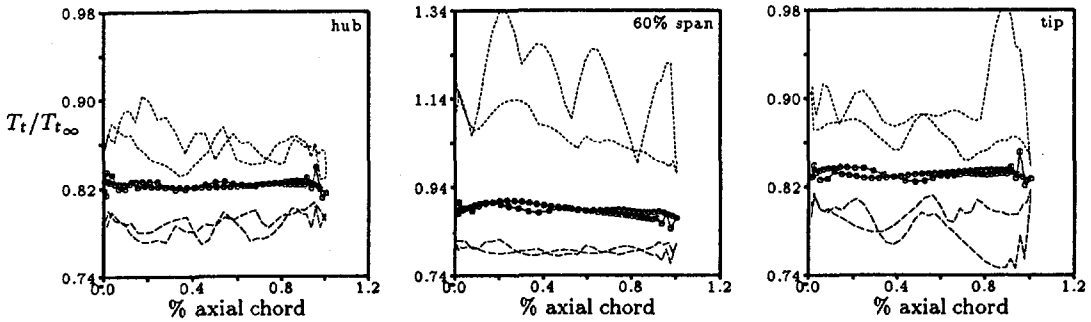


Fig. 8 Time-averaged and unsteady rotor-relative stagnation temperature on rotor blade

Downloaded 01 Jun 2010 to 171.66.16.53. Redistribution subject to ASME license or copyright; see http://www.asme.org/terms/Terms_Use.cfm

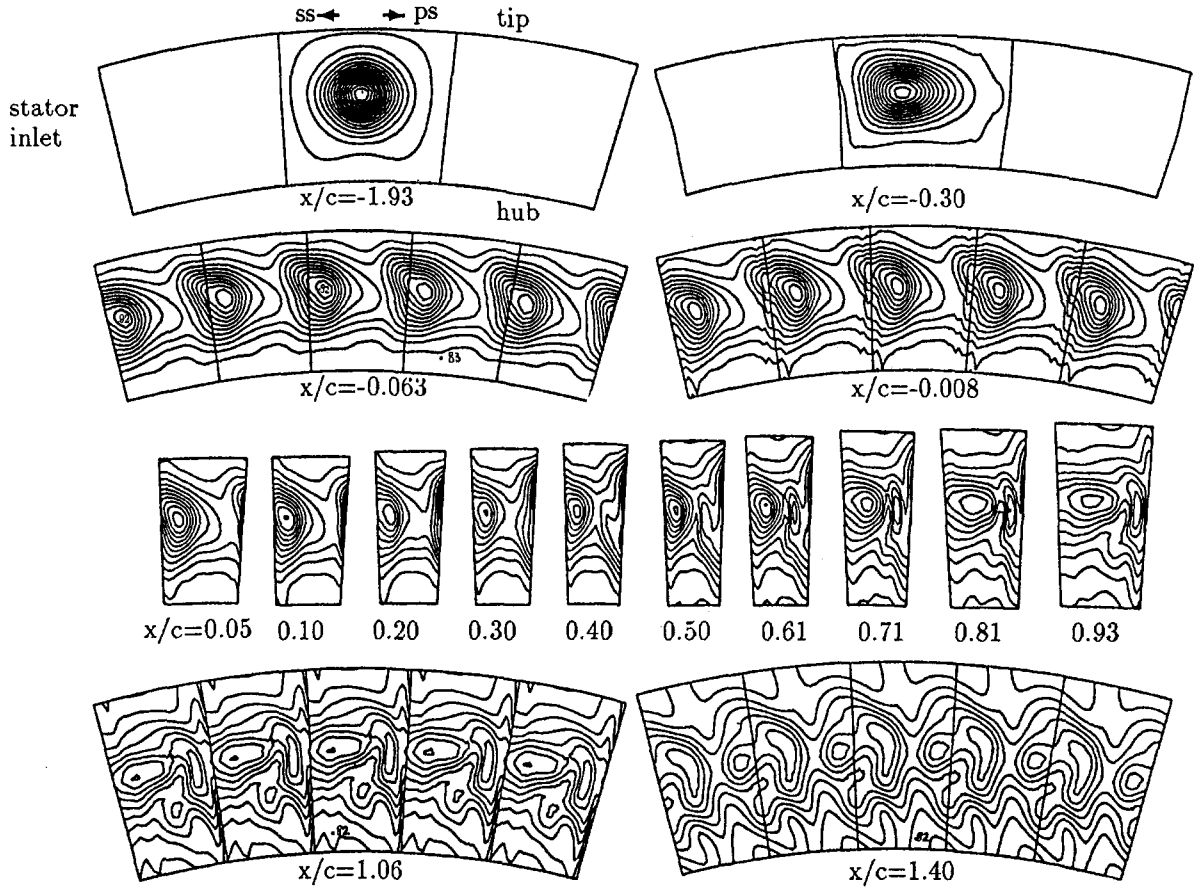


Fig. 9 Stagnation temperature contours on axial cuts for the time-averaged solution ($\Delta T_t/T_{t_\infty}$ = 0.01, for x/c = −1.93 & −0.30 $\Delta T_t/T_{t_\infty}$ = 0.06) (ss: suction side, ps: pressure side)

Table 1 Steady and time-averaged flow parameters for transonic turbine stage (*same mass flow in both cases*)

parameter		steady no streak	time-averaged hot streak
Stator inlet tangential angle	hub	0.0°	0.0°
	60% span	0.0°	0.0°
	tip	0.0°	0.0°
Stator outlet tangential angle	hub	74.8°	74.6°
	60% span	75.0°	75.0°
	tip	72.4°	72.5°
Rotor-relative inlet tangential angle	hub	55.0°	55.0°
	60% span	48.7°	50.8°
	tip	38.0°	36.8°
Rotor-relative outlet tangential angle	hub	-59.1°	-60.1°
	60% span	-70.1°	-69.0°
	tip	-70.6°	-71.1°
Stator inlet Mach	hub	0.15	0.15
	60% span	0.13	0.13
	tip	0.13	0.13
Stator outlet Mach	hub	1.31	1.30
	60% span	1.22	1.22
	tip	1.21	1.21
Rotor-relative inlet Mach	hub	0.69	0.61
	60% span	0.52	0.50
	tip	0.44	0.46
Rotor-relative outlet Mach	hub	1.20	1.20
	60% span	1.08	1.10
	tip	1.03	1.03
Rotor Mach	hub	0.76	0.75
	60% span	0.80	0.79
	tip	0.87	0.88
Rotor wheel speed $\Omega/[c_{t_{inl}}/L_{hub}]$		0.097	0.097
Ratio of specific heats γ		1.27	1.27

represented on several interblade axial cuts ranging from the stator inlet to the rotor exit. The position of the cuts is marked at the top of Fig. 10. Absolute and relative stagnation temperatures are plotted in the stator and the rotor, respectively. The decrease of the peak temperature from the stator inlet to the stator exit is an indication of the numerical dissipation acting upon the streak core supported by too few grid nodes.

From a time-averaged point of view the "one hot streak in three stator passages" has been transformed into a "one lukewarm streak in each of the five rotor channels," with a reduced core peak temperature level. For example, the maximum un-

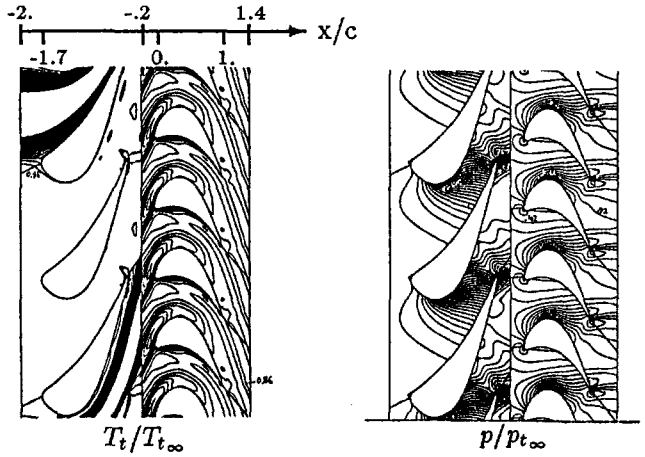


Fig. 10 Stagnation temperature and static pressure contours at 60 percent span for the time-averaged solution ($\Delta T_t/T_{t_\infty}$ = 0.01, $\Delta p/p_{t_\infty}$ = 0.02)

Downloaded 01 Jun 2010 to 171.66.16.53. Redistribution subject to ASME license or copyright; see http://www.asme.org/terms/Terms_Use.cfm

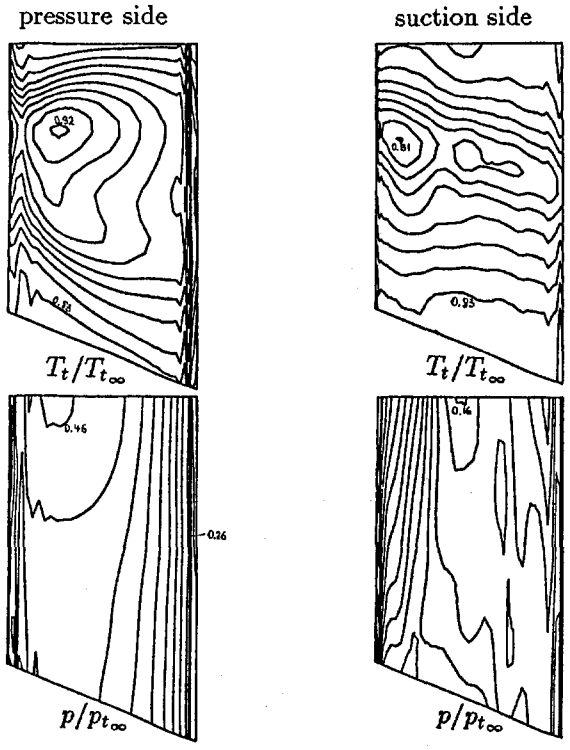


Fig. 11 Rotor-relative stagnation temperature and static pressure for the time-averaged solution ($\Delta T_t/T_{t_\infty} = 0.01$, $\Delta p/p_{t_\infty} = 0.02$)

steady nondimensionalized inlet rotor total temperature is about 1.58, which compares to 0.92 in the time-averaged solution. The ratio of these numbers corresponds approximately to the ratio of stator-to-rotor pitch. On a time-averaged basis in the rotor, the suction side core of the streak retains its original shape but migrates slowly towards the pressure side. As opposed to the pressure surface, the maximum temperature stays off the blade suction surface.

In Fig. 10, the time-averaged stagnation temperature and static pressure are represented on a cut at 60 percent span. An interesting feature to notice is that the maximum temperature in the rotor domain occurs in the field near the leading edge, and not on the blade itself or at the rotor inlet.

The time-averaged rotor-relative stagnation temperature is larger on the pressure surface than on the suction side; see Fig. 11. Also, the areas of high temperatures cover a broader portion of the pressure surface than on the suction surface. This is a consequence of the radial secondary flow occurring on the pressure side and mentioned in Section 3.2. This effect can be

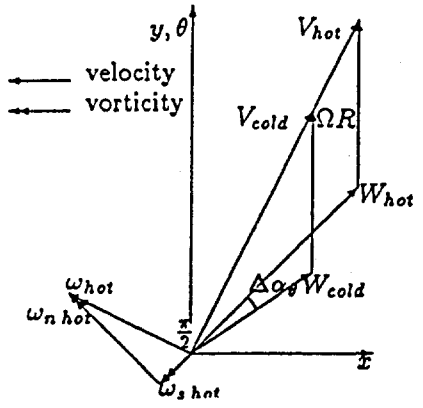


Fig. 12 Velocity and vorticity triangles at stator/rotor interface

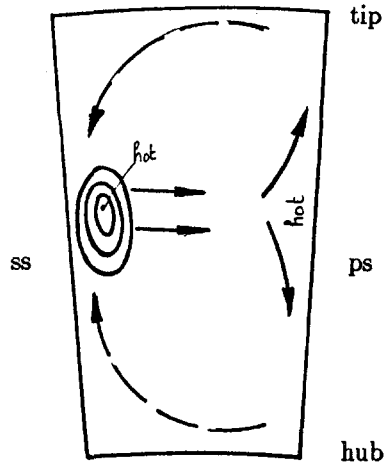


Fig. 13 Schematic of rotor-relative secondary flow for the time-averaged solution (ss: suction side, ps: pressure side)

qualitatively explained by using vorticity and velocity triangles arguments and simple dynamics (Butler et al., 1986; Saxer, 1992). Figure 12 is a schematic of the vorticity and the velocity triangles at the stator/rotor interface. In the relative frame, the stator vorticity (normal to the absolute flow) can be decomposed into a normal and a streamwise component, which will strengthen as the normal component turns into the rotor passage producing a three-dimensional secondary flow. From the velocity triangle it can be inferred that in the rotor frame the hot core fluid is streaming with a relatively higher velocity than the cold surrounding fluid, and with a larger incidence angle. The hot gas has a "slip velocity" component normal to the surrounding cooler fluid that drives it toward the pressure surface. The overall effect is the collection of hotter gas on the rotor pressure side than on the suction side. On the pressure side, the hot fluid is spreading from midspan toward the hub and the tip endwalls

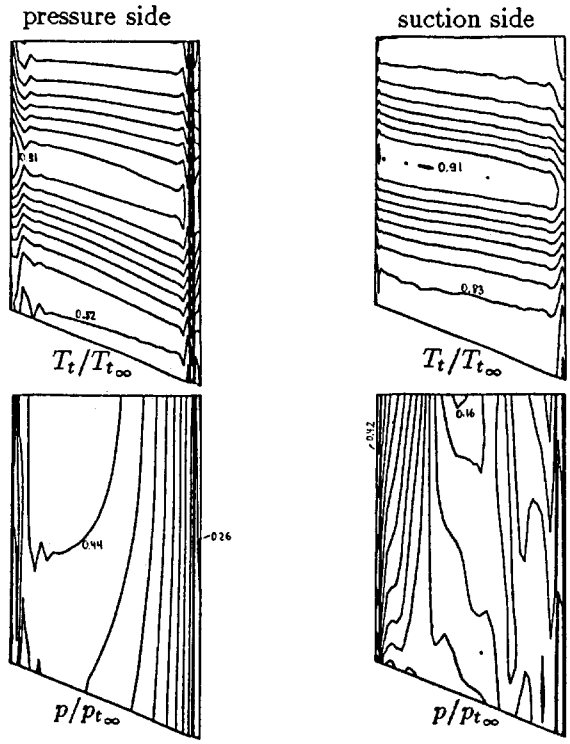


Fig. 14 Rotor-relative stagnation temperature and static pressure for the steady-state solution ($\Delta T_t/T_{t_\infty} = 0.01$, $\Delta p/p_{t_\infty} = 0.02$)

Downloaded 01 Jun 2010 to 171.66.16.53. Redistribution subject to ASME license or copyright; see http://www.asme.org/terms/Terms_Use.cfm

resulting in the heating of the upper and lower walls. On the suction side, cool endwall gas flows toward midspan. Under the influence of the secondary flow, as schematized in Fig. 13, the general motion of the hot core moving across the passage toward the rotor pressure surface can be seen in Fig. 9. Notice that the time-averaged surface total temperature downstream of the leading edge on both the pressure and the suction sides is higher than at the leading edge itself.

Figure 14 represents the steady-state stagnation temperature and static pressure distributions on the rotor pressure and suction surfaces. This computation was performed using the steady-state nonreflecting boundary conditions and flux-averaging procedure mentioned in Section 2.1, where the tangential components of the hot streak at the exit of the stator have been flux averaged, retaining only its radial variations in the rotor frame. By comparing Fig. 14 with Fig. 11 one infers that, regarding the pressure distribution, the steady-state procedure is in very good agreement with the time-averaged of the periodic unsteady solution. However, the radial extent of the temperature distortion is much weaker than in the unsteady case. This suggests that the streak tangential variations that have been retained in the rotor time-averaged solution are of prime importance in the generation of the radial secondary flow on the blade pressure surface.

5 Summary and Conclusions

This paper has presented a numerical simulation of the unsteady inviscid and three-dimensional flow in a generic industrial transonic first turbine stage in the presence of streaks of hot gas. Realistic flow conditions were obtained by setting a streak peak-to-free stream temperature ratio of 1.97 at the inlet of one out of every three stator passages and by using a 3-to-5 stator-to-rotor blade count ratio.

Due to the impact of the stator trailing edge shock wave off the downstream rotor, a shock motion was captured as part of the three-dimensional solution. The unsteady shock interaction included a primary reflection off the rotor suction surface and a secondary reflection off the adjacent rotor pressure side. The primary reflection moves back toward the upstream stator, striking it on the suction side close to the trailing edge. In addition, the secondary reflection crosses back toward the original rotor and intensifies into a discernable shock. This shock motion is consistent with previous two-dimensional numerical simulations. The computed unsteady static pressure fluctuations are the largest on the forward portion of the rotor suction surface and can exceed half of the stator inlet stagnation pressure.

Due to the invariance of the inlet stagnation pressure, the hot streak is convected without redistribution in the stator passage. The different phases of the hot streak chopping and migration in the rotor frame were presented and discussed. In particular, the presence of a secondary flow forces the chopped pressure side leg of the hot streak to migrate toward the hub and the tip endwalls. The unsteadiness produced by the transonic interaction affects the streak peak stagnation temperature at the rotor inlet by more than 10 percent of the stator inlet temperature distortion. As an estimate, the streak crossing time from the rotor leading edge to the trailing edge corresponds approximately to 4 rotor periods on the pressure surface and 2 rotor periods on the suction side. As a consequence, the time-averaged rotor surface stagnation temperature is larger on the pressure side than on the suction side, but surprisingly only to a small extent. It is suggested that the increase in the local rotor-relative stagnation temperature is produced by the unsteady shock wave interaction particularly active on the forward portion of the suction side area, thus increasing the level of the time-averaged value to nearly the one obtained on the pressure surface.

On a time-averaged basis, each rotor passage experiences the effects of an inlet hot streak of circular shape and reduced core temperature with respect to the streak temperature at the exit of the stator. Due to the secondary flow, the maximum time-averaged temperature on the rotor blade occurs on the pressure surface in a region centered at 10 percent rotor inlet span above the rotor inlet core position.

A comparison between the time-averaged solution and the steady-state solution, in which the circumferential variations introduced by the streak are cut off (but not the radial variations), was performed. The pressure field compares very well between the two solutions, but not the stagnation temperature distribution. This suggests that the tangential temperature distortions at the rotor inlet have a stronger effect on the radial secondary flow than the streak radial variations. Hence, accurate predictions of temperature distributions in the presence of streaks of hot gas require any numerical procedure to account for unsteady as well as three-dimensional effects.

Acknowledgments

Partial funding has been provided by Rolls-Royce PLC, Dr. P. Stow technical supervisor, and by the Air Force Office of Scientific Research, Major D. Fant technical monitor. The authors acknowledge the contributions of Mr. R. Amat for the preliminary computation, and of Mr. E. Casartelli for the elaboration of the figures.

References

Butler, T. L., Sharma, O. P., Joslyn, H. D., and Dring, R. P., 1986, "Redistribution of an Inlet Temperature Distortion in an Axial Flow Turbine Stage," AIAA Paper No. 86–1468.

Collie, J. C., Moses, H. L., Schetz, J. A., and Gregory, B. A., 1993, "Recent Advances in Simulating Unsteady Flow Phenomena Brought About by Passage of Shock Waves in a Linear Turbine Cascade," ASME JOURNAL OF TURBOMACHINERY, Vol. 115, pp. 687–698.

Doorly, D. J., and Oldfield, M. L. G., 1985, "Simulation of the Effects of Schock Wave Passing on a Turbine Rotor Blade," ASME *Journal of Engineering for Gas Turbines and Power,* Vol. 107, No. 4.

Dorney, D. J., Roger, L. D., Edwards, D. E., and Madavan, N. K., 1990, "Unsteady Analysis of Hot Streak Migration in a Turbine Stage," AIAA Paper No. 90-2354.

Giles, M. B., 1990, "Stator/Rotor Interaction in a Transonic Turbine," *AIAA Journal of Propulsion and Power,* Vol. 6, No. 5.

Harasgama, S. P., 1990, "Combustor Exit Temperature Distortion Effects on Heat Transfer Aerodynamics Within a Rotating Turbine Blade Passage," ASME Paper No. 90-GT-174.

Hawthorne, W. R., 1974, "Secondary Vorticity in Stratified Compressible Fluids in Rotating Systems," Technical Rept. CUED/A-Turbo/TR 63, Cambridge University, United Kingdom.

Holmes, D. G., and Connell, S. D., 1989, "Solution of the 2-D Navier–Stokes Equations on Unstructured Adaptive Grids," AIAA Paper No. 89-1932-CP.

Horlock, J. H., and Lakshminarayana, B., 1973, "Secondary Flows: Theory, Experiment, and Application in Turbomachinery Aerodynamics," *Annual Review of Fluid Mechanics,* Vol. 5.

Johnson, A. B., Oldfield, M. L. G., Rigby, M. J., and Giles, M. B., 1990, "Nozzle Guide Vane Shock Wave Propagation and Bifurcation in a Transonic Turbine Rotor," ASME Paper No. 90-GT-310.

Johnson, M. W., 1978, "Secondary Flow in Rotating Bends," Technical Rept. CUED/A-Turbo/TR 92, Cambridge University, United Kingdom.

Krouthén, B., and Giles, M. B., 1988, "Numerical Investigation of Hot Streaks in Turbines," AIAA Paper No. 88-3015.

Munk, M., and Prim, R. C., 1947, "On the Multiplicity of Steady Gas Flows Having the Same Streamline Pattern," *Proceedings of the National Academy of Sciences,* U.S., Vol. 33, pp. 137–141.

Ni, R.-H., 1981, "A Multiple Grid Scheme for Solving the Euler Equations," *AIAA Journal,* Vol. 20, No. 11, pp. 1565–1571.

Ni, R.-H., and Sharma, O. P., 1990, "Using 3-D Euler Flow Simulations to Assess Effects of Periodic Unsteady Flow Trough Turbines," AIAA Paper No. 90-2357.

Saxer, A. P., and Giles, M. B., 1993, "Quasi-Three-Dimensional Nonreflecting Boundary Conditions for Euler Equations Calculations," AIAA *Journal of Propulsion and Power,* Vol. 9, No. 2.

Saxer, A. P., 1992, "A Numerical Analysis of 3-D Inviscid Stator/Rotor Interactions Using Non-reflecting Boundary Conditions," Ph.D. Thesis, Massachusetts Institute of Technology, Cambridge, MA, June.

Takahashi, R. K., and Ni, R.-H., 1990, "Unsteady Euler Analysis of the Redistribution of an Inlet Temperature Distortion in a Turbine," AIAA Paper No. 90-2262.

Downloaded 01 Jun 2010 to 171.66.16.53. Redistribution subject to ASME license or copyright; see http://www.asme.org/terms/Terms_Use.cfm

M. Y. Jabbari[1]

K. C. Marston[2]

E. R. G. Eckert

R. J. Goldstein

Department of Mechanical Engineering,
University of Minnesota,
Minneapolis, MN 55455

Film Cooling of the Gas Turbine Endwall by Discrete-Hole Injection

Film cooling performance for injection through discrete holes in the endwall of a turbine blade is investigated. The effectiveness is measured at 60 locations in the region covered by injection. Three nominal blowing rates, two density ratios, and two approaching flow Reynolds numbers are examined. Analysis of the data reveals that even 60 locations are insufficient for the determination of the field of film cooling effectiveness with its strong local variations. Visualization of the traces of the coolant jets on the endwall surface, using ammonium-diazo-paper, provides useful qualitative information for the interpretation of the measurements, revealing the paths and interaction of the jets, which change with blowing rate and density ratio.

Introduction

Designers of aircraft engines strive to increase engine operating temperatures in order to attain higher thrust and improved efficiency. The main limitation on higher temperatures is the structural integrity of engine parts, especially those subject to high stresses. Uncooled metal alloys are not strong enough to withstand the severe conditions within the engine; therefore components must be cooled to avoid structural failure. One popular method used to maintain surface temperatures at acceptable levels is film cooling.

In film cooling, a secondary or coolant flow is injected into the boundary layer through a slot or an array of holes in the surface to be protected. The coolant serves to decrease the temperature in the boundary layer for some distance downstream of injection. The temperature an adiabatic wall would assume in this process is called the adiabatic wall temperature, T_{aw}. It is conventionally described by a dimensionless parameter, the film cooling effectiveness:

$$\eta = (T_{aw} - T_r)/(T_j - T_r) \quad (1)$$

T_j in this equation denotes the temperature with which the coolant jet is injected into the boundary layer and T_r is the recovery temperature the wall assumes under the influence of aerodynamic heating by the mainstream to which it is exposed in the absence of film cooling (Eckert, 1992).

Often the wall is cooled not only by the coolant injected into the boundary layer but also by convection on the other side. The heat flux q_w required to achieve a desired wall temperature, T_w, in the combined process is calculated with the equation

$$q_w = h(T_w - T_{aw}) \quad (2)$$

In numerous experiments it was found that the heat transfer coefficient, h, on the solid wall downstream of the cooling holes can be approximated by the values occurring in normal convection without injection, except in the immediate neighborhood downstream of the cooling holes. This does, however, not apply to the surface area with the cooling hole arrangement as it is studied in the present paper. Some information on those heat transfer coefficients, expressed in Stanton numbers, is found in Eckert (1984) based on measurements performed at Stanford University.

The focus of the present work is determination of the film cooling effectiveness of the endwall (or platform) to which the blades of a high-pressure turbine are attached. The end-wall cooling problem has attained greater importance in recent years since low aspect ratio and low solidity turbine designs have a higher ratio of endwall to blade surface area. Mass (heat) transfer measurements have shown regions on the endwall with very high transfer coefficient that need protection (Goldstein and Spores, 1988). While considerable research has been done on three-dimensional flows in a turbine passage and their effects on the heat transfer coefficient at the endwall, little published work is available concerning endwall film cooling. Results of this investigation would also be complementary to the earlier film cooling, heat transfer, and flow visualization studies carried out in the same rig (Goldstein and Chen, 1985, 1987; Goldstein and Spores, 1988; Chen and Goldstein, 1992; Jabbari et al., 1992).

Blair (1974), in a pioneering work on turbine endwall heat transfer, studied film cooling injection from a thin angled slot in the endwall slightly upstream of the blade passage. Film effectiveness values were found to be quite high near the slot, but dropped off rapidly downstream. It was noted that, due to the secondary flows in the passage, the injected coolant is swept away from the pressure surface of one blade toward the suction surface of the other. Yamao et al. (1987) investigated the film cooling performance resulting from the leakage of sealing air through the flexible joints between adjacent blade platforms. Two slots were used to simulate these joints: one at the leading edge of the passage (similar to Blair) and one down the middle of the passage between the two blades. Sparse measurements of the adiabatic wall effectiveness showed agreement with Blair concerning injection through the leading edge slot. The intrapassage slot produced very little cooling effect on the endwall except in the corner near the trailing edge of the blade suction surface. Granser and Schulenberg (1990) also measured the adiabatic wall effectiveness due to injection from a slot at the cascade leading edge and compared these results to a partially parabolic numerical calculation.

Film cooling performance by discrete-hole coolant injection was investigated by Bourguignon (1985) and Sato et al. (1987). Bourguignon gives a general discussion on the effects of coolant injection on endwall secondary flows and heat transfer coefficients. Sato et al. determined the adiabatic wall effectiveness distribution on the endwall resulting from heated injection through an array of approximately 80 film cooling holes.

[1]Current address: Department of Mechanical Engineering, Saginaw Valley State College, 7400 Bay Rd., University Center, MI 48710.

[2]Presently at IBM Corporation, 522 South Rd., Poughkeepsie, NY 12601.

Contributed by the International Gas Turbine Institute and presented at the 39th International Gas Turbine and Aeroengine Congress and Exposition, The Hague, The Netherlands, June 13–16, 1994. Manuscript received by the International Gas Turbine Institute February 9, 1994. Paper No. 94-GT-67. Associate Technical Editor: E. M. Greitzer.

Copyright © 1996 by ASME

Downloaded 01 Jun 2010 to 171.66.16.53. Redistribution subject to ASME license or copyright; see http://www.asme.org/terms/Terms_Use.cfm

The present study is also concerned with endwall film cooling by discrete hole injection. The adiabatic wall effectiveness distribution resulting from coolant injection through a small array of 14 film cooling holes is determined using mass transfer measurements and visualizations produced using ammonia gas and diazo paper. The use of only 14 injection holes leads to a vast reduction in the total mass flow of coolant when compared to the 80 holes used by Sato et al. Also, creative use of the ammonia-diazo visualizations in combination with the mass transfer measurements produces a reasonably detailed picture of the adiabatic wall effectiveness distribution on the endwall.

Experimental Apparatus and Measurement Technique

Experiments are conducted in a low-speed wind tunnel with a planar cascade of six scaled-up turbine blades. This is essentially the same apparatus described by Ito et al. (1978). The blades have a chord length of 169.1 mm, a span to chord ratio of 3.55, an inlet flow angle of 44.3 deg, and an outlet flow angle of 62.7 deg. Some details of the cascade and the film cooling hole arrangement are shown in Fig. 1. Fourteen 1.905-mm-dia film cooling holes are drilled through the endwall between the middle blades at an angle of 25 deg with respect to the endwall. The length to diameter ratio, L/D, for each hole is 15.77. Ten of the holes are intended for in-line injection, and the other four for transverse injection. The coordinate location and angular orientation of each hole are also given. The smallest spacing between neighboring holes (holes 4 and 8) is 7.32 hole diameters. Sixty taps in the wall, 0.635 mm in diameter, are used to draw samples of the flow or measure wall pressures. The taps, designated by small solid circles in Fig. 1(a), are aligned (within the design constraints) with the symmetry planes of the holes 1-10. An 8 mm clay fillet is formed at the junction of the blade and endwall to eliminate the sharp corner and produce a more realistic endwall geometry. Its extent on the endwall is indicated by the dashed contour in Fig. 1(a).

Film effectiveness values are obtained using a mass transfer technique described by Goldstein (1971). Air with a foreign gas tracer (a mixture of air with helium or sulfur hexafluoride) is injected into the mainstream and the resulting mass concentration of admixed gas on the impermeable wall (C_{iw}) is measured by analyzing gas samples obtained through the sampling taps in the endwall. The corresponding impermeable wall effectiveness is defined as:

$$\eta_{iw} = (C_{iw} - C_i)/(C_j - C_i) \qquad (3a)$$

In this experiment, $C_i = 0$, therefore:

$$\eta_{iw} = C_{iw}/C_j \qquad (3b)$$

The temperature field in film cooling of an adiabatic surface and the concentration field in the mass transfer experiment on an impermeable surface are similar as long as the transport properties do not vary within the field (extension of Reynolds analogy between heat and momentum transfer). Subject to this restriction the two effectiveness parameters are then equal ($\eta = \eta_{iw}$). This condition is satisfied in the experiment with mixture of air and helium by the small amount of the tracer gas. Sulfur hexafluoride was mixed in the secondary air stream to produce a density ratio, R, of the injected gas to the air in the mainstream near a value 2. This is characteristic of the density ratio of the cooling air to the hot mainstream gas in gas turbines. For this condition, the analogy between heat and mass transfer is only approximately fulfilled (Shadid and Eckert, 1991).

The effect of the injected jets on the endwall is visualized using ammonia gas and diazo paper in a manner similar to the tests of Dring et al. (1980). Commercial grade blue-line diazo paper is attached to the endwall. Small amounts of ammonia and water vapor are added to the flow passing through the film cooling holes. Diazo paper contains an aromatic diazo compound and a coupler that, when allowed to react, will produce a colored dye. However, this reaction is suppressed by an acid embedded in the paper. In order to effect a color change, ammonia and water vapor are introduced to neutralize the acid and allow the coupling reaction to occur. The blue shadings left on the diazo paper not only show the positions of the cooling jets and their interaction along the endwall, they also relate to the amount of ammonium absorbed by the paper (mass transfer at the wall), which is due to the combined effect of the local ammonia concentration and the local mass transfer coefficient.

Test Conditions

Experiments are conducted for two approaching free-stream velocities ($\mathrm{Re}_c \approx 0.86 \times 10^5$ or 1.23×10^5), three nominal blowing rates ($\bar{M} \approx 1.0$, 1.5, or 2.0), and two density ratios ($R \approx 1.0$ or 2.0). The endwall boundary layer is tripped and for $\mathrm{Re}_c = 1.23 \times 10^5$, a free-stream velocity of 11.79 m/s, a boundary layer thickness of 28.51 mm, a displacement thickness of 3.10 mm, and a momentum thickness of 2.20 mm, are measured at a location 14.5 cm upstream of the blade's leading edge.

Nomenclature

A = total cross-sectional area of injection holes = $14A_j$
A_j = cross-sectional area of injection hole = $\pi D^2/4$
c = chord length = 16.91 cm (Fig. 1(a))
C_i = approaching flow concentration
C_{iw} = impermeable wall concentration
C_j = injected flow concentration (the same for all jets)
D = injection hole diameter = 1.905 mm (the same for all holes)
h = heat transfer coefficient
I_j = momentum ratio
L = length of the injection hole; L/D = 15.77
$\dot{m}$ = total mass flow rate of coolant = $\sum_{j=1}^{j=14} \dot{m}_j$
$\dot{m}_j$ = mass flow rate of a single coolant jet (varies with holes)
M_j = blowing rate of a single jet = $(\dot{m}_j/A_j)/(\rho_\infty u_\infty)$
$\bar{M}$ = nominal blowing rate = $(\dot{m}/A)/(\rho_i u_i)$, see Table 1
$P_{i,s}$ = approaching flow static pressure
$P_{i,t}$ = approaching flow total pressure
P_w = wall pressure
q_w = wall heat flux
R = density ratio = ρ_j/ρ_i
Re_c = Reynolds number = $u_i c/\nu_i$
T_{aw} = adiabatic wall temperature
T_j = injectant temperature
T_r = recovery temperature
T_w = wall temperature
u_i = approaching flow velocity $\approx$ 8.2 or 11.8 m/s
u_∞ = free-stream velocity (varies with hole location)
η = film cooling effectiveness
η_{iw} = impermeable wall effectiveness
ν_i = kinematic viscosity of approaching flow
ρ_i = approaching flow density
ρ_j = injectant density (in plenum chamber)
ρ_∞ = free-stream density $\approx \rho_i$
χ = distance from downstream edge of injection hole along a row (Fig. 1(b))

Downloaded 01 Jun 2010 to 171.66.16.53. Redistribution subject to ASME license or copyright; see http://www.asme.org/terms/Terms_Use.cfm

Injection Hole Coordinates			
hole #	X (mm)	Y (mm)	β (°)
1	64.4	186.9	70
2	81.0	172.4	70
3	99.2	157.1	70
4	117.1	139.9	70
5	72.6	149.3	70
6	85.3	142.6	70
7	100.4	135.3	70
8	116.1	126.0	70
9	129.0	119.5	70
10	145.0	109.1	70
11	100.0	117.3	20
12	115.5	109.4	20
13	129.5	102.0	20
14	144.3	93.8	20

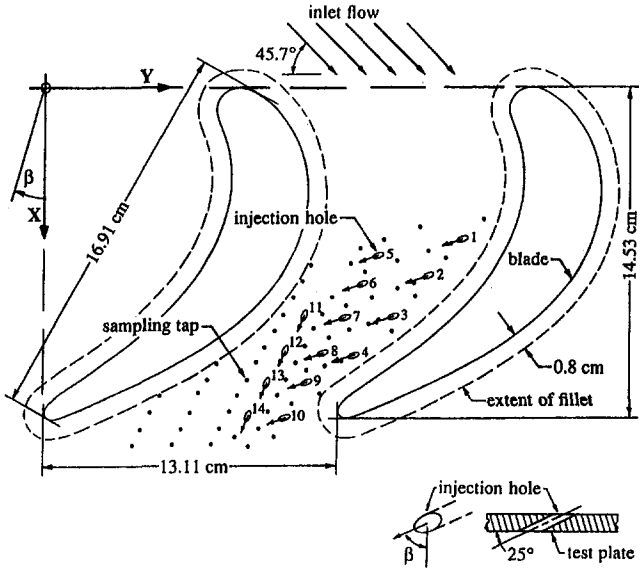


Fig. 1(*a*) Sketch of the test section

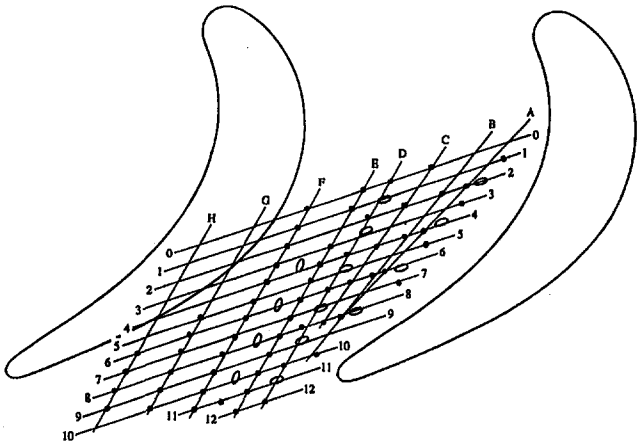


Fig. 1(*b*) Sampling tap and injection hole row designation

Over the endwall, the local free-stream velocity varies due to the passage geometry. In Fig. 2, a contour plot of measured endwall pressure distribution is presented as:

$$(P_w - P_{i,s})/(P_{i,t} - P_{i,s})$$

which is equivalent to:

$$[1 - (u_\infty/u_i)^2]$$

assuming potential flow through the passage. Contours shown in Fig. 2 remain almost the same for both of the Reynolds number used in this experiment. Additional information regarding the flow field in the passage is available from Chung and Simon (1990), Chen and Goldstein (1992), and Jabbari et al. (1992).

Since the injection holes are fed from a single plenum chamber, it is clear that the flow rate through the film cooling holes is influenced by the endwall distribution. Therefore, to study the jets' performance collectively, rather than individually, a nominal blowing rate is defined as total coolant mass flow divided by total injection area and mass velocity of the approaching free stream:

$$\bar{M} = (\dot{m}/A)/(\rho_i u_i)$$

The nominal blowing rate, as indicated in Table 1, is, in fact, a weighted average of the injection hole blowing rates (M_j). The injection hole blowing rate is the mass flow rate of the coolant through each hole divided by the hole's flow area and the local freestream mass velocity:

$$M_j = (\dot{m}_j/A_j)/(\rho_\infty u_\infty).$$

The individual hole mass flow rate ($\dot{m}_j$) is evaluated from the pressure drop across the coolant passage and a discharge coefficient obtained by calibration. The local free-stream velocity (u_∞) at each injection hole is determined from the measured wall pressure distribution given in Fig. 2. In Table 1 values of M_j and u_∞/u_i are given for $\mathrm{Re}_c = 1.23 \times 10^5$. It is important to note that the change in hole blowing rate (going from hole 1 to hole 14) at $\bar{M} = 1.07$ is opposite that of $\bar{M} = 2.06$ (as seen in Table 1). This is because of the diminishing difference between plenum chamber pressure and the endwall pressure at some hole locations, leading to a very small flow rate through those holes. In fact, reverse flow into the plenum chamber through holes 1 or 2 (see Fig. 1(*a*)) is a possibility at nominal

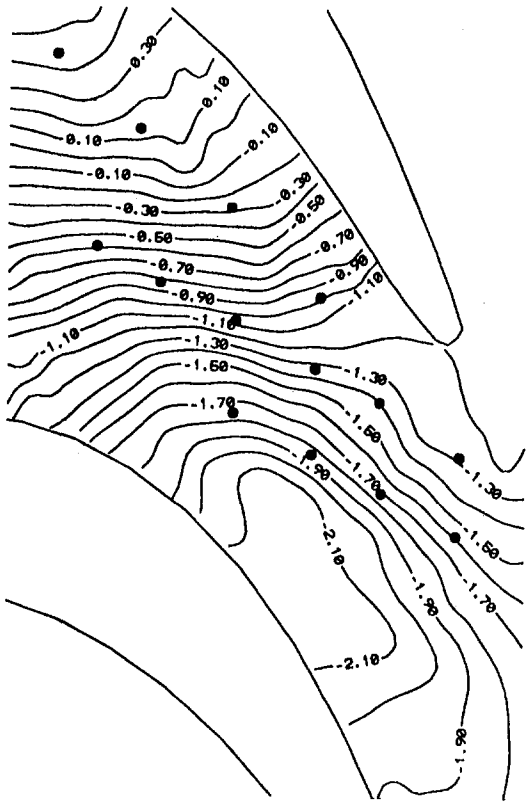


Fig. 2 Dimensionless pressure contours on the endwall $(P_w - P_{i,s})/(P_{i,t} - P_{i,s})$ for Re_c = 125,000

Downloaded 01 Jun 2010 to 171.66.16.53. Redistribution subject to ASME license or copyright; see http://www.asme.org/terms/Terms_Use.cfm

Table 1 Blowing rates and free-stream velocities at injection holes; $\bar{M} = \frac{1}{14}\sum_{j=1}^{14} M_j(\rho_\infty u_\infty/\rho_j u_j)$

$Re_c \approx 1.24 \times 10^5$				
	R=2.02		R=0.93	
Hole	$\bar{M}$=1.07	$\bar{M}$=2.06	$\bar{M}$=2.02	
j	M_j	M_j	M_j	u_∞/u_i
1 (A2)	0.35	2.30	2.53	0.73
2 (A4)	0.57	1.90	2.03	0.94
3 (A6)	0.69	1.67	1.71	1.14
4 (A8)	0.78	1.48	1.45	1.39
5 (D1)	0.75	1.55	1.55	1.28
6 (D3)	0.78	1.48	1.45	1.39
7 (D5)	0.80	1.43	1.39	1.47
8 (D7)	0.82	1.40	1.34	1.54
9 (D9)	0.82	1.40	1.34	1.54
10 (D11)	0.81	1.42	1.36	1.51
11 (F4)*	0.84	1.35	1.27	1.67
12 (F6)*	0.84	1.34	1.25	1.69
13 (F8)*	0.84	1.35	1.27	1.66
14 (F10)*	0.83	1.37	1.30	1.61

* Injection holes F4, F6, F8, F10 are actually located between rows E and F (see Fig. 1b)

blowing rates less than 1.0. For the values of Re_c examined, the dimensionless velocities (or the endwall pressure coefficient) show slight dependence on Re_c. This is also true for the hole blowing rates at a fixed nominal blowing rate.

Discussion of Results

In Figs. 3 and 4 measurements of effectiveness for nominal blowing rates 1.0 and 2.0 are presented, respectively. The effectiveness (in percent) is written next to the sampling taps where it is measured. Plots of effectiveness variation along several rows (labeled in Fig. 1(b)) are shown in Figs. 5 and 6. Visualization of the trace of the film cooling jets on the endwall are obtained and presented in Figs. 7, 8, and 9. The uncertainties of the presented data, employing the method suggested by Moffat (1982), are: 5.7 percent for film cooling effectiveness, 3.1 percent for nominal blowing rate, and 2.9 percent for density ratio. In the discussion that follows, the injection holes and the sampling taps are referred to by the grid nearest to them (see Fig. 1(b)), for example, injection hole A2, D3, F6 (injection holes F4, F6, F8, F10 are actually between rows E and F) or sampling tap A2, C4, E6, F7, etc.

Considering the large spacing between the injection holes A2, A4, and A6 (more than seven hole diameters), one may expect the effectiveness distribution downstream of these holes to resemble those previously reported for injection through a single or a row of holes (Goldstein, 1971). To verify this, comparison is made with the measurements reported by Pedersen et al. (1977) in Fig. 5. Pedersen's data are a centerline effectiveness for injection through a row of tubes (L/D = 60) into a mainstream that has a uniform velocity field outside its boundary layer. The tubes are spaced three diameters apart and are inclined at 35 deg. The present data are effectiveness along rows 2, 4, 6 (between rows A and D), for injection through holes A2, A4, and A6, into a mainstream with varying velocity field. The holes have L/D = 15.77 and the injection angle is 25 deg. Although the mainstream flow fields and the injection geometries of the two sets of data are different, the comparison proves useful in interpreting some features of the present data.

For a density ratio of about 2, and at low to moderate blowing rates, the differences between the present data and those of Pedersen et al. (1977) are not substantial (Fig. 5(a)). Similar results are found along row 4 (M_j = 0.57, I_j = 0.16) though not shown in the figure. At higher blowing rates ($M_j \approx 2$), however, while the effectiveness values along row 4 (except close to the injection point) are close to those of Pedersen's, considerably lower values are measured along row 2 (Fig. 5(b)). This deviation seems rather peculiar and will be discussed later when the visualization results are examined.

Examination of the present effectiveness distribution along transverse rows (rows C, E, F, G shown in Fig. 6) reveals other peculiar features: For example, at the same distance downstream of injection holes D5, D7, D9, and for approximately the same blowing rates through them, the effectiveness downstream of injection hole D7 is much higher than those of holes D5 or D9 (compare readings of sampling taps E7, E5, and E9 along row E in Fig. 6). Along row F, a higher effectiveness is measured at sampling tap F2—farther away from its aligned injection hole A2—than is measured at either of the taps F1 or F3, which are closer to their respective injection holes D1 and D3. While taps G6, G8, G10 (downstream of injection holes F6, F8, F10) indicate values of effectiveness that change with blowing rates, the off-center taps G5, G7, and G9 (between the same injection holes) show approximately the same values of effectiveness independent of blowing rate.

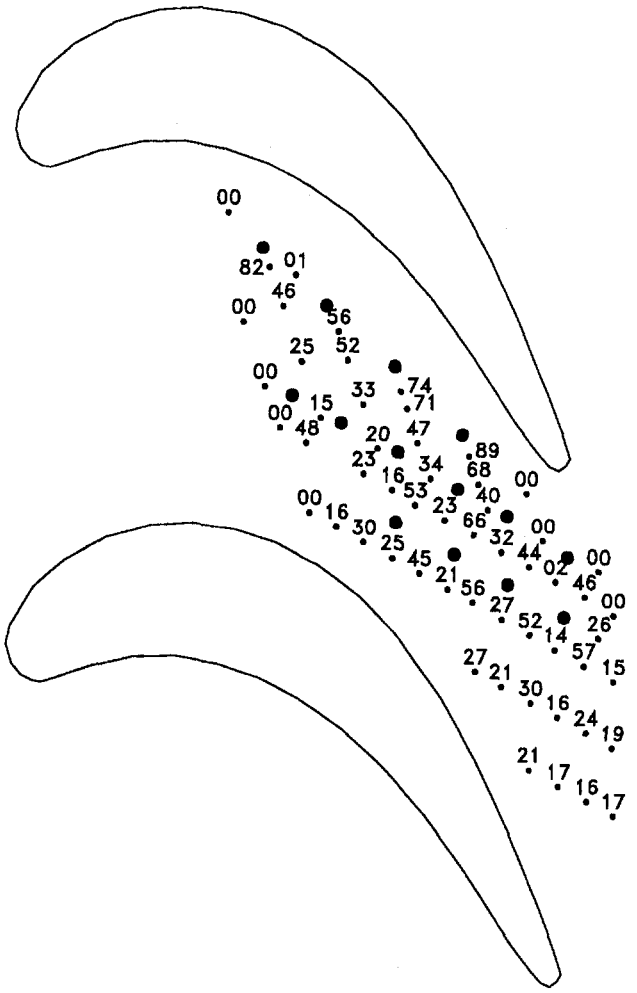


Fig. 3 Endwall effectiveness distribution: $\bar{M}$ = 1.07, R = 2.01, Re_c = 123600

Downloaded 01 Jun 2010 to 171.66.16.53. Redistribution subject to ASME license or copyright; see http://www.asme.org/terms/Terms_Use.cfm

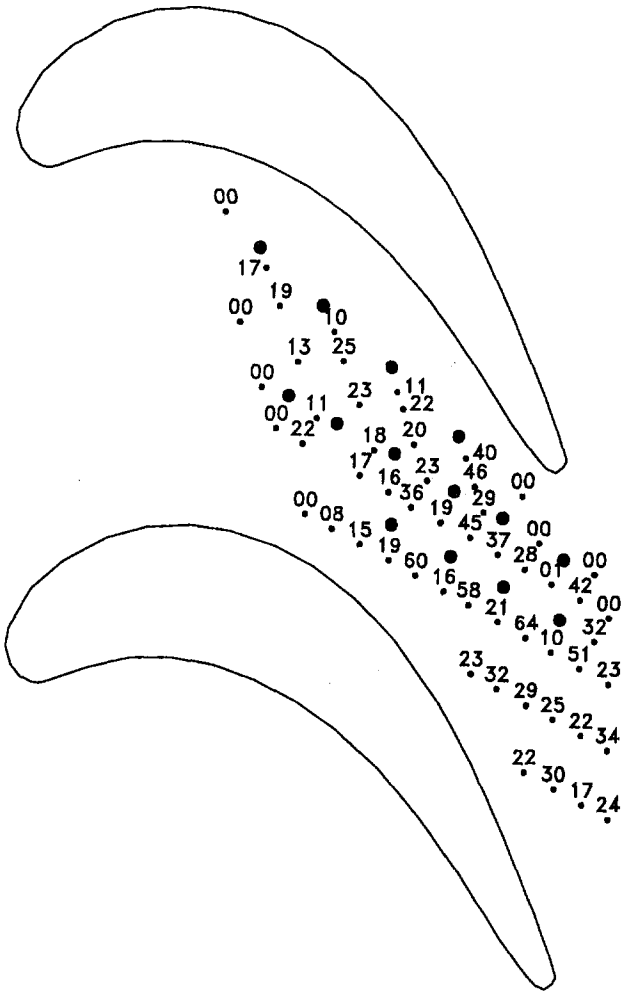


Fig. 4 Endwall effectiveness distribution: $\bar{M}$ = 2.06, R = 2.02, Re_c = 123100

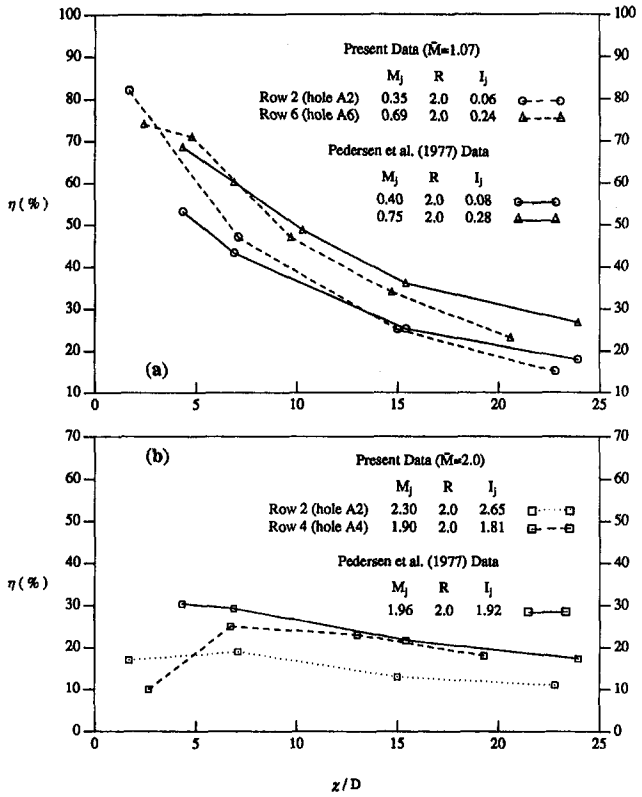


Fig. 5 Comparison of the present effectiveness data with those of Pedersen et al. (1977)

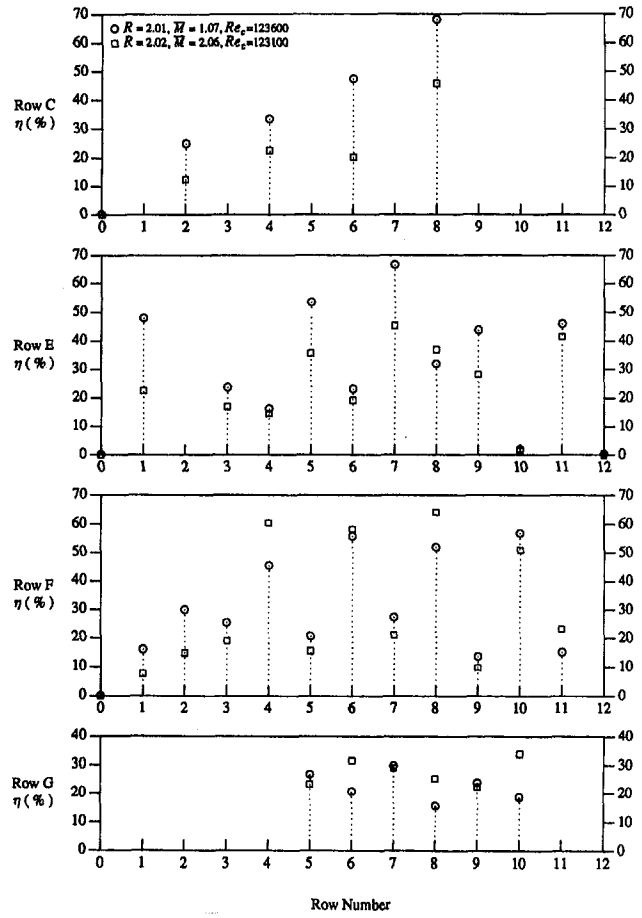


Fig. 6 Effect of change in blowing rate on effectiveness distribution

It must be emphasized that the mainstream velocity field in this study is three dimensional and that the velocity varies, both in magnitude and direction, along and above the endwall. That is, each jet encounters a different velocity as it enters the mainstream and interacts with a varying flow field along its path. This could force changes on the jets and their trajectories, thus altering the distribution of effectiveness. To provide information on the jet paths needed for the interpretation of the data, ammonium-diazo visualization of the jets' traces on the endwall is employed.

In Figs. 7 and 8 results of visualization for nominal blowing rates ($\bar{M}$) of 1.0 and 2.0 (density ratio $\approx$ 2) are presented. These figures correspond, respectively, to the data shown in Figs. 3 and 4. In Fig. 9 visualization for $\bar{M}$ = 2 and R = 0.93 is shown. In the visualization figures, traces of the film cooling jets on the endwall (blue colors) and their location relative to the sampling taps are visible. This shows which regions of the endwall are covered by the jets and how the boundaries of these regions have changed with a change in blowing rate and/or density ratio. Closer examination reveals details that help to explain the unusual features of the effectiveness data which were discussed earlier.

Focusing on the trace of the jet from hole A2 in Fig. 7, it is seen that the trace centerline is close to the first two sampling taps (A2 and B2) but farther downstream shifts away from the third (C2) and the fourth (D2) taps. This is what the data in Fig. 5(a) along row 2 (M_j = 0.35) show: The effectiveness at tap A2 (χ/D = 1.7) and tap B2 (χ/D = 7.1) are higher than those of Pedersen's but fall below them at taps C2 (χ/D =

Downloaded 01 Jun 2010 to 171.66.16.53. Redistribution subject to ASME license or copyright; see http://www.asme.org/terms/Terms_Use.cfm

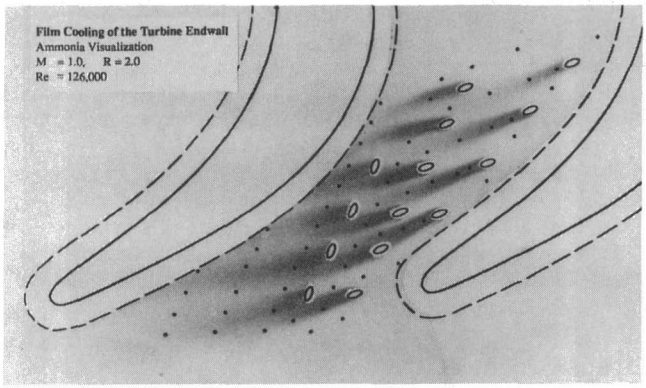


Fig. 7 Visualization of jet traces on the endwall: $\bar{M}$ = 1.0, R = 2.0, Re_c = 126,000

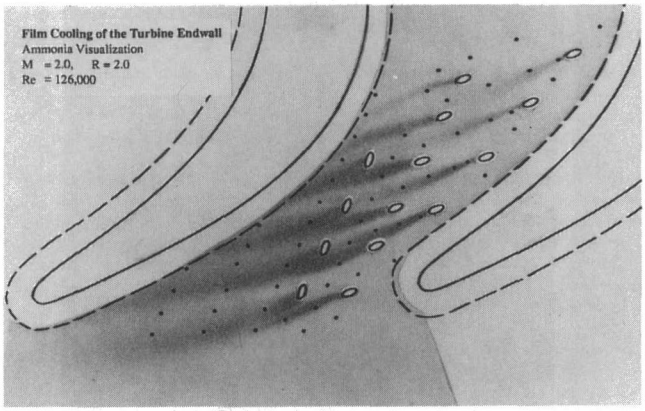


Fig. 8 Visualization of jet traces on the endwall: $\bar{M}$ = 2.0, R = 2.0, Re_c = 126000

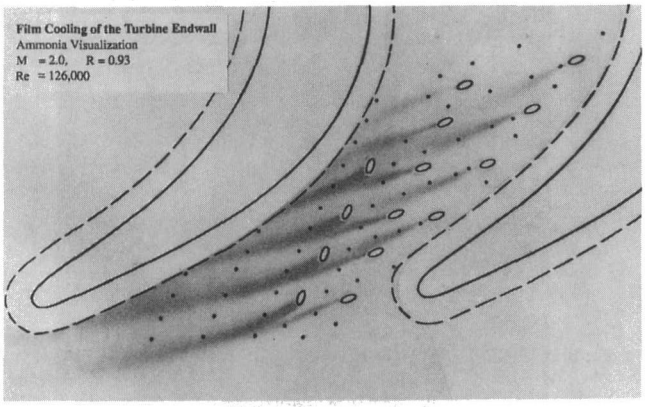


Fig. 9 Visualization of jet traces on the endwall: $\bar{M}$ = 2.0, R = 0.93, Re_c = 126,000

15.4) and D2 (χ/D = 23.9). The near centerline effectiveness of the present study is higher than Pederson's, possibly due its shallower injection angle (Goldstein and Stone, 1994) and its mainstream acceleration (Jabbari and Goldstein, 1978), and those at taps C2 and D2 are lower because they are off-centerline values. The displacement of the trace centerline from the sampling taps is more pronounced for row 2 in Fig. 8, revealing that the data for M_j = 2.3 in Fig. 5(b) are also off-centerline effectiveness, and therefore lower than the centerline values, which may have been comparable to Pedersen's data (as are for row 4). Agreement/disagreement between effectiveness distribution along row 6 and data of Pedersen (see Fig. 5(a)) is explained in similar fashion. The lower effectiveness measured at tap A4 (χ/D = 2.67) of row 4, the first data point of row 4 in Fig. 5(b), appears to be a result of the jet not covering this tap because of its higher penetration and the tap's misalignment (see Fig. 8 and compare it with Fig. 7).

Earlier, it was noted that effectiveness at tap E7 was higher than those at taps E5 and E9 (as seen in Fig. 6). Examination of the visualization results, particularly the one in Fig. 8, shows that the tap E7 is closer to the jet centerline than are taps E5 and E9. It is also interesting to note that some jets, for example D1 and D3 in Fig. 7, influenced by the local variation of the mainstream flow, follow a curved path and pass between the taps. In particular, the trace of jet D3 is not aligned with taps E3 and F3; instead, it is displaced upstream over tap F2 (Fig. 7). This explains the higher effectiveness that is measured at tap F2 relative to its neighbors F1 or F3. Noticeable in the visualization results are regions, without sampling taps in them, where two or more jets have merged. Judging from the strength of the intensity of color in these regions, and deducing from readings of taps F4, F6, and F8 in areas of comparable shade, very high levels of effectiveness prevail in these regions.

Comparison of traces in Figs. 8 and 9 show that jets of comparable blowing rates ($\bar{M} \approx 2$) but lower density ratio (higher momentum ratio) leave narrower traces on the endwall. This points to the higher penetration of the lower density jets into the mainstream, which leads to lower effectiveness at all of the measurement taps as are seen in Fig. 10. The reduction in effectiveness, however, is greater for taps closer to the jet centerline than those away from it (cf. readings of taps F4–F8 with the visualizations) which may indicate lateral as well as vertical change in the jet position. Moreover, the distribution of effectiveness along Row G has become more nonuniform at

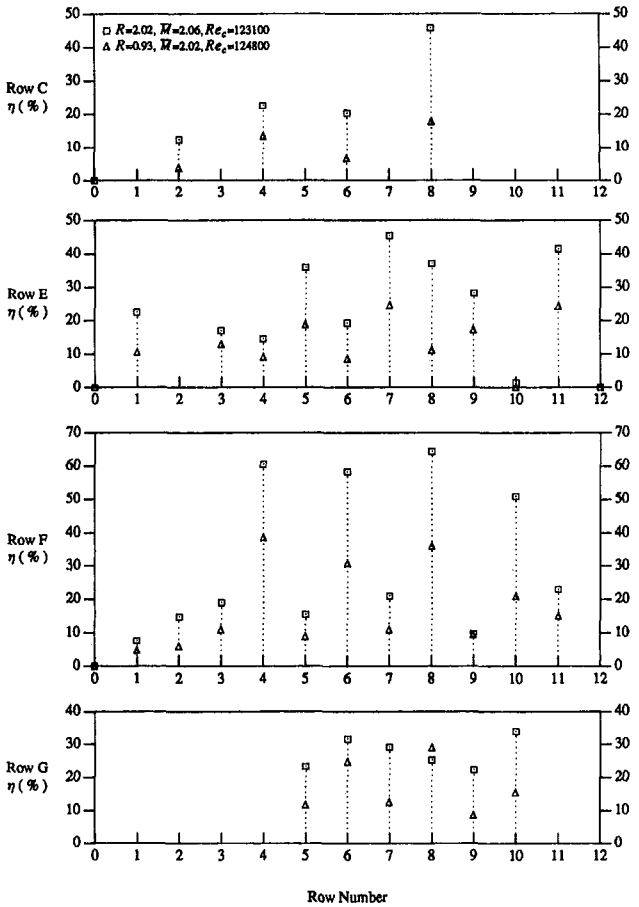


Fig. 10 Effect of change in density ratio on effectiveness distribution

Downloaded 01 Jun 2010 to 171.66.16.53. Redistribution subject to ASME license or copyright; see http://www.asme.org/terms/Terms_Use.cfm

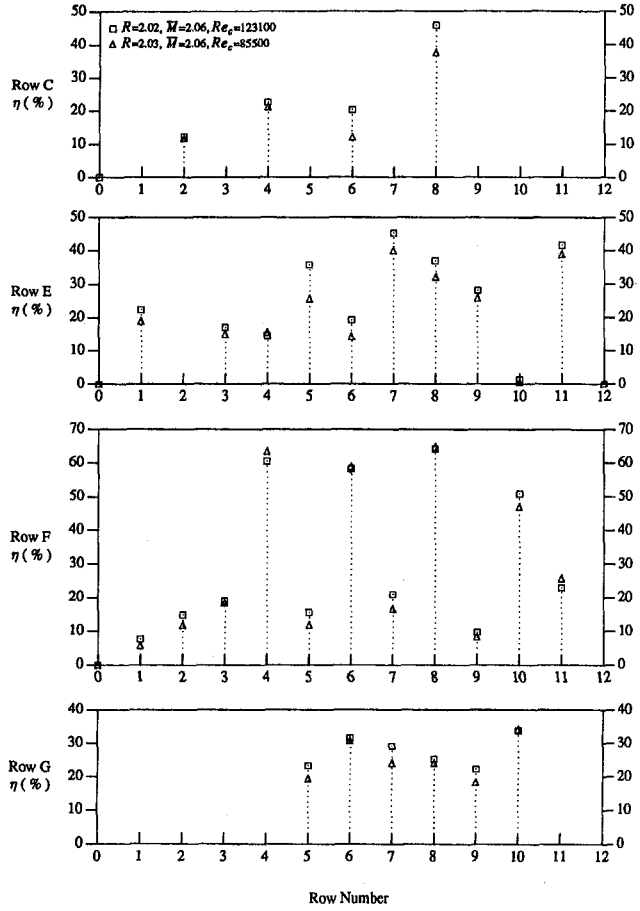


Fig. 11 Effect of change in Reynolds number on effectiveness distribution

lower density ratio, indicating that the trajectories of the laterally injected jets (holes F4, F6, F8, F10) are slightly shifted by the change in the density ratio. When the jet traces (as seen in Figs. 8 and 9) and traces of the endwall flow obtained without injection (Jabbari et al., 1992) are compared, it is found that these jets do not follow the endwall flow direction; their paths lie closer to the potential flow direction in the passage. This, particularly, is more pronounced for the laterally injected jets (F4, F6, F8, F10).

The effect of the approaching flow Reynolds number on effectiveness, for the Reynolds numbers examined, are insignificant except close to the injection point downstream of jets A6, A8, and D5 (Fig. 11). Comparison of the corresponding visualization results indicates that only these jets are slightly displaced. This is in agreement with observation of Goldstein and Spores (1988) who found that a change in Reynolds number (of the same magnitude as in this study) had an insignificant effect on the endwall mass transfer distribution. Also, as was stated earlier, the endwall pressure distribution (Fig. 2) is not very sensitive to the change in Reynolds number. These indicate that the flow field near the endwall is not a strong function of Reynolds number in the range examined here.

All together, it is evident that the jet centerlines may depart from that of the injection hole depending on the jet's parameters and the mainstream velocity field and that the sampling taps (or thermocouples) aligned with the hole centerline may be indicating off-centerline values. Consequently, it becomes necessary to use other techniques, such as ammonium visualization or infrared photography, to scan the entire endwall surface in order to obtain a true picture of the effectiveness distribution.

Conclusions

A wide variation in the level of film cooling effectiveness is observed on the endwall of a gas turbine blade. Several factors including large spacing between injection holes, variation in the mainstream velocity field, and displacement of the jet trajectories are responsible. Flow visualization results indicate that the jet centerline on the endwall, and thus the maximum effectiveness, are displaced with blowing rate and density ratio; suggesting that interpolation of the sparsely measured data should be done cautiously. The streamwise distribution of effectiveness, so far as the jets have not merged or changed lateral position, is predictable from the data available in literature. The color shade in the visualization results, particularly in regions where variation of the mass transfer coefficient is not appreciable, provides qualitative information on the effectiveness distribution.

Acknowledgments

The financial support of United Technologies (Pratt & Whitney) and contributions of Dr. T. J. Hajek and Dr. S. I. Tanrikut are gratefully acknowledged. This work was also partially paid for by the Air Force Office of Scientific Research.

References

Blair, M., 1974, "An Experimental Study of Heat Transfer and Film Cooling on Large-Scale Turbine Endwalls," ASME Paper No. 74-GT-33.

Bourguignon, A. E., 1985, "Etudes des Transfers Thermiques sur les Plates-Formes de Distributeur de Turbine avec et sans Film de Refroidissement," AGARD-CP-390.

Chen, P. H., and Goldstein, R. J., 1992, "Convective Transport Phenomena on the Suction Surface of a Turbine Blade Including the Influence of Secondary Flows Near the Endwall," ASME JOURNAL OF TURBOMACHINERY, Vol. 114, pp. 776–787.

Chung, J. T., and Simon, T. W., 1990, "Three-Dimensional Flow Near the Blade/Endwall Junction of a Gas Turbine: Visualization in a Large-Scale Cascade Simulator," ASME Paper No. 90-WA/HT-4.

Dring, R. P., Blair, M. F., and Joslyn, H. D., 1980, "An Experimental Investigation of Film Cooling on a Turbine Rotor Blade," ASME *Journal of Engineering for Power,* Vol. 102, pp. 81–87.

Eckert, E. R. G., 1984, "Analysis of Film Cooling and Full-Coverage Film Cooling of Gas Turbine Blades," ASME *Journal of Heat Transfer,* Vol. 106, pp. 206–213.

Eckert, E. R. G., 1992, "Similarity Analysis of Model Experiments for Film Cooling in Gas Turbines," *Warme- und Stoffubertragung,* Vol. 27, pp. 217–223.

Goldstein, R. J., 1971, "Film Cooling," *Advances in Heat Transfer,* T. F. Irvine, Jr., and J. P. Hartnett, eds., Academic Press, New York, Vol. 7, pp. 321–379.

Goldstein, R. J., and Chen, P. H., 1985, "Film Cooling on a Gas Turbine Blade Near the Endwall," ASME *Journal of Engineering for Gas Turbines and Power,* Vol. 107, pp. 117–122.

Goldstein, R. J., and Chen, P. H., 1987, "Film Cooling of a Turbine Blade With Injection Through Two Rows of Holes in the Near-Endwall Region," ASME JOURNAL OF TURBOMACHINERY, Vol. 109, pp. 588–593.

Goldstein, R. J., and Spores, R. A., 1988, "Turbulent Transport on the Endwall in the Region Between Adjacent Turbine Blades," ASME *Journal of Heat Transfer,* Vol. 110, pp. 862–869.

Goldstein, R. J., and Stone, L. D., 1994, "Row-of-Holes Film Cooling of a Convex and a Concave Wall at Low Injection Angles," manuscript.

Granser, D., and Schulenberg, T., 1990, "Prediction and Measurement of Film Cooling Effectiveness for a First-Stage Turbine Vane Shroud," ASME Paper No. 90-GT-95.

Ito, S., Goldstein, R. J., and Eckert, E. R. G., 1978, "Film Cooling of a Gas Turbine Blade," ASME *Journal of Engineering for Power,* Vol. 100, pp. 476–481.

Jabbari, M. Y., and Goldstein, R. J., 1978, "Effect of Mainstream Acceleration on Adiabatic Wall Temperature and Heat Transfer Downstream of Gas Injection," *Proceedings, 6th International Heat Transfer Conference,* Toronto, Canada, Vol. 5, pp. 249–254.

Jabbari, M. Y., Goldstein, R. J., Martson, K. C., and Eckert, E. R. G., 1992, "Three Dimensional Flow at the Junction Between a Turbine Blade and the End-Wall," *Warme- und Stoffubertragung,* Vol. 27, pp. 51–59.

Moffat, R. J., 1982, "Contribution to the Theory of Single-Sample Uncertainty Analysis," ASME *Journal of Fluids Engineering,* Vol. 104, pp. 250–260.

Pedersen, D. R., Eckert, E. R. G., and Goldstein, R. J., 1977, "Film Cooling With Large Density Differences Between the Mainstream and the Secondary Fluid Measured by the Heat-Mass Transfer Analogy," ASME *Journal of Heat Transfer,* Vol. 99, pp. 620–627; also Pedersen's Ph.D. Thesis, Mech. Eng. University of Minnesota, 1972.

Sato, T., Aoki, S., Takeishi, K., and Matsuura, M., 1987, "Effect of Three-Dimensional Flow Field on Heat Transfer Problems of a Low Aspect Ratio Turbine Nozzle," 87-TOKYO-IGTC-59.

Shadid, J. N., and Eckert, E. R. G., 1991, "The Mass Transfer Analogy to Heat Transfer in Fluids With Temperature-Dependant Properties," ASME JOURNAL OF TURBOMACHINERY, Vol. 113, pp. 27–33.

Yamao, H., Aoki, S., Takeishi, K., and Takeda, K., 1987, "An Experimental Study for Endwall Cooling Design of Turbine Vanes," 87-TOKYO-IGTC-67.

Downloaded 01 Jun 2010 to 171.66.16.53. Redistribution subject to ASME license or copyright; see http://www.asme.org/terms/Terms_Use.cfm

D. R. H. Gillespie

A. R. Byerley

P. T. Ireland

Z. Wang

T. V. Jones

Department of Engineering Science,
University of Oxford,
Oxford, United Kingdom

S. T. Kohler
Rolls Royce
Bristol, United Kingdom

Detailed Measurements of Local Heat Transfer Coefficient in the Entrance to Normal and Inclined Film Cooling Holes

The local heat transfer inside the entrance to large-scale models of film cooling holes has been measured using the transient heat transfer technique. The method employs temperature-sensitive liquid crystals to measure the surface temperature of large-scale perspex models. Full distributions of local Nusselt number were calculated based on the cooling passage centerline gas temperature ahead of the cooling hole. The circumferentially averaged Nusselt number was also calculated based on the local mixed bulk driving gas temperature to aid interpretation of the results, and to broaden the potential application of the data. Data are presented for a single film cooling hole inclined at 90 and 150 deg to the coolant duct wall. Both holes exhibited entry length heat transfer levels that were significantly lower than those predicted by entry length data in the presence of crossflow. The reasons for the comparative reduction are discussed in terms of the interpreted flow field.

Introduction

The continuous drive to higher turbine entry temperatures together with the requirement for longer component life means that designers must be able to predict blade temperature fields with ever increasing accuracy. An accurate thermal model requires detailed specification of the convective boundary condition on both the external and internal surfaces of the blade. The current work has succeeded in measuring the detailed local heat transfer coefficient distributions in the entrance to discrete film cooling holes, which were normal and inclined to the cooling duct wall. The cooling passage was modeled as a high aspect ratio rectangular section duct and, for all the tests, the flow ahead of the hole was fully developed turbulent two-dimensional channel flow. The length-to-diameter ratio of the hole, the duct height-to-hole diameter ratio, and the turbulence intensity (Ireland, 1987) were all engine representative. A single duct Reynolds number of 26,000 was maintained throughout the series of tests while the ratio of average hole velocity divided by the duct centerline velocity (defined as the suction ratio, SR) was varied from 0 to 8. This range is representative of different engine conditions caused by the reduction in passage flow as air feeds the film cooling holes or by the variation in the pressure distribution around the aerofoil.

Previous Work. In the literature, there are numerous reports of detailed heat transfer measurements on both the turbine blade internal and external surfaces surrounding film cooling holes. Byerley et al. (1988) applied the transient heat transfer method to the measurement of local heat transfer coefficients within the cooling passage around the entrance to normal and then inclined film cooling holes. They reported considerable cooling passage heat transfer coefficient enhancement (local values can exceed six times the plain duct local values) in the region immediately downstream of the hole. Heat transfer levels were predicted on the cooling passage wall by Byerley et al. (1992) using computational fluid dynamics. Qualitatively the distributions agreed well with the experimental measurements, and the existence of a vortex pair in the cooling passage, which trailed downstream from the hole at high suction ratios, was confirmed. Shen et al. (1991) investigated the effect of combining multiple film cooling holes on the cooling passage heat transfer levels and later (Shen et al., 1994) went on to quantify the cooling performance of film cooling holes with rib roughness elements. Local heat transfer coefficients and adiabatic wall temperature around the outlet to film cooling holes were measured by Vedula and Metzger (1991) who also used liquid crystals and a transient heat transfer technique. Local heat transfer coefficient distributions *within* film cooling holes had not been published prior to the experimental work performed at Oxford. Metzger and Cordaro (1979) performed an experimental investigation that yielded circumferentially and axially averaged heat transfer coefficients based on the mean mixed bulk gas temperature for a range of hole length to diameter ratios. Only holes normal to the duct were considered. The results indicated that increases in crossflow increase the heat transfer levels relative to those in the absence of crossflow. Morland (1989) analytically predicted the flow local to the film cooling hole entrance. He showed that, above a certain suction ratio, the stagnation point moved outside the hole onto the passage wall. Flow features are further described in Fig. 1. Haidar and Dixon (1988) measured loss coefficients for branched ducts under compressible flow conditions. Dunne (1982) observed the effect on local heat transfer of a region of separation just inside the hole upstream edge in an investigation of film cooling bleed along one edge of a cooling passage.

Test Technique and Experimental Apparatus

The transient liquid crystal technique, first applied to internal cooling geometries by Ireland and Jones (1985), was used to obtain full surface heat transfer coefficient distributions in single tests. The experimental apparatus and procedure have been fully described by Byerley et al. (1988) and hence only a brief description is given here for the sake of completeness. The test section, manufactured from perspex, is used to model, at approximately 50 times engine scale, the flow from an idealized cooling duct to a single film cooling hole. The model is initially at room temperature and, at the start of the test, is suddenly

Contributed by the International Gas Turbine Institute and presented at the 39th International Gas Turbine and Aeroengine Congress and Exposition, The Hague, The Netherlands, June 13–16, 1994. Manuscript received by the International Gas Turbine Institute January 28, 1994. Paper No. 94-GT-1. Associate Technical Editor: E. M. Greitzer.

Copyright © 1996 by ASME

Downloaded 01 Jun 2010 to 171.66.16.53. Redistribution subject to ASME license or copyright; see http://www.asme.org/terms/Terms_Use.cfm

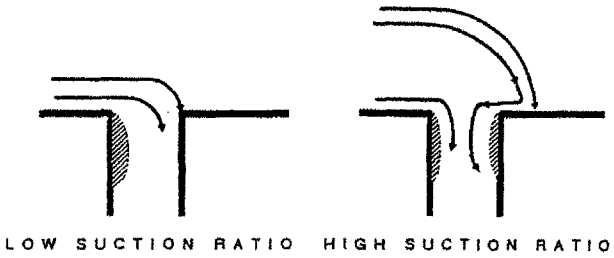


Fig. 1 Flow field within 90 deg holes at low and high suction ratios

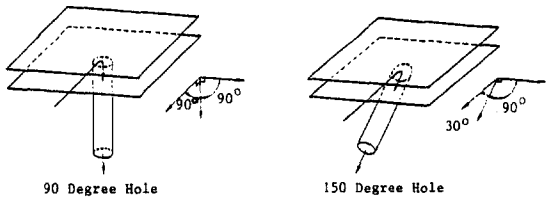


Fig. 2 Inclination of film cooling holes to cooling duct

subjected to a step increase in gas temperature. The subsequent surface temperature distribution is measured using temperature-sensitive liquid crystals. The method allows the full surface heat transfer coefficient distribution based on the measured gas temperature to be determined with an uncertainty of about 7 percent (Byerley et al., 1988). In the present work, two geometries representative of typical engine film cooling holes were investigated. A schematic diagram of the working section is shown in Fig. 3. The model hole diameter was 22 mm and the hole length-to-diameter ratio was 10. The holes were inclined at 90 and 150 deg to the main duct flow (Fig. 2). The rectangular duct cross section was 60 × 600 mm. The liquid crystal color play was monitored using a color video camera and recorded on video tape. The video data were then processed using the computerized intensity history method developed by Wang et al. (1995).

Data Analysis

The local heat transfer coefficient can be found from the surface temperature rise through the solution to the one-dimensional Fourier equation:

$$\frac{T_w - T_{\text{init}}}{T_{aw} - T_{\text{init}}} = 1 - e^{\beta^2}\text{erfc}\ \beta \tag{1}$$

where

$$\beta = \frac{h\sqrt{t}}{\sqrt{\rho c_p k}} \tag{2}$$

A single event narrow band liquid crystal with the peak intensity calibrated to 35.6°C was used in the investigation of the 90 deg film cooling hole whereas a double event liquid crystal coating with peaks calibrated at 36.2°C and 40.7°C was used in the inclined hole tests. Using conventional transient heat transfer data reduction (see Byerley et al., 1988), a detailed distribution of heat transfer coefficient based on the duct centerline temperature three hole diameters upstream of the hole was obtained.

A particularly useful way of presenting transient heat transfer data is to calculate values based on local mixed bulk gas temperature. Such values, unlike those based on a single measured temperature, become independent of distance from the entrance of the cooling passage. Results from transient heat transfer experiments based on local mixed bulk temperature were presented by Ireland (1987) and later Wang (1991) for arrays of pedestals. The values were then directly comparable to data obtained by other workers who used steady-state methods to determine heat transfer levels. Furthermore, the heat transfer measurements presented below based on local mixed bulk temperature were determined using an analysis method that is independent of the uncertainty in the experimental temperatures. The uncertainty in the entry length enhancement factor is typically 5 percent for the data presented below.

It has been shown that the heat transfer coefficient governing convection during transient heat transfer experiments corresponds to the isothermal wall heat transfer coefficient for many different flow fields (Dunne, 1982; Ireland, 1987; Byerley et al., 1988; Baughn and Yan, 1992). This means that as the wall surface temperature increases during the experiment, the local heat transfer coefficient remains constant. The local heat flux can be defined in terms of the local heat transfer coefficient, h, and the difference in temperature between the wall temperature, T_w, and a gas temperature, T_g:

$$q = h(T_g - T_w) \tag{3}$$

Since the energy equation is linear in temperature, superposition can be used to show that the difference between this chosen gas temperature and the wall temperature is directly proportional to the difference between any other gas temperature and the wall temperature. In other words, q can be written

$$q = h \times \text{constant} \times (T_g - T_w)$$

or

$$q = h_R(T_R - T_w) \tag{4}$$

Since q is the same in both equations,

$$h_R(T_R - T_w) = h(T_g - T_w) \tag{5}$$

and Eq. (6) then follows when h_{mb} is the heat transfer coefficient based on local mixed bulk temperature, T_{mb}.

Nomenclature

A = hole surface area, m^2
c_p = specific heat capacity, J/kg K
d = film cooling hole diameter, m
erfc( ) = 1 − erf( )
h = heat transfer coefficient, W/m^2 K
k = thermal conductivity, W/m K
L = film cooling hole length, m
$\dot{m}$ = mass flow, kg/s
Nu = Nusselt number
$\overline{\text{Nu}}$ = axially averaged Nusselt number
Pr = Prandtl number
$\dot{q}$ = heat flux, W/m^2
Re = Reynolds number
SR = Suction Ratio = hole average velocity/duct centerline velocity
St = Stanton number
t = time, s
T = temperature, °C
z = distance along hole from inlet, m
β = defined in Eq. (2)
ρ = density, kg/m^3

Subscripts

avg = average
aw = adiabatic wall
cl = based on upstream duct centerline temperature
init = initial
mb = based on local mixed bulk temperature
R = reference
O = reference or outlet
w = wall

Downloaded 01 Jun 2010 to 171.66.16.53. Redistribution subject to ASME license or copyright; see http://www.asme.org/terms/Terms_Use.cfm

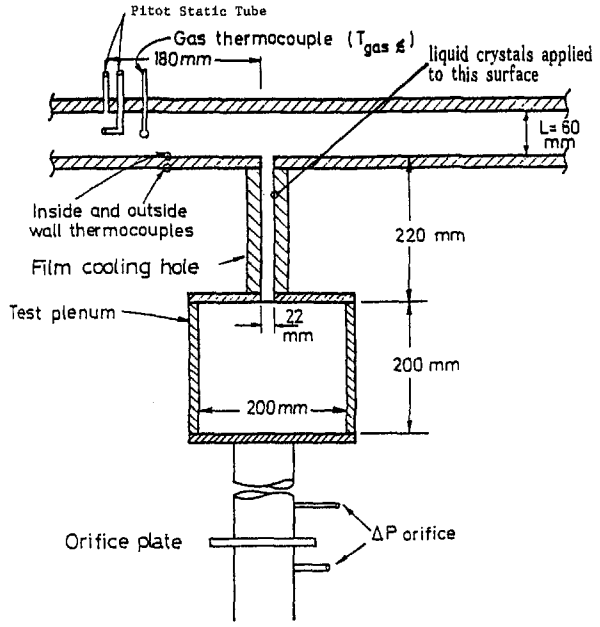


Fig. 3 Experimental working section

$$\frac{h_{mb}}{h_R} = \frac{T_R - T_w}{T_{mb} - T_w} \tag{6}$$

An energy balance between the hole outlet, where the mixed bulk temperature is T_{mbO}, and the region where the local heat transfer coefficient is evaluated yields

$$T_{mbi} - T_w = T_{mbO} - T_w + \frac{\int_A h_R(T_R - T_w)dA}{\dot{m}c_p} \tag{7}$$

In this equation the integral is performed over the hole surface area, A, between the outlet and the plane at which the heat transfer coefficient is determined. Combining Eqs. (6) and (7), we obtain:

$$\frac{h_{mb}}{h_R} = \frac{T_R - T_w}{T_{mbO} - T_w + \frac{(T_R - T_w)}{\dot{m}c_p}\int_A h_R dA} \tag{8}$$

The expression for heat transfer in terms of the time for the liquid crystal intensity to peak, Eq. (2), is then used to eliminate h_R and $(T_R - T_w)$. The local heat transfer coefficient based on local mixed bulk temperature becomes:

$$h_{mb} = \frac{\frac{1}{\sqrt{t}}}{\frac{1}{\sqrt{t_O}h_{mbO}} + \frac{1}{\dot{m}c_p}\int_A \frac{1}{\sqrt{t}}dA} \tag{9}$$

This allows the heat transfer coefficient to be determined independently from measured experimental temperatures, though a reference value of the heat transfer coefficient based on the mixed bulk temperature is required.

The most appropriate data available in the literature to determine the Nusselt number at the hole outlet were obtained by considering the results of Metzger and Cordaro (1979). They measured the heat transfer coefficient in tubes with different length to diameter ratios subject to varying crossflows. The Nusselt number was based on the average of the inlet and outlet mixed bulk temperatures and was averaged over the full inside surface of the tube. They correlated data on the hole Reynolds number, suction ratio, and length-to-diameter ratio as:

$$\overline{\mathrm{Nu}}_{mb\mathrm{avg}} = 0.023\,\mathrm{Re}^{0.8}\,\mathrm{Pr}^{0.67}\left[1 + \left(\frac{d}{L}\right)^{0.7}\right] \times \left[1 + 45\mathrm{SR}^{-0.54}\,\mathrm{Re}^{-0.38}\left(\frac{d}{L}\right)^{0.54}\right] \tag{10}$$

The average Nusselt number based on the local mixed bulk temperature at the outlet of the tube can then be found again using an energy balance over the length of the tube:

$$\overline{\mathrm{Nu}}_{mbO} = \left(\frac{\overline{\mathrm{Nu}}_{mb\mathrm{avg}}}{1 + 2\mathrm{St}\left(\frac{L}{D}\right)}\right) \tag{11}$$

Evaluation of Eq. (11) for the Reynolds numbers and length of film cooling holes investigated showed that the difference between the average Nusselt number based on outlet mixed bulk temperature and that based on the average of inlet and outlet temperatures was as high as 10 percent. If the reasonable assumption is made that truncating the pipe does not influence the local heat transfer coefficient, then it is possible to infer local values from the correlation. This is achieved by differentiating the integral of local Nusselt number over the length of the tube:

$$\overline{\mathrm{Nu}}L = \int_O^L \mathrm{Nu}\,dx \Rightarrow \mathrm{Nu}(x) = \overline{\mathrm{Nu}} + L\frac{d\overline{\mathrm{Nu}}}{dL} \tag{12}$$

The value of the enhancement factor calculated from this analysis of Metzger and Corado's data is presented as a function of the hole Reynolds number in Fig. 4, where the hole Reynolds number is based on the average velocity in the hole and the hole diameter. The effect of crossflow can be seen to be small at this position since the flow is well mixed at the hole outlet (8d from the hole entrance).

Results

Local Heat Transfer Distribution. The local heat transfer distribution within the holes was calculated based on the gas temperature on the duct centerline eight diameters upstream of the hole. The average temperature of gas drawn into the hole during the test is somewhat lower than this temperature as proportionally more air is drawn into the hole from near the wall than from the middle of the duct (Byerley, 1989). When uniformly normalized with respect to Nusselt number calculated from the Dittus–Boelter correlation, the values can be seen to fall below unity. This is expected since the analysis based on a single inlet temperature does not account for the reduction in

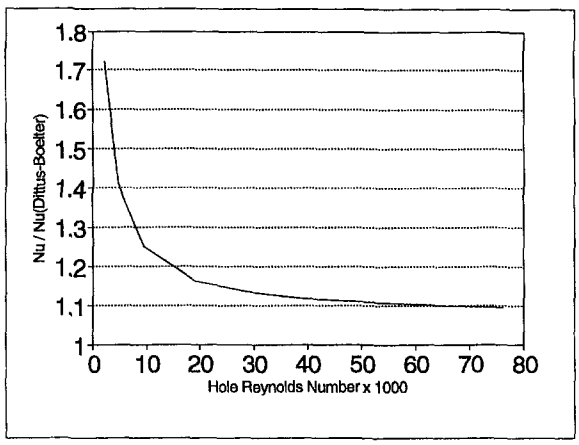


Fig. 4 Baseline Nusselt number at eight hole diameters from entrance

Downloaded 01 Jun 2010 to 171.66.16.53. Redistribution subject to ASME license or copyright; see http://www.asme.org/terms/Terms_Use.cfm

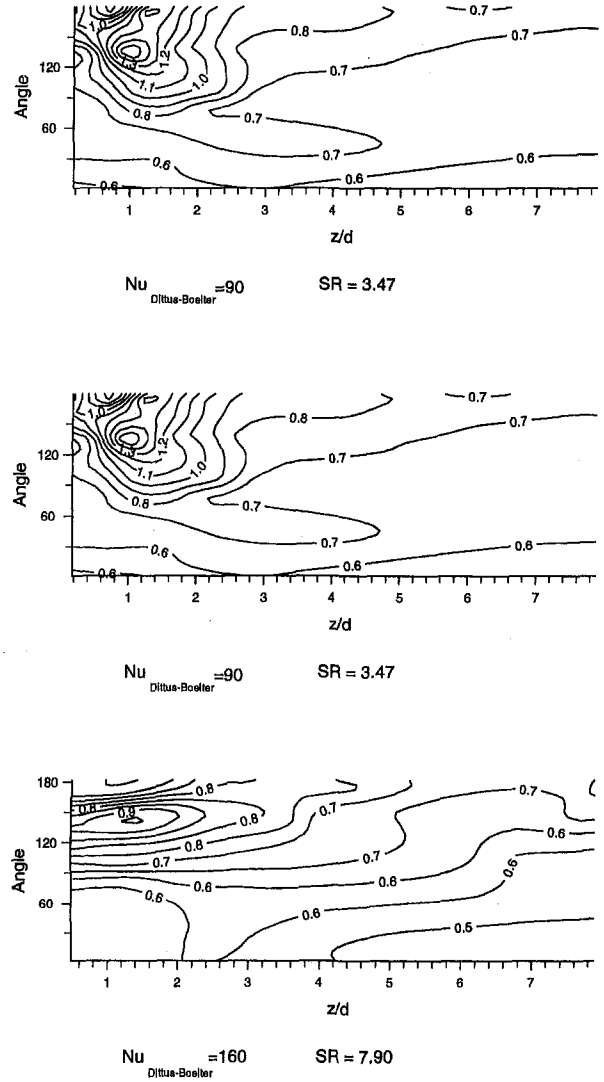


Fig. 5 Local Nusselt number distribution, 90 deg hole, based on centerline duct temperature

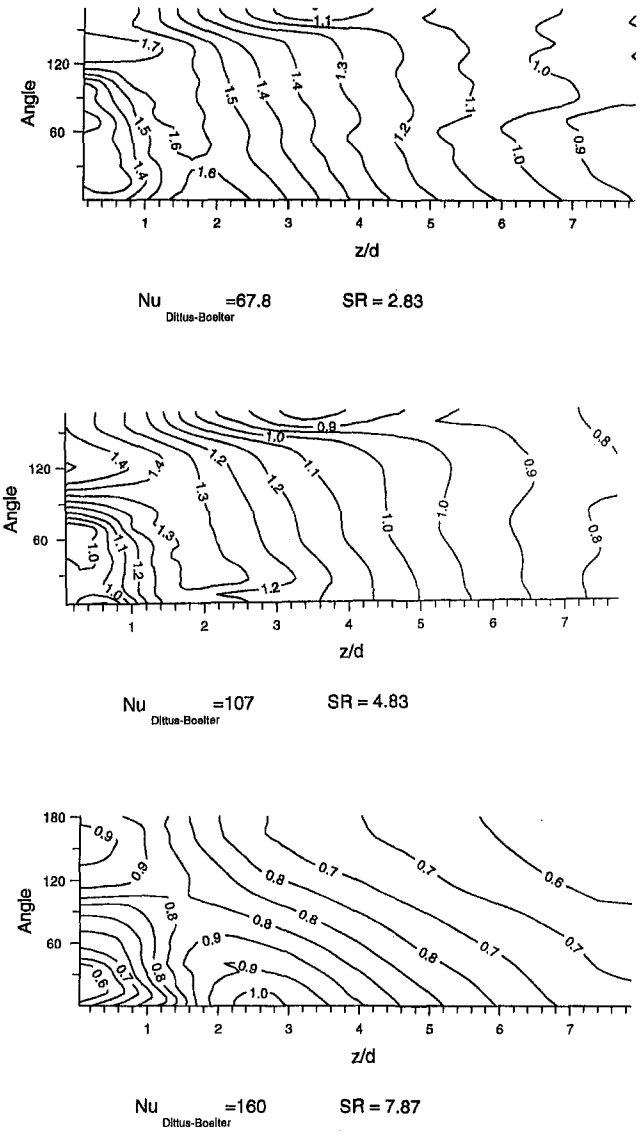


Fig. 7 Local Nusselt number distribution, 150 deg hole, based on centerline duct temperature

the difference between the gas temperature and wall temperature as the gas travels down the hole. Furthermore, the average temperature potential of flow drawn into the hole is significantly lower than the measured centerline temperature. Byerley (1989) showed that the capture area enlarged with increasing suction ratio, to include progressively more of the channel flow near the duct walls. This causes the normalized values of Nusselt number to decrease with increasing suction ratio as shown. Results at several suction ratios are shown for tests with the hole inclined at 90 and 150 deg in Figs. 5 and 7. For each test, more than 120 data points were used to determine the heat transfer contours using the automated image processing system described by Wang et al. (1993). In these figures, the angle

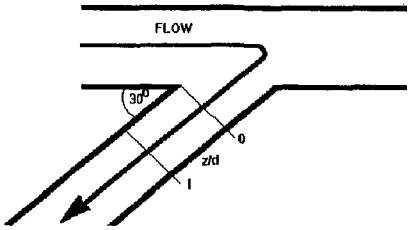


Fig. 6 Coordinate system in 150 deg hole

coordinate is measured between the line connecting the hole surface to the hole axis and a line in the undisturbed crossflow direction. z is the surface distance from the hole entry measured in the direction of the hole axis, as shown for the 150 deg hole in Fig. 6.

The effect of the crossflow is considerable and produces a Nusselt number distribution within the 90 deg hole that is far from symmetric about the 90 deg line. Along the 0 deg line there is always a region of low heat transfer due to the presence of a separation bubble attached to the upstream edge of the inlet to both geometries. Heat transfer enhancement can be seen in the first 2.5 diameters outside the separated region. For the 90 deg hole, a second region of relatively low heat transfer appears at the back edge of the hole at higher suction ratios. This phenomenon is consistent with the movement of the dividing streamline stagnation point to the channel wall outside the hole, as predicted by Morland (1989), and the appearance of a second separation bubble at the hole edge downstream relative to the mainstream flow (Fig. 1).

Flow field diagnostics have not been applied to the separation at the back of the 150 deg hole; however, the region of maximum enhancement consistently occurs at 120–180 deg around the circumference of the hole, suggesting that there is a large

Downloaded 01 Jun 2010 to 171.66.16.53. Redistribution subject to ASME license or copyright; see http://www.asme.org/terms/Terms_Use.cfm

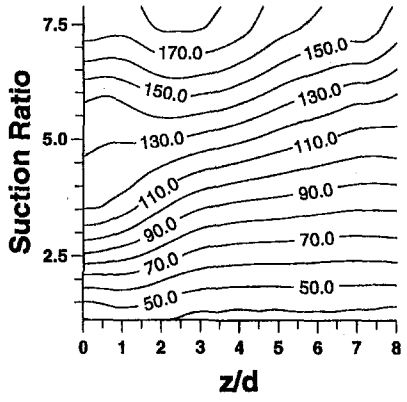


Fig. 8 Total Nusselt number distribution, 90 deg hole

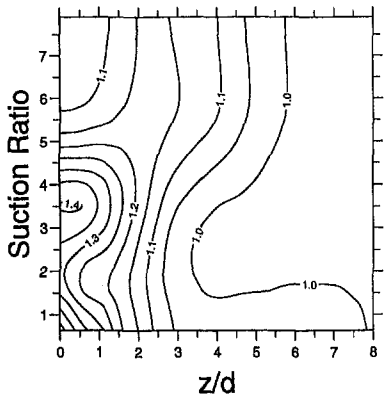


Fig. 10 $Nu/Nu_{Dittus-Boelter}$, 90 deg hole

separation bubble at the front edge of the hole. The heat transfer distribution becomes more uniform around the circumference of the 150 deg hole with increasing suction ratio, corresponding to a lower relative crossflow at the hole entrance. Byerley et al. (1988) reported that the discharge coefficient was 10–30 percent lower for a 150 deg hole than for a 90 deg hole due to the greater angle through which the flow is turned and the resulting increased extent of the separation.

Circumferentially Averaged Results Based on Local Mixed Bulk Temperature. The results presented above have shown that the heat transfer levels are sensitive to the gas temperature drawn into the hole. An attempt was made to make the data less dependent on the geometry of the supply passage by calculating heat transfer levels based on local mixed bulk temperature. It is thought that these levels will then be of use in situations where the flow and boundary conditions upstream of the hole are different from the current configuration, but where estimates can be made of the coolant mixed bulk temperature entering the hole.

The circumferentially averaged Nusselt number distributions for both hole configurations investigated determined using the analysis described above are presented in Figs. 8 and 9. Tests were processed at twelve different suction ratios to evaluate each of these plots. As expected, since the same procedure is used to determine the heat transfer coefficient at the outlet, the value of the Nusselt number is identical for both geometries along the $z/d = 8$ line. At the hole inlet, the 150 deg hole is less than the 90 deg data. Interestingly, the overall circumferentially averaged Nusselt numbers for the 150 deg holes are higher than those for the 90 deg hole. The highest Nusselt number is found between 0 and 2.5 diameters at all suction ratios, with the peak value moving further down the film cooling hole with increasing SR. The heat transfer coefficient enhancement over a simple Dittus–Boelter fully developed flow Nusselt number is shown in Figs. 10 and 11.

In the case of the 90 deg hole, the maximum enhancement is seen at the entrance to the hole at suction ratios up to 3.5, where a maximum enhancement of 1.4 is found. At greater suction ratios the peak moves down into the hole. This is thought to be due to the nature of the separation at the entrance of the 90 deg hole. At low suction ratios, the Reynolds number in the hole is low, and the effect of the relatively high crossflow causes the maximum local heat transfer to occur at the entrance to the film cooling hole. This peak in heat transfer is enough to increase the circumferentially averaged value even though a patch of low heat transfer occurs at the separation formed at its leading edge. However, as the suction ratio increases, the size of the entrance separation increases, see Fig. 5, while the relative crossflow decreases, and the flow field tends towards the no-crossflow case, where the maximum Nusselt number is found 1–2 diameters downstream of an abrupt entrance (Boelter et al., 1948).

The cross-over between these two conditions is governed by the formation of the separation just inside the back edge of the hole when the stagnation point moves from the inside of the film cooling hole to the cooling channel outside. A portion of the flow along the downstream duct wall is turned and accelerated into the hole causing an additional region of separation. Byerley et al. (1988) report this to occur at a suction ratio between 3.24 and 4.21.

In the case of the 150 deg hole, the large inlet separation at the front of the hole dominates the heat transfer obtained at all suction ratios. The maximum enhancement of 2.3 is obtained at the hole entrance with the lowest suction ratio, where the separation is smallest and the crossflow is dominant. As the

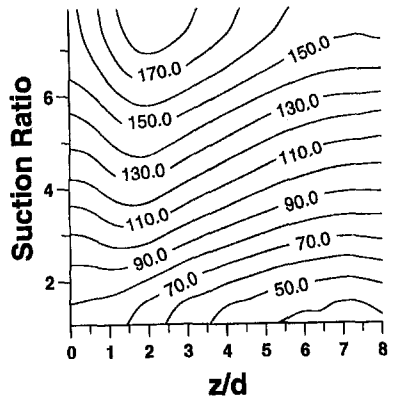


Fig. 9 Total Nusselt number distribution, 150 deg hole

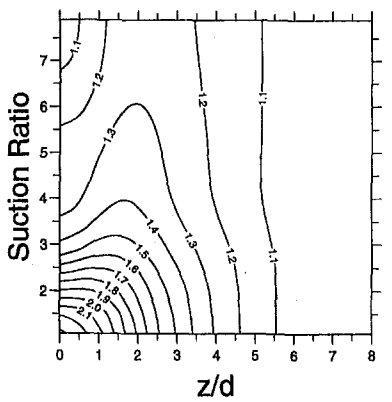


Fig. 11 $Nu/Nu_{Dittus-Boelter}$, 150 deg hole

Downloaded 01 Jun 2010 to 171.66.16.53. Redistribution subject to ASME license or copyright; see http://www.asme.org/terms/Terms_Use.cfm

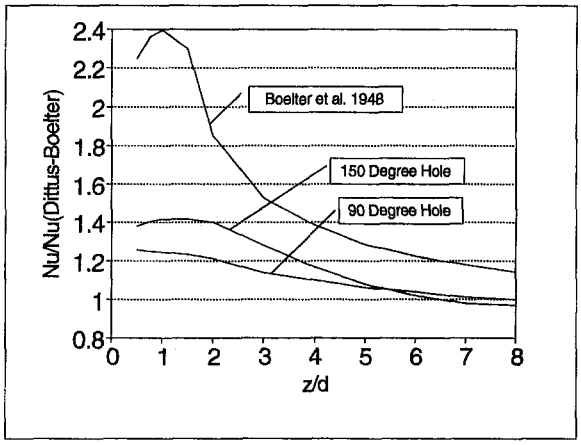


Fig. 12 Nu(Local)/Nu(Dittus-Boelter) suction ratio averaged

suction ratio is increased, the separation at the hole entrance increases and the growth of the separation causes the peak enhancement to move into the hole. The Nusselt number enhancement obtained in the 150 deg hole over the first four hole diameters is considerably greater than in the 90 deg hole for suction ratios under 3.0.

The enhancement in heat transfer coefficient measured for both the hole geometries investigated at the highest suction ratio is small in comparison to the findings of Boelter et al. (1948) for an abrupt-contraction entrance in the absence of crossflow, Fig. 12. Here, the very high levels between one and two diameters from the entrance arise from the reattachment of the separated flow in a ring around the pipe. The much lower circumferentially averaged values measured in the current work are caused by the greatly increased extent of the inlet separations under crossflow. In other words, the region of high heat transfer at reattachment is reduced from a continuous circle to a small patch, Figs. 5 and 7.

Summary

A new method of analyzing the heat transfer data has succeeded in uncoupling the influence of the different driving temperatures between the present work and previous data from the effects of crossflow. The experimental results show that there is a significant effect of crossflow on local heat transfer in film cooling holes. Enhancement is greater at low suction ratios where there is a high level of crossflow, and the maximum enhancement is seen to take place within three to four hole diameters of from the hole entrance, while the effect of the crossflow is almost imperceptible eight diameters downstream. When the film cooling hole was inclined at 150 deg to the cooling duct, the cooling enhancement was increased by up to 50 percent compared to a film cooling hole perpendicular to the flow at low suction ratios. Higher heat transfer was measured over the entire length of the hole in the 150 deg hole for suction ratios under 3.0. As the suction ratio was further increased this relative enhancement was reduced, producing similar heat transfer over the entire length of the tube at the highest suction ratio. When present data based on local mixed bulk temperature are compared to previous work, crossflow is seen to reduce the heat transfer enhancement by a large amount. This phenomenon is discussed in terms of the interpreted flow field.

Acknowledgments

The authors gratefully acknowledge the support of the Ministry of Defence (Procurement Executive) for part of the work, and the permission of Rolls Royce plc. to publish the paper. The authors also thank Mr. P. J. Timms for his expert technical assistance.

References

Baughn, J. W., and Yan, X., 1992, "Heat Transfer Measurements in Square Ducts With Transverse Ribs," presented at the National Heat Transfer Conference, Aug.

Boelter, L. M. K., Young, G., and Iversen, H. W., 1948, "An Investigation of Aircraft Heaters XXVII: The Distribution of Heat Transfer Rate in the Entrance Region of a Circular Tube," NACA TN1451, Washington, DC.

Byerley, A. R., Ireland, P. T., Jones, T. V., and Ashton, S. A., 1988, "Detailed Heat Transfer Measurements Near and Within the Entrance of a Film Cooling Hole," ASME Paper No. 88-GT-155.

Byerley, A. R., Jones, T. V., and Ireland, P. T., 1992, "Internal Cooling Passage Heat Transfer Near the Entrance to a Film Cooling Hole: Experimental and Computational Results," ASME Paper No. 92-GT-241.

Byerley, A. R., 1989, "Heat Transfer Near the Entrance to a Film Cooling Hole in a Gas Turbine Blade," D. Phil Thesis, Department of Engineering Science, University of Oxford, United Kingdom.

Dunne, S. T., 1982, "A Study of Flow and Heat Transfer in Gas Turbine Blade Cooling Passages," D. Phil Thesis, Department of Engineering Science, University of Oxford, United Kingdom.

Haidar, N. I. A., and Dixon, S. L., 1988, "Compressible Flow Losses in Branched Ducts," ASME HTD-Vol. 104, No. 2, pp. 17–23.

Ireland, P. T., and Jones, T. V., 1985, "The Measurement of Local Heat Transfer Coefficients in Blade Cooling Geometries," presented at the AGARD Conference on Heat Transfer and Cooling in Gas Turbines, CP 390, Paper 28.

Ireland, P. T., 1987, "Internal Cooling of Turbine Blades," D. Phil Thesis, Department of Engineering Science, University of Oxford, United Kingdom.

Metzger, D. E., and Cordaro, J. V., 1979, "Heat Transfer in Short Tubes Supplied From a Cross-Flowing Stream," ASME Paper No. 79-WA/HT-16.

Morland, L. C., 1989, "Mathematical Models for a Fluid Flow Arising in Turbine Blade Cooling Passages," D. Phil Thesis, University of Oxford, United Kingdom.

Shen, J.-R., Ireland, P. T., Wang, Z., and Jones, T. V., 1991, "Heat Transfer Coefficient Enhancement in a Gas Turbine Blade Cooling Passage Due to Film Cooling Holes," *Proceedings of the Institution of Mechanical Engineers, Turbomachinery,* London, pp. 219–226.

Shen, J.-R., Ireland, P. T., Wang, Z., and Jones, T. V., 1994, "Heat Transfer Enhancement Within a Turbine Blade Cooling Passage Using Ribs and Combinations of Ribs With Film Cooling Holes," ASME Paper No. 94-GT-232; accepted for publication in the ASME JOURNAL OF TURBOMACHINERY.

Vedula, R. J., and Metzger, D. E., "A Method for the Simultaneous Determination of Local Effectiveness and Heat Transfer Distributions in Three-Temperature Convection Situations," ASME Paper No. 91-GT-345.

Wang, Z., 1991, "The Application of Thermochromatic Liquid Crystals to Detailed Turbine Cooling Measurements," D. Phil Thesis, Department of Engineering Science, University of Oxford, United Kingdom.

Wang, Z., Ireland, P. T., and Jones, T. V., 1995, "An Advanced Method of Processing Liquid Crystal Video Signals From Transient Heat Transfer Experiments," ASME JOURNAL OF TURBOMACHINERY, Vol. 117, pp. 184–189.

Yan, X., Baughan, J. W., and Mesbah, M., 1992, "The Effect of Reynolds Number on the Heat Transfer Distribution From a Flat Plate to an Impinging Jet," ASME HTD-Vol. 226, pp. 1–8.

Downloaded 01 Jun 2010 to 171.66.16.53. Redistribution subject to ASME license or copyright; see http://www.asme.org/terms/Terms_Use.cfm

Investigation of the Flow Field Downstream of a Turbine Trailing Edge Cooled Nozzle Guide Vane

C. H. Sieverding

T. Arts

R. Dénos

von Karman Institute for Fluid Dynamics, Rhode-Saint-Genèse, Belgium

F. Martelli

University of Florence, Florence, Italy

A trailing edge cooled low aspect ratio transonic turbine guide vane is investigated in the VKI Compression Tube Cascade Facility at an outlet Mach number $\bar{M}_{2,is}$ = 1.05 and a coolant flow rate $\dot{m}c/\dot{m}g$ = 3 percent. The outlet flow field is surveyed by combined total-directional pressure probes and temperature probes. Special emphasis is put on the development of low blockage probes. Additional information is provided by oil flow visualizations and numerical flow visualizations with a three-dimensional Navier–Stokes code. The test results describe the strong differences in the axial evolution of the hub and tip endwall and secondary flows and demonstrate the self-similarity of the midspan wake profiles. According to the total pressure and temperature profiles, the wake mixing appears to be very fast in the near-wake but very slow in the far-wake region. The total pressure wake profile appears to be little affected by the coolant flow ejection.

Introduction

In recent years the turbomachinery community has focused its attention increasingly on the unsteady effects in turbine and compressor stages resulting from the interference of rotor blades with the pressure and temperature gradient fields of the preceding stator blade row or vice versa (Sharma et al., 1992). The intensity of the interaction depends of course on the strength of the pressure and temperature gradients in the interblade row space; these in turn are functions of the blade loading and the aspect ratio of the upstream blade row as well as of the outlet Mach number and the axial distance. In turbines the interference is particularly complex in the HP stages where the flow patterns are often dominated by secondary and tip clearance flows. The axial evolution of the interblade row flow field is a combined diffusion–convection process in which radial and circumferential pressure gradients as well as a complex vortex system, generated by the upstream blade row, play equally important roles.

Systematic measurements of the axial evolution of the downstream flow field behind turbine blade rows are rather scarce. Nearly all investigations are done on low-aspect-ratio high turning nozzle guide vanes. Binder and Romey (1983) were probably the first to study in great detail the outlet flow field behind an annular stator blade row. The authors used the Laser-2-Focus technique to determine the velocity field in several axial planes. They derived from the yaw angle distribution the location of vortices as well as their type. The downstream mixing process was largely attributed to the action of these vortices. Sieverding et al. (1984) surveyed the outlet flow field of a low-speed annular cascade with four-hole pressure probes at three axial locations and gave a detailed account of the radial migration of low-momentum boundary layer material through the wake region under the influence of the radial pressure gradient. These results confirmed previous observations by Rohlik et al. (1954) in a transonic guide vane. Yamamoto and Yanagi (1985), carrying out very similar measurements to those of Sieverding et al., added further information on the radial redistribution of losses through the action of the trailing edge vorticity. Williamson and Moustapha (1986) reported test results on a highly loaded transonic three-dimensional guide vane with endwall contraction for mean outlet Mach numbers from M_2 = 0.65 to 1.04. Similarly to the other authors, they found the hub endwall losses significantly higher than the tip region losses. The higher hub losses were attributed to the higher adverse pressure gradients downstream of the throat—due to the higher Mach numbers at the hub—and the radial migration of vane surface boundary layers. With the onset of transonic conditions at the hub, the losses undergo a sharp rise and accentuate thereby the spanwise loss variation. The outlet flow angle showed a marked decrease of the flow turning toward the hub with increasing Mach numbers. This phenomenon was attributed to the action of the passage vortex. The authors concluded that the observed nozzle hub separation, stemming from shock–boundary layer interaction, could be significantly reduced by a downstream rotor. Dominy and Harding (1989) compared the outlet flow characteristics of a very highly loaded constant section HP guide vane with two three-dimensional guide vanes with different degrees of trailing edge bowing for unloading the endwall regions and controlling secondary flows.

The present investigation extends the aerodynamic research in annular cascades to transonic turbine guide vanes with trailing edge coolant flow ejection. The coolant flow is ejected from a slot on the rear pressure side. Most of the tests are done with a coolant flow rate of 3 percent, but some tests were also done at zero flow rate for comparison purpose. In addition to previous research, the test program included wake temperature measurements, and an attempt was made to quantify the wake turbulence with high-frequency total pressure probes measurements. Particular attention was given to the wake decay process. This work was carried out as part of a BRITE EURAM turbine research program in collaboration with ALFA AVIO, MTU, SNECMA, DLR, and the University of Florence. The annular cascade tests were complemented by straight cascade tests at DLR (Kapteijn

Contributed by the International Gas Turbine Institute and presented at the 39th International Gas Turbine and Aeroengine Congress and Exposition, The Hague, The Netherlands, June 13–16, 1994. Manuscript received by the International Gas Turbine Institute February 19, 1994. Paper No. 94-GT-209. Associate Technical Editor: E. M. Greitzer.

Copyright © 1996 by ASME

Downloaded 01 Jun 2010 to 171.66.16.53. Redistribution subject to ASME license or copyright; see http://www.asme.org/terms/Terms_Use.cfm

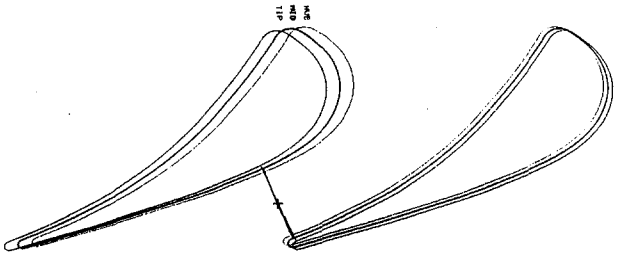


Fig. 1(*a*) Three-dimensional stacking of blade base profile

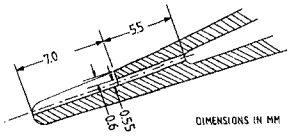


Fig. 1(*b*) PS ejection blade

et al., 1994). Reference will be made to the straight cascade tests whenever necessary.

Annular Cascade Geometry

The guide vane has cylindrical blades. The uncooled blade profile was optimized by ALFA AVIO for midspan flow conditions using a semi-inverse blade design method. Its main characteristics are presented below:

- Chord length, c = 72.0 mm
- Axial chord length, c_{ax} = 43.1 mm
- Pitch to chord ratio, g/c = 0.75
- Throat width, o = 14.98 mm
- Gaging angle, arccos (o/g) = 73.9 deg
- Stagger angle, γ = 51.90 deg
- Trailing edge thickness, te = 1.70 mm
- Trailing edge thickness to chord ratio, te/c = 2.36 percent
- Trailing edge wedge angle, δ_{te} = 6.4 deg

The blade coordinates are given in the appendix. The blade sections from hub to tip (constant sections) are stacked along the vector radius through the centers of the throats, Fig. 1(*a*). The base profile was modified to allow for coolant flow ejection from the rear pressure side by cutting back the rear pressure side as indicated in Fig. 1(*b*). The coolant flow is ejected from behind the backward-facing step.

The cascade was tested in the VKI Compression Tube Annular Cascade Facility (Sieverding and Arts, 1992). Figure 2 shows a meridional view of the test section. The contraction preceding the guide vane simulates the exit of a combustion chamber. The cylindrical endwalls continue downstream of the blade row for about 450 mm at the tip and 100 mm at the hub. The coolant air is injected into a large space between the guide vane endwall and the guide vane housing. From there the cooling air enters the hollow blades and is ejected through a pressure side trailing edge slot spanning the entire blade height.

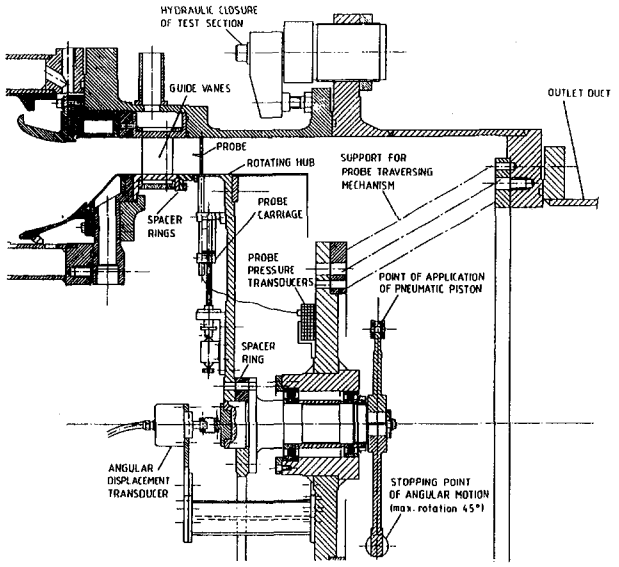


Fig. 2 Meridional view of test section

The main annular cascade characteristics are:

	Diameter mm	Throat mm	Pitch mm
Hub	689	13.56	50.34
Mean	739.7	14.98	54.04
Tip	790.4	16.50	57.75

The throat dimensions are those of the base profile.

The cut back on the rear pressure side moves the position of the throat upstream and increases the throat width by about 2 percent.

Testing Program

Tests are run at design Mach number and Reynolds number and nominal coolant flow rate. The test conditions are summarized below:

- Isentropic Mach number at midspan $M_{2,is}$ = 1.05
- Reynolds number based on chord length and outlet velocity at midspan Re = 10^6
- Turbulence intensity Tu = 1.8 percent
- Coolant mass flow rate $\dot{m}c/\dot{m}g$ = 3 percent
- Inlet total pressure P_{01} = 1.62 bar
- Inlet total temperature T_{01} = 440 K
- Coolant flow temperature T_{0c} = 287 K
- Blade temperature T_{bl} = 287 K

Nomenclature

c = chord
g = pitch
h = blade height
$\dot{m}$ = mass flow
M = Mach number
o = throat
P = pressure
Re = Reynolds number based on chord and outlet velocity
te = trailing edge thickness
T = temperature
Tu = turbulence intensity, percent
V = absolute velocity
X, Y = coordinates
α = absolute flow angle referred to axial direction
γ = radial flow angle
ζ = kinetic energy loss
ϑ = variable
κ = specific heat ratio

Subscripts

ax = axial
c = coolant
g = main flow
is = isentropic
l = local
r = radial
te = traling edge
0 = total
1 = inlet
2 = outlet

Downloaded 01 Jun 2010 to 171.66.16.53. Redistribution subject to ASME license or copyright; see http://www.asme.org/terms/Terms_Use.cfm

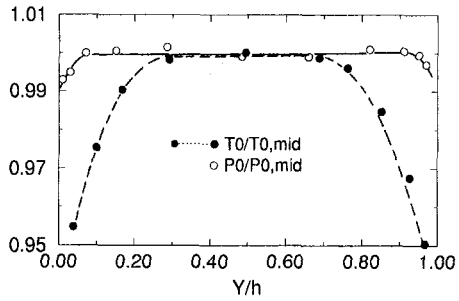


Fig. 3 Spanwise variation of upstream total pressure and temperature

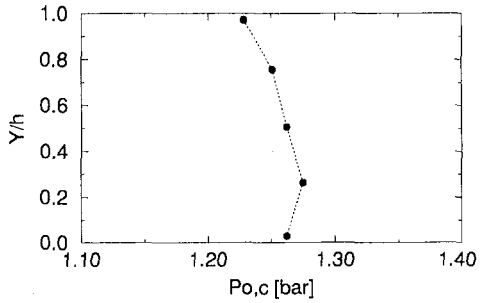


Fig. 4 Total pressure distribution along coolant slot

The coolant flow to main flow temperature ratio is $T_{0c}/T_{0g} = 0.65$. Ideally this ratio should have been close to 0.5 to simulate correctly the conditions in advanced turbo engines. However, this would have required to cool the coolant air down to ≈220 K, which would have caused considerably more complications in the experimental setup and longer testing times. Due to the fundamental character of this study, this was not deemed to be necessary. For comparison reasons a few tests were run with zero coolant flow ejection.

The bulk of the experimental data consists of loss and angle measurements in three axial planes, $x/c_{ax} = 0.25$, 0.54, and 1.0, over the entire blade height. These aerodynamic measurements are completed by the measurement of the midspan thermal wake profile. Total pressure fluctuations in the wake were recorded at midspan in the first traverse plane.

General Flow Conditions

Upstream Flow Conditions. Figure 3 shows the radial variation of the inlet total pressure as measured with a total pressure rake, each pressure tube being connected to a separate Sensym absolute pressure transducer. The boundary layer thickness is very small on both endwalls, around 5 percent of the blade height. At the hub, the first measurement point is at 0.5 mm from the wall. The ratio between the total pressure in this point and the free-stream total pressure is $P_{ol}/P_{01} = 0.993$.

The drop-off of the temperature profile near the endwall was higher than anticipated based on previous experiments with albeit higher Reynolds numbers than in the present case, i.e., 2.5×10^6 instead of 10^6. The possibility of blowing off the endwall boundary layer before the inlet guide vane contraction was not used.

The inlet flow angle is not measured, but considering the construction of the tunnel with its axisymmetric settling chamber preceding the test section, it can reasonably be assumed that the inlet flow direction is axial.

The turbulence intensity at midspan, measured with a constant temperature hot wire probe, is $Tu \approx 1.8$ percent.

Outlet Flow Conditions. In the absence of a downstream rotor, it is important to verify that the far downstream uniform pressure field does not affect the radial pressure gradient field at the stator exit. The table below compares the measured pitch-averaged isentropic Mach numbers at hub and tip in the axial plane $x/c_{ax} = 0.54$ with the results of a three-dimensional Euler calculation.

$M_{2,is} = f(P_2/P_{01})$		
	3-D Euler code	Experiments
hub	1.13	1.12
mean	1.05	-
tip	0.987	0.98

The good agreement is an indication for correct flow conditions at least up to this measurement plane.

The outlet flow field is typically surveyed over three to four pitches. The pitchwise isentropic Mach number distributions along hub and tip, based on wall static pressure measurements showed a good periodicity. The pitchwise averaged mean Mach numbers differ at most by 1–2 percent. However, the blade-to-blade loss variations are bigger, as will be discussed later.

Coolant Flow. The coolant mass flow is measured via a sonic hole in the coolant flow admission pipe. The coolant flow total pressure and temperature are measured just before entering the space above the guide vane platform. Unfortunately it was not possible also to measure the coolant flow conditions along the trailing edge coolant slot in the presence of the main stream. While it may be assumed that the total temperature is constant along the span (except very close to the endwalls), the same may not be true for the total pressure: (1) because of nonuniform flow mixing inside the blade and (2) because of the static pressure gradient along the trailing edge. The first point was investigated by measuring the coolant flow total pressure along the span in absence of the main flow with five flattened total pressure tubes immersed 2–3 mm into the slot. The total pressure in the coolant flow admission pipe was the same as during a test run, i.e., $P_{oc,1} = 1.3$ bar. The flow discharged at a constant static pressure of $P = 1.02$ bar instead of $P = 0.8$ and 0.9 bar at hub and tip, respectively, in presence of the main flow. Figure 4 shows that from $y/h = 0.25$ to 0.75 the measured total pressure decreases linearly from 1.275 to 1.255 bar, i.e., a pressure change of ~1.5 percent. The drop off at the walls to 1.268 bar at the hub and 1.23 at the tip, respectively, is probably due to endwall effects in the internal cooling channel.

Measurement System

The outlet flow field is surveyed by combined total-directional pressure probes, combined total pressure–temperature probes, and fast response Kulite total pressure probes. The corresponding static pressure field is obtained by linear interpolation between hub and tip endwall static pressure distributions. The assumption of a linear spanwise pressure variation was confirmed by three-dimensional Euler and Navier–Stokes calculations. To allow circumferential traversing of the probes with minimum perturbation of the flow, the hub endwall is divided into a small fixed part followed by a rotatable part carrying the probes. Spacer rings allow extending the fixed part and shifting the rotatable part with the probes downstream and thereby displacing the measurement plane. The disk carrying the rotatable endwall is mounted on a shaft with on its right side a lever, which is actuated by a pneumatic piston, Fig. 2.

Pressure Probes. The main constraints for the probe design are:

(*a*) a sufficient short response time of the probe/transducer ensemble;

Downloaded 01 Jun 2010 to 171.66.16.53. Redistribution subject to ASME license or copyright; see http://www.asme.org/terms/Terms_Use.cfm

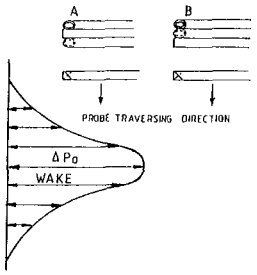


Fig. 5 Various types of three-hole pressure probes

(b) the use of the probes in strong pressure gradient fields;
(c) the minimization of the probe blockage effect;

(a) determines the minimum dimensions of the probe head, (b) determines to a large extent the arrangement of the differential tubes for the angle measurements, and (c) affects in particular the probe stem size and the distance between probe stem and probe nose.

The relative high probe traversing speed of about 500 mm/s requires short probe-transducer system response times. Extensive testing of various probe-pressure line-transducer systems at VKI (Sieverding et al., 1988) have shown adequate response times for probes made of 1 × 0.8 mm ϕ tubes connected via flexible pressure lines to Sensym differential pressure transducers located at 400 mm from the probe head. With these tube diameters, the diameter of the probe head of a five-hole probe would be typically 3 mm.

Calculations showed that traversing the midspan wake in the axial plane $x/c_{ax} = 0.25$ with such a five-hole probe would have resulted in local errors in the α-angle measurements of ±1.8 deg. The traversing of a shock would of course entail even bigger errors. This led to the choice of three-hole probes with the tubes arranged in a plane normal to the wake profile, Fig. 5. However, the use of this type of probe head is problematic near the endwalls where the spanwise total pressure gradients associated with the endwall boundary layers and secondary flows are even bigger than the pitchwise gradients of the wake profiles. Calculations showed that angle measurements with probe head A—the total pressure tube placed between the two directional tubes—in the region of the secondary loss peak at the hub would be in error by as much as ±2 deg and angle measurements within the endwall boundary layer should be disregarded altogether. Type "B" probe heads, with the differential pressure tubes side by side, are better in the endwall regions. With this probe the maximum error in the region of the hub secondary loss peak drops to ±1 deg. However, within the endwall boundary layers, the errors are still high and angle measurements for wall distances $Y < 2.5$ mm (5 percent of blade height) are not to be trusted. The wake traverses between 15 and 85 percent blade height were carried out with probes of type A; for traverses closer to the walls use was made of probes of type B.

Because of the above-mentioned problems, it was not attempted to measure the radial flow angles ($\gamma = \arctan V_{r,2}/V_2$). Navier–Stokes calculations, carried out at the University of Florence, showed that γ did not exceed 3 to 4 deg in all measurement planes.

The calibration of the three-hole probes showed that such variations had no significant effect on the α-angle measurements.

Probe Blockage Effect—Probe Design. The immersion of a probe into a transonic or low supersonic flow inevitably alters the local flow conditions due to the blockage of the probe, in particular of the probe stem, if this stem is directed normal to the flow, which is typically the case when testing annular cascades. Several authors have addressed this problem (e.g., Sieverding, 1985; Schaub et al., 1990; Depolt et al., 1990; Harasgama and Chana, 1990; each of them defining his own acceptance criterion for reliable probe measurements).

In the authors' opinion the best way of evaluating the importance of the probe blockage effect on the downstream measurements is to compare the endwall static pressure distributions in the measurement plane in the absence and in presence of the probe. Ideally the probe stem should be so small and far removed that the flow in the measurement plane is not at all affected by its presence. This appears to be unrealistic in transonic annular cascades because it implies either unreasonably long probe heads or too small probe stem dimensions, either or both leading to undesirable probe vibrations. A less stringent, but sufficient requirement is to ensure that the endwall static pressure at the point of measurement and upstream of it is not affected, i.e., the wall pressure tappings to the right of the probe nose in Fig. 6(a), while the flow downstream of the probe nose, i.e., to the left of it, may be disturbed.

An entirely new probe was designed, Fig. 6(b). The end of the rectangular shaped probe stem (7 × 3.3 mm) is bent laterally at 90 deg. A 110 mm probe head is attached to this transverse piece. A cross arm provides the required stiffness for the probe head. The probe head is curved to align it with the midspan cylindrical stream surface. Aligning the probe head with the mean flow direction puts the probe stem at more than two pitches away from the probe nose. To avoid the blockage effect variation with probe immersion depth, the probe stem is backed up by a fixed cylinder, which spans the whole passage height and has the same width as the probe stem. Figure 6(c) compares the hub endwall isentropic Mach number distributions at x/c_{ax}

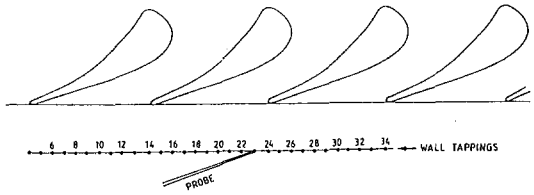


Fig. 6(a) Probe in downstream measurement plane

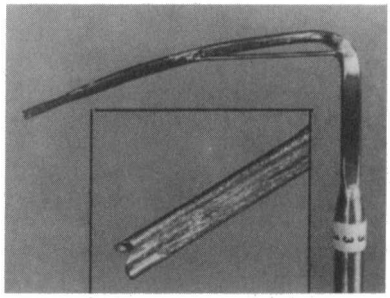


Fig. 6(b) New low-blockage pressure probe

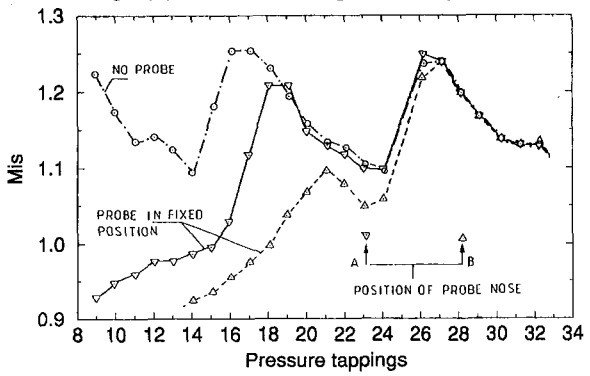


Fig. 6(c) Effect of probe blockage on Mach number distribution at hub endwall

Downloaded 01 Jun 2010 to 171.66.16.53. Redistribution subject to ASME license or copyright; see http://www.asme.org/terms/Terms_Use.cfm

= 0.54, recorded at two different circumferential positions of the probe, with the Mach number distributions in the absence of the probe. For probe position A the first significant influence of the probe stem is felt five tappings downstream of the probe nose, i.e., at 50 percent of the pitch; for probe position B the influence is felt at 4 tappings or 40 percent of the pitch downstream of the nose. These results demonstrate clearly that the probe blockage problem for the present cascade testing has been solved satisfactorily.

Measurement Assessment

The measurement uncertainties are dependent on the linearity and stability of the pressure transducers and the accuracy of the calibration procedures. The uncertainty on the blade losses is affected by the individual errors in the measurement of the upstream and downstream total pressures P_{01} and P_{02} and the downstream static pressure P_2. The measurement error for these quantities is estimated to be of the order of $\Delta P/P = 0.2$–0.3 percent. The uncertainty of the blade kinetic energy loss is evaluated as $\delta\zeta/\zeta = 10$ percent.

The uncertainty on the angle measurements is much more difficult to evaluate, because it relies additionally on the calibration of the directional probe over a wide range of Mach numbers and flow angles and on its behavior in strong gradient fields. In weak pressure gradient fields the flow angle uncertainty is estimated to ± 0.8 deg, but in high spanwise gradient fields the local errors may be considerably higher; see section on "Pressure Probes."

Repeat tests are also an excellent mean for the assessment of measurement uncertainty. Repeat tests in plane $x/c_{ax} = 0.25$, separated by several months with complete dismantling of the probe traverse mechanism in between, showed that out of eight repeat tests at various spanwise positions between 20 and 80 percent of the blade height, the difference in blade losses (averaged over three wakes) was less than 5 percent for five spanwise positions and 10–12 percent for the other three. These data corroborate the values of the uncertainty on the losses of $\delta\zeta/\zeta = 10$ percent quoted above.

To evaluate globally the blade-to-blade loss variations, the results of some 60 traverses from all three measurement planes, covering each three wakes, have been examined. For each traverse the loss of each individual blade was compared with the loss value obtained by averaging the losses over three wakes.

The differences are summarized in the table below:

$\frac{\zeta_{blade} - \zeta_{3\ blades}}{\zeta_{3\ blades}}$	percentage of traverses
0-10%	60%
10-20%	28%
>20%	12%

Note that the highest differences are recorded in the secondary and endwall boundary layer regions, where spanwise gradients are predominant.

The differences are surprisingly high, considering the expected "inherent periodicity" of blade flows through annular cascades. Obviously, minor differences in blade and cascade geometry are able to affect considerably the boundary layer development on the blades and endwalls.

Performance Measurements

Blade losses and outlet flow angles are presented in the form of carpet plots and spanwise distributions of pitch-averaged values. Except for a few, all data are averaged data over three pitches. In view of the comparison with numerical predictions, losses and angles are presented under the form of area-averaged

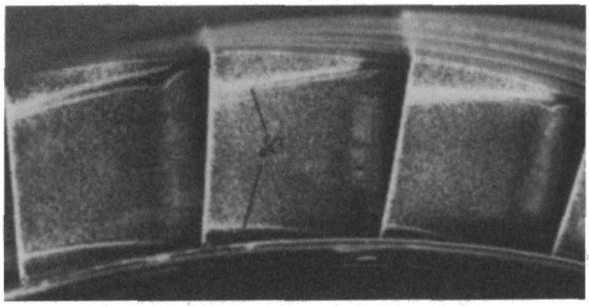


Fig. 7 Oil flow visualization at nominal outlet Mach number and coolant flow ejection

data. However, the blade losses were also calculated under the form of mixed-out values using the conservation equations for mass, momentum, and energy between the measurement plane and a plane infinitely far downstream. For all measurement points the difference between area-averaged and mixed-out losses was $\Delta\zeta < 0.2$ percent, the mixed-out values being bigger.

The blade losses are expressed by the kinetic loss coefficient

$$\zeta = 1 - \frac{1 - (P_2/P_{02})^{(k-1)/k}}{1 - (P_2/P_{01})^{(k-1)/k}}$$

To account for differences between mainflow and coolant flow energies, the losses have to be calculated as

$$\zeta_c = 1 - \frac{\left[1 - \left(\frac{P_{S2}}{P_{02}}\right)^{(k-1)/k}\right](\dot{m}_1 \cdot T_{01} + \dot{m}_c \cdot T_{0c})}{\dot{m}_1 \cdot T_{01}\left(1 - \left(\frac{P_{S2}}{P_{01}}\right)^{(k-1)/k}\right) + \dot{m}_c \cdot T_{0c}\left(1 + \left(\frac{P_{S2}}{P_{0c}}\right)^{(k-1)/k}\right)}$$

The differences between ζ and ζ_c can be important and are illustrated at the example of the midspan losses measured at $X/C_{ax} = 0.54$:

- upstream main flow conditions: $P_{01} = 1.62$ bar, $T_{01} = 440$ K
- coolant flow at TE slot exit: $P_{0c} = 1.265$ bar, $T_{0c} = 287$ K
- measured downstream conditions: $P_{02} = 1.58$ bar, $P_{S2} = 0.806$ bar

With these conditions the loss coefficients are, respectively, $\zeta = 3.2$ percent and $\zeta_c = 2.6$ percent.

Because of lack of space for presenting systematically both loss coefficients and to ease comparison with numerical calculations it was decided to present only ζ values.

Losses. The spanwise evolution of the losses is the result of the combined effect of secondary flows, of Mach number variation along the blade height and radial pressure gradient. The variation of the pitch-to-chord ratio g/c along the blade height may also play an effect, but the optimum g/c is Mach number dependent as shown by Dejc and Trojanovskij (1973). It turns out that the variation of g/c along the span of ~15 percent corresponds approximately to the change in the optimum g/c suggested by Dejc for the Mach number variation of $M_{2,is} = 0.98 \rightarrow 1.12$ from tip to hub. Therefore, it appears reasonable to neglect this parameter in the following discussion.

Near the endwalls, Mach number effects are masked by secondary flow effects. As indicated by the oil flow visualizations in Fig. 7, the extension of the secondary flow zone is larger at the tip than at the hub. At the trailing edge this zone covers about 10 percent of the span at the hub and 20 percent of the span at the tip. With increasing distance the secondary flows will continue to expand radially thanks to the continuously growing endwall boundary layer, the radial pressure gradient, and the

Downloaded 01 Jun 2010 to 171.66.16.53. Redistribution subject to ASME license or copyright; see http://www.asme.org/terms/Terms_Use.cfm

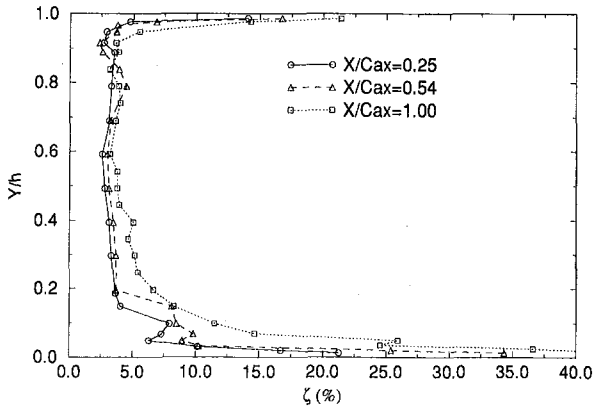


Fig. 8 Spanwise loss distributions in downstream planes

combined action of passage and trailing edge vortex (sum of trailing filament vortices and trailing edge shed vorticity). The overall aspect of the loss distribution in the planes $x/c_{ax} = 0.25$ and 0.54, Fig. 8, follows the typical pattern: at the endwall high losses due to the endwall boundary layer; at some distance from the endwall a relative loss maximum (secondary loss core) associated with the passage vortex; beyond that, a slow decrease down to the level of profile losses. The secondary loss core at the tip is not very prominent and the position of its maximum is not well defined. The secondary loss maximum exceeds the profile losses hardly by one point. The maximum moves from about $y/h = 0.85$ in the axial plane $x/c_{ax} = 0.25$ to $y/h = 0.8$ and 0.75 at the downstream planes $x/c_{ax} = 0.54$ and 1.0. Contrary to the tip, at the hub one observes a very prominent loss core. Its extension grows from $y/h = 0.15$ at the plane $x/c_{ax} = 0.25$ to $y/h = 0.25$ at $x/c_{ax} = 0.54$. The big difference between hub and tip is explained at least partially through the action of the radial pressure gradient, which causes a radial migration of low-momentum boundary layer from tip to hub through the trailing edge base flow region. Such a radial migration was observed by many researchers as described in the introduction and appears also very clearly on the flow visualization in Fig. 9, obtained with a Navier–Stokes for the present cascade.

In the plane $x/c_{ax} = 1.0$, Fig. 8, the loss distribution at the hub has taken a parabolic shape, extending from the hub endwall to midspan. Obviously the endwall boundary growth has become the dominating factor. One of the reasons for the strong change in the hub loss profile may be looked for in the evolution of the static pressure field.

plane	x/c$_{ax}$	$\overline{P_2/P_{01}}$ tip	$\overline{P_2/P_{01}}$ hub	$\overline{M_{2,is}}$ tip	$\overline{M_{2,is}}$ hub
1	0.25	0.550	0.4545	0.967	1.124
2	0.54	0.5426	0.4562	0.977	1.121
3	1.0	0.5345	0.4824	0.987	1.076

Between $x/c_{ax} = 0.25$ and 0.54, the pitch-averaged pressure at the hub remains nearly identical, but between $x/c_{ax} = 0.54$ and 1.0 the pressure rises by almost 6 percent. At the tip the pressure change is only 1.5 percent over the same axial distance. Contrary to the experiments Navier–Stokes calculations show that the spanwise pitch-averaged static pressure distribution is nearly identical in all three measurement planes. The reason for the pressure rise at the hub is therefore most probably to be attributed to the upstream influence of the constant pressure field at the exit of the cylindrical flow duct; see Fig. 2.

The effect of Mach number variation on the spanwise loss distribution is best observed in the measurement planes $x/c_{ax} = 0.25$ and 0.54. Minimum profile losses occur at the spanwise

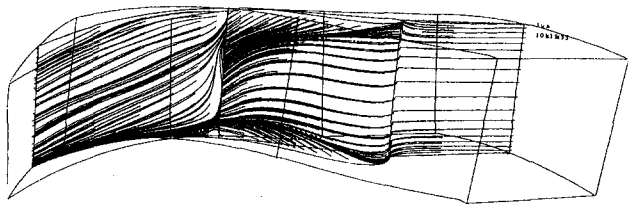


Fig. 9 Flow visualization of the blade suction side obtained from three-dimensional Navier–Stokes solver

position $y/h = 0.6$. (This position of minimum losses is confirmed also by other tests, e.g., measurements in plane $x/c_{ax} = 1.0$.) At this spanwise position, the mean isentropic Mach number is $\overline{M_{2,is}} = 1.03$ and the losses at $x/c_{ax} = 0.25$ amount to $\zeta = 2.8$ percent. From $y/h = 0.6$ downward, there is a slow linear increase in losses up to $\zeta = 4$ percent at $y/h = 0.15$. From $y/h = 0.6$ upward, the losses also rise slowly, but when accounting for some secondary losses, the profile losses will never exceed $\zeta = 3.2$ percent. At no place does one observe a sudden strong increase of the losses with Mach number, as found in the straight cascade tests at DLR, where the losses undergo a sudden rise from $\zeta = 3.5$ percent at $M_{2,is} = 1.0$ to $\zeta = 7$ percent at $M_{2,is} = 1.08$; see Kapteijn et al. (1994). The most likely explanation for this difference are strong three-dimensional flow effects in the trailing edge region, already referred to, with possible effects on the trailing edge base pressure and the shock intensity. As regards the latter, the oil flow visualization in Fig. 7 suggests that the suction side shock boundary layer interaction is weak over the entire span.

Figure 10 presents the blade losses in plane $X/C_{ax} = 0.54$ between 20 and 80 percent blade height with and without coolant flow ejection. Except at $Y/h = 0.7$ and 0.8, the ejection of coolant flow results in a reduction of the profile losses and this reduction increases toward the hub, i.e., to the region of higher Mach numbers. The higher losses at zero coolant flow rate are to be attributed to the backward-facing step on the rear pressure side. At chocked conditions, the corner will produce a strong Prandtl–Meyer expansion, followed by a reattachment shock at short distance form the corner. On the suction side the flow will experience first a strong acceleration due to the Prandtl–Meyer expansion from the pressure side corner and then undergo, one after the other, the corner shock and the trailing edge shock. The ejection of coolant will reduce the effective step height. Hence both the corner expansion and the intensity of the reattachment shock will diminish and the blade losses will be reduced.

The lower losses at zero coolant flow ejection at $Y/h = 0.7$ and 0.8 are difficult to understand. The radial migration of low-

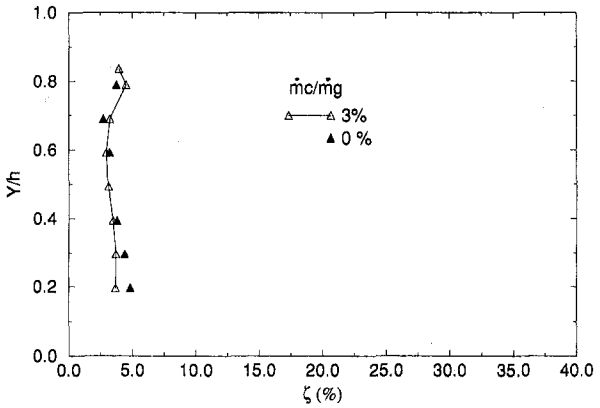


Fig. 10 Comparison of losses at zero and 3 percent ejection in the plane $X/C_{ax} = 0.54$

Downloaded 01 Jun 2010 to 171.66.16.53. Redistribution subject to ASME license or copyright; see http://www.asme.org/terms/Terms_Use.cfm

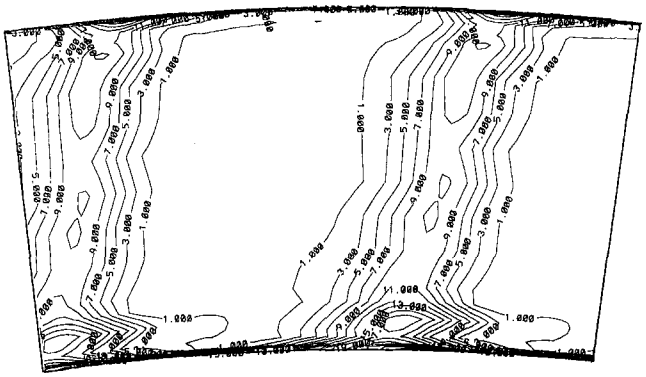


Fig. 11(*a*) Carpet loss plot at downstream plane $X/C_{ax} = 0.25$

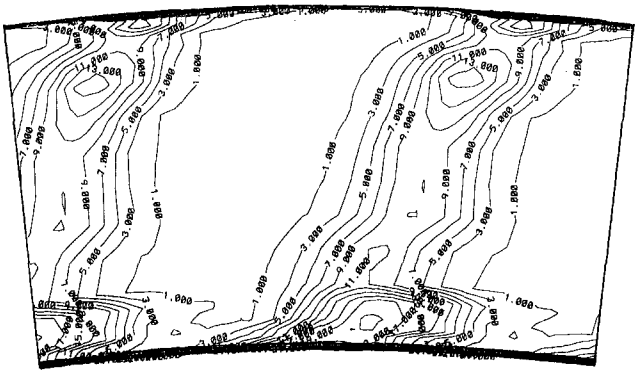


Fig. 11(*b*) Carpet loss plot at downstream plane $X/C_{ax} = 0.54$

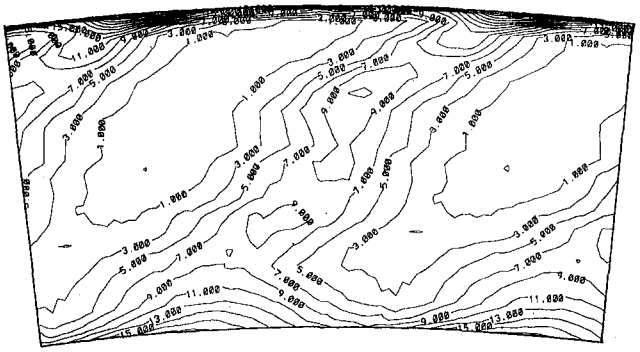


Fig. 11(*c*) Carpet loss plot at downstream plane $X/C_{ax} = 1.0$

momentum flow in the separated region behind the backward-facing step could have an effect similar to a coolant flow ejection. Differences in secondary flows with and without coolant ejection may be another possibility.

The loss carpet plots for the three downstream measurement planes are presented in Figs. 11(*a*), (*b*), (*c*). Due to problems with the opto-electronic encoder for the angular displacement, the probe position is measured within an accuracy of ±0.5 deg only. In the axial plane $x/c_{ax} = 0.25$ the wake covers about 45–50 percent of the blade pitch, except near the endwalls. Secondary flows are not very important. The only distinct secondary loss core appears at the hub, with its peak nearly in the center of the wake. Outside of the wake the end-wall boundary layer is extremely thin. At the axial distance $x/c_{ax} = 0.54$ the wake has broadened and the hub secondary loss core has taken considerable proportions. The secondary loss core at the tip appears like an island in the wake center at some distance from the endwall. Right at the endwall appears a new loss maximum. In the following downstream plane at $x/c_{ax} = 1.0$ the upper secondary loss island has migrated further toward midspan. At the casing the endwall boundary layer appears to be sucked in the wake by the action of the radial pressure gradient. Outside the wake the endwall boundary layer remains thin. In the lower half, the flow field has completely changed. The wake and/or the hub endwall boundary layer have spread over the entire passage. The secondary loss core has entirely merged with the endwall boundary layer. As pointed out before, the strong increase of the hub endwall boundary layer between $x/c_{ax} = 0.54$ and 1.0 is probably related to the significant static pressure rise for $x/c_{ax} > 0.54$ caused by the uniform far downstream conditions.

Wake Profile. Let us at present consider more closely the downstream evolution of the midspan blade wake. There are different ways of describing the wake profile. In low-speed flow the wake mixing behind cylinders is looked at in terms of the wake velocity distribution. This is not appropriate for the wake behind blades with transonic and supersonic outlet flow conditions, because the static pressure field is strongly nonuniform, with the consequence that the wake crosses a constantly varying static pressure field. Hence, the local velocity in the wake does depend not only on the wake diffusion process but also on the local static pressure. Of course, the same is to be said when describing the wake by its kinetic energy loss profile. Therefore, the evolution of the wake shape will be studied with regard to its total pressure profile, $1 - P_{02}/P_{01}$. Figure 12(*a*) presents these profiles for midblade height at the 3 axial positions $x/c_{ax} = 0.25$, 0.54, and 1.0. The profiles in the first two planes were obtained by averaging over three wakes, the last by averaging over two wakes. The gradual lateral spreading of the wake, accompanied by a progressive reduction of the wake depth, indicates a rather slow mixing process. It is worth noting that the wake profiles do not show any noticeable signature of the pressure side coolant flow ejection.

The total pressure profiles were also approximated by Gaussian distribution functions. The distribution parameter σ, characterizing the wake shape, was calculated for the two cases by using either a single symmetric distribution curve or an asymmetric distribution with different shape parameters σ for the suction side and pressure side of the wake, Fig. 12(*b*). The comparison of the measured and the Gaussian wake profiles show an excellent agreement, Fig. 12(*a*).

Using the reduced variable $u = (y - \bar{y})/\sigma$ the distribution law

$$\vartheta(y) = \frac{1}{\sqrt{2\pi\sigma}} \exp\left(-\frac{(y-\bar{y})^2}{2\sigma^2}\right)$$

can be written as

$$\vartheta_r(y) = \frac{1}{\sqrt{2\pi}} \exp\left(-\frac{u^2}{2}\right)$$

This is the standardized normal distribution; the variable has a null mean value and a standard deviation equal to one. This means that choosing an appropriate reduction for a set of Gaussian curves with different σ values will lead to collapse them in a unique curve. This is presented in Fig. 12(*c*). The figure demonstrates that the total pressure loss curves are self-similar.

It is evident that the wake profiles will not conserve their self-similarity in regions of strong secondary and endwall flows.

Outlet Flow Angle. The spanwise variation of the outlet flow angle is presented in Fig. 13. In the section "Pressure Probes," it was stated that angle measurements for wall distances <5 percent were not to be trusted and therefore any data within this zone are omitted from the angle plots. As to the remaining data, the accuracy is estimated to be of the order of ±0.5 to 0.8 deg, based on previous experiences with similar probes in two-dimensional transonic flow measurements. An exact error estimation is not possible. The pressure gradient

Downloaded 01 Jun 2010 to 171.66.16.53. Redistribution subject to ASME license or copyright; see http://www.asme.org/terms/Terms_Use.cfm

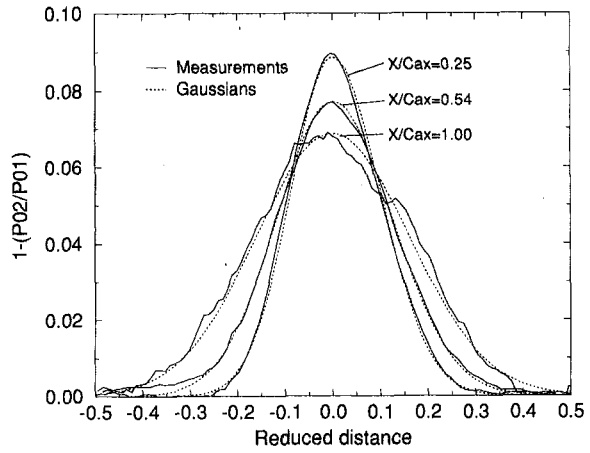


Fig. 12(*a*) Comparison of measured and Gaussion wake profiles

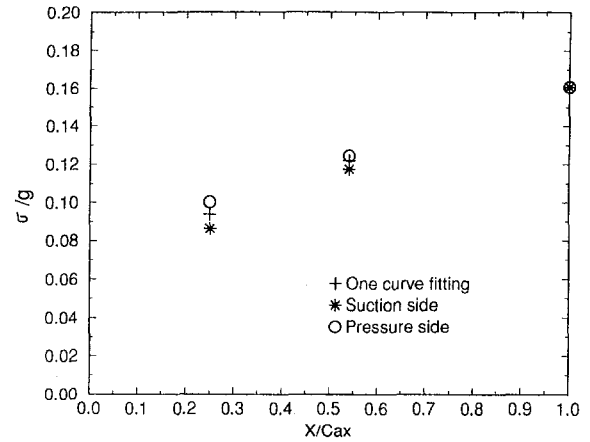


Fig. 12(*b*) Evolution of wake shape parameter σ for Gaussian distribution

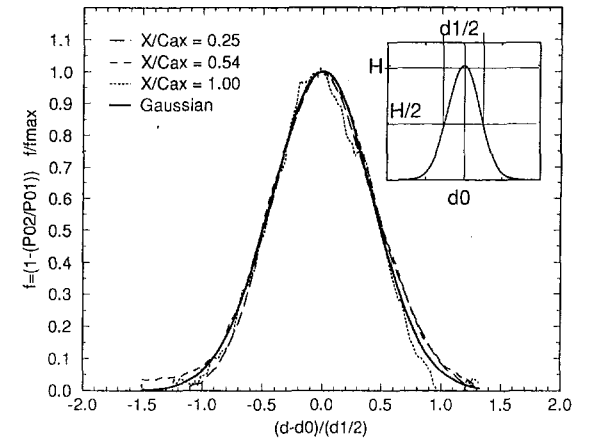


Fig. 12(*c*) Self-similarity of total pressure loss profiles

fields are too complex to evaluate the measurements errors related to the probe head size for all conditions.

The outlet flow angle curves for the planes at $x/c_{ax} = 0.25$ and 0.54, are the most important from the point of view of a turbine design. The overall differences between the two curves are small. Except near hub and tip where maximum local differences of the order of 1 deg are recorded, the angles differ by less than 0.5 deg over the major part of the span. The α_2 angle varies from about 71 deg at the tip to 73 deg at the hub. The angle variation in the upper half span is more important than in the lower half span. The nearly constant α_2 in this region is possibly a Mach number effect (supersonic deviation for a convergent blading), which compensates at least partially for the change in the gaging angle $\alpha_2^* = \arccos o/g$ which increases from tip to hub. The typical under- and overturning near the endwalls due to the passage vortex is observed only at the hub. The flow angle distribution at the tip does not allow us to draw any conclusions as to the action of the tip passage vortex on the outlet flow angle distribution. Any such effects appear to be small and subdued by the data scatter.

Compared to the planes $X/C = 0.25$ and 0.54, the spanwise angle variation in plane $X/C = 1.0$ has become much more important. The change is particularly important in the lower half span. This change is naturally related to the strong increase of the hub endwall boundary layer, put into evidence in Fig. 8, which affects more the axial than the circumferential component of velocity. This strong change in the spanwise outlet angle variation between the axial planes $x/c_{ax} = 0.54$ and 1.0 is also evident in the carpet loss plots, Figs. 11(*b*) and 11(*c*), which indicate an important inclination of the wake between both planes.

Wake Total Pressure Fluctuations. Many researchers have developed over the past years multisensor fast response pressure probes for unsteady flow measurements in rotating machines. In a few cases, e.g., Ruck and Stetter (1990), Moss and Oldfield (1990), it has been attempted to use such probes for turbulence measurements. However, the relatively large probe heads pose problems as regards the spatial resolution of the measurements. To circumvent the problem of size and get nevertheless some useful information on the unsteady wake character, it was decided to use a single total pressure probe with a Kulite pressure transducer mounted in the nose to record the turbulent fluctuations in the wake, Fig. 14(*a*). The assumption is made that the wake turbulence is mainly caused by total pressure fluctuations, while static pressure and temperature fluctuations can be considered small. This assumption does certainly not hold in the near wake, but in the first measurement plane at $x/c_{ax} = 0.25$ the streamwise distance from the trailing edge amounts already to 80 percent of the chord length.

The measurements were carried out in plane $x/c_{ax} = 0.25$ at midspan. Figure 14(*b*) shows both the turbulence and the time-averaged total pressure profile. The data are derived from a continuous midspan traverse over two wakes at $x/c_{ax} = 0.25$. The Kulite data are filtered at 50 kHz. Each point in the figure presents the average of 2000 successive data points. Control measurements with the probe in fixed positions with an averaging over a much longer time agree very well with the results from the continuous traverse.

Maximum values of $Tu = 4.2$ percent are recorded in the wake center. Considering that due to the finite size of the probe head, 1.6 mm diameter, the pressure fluctuations are averaged over a nonnegligible distance, one may expect that the real

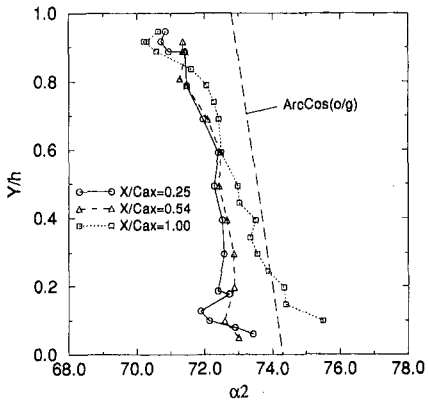


Fig. 13 Comparison of spanwise outlet angle distributions

Downloaded 01 Jun 2010 to 171.66.16.53. Redistribution subject to ASME license or copyright; see http://www.asme.org/terms/Terms_Use.cfm

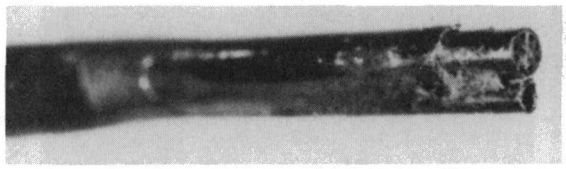


Fig. 14(*a*) Conventional pitot pressure probe combined with fast-response Kulite pressure probe

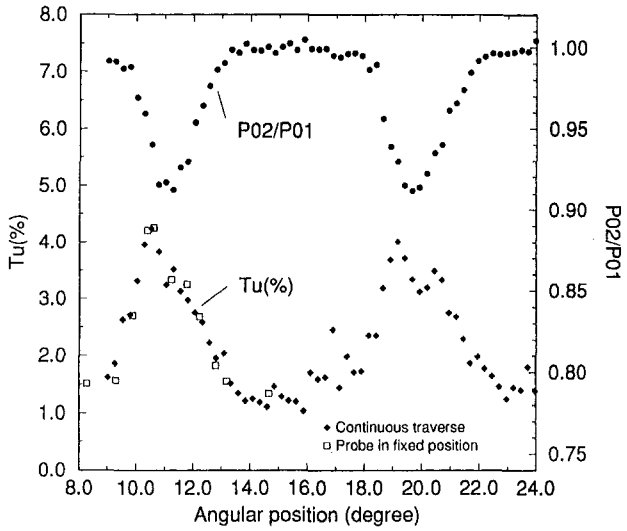


Fig. 14(*b*) Turbulence intensity and total pressure profile at midspan in plane $X/C_{ax} = 0.25$

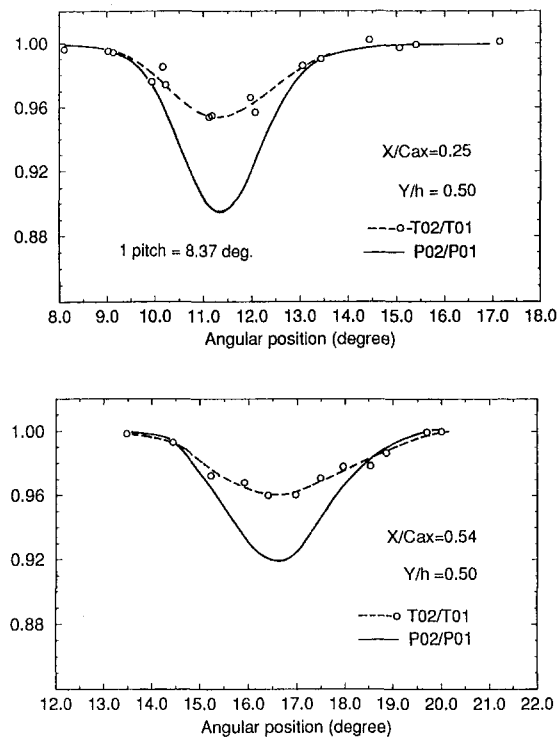


Fig. 16 Midspan wake temperature and total pressure profiles at $X/C_{ax} = 0.25$ and 0.54

turbulence levels are slightly higher. In between the wakes the turbulence level drops to $Tu \simeq 1.2$ percent. Compared to an inlet turbulence level of $Tu \simeq 1.8$ percent, measured with a hot-wire probe, the downstream value of 1.2 percent seems to be slightly high because the magnitude of the velocity fluctuations can be assumed to remain constant from inlet to outlet while the mean-velocity increases strongly across the cascade. A possible explanation is that the time-varying wake shedding process induces slight trailing edge shock oscillations, which affect the entire flow field.

An interesting feature is the double peak in the right Tu profile, which may be explained by the effect of the coolant jet. The left Tu profile does not show this peak but the profile exhibits a singular inversion in the same region.

Wake Temperature Profiles

Figure 15 shows a sketch of the probe: two bare thermocouples of 0.1 mm diameter chromel alumel wires mounted side by side with the total pressure probe. Bare thermocouples were chosen to keep the probe head size small. The disadvantage of bare thermocouples is their sensitivity to gas velocity. To reduce this effect, measures have to be taken to ensure a low gas velocity at the junction. For the probe in Fig. 15, the junction velocity depends on its proximity to the pitot probe and on the distance between the junction and the tubes from which the wires emerge. The measuring accuracy of the probe was evaluated by comparing the measurements in the downstream planes, probe positioned between two wakes, with the temperature recorded by a thermocouple probe upstream of the cascade where the Mach number is of the order of $M_1 = 0.15$ only. Through careful adjustment of the position of the thermocouple junctions of the probe, it was possible to obtain an agreement within 1 percent. The measurement uncertainty of the upstream probe is estimated to ±0.3 percent. Due to the slow response of thermocouple probes, it was decided to use a point by point measurement procedure, rather than continuous traversing.

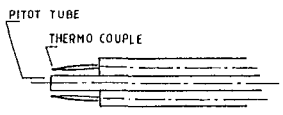


Fig. 15 Thermocouple temperature probe

Figure 16 shows the midspan temperature and total pressure profiles for the axial planes $x/c_{ax} = 0.25$ and 0.54. For clarity the experimental points of the total pressure measurements have been omitted from these graphs. Two aspects are particularly striking: (*a*) the lateral extension of the thermal profiles coincides very closely with that of the total pressure profiles and (*b*) the temperatures in the wake centers differ only by ≈4 percent from the inlet total temperature. Considering the evolution of the temperature ratio from $T_{02}/T_{01} = 0.65$ at the coolant slot exit to 0.955 and 0.96 at the axial distances $x/c_{ax} = 0.25$ and 0.54, respectively, it appears that the thermal diffusion is very strong in the near-wake region, but very slow in the far-wake region in which the measurement planes are situated. Very similar results were obtained by Kapteijn et al. (1994) with their straight cascade tests measuring the evolution of the CO_2 coolant flow concentration in the wake. At 25 percent of the axial chord, the maximum concentration has already dropped to 10 percent, but it needs another 50 percent of the axial chord to decrease by further 5 percent.

Conclusions

1 The far-downstream uniform flow field does apparently not influence the cascade outlet flow field in the first two measurement planes at 25 and 54 percent of the axial chord, which are the most important from the point of view of turbine design.

2 Considering the design of the cascade with simple cylindrical blades, the cascade performs remarkably well from the point of view of both profile and secondary losses. Surprisingly the profile losses are smaller than what was to be expected from straight cascade results. Radial flow migration in the trailing

Downloaded 01 Jun 2010 to 171.66.16.53. Redistribution subject to ASME license or copyright; see http://www.asme.org/terms/Terms_Use.cfm

edge region affects the trailing edge losses, possibly significantly.

3 The coolant flow ejection does not produce any unusual wake flow patterns in the measurement planes, which points to a rapid mixing with the main flow. This fast mixing is particularly evident from wake temperature measurements, which show that the ratio between the coolant to mainflow temperature rises from $T_{oc}/T_{01} = 0.65$ at the coolant slot exit to 0.955 at 25 percent of the axial chord from the trailing edge.

4 The evolution of the midspan wake total pressure profile can be approximated by Gaussian curves, which prove to be self-similar with increasing downstream distance.

Acknowledgments

This research was carried out under contract for the CEC as part of the BRITE EURAM Aero 001 Project "Investigation of the Wake Mixing Process Behind Transonic Turbine Guide Vanes With Trailing Edge Coolant Flow Ejection." The authors wish to acknowledge this financial support as well as the contributions by ALFA AVIO, MTU, and SNECMA, who made this research possible.

References

Binder, A., and Romey, R., 1983, "Secondary Flow Effects and Mixing of the Wake Behind a Turbine Stator," ASME *Journal of Engineering for Power,* Vol. 105, pp. 40–46.

Dejc, M. E., and Trojanovskij, B. M., 1973, "Untersuchung und Berechnung Axialer Turbinenstufen," VEB Verlag Technik, Berlin.

Depolt, Th., Vinnemaier, F., and Koschel, W., 1990, "Investigation on Minimizing Blockage Effects of Multi-hole Pressure Probes in Transonic Flow," *Proc. of 10th Symp. on Measuring Techniques for Transonic and Supersonic Flows in Cascades and Turbomachines,* VKI.

Dominy, R. G., and Harding, S. G., 1989, "An Investigation of Secondary Flows in Nozzle Guide Vanes," AGARD CP 469.

Harasgama, S. P., and Chana, K. S., 1990, "Turbine Nozzle Guide Vane Exit Area Traversing in a Short Duration Light Piston Test Facility," *Proc. of 10th Symp. on Measuring Techniques for Transonic and Supersonic Flows in Cascades and Turbomachines,* VKI.

Kapteijn, C., Amecke, J., and Michelassi, V., 1994, "Aerodynamic Performance of a Transonic Turbine Guide Vane With Trailing Edge Coolant Ejection," ASME Paper No. 94-GT-288 to be published in the ASME JOURNAL OF TURBOMACHINERY, Vol. 118, July 1996.

Moss, R. W., and Oldfield, M. L. G., 1990, "Comparison Between Turbulence Spectra Measured With Fast Response Pressure Probes and Hot Wires," *Proc. of the 10th Symp. on Measuring Techniques for Transonic and Supersonic Flows in Cascades and Turbomachines,* VKI.

Ng, W., and Epstein, A., 1983, "High Frequency Temperature and Pressure Probe for Unsteady Compressible Flow," *Review of Scientific Instruments,* Vol. 54, No. 12.

Rohlik, H. E., Kofokey, M. G., Allen, H. W., and Herzig, H. Z., 1954, "Secondary Flows and Boundary Layer Accumulations in Turbine Nozzles," NACA TR 1168.

Ruck, G., and Stetter, H., 1990, "Unsteady Velocity and Turbulence Measurements With a Fast Response Probe," ASME Paper No. 90-GT-232.

Schaub, U. W., Williamson, R. G., Huot, J. P., and Moustapha, S. H., 1990, "An Experimental Assessment of the Influence of Downstream Conditions on the Performance of a Transonic Turbine Nozzle of High Turning," ASME JOURNAL OF TURBOMACHINERY, Vol. 112, pp. 286–293.

Sharma, O. P., Pickett, G. F., and Ni, R. H., 1992, "Assessment of Unsteady Flows in Turbines," ASME JOURNAL OF TURBOMACHINERY, Vol. 114, No. 1, pp. 79–90.

Sieverding, C. H., van Hove, W., and Boletis, E., 1984, "Experimental Study of the Three-Dimensional Flow Field in an Annular Turbine Nozzle Guide Vane," ASME *Journal of Engineering for Gas Turbines and Power,* Vol. 106, No. 2.

Sieverding, C. H., 1985, "Aerodynamic Development of Axial Turbomachinery Blading—Testing Techniques and Steady State Performance Measurements," in: *Thermodynamics and Fluid Mechanics of Turbomachinery,* NATO ASI Series E, No. 97A, Nijhoff.

Sieverding, C. H., Arts, T., and Pasteels, H., 1988, "Transonic Cascade Performance Measurements Using a High Speed Probe Traversing Mechanism in a Short Duration Wind Tunnel," *Proc. 9th Symp. on Measuring Techniques for Transonic and Supersonic Flow in Cascades and Turbomachines,* Oxford.

Sieverding, C. H., and Arts, T., 1992, "The VKI Compression Tube Annular Cascade Facility," ASME Paper No. 92-GT-336.

Williamson, R. G., and Moustapha, S. H., 1986, "Annular Cascade Testing of Turbine Nozzles at High Exit Mach Numbers," ASME *Journal of Fluid Engineering,* Vol. 108.

Yamamoto, A., and Yanagi, R., 1985, "Production and Development of Secondary Flows and Losses Within a Three Dimensional Turbine Stator Cascade," ASME Paper No. 85-GT-217.

APPENDIX

Blade coordinates

X(mm)	Yss(mm)	Yps(mm)
0.000	0.000	0.000
1.207	2.830	-2.468
2.318	4.479	-3.282
3.498	5.925	-4.039
4.745	7.159	-4.881
6.057	8.171	-5.807
7.430	8.961	-6.813
8.861	9.526	-7.898
10.344	9.864	-9.065
11.874	9.969	-10.307
13.446	9.830	-11.627
15.054	9.427	-13.024
16.690	8.739	-14.502
18.348	7.738	-16.067
20.020	6.402	-17.724
21.701	4.679	-19.483
23.381	2.506	-21.358
25.054	-0.171	-23.358
26.712	-3.417	-25.495
28.348	-7.141	-27.771
29.955	-11.141	-30.193
31.527	-15.261	-32.756
33.058	-19.600	-35.446
34.541	-24.107	-38.245
35.971	-28.693	-41.126
37.344	-33.282	-44.062
38.656	-37.730	-47.009
39.903	-42.050	-49.926
41.083	-46.155	-52.867
42.194	-49.998	-54.550
43.234	-53.721	-53.720

Downloaded 01 Jun 2010 to 171.66.16.53. Redistribution subject to ASME license or copyright; see http://www.asme.org/terms/Terms_Use.cfm

Simulation of Cooling Systems in Gas Turbines

G. Ebenhoch

T. M. Speer

MTU Motoren- und Turbinen-Union München GmbH, München, Federal Republic of Germany

The design of cooling systems for gas turbine engine blades and vanes calls for efficient simulation programs. The main purpose of the described program is to determine the complete boundary condition at the coolant side to support a temperature calculation for the solid. For the simulation of convection and heat pick up of the coolant flow, pressure loss, and further effects to be found in a rotating frame, the cooling systems are represented by networks of nodes and flow elements. Within each flow element the fluid flow is modeled by a system of ordinary differential equations based on the one-dimensional conservation of mass, momentum, and energy. In this respect, the computer program differs from many other network computation programs. Concerning cooling configurations in rotating systems, the solution for a single flow element or the entire flow system is not guaranteed to be unique. This is due to rotational forces in combination with heat transfer and causes considerable computational difficulties, which can be overcome by a special path following method in which the angular velocity is selected as the parameter of homotopy. Results of the program are compared with measurements for three applications.

1 Introduction

The demand for high overall efficiency of today's gas turbines requires that turbine inlet temperatures be much higher than the melting point of the blade materials. This means that hot section components, especially blades and vanes, must be cooled in order to comply with life requirements. In the thermodynamic gas turbine cycle, coolant mass flows are parasitic and reduce the overall efficiency of the engine. They must accordingly be minimized, and in order to do this, it is highly important to be able to predict them.

On the other hand, convective cooling configurations cause temperature gradients in the solid, which reduce the life of the hot section parts as a result of thermal stresses. Knowledge of the coolant side heat transfer coefficient (besides the hot gas side heat transfer distribution) as well as local coolant temperature is necessary for cooling design. Physical phenomena such as pressure loss, increase or decrease of enthalpy in the coolant mass flow, and effects in a rotating frame have to be described.

As the wall temperature is a boundary condition for the method presented, it is held constant during the computation of the coolant flow. It is, however, adjusted within an iterative process with a thermal analysis program until the global energy balance of the cooling system is achieved.

For practical application of a simulation program, a further aspect should be mentioned. In the early phase of the design process, geometry has still to be defined, meaning that a surface model of the geometry is not available. In this design phase a "gridless" and flexible method of varying the geometry is very useful.

Several methods are presented in the literature (e.g., Tietz and Koschel (1991), Kutz and Speer (1994), and the references therein). Most of them do not describe all phenomena in a coolant flow or seem to be not very flexible.

Here, a method is described for the efficient design of cooling systems based on a network technique. This method simulates steady-state coolant mass flow in nearly all relevant convective airfoil cooling configurations, using correlations for pressure loss and heat transfer coefficient. The governing equations, derived from the one-dimensional conservation of mass, momentum, and energy, as well as specific problems and an efficient solution method are discussed.

Finally, results from measurements and calculations are compared for three applications.

2 Mathematical Model of Cooling Systems

2.1 Cooling Systems as Networks. Cooling systems are represented by networks of flow elements. These are connected at nodes. The flow passes through the elements; flow paths split up or join together at the nodes as shown in Fig. 1.

Each flow element represents a section of the flow channel that can be described as a closed entity and is distinct from its neighbors. There is a wide variety of elements; among these are ribbed channels, U-turns of a certain cross-sectional shape and length, impingement cooling, and orifices.

The type and geometry of an element determine the calculation procedure for pressure loss and heat transfer coefficients ζ and α, respectively, which may further depend on the local thermodynamic condition. These calculation procedures represent correlations based upon the company's experience or upon literature.

Modeling of the flow through elements and their connection at nodes satisfies the conservation of mass and energy.

At those boundary nodes where the flow enters the system, pressure and temperature values must be prescribed; at outlet boundaries only pressures are required. However, as the flow direction that is determined by the program on its own may differ from the direction expected a priori, both pressure and temperature must be provided at all boundary nodes.

The task now consists in computing pressures and temperatures at internal nodes and mass flows through elements.

2.2 Differential Equations for Flow Elements. Each element can be handled in isolation because its throughflow is completely determined by its inlet pressure and temperature and its outlet pressure. These in turn must meet the values at the adjacent nodes.

The flow at location x is described by the following pair of coupled differential equations:

Contributed by the International Gas Turbine Institute and presented at the 39th International Gas Turbine and Aeroengine Congress and Exposition, The Hague, The Netherlands, June 13–16, 1994. Manuscript received by the International Gas Turbine Institute February 4, 1994. Paper No. 94-GT-49. Associate Technical Editor: E. M. Greitzer.

Copyright © 1996 by ASME

Downloaded 01 Jun 2010 to 171.66.16.53. Redistribution subject to ASME license or copyright; see http://www.asme.org/terms/Terms_Use.cfm

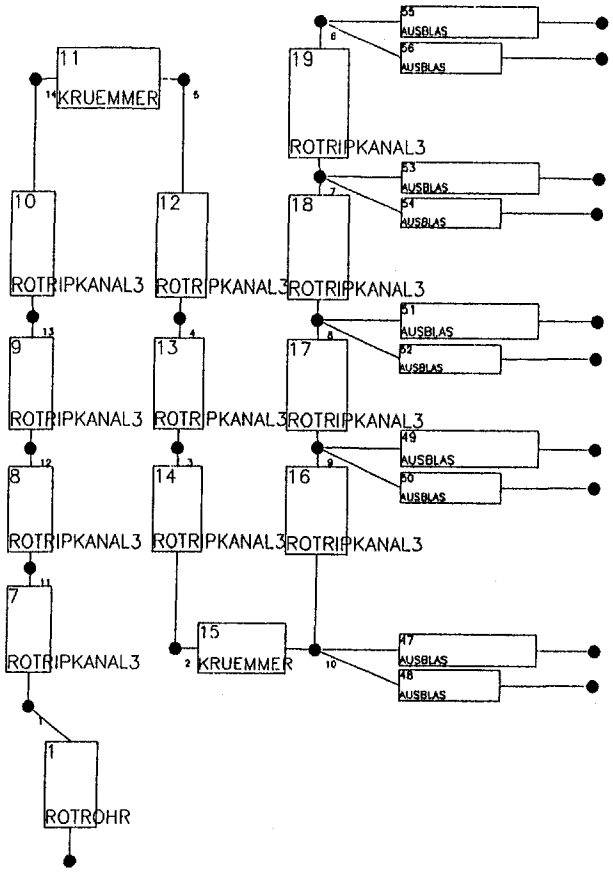


Fig. 1 Complex cooling system network

$$\frac{dp_t}{dx} = p_t\left[\frac{\omega^2 r\Delta r}{RT_t} - \frac{\kappa}{2}\mathrm{M}^2\frac{\alpha UL}{c_p m}\frac{T_W - T_t}{T_t} - \zeta\frac{\kappa}{2}\mathrm{M}^2\right], \quad (1)$$

$$\frac{dT_t}{dx} = \frac{1}{c_p}\left[\omega^2 r\Delta r + \frac{\alpha UL}{m}(T_W - T_t)\right], \quad (2)$$

where x denotes a normalized coordinate running from 0 (inlet) to 1 (outlet) along each single element.

As m does not depend on x, Eqs. (1) and (2) guarantee the conservation of mass, momentum, and energy flow.

They describe a general pipe flow and account for the following phenomena:

- Pumping effect caused by rotation with angular velocity ω, which depends further on the radial position r of the element and the radial distance $\Delta r := r(1) - r(0)$ (first term in both equations).
- Heat flux (second term in both equations), described by $\alpha UL/m(T_W - T_t)$. Here, T_W is the wall temperature of the component to be cooled down; U and L denote circumference and length, respectively. Geometry and radial position may vary linearly with x.
- Pressure loss due to friction, characterized by the pressure loss coefficient ζ (third term in pressure Eq. (1)).

Equation (1) contains the Mach number M; this has to be computed from the corrected mass flow m_{corr} from one-dimensional gas dynamics:

$$m_{\mathrm{corr}} = \frac{m\sqrt{T_t}}{Ap_t} = \sqrt{\frac{\kappa}{R}}\frac{\mathrm{M}}{\left(1 + \frac{\kappa - 1}{2}\mathrm{M}^2\right)^{(1/2)[(\kappa+1)/(\kappa-1)]}}. \quad (3)$$

Based on the solution of Eqs. (1) and (2), the first law of thermodynamics gives the total energy u at location x as

$$u(x) = m(c_p T_t(x) - RT(x)). \quad (4)$$

The differential Eqs. (1) and (2) are supplemented by the boundary conditions

$$p_t(0) = p_t^0, \quad T_t(0) = T_t^0, \quad p_t(1) = p_t^1, \quad (5)$$

where the superscripts 0 and 1 denote the nodes at element inlet and outlet, respectively.

2.3 Nodal Equations. The nodal equations guarantee the balance of incoming and outgoing mass and energy flows for each node k. For the subsets $I(k) := \{j$: stream flows into node $k\}$ and $0(k) := \{j$: stream flows out of node $k\}$ of flow elements, this leads to the nodal equations

$$F^k := \sum_{j\in I(k)} m_j - \sum_{j\in O(k)} m_j = 0 \quad (6)$$

$$G^k := \sum_{j\in I(k)} u_j(1) - \sum_{j\in O(k)} u_j(0) = 0. \quad (7)$$

Within Eqs. (6) and (7), m_j and u_j are to be computed from Eqs. (1)–(5).

Collecting all nodal equations, we end up with the nonlinear system

$$F(P, T) = 0 \quad (8)$$

$$G(P, T) = 0 \quad (9)$$

of equations for the unknowns P and T, where F, G, P, and T are K-dimensional vectors of the nodal values F^k, G^k, p^k, and T^k, respectively.

Nomenclature

A = cross-sectional area
c_p = specific heat at constant pressure
F, G = vectors of nodal mass and energy flow balance defects
I = subset of flow elements
j = number of flow element
k = number of node
L = length
m = mass flow
M = Mach number
O = subset of flow elements
p = pressure
P = vector of nodal pressure values
Q = factor in Eq. (12)
r = radius
R = gas constant
T = temperature (scalar or vector of nodal values)
u = energy
U = circumference
x = normalized coordinate along flow element
α = heat transfer coefficient
κ = ratio of specific heats
ω = angular velocity
ζ = pressure loss coefficient

Subscripts

corr = corrected
j = refers to flow element
nom = nominal
t = total
W = wall

Superscripts

0, 1 = inlet and outlet
k = refers to node
* = critical

Downloaded 01 Jun 2010 to 171.66.16.53. Redistribution subject to ASME license or copyright; see http://www.asme.org/terms/Terms_Use.cfm

2.4 Existence and Uniqueness of Solutions. It can be proved (with the aid of Frommer (1992a, b), Rheinboldt (1970), cf. Kutz and Speer (1992)) that a solution of the total system (1)–(9) exists under reasonable assumptions and that it is unique, if the following monotonicity condition is satisfied for all elements: For any fixed pair $p_t(0)$, $T_t(0)$ of inlet values, the outlet pressure decreases monotonically when the mass flow is increased from 0 (resting fluid) to m^* (choking flow).

For nonrotating systems (i.e., $\omega = 0$, e.g., vanes) this can be guaranteed by calculation procedures for α and ζ that preserve monotonicity in α and friction pressure loss.

For rotating systems (e.g., rotor blades), however, this monotonicity condition cannot be guaranteed for very small mass flow values. This is discussed below (see section 3.2). Consequently, the uniqueness of the solution cannot be proven (except for tree-structured networks).

This could be ignored as of theoretical interest only, but unfortunately the existence of two or more solutions of the boundary value problem for one single element does not only irritate the iterative computation procedure but prevents it from convergence if it happens to oscillate between these elemental solutions. This is overcome by applying a homotopy or continuation method for rotating systems (see section 4.4).

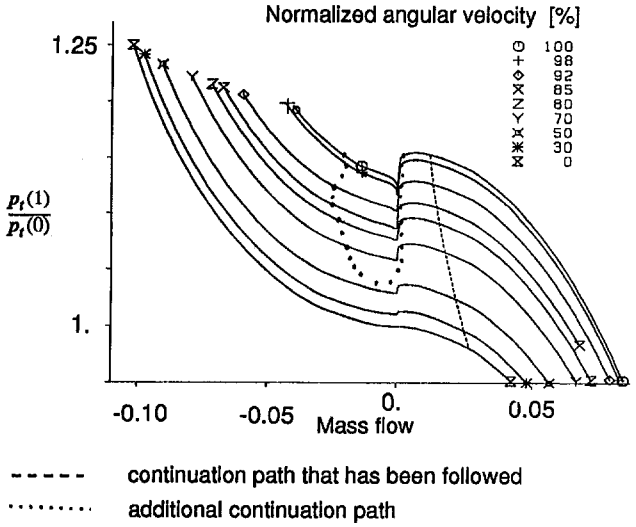


Fig. 2 Nonmonotonic behavior of rotating elements

3 Problems in Flow Element Computation

3.1 Choking Elements. Within the cooling system, the flow is defined to be subsonic because the use of nozzles is not permitted. Except for isolated shocks at local minima of the cross-sectional area the flow must be subsonic. Because of the assumption of linear (and thus monotonic) variation of the cross section, this can occur only at the element boundaries (with the exception of an orifice, see below).

Let the critical mass flow m^* be that value of the mass flow for which the maximum corrected value just reaches the critical corrected mass flow m^*_{corr}, which is gained from Eq. (3) by setting M = 1:

$$\max\left\{\frac{m^*\sqrt{T_t(x)}}{A(x)p_t(x)} : x \in [0, 1]\right\}$$

$$= m^*_{\text{corr}} := \left(\frac{2}{\kappa + 1}\right)^{1/(\kappa-1)} \sqrt{\frac{2\kappa}{R(\kappa + 1)}}. \quad (10)$$

Obviously, the mass flow m to be computed cannot exceed m^*.

Let $p_t^*(1)$ be the outlet pressure corresponding to m^*. If now the inequality $p_t^*(1) \le p_t^!$ holds, then the boundary value problem (1)–(5) has a solution. Otherwise, the outlet condition must be relaxed to $p_t(1) = p_t^*(1)(> p_t^!)$, and at the outlet the flow expands to the nodal pressure.

Orifices are modeled by incorporating them together with their upstream and downstream passage into a single orifice element. Except for the orifice itself, which is assumed to be located at $x = \frac{1}{2}$, its cross section varies smoothly.

For the solution of the boundary value problem for an orifice element, at first this is computed as a pipe while ignoring the narrow cross section of the orifice itself. If the resulting mass flow passes the orifice without choking, it is accepted as a solution. For large pressure ratios and small orifice areas, however, the orifice causes the flow to choke. Then, the above-computed mass flow must be decreased until at $x = \frac{1}{2}$ its corrected value becomes critical.

3.2 Ambiguity of Rotating Systems. Figure 2 shows the dependence of outlet pressure on mass flow over a variety of angular velocity values for a certain nonadiabatic element, which is directed radially outwards ($\Delta r > 0$). Negative m values denote opposite flow direction. Inlet pressure and temperature are kept constant. The dashed and dotted lines are explained in section 4.4.

The initial increase of $p_t(1)$ for small mass flow values is remarkable for high angular velocities; for $\omega = 0$ the curve decreases monotonically.

A discussion of the differential equations shows: The rotational term causes pressure increase (along the element coordinate x); friction and heat pick up take care of pressure loss.

By passing to the limit $m = 0$ it follows that $T_t(x) = T_W$ for all x and

$$\frac{p_t(1)}{p_t(0)} = \exp\left(\frac{\omega^2 r \Delta r}{RT_W}\right) > 1. \quad (11)$$

With increasing mass flow the temperature approach toward T_W needs an increasing distance; the fluid remains colder than the wall for a long distance or all over the element; the density exceeds its value for $m = 0$. Therefore the rotational term becomes more important than in the case $m = 0$.

If the angular velocity is sufficiently high in comparison with α and ζ, then for small positive mass flows the outlet pressure can exceed the outlet pressure for resting fluid ($m = 0$). For higher mass flow values this cannot happen because then pressure loss due to friction and heat transfer predominate the pumping effect.

As a consequence, the boundary value problem can have up to three solutions: two for small positive mass flows, one solution for $m < 0$.

Presumably, for a fluid nearly at rest, the flow is instable, and the underlying physical model and thus the differential equations are not applicable. A solution that contains such a small mass flow in an ambiguous situation is marked "unreliable" by the program.

If, in a real physical experiment, one starts with the well-defined steady-state solution for a nonrotating system and increases the angular velocity up to its nominal value, one ends up with a specific solution. This is uniquely defined by the initial steady state (or its boundary conditions) and the transient development of ω provided the solution path one is following does not contain any branching point (which has never been encountered although the program performs tests for its existence).

This mechanism is copied by the path-following method (see section 4.4), which constructs an auxiliary sequence of steady-state solutions (this must not be confused with a transient simulation).

Downloaded 01 Jun 2010 to 171.66.16.53. Redistribution subject to ASME license or copyright; see http://www.asme.org/terms/Terms_Use.cfm

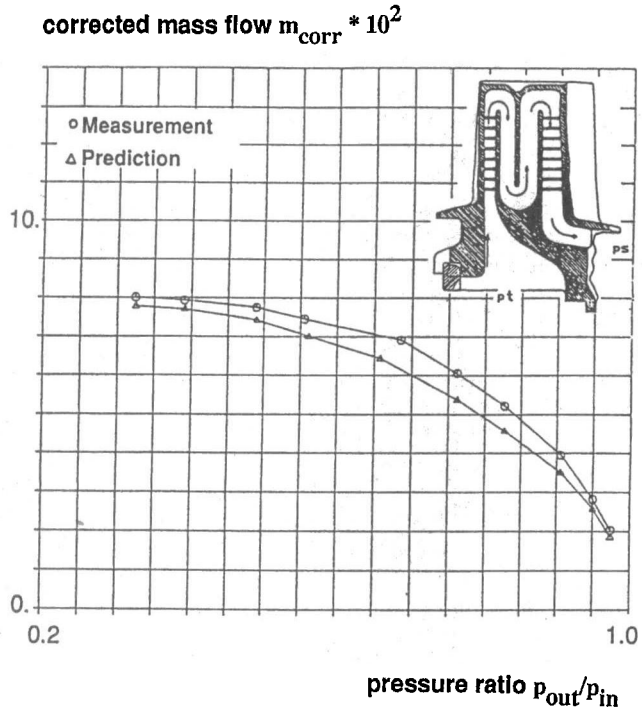


Fig. 3 Flow function in a multipass blade cooling system, comparison of measurement and calculation

4 Numerical Solution of the Equations

4.1 Overview. The solution of Eqs. (1) – (9) is computed by a hierarchy of several iterative procedures that are ordered into each other. This structure follows the separation of the total system into flow elements and the separation of the influences of nodal pressures (onto mass balances) on one hand and of nodal temperatures (onto energy balances) on the other. Rotation as an additional feature is taken into account by stepwise increase of the angular velocity.

The large number of unknown mass flow and nodal pressure and temperature values (more than two hundred for the nozzle of section 5.2) together with the heterogeneous structure of the model (differential and algebraic equations) require this decoupling of system components and their influencing quantities.

Corresponding to their position within that hierarchy and to the according frequency of their execution, the innermost iterative procedures must perform particularly efficient in order to reduce total computation time. Specially, the number of evaluations of α and ζ should not be too large.

Except for the integration of the differential equations and the consideration of rotation, this computational scheme follows the one described by Kutz and Speer (1992). Some selected additional features of the computation method are discussed below.

4.2 Integration of the Differential Equations. Within a shooting method, the differential Eqs. (1), (2) are integrated for a sequence of mass flow values until the boundary conditions (5) are satisfied.

The heat flux term in the temperature equation causes the system to be stiff, especially for small mass flows. In general, the integration of a stiff system requires either very short steps or an implicit method. The disadvantages of both are avoided by the following noniterative procedure, which needs only a few steps:

The nonstiff pressure Eq. (1) is integrated with the classical fourth-order, four-stage Runge–Kutta method (for the transformed variable log p_t instead of p_t), while the Implicit Euler method is used four times for the stiff temperature equation (2) (see, e.g., Hairer et al. (1987)). Of course, the equations are not integrated separately, but both methods are geared together stage by stage.

This computation can be done explicitly, which accelerates the computation considerably and is crucial for the performance of the shooting method because it makes the outlet pressure depend noniteratively on the mass flow and thus preserves smoothness.

4.3 Computation of Nodal Pressures. Equation (8), $F(P, T) = 0$, is solved for the nodal pressure vector P while the nodal temperatures T are kept fixed by the Hybrid Method of Powell (1970), which is part of the MINPACK-library (see Moré et al. (1980)).

As the throughflow for each element depends on two nodal pressures only, at each node k the mass balance defect $F^k(P)$ (left-hand side of Eq. (6)) does not depend on more than a few adjacent nodal pressure values. This is exploited in several ways: It accelerates the computation of the Jacobian matrix $\delta F/\delta P$ because this is nearly a byproduct of the evaluation of $F^k(P)$ itself.

Further, the Hybrid method is modified such that the computation of the next iterative vector P is restricted to what we call the "essential subspace." This means that a nodal pressure value is not changed unless this would result in a significant improvement in the mass balance defect. This restricts the computational effort to those network regions with the largest mass balance defects where it is most promising and can lead to a "freezing" of up to 80 percent of the nodal pressure values for one or more iteration steps.

Further it is possible to update the Jacobian matrix whenever an iteration step gained an improvement at nearly no cost by exploiting the approximative relationship

$$\frac{dp_t(1)}{dp_t(0)} \approx Q \frac{p_t(0)}{p_t(1)} . \tag{12}$$

This describes a relation between inlet and outlet pressure for fixed mass flow and inlet temperature. Q is an element specific factor that depends on the angular velocity only; it is $Q = 1$ for $\omega = 0$.

Relation (12) has been found empirically to hold for three and more figures precision and can be backed up by a detailed discussion of the differential equations with the help of the corresponding variational equation and the fundamental lemma (see Hairer et al. (1987), pp. 97 and 56, respectively).

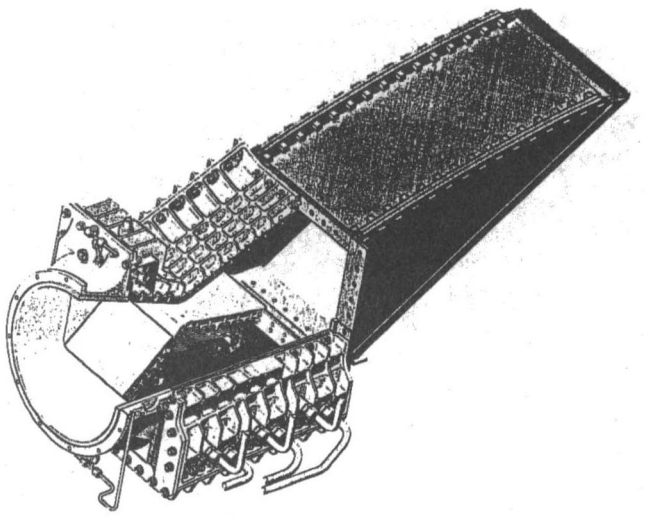


Fig. 4 Test model of a nozzle of a hypersonic vehicle

Downloaded 01 Jun 2010 to 171.66.16.53. Redistribution subject to ASME license or copyright; see http://www.asme.org/terms/Terms_Use.cfm

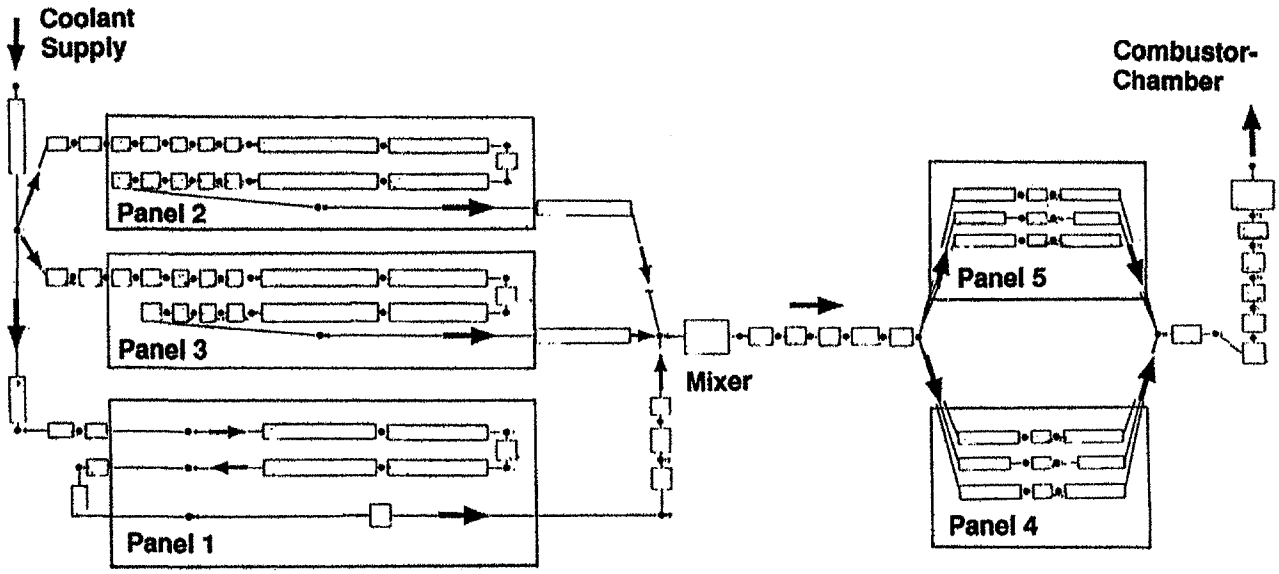


Fig. 5 Network of the cooling system of the nozzle

Thereby, the algorithm can always rely on a rather actual (i.e., up to date) Jacobian matrix and thus avoids the majority of nonimproving iteration steps, which can halve the total step number.

4.4 Path Following Method for Rotating Systems. The path following method computes a solution for the nominal value ω_{nom} of the angular velocity by constructing a sequence of solutions for increasing ω values, starting with $\omega = 0$. As each solution serves as an initial estimate for the next ω value, subsequent solutions stay close to each other and it is unlikely that the procedure leaves the solution path once chosen and skips to a completely different path.

Further names for this method in the literature are incremental loading and homotopy method; here, ω serves as the parameter of homotopy. It is described, e.g., by Ortega and Rheinboldt (1970) and Seydel (1988).

Table 1 Normalized local pressure and temperature values for hypersonic nozzle: $[p_{local}^{normalized} = (p_{local} - p_{outlet}^{measured})/(p_{inlet}^{measured} - p_{outlet}^{measured})$; $T_{local}^{normalized} = (T_{local} - T_{inlet}^{measured})/(T_{outlet}^{measured} - T_{inlet}^{measured})]$

Position	calculat. pressure	measured pressure	calculat. temperat.	measured temperat.
Panel 1 inlet	1.	1.	0.02	0.
Panel 2 inlet	1.	1.	0.02	0.02
Panel 3 inlet	1.	1.	0.02	0.006
Panel 1 outlet	0.65	0.648	0.98	1.07
Panel 2 outlet	0.944	0.877	0.99	0.96
Panel 3 outlet	0.77	0.76	0.7	0.74
Panel 4/5 inlet	0.34	0.42	0.86	0.89
Panel 4/5 outlet	0.027	0.	1.01	1.

Figure 2 shows as a dashed line the path that has been followed. An additional, U-shaped continuation path is sketched as a dotted line, which connects all other points with the same pressure and angular velocity values as the dashed path. This second path leads to the other two solutions at $\omega = \omega_{nom}$, which, however, cannot be results of any path following method because this path cannot be reached from the nonrotating solution (0 percent line).

5 Comparison of Measurements and Calculations

The presented method is tested in three cases of different applications. In each bench mark different physical phenomena are predominant.

5.1 Isothermal Flow in a Multipass System. A simple test case is a nonrotating multipass system of a blade as shown in Fig. 3. The flow function of a multipass blade cooling system is measured and compared with results of a calculation over a wide range of pressure ratios. This is an isothermal test case, so pressure loss is the only physical phenomenon.

It can be seen that the maximum difference between measurement and calculation (prediction) is about 10 percent and occurs at a pressure ratio of about 0.7. At smaller pressure ratios, calculation and measurement fit quite well. Here the difference is only about 4 percent. In this range, the corresponding Reynolds number represents real engine conditions in the blade.

5.2 Coolant Flow With High-Density Heat Transfer. As a second test case, the coolant flow passing a cooling panel in a nozzle of an hypersonic vehicle is presented; see Fig. 4. The corresponding network is shown in Fig. 5.

Because of extremely high gas temperatures and hot gas side heat transfer coefficients, there is a significant increase in coolant enthalpy when passing the panel. Coolant flows in different

Table 2 Normalized local mass flow values for hypersonic nozzle

Mass flow at position	calculated	measured
Panel 1	0.40	0.4
Panel 2	0.19	0.2
Panel 3	0.37	0.4
Overall	0.96	1.0

Downloaded 01 Jun 2010 to 171.66.16.53. Redistribution subject to ASME license or copyright; see http://www.asme.org/terms/Terms_Use.cfm

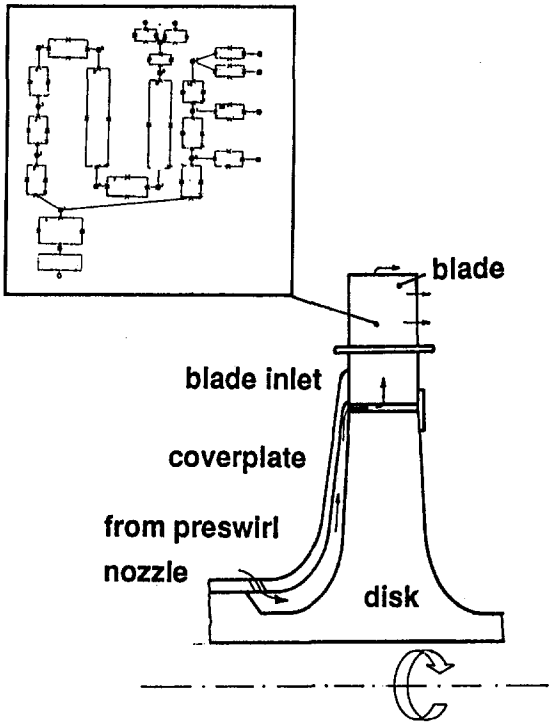


Fig. 6 Scheme of rotor geometry with network of blade cooling configuration

panels of the whole nozzle as well as temperature and pressure in the cooling system were measured in a test sequence under real engine condition.

Table 1 shows calculated and measured normalized static pressure values at several locations. It can be seen that the pressure drop over panels 1 to 3 is predicted quite well. On the other hand, the maximum discrepancy in pressure drop occurs over the mixer (panel 4 inlet) and is overpredicted. Obviously, for the newly developed mixer, the correlation for pressure loss has been assumed too pessimistic.

This leads to an overall coolant mass flow, which is predicted as too small. In Table 2, mass flow values for several panels are presented. The flows are normalized by the overall mass flow in the system. Despite the enormous heat pickup, the overall mass flow is predicted with a discrepancy of less than 4 percent.

As a further parameter, the temperature of the coolant flow, measured at the same locations as the static pressure, is compared with the calculation in a dimensionless form (Table 1). It is shown that the maximum discrepancy is about 8 percent. This difference can be reduced by using more elements for the modeling of panel 1 where the local heat flux varies very strongly.

Nevertheless, the results are encouraging.

5.3 Coolant Mass Flow in a Rotating Blade With Pressure Loss and Heat Transfer. This last test case is a complex overall blade cooling configuration of a high pressure turbine. A cover plate supplies the cooling air for the rotor blade. Figure 6 shows a scheme of its geometry and the network of the blade cooling configuration. After a preswirl nozzle the coolant flow passes a cover plate up to the blade inlet. The coolant flow leaves the multipass system of the blade through film cooling holes.

Pretest simulations have been performed in order to establish the flow characteristics of this system. In an intensively instrumented engine the mass flows are well known.

For the validating calculation, pressure and temperature at the blade inlet and the pressure on the airfoil surface at the exit are prescribed.

In this engine the physical effects cannot be separated from each other. Therefore, the values of the mass flow as the global indicator have been compared. At the aerodynamic design point, the calculated mass flow agrees with the measured one within two-figure accuracy.

Despite the low corrected mass flow value the ambiguities mentioned in section 3.2 were not encountered; the program performed robustly.

6 Conclusion

In this paper, a method for simulating cooling systems in gas turbines is presented. The governing equations based on the steady state one-dimensional conservation of mass, momentum, and energy, are discussed as well as their solution with an efficient integration method. Complex cooling systems are simulated by a network.

The major requirements for industrial application that influenced the development of this simulation program are:

- sufficient accuracy in predicting coolant mass flow, regional coolant side heat transfer coefficients, and local coolant temperatures,
- robustness and efficiency of the computation procedure,
- flexibility in generating different cooling configurations,
- flexibility in varying the geometry,
- transparent display of the comprehensive results in complex cooling systems.

The accuracy of the method is demonstrated in three test cases, where different physical phenomena are predominant.

CPU-time consumption varies from 15 s for the examples presented up to 100 s for large rotating systems on a computer with 45 Mflops.

The simulation program is completed by a graphic preprocessor for the construction and parameterization of networks and a graphic postprocessor for the display of results.

On this platform, generation and modification of different geometric cooling configurations are very flexible. Because of the network technique, no surface model is necessary. In an early design phase, this method is a suitable tool for optimizing cooling systems.

The knowledge basis of the program is formed by the library of calculation procedures for pressure loss and heat transfer coefficients. This can be handled flexibly and the resulting data base will be further enlarged in future.

References

Frommer, A., 1992a, "Verallgemeinerte Diagonaldominanz bei nichtlinearen Funktionen. I," *ZAMM*, Vol. 72, pp. 431–444.

Frommer, A., 1992b, "Verallgemeinerte Diagonaldominanz bei nichtlinearen Funktionen. II," *ZAMM*, Vol. 72, pp. 591–605.

Hairer, E., Nørsett, S. P., and Wanner, G., 1987, *Solving Ordinary Differential Equations, Vol. 1*, Springer-Verlag, Berlin–Heidelberg.

Kahaner, D., Moler, C., and Nash, S., 1989, *Numerical Methods and Software*, Englewood Cliffs, NJ.

Kutz, K. J., and Speer, T. M., 1994, "Simulation of the Secondary Air System of Aero Engines." ASME JOURNAL OF TURBOMACHINERY, Vol. 116, pp. 306–315.

Moré, J. J., Garbow, B. S., and Hillstrom, K. E., 1980, *User Guide for MINPACK-1*, Argonne National Laboratory, Argonne, IL.

Ortega, J. M., and Rheinboldt, W. C., 1970, *Iterative Solution of Nonlinear Equations in Several Variables*, New York.

Powell, M. J. D., 1970, "A Hybrid Method for Nonlinear Equations," *Numerical Methods for Nonlinear Algebraic Equations*, Rabinowitz, ed., Gordon and Breach, pp. 87–114.

Rheinboldt, W. C., 1970, "On M-Functions and Their Application to Nonlinear Gauss–Seidel Iterations and to Network Flows," *J. of Math. Anal. and Appl.*, Vol. 32, pp. 274–307.

Seydel, R., 1988, *From Equilibrium to Chaos. Practical Bifurcation and Stability Analysis*, Elsevier, New York.

Tietz, T. A., and Koschel, W. W., 1991, "Computer Code for the Calculation of the Temperature Distribution of Cooled Turbine Blades," ISABE Paper No. 91-7017.

Downloaded 01 Jun 2010 to 171.66.16.53. Redistribution subject to ASME license or copyright; see http://www.asme.org/terms/Terms_Use.cfm

Transition Modeling Effects on Turbine Rotor Blade Heat Transfer Predictions

A. A. Ameri[1]
University of Kansas Center for Research Inc., Lawrence, KS

A. Arnone
Assistant Professor, Department of Energy Engineering, University of Florence, Florence, Italy

The effect of transition modeling on the heat transfer predictions from rotating turbine blades was investigated. Three-dimensional computations using a Reynolds-averaged Navier–Stokes code were performed. The code utilized the Baldwin–Lomax algebraic turbulence model, which was supplemented with a simple algebraic model for transition. The heat transfer results obtained on the blade surface and the hub endwall were compared with experimental data for two Reynolds numbers and their corresponding rotational speeds. The prediction of heat transfer on the blade surfaces was found to improve with the inclusion of the transition length model and wake-induced transition effects over the simple abrupt transition model.

Introduction

Prediction of the rate of heat transfer on hot surfaces of turbine passages is an important step in the design of optimum blade cooling schemes. In order to predict this quantity accurately in turbine passages, it is necessary to pay special attention to issues relating to physical modeling of turbulence and laminar-turbulent transition. For a given Reynolds number, the turbulent heat transfer rate can be two to three times larger than the laminar value. The transition between the laminar and turbulent regimes can be very long. Thus the boundary layer over a large area of the blade surface can be in a state of transition. In addition to the normal transition process, which is usually of the bypass type, passing of wakes originating from upstream blade rows through the blade passage results in a second independent transition process, which is unsteady. The latter mode of transition, known as wake-induced transition, has been extensively investigated by many researchers (see, for example, Mayle, 1991) and has been shown to be an important process. It enhances the blade heat transfer and should be accounted for in order to obtain an accurate estimate of the passage wall heat transfer.

A thorough review of literature on the topic of heat transfer in turbomachinery can be found in Simoneau and Simon (1993). Previous transition and turbulence modeling efforts aimed at predicting the rate of heat transfer in turbine passages have mostly utilized either an algebraic model or a low-Reynolds-number two-equation model.

With an algebraic model it is necessary to provide the location of the onset and the evolution path of transition. Rao and Delaney (1992) assumed instantaneous transition past the stagnation point for their unsteady full stage calculations. Ameri and Arnone (1991) and Dorney and Davis (1991) used the experimental results to prescribe the onset of transition on the blade surface. Recently Boyle and Giel (1992) applied a transition model to the midspan plane of the blade and extended the result to the whole span.

Choi and Knight (1988) and Hah (1989) were among the first workers to predict the heat transfer on the surfaces of turbine blades using low Reynolds number two-equation models. The work of Schmidt and Patankar (1988) and their PTM (Production Term Modification) model was performed to include physically based criteria in this type of modeling. Although these models perform well in the fully turbulent regime, they do not perform sufficiently well in the transitional regime. Much work needs to be done to bring the transition modeling ability of these models to a consistent and reliable level for routine use.

It is the purpose of this work to investigate the effect of transition modeling on the surface heat transfer of turbine blades as predicted by three-dimensional Reynolds averaged Navier–Stokes computations. In this work prediction of time-averaged heat transfer rates from the surfaces of a rotating blade passage will be addressed. The wake-induced transition, which is a periodic unsteady effect, is accounted for in a time averaged sense. As the utilization of algebraic modeling affords the possibility to manipulate the eddy viscosity field with relative ease this type of modeling approach was selected for this work.

In the following sections the transition models employed will be described and the method of implementation will be presented. Finally the results of the application of the models to three-dimensional turbine rotor flows will be discussed and comparison of heat transfer results with experimental data of Blair (1991) will be provided.

Transition and Turbulence Models

Transition Model. Mayle (1991), in his review paper, describes the transition process on the blade as the total effect of two independent transition processes, namely, a "normal mode" and an unsteady "wake-induced transition." For each mode he suggests models to account for the start of transition and distribution of intermittency factor downstream of that location. To estimate the location of the start of transition the following correlation suggested by Mayle (1991) was used:

$$\mathrm{Re}_\theta = 400Tu^{-5/8} \quad \text{for} \quad Tu \geq 3.0 \tag{1}$$

Here Re_θ is the Reynolds number based on the momentum thickness and Tu is turbulence intensity expressed as a percent of free-stream velocity. As can be seen, the effect of turbulence intensity is to hasten the onset of transition by lowering the transition momentum thickness Reynolds number. The value of θ is calculated as was done by Boyle (1992) using Thwaite's approximation:

$$\theta^2(s1) = \frac{0.45\nu}{U_e^6(s1)} \int_0^{s1} U_e^5 ds \tag{2}$$

[1] Present address: AYT Corp., c/o NASA Lewis Research Center, Cleveland, OH 44135.

Contributed by the International Gas Turbine Institute and presented at the 39th International Gas Turbine and Aeroengine Congress and Exposition, The Hague, The Netherlands, June 13–16, 1994. Manuscript received by the International Gas Turbine Institute February 4, 1994. Paper No. 94-GT-22. Associate Technical Editor: E. M. Greitzer.

Copyright © 1996 by ASME

Downloaded 01 Jun 2010 to 171.66.16.53. Redistribution subject to ASME license or copyright; see http://www.asme.org/terms/Terms_Use.cfm

This eliminated the requirement of a priori knowledge of location of the edge of the boundary layer. In this expression ν is the free-stream kinematic viscosity and s is the local surface distance from the leading stagnation point. The quantity U_e is the edge velocity, which is computed using the blade surface static to local total relative pressure ratio. The integration is carried out along the streamwise grid lines. This is acceptable as long as the inviscid streamlines are reasonably aligned with the grid lines.

Downstream of the onset of transition the following expression was used for the distribution of intermittency:

$$\gamma_n(s) = (1. - \exp[-\hat{n}\sigma(\mathrm{Re}_s - \mathrm{Re}_{st})^2]) \tag{3}$$

where $\hat{n}\sigma$ is a dimensionless spot production rate, Re_s is the local Reynolds number, and the subscript t signifies the value at the onset of transition. For zero pressure gradient the parameter was calculated using a correlation provided by Mayle (1991), namely,

$$\hat{n}\sigma = 1.5(10)^{-11}Tu^{7/4} \tag{4}$$

For nonzero pressure gradients, values of the turbulent spot production rate at transition were obtained by employing a graphic correlation suggested by Mayle (1991). The transition length has been shown to be dependent upon the acceleration parameter at transition, with the effect of turbulence intensity on transition being more pronounced for favorable than that for unfavorable pressure gradients.

For the time-averaged wake induced intermittency Mayle and Dullenkopf (1991) suggested the following expression:

$$\gamma_w(s) = 1 - \exp\left[-0.302\omega_r\left(\frac{s - s_{tw}}{c}\right)\right] \tag{5}$$

where c is the axial chord, $\omega_r = \omega c/U$ is the reduced wake passing frequency with U representing the magnitude of the incident velocity, and ω is the wake passing frequency equal to the product of the rotation rate and the number of upstream blades. Here we have assumed that the location of the onset of wake-induced transition, s_{tw}, follows the same expression (1) that was used for the onset of normal transition, with the maximum intensity of turbulence in the wake replacing the free-stream turbulence. The use of expression (1) was adopted in the absence of a commonly accepted correlation for the onset of wake induced transition. Given all of the above the resultant time-averaged intermittency can be calculated using the expression suggested by Mayle and Dullenkopf (1991):

$$\tilde{\gamma}(s) = 1 - [1 - \gamma_n(s)][1 - \tilde{\gamma}_w(s)] \tag{6}$$

Turbulence Model. The Baldwin–Lomax (1978) model has been used to account for turbulence effects. The resultant eddy viscosity is calculated as a weighted average of contributions from the endwalls μ_{ew} and the blade surface μ_{bl} as follows:

$$f = \frac{1/d_{ew}^2}{1/d_{bl}^2 + 1/d_{ew}^2} \tag{7}$$

$$\mu_t = f\mu_{ew} + (1 - f)\mu_{bl}\tilde{\gamma}(s) \tag{8}$$

where d stands for distance from the no-slip boundary. The turbulent thermal diffusivity is calculated from:

$$\alpha_t = \frac{\mu_t}{\rho\ \mathrm{Pr}_t} \tag{9}$$

where ρ is the density. For the calculation of the turbulent heat flux a constant value of turbulent Prandtl number, $\mathrm{Pr}_t = 0.9$, was used. It is a fact that the value of Pr_t is not constant and is quite large very near the no-slip boundaries (Kays and Crawford, 1980). However, it was shown by Boyle (1991) that the difference between the solutions with constant and variable turbulent Prandtl number is very small.

Table 1 Run conditions

	CASE A	CASE B
Re_2	2.73E5	5.84E5
N(rpm)	160	410
β_1(degrees)	40°	40°

Computational Method

The code TRAF3D (TRAnsonic Flow 3D) (Arnone, 1994), which uses a cell-centered finite volume approach, was employed for the present computations. The governing equations solved are the conservative form of the Reynolds-averaged Navier–Stokes equation in a curvilinear coordinate system in terms of the absolute velocity and specific total energy. Perfect gas law is used as the equation of state. Variation of viscosity with temperature was assumed to follow Sutherland's law (Schlichting, 1979). The equations are solved using a four-stage Runge–Kutta time-stepping method. To accelerate convergence, the code employs the Full Approximation Storage (FAS) multigrid method originally devised by Brandt (1979) and Jameson (1983). Variable coefficient implicit smoothing of the residuals is performed to further increase the rate of convergence. A three-dimensional extension of eigenvalue scaling of the artificial dissipation terms, first devised by Martinelli (1987), was adopted to prevent odd-even decoupling and to capture shocks. Further details of the numerical scheme and the implementation of the boundary conditions are given by Arnone (1994), Arnone et al. (1992) and Ameri and Arnone (1991). The tip clearance is handled by imposing periodicity conditions across the airfoil without solving for the flow in the tip clearance.

Computational Grid

A nonperiodic C-type grid (Arnone et al., 1992), which uses unequal numbers of grid points on the pressure side and suction side of the blade, is employed for the discretization of the flow field. The pitchwise grid is constructed first by generating an inviscid grid using an elliptic procedure. The viscous grid is then made by embedding grid lines in the vicinity of the no-slip boundaries with the desired wall spacing. The hub-to-tip grid is generated by stacking. A geometric stretching is used in the spanwise direction with the spacing of the grid at the hub and tip specified.

With nonperiodic grids, the relative skewness of the grid lines is minimized and the grid lines are reasonably orthogonal to the blade surface throughout the boundary layer.

Results

The experimental results of Blair (1991) were used to validate the numerical calculations. These experiments provide heat transfer measurements on the surface of a turbine rotor blade and its hub endwall. The measurements were performed for the design and off-design conditions, and cover a range of inlet incidence, Reynolds numbers, and surface roughness parameters. The cases examined here are for a smooth surface with design incidence and two Reynolds numbers at their corresponding rotational speeds. The flow conditions considered are given in Table 1.

For the present calculations the free-stream turbulence intensity, Tu_e, was measured to be 3.5 percent (Dring et al., 1987) and was assumed to vary along the blade using the following relationship:

Downloaded 01 Jun 2010 to 171.66.16.53. Redistribution subject to ASME license or copyright; see http://www.asme.org/terms/Terms_Use.cfm

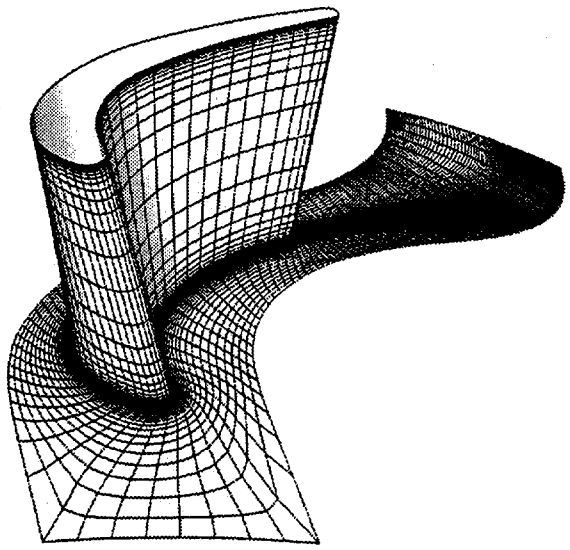


Fig. 1 UTRC rotor and a typical grid

$$Tu_e \times U_e = \text{const} \qquad (10)$$

The maximum turbulence intensity in the wake was reported to be 10.5 percent. The turbulence intensity values given here are percentages of the relative incoming velocities.

The heat transfer results were calculated in terms of the Stanton number in a manner consistent with the experimental results. The definition used for the Stanton number is:

$$\text{St} = \frac{-\partial T/\partial n|_w c}{(T_w - T_0)(\text{Re}_2 \text{ Pr})}$$

Here T is the static temperature, n is the direction vector normal to the blade, Re_2 is the Reynolds number based on relative exit conditions, and the subscripts w and 0 refer to wall and total absolute conditions. The boundary layer on the endwall is assumed to be fully turbulent starting from the inlet boundary condition with a specified 5 percent boundary layer thickness. The inlet velocity profile is assumed to follow the $\frac{1}{7}$th power law. The experiments were performed with constant flux thermal boundary condition on the blade surface and the endwalls. In order to achieve faster convergence speeds, preliminary calculations aimed at establishing grid independence of the solutions as well as showing the effect of transition models on heat transfer were performed with a constant temperature boundary condition. Final results are provided using constant heat flux boundary conditions.

Blade Surface Heat Transfer. Figure 1 shows the blade and the basic constructs of the grid. The density of the pitchwise grid was chosen by experimentation using a two-dimensional code. Boyle and Giel (1992) report that a minimum of 50 grid planes in the spanwise direction is necessary to obtaining an accurate heat transfer solution. The grid densities chosen for computations were $193 \times 49 \times 65$ or $193 \times 49 \times 97$. The finer grid was constructed by holding the grid spacing at the solid surfaces constant and refining the grid in the spanwise direction. The same grids were used for both the high and the low-Reynolds-number calculations. The grid spacing of the first grid point away from the blade surface in terms of $y+$, nondimensional distance in wall coordinates, for the higher Reynolds number calculation is presented in Fig. 2. The spacing is specified such that the maximum value of $y+$ computed at the first grid point away from the solid surfaces is close to unity.

Calculations using abrupt transition, normal transition, and normal plus wake-induced transition models were carried out to compare the heat transfer predictions and their agreement

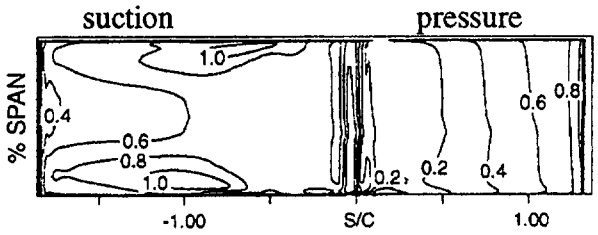


Fig. 2 Blade surface y^+ contours, case *B*; $193 \times 49 \times 65$ grid

with the experimental data at midspan and are shown in Fig. 3. As described in the previous section, the preliminary calculations were carried out using the constant temperature boundary condition. Calculations using this boundary condition are shown by the symbol "*T*" and those performed with constant heat flux boundary condition are shown by the symbol "*H*" in the legend of these figures. Also calculations using the abrupt transition, normal (with transition length) transition and normal plus wake transition are signified by symbols *A*, *N*, and *NW*, respectively.

Results of the calculations with constant-temperature boundary condition using the abrupt or normal transition models as can be seen from Fig. 3, do not match the experimental data outside the fully turbulent regime. The results obtained with the normal intermittency model constitute the lower bound on heat transfer as the wake passing frequency in Eq. (5) approaches zero. Inclusion of the wake-induced transition model results in the distributions shown with the dotted lines. The improvement in the prediction of heat transfer on the suction side is quite significant. The pressure side heat transfer predictions are, however, not as satisfactory. Application of the constant heat flux boundary condition results in the predictions shown as solid lines. As can be seen, while the predictions on the suction side are within the experimental error, the prediction of the heat transfer on the pressure side of the blade is limited only to the downstream portion. The line plots show that overall best results are obtained using the combined normal mode and wake-induced transition model.

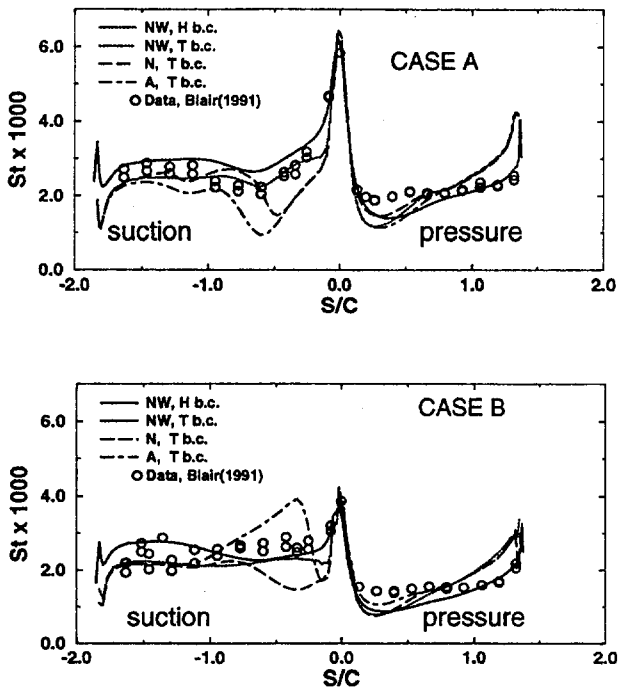


Fig. 3 Midspan Stanton number, three-dimensional calculations

Downloaded 01 Jun 2010 to 171.66.16.53. Redistribution subject to ASME license or copyright; see http://www.asme.org/terms/Terms_Use.cfm

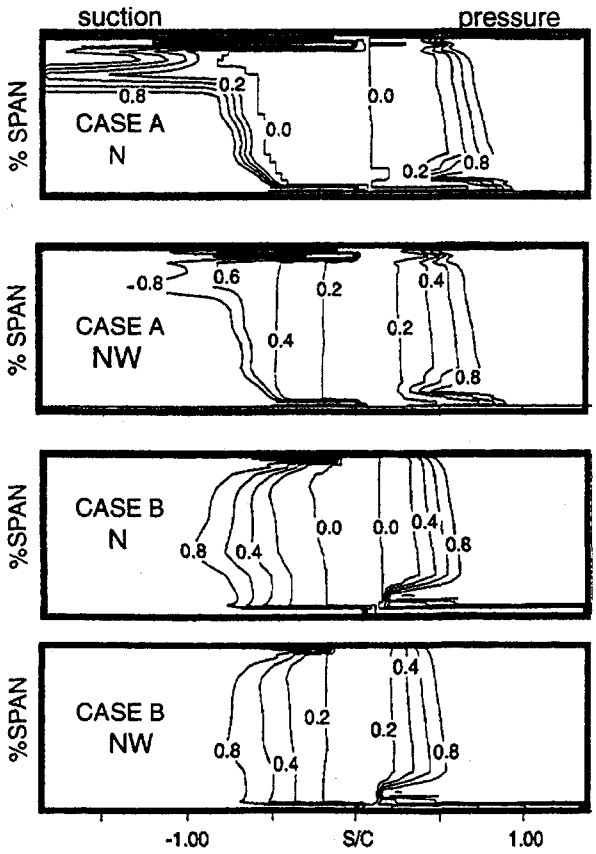


Fig. 4 Contours of intermittency factor, normal (*N*) and normal + wake (*NW*) transition models, 193 × 49 × 65 grid

Figure 4 presents the distribution of the normal (N) and normal plus wake intermittency factor (NW) on the blade for both cases considered. Contours of "0.0" intermittency were added to the normal intermittency contours to delineate the location of the start of transition. The extent of transition is governed by the free-stream turbulence and by the value of acceleration parameter at the location of the onset of transition. Thus, if the acceleration parameter indicates the pressure gradient is favorable, transition will be drawn out and vice versa. It should be noted that the value of intermittency approaches unity exponentially as shown in Eqs. (3) and (5). The variation of the intermittency parameter, close to the endwalls calculated here, is due to the manner in which the location of stagnation point was calculated. The flow in the vicinity of endwalls experiences some overturning, thereby deviating from the nominal design inlet angle and hence shifting the location of maximum pressure (stagnation point) farther downstream away from the geometric stagnation point along the pressure side.

The experimental measurements along with the computed contours of Stanton number distribution on the blade surface for the two cases considered are shown in Figs. 5 and 6. The surface and hub endwall heat transfer contour plots presented in this paper were obtained using the combined normal mode and wake induced modeling.

Results of the grid study are presented in Figs. 5(a) and 5(b) for case A and 6(a) and 6(b) for case B. Those figures show that the predictions obtained with the 193 × 49 × 65 grid are sufficiently grid independent. The measured contours of Stanton number are presented in Figs. 5(c) and 6(c) and the final predictions using the chosen grid and constant heat flux boundary condition are shown in Figs. 5(d) and 6(d). The major discrepancy between the predicted and experimental results occurs on the pressure side of the blade where the flow is transitional. A possible explanation for this discrepancy can perhaps be the enhancement of the heat transfer due to free-stream turbulence. This mechanism, not dealt with in this paper, has been recently revisited by Dullenkopf and Mayle (1994). As can be seen from the plots, the comparison between the experiments and the computations is generally favorable. All the salient features such as the enhancement of heat transfer in the vicinity of the hub and casing endwall as well as the increase in the leading edge region close to the hub endwall are captured.

Endwall Heat Transfer. In the course of this study the hub endwall heat transfer was also predicted. The reader is reminded that the endwall boundary layer is assumed to be fully turbulent starting from the upstream boundary and no transition modeling was performed for the endwall. The heated endwall surface in the experiment extended from 0.24 × axial chord upstream of the leading edge to a location of 0.21 × axial chord

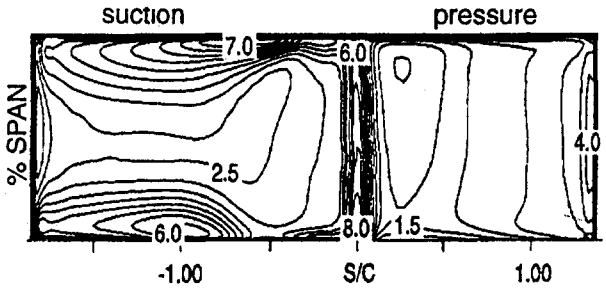


Fig. 5(a) Calculated surface Stanton number × 1000 contours, case A, 193 × 49 × 65 grid; constant wall temperature

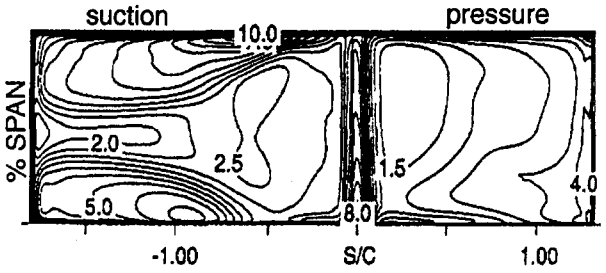


Fig. 5(b) Calculated surface Stanton number × 1000 contours, case A, 193 × 49 × 97 grid; constant wall temperature

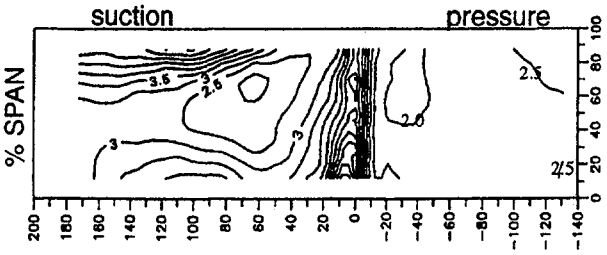


Fig. 5(c) Surface Stanton number × 1000 contours, Case A, data of Blair (1991)

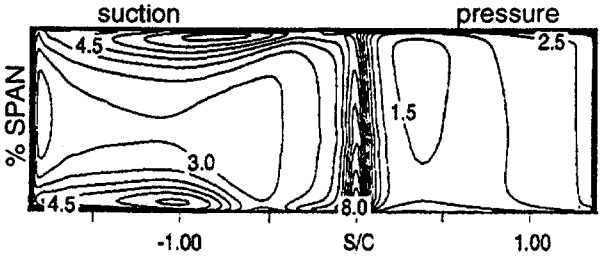


Fig. 5(d) Calculated surface Stanton number × 1000 contours, case A, 193 × 49 × 65 grid; constant wall heat flux

Downloaded 01 Jun 2010 to 171.66.16.53. Redistribution subject to ASME license or copyright; see http://www.asme.org/terms/Terms_Use.cfm

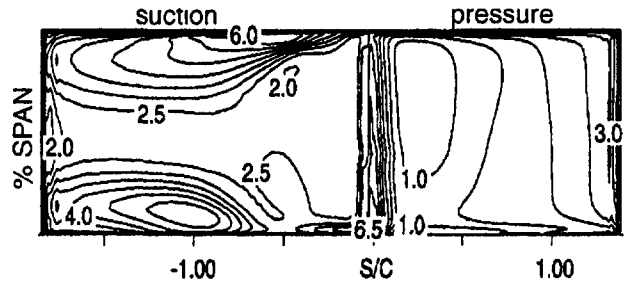


Fig. 6(*a*) Calculated surface Stanton number × 1000 contours, case *B*, 193 × 49 × 65 grid; constant wall temperature

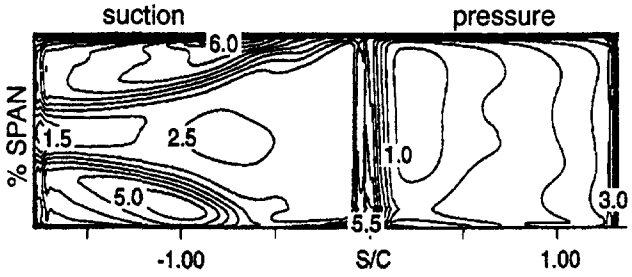


Fig. 6(*b*) Calculated surface Stanton number × 1000 contours, case *B*, 193 × 49 × 97 grid; constant wall temperature

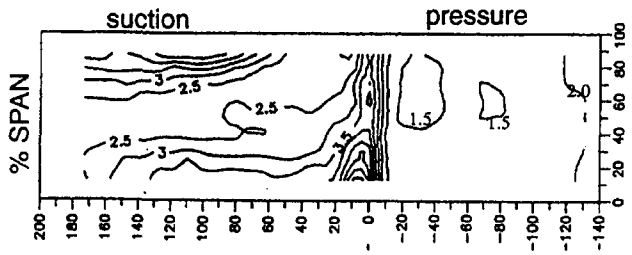


Fig. 6(*c*) Surface Stanton × 1000 contours, case *B*, data of Blair (1991)

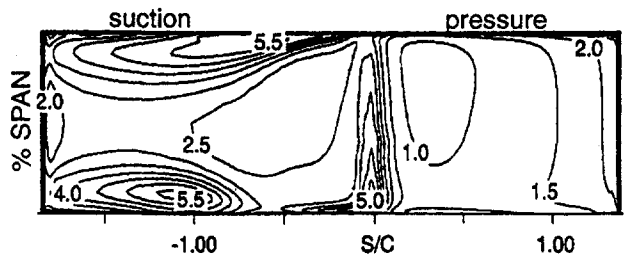


Fig. 6(*d*) Calculated surface Stanton number × 1000 contours, case *B*, 193 × 49 × 65 grid; constant wall heat flux

downstream of the trailing edge. These locations are very near the edges of the rotor. The calculation domain extended from 60 percent axial chord upstream of the leading edge where heating of the endwall was initiated, to 100 percent axial chord downstream of the blade trailing edge. Some calculations were also performed with the location of start and end of heating, and beginning and end of rotation similar to the experimental setup. It was found that the predictions of heat transfer so obtained were very close to the simpler setup, within the area covered by the experimental measurements.

Figure 7 presents the variation of the distance of the first grid point away from the hub endwall in dimensionless wall coordinates for the higher Reynolds number case considered. The location of the first grid plane away from the endwall is seen to be well within the viscous sublayer.

Figures 8 and 9 present the experimental as well as the computed contours of Stanton number on the endwalls. The

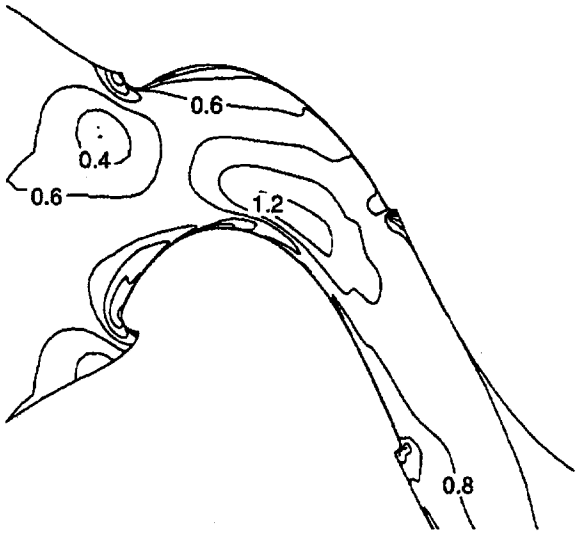


Fig. 7 Endwall $y+$ distribution, case *B*

results presented here were obtained with the baseline 193 × 49 × 65 grid. Calculations made with the finer grid showed that space convergence was achieved; however, those results will not be presented here in the interest of space economy. Generally the results exhibit good agreement with the experimental data. Some notable features of the results and their comparison with the experimental measurements follow: The enhancement of heat transfer close to the blade leading edge is shown in the experimental measurements and captured by the numerical calculations. Within the passage, the maximum level of heat transfer predicted by the numerical calculations in case *A* was computed to be 0.0045 while the experimental results show a maximum value of 0.0035. In case *B*, this maximum is only off by 12.5 percent. The contours of Stanton number of 0.003 and 0.0035 for case *A*, and contours of 0.0025 and 0.003 for case *B* are remarkably well captured by the numerical calculations.

Computational Requirements

The code requires 60 words of memory per grid point. The CPU time requirement was 21.0E-6 seconds per iteration per grid point on the NAS Cray C90. Typically the computations required 800 multigrid cycles for the constant temperature boundary condition runs and 2000 to 3000 cycles for the constant heat flux boundary condition runs to converge. The calculations were deemed converged, once the heat transfer results stopped changing during the iteration process. The calculations were performed with two or three levels of multigrid. It should be noted that the predictions were made for experimental conditions that were in the incompressible flow regime. The present code is best suited to the transonic flow regime. It is expected that the speed of convergence in the more realistic Mach number regimes typical of gas turbine operations will be improved.

Summary and Conclusions

In this work the effect of transition modeling on the prediction of heat transfer on the surfaces of a rotating turbine blade passage was studied. The results from the large-scale rotating rig of Blair (1991) were used for comparison. Grid study was undertaken to ensure reasonable grid independence of the solutions. This was done using constant wall temperature boundary condition since the constant flux condition required longer CPU time for complete convergence. The inclusion of a simple model to account for the time average of unsteady effect of wake passing on transi-

Downloaded 01 Jun 2010 to 171.66.16.53. Redistribution subject to ASME license or copyright; see http://www.asme.org/terms/Terms_Use.cfm

tion was found to improve the prediction of heat transfer on the blade surface where the predicted contours of heat transfer matched the experimental results very well. The heat transfer predictions on the endwall were found to be satisfactory. With the exception of the maximum level of heat transfer inside the passage for the low Reynolds number case, the computed contours reasonably matched the measured contours.

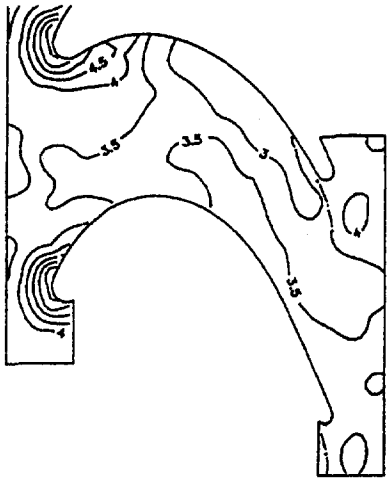


Fig. 8(*a*) Endwall Stanton number × 1000, case *A*, data of Blair et al. (1991)

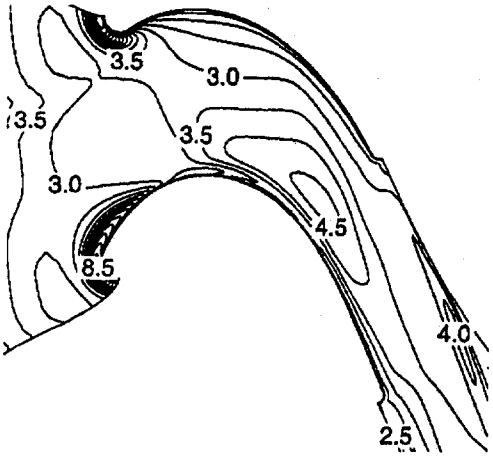


Fig. 8(*b*) Calculated Stanton number × 1000 contours, case *A*, constant heat flux B.C., 193 × 49 × 65 grid

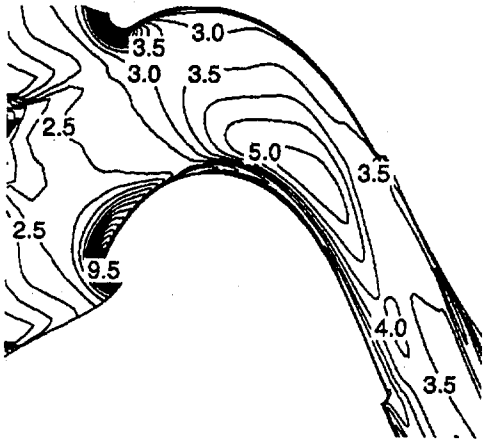


Fig. 8(*c*) Calculated Stanton number × 1000 contours, case *A*, constant temperature B.C., 193 × 49 × 65 grid

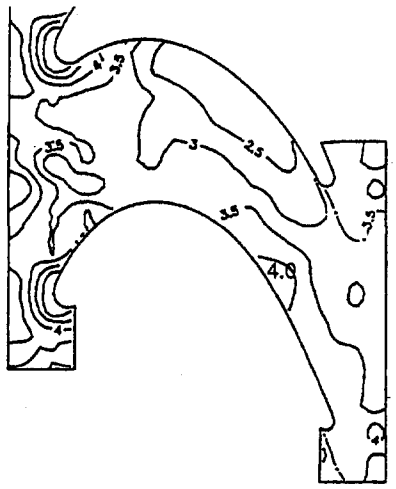


Fig. 9(*a*) Endwall Stanton number × 1000, case *B*, data of Blair et al. (1991)

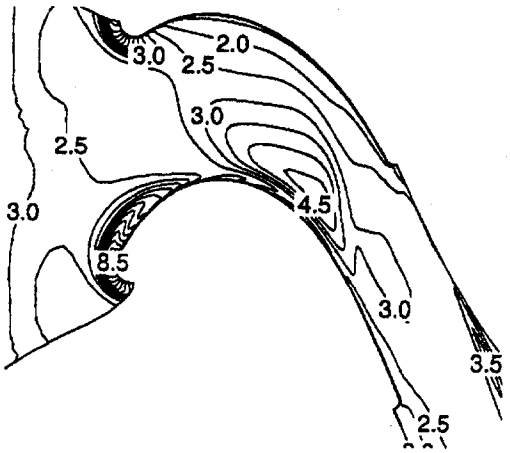


Fig. 9(*b*) Calculated Stanton number × 1000 contours, case *B*, constant heat flux B.C., 193 × 49 × 65 grid

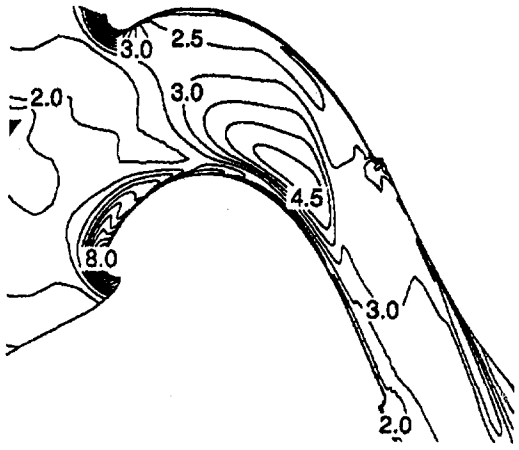


Fig. 9(*c*) Calculated Stanton number × 1000 contours, case *B*, constant temperature, B.C., 193 × 49 × 65 grid

Acknowledgments

The authors wish to thank Dr. Raymond Gaugler, chief of Turbomachinery Flow Physics branch of NASA Lewis Research Center, and Dr. Louis Povinelli, chief of the Internal Fluid Mechanics Division of NASA Lewis Research Center, for their support of this work. Thanks are also due to Mr.

Downloaded 01 Jun 2010 to 171.66.16.53. Redistribution subject to ASME license or copyright; see http://www.asme.org/terms/Terms_Use.cfm

Robert Boyle for his invaluable suggestions. The calculations performed in this work were performed on the Cray-C90 supercomputer of the NAS facility at NASA Ames Research Center.

References

Ameri, A. A., and Arnone, A., 1991, "Three Dimensional Navier–Stokes Analysis of Turbine Passage Heat Transfer," AIAA Paper No. 91–2241.

Ameri, A. A., and Arnone, A., 1994, "Comparison of Heat Transfer Predictions Using a Zero Equation and a Two-Equation Turbulence Model," ASME Paper No. 94-GT-122.

Arnone, A., 1994, "Viscous Analysis of Three-Dimensional Rotor Flow Using a Multigrid Method," ASME JOURNAL OF TURBOMACHINERY, Vol. 116, pp. 435–445.

Arnone, A., Liou, M. S., and Povinelli, L. A., 1992, "Navier–Stokes Solutions of Transonic Cascade Flows Using Non-periodic *C*-Type Grids," *AIAA Journal of Propulsion and Power,* Vol. 8, No. 2, pp. 410–417.

Baldwin, B. S., and Lomax, H., 1978, "Thin Layer Approximation and Algebraic Model for Separated Turbulent Flows," AIAA Paper No. 78-0257.

Blair, M. F., 1991, "The Effects of Reynolds Number, Rotor Incidence Angle, and Surface Roughness on the Heat Transfer Distribution in a Large Scale Turbine Rotor," UTRC report No. R91-970057-3.

Boyle, R. J., 1991, "Navier–Stokes Analysis of Turbine Blade Heat Transfer," ASME JOURNAL OF TURBOMACHINERY, Vol. 113, pp. 392–403.

Boyle, R. J., and Giel, P. W., 1992, "Three-Dimensional Navier–Stokes Heat Transfer Predictions for Turbine Blade Rows," AIAA Paper No. 92-3068.

Brandt, A., 1979, "Multi-level Adaptive Computations in Fluid Dynamics," AIAA Paper No. 79-1455.

Choi, D., and Knight, C. J., 1988, "Computation of 3d Viscous Cascade Flows," AIAA Paper No. 88-0363.

Dorney, D. J., and Davis, R., 1991, "Navier–Stokes Analysis of Turbine Blade Heat Transfer and Performance," ASME JOURNAL OF TURBOMACHINERY, Vol. 114, pp. 795–806.

Dring, R. P., Joslyn, H. D., and Blair, M. F., 1987, "The Effects of Inlet Turbulence and Rotor/Stator Interactions on the Aerodynamics and Heat Transfer of a Large-Scale Rotating Turbine Model," NASA Contractor Report 179469.

Dullenkopf, M., and Mayle, R. E., 1994, "The Effects of Incident Turbulence and Moving Wakes on Laminar Heat Transfer in Gas Turbines," ASME JOURNAL OF TURBOMACHINERY, Vol. 116, pp. 23–28.

Hah, C., 1989, "Numerical Study of Three-Dimensional Flow and Heat Transfer Near the Endwall of a Turbine Blade Row," AIAA Paper No. 89-1689.

Jameson, A., 1983, "Transonic Flow Calculations," MAE Report 1651, MAE Department, Princeton University.

Kays, W. M., and Crawford, M. E., 1980, *Convective Heat and Mass Transfer,* 2nd ed., McGraw-Hill, New York.

Martinelli, L., 1987, "Calculations of Viscous Flows With a Multigrid Method," Ph.D. thesis, Princeton University, Princeton, NJ.

Mayle, R. E., 1991, "The Role of Laminar–Turbulent Transition in Gas Turbine Engines," ASME JOURNAL OF TURBOMACHINERY, Vol. 113, pp. 509–537.

Mayle, R. E., and Dullenkopf, K., 1991, "More on the Turbulent-Strip Theory for Wake-Induced Transition," ASME JOURNAL OF TURBOMACHINERY, Vol. 113, pp. 428–432.

Rao, K. V., and Delaney, R. A., 1992, "Vane-Blade Interaction in a Transonic Turbine, Part II—Heat Transfer," AIAA Paper No. 92-3324.

Schlichting, H., 1979, *Boundary Layer Theory,* 7th ed., McGraw-Hill, New York.

Schmidt, R. C., and Patankar, S. V., 1988, "Two Equation Low-Reynolds Turbulence Modeling of Transitional Boundary Layer Flow Characteristic of Gas Turbine Blades," NASA-CR 4145.

Simoneau, R. J., and Simon, F. F., 1993, "Progress Towards Understanding and Predicting Heat Transfer in the Turbine Gas Path," *International Journal of Heat and Fluid Flow,* Vol. 14, No. 2, pp. 106–127.

Downloaded 01 Jun 2010 to 171.66.16.53. Redistribution subject to ASME license or copyright; see http://www.asme.org/terms/Terms_Use.cfm

Flow and Heat Transfer Behavior in Transitional Boundary Layers With Streamwise Acceleration

F. J. Keller

T. Wang

Department of Mechanical Engineering,
Clemson University,
Clemson, SC

The effects of streamwise acceleration on a two-dimensional heated boundary layer undergoing natural laminar–turbulent transition were investigated with detailed measurements of momentum and thermal transport phenomena. Tests were conducted over a heated flat wall with zero pressure-gradient and three levels of streamwise acceleration: $K \equiv (\nu/\bar{U}_\infty^2)(d\bar{U}_\infty/dx) = 0.07$, 0.16, and 0.25×10^{-6}. Free-stream turbulence intensities were maintained at approximately 0.5 percent for the baseline case and 0.4 percent for the accelerating cases. A miniature three-wire probe was used to measure mean velocity and temperature profiles, Reynolds stresses, and Reynolds heat fluxes. Transition onset and end were inferred from Stanton numbers and skin-friction coefficients. The results indicate that mild acceleration delays transition onset and increases transition length both in terms of distance, x, and Reynolds number based on x. Transition onset and length are relatively insensitive to acceleration in terms of momentum thickness Reynolds number. This is supported by the boundary layer thickness and integral parameters, which indicate that a favorable pressure gradient suppresses boundary layer growth and development in the transition region. Heat transfer rates and temperature profiles in the late-transition and early-turbulent regions lag behind the development of wall shear stress and velocity profiles. This lag increases as K increases, indicating that the evolution of the heat transport is slower than that of the momentum transport. Comparison of the evolution of rms temperature fluctuations to the evolution of Reynolds normal stresses indicates a similar lag in the rms temperature fluctuations.

Introduction

Knowledge of the physics involved in momentum and thermal transport in the transitional boundary layer can be applied to the external flow over gas turbine vanes and blades. For a commercial gas turbine engine, it is common for as much as 50 to 80 percent of the turbine blade surface to be covered with flow undergoing transition (Turner, 1971). Most modeling codes for heat transfer rely on some form of Reynolds analogy to predict thermal loading, i.e., inferring the thermal transport directly from the momentum transport. Recent experimental investigations indicate a breakdown in this analogy in the transitional flow process (Blair, 1982, 1992; Wang et al., 1985; Sharma, 1987; Volino and Simon, 1991). Therefore, the conventional technique of basing heat transfer modeling on a constant value or a multiple-layer model of the turbulent Prandtl number may be inadequate. Since turbine blades are exposed to a wide range of pressure gradients (Mayle, 1991), the reported discrepancy between fluid mechanics and heat transfer is especially important. Recognition and understanding of the underlying mechanisms involved in this discrepancy between momentum and thermal transport are essential to improving the accuracy of thermal load predictions. The purpose of this research program is to investigate the effects of streamwise acceleration on a two-dimensional boundary layer undergoing natural transition. The transport mechanisms within the boundary layer must be explored to determine what discrepancies exist between the momentum and thermal transport, thereby addressing the validity of Reynolds analogy for use in the transition process. The results of this study have served as a valuable reference for comparison with the results of streamwise acceleration in elevated free-stream turbulence conditions (Zhou and Wang, 1993).

Most correlations for transition onset incorporate the combined effects of free-stream turbulence intensity (FSTI) and pressure gradient. In flows with low free-stream turbulence, large discrepancies exist between these methods in predicting transition onset, especially for favorable pressure gradients (Arnal, 1984). For flows with low FSTI, the pressure gradient significantly affects the transition onset. As FSTI increases, the pressure gradient has less of an effect (Abu-Ghannam and Shaw, 1980). The experimental results of many researchers, for example, Turner (1971), Abu-Ghannam and Shaw (1980), Blair (1982, 1992), Narasimha (1985), and Rued and Wittig (1985, 1986), showed that a favorable pressure gradient increases the length of transition. These results can be used to predict the fluid mechanics and momentum transport in transitional boundary layers and to predict heat transfer, provided that some form of Reynolds analogy holds. However, for favorable pressure gradient flow, experimental evidence indicates a breakdown of Reynolds analogy. Blair (1982, 1992), Sharma (1987), and Volino and Simon (1991) determined that the length of transition for accelerating flows is longer for the thermal than the momentum boundary layer. By comparing the Stanton numbers and temperature profiles to the shape factor and velocity profiles, Blair (1992) determined that the physical length of transition is one-third longer for heat transfer than it is for flow with $K = 0.20 \times 10^{-6}$. Blair reasoned that the difference between the velocity and the temperature profiles is produced by the streamwise pressure distribution. The boundary layer velocity distribution depends directly on mainstream acceleration, as shown by the equations of motion. The temperature distribution is only indirectly linked to the pressure gradient through the effect of acceleration on the turbulent transport of heat. These results indicate that inferring transition information

Contributed by the International Gas Turbine Institute and presented at the 39th International Gas Turbine and Aeroengine Congress and Exposition, The Hague, The Netherlands, June 13–16, 1994. Manuscript received by the International Gas Turbine Institute February 4, 1994. Paper No. 94-GT-24. Associate Technical Editor: E. M. Greitzer.

Copyright © 1996 by ASME

Downloaded 01 Jun 2010 to 171.66.16.53. Redistribution subject to ASME license or copyright; see http://www.asme.org/terms/Terms_Use.cfm

from the heat transfer measurements alone is unreliable for accelerating flow and that transition prediction based on fluid mechanics measurements will not accurately predict the heat transfer in transition.

Information regarding the mean flow structure within the transitional boundary layer for a zero-pressure gradient is well documented. Most of the results isolate the effects of FSTI on heat transfer and flow structure. Typical parameters investigated are mean velocity and temperature profiles, fluctuating turbulent velocity and Reynolds shear stresses (u'^2, v'^2, $\overline{uv}$), and Reynolds heat fluxes ($\overline{vt}$, $\overline{ut}$). The highlights of these results are listed below.

1 The streamwise fluctuating turbulent velocity (u') reaches a peak value of approximately 18 percent of U_∞, regardless of the level of FSTI (Schubauer and Klebanoff, 1956; Wang et al., 1985; Kim et al., 1989; Kuan and Wang, 1990). This value is greater than the value for fully turbulent flow.
2 The u' profiles in the transition region are characterized by two peaks, one near-wall peak and a second peak midway through the boundary layer (Wang et al., 1985; Sohn et al., 1989; Kuan and Wang, 1990). The cause of the second peak is still the subject of controversy.
3 The cross-stream fluctuating turbulent velocity (v') reaches a constant value much earlier than u', indicating that the flow in a transitional boundary layer is less isotropic than the flow of a fully turbulent boundary layer. The location of the peak in v' in the streamwise direction coincides with the location of the peak in u' in the streamwise direction (Kuan and Wang, 1990).
4 Measurements of the average Reynolds cross-stream heat flux ($\overline{vt}$) have resulted in negative values near the wall for some researchers (Sohn et al., 1989; Wang et al., 1992), while they remain positive for others (Kim et al., 1989). The reasons for this are as yet unknown.

Current documentation of the mean flow structure within transitional flows with favorable pressure gradients is extremely limited. Blair (1992) presented velocity and temperature profiles through the transition region for boundary layer flow with $K = 0.20 \times 10^{-6}$ and FSTI = 2 percent (high FSTI transition). The results showed that the development of the temperature profiles lags behind those of the respective velocity profiles. This strongly indicates that acceleration affects heat transfer differently than it does flow structure. The cause of these differences remains to be determined. To the knowledge of these authors, no further information is available regarding detailed flow and thermal structure within the transitional boundary layer with a favorable pressure gradient.

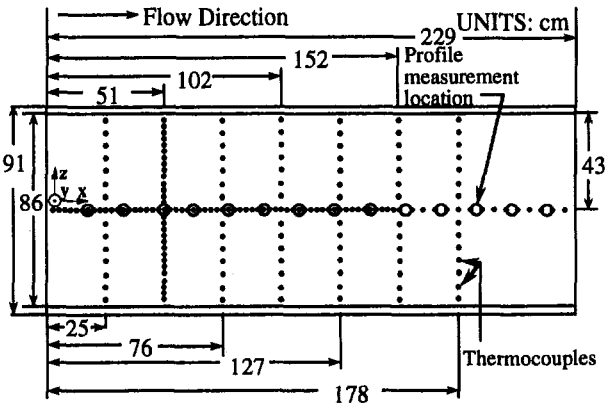


Fig. 1 Thermocouple layout on heated test wall

Experimental Program

Test Facility. The experiments were conducted in a two-dimensional, open circuit, blowing-type wind tunnel capable of a maximum air speed of 35 m/s, uniform within 0.7 percent and steady within 1 percent over a 20-hour period. Rayon-viscous felt capable of filtering out particles larger than 5 μm was used to filter the inlet airflow. The free-stream air temperature, controlled by the heat exchanger and the air-conditioning system in the laboratory, could be maintained within 0.5 °C over a period of 20 hours and uniformly within 0.1°C. To ensure that the boundary layer began at the leading edge of the test wall, a suction fan and low-pressure plenum were installed to provide suction. A detailed description of the wind tunnel is provided by Kuan (1987) and Kuan and Wang (1990).

The test section was designed with a large aspect ratio of 6, which provided the two-dimensional flow required in this investigation. The test section was 0.15 m wide, 2.4 m long, and 0.92 m high. A composite construction was utilized for the rectangular 2.4 × 0.92-m heated test wall. This design allows for flexibility, so that the test wall can be bent to varying degrees of streamwise curvature for future studies. The back surface was insulated with 25.4 cm of R30 fiberglass to minimize backplane conduction losses. The heating pad consisted of a heater foil sandwiched between glass cloth and silicon rubber sheets. A 1.56-mm-thick aluminum sheet was vulcanized to the front surface of the heater pad to improve the uniformity of the heat flux. A 1.56-mm polycarbonate sheet was placed on the front surface to provide a smooth test surface on which the air flows and from which measurements were taken. One hundred eight-

Nomenclature

C_f = skin-friction coefficient = $\tau_w/(\rho \bar{U}_\infty^2(x)/2)$
C_p = pressure coefficient = $(P - P_{\text{ref}})/\frac{1}{2}\rho \bar{U}_{\infty_{\text{ref}}}^2$
c_p = specific heat
K = pressure gradient parameter = $(\nu/\bar{U}_\infty^2(x))\,(d\bar{U}_\infty(x)/dx)$
P = static pressure
q_w'' = wall heat flux
Re_x = Reynolds number = $\bar{U}_\infty(x)x/\nu$
t = instantaneous fluctuation in temperature
t' = rms value of temperature fluctuation
T = instantaneous temperature
$\bar{T}$ = mean temperature
u, v = instantaneous velocity fluctuations in streamwise and cross-stream directions
u', v' = rms values of velocity fluctuations
u_τ = friction velocity = $\sqrt{\tau_w/\rho}$
U, V = instantaneous velocities
$\bar{U}$ = mean velocity
U^+ = $\bar{U}/u_\tau$
$\overline{uv}$ = mean Reynolds shear stress
$\overline{ut}$ = mean Reynolds streamwise heat flux
$\overline{vt}$ = mean Reynolds cross-stream heat flux
x = coordinate in streamwise direction
y = coordinate normal to the surface
Y^+ = yu_τ/ν
Γ = intermittency factor
δ = boundary layer thickness at 0.995 U_∞
δ^* = displacement thickness
θ = momentum thickness
ν = kinematic viscosity
ρ = density
τ_w = shear stress on the wall

Subscripts

end = end of transition
ref = reference location at x = 20 cm
s = onset of transition
w = at the wall
∞ = free-stream value

Downloaded 01 Jun 2010 to 171.66.16.53. Redistribution subject to ASME license or copyright; see http://www.asme.org/terms/Terms_Use.cfm

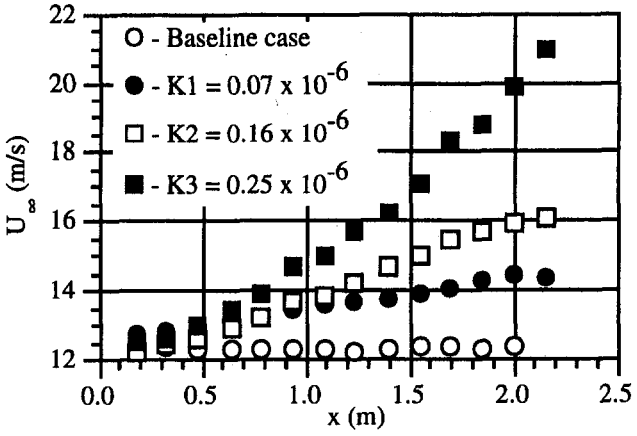


Fig. 2 Free-stream velocity for each case

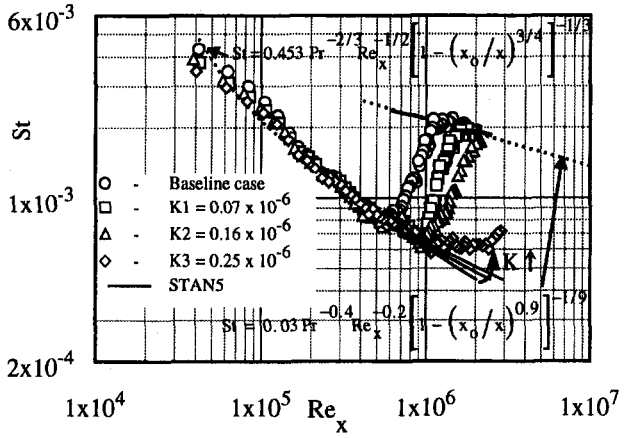


Fig. 4 Centerline Stanton number distribution for all cases

five 3-mil E-type thermocouples were embedded beneath the test surface and were strategically placed along the test surface to capture the spanwise and streamwise evolution of the wall heat transfer during the transitional flow process (Fig. 1).

Fourteen measuring holes of 2.54-cm diameter were drilled along the centerline axis in the outer observation wall. The first centerline measuring hole (station 1) was located 20 cm from the leading edge, with the remaining measuring holes placed every 15 cm (labeled sequentially station 2 through 14). When the probe was placed through the measuring hole into the test section, the length of the probe extended 2 cm upstream of the hole location. Plexiglas plugs, flush with the inner surface, were used to plug the holes when measurements were not being taken. Slots cut into the bottom wall and the top wall provided for adjustment of the outer observation wall in order to vary the pressure gradient in the test section. A detailed description of the test section and heated test wall was documented by Wang et al. (1992).

Geometry of the Test Section. The geometry of the test section used in this investigation was first described by Keller and Wang (1993), and is repeated here for clarity. For the baseline case, with no acceleration, the outer wall of the test section was adjusted to account for the growth of the boundary layer and to maintain a near-zero pressure distribution inside the test section with a variation of pressure coefficient, Cp, within 1 percent. Three different favorable pressure gradients were utilized in this investigation. A constant pressure gradient parameter, K, was maintained during each case. One of the advantages of using a constant K over other pressure gradient parameters is that a constant K can be conveniently obtained by linearly decreasing the width of the test section from the inlet to the exit. Fine tuning of the local width of the test section removed the effect of boundary layer growth on the pressure gradient. For each acceleration case, the width of the test section inlet was maintained at 15.24 cm, and the downstream width was arranged to decrease linearly to the exit plane. An exit width of 14.6 cm was used for the lowest acceleration case of $K = 0.07 \times 10^{-6}$, while an exit width of 8.9 cm was used for the highest acceleration case of $K = 0.25 \times 10^{-6}$. It should be noted that a constant K flow is inherently different from a Falkner–Skan flow, which has a constant $\Lambda(\equiv (\delta^2/\nu)\ (dU_\infty(x)/dx))$ value. Detailed explanations concerning the physical meaning of flow and thermal features of accelerated boundary layers with constant K values and the differences between a constant K and a constant Λ flow were made by Zhou and Wang (1992).

Three-Wire Sensor. A specially designed, miniature three-wire probe was used to measure the boundary layer velocity and temperature data. An "X" array, consisting of two 1.0-mm-long and 2.5-μm-dia Wollaston-type platinum-coated tungsten wires was used as the velocity sensor. An active sensing length of 0.5 mm was etched in the center. The "X" wires were placed orthogonal to each other with a spacing of 0.35 mm. The temperature sensor is a 0.35-mm-long unplated platinum wire 1.2 μm in diameter placed normal to the mean flow direction, in a plane parallel to the plane of the cross wire and spaced 0.35 mm from the "X" array. A complete description of the probe design and qualification, specifically in a heated transitional boundary layer, can be found in Shome (1991).

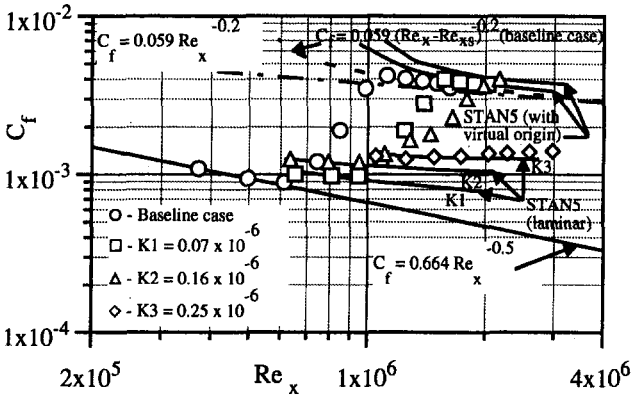


Fig. 3 Skin friction coefficient versus Reynolds number for each case

Table 1 Reynolds numbers at onset and end of transition for all test cases (note: **** indicates that no end of transition was observed in the test facility)

		Baseline	K1 0.07×10^{-6}	K2 0.16×10^{-6}	K3 0.25×10^{-6}
FSTI at x_s		0.5	0.4	0.4	0.4
U_∞ (m/s) Sta01 x = 18 cm		12.24	12.68	12.20	12.45
Onset of transition	x(cm)	68	107	115	122
	Re_x	5.50×10^5	9.46×10^5	10.3×10^5	12.5×10^5
	$Re_{\delta*}$	1294	1322	1233	1233
	Re_θ	492	541	544	552
End of transition	x(cm)	137	168	213	****
	Re_x	11.2×10^5	15.7×10^5	21.7×10^5	****
	$Re_{\delta*}$	1826	1874	1880	****
	Re_θ	1302	1282	1235	****
Length of transition	x(cm)	69	61	98	****
	Re_x	5.70×10^5	6.24×10^5	11.4×10^5	****
	$Re_{\delta*}$	532	552	647	****
	Re_θ	810	741	691	****

Downloaded 01 Jun 2010 to 171.66.16.53. Redistribution subject to ASME license or copyright; see http://www.asme.org/terms/Terms_Use.cfm

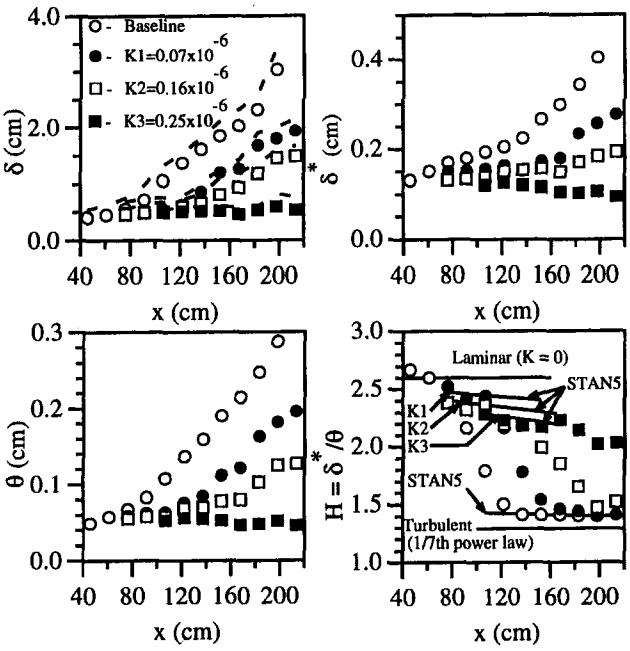


Fig. 5 Boundary layer integral parameters for all cases (--- thermal boundary layer thickness)

Measurements and Instrumentation. The velocity sensors were operated in a constant-temperature mode, using a TSI model IFA 100 Intelligent Flow Analyzer. A DISA M20 temperature bridge was used to operate the temperature sensor in the constant current mode. For future turbulent power and thermal power spectral analyses, TSI Model 157 signal conditioners were used to low-pass filter signals from all three sensors. The "X" wires of the three-wire sensor were operated at overheat ratios of 1.43 and 1.66. The temperature sensor was operated with a very low overheat ratio. The probe current was set at 0.1 mA, and an amplifier gain of 3500 was used. For convenience, the velocity wires are referred to as hot wires, and the temperature wire is referred to as a cold wire in this study. The optimum frequency response found for each velocity wire was approximately 200 kHz. The frequency response of the temperature sensor was experimentally determined to range from 4800 to 6400 Hz, depending on the velocity, by using the DISA M20 constant current bridge (see Wang et al., 1992, and Keller, 1993, for details). In addition to the three-wire sensor, a single hot wire was used to cross-check the results obtained from the three-wire sensor and to provide guidance for calculating the skin-friction coefficient in the near-wall region. The data from all of the sensors were subsequently sampled at 2 kHz for 20 seconds with the low-pass filter set at 1 kHz.

The wind tunnel, the test wall power supply, and the cooling water supply were started at least 12 hours prior to the experiment. A global measurement for wall temperature distribution was performed by scanning the temperature approximately every two hours. Each time, an average of three different scans, each made at a sample rate of 1 channel/second, was obtained. The local wall temperature was checked before, midway through, and after each measurement of the boundary layer temperature profile to ensure that it remained steady. Both the global and local check served to monitor the steadiness and the

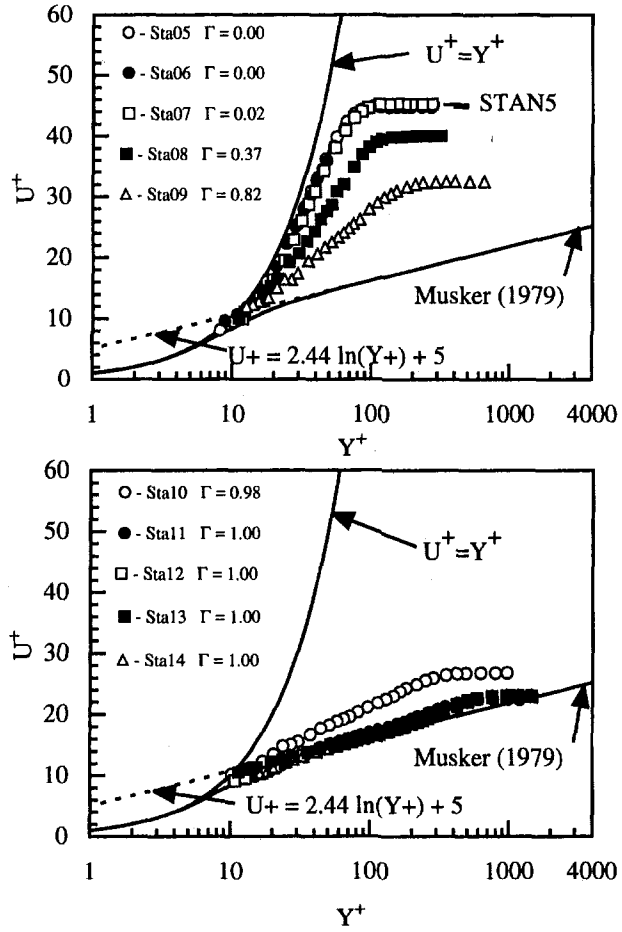


Fig. 6 Mean velocity profiles for $K1 = 0.07 \times 10^{-6}$ in wall units

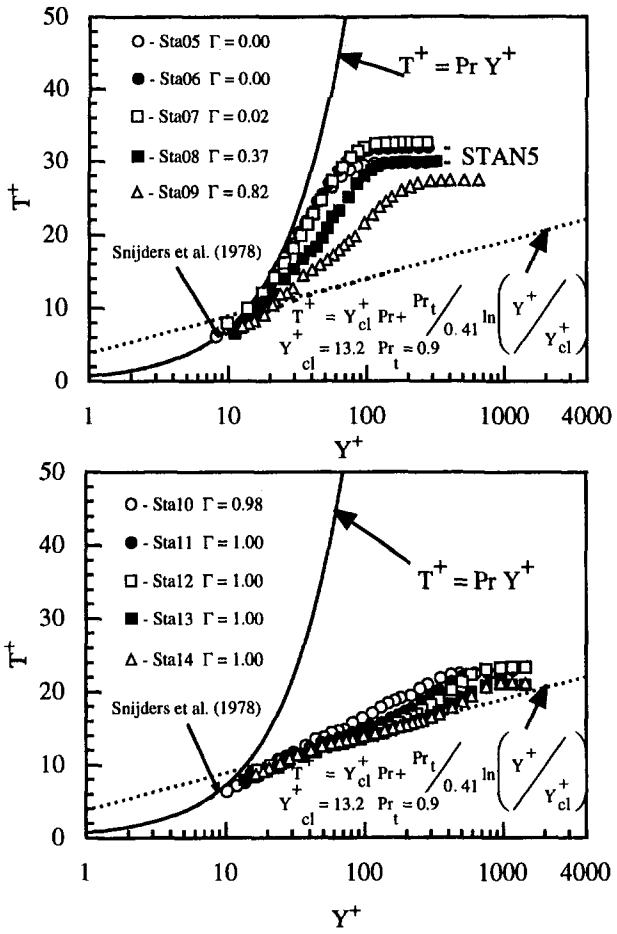


Fig. 7 Mean temperature profiles for $K1 = 0.07 \times 10^{-6}$ in wall units

Downloaded 01 Jun 2010 to 171.66.16.53. Redistribution subject to ASME license or copyright; see http://www.asme.org/terms/Terms_Use.cfm

free-stream temperature as well as the wall temperature. The thermocouple measurements were made through a Fluke 8842A 5-1/2 digit digital multimeter and a Fluke 2205A switch controller. For each case, a uniform heat flux of 335 W/m^2 was applied to the test wall, and the free-stream temperature was maintained at approximately 15°C. The resulting wall temperatures ranged from 24°C to 41°C. All fluid properties were evaluated at atmospheric pressure and free-stream temperature.

Results and Discussion

In the following discussion, the results of the baseline case are used for comparison with the accelerating cases. Please refer to Keller (1993) or Wang et al. (1992) for detailed documentation of the baseline case. After the sampled data were reduced, the intermittency function was obtained. The value of this function is 1 if the flow is turbulent, and 0 otherwise. The total percentage of time that the intermittency function is 1 determines the intermittency factor, Γ. For a complete description of the method used to determine the intermittency factor, refer to Keller and Wang (1993). The free-stream velocities for each of the three accelerating cases, along with the velocity of the baseline case, are shown in Fig. 2. For each accelerating case, the free-stream velocity at station 1 (the reference station for the *Cp* measurements) was maintained as close to the value used during the baseline case as possible. The K values obtained were $K = 0.07 \times 10^{-6}$, $K = 0.16 \times 10^{-6}$, and $K = 0.25 \times 10^{-6}$. These values are termed $K1$, $K2$, and $K3$ for the remainder of the discussion.

Skin Friction, Stanton Number, and Integral Parameters. Station numbers are used when referencing all measurement locations. The variation of skin-friction coefficient for each case is shown in Fig. 3. All skin-friction values were obtained from the mean velocity profiles, including single hot-wire measurements for use as a guide. Mean velocity profile outputs from the STAN5 code (NASA/Lewis version, expanded from the original version from Crawford and Kays, 1976) were used to compare the laminar stations. The skin-friction values for laminar and turbulent flow from the STAN5 solutions are also shown in Fig. 3. For the laminar region, an increasing K makes the mean velocity profiles fuller, and thus increases the skin-friction coefficient. The same effect occurs in fully turbulent flow. From Fig. 3, it is observed that a higher K value delays the onset of transition and increases the length of transition. These observations are consistent with the experimental results of Turner (1971), Abu-Ghannam and Shaw (1980), Blair (1982, 1992), Narasimha (1985), and Rued and Wittig (1985, 1986).

The distribution of centerline Stanton numbers for each case is shown in Fig. 4. The Stanton numbers for all three accelerating cases follow their corresponding laminar correlations for zero pressure gradient up to the point of transition, and then approach the fully turbulent correlation at the end of transition. This is consistent with the experimental results of Blair (1982), which indicated no significant deviation from the laminar or turbulent correlations for flows with K values of 0.2×10^{-6} and 0.75×10^{-6}. For a strongly accelerating flow, such as $K = 3.2 \times 10^{-6}$, Rued and Wittig (1985) observed a 20 percent increase in Stanton number over their zero pressure gradient case for the early laminar region, followed by a slight decrease below the zero pressure gradient laminar correlation as the Reynolds number increases. The effects of streamwise acceleration on Stanton number in the laminar and turbulent boundary layer are not significant until a relatively large value of K is obtained.

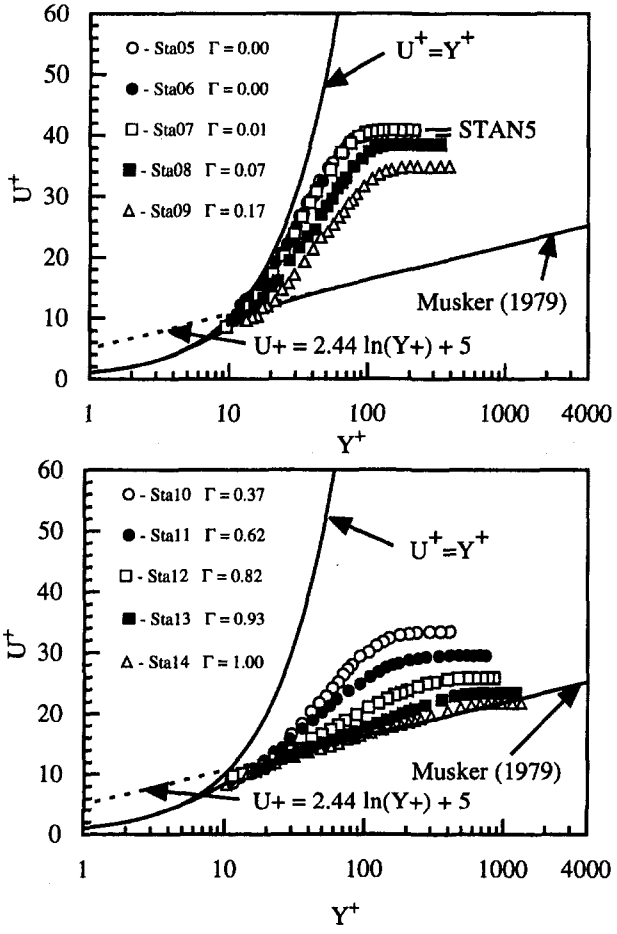


Fig. 8 Mean velocity profiles for $K2 = 0.16 \times 10^{-6}$ in wall units

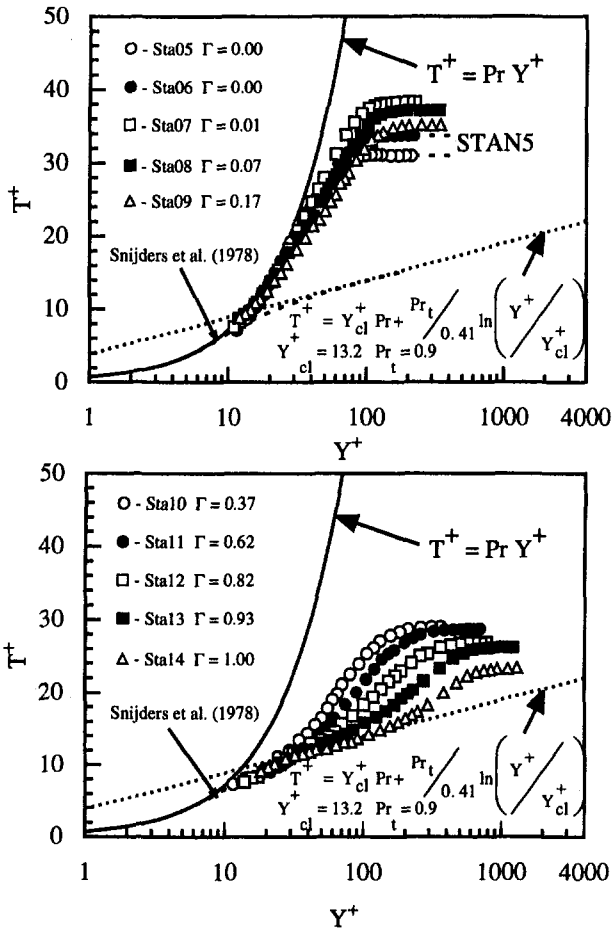


Fig. 9 Mean temperature profiles for $K2 = 0.16 \times 10^{-6}$ in wall units

Downloaded 01 Jun 2010 to 171.66.16.53. Redistribution subject to ASME license or copyright; see http://www.asme.org/terms/Terms_Use.cfm

In this investigation, transition onset was defined by the location, L, where the skin-friction coefficient (and/or Stanton number) deviates from the laminar correlation, and the end of transition was defined as the point of maximum skin friction (and/or Stanton number) immediately following the rise of C_f. The onset and end of transition were inferred from Figs. 3 and 4, and are listed in Table 1. As K increases, the location of transition onset is delayed both in terms of physical distance, x, and Reynolds number based on x. For the three accelerating cases, $Re_{\theta s}$ appears insensitive to the point of transition, which is consistent with the observations of Blair (1992). This is also consistent with the observation made by Abu-Ghannam and Shaw (1980), that a favorable pressure gradient has an insignificant effect on the onset of transition in terms of Re_θ. The physical length of transition, in terms of x, for the $K1$ case is actually shorter than that of the baseline case by approximately 12 percent (7 cm). This is attributed to the spacing of the measuring stations and the difficulty in obtaining an exact transition start and end point. Determination of the onset and end of transition was limited to a measuring station location or a point midway between two stations. If the point was determined to be midway between two stations, then the free-stream velocity and integral parameters were estimated by linearly interpolating between the values at the adjoining stations. For the $K2$ case, the physical length of the transition region is much longer (42 percent) than the baseline case or the $K1$ case. The length of transition in terms of Re_x and $Re_\delta{}^*$ increases as K increases, whereas the length of transition decreases in terms of Re_θ as K increases. For the $K3$ case, the length of the test section was insufficient to obtain fully turbulent conditions.

The momentum boundary layer thickness, thermal boundary layer thickness, and integral parameters for each case are shown in Fig. 5. Increasing the pressure gradient suppresses boundary layer growth and development through the transition region. For the strongest accelerating case, $K3$, the boundary layer displacement thickness and the momentum thickness actually decrease in the downstream direction. This is consistent with the analytical results of Zhou and Wang (1992) for laminar flows with constant K values.

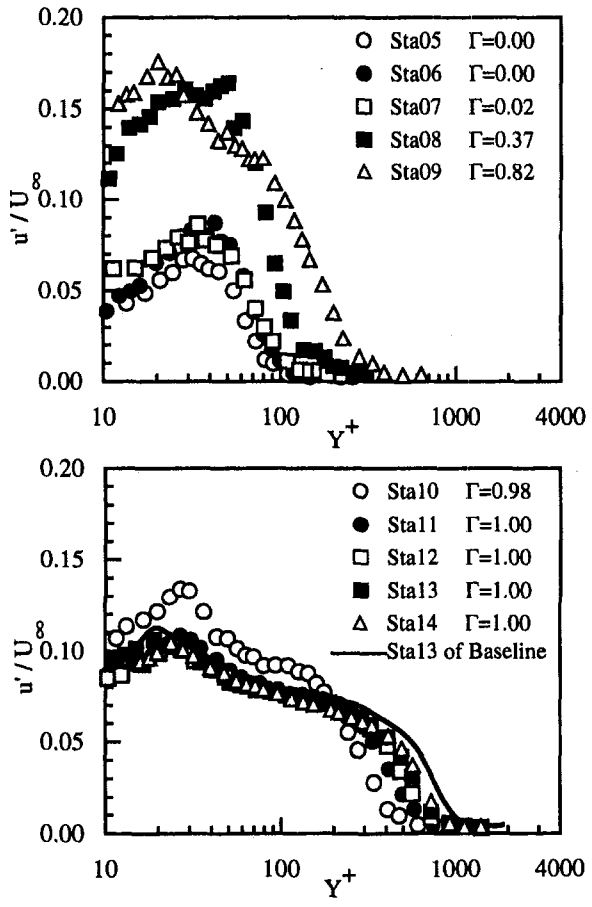


Fig. 10 Streamwise fluctuating turbulent velocity distributions for $K1 = 0.07 \times 10^{-6}$ in wall units

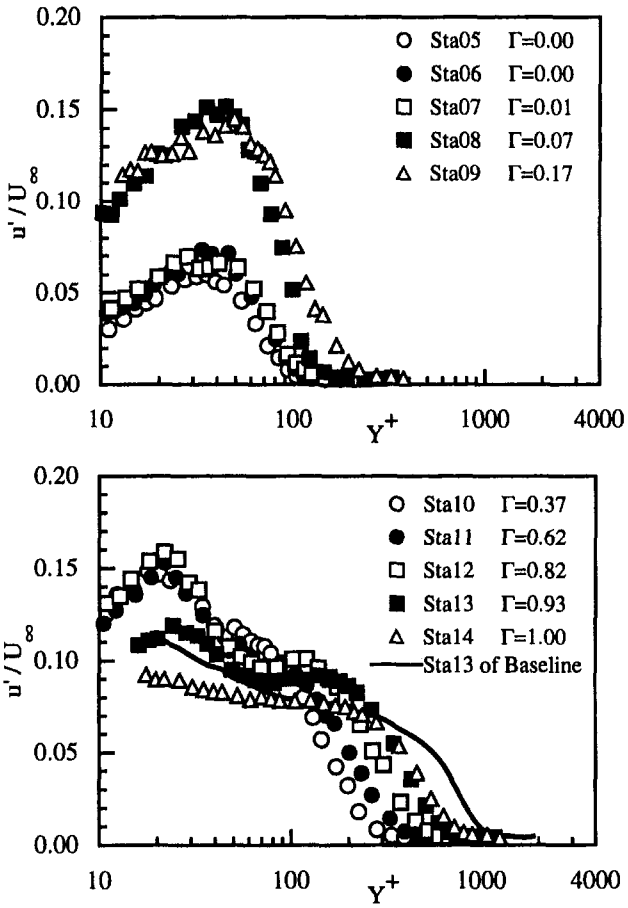


Fig. 11 Streamwise fluctuating turbulent velocity distributions for $K2 = 0.16 \times 10^{-6}$ in wall units

Mean Velocity and Mean Temperature Profiles. The mean velocity and temperature profiles for cases $K1$ and $K2$ are shown in wall units in Figs. 6–9. The results of the $K3$ case are omitted from further discussion since the flow for this case never reached beyond the early transition region, and no additional information was obtained. For the lowest accelerating case, $K1$, the mean velocity profiles followed the laminar solution up through station 7. The flow was transitional from stations 8 through 10 and matched the fully turbulent correlation for a zero pressure gradient flow from station 11 to station 14 (Fig. 6). Blair (1982, 1992) reported that the velocity profiles for fully turbulent flow with $K = 0.2 \times 10^{-6}$ also matched the zero pressure gradient correlation. However, Julien et al. (1969) reported that for K values greater than 0.57×10^{-6}, the fully turbulent velocity profiles slightly "overshoot" the log-linear region of the zero pressure gradient turbulent correlation. Apparently, low K values, although sufficient to affect the onset of transition, are insufficient to cause significant deviation from the zero-pressure gradient turbulent correlation. The mean temperature profiles for the $K1$ case are shown in Fig. 7. The mean temperature profiles begin to deviate from the laminar solution at the same location as the mean velocity profiles; however, comparison of the transitional profiles reveals that the streamwise evolution of temperature lags behind the velocity distribu-

Downloaded 01 Jun 2010 to 171.66.16.53. Redistribution subject to ASME license or copyright; see http://www.asme.org/terms/Terms_Use.cfm

tions. This lag is evident at stations 11 and 12, where the velocity profiles are in close agreement with the law of the wall, but the temperature profiles exhibit a much shorter logarithmic region and are still approaching the fully turbulent profile. A similar observation was made by Blair (1982, 1992). For the $K2$ case, the same observation is made in Figs. 8 and 9. The mean velocity profiles in the turbulent region have a slightly steeper slope in the linear-log region than does the zero pressure gradient turbulent correlation. No obvious wake region is observed. This is similar to the "overshoot" in the log-linear region observed by Julien et al. (1969). For the transitional process, the lag of the temperature profiles behind the velocity profiles is more clear in the $K2$ case. These results indicate that the development of momentum transport in accelerating transitional flows leads the development of thermal transport. Sharma (1987) showed that current transition modeling schemes predict the momentum boundary layer in accelerating flows well, but fail to predict the thermal boundary layer. This failure was determined to be due to the different paces of development of the momentum and thermal transport. Sharma stressed the need to model this discrepancy correctly so that accurate predictions can be obtained. These authors believe that an improved understanding of the physical mechanisms can be obtained by investigating the Reynolds stresses and heat fluxes inside the boundary layer, as shown in the following sections.

Streamwise and Cross-Stream Turbulent Fluctuating Velocities (u' and v'). The streamwise evolution of turbulent fluctuating velocity, u', for $K1$ and $K2$ is shown in Figs. 10 and 11, respectively. The turbulent fluctuating velocities (u' and v') are related to the Reynolds stresses as $\rho u'^2$ and $\rho v'^2$. The laminar stations exhibit a peak in u' at approximately $Y^+ =$ 40. The magnitude of the peak intensity in the baseline case is approximately 5 percent of the free-stream velocity. The magnitudes of the peak intensities for the pressure gradient cases range from 7 to 9 percent of the free-stream velocity. These values are similar in magnitude to the intensities observed at the onset of transition for the baseline case. This indicates that in the presence of a favorable pressure gradient, a laminar boundary can tolerate a higher u' without undergoing transition than it can in the zero pressure gradient case. Within the transition region, the peak intensity observed in u'/U_∞ decreases as K increases. For the baseline case, the maximum u' in the transition region was 19 percent of the free-stream velocity. This maximum value slightly decreased to 18 percent for $K1$ and to 16 percent for $K2$. For all three cases, the peak intensity in u' occurred in the transition region at approximately $Y^+ =$ 30, near the beginning of the velocity log-linear region. For the fully turbulent region, as K increases, the peak intensity in u' is suppressed in the near-wall region between $10 < Y^+ < 50$, but it remains at the same level at the end of the log-linear region, $200 < Y^+ < 300$. This decrease is most likely due to a thickening of the viscous sublayer relative to the boundary layer thickness. It should be noted that the growth of both the viscous sublayer and the boundary layer is suppressed by a favorable pressure gradient; however, the viscous sublayer is suppressed less than the boundary layer.

The cross-stream turbulent fluctuating velocities, v', for $K1$ and $K2$ are shown in Figs. 12 and 13, respectively. The trend in the development of v' for the accelerating cases is similar to that observed in the baseline case, but with less magnitude in the transition region as K increases. However, one distinct difference is observed in the fully turbulent region. For the

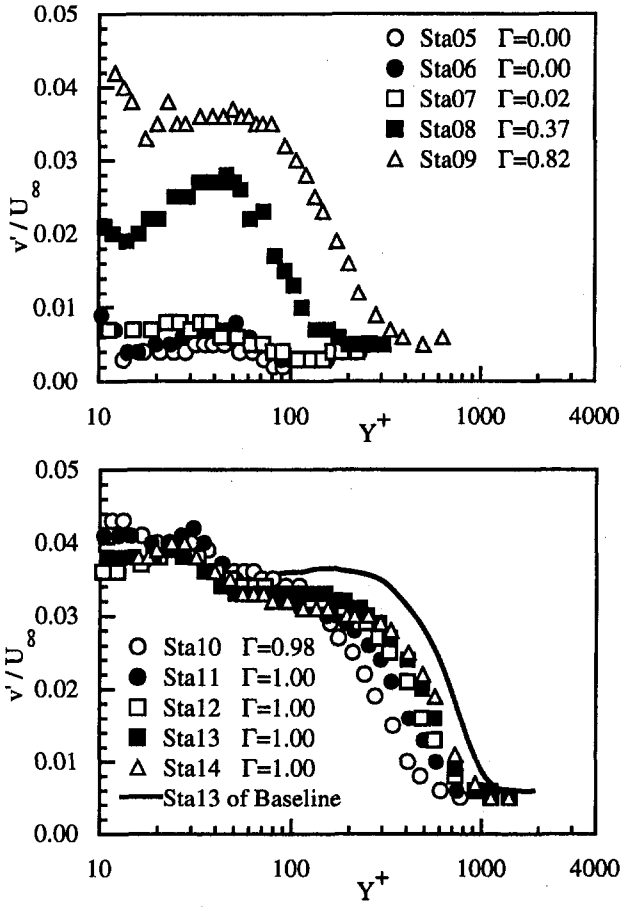


Fig. 12 Cross-stream fluctuating turbulent velocity distributions for $K1 = 0.07 \times 10^{-6}$ in wall units

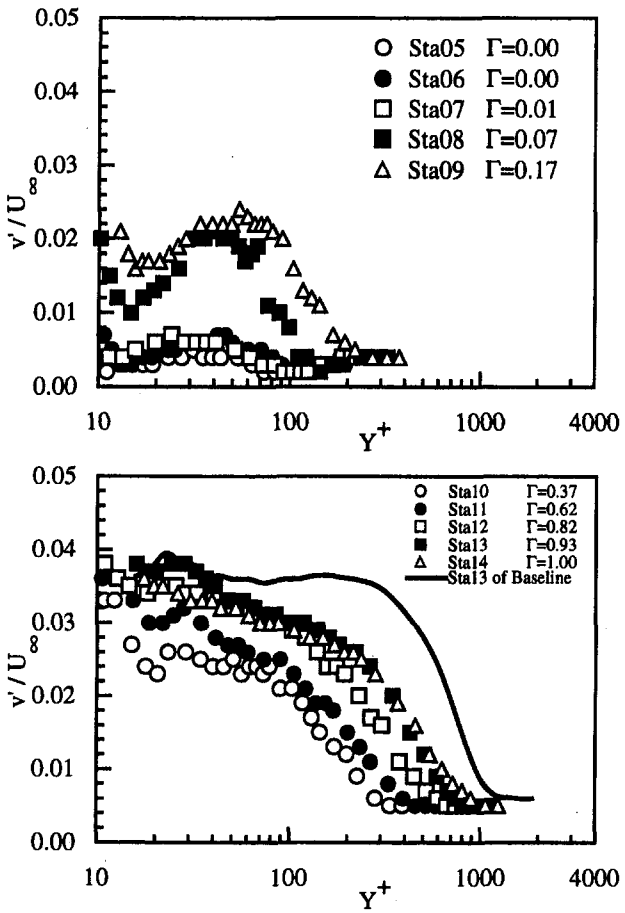


Fig. 13 Cross-stream fluctuating turbulent velocity distributions for $K2 = 0.16 \times 10^{-6}$ in wall units

Downloaded 01 Jun 2010 to 171.66.16.53. Redistribution subject to ASME license or copyright; see http://www.asme.org/terms/Terms_Use.cfm

baseline case, the value of v' in the velocity log-linear region ($40 < Y^+ < 200$) is fairly constant, with a value of about 3.7 percent of the free-stream velocity. As K increases, this value is suppressed, and does not extend as far out into the boundary layer. For the $K2$ case, v' never maintains a constant value, but progressively decreases from the near-wall maximum. It appears that pressure gradient affects v' more in the outer boundary layer than in the near-wall region.

The evolution of the maximum u' and v' for $K1$ and $K2$ is compared to the baseline case in Fig. 14. The streamwise locations are aligned with the onset and the end of transition. The results are similar to those observed from the baseline case, i.e., that u' increases to a maximum value in the early stage of transition and reduces in the late transition region. However, v' reaches the maximum value at about the same location that u' reaches the maximum, but it maintains this maximum value up through the turbulent flow region (see Kuan and Wang, 1989). The location of the peak value of u' migrates closer to the wall as the flow progresses downstream. Compared to the values of u' and v', the flow in the transition region is much less isotropic than the flow in a fully turbulent boundary layer.

Reynolds Shear Stress ($\overline{uv}$). Figures 15 and 16 show the evolution of Reynolds shear stress for cases $K1$ and $K2$, respectively. As the K value is increased, the ratio of the turbulent shear to the wall shear is reduced at each corresponding Γ value. For example, the values of $\overline{uv}/u_\tau$ at station 8 ($\Gamma = 0.37$) for the $K1$ case in Fig. 15 are higher than those at station 10 ($\Gamma = 0.37$) for the $K2$ case in Fig. 16 (note: the large scatter observed for station 8 is due to the low intermittency in the early transition region). This is due to the increased pressure gradient, which acts to make the velocity profiles fuller, thus increasing the viscous shear near the wall. In the pretransitional region, negative values occur for $30 < Y^+ < 80$. The cause of these negative values is not clear. In the transition region of the $K1$ case, the peak values of $\overline{uv}$ at station 9 are approximately 50 percent

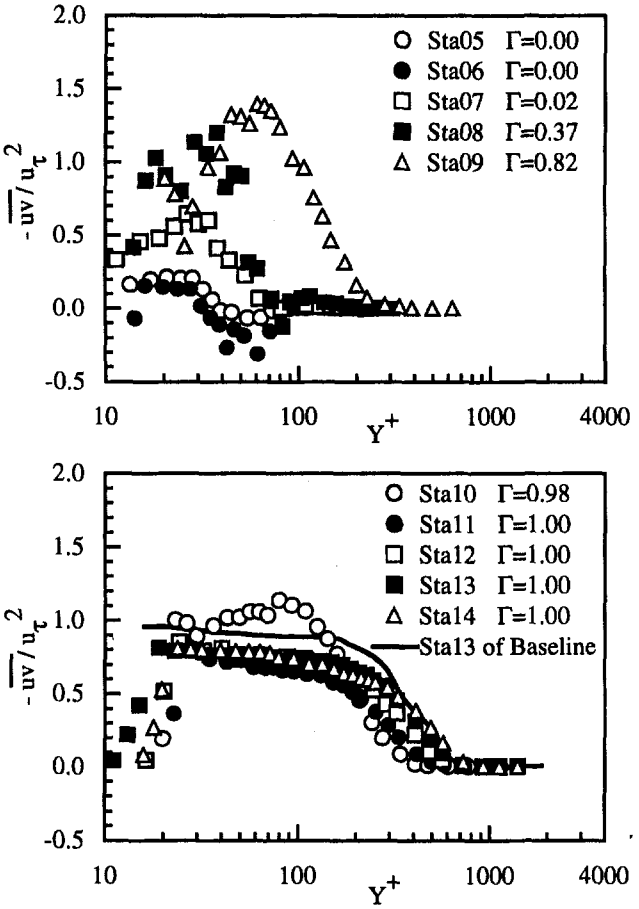


Fig. 15 Reynolds shear stress distributions for $K1 = 0.07 \times 10^{-6}$ case in wall units

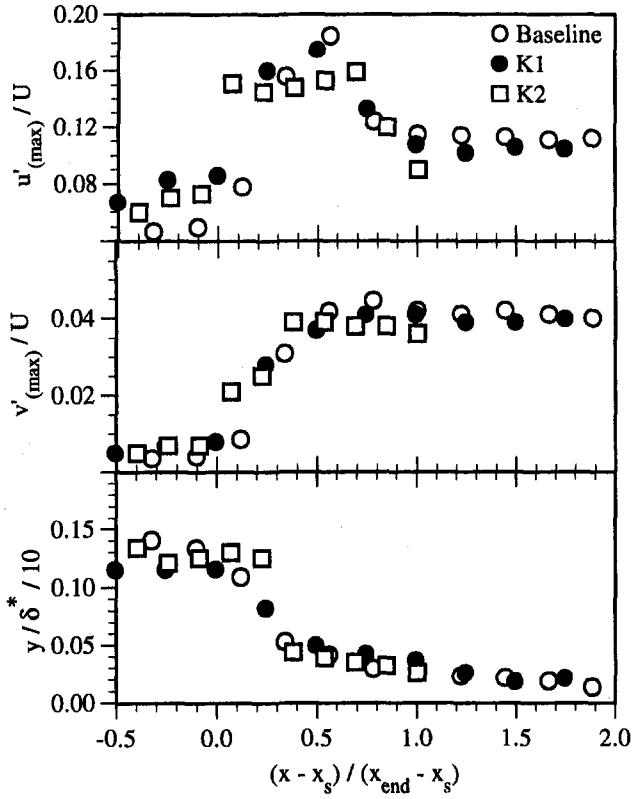


Fig. 14 Distributions of maximum fluctuating turbulent velocity and the corresponding y positions in the streamwise direction

larger than the wall shear. This indicates that the turbulent shear is generated within the boundary layer and imposes itself on the wall shear, as in the baseline case (see Wang et al., 1992). For the $K2$ case, the turbulent shear never exceeds the wall shear. At station 12, shown in Fig. 16, the turbulent shear reaches a maximum value of approximately 90 percent of the wall shear. This value is only 30 percent greater than the fully turbulent value of station 14. This may be due to the applied pressure gradient suppressing the local turbulent shear generation at $Y^+ \approx 100$. This might also be explained as follows: The applied pressure gradient results in an effective communication between local high turbulent shear, generated around $Y^+ \approx 100$, and the wall, such that the wall shear is quickly adjusted to the produced shear away from the wall. Also, a comparison of the Reynolds shear stress shown in Figs. 15 and 16 and the u' shown in Figs. 10–13 reveals that the amplification process of the Reynolds shear stress near the onset of transition between stations 6 and 7 is faster than that of the Reynolds normal stress.

The rms Temperature Fluctuation. The evolution of the rms temperature fluctuations normalized by the temperature difference ($T_w - T_\infty$) is shown in Figs. 17 and 18. In the laminar region, the t' profiles are similar to the u' profiles. A peak occurs at approximately $Y^+ = 40$, which is greater in magnitude than the corresponding profiles for the baseline case. In this region, a favorable pressure gradient has similar effects on t' and u'. As in the evolution of u', shown in Figs. 10 and 11, there is little change in t' between stations 6 and 7.

As transition proceeds, the peak of t' rapidly increases in magnitude, similar to the increase observed in u'. Direct comparison of the evolution of t', shown in Figs. 17 and 18, to the evolution of u' and v', shown in Figs. 10–13, indicates a lag

Downloaded 01 Jun 2010 to 171.66.16.53. Redistribution subject to ASME license or copyright; see http://www.asme.org/terms/Terms_Use.cfm

in the evolution of the rms temperature fluctuations relative to the fluctuating velocities. For the $K1$ case, the t' profiles continue to develop up through station 13, while u' in Fig. 10 reaches an equilibrium state by station 11. This lag of t' behind u' in reaching equilibrium is more pronounced for the $K2$ case, as a comparison of Figs. 11 and 18 reveals. In Fig. 17, station 13 has two distinctive peaks at $Y^+ = 40$ and 200, respectively; station 14 has a constant value on the region of $20 < Y^+ < 100$ and a peak value at $Y^+ = 300$. This supports the observation drawn from the mean temperature and velocity profiles that the thermal transport lags behind the momentum transport in the transition region.

There are secondary t' peaks occurring at the outer portion of the log-linear region in the late-transitional and early-turbulent stations (stations 12–14 in Fig. 17 and stations 11–13 in Fig. 18). The magnitude of this second peak (located at approximately $Y^+ = 200$) increases as K increases, and actually exceeds the near-wall peak (located at approximately $Y^+ = 30$). This effect was not present in the fluctuating velocities, which indicates that an applied pressure gradient affects the thermal structures differently in this region than it does the flow structure. This may be a result of the differences between the transport mechanisms of momentum and heat.

Reynolds Heat Fluxes ($\overline{vt}$) and ($\overline{ut}$). Measurement of the cross-stream Reynolds heat flux, $\overline{vt}$, for the baseline case was discussed in detail by Wang et al. (1992) and Keller (1993). The results for station 5 are not shown since the flow was pretransitional and $\overline{vt}$ and $\overline{ut}$ are near zero. Large negative values of $\overline{vt}$ were obtained in the inner boundary layer. The magnitude and boundary layer penetration of these negative values were the greatest in the midtransition region. As the transition process

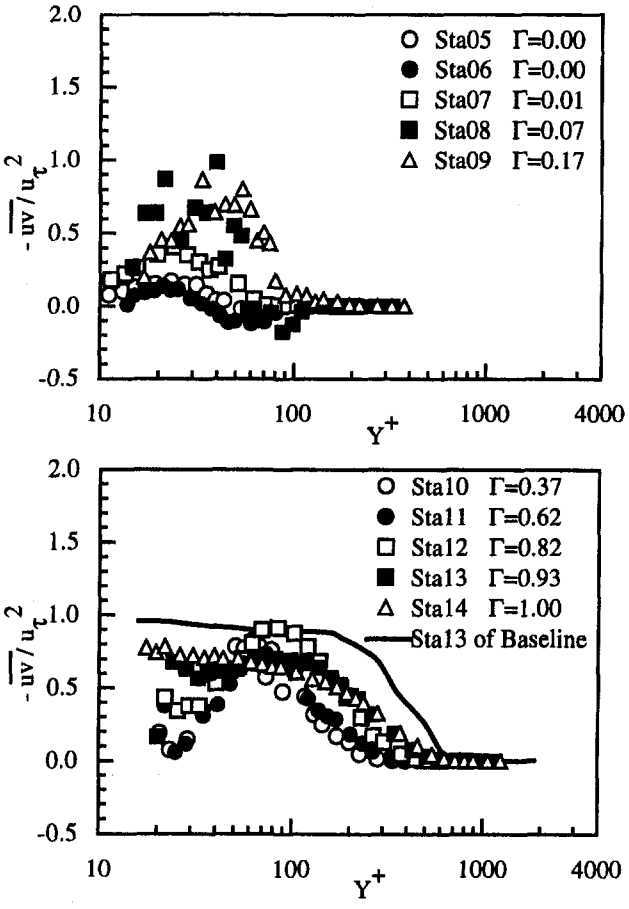


Fig. 16 Reynolds shear stress distributions for $K2 = 0.16 \times 10^{-6}$ case in wall units

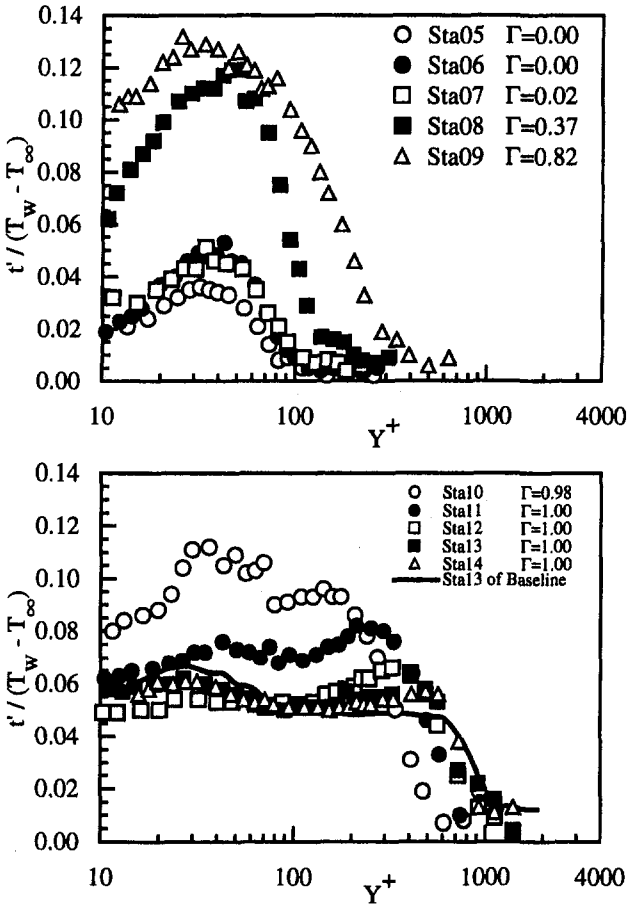


Fig. 17 The rms temperature fluctuations for $K1 = 0.07 \times 10^{-6}$ in wall units

advanced, the near-wall region of negative $\overline{vt}$ became narrower, finally occupying the inner 5–10 percent of the boundary layer. A negative time-averaged $\overline{vt}$ in a thermal field of negative mean-temperature gradient results in a negative eddy thermal diffusivity, which is physically inappropriate. To explore this issue more fully and to attempt to determine whether the occurrence of a negative $\overline{vt}$ within the boundary layer was a real physical phenomenon or an induced measurement error, several possible explanations were investigated: (1) insufficient frequency response of the cold wire (thermal lag), (2) thermal cross-talk between the hot and cold wires, (3) spatial resolution of the three-wire probe, and (4) three dimensionality of the transitional flow.

The issues of frequency response and thermal cross-talk were investigated experimentally and determined not to contribute to the negative $\overline{vt}$ measurements (see Keller, 1993).

The issue of spatial resolution of the probe is of special concern near the wall since the eddy size decreases as the wall is approached, which may result in the two crossed wires sensing different velocities. This subject was investigated by Ligrani and Bradshaw (1987), who recommended that the spanwise distance between the sensors be $S^+ < 20 \sim 25$, where S^+ is the spacing between the wires in the wall coordinates. For the baseline case, S^+ ranged from 12 to 23, which satisfied the recommended spacing. Sohn et al. (1989) also observed negative $\overline{vt}$ in the transitional boundary layer and discussed the issue of spatial resolution. They believe that the negative $\overline{vt}$ values may be due to sensor spacing; they have outlined a plan to investigate the effects of S^+, but no results have been published to date. To reduce the impact of spatial resolution, the flow speed was reduced to 8 m/s, so that a relatively thicker boundary

Downloaded 01 Jun 2010 to 171.66.16.53. Redistribution subject to ASME license or copyright; see http://www.asme.org/terms/Terms_Use.cfm

layer could be obtained. Similar large negative values of $\overline{vt}$ were again measured. A further reduction of the flow speed below 8 m/s resulted in total laminar flow in the present facility, so the effect of spatial resolution is not resolved.

The issue of three-dimensional effect is also of special concern for two reasons: (a) the uncertainty of the yaw angle can significantly contribute to the overall measurement uncertainty, and (b) the spanwise Reynolds heat flux, wt, would be important for transferring thermal energy. An uncertainty analysis showed that a ±2° uncertainty in the flow angle relative to the wire can contribute to ±20 percent uncertainty in $\overline{vt}$ measurement. Although 20 percent uncertainty may seem large, it does not alter the sign from a negative to a positive value. If the effect of three dimensionality is significant, the negative $\overline{vt}$ might be valid, because the downwash flow surrounding the turbulent spot brings in cooler flow from the mainstream toward the wall. This implies that further study is needed to measure $\overline{vt}$ and to verify that the measured energy transport is conserved in a control volume in the transitional boundary layer. The effect of fluid convection due to thermal gradients in the heated boundary layer was estimated by comparing the ratio of Grashof number to the Reynolds number squared. The ratio was below 0.1; therefore thermal gradients were determined to be insignificant, and were not considered to be a contributor to the effect of three dimensionality.

The evolution of normalized $\overline{vt}$ for the accelerating cases is shown in Figs. 19 and 20. The results are very similar to the results of the baseline case, with the following exception. As K increases, the negative values of normalized $\overline{vt}$ in the transition region increase in magnitude (i.e., become more negative), extend further into the boundary layer, and remain longer downstream. As the velocity increases under the influence of a favorable pressure gradient, the spanwise distance between the sensors (in terms of S^+) increases, although S^+ for the accelerating cases met the criteria recommended by Ligrani and Bradshaw (1987), $S^+ < 20 \sim 25$. If spatial resolution of the sensor is the cause of the negative $\overline{vt}$ measurements, then the thinning of the boundary layer as K increases might explain the increase in the magnitude and the boundary layer penetration of the negative $\overline{vt}$ values. This topic is discussed in detail by Keller (1993).

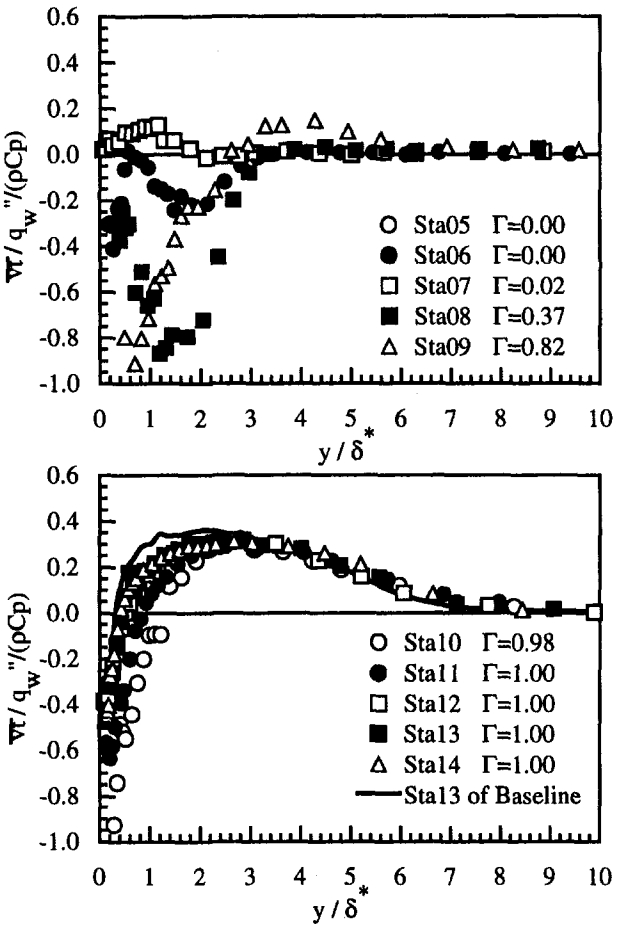


Fig. 19 Cross-stream Reynolds heat flux distributions for $K1 = 0.07 \times 10^{-6}$ case

The streamwise Reynolds heat flux, $\overline{ut}$, normalized by the wall heat flux, is shown in Figs. 21 and 22. For the baseline case, the magnitude of the peak value of normalized $\overline{ut}$ in the transition region was approximately 17 times that of the wall heat flux. For the accelerating cases, this magnitude increased to approximately 20 times the wall heat flux. The location of this peak value moves away from the wall as K increases. For the baseline case, the peak intensity occurs at approximately $Y^+ = 30$, while for the $K2$ case, the peak has moved to about $Y^+ = 50$. This may be caused by a thickening of the conduction layer relative to the boundary layer. The second peak at $Y^+ = 200$ that was observed to occur in t' is also seen in the normalized $\overline{ut}$ profiles. The magnitude of this second peak, relative to the magnitude of the near-wall peak, also increases as K increases. This indicates that a favorable pressure gradient has a similar impact on the streamwise Reynolds heat flux as it has on t'.

The observations made from the Reynolds stresses, Reynolds heat fluxes, and rms temperature fluctuations within the boundary layer indicate that a favorable pressure gradient affects thermal structures differently than it affects flow structures in the

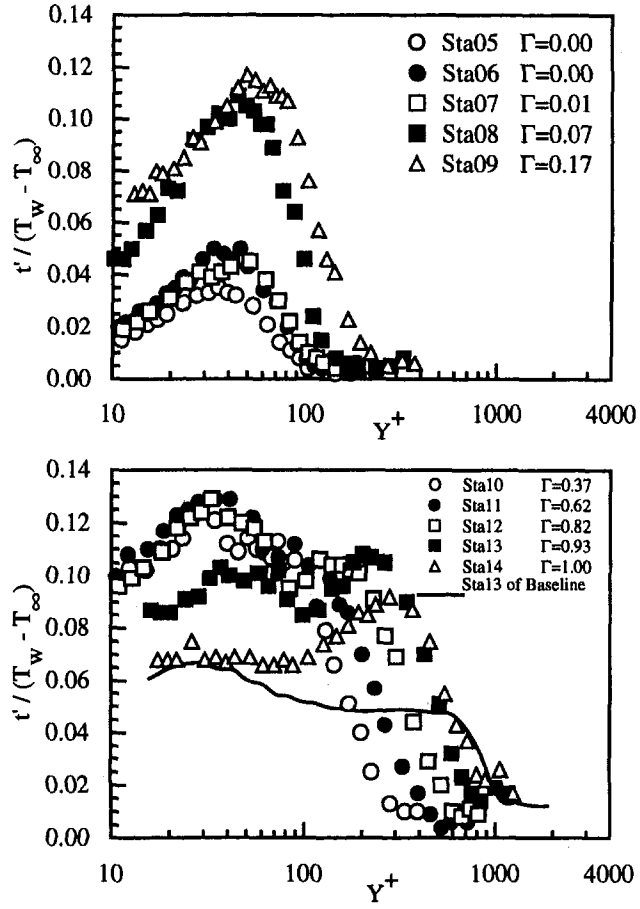


Fig. 18 The rms temperature fluctuations for $K2 = 0.16 \times 10^{-6}$ in wall units

Downloaded 01 Jun 2010 to 171.66.16.53. Redistribution subject to ASME license or copyright; see http://www.asme.org/terms/Terms_Use.cfm

transitional boundary layer. Conditional sampling must be used to investigate further the intermittent flow and thermal structures in separate nonturbulent and turbulent portions to determine the causes of the differences observed and to address the impact of the large-scale eddy motion on these structures in transitional boundary layers.

Eddy Viscosity (ϵ_M). Since the issue of negative $\overline{vt}$ measurements was not resolved, eddy diffusivities and turbulent Prandtl numbers for the accelerating cases are not presented. The evolution of the eddy viscosities for the accelerating cases normalized by their viscous counterparts is shown in Figs. 23 and 24. In the early transition region, ϵ_M is approximately zero. As transition progresses, ϵ_M grows rapidly, reaching a peak magnitude at $y/\delta = 0.4$ for both the $K1$ and $K2$ cases, similar to that observed in the baseline case. While the y/δ location of this maximum value does not change as the flow moves downstream, the magnitude of the maximum value continues to increase. As K increases, the peak magnitude of the eddy viscosity is reduced. This supports the observation from Figs. 15 and 16 that the ratio of turbulent shear to the wall shear is suppressed as K increases.

Uncertainty Analysis

Uncertainty analyses were conducted for the surface measurements, C_f and St, the boundary layer measurements, $\overline{U}$, $\overline{T}$, u', $\overline{uv}$, and $\overline{vt}$, and the integral parameters, δ^*, θ, and H. The propagation of the individual uncertainties into the final results was determined using the procedure set forth by Kline and McClintock (1953). The resultant uncertainties are listed in Table 2. A complete listing of the uncertainties and details of the methods used are documented by Keller (1993).

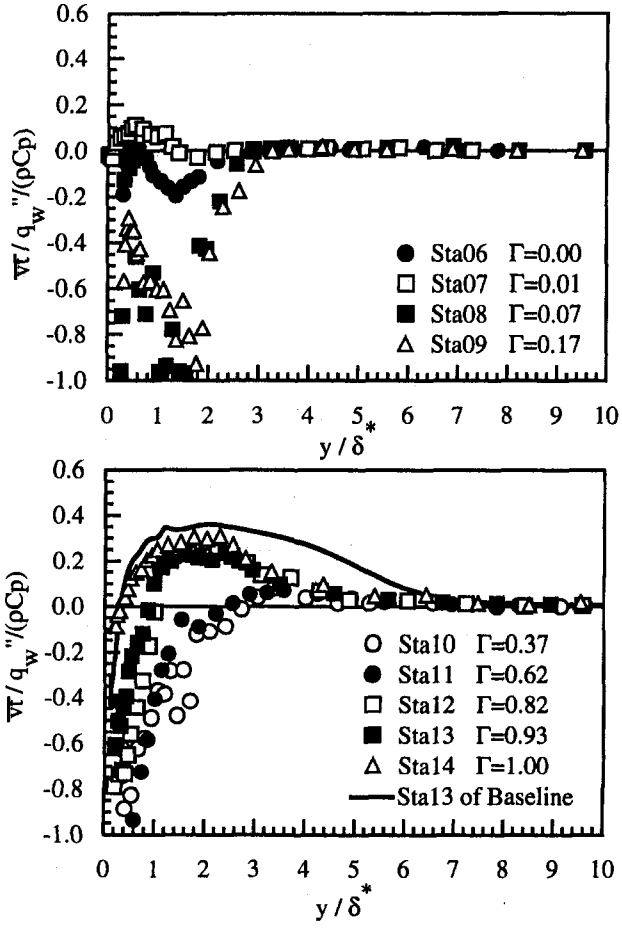


Fig. 20 Cross-stream Reynolds heat flux distributions for $K2 = 0.16 \times 10^{-6}$ case

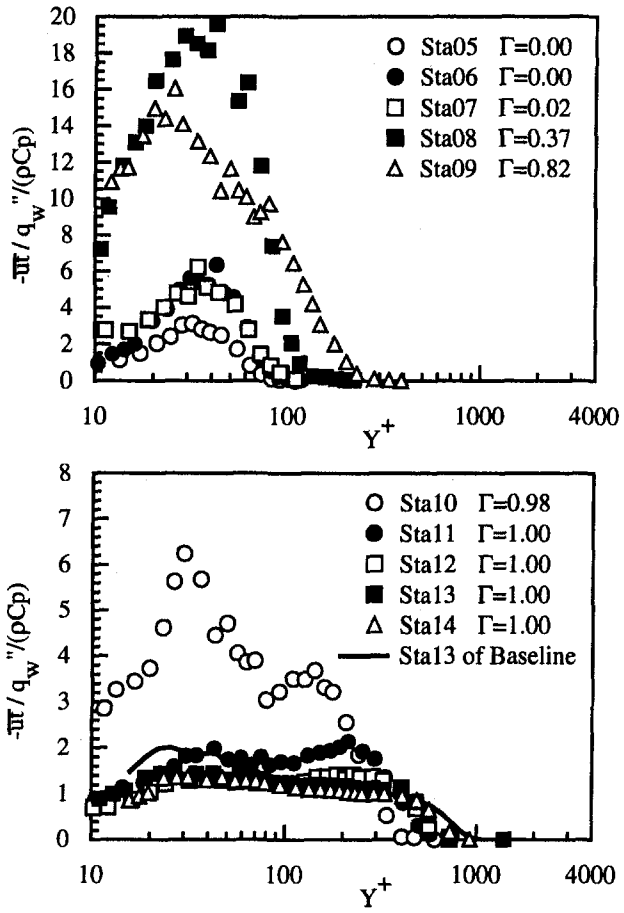


Fig. 21 Streamwise Reynolds heat flux distributions for $K1 = 0.07 \times 10^{-6}$ in wall units

Conclusions

The effects of streamwise acceleration on the flow and thermal structures of a two-dimensional heated boundary layer undergoing natural transition from laminar to turbulent flow were investigated in detail. A specially designed, miniature three-wire probe was used to measure the Reynolds stresses and

Table 2 Resultant uncertainties

Parameter	Uncertainty magnitude (%)
C_f	5
Cf (transition)	13
St	4
$\overline{U}$	2.8
$\overline{T}$	~0
u'	7.1
$\overline{uv}$	11.9
$\overline{vt}$	21.0
δ^*	3.6
θ	7.5
H	5.9
Y^+	4.7
U^+	4.7
T^+	3.2

Downloaded 01 Jun 2010 to 171.66.16.53. Redistribution subject to ASME license or copyright; see http://www.asme.org/terms/Terms_Use.cfm

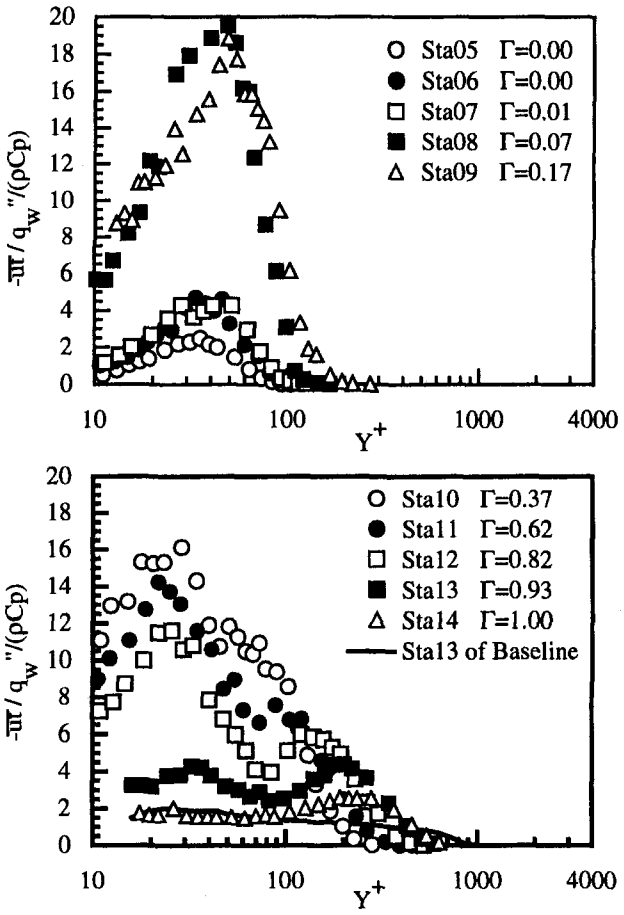


Fig. 22 Streamwise Reynolds heat flux distributions for $K2 = 0.16 \times 10^{-6}$ in wall units

heat fluxes within the transitional boundary layer. The primary conclusions are summarized below.

Streamwise acceleration was shown to delay the point of transition onset both in terms of physical distance, x, and Reynolds number based on x. The transition onset momentum Reynolds number, $Re_{\theta s}$, was relatively insensitive to acceleration. In general, the physical length of transition increased with increasing K. However, the transition length in terms of Re_θ was relatively constant with increasing K. This was supported by the boundary layer thickness and integral parameters, which indicated that an increasing pressure gradient suppresses boundary layer growth and development through the transition region. The streamwise fluctuating turbulent velocities were suppressed in the near-wall region ($Y^+ < 50$) relative to the baseline case as K increased. This was believed to be caused by an increased viscous dampening resulted from a thickening of the viscous sublayer relative to the boundary layer thickness. The lag that was observed between the mean temperature profiles and the mean velocity profiles for the baseline case became more pronounced with increasing K. Comparison of the evolution of rms temperature fluctuations to the evolution of u' indicated a lag in the rms temperature fluctuations. This supports the observation drawn from the mean temperature and velocity profiles that the thermal transport lags behind the momentum transport in the transitional process and that the effect is more pronounced as K increases.

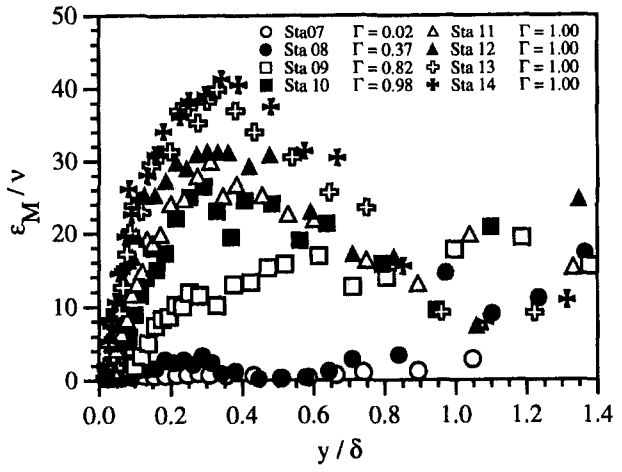


Fig. 23 Distribution of eddy viscosity for $K1 = 0.07 \times 10^{-6}$

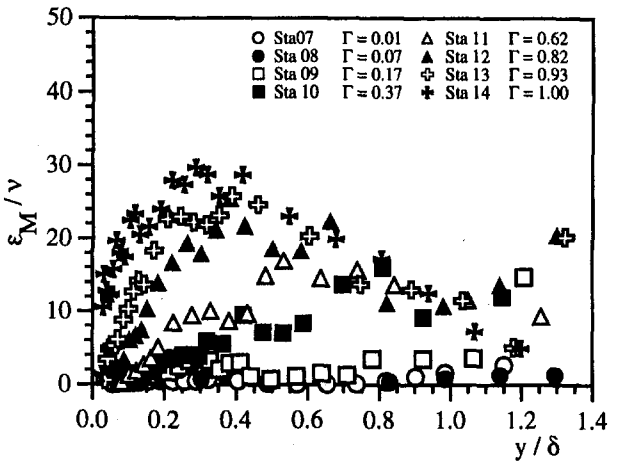


Fig. 24 Distribution of eddy viscosity for $K2 = 0.16 \times 10^{-6}$

These results suggest that in performing numerical analyses of transitional boundary layers, the thermal transport should not be directly inferred from the momentum transport by a simple extension of Reynolds analogy.

Acknowledgments

This program was primarily sponsored by the Air Force Office of Scientific Research (Grant No. AFOSR-89-0324). The program monitors were Major Daniel Fant and Dr. James M. McMichael. Partial funding was provided by The Office of Naval Research (Grant No. N00014-89-J-3105). The program monitor was Dr. Gabriel Roy.

References

Abu-Ghannam, B. J., and Shaw, R., 1980, "Natural Transition of Boundary Layers—The Effects of Turbulence, Pressure Gradient and Flow History," *J. Mech. Engr. Sci.*, Vol. 22, pp. 213–228.

Arnal, D., 1984, "Description and Prediction of Transition in Two-Dimensional, Incompressible Flow," AGARD-R-709, Vol. 2-1.

Blair, M. F., 1982, "Influence of Free-Stream Turbulence on Boundary Layer Transition in Favorable Pressure Gradients," ASME *Journal of Engineering for Power*, Vol. 104, pp. 743–750.

Blair, M. F., 1992, "Boundary Layer Transition in Accelerating Flows With Intense Free-Stream Turbulence; Part 1—Disturbances Upstream of Transition Onset; Part 2—The Zone of Intermittent Turbulence," ASME *Journal of Fluids Engineering*, Vol. 114, pp. 313–332.

Crawford, M. E., and Kays, W. M., 1976, "STAN5—A Program for Numerical Computations of Two-Dimensional Internal and External Boundary-Layer Flows," NASA CR-2742.

Julien, H. L., Kays, W. M., and Moffat, R. J., 1969, "The Turbulent Boundary Layer on a Porous Plate: An Experimental Study of the Effects of a Favorable Pressure Gradient," Report No. HMT-4, Thermosciences Division, Dept. of Mech. Engr., Stanford University, Stanford, CA.

Keller, F. J., 1993, "Flow and Thermal Structures in Heated Transitional Boundary Layers With and Without Streamwise Acceleration," Ph.D. Dissertation, Dept. of Mech. Engr., Clemson University, Clemson, SC.

Downloaded 01 Jun 2010 to 171.66.16.53. Redistribution subject to ASME license or copyright; see http://www.asme.org/terms/Terms_Use.cfm

Keller, F. J., and Wang, T., 1993, "Effects of Criterion Functions on Intermittency in Heated Transitional Boundary Layers With and Without Streamwise Acceleration," ASME Paper 93-GT-67; also ASME JOURNAL OF TURBOMACHINERY, Vol. 117, 1995, pp. 154–165.

Kim, J., Simon, T. W., and Kestoras, M., 1989, "Fluid Mechanics and Heat Transfer Measurements in Transitional Boundary Layers Conditionally Sampled on Intermittency," *Heat Transfer in Convective Flows,* ASME HTD-Vol. 107, pp. 69–81.

Kuan, C. L., 1987, "An Experimental Investigation of Intermittent Behavior in the Transitional Boundary Layer," M.S. Thesis, Dept. of Mech. Engr., Clemson University, Clemson, SC.

Kuan, C. L., and Wang, T., 1989, "Some Intermittent Behavior of Transitional Boundary Layers," AIAA Paper No. 89–1890.

Kuan, C. L., and Wang, T., 1990, "Investigation of Intermittent Behavior of Transitional Boundary Layers Using a Conditional Averaging," *Exp. Thermal and Fluid Sci.,* Vol. 3, pp. 157–170.

Ligrani, P. M., and Bradshaw, P., 1987, "Spatial Resolution and Measurement of Turbulence in the Viscous Sublayer Using Subminiature Hot-Wire Probes," *Experiments in Fluids,* Vol. 5, pp. 407–417.

Mayle, R. E., 1991, "The Role of Laminar–Turbulent Transition in Gas Turbine Engines," ASME JOURNAL OF TURBOMACHINERY, Vol. 113, pp. 509–537.

Musker, A. J., 1979, "Explicit Expression for the Smooth Wall Velocity Distribution in a Turbulent Boundary Layer," *AIAA Journal,* Vol. 17, No. 6, pp. 655–657.

Narasimha, R., 1985, "The Laminar-Turbulent Transition Zone in the Boundary Layer," *Prog. Aerospace Sci.,* Vol. 22, pp. 29–80.

Rued, K., and Wittig, S., 1985, "Free-Stream Turbulence and Pressure Gradient Effects on Heat Transfer and Boundary Layer Development on Highly Cooled Surfaces," ASME *Journal of Engineering for Gas Turbines and Power,* Vol. 107, pp. 54–59.

Rued, K., and Wittig, S., 1986, "Laminar and Transitional Boundary Layer Structures in Accelerating Flow With Heat Transfer," ASME JOURNAL OF TURBOMACHINERY, Vol. 108, pp. 116–123.

Schubauer, G. B., and Klebanoff, P. S., 1956, "Contributions on the Mechanics of Boundary-Layer Transition," NACA Technical Note #1289, supersedes NACA TN #3489.

Sharma, O. P., 1987, "Momentum and Thermal Boundary Layer Development on Turbine Airfoil Suction Surfaces," AIAA Paper No. 87-1918.

Shome, B., 1991, "Development of a Three-Wire Probe for the Measurement of Reynolds Stresses and Heat Fluxes in Transitional Boundary Layers," M.S. Thesis, Dept. of Mech. Engr., Clemson University, Clemson, SC.

Sohn, K. H., O'Brien, J. E., and Reshotko, E., 1989, "Some Characteristics of Bypass Transition in a Heated Boundary Layer," NASA TM102126.

Turner, A. B., 1971, "Local Heat Transfer Measurements on a Gas Turbine Blade," *J. of Mech. Engr. Sci.,* Vol. 13, No. 1, pp. 1–12.

Volino, R. J., and Simon, T. W., 1991, "A Review of Bypass Transition in Boundary Layers," NASA CR-187187.

Wang, T., Simon, T. W., and Buddhavarapu, J., 1985, "Heat Transfer and Fluid Mechanics Measurements in Transitional Boundary Layer Flows," ASME *Journal of Engineering for Gas Turbines and Power,* Vol. 107, pp. 1007–1015.

Wang, T., Keller, F. J., and Zhou, D., 1992, "Experimental Investigation of Reynolds Shear Stresses and Heat Fluxes in a Transitional Boundary Layer," *Fundamental and Applied Heat Transfer Research for Gas Turbine Engines,* ASME HTD-Vol. 226, pp. 61–70.

Zhou, D., 1993, "Flow and Thermal Structures in Heated Transitional Boundary Layers With Elevated Free-Stream Turbulence and Pressure Gradients," Ph.D. Dissertation, Dept. of Mech. Engr., Clemson University, Clemson, SC.

Zhou, D., and Wang, T., 1992, "Laminar Boundary Layer Flow and Heat Transfer With Favorable Pressure Gradient at Constant K Values," ASME paper 92-GT-246.

Zhou, D., and Wang, T., 1993, "Combined Effects of Elevated Free-Stream Turbulence and Streamwise Acceleration on Flow and Thermal Structures in Transitional Boundary Layers," *Gas Turbine Heat Transfer,* ASME HTD-Vol. 242, pp. 41–52; also to appear in *Experimental Thermal and Fluid Science,* 1996.

Downloaded 01 Jun 2010 to 171.66.16.53. Redistribution subject to ASME license or copyright; see http://www.asme.org/terms/Terms_Use.cfm

Unsteady Boundary Layers on a Flat Plate Disturbed by Periodic Wakes: Part I—Measurement of Wake-Affected Heat Transfer and Wake-Induced Transition Model

K. Funazaki
Department of Mechanical Engineering,
Iwate University,
Morioka, Iwate,
Japan

Measurements of wake-affected heat transfer distributions on a flat plate are made by use of a wake generator that consists of a rotating disk and several types of circular cylinder. The main purpose of this study is to construct a wake-induced transition model in terms of an intermittency factor, considering the evolution of the wake-induced turbulent region, a so-called turbulent patch in a distance–time diagram. A comparison between the proposed transition model and the measured heat transfer data reveals that the transition model yields good agreement with the measured data of all test conditions in this study.

Introduction

Transition phenomena in gas turbine engines have been one of the most important issues facing aerodynamists as well as cooling designers of turbine blades. Recently, wake-induced transition of boundary layers over blade surfaces has received much attention from a large number of researchers. Considerable amounts of observation about transition phenomena have been made, for example by Pfeil and Herbst (1979), Pfeil et al. (1983), LaGraff et al. (1989), Addison and Hodson (1990a, b), and Dullenkopf et al. (1991), and accordingly several models of the wake-induced transition are proposed in a somewhat phenomenological fashion by Addison and Hodson (1992), Dong and Cumpsty (1990) or in semi-analytical ways by Addison and Hodson (1990a, b), Mayle and Dullenkopf (1990, 1991). In a practical sense, the Mayle–Dullenkopf model seems to be useful for predicting wake-affected heat transfer along a blade surface, which is described in terms of the intermittency factor as follows:

$$\gamma_w(x) = 1 - \exp\left[-C\left(\frac{x - x_w}{U_\infty T}\right)\right], \quad C = 1.9 \qquad (1)$$

where x_{tw} is a wake-induced transition point, U_∞ is a free-stream velocity and T is a wake-passing period. This Mayle–Dullenkopf model, which was developed on the basis of a statistical approach by Emmons (1951) in conjunction with some experimental data, reportedly yielded good agreements with the experimental data employed in their studies.

On the other hand, Funazaki et al. (1993) conducted an experimental simulation for wake–blade interaction, using a bar-type wake generator and a flat plate, in order to investigate wake-affected heat transfer distributions over the plate surface with no pressure gradient, whose results were then compared with the Mayle–Dullenkopf model. Consequently, it was found that the wake-affected heat transfer distributions obtained in several cases of the wake-passing frequency could not be adequately reproduced by Eq. (1) with no manipulation of the constant C in Eq. (1), x_{tw} being regarded as a constant for a fixed Reynolds number. In addition, in the highest wake-passing frequency, any attempts using the Mayle–Dullenkopf model failed to produce a reasonable agreement with the experimental data. A similar finding is recently reported by Han et al. (1993). Using the results obtained, Funazaki et al. proposed another transition model. It was based on the evolution of wake-induced turbulent spots (or turbulent patch) in the distance–time diagram as shown in Fig. 1, which was similar to that of Pfeil et al. (1983). Their transition model is expressed as follows:

$$\gamma_w(x) = \left(\frac{1}{U_E} - \frac{1}{U_F}\right)\frac{x - x_{tw}}{T}$$

$$= \left(\frac{1}{\beta_E} - \frac{1}{\beta_F}\right)\frac{x - x_{tw}}{L}S$$

$$S = \frac{L}{U_\infty T},$$

where $U_E \equiv \beta_E U_\infty$ and $U_F \equiv \beta_F U_\infty$ are propagation speeds of the preceding and following portions of the turbulent patch. Note that the values of coefficients β_E and β_F are assumed to be 0.55 and 1.0, respectively. It was somewhat surprising to see that this simple transition model successfully predicted the wake-affected heat transfer distributions for all of the unsteady flow conditions employed in that study, where the wake-induced transition point was experimentally determined.

Although the proposed model in Eq. (2) is verified to yield a reasonable prediction of wake-affected heat transfer on a flat plate surface with no pressure gradient, there still remain several points to be considered for a more accurate and reliable transition model. For example, the effects of incident wake characteristics, e.g., turbulence intensity involved within the wake or wake duration, on the transition are not fully discussed. Furthermore, there is no clear criterion of a wake-induced transition point to date.

Contributed by the International Gas Turbine Institute and presented at the 39th International Gas Turbine and Aeroengine Congress and Exposition, The Hague, The Netherlands, June 13–16, 1994. Manuscript received by the International Gas Turbine Institute February 24, 1994. Paper No. 94-GT-429. Associate Technical Editor: E. M. Greitzer.

Copyright © 1996 by ASME

Downloaded 01 Jun 2010 to 171.66.16.53. Redistribution subject to ASME license or copyright; see http://www.asme.org/terms/Terms_Use.cfm

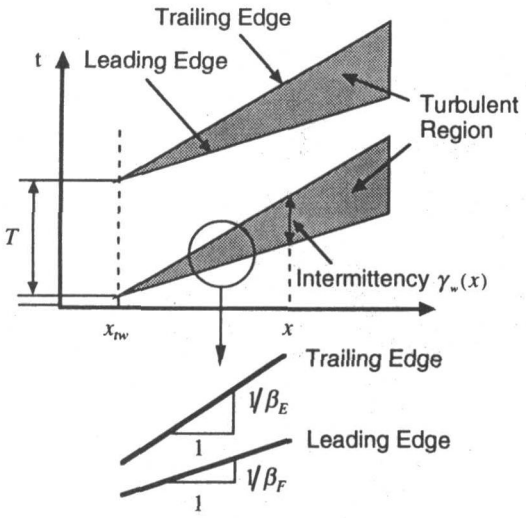


Fig. 1 Schematic of wake-induced transition model in a distance-time diagram (Funazaki et al., 1993)

Accordingly, the emphasis of this experimental study as Part I is placed on the investigation of the wake characteristics effects, from which results are utilized to develop a more accurate wake-induced transition model. In Part II, the onset of the transition will be argued on the basis of the hot-wire measurements of the unsteady transitional boundary layers in conjunction with the heat transfer data obtained in Part I.

Experimental Investigation

Test Apparatus. A brief explanation on the test apparatus and the measurement system is made, because it is largely the same as the previous study of Funazaki et al. (1993). Figure 2 shows the test apparatus used in this study. Air from the nozzle with a speed of 30 m/s and a turbulence intensity less than 1.0 percent is fed to the test section through the wake generator, as shown in the lower portion of Fig. 2. This wake generator consists of a rotating disk with diameter of 400 mm and several circular cylinders attached on the disk rim. Three types of cylinders with different diameters, i.e., 2 mm, 5 mm, and 10 mm, are used to observe how such differences in wake characteristics can affect the wake-induced transition. The test section is a rectangular acrylic resin duct with 120 mm × 240 mm cross section and has slots through which the cylinders can pass. The rotational speed of the disk is changed with a transmission gear

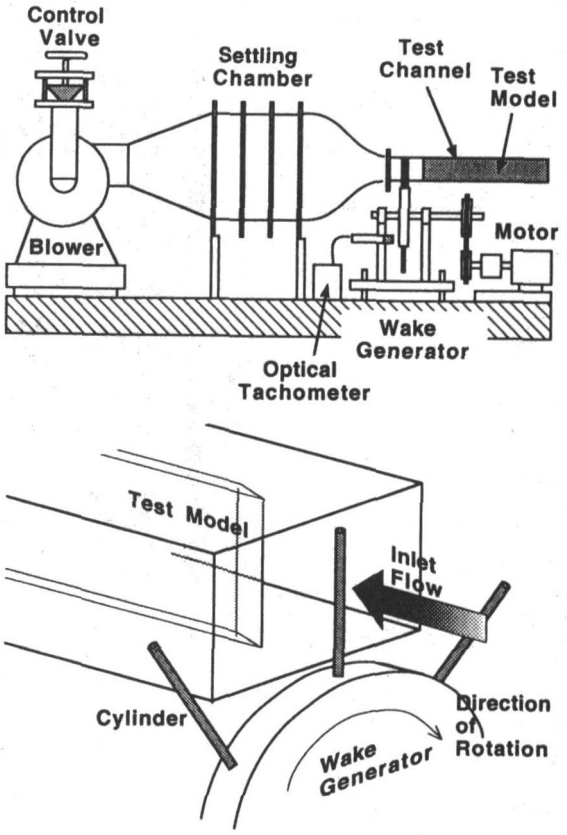


Fig. 2 Test apparatus (upper), wake generator (lower)

Nomenclature

d = diameter of cylinder
f = wake passing frequency
h = heat transfer coefficient
L = length of the flat plate
l_D = distance between the wake generating cylinder and the leading edge of the flat plate
max[ ], min[ ] = functions that select maximum and minimum values from the values in the brackets
n = revolution number
n_c = number of cylinders
$\dot{q}_w$, $\dot{q}_{\text{loss}}$, $\dot{q}_{\text{supply}}$ = surface heat flux, heat loss, supplied heat flux
Re = Reynolds number = $U_\infty L/\nu$
Re_x = Reynolds number based on the length measured from the leading edge of the plate
Re_θ = momentum thickness Reynolds number
S = Strouhal number
S_w = wake passing Strouhal number = $L/(U_\infty T)$
$\text{St}(x)$ = local Stanton number
$\text{St}_{NW}(x)$ = local Stanton number obtained in the no-wake case
$\text{St}_T(x)$ = local Stanton number obtained in the fully turbulent case
T = wake passing period
t = time
Tu = ensemble-averaged turbulence intensity
$T_w(x)$, T_∞ = local surface temperature, free-stream temperature
U_E, U_F = trailing edge and leading edge propagation velocities of turbulent spot
U_∞ = free-stream velocity
$u(t_j)$ = instantaneous velocity
$\tilde{u}(t_j)$, $u'^2(t_j)$ = ensemble-averaged velocity, ensemble-averaged variation of velocity
x = surface length from the leading edge
x_{tw} = start point of forced transition
y = distance from the plate surface
$\gamma_w(x)$ = wake-induced local intermittency factor of the boundary layer
τ_w = wake duration time

Subscripts

NW = no wake
T = turbulent

Downloaded 01 Jun 2010 to 171.66.16.53. Redistribution subject to ASME license or copyright; see http://www.asme.org/terms/Terms_Use.cfm

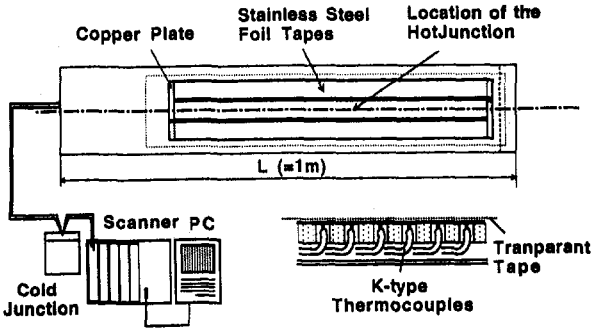


Fig. 3 Test model for heat transfer measurement, showing the installation of the thermocouples

box connected to the induction motor and is sensed by an optical tachometer. Flow rate through the test section can be controlled by the valve of the blower intake and is monitored by a Pitot tube installed at the duct.

A sharp-edged flat plate of 1000 mm length and 10 mm thickness is used for the measurement of the heat transfer rate; it is placed within the duct aligned almost along its centerline. The distance between the plate and the wake generator, l_D, is usually fixed to be 0.12 m, but it can be changed in order to vary wake characteristics, e.g., wake depth, on the flat plate. Sixty equally spaced holes of 5 mm diameter are drilled through the plate along the center line. As shown in Fig. 3, each of the holes is plugged with urethane foam and a hot junction of K-type (chromel-alumel) thermocouple is then flush-mounted on the surface to be measured, penetrating back through the foam. The wires of the thermocouples are buried inside a slot on the back of the plate. Both sides of the plate are covered with stainless steel foil adhesive tapes of 30 μm thickness, which are soldered onto copper plates and heated by electricity. For the purpose of preventing the buckling of the foils during heating, transparent tapes (3M Book Tape 845, 90 μm thickness) is pasted on the stainless foils. Temperature drop through this tape is about 0.025°C.

Smooth inflow to the flat plate is achieved by adjusting the open area of the duct exit, which is confirmed by the oil flow pattern on the plate. This is also the case in the unsteady flow conditions since even in the wake the inflow has a slight negative incidence to the measured surface of the plate at most and causes no flow separation around the leading edge.

Measuring System

Wake Characteristics. Figure 4(a) shows the wake measuring system in this study. An I-type hot-wire probe (Kanomax, Model 0251R) is used not only to detect the wake profile in front of the flat plate, but also to investigate the streamwise variation of wake characteristics above the plate, as will be shown in Fig. 5. Signals from the hot-wire probe are processed by a constant-temperature anemometer (Kanomax, System 7201) and the linearized signals are then A/D converted by the computer-controlled digitizer (Autonix, APC-204), with a sampling frequency of 50 kHz and memory size of the logged data per process 2048 words. Each of the data-acquisition processes is triggered by a signal from the optical tachometer, which yields test data synchronized with the disk revolution.

For one test condition, 256 lines of time-serial digitized data for velocity, $v_i(t_j)$ ($j = 1, \ldots, 2048$), are logged. They are transferred back to the computer, and then stored in the auxiliary memory unit for subsequent off-line calculation, as described in the following.

Ensemble-averaged velocity $\tilde{v}_i(t_j)$ and its variance $v'^2(t_j)$ are calculated as

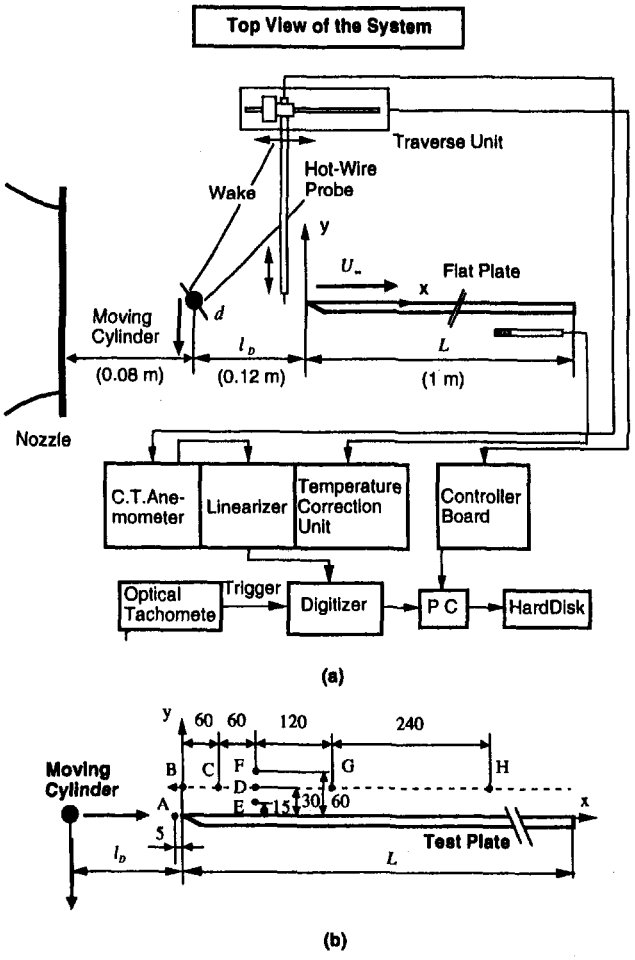


Fig. 4 (a) Measuring system (upper); (b) locations for the wake profile measurement (lower)

$$\tilde{v}(t_j) = \frac{1}{k}\sum_{i=1}^{k} v_i(t_j), \quad k = 256 \tag{3}$$

$$v'^2(t_j) = \frac{1}{k-1}\sum_{i=1}^{k} [v_i(t_j) - \tilde{v}(t_j)]^2. \tag{4}$$

Local turbulence intensity is then defined as

$$Tu(t_j) = \frac{\sqrt{v'^2(t_j)}}{U_\infty}. \tag{5}$$

Heat Transfer. After confirming thermal equilibrium conditions by monitoring the surface temperature distribution, the signals from all the thermocouples embedded in the flat plate

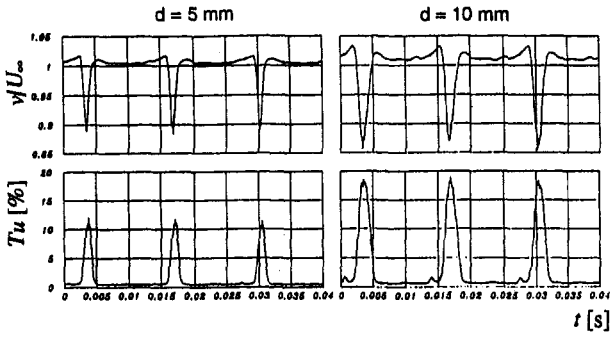


Fig. 5 Ensemble-averaged wake profiles obtained at point A in Fig. 4 for d = 5 mm and d = 10 mm

Downloaded 01 Jun 2010 to 171.66.16.53. Redistribution subject to ASME license or copyright; see http://www.asme.org/terms/Terms_Use.cfm

are scanned 10 times during about 30 seconds. They are then averaged for each measuring point to obtain time-averaged heat transfer characteristics, i.e., Stanton number distribution St or heat transfer coefficient distribution h, which are determined as follows:

$$\mathrm{St}(x) = \frac{\dot{q}_w}{c_p U_\infty (T_w(x) - T_\infty)} = \frac{\dot{q}_{\text{supply}} - \dot{q}_{\text{loss}}}{c_p U_\infty (T_w(x) - T_\infty)} \quad (6)$$

$$h(x) = \frac{\dot{q}_w}{(T_w(x) - T_\infty)} = \frac{\dot{q}_{\text{supply}} - \dot{q}_{\text{loss}}}{(T_w(x) - T_\infty)}, \quad (7)$$

where $T_w(x)$ is the time-averaged surface temperature, T_∞ is the free-stream temperature measured at the aft portion of the test section, and $\dot{q}_w$ is the surface heat flux. Preliminary experiments determined the correlation for the heat flux $\dot{q}_{\text{loss}}$ that did not contribute to the convective heat transfer. Attention was paid to maintaining the same level of the average of the temperature difference $T_w(x) - T_\infty$ almost constant (≈ 10°C) in every test run as well as to avoiding overheating of the foils, because the air temperature sometime rose to more than 30°C. Average uncertainty in the Stanton number is estimated by the method of Kline and McClintock (1953) and is about ± 7 percent.

Results

Wake Profiles. Figure 4(b) shows the locations of wake measurement points around the test plate. Wake profiles obtained ahead of the leading edge of the plate (point A in Fig. 4(b)) are presented in Fig. 5 for the two wake-generating cylinders, which are expressed in terms of the ensemble-averaged velocity distribution as well as the ensemble-averaged turbulence intensity distribution with respect to time. Maximum values of turbulence intensity measured within the wakes, $Tu_{\max}$, for the cylinders with diameters of 2 mm, 5 mm, and 10 mm are about 6, 12, and 18 percent, respectively. These values are found to be almost unchanged even at a doubled rotational speed of the disk in the wake generator. It is also discovered that the turbulence intensity distributions, not in a rigorous sense, can be approximated by a Gaussian distribution, namely

$$Tu(t) = \max\left[Tu_b,\ Tu_{\max}\exp\left(-\ln 2\left(\frac{t}{\tau_{1/2}}\right)^2\right)\right], \quad (8)$$

where Tu_b is a background turbulence intensity, i.e., free-stream turbulence intensity; $\tau_{1/2}$ is a semi-depth width for a turbulence intensity profile. From a comparison between the velocity profiles and the turbulence intensity profiles, it is found that a semi-depth width for the turbulence intensity profile is about 1.5 times as large as that of the corresponding velocity profile, that is,

$$\tau_{1/2,Tu} \cong 1.5\tau_{1/2,\text{velocity}}. \quad (9)$$

Measurements at several points in Fig. 5 demonstrate some of the wake profile variations in the streamwise and crossflow direction. Figures 6(a) and (b), in the cases of 5-mm and 10-mm-dia cylinders, show streamwise variations of wake profiles measured along the plane with 30 mm distance from the test plate surface. Despite the streamwise wake decay, wakes measured at the farthest point downstream from the leading edge still retain considerable amount of the turbulence intensities. In the velocity profiles of the wakes, shown in the upper portion of each of the graphs, there always appears a slight acceleration before the velocity deficit. Such acceleration tends to be pronounced in the case of larger cylinder diameter, as well as in the case of closer measurement point to the plate surface as shown in Figs. 7(a) and 7(b). Meyer (1957) explained these phenomena as a negative jet effect. One of the interesting findings in Fig. 7 is that the turbulence intensity profiles within the wakes do no exhibit any drastic changes even when the measurement point moves close to the wall, in contrast to the corresponding velocity profiles, which suffer from deformation so severely that one may not identify the extent of the wake correctly. Hence, the present author holds that wake characteristics, e.g., wake duration, must be defined in terms of turbulence intensity, not velocity.

Wake-Affected Heat Transfer

Effect of Wake-Passing Frequency. It is understood from the previous studies by Mayle and Dullenkopf (1990) as well as by Funazaki et al. (1993) that wake-affected heat transfer becomes more enhanced in the higher wake-passing frequencies. This is also the case in the present study as shown in Figs. 8(a) for the 5-mm-dia case and 8(b) for the 10-mm-dia case. In these figures the data referred to as "Turbulent" were obtained with one of the cylinders on the disk rim being fixed just in front of the plate leading edge so that the wake from that cylinder covers the plate surface all the time, while the data referred to as "No Wake" mean the heat transfer distribution under no-wake flow condition. It should be noted that an inlet Reynolds number, Re ($= U_\infty L/\nu$) adopted in this study is unchanged and is 2×10^6 for all cases. Also shown in these figures are the results obtained from the correlations for constant surface heat flux case given by Kays and Crawford (1980), which are for a laminar boundary layer,

$$\mathrm{St} = 0.453\mathrm{Pr}^{-2/3}\mathrm{Re}_x^{-1/2}, \quad (10)$$

and for a turbulent boundary layer,

$$\mathrm{St} = 0.0287\mathrm{Pr}^{-0.4}\mathrm{Re}_x^{-0.2}. \quad (11)$$

Note that the unheated starting length ($\cong 0.04$ m) is taken into account for both cases. The obtained Stanton numbers for the "No Wake" and the "Turbulent" mostly follow Eqs. (10) and (11), although slight differences appear.

By changing the disk rotational speed from 900 rpm to 1500 rpm, which corresponds to Strouhal numbers ranging from 1.5 to 2.5, the measured Stanton number distributions along the surface accordingly increase from the base line data, i.e., "steady flow," toward the turbulent flow case. This means that the boundary layer under the influence of the periodic wakes is in a transitional state and such wakes surely promote earlier transition of the boundary layer. At the highest wake-passing frequency, as shown in Fig. 9, the boundary layer completes its transition process so quickly that a larger portion of the test plate is covered with the turbulent boundary layer. Figure 10 demonstrates dominant effects of the wake-passing frequency on the wake-affected heat transfer. In such a case, remarkable agreement is obtained between the two heat transfer distributions under the same wake-passing frequency, even though combinations of the disk rotation speed and the number of cylinders on the disk rim are quite different.

Effect of Cylinder Diameter. Quantitative differences in heat transfer enhancement by wakes became very obvious among the experimental data obtained for the three different cylinders. Such a difference is more visible in Fig. 11. It is not difficult to predict this difference when recalling the above-mentioned large differences in the wake characteristics, but the present author would like to draw the readers' attention to the point that the original Mayle–Dullenkopf model of Eq. (1) as well as the previously proposed model of Eq. (2) takes no account of any information about the wake structure in an explicit manner. Therefore, they cannot explain the difference in heat transfer without manipulation of the transition point, x_{tw}. In the next section, it will be shown that Eq. (2) can be modified in a very simple fashion to include effects originating from the wake structure.

Effect of the Distance Between the Test Plate and the Moving Cylinders. Figure 12 shows a sample of wake-affected heat transfer distributions obtained by changing the distance between

Downloaded 01 Jun 2010 to 171.66.16.53. Redistribution subject to ASME license or copyright; see http://www.asme.org/terms/Terms_Use.cfm

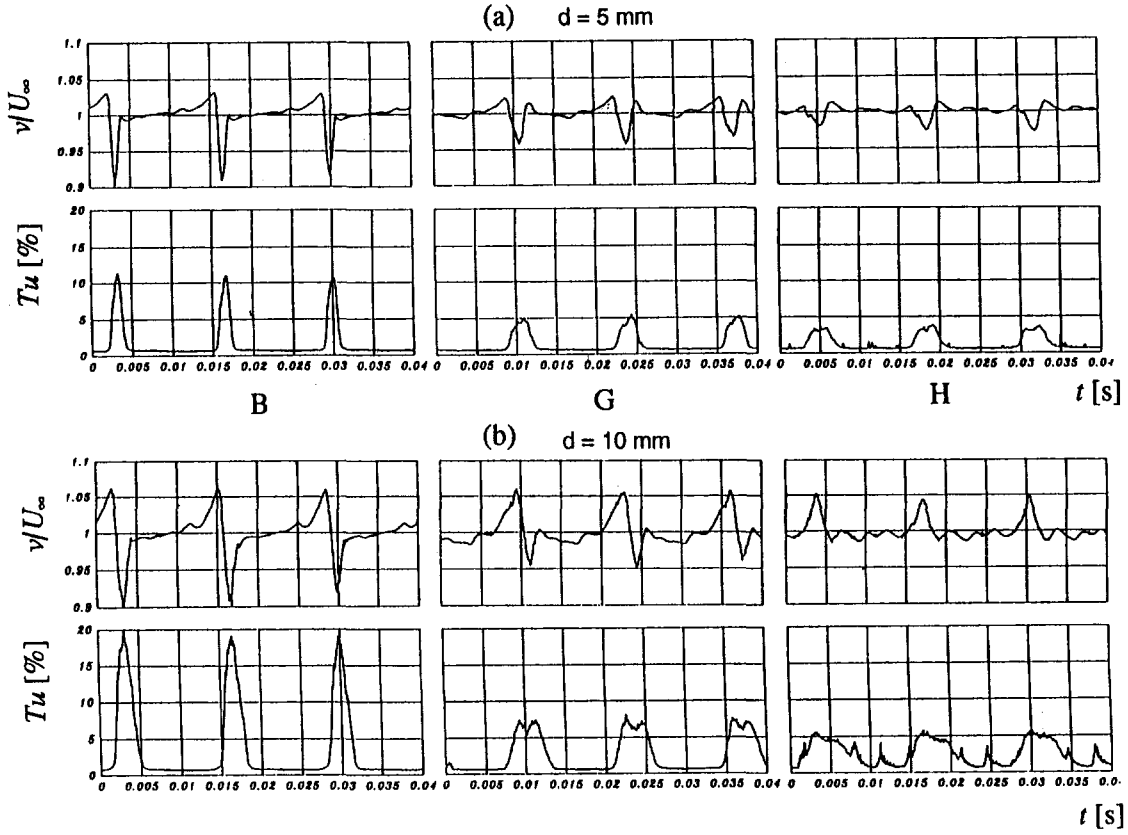


Fig. 6 Streamwise variations of the ensemble-averaged wake profiles: (*a*) d = 5 mm, (*b*) d = 10 mm

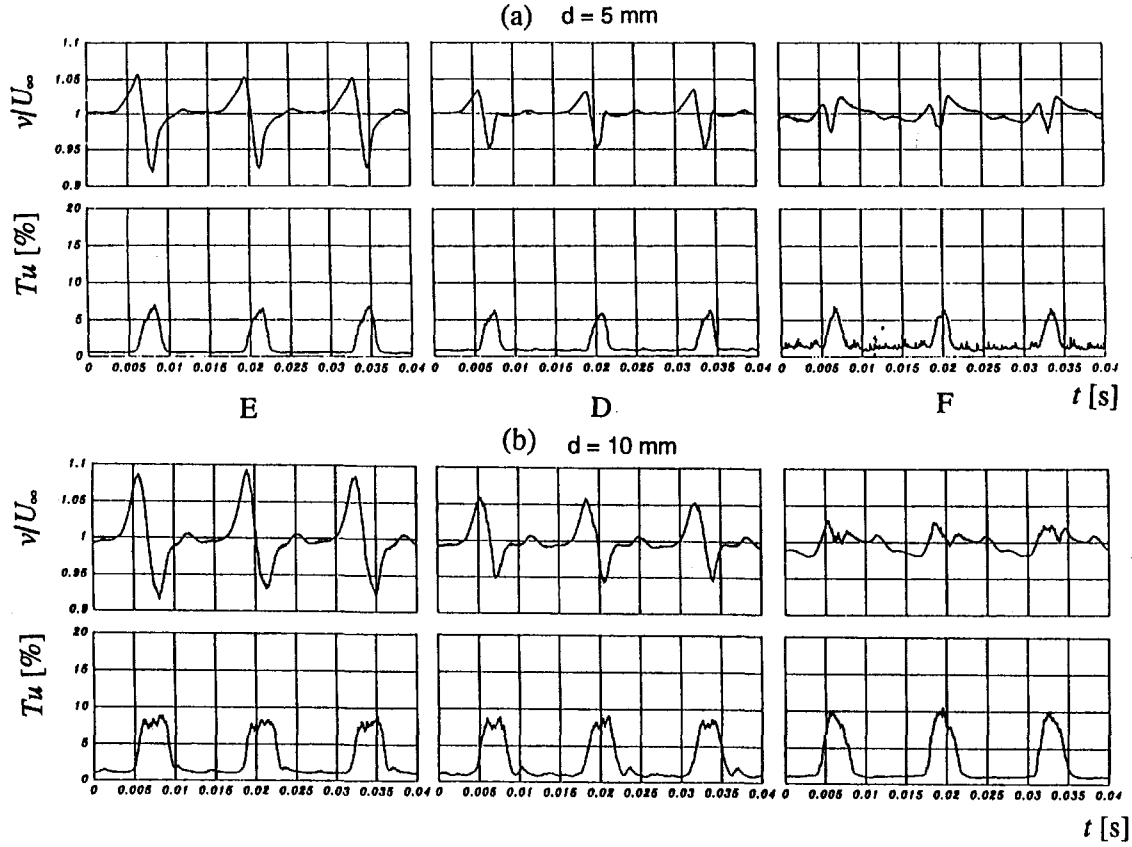


Fig. 7 Effect of the gap between the measuring point and the plate surface on the wake profiles: (*a*) d = 5 mm, (*b*) d = 10 mm

Downloaded 01 Jun 2010 to 171.66.16.53. Redistribution subject to ASME license or copyright; see http://www.asme.org/terms/Terms_Use.cfm

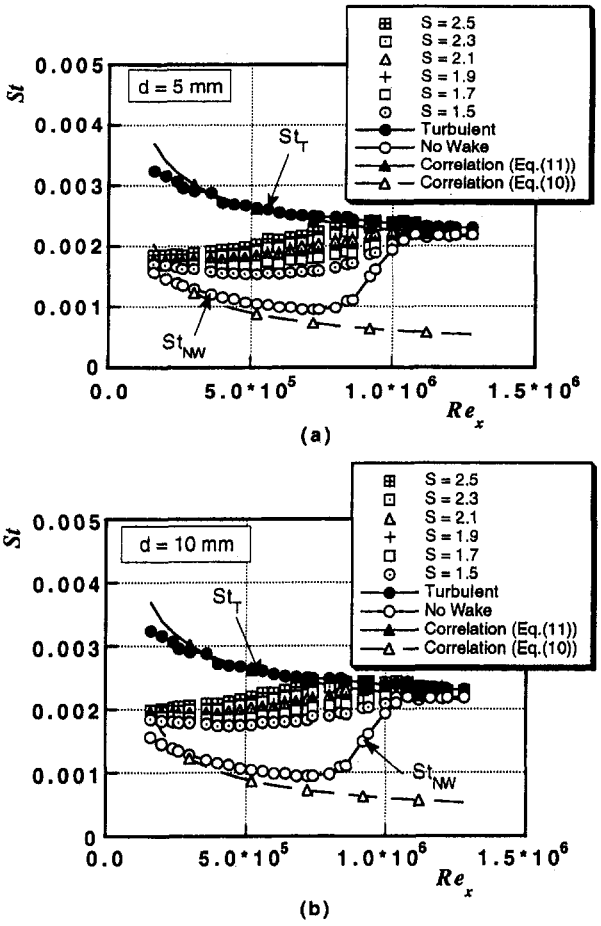


Fig. 8 Stanton number distributions for several Strouhal numbers: (*a*) d = 5 mm, (*b*) d = 10 mm

the plate and the moving cylinders from 0.06 m to 0.24 m. These cases correspond to $X/d \cong 10$ through 40, where X is a distance measured along the relative exit flow direction from the cylinder. Such a wake-affected heat transfer is seemingly most enhanced at $l_D = 0.06$, but the difference among the data in Fig. 12 is not as noticeable as was expected from the enlarged relative distance between the cylinders and the test plate.

Modified Wake-Induced Transition Model

As mentioned above, the published wake-induced transition models need to be modified in order to reproduce the heat

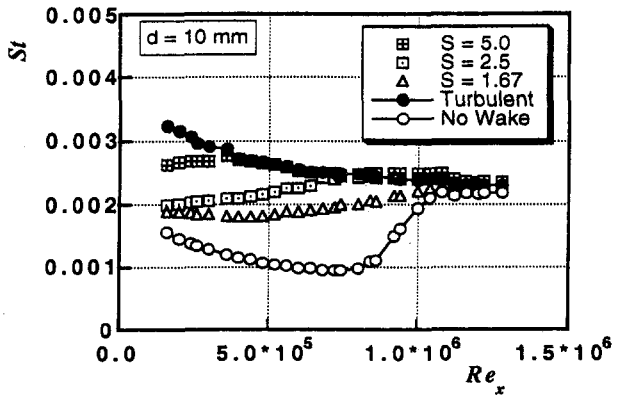


Fig. 9 Stanton number distributions for several Strouhal numbers, including the highest Strouhal number case (d = 10 mm)

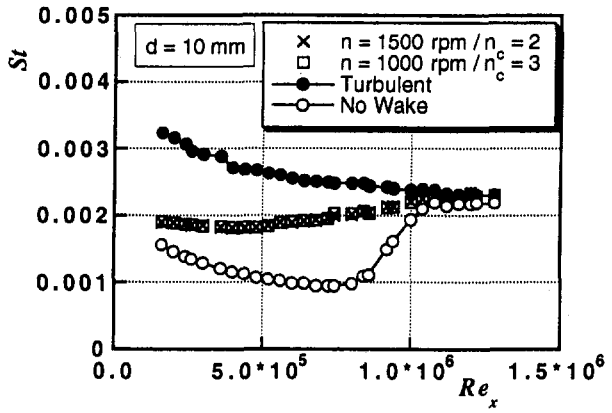


Fig. 10 Dominant effect of the Strouhal number on the heat transfer augmentation by the wake passage

transfer enhancement caused by wakes of larger diameter cylinders. One way to achieve this end is to shift the forced transition point in the upwind direction. Best fitting of the measured intermittency factor, namely

$$\gamma(x) = \frac{\mathrm{St}(x) - \mathrm{St}_{NW}(x)}{\mathrm{St}_T(x) - \mathrm{St}_{NW}(x)}, \qquad (12)$$

with Eq. (2) yields new forced transition points, which are, for the data in Fig. 11, about −0.02 m for 5-mm-dia cylinder and

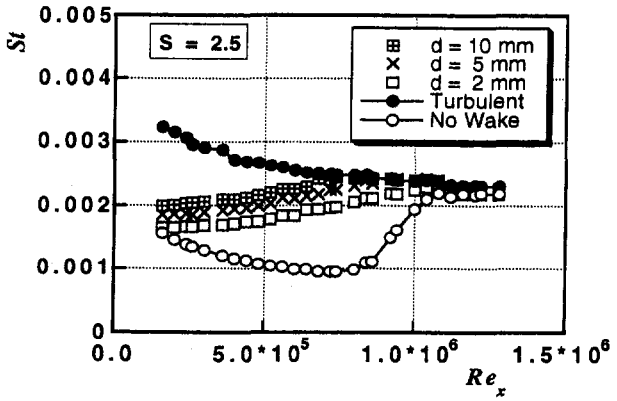


Fig. 11 Effect of the cylinder diameters on the heat transfer (S = 2.5)

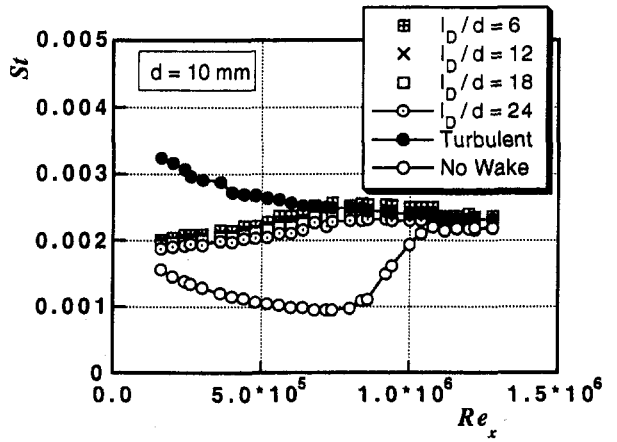


Fig. 12 Effect of the axial distance between the wake-generating cylinders and the plate leading edge upon the heat transfer (S = 2.5)

Downloaded 01 Jun 2010 to 171.66.16.53. Redistribution subject to ASME license or copyright; see http://www.asme.org/terms/Terms_Use.cfm

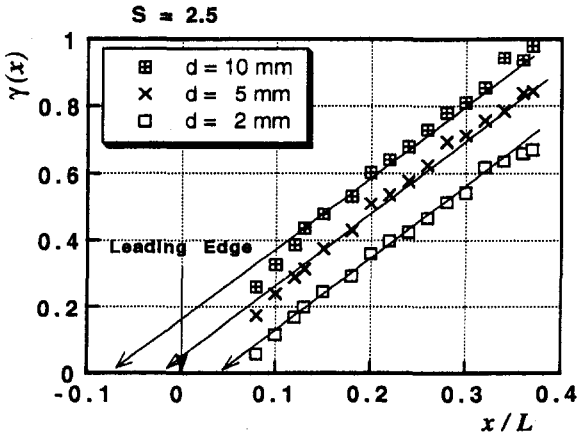


Fig. 13 Intermittency factor plots against the distance from the leading edge

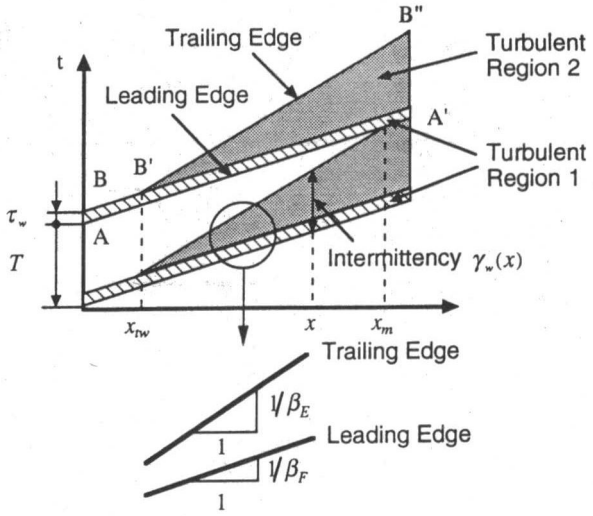


Fig. 14 Schematic of the modified wake-induced transition model in a distance–time diagram

about −0.08 m for 10-mm-dia cylinder as shown in Fig. 13. These negative values indicate that wake-induced transitions start before the plate leading edge, therefore they are unacceptable for wake-induced transition points because they don't have any physical meanings. Thus we must seek another approach for modifying the transition model.

According to Addison and Hodson (1990a, b), the time taken for wake turbulence to diffuse into a laminar boundary layer is very short compared to the wake-passing period. They have shown that the ratio of the diffusion time to the period is approximately represented by the ratio of a molecular kinematic viscosity to a wake-associated eddy viscosity. This means that the boundary layer over which the wake is passing may be immediately activated to become turbulent by the turbulence kinetic energy pouring in. While the laminar boundary layer thickness is very thin and velocity gradient is large, a viscous effect around there is strong enough to dissipate the turbulence kinetic energy quickly, so that the boundary layer is supposed to return to a nondisturbed condition after the wake goes away. This supposition implies that the turbulent state of the boundary layer lasts only for the wake duration, and the wider a wake width, the longer the boundary layer remains turbulent. A similar approach was used by Dullenkopf and Mayle (1994) in order to evaluate the effect of the wake passing on the laminar boundary layer. After the boundary layer grows to some extent, it becomes more susceptible to the turbulence kinetic energy diffused from the wake, then turbulent spots finally emerge inside the boundary layer causing the onset of wake-induced transition.

On the basis of this idea of the wake-induced transition, a distance–time diagram for the boundary layer state under the influence of periodic wakes can be illustrated as shown in Fig. 14. Equation (2) is then modified so as to have the following transition model, namely

$$\gamma_w(x) = \min\,[1,\ \Gamma(x)]$$

$$\Gamma(x) = \left(\frac{1}{\beta_E} - \frac{1}{\beta_F}\right)\frac{x - x_{tw}}{U_\infty T} + \frac{\tau_w}{T}$$

$$= \left(\frac{1}{\beta_E} - \frac{1}{\beta_F}\right)\frac{x - x_{tw}}{L}\,\mathrm{S} + \frac{\mathrm{S}}{\mathrm{S}_w}, \quad x \geq x_{tw}$$

$$\Gamma(x) = \frac{\mathrm{S}}{\mathrm{S}_w}, \quad x < x_{tw},$$

$$\mathrm{S} = \frac{L}{U_\infty T}, \quad \mathrm{S}_w = \frac{L}{U_\infty \tau_w}, \tag{13}$$

where S is the Strouhal number and τ_w is the wake duration. The diagram in Fig. 14, similar to that of Hodson (1990), has several features to be noted. First, the duration of a turbulent region caused just beneath an incoming wake, which we refer to as "Turbulent Region 1," is assumed constant from the plate leading edge throughout to the end of the transition, despite the fact that the wake profile of turbulence intensity suffers from somewhat gradual deformation as observed in the previous section. Second, for simplicity a wake-induced point is defined by the location where another turbulent region referred to as "Turbulent Region 2" appears and starts to follow the preceding wake. This turbulent region 2 has its origin from wake-induced turbulent spots, so that the moving speed of the trailing edge should be the same with that of turbulent spots, i.e., 0.55 U_∞ in this case.

One might feel that the expression for the intermittency by Eq. (13) or the diagram in Fig. 14 is too deterministic when considering the randomness of the transition process as well as of the wake itself. This is critical for determining the onset of the wake-induced transition, as described by Mayle (1991). When averaged, however, the effect of the randomness can be expected to become confined, consequently Eq. (13) works fairly well to predict the wake-affected heat transfer as will be shown later.

The present author is aware that there have been some discussions on the relationship between a wake-induced transition and wake characteristics. One of the latest discussions was made by Cumpsty to the study of Walker (1993), in which they argued about whether the passage of wakes has any direct connection with a forced boundary layer transition. Quoting some experimental findings from the study of Orth (1993), Walker inferred that there existed both direct and indirect mechanisms of the transition caused by the periodic passing wake (or wake turbulence). In the present wake-induced transition model, such indirect mechanisms are not finally taken into account. This is because in the heat transfer measurements of this study, as well as in the second part of the study (Part II), the effect of the indirect mechanism could not be identified. Detailed arguments about the reason for these somewhat conflicting results are made in Part II.

The unknown in Eq. (13), x_{tw} and τ_w, could be determined by a best fitting of the experimental data with the corresponding curves of Eq. (13), but such a straightforward operation seems a very cumbersome task. Whence, an assumption is made about the wake-induced transition point. Addison and Hodson (1990a, b) have found in their experiment using an annular cascade that

Downloaded 01 Jun 2010 to 171.66.16.53. Redistribution subject to ASME license or copyright; see http://www.asme.org/terms/Terms_Use.cfm

Table 1

Cylinder diameter [mm]	Assumed wake duration [msec]
10	3.40
5	1.77
2	0.15

the wake-induced transition starts at the place where a Reynolds number based on momentum thickness, Re_θ, is around 200. This value corresponds to the instability point of the laminar boundary layer with a Blasius-type velocity profile; accordingly, it seems reasonable to use the following relation as a criterion for determining x_{tw}:

$$Re_\theta = 200 \text{ at } x = x_{tw}. \quad (14)$$

In the present case, x_{tw} is about 0.045 m measured from the leading edge. This simple criterion, which implies that a wake-induced transition is determined mainly by the state of time-averaged boundary layer irrespective of wake characteristics, is employed here for convenience. As will be shown in Part II, however, the wake-induced transition point shows a considerable dependency on the wake characteristics, especially by wake duration. Nevertheless, Eq. (14) works fairly well, as shown below.

By means of a best-fit technique with the experimental data, wake duration τ_w is determined for each of the wake-generating cylinders and the results are listed in Table 1. Some comparisons are then made between the experimental heat transfer data and the corresponding estimations by using the proposed transition model of Eq. (13) in conjunction with the relation of

$$St(x) = (1 - \gamma(x))St_{NW}(x) + \gamma(x)St_T(x), \quad (15)$$

where $x_{tw} = 0.045$. Figures 15–18 show the comparisons for three Strouhal number cases. It follows that the experimental data, even at the highest Strouhal number as shown in Fig. 18, are successfully reproduced by the transition model of Eq. (13) and Eq. (15), which indicates the usefulness of the proposed transition model, as well as the assumption for the wake-induced transition point.

In this study, it is shown that the proposed transition model works well to predict the wake-affected heat transfer on the flat plate. Actual flow fields in turbomachines, however, are very complicated compared to that of the present experiment and have several factors that are not taken into account in the model, which are for example effects of curvature, pressure gradient, compressibility and so on. Nevertheless, the author believes that the model will do in that case as a basic model of the wake-induced transition, in which the effects of those factors could be incorporated afterward.

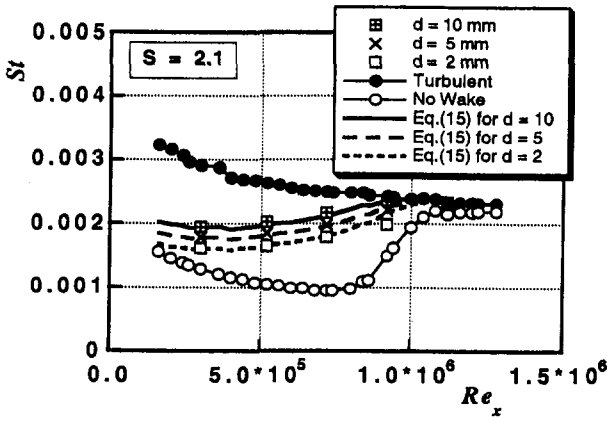


Fig. 16 Comparisons between the estimations by Eq. (15) and the experiments (S = 2.1)

Discussion

Examining the experimental data obtained at relatively low Strouhal numbers such as those in Fig. 15, there appear some

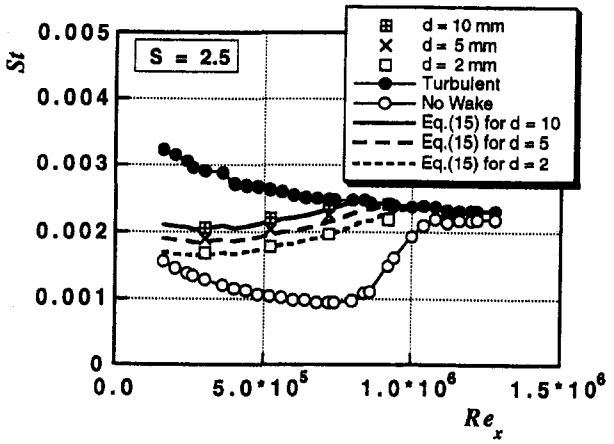


Fig. 17 Comparisons between the estimations by Eq. (15) and the experiments (S = 2.5)

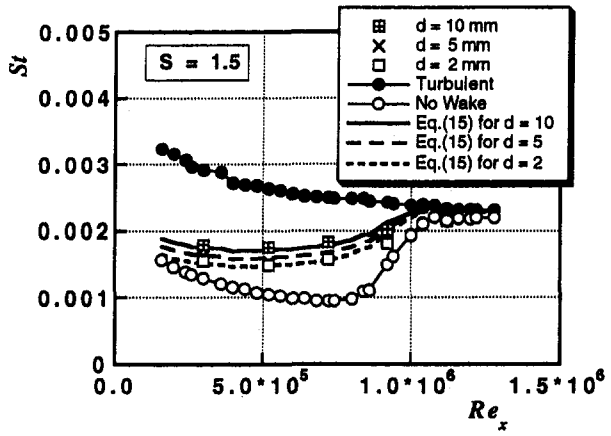


Fig. 15 Comparisons between the estimations by Eq. (15) and the experiments (S = 1.5)

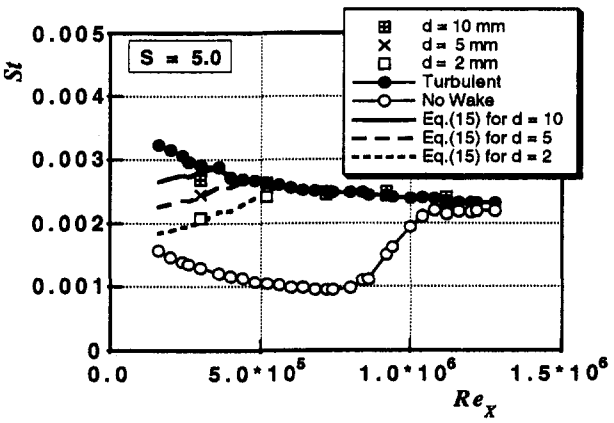


Fig. 18 Comparisons between the estimations by Eq. (15) and the experiments (S = 5.0)

Downloaded 01 Jun 2010 to 171.66.16.53. Redistribution subject to ASME license or copyright; see http://www.asme.org/terms/Terms_Use.cfm

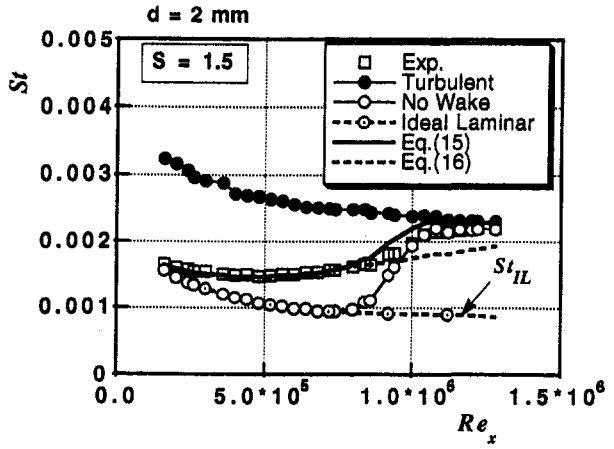


Fig. 19 Estimation of the wake-affected heat transfer by use of data for an ideal laminar boundary layer (S = 1.5)

discrepancies between the data and the estimates near the end of the transition, where the estimated values become larger than the experimental data. At first glance it seemed that such discrepancies were due to the steady heat transfer distributions $St_{NW}(x)$ that contained some effects of the natural transition occurring around there. In order to check this supposition, ideal laminar heat transfer distributions free from the effect of the natural transition, $St_{IL}(x)$ were derived by extending the data smoothly from the natural transition point ($x/L = 0.4$ in this case), and are used in Eq. (15), instead of the measured $St_{NW}(x)$ as follows;

$$St(x) = (1 - \gamma(x))St_{IL}(x) + \gamma(x)St_T(x). \qquad (16)$$

Such modified estimations are then compared with the corresponding experimental data for the cylinder of 2 mm, as presented in Figs. 19 and 20. Compared to the experimental data as well as to the corresponding "original" estimations, use of the ideal laminar heat transfer distributions considerably underestimates wake-affected heat transfer when the Strouhal number is low (Fig. 19). As the Strouhal number increases (Fig. 20), newly estimated curves of wake-affected heat transfer gradually tend to follow the experimental data more precisely than the original estimations do. This indicates that the passage of periodic wakes surely influences time-averaged characteristics of the boundary layer as the wake-passing Strouhal number increases and considerably suppresses its natural transition process.

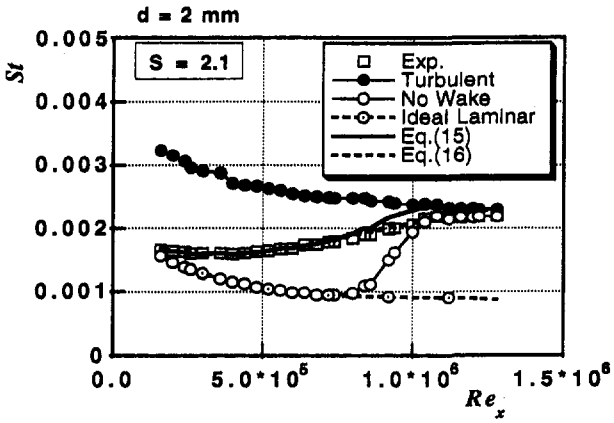


Fig. 20 Estimation of the wake-affected heat transfer by use of data for an ideal laminar boundary layer (S = 2.1, effect of the natural transition on the wake-affected heat transfer is completely suppressed)

Conclusions

Measurements of wake-affected heat transfer distributions on a flat plate are made by use of the wake generator, and a modified wake-induced transition model in terms of intermittency factor is proposed. Findings in this study are summarized as follows;

1 A wake-induced transition model with no consideration of the difference in wake characteristics failed to reproduce the experimental data of wake-affected heat transfer.

2 A modification on the transition model was made in order to incorporate the effects of wake duration. Also proposed was a criterion for a wake-induced transition point, which stated that the transition point corresponded to the place where the momentum thickness Reynolds number was 200.

3 Wake-affected heat transfer distributions for all unsteady flow conditions were well-reproduced by the proposed transition model, where the wake durations were experimentally determined.

4 Small discrepancies between the experiments and the model were recognized over the region where natural transition appeared. It was found that in some cases great improvement on estimation of wake-affected heat transfer was achieved by use of an ideal heat transfer distribution free from natural transition instead of the measured data.

Acknowledgments

This study is supported by IHI, Ishikawajima-Harima Heavy Industries Co., with supervision of S. Yamawaki and R. Henk. Great help in executing all experimental works was provided by K. Meguro and Y. Yamashita and is gratefully acknowledged.

References

Addison, J. S., and Hodson, H. P., 1990a, "Unsteady Transition in an Axial-Flow Turbine: Part I—Measurements on the Turbine Rotor," ASME JOURNAL OF TURBOMACHINERY, Vol. 112, pp. 206–214.

Addison, J. S., and Hodson, H. P., 1990b, "Unsteady Transition in an Axial-Flow Turbine: Part II—Cascade Measurements and Modeling," ASME JOURNAL OF TURBOMACHINERY, Vol. 112, pp. 215–222.

Addison, J. S., and Hodson, H. P., 1992, "Modeling of Unsteady Transition Boundary Layers," ASME JOURNAL OF TURBOMACHINERY, Vol. 114, pp. 580–589.

Dong, Y., and Cumpsty, N. A., 1990, "Compressor Blade Boundary Layers: Part 2—Measurements With Incident Wakes," ASME JOURNAL OF TURBOMACHINERY, Vol. 112, pp. 231–240.

Dullenkopf, K., Schulz, A., and Witting, S., 1991, "The Effect of Incident Wake Conditions on the Mean Heat Transfer of an Airfoil," ASME JOURNAL OF TURBOMACHINERY, Vol. 113, pp. 412–418.

Dullenkopf, K., and Mayle, R. E., 1994, "The Effects of Incident Turbulence and Moving Wakes on Laminar Heat Transfer in Gas Turbine," ASME JOURNAL OF TURBOMACHINERY, Vol. 116, pp. 23–28.

Emmons, H. W., 1951, "The Laminar–Turbulent Transition in a Boundary Layer—Part I," *Journal of Aeronautical Science,* Vol. 18, pp. 490–498.

Funazaki, K., Meguro, T., and Yamawaki, S., 1993, "Studies on the Unsteady Boundary Layer on a Flat Plate Subjected to Incident Wakes (Forced Transition Models of the Boundary Layer)," *JSME International Journal,* Vol. 36, pp. 532–539.

Han, J. C., Zhang, L., and Ou, S., 1993, "Influence of Unsteady Wake on Heat Transfer Coefficient From a Gas Turbine Blade," ASME *Journal of Heat Transfer,* Vol. 115, pp. 904–911.

Hodson, H. P., 1990, "Modeling Unsteady Transition and Its Effect on Profile Loss," ASME JOURNAL OF TURBOMACHINERY, Vol. 112, pp. 619–701.

Kays, W. M., and Crawford, M. E., 1980, *Convective Heat and Mass Transfer,* McGraw-Hill, New York, p. 140.

Kline, S. J., and McClintock, F. A., 1953, "Describing Uncertainties in Single Sample Experiments," *Mechanical Engineering,* Jan., pp. 3–8.

LaGraff, J. E., Ashworth, D. A., and Schultz, D. L., 1989, "Measurement and Modeling of the Gas Turbine Blade Transition Process as Disturbed by Wakes," ASME JOURNAL OF TURBOMACHINERY, Vol. 111, pp. 315–322.

Mayle, R. E., 1991, "The Role of Laminar-Turbulent Transition in Gas Turbine Engines," ASME JOURNAL OF TURBOMACHINERY, Vol. 113, pp. 509–537.

Mayle, R. E., and Dullenkopf, K., 1990, "A Theory for Wake-Induced Transition," ASME JOURNAL OF TURBOMACHINERY, Vol. 112, pp. 188–195.

Downloaded 01 Jun 2010 to 171.66.16.53. Redistribution subject to ASME license or copyright; see http://www.asme.org/terms/Terms_Use.cfm

Mayle, R. E., and Dullenkopf, K., 1991, "More on the Turbulent-Strip Theory for Wake-Induced Transition," ASME JOURNAL OF TURBOMACHINERY, Vol. 113, pp. 428–432.

Meyer, R. X., 1957, "The Effect of Wakes on the Transient Pressure and Velocity Distributions in Turbomachines," ASME *Journal of Basic Engineering*, Vol. 80, pp. 1544–1552.

Orth, U., 1993, "Unsteady Boundary-Layer Transition in Flow Periodically Disturbed by Wakes," ASME JOURNAL OF TURBOMACHINERY, Vol. 115, pp. 707–713.

Pfeil, H., and Herbst, R., 1979, "Transition Procedure of Instationary Boundary Layer," ASME Paper No. 79-GT-128.

Pfeil, H., Herbst, R., and Schroder, T., 1983, "Investigation of the Laminar–Turbulent Transition of Boundary Layers Disturbed by Wakes," ASME *Journal of Engineering for Power*, Vol. 105, pp. 130–137.

Walker, G. J., 1993, "The Role of Laminar–Turbulent Transition in Gas Turbine Engines: A Discussion," ASME JOURNAL OF TURBOMACHINERY, Vol. 115, pp. 207–217.

Downloaded 01 Jun 2010 to 171.66.16.53. Redistribution subject to ASME license or copyright; see http://www.asme.org/terms/Terms_Use.cfm

Unsteady Boundary Layers on a Flat Plate Disturbed by Periodic Wakes: Part II—Measurements of Unsteady Boundary Layers and Discussion

K. Funazaki
Department of Mechanical Engineering,
Iwate University,
Morioka, Iwate,
Japan

As the second part of the study, detailed hot-wire anemometry measurements of wake-affected boundary layers on the flat plate are made. These measurements are organized in order, first, to check the standpoint of the modeling of the wake-induced transition proposed in Part I, and second, to observe wake–boundary layer interaction in detail from a viewpoint of direct and indirect effect of the wake passage upon turbulent spot generation within the boundary layer, as described by Walker (1993). The validity of the presumed state of the wake-affected boundary layer in the distance–time domain, which constitutes the basis of the transition model, is confirmed to great extent. However, it is also found that the criterion for the onset of the wake-induced transition adopted in Part I should be reconsidered. Some successful attempts are therefore made to specify the transition onset.

Introduction

In Part I, wake-affected heat transfer distributions on the test plate subjected to periodic wakes were measured, and on the basis of those data, a new wake-induced transition model in terms of an intermittency factor was proposed. Although this transition model, which takes the effect of wake duration into account, has successfully reproduced the experimental data, further investigation is necessary because that model employs several assumptions about the wake-induced transition point and wake duration. In addition, as pointed out in Part I, some argument is necessary about direct and indirect effects of the wake-passing upon the boundary layer transition, which was mentioned by Orth (1992) and by Walker (1993). For the purpose of examining these issues, it is useful to conduct detailed boundary layer measurement by use of hot-wire anemometry techniques.

In this study, a large number of experimental data about the instantaneous velocity are obtained, which are then processed to obtain ensemble-averaged velocity and turbulence intensity. Attention is focused on the wake-induced transition onset as well as on the growth pattern of the induced turbulent spots or turbulent patch along the flow direction. These observations are compared with the transition model proposed in Part I and with the heat transfer data. A somewhat unique approach is used to determine a threshold of turbulence intensity that defines the extent of the turbulent region of the boundary layer in the distance–time domain.

The present study shows that the transition model works fairly well, but it also reveals a necessity to modify the criterion for the transition onset. Taking into account quasi-steadiness of wake turbulence diffusing into the boundary layer, the transition model is corrected by the well-known correlation for natural transition by Abu-Ghannam and Shaw (1980). With this modification, the model describes the experimental findings, especially the upward movement of the transition onset by the intense wake, quite well.

Contributed by the International Gas Turbine Institute and presented at the 39th International Gas Turbine and Aeroengine Congress and Exposition, The Hague, The Netherlands, June 13–16, 1994. Manuscript received by the International Gas Turbine Institute February 24, 1994. Paper No. 94-GT-430. Associate Technical Editor: E. M. Greitzer.

Experimental Investigation

Test Apparatus and Measuring System. The experimental setup in the present study is schematically shown in Fig. 1, which is quite similar to that of Part I. An *I*-type hot-wire probe is used for the measurement of wake-affected boundary layers on the flat plate. The number of measuring points amounts to 220: 10 points in the normal direction from $y/L = 0.2 \times 10^{-3}$ to $y/L = 4.8 \times 10^{-3}$ at each of 22 streamwise locations from $x/L = 0.0$ to $x/L = 0.6$. A computer-controlled traverse unit positions the probe along the y coordinate. The measurement origin ($y = 0.0$) is determined with great care at every streamwise location because of slight waviness in the surface of the test plate. The instantaneous velocity data obtained are ensemble-averaged (or phase-locked-averaged) and processed as before (see Eqs. (3)–(5) in Part I), which yields time-resolved velocity as well as turbulence intensity within the boundary layer.

Test Conditions. Throughout this experiment, the inlet flow velocity U_∞ is fixed at 30 m/s and the Reynolds number based on the plate length is then 2×10^6. All flow conditions adopted here are listed in Table 1, where the Strouhal number is defined as

$$S = \frac{fL}{U_\infty}, \quad f = \frac{nn_c}{60}. \tag{1}$$

Note that due to a mechanical restriction of the traverse unit, measurements of the boundary layers over $x/L = 0.0$ to 0.15 are not conducted for the case of $l_D/L = 0.12$.

Uncertainty Analysis. Uncertainty of the measured velocity data is estimated by the method of Kline and McClintock (1953), and it is about ±6 percent.

Results

Measurements of Boundary Layers Near the Leading Edge ($x/L = 0.0$–0.15). Figure 2 shows the contours of

Copyright © 1996 by ASME
Downloaded 01 Jun 2010 to 171.66.16.53. Redistribution subject to ASME license or copyright; see http://www.asme.org/terms/Terms_Use.cfm

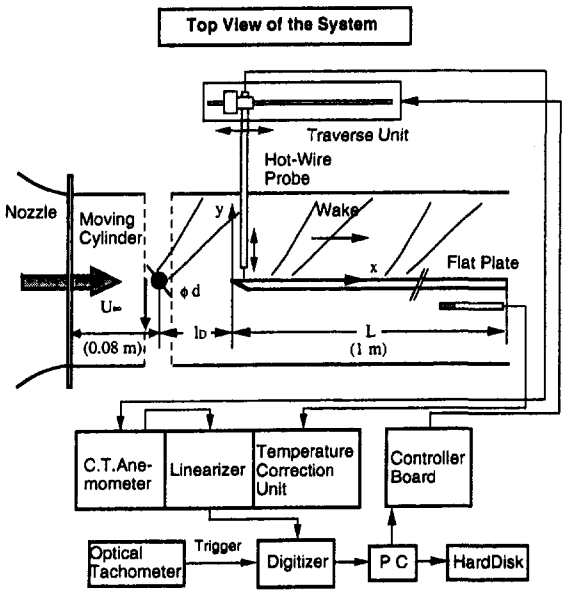


Fig. 1 Schematic layout of the test apparatus and the measurement system

phase-locked-averaged turbulence intensity within the $x-y$ plane at several instants during one wake-passing period for the test case of No. 5, where $d = 2$ mm and $l_D/L = 0.24$. In this figure solid lines marked with $\langle\delta_{95}\rangle$ indicate the contours of 95 percent free-stream velocity, from which one may spot incident wakes from the cylinders as well as a boundary layer on the test plate. Note that the scales for the x coordinate and the y coordinate are different. At the instant of $t/T = 0.45$, a wake with more than 4 percent turbulence intensity reaches the leading edge of the plate. As the wake is convected downstream, its turbulence intensity gradually decreases. At $t/T = 0.50$, a small region with 4 percent turbulence intensity marked with S as well as with slight shade appears at the foot of the wake. After that, the small region moves downstream about at a half speed of the free-stream so that it tends to retard behind the wake; at the same time it keeps growing until it penetrates the free stream at $t/T = 0.60$. This sequence means that the highly turbulent region is a wake-induced turbulent patch, i.e., a group of turbulent spots induced by a direct interaction between the wake and the boundary layer. It is revealing to recast the above data into distance–time diagrams for turbulence intensity on the horizontal plane closest to the wall ($y/L = 0.2 \times 10^{-3}$) as shown in Fig. 3. This figure clearly shows the appearance and the growth of the turbulent patch. From this diagram, it is quite natural to think that the turbulent patch is caused by the wake passage. The occurrence of a turbulent patch around at $x/L =$ 0.03 can be seen during $t/T = 0.45$ to 0.50. Being convected downstream, such a turbulence patch gradually extends in length. This is because a downstream edge of the turbulent patch or the patch leading edge moves almost with the wake, while the trailing edge moves slower than the wake. As will be detailed later, the moving speeds of the leading and trailing edges are derived from these diagrams and are respectively found to be about 100 and 54 percent of the free-stream velocity. These values agree with the heat transfer measurements in Part I. As the distance from the surface increases, the effect of the turbulent patch tends to disappear as only a region of high turbulence intensity associated with the wake can be recognized.

Figure 4 shows contours of the phase-locked-averaged turbulence intensity in the case of No. 6, where the unsteady condition is the same with the case of No. 5 except that the distance between the wake generator and the flat plate is enlarged ($l_D/L = 0.48$). Although the instant when the wake reaches the plate leading edge is different from the previous cases of Figs. 2 and 3 due to the extra distance, relative wake positions in Fig. 4 are almost the same as those of the corresponding diagrams in Fig. 2. Compared to the previous cases, wake turbulence in Fig. 4 decays slightly. Under such circumstances, it takes longer for a 4 percent turbulence intensity region to appear inside the boundary layer after the wake arrives at the leading edge. Moreover, the growth rate of the induced turbulent patch in this decayed wake case is smaller than that of the previous wake case shown in Fig. 2.

At first glance, such a phenomenon seemed to be explained by the difference in diffusive time scale of the turbulent kinetic energy between the two wake cases as pointed out by Addison and Hodson (1990a, b). They have shown that the time needed for the turbulent kinetic energy of wake to diffuse into a boundary layer is in inverse proportion to the corresponding eddy viscosity inside the wake. In the case of a two-dimensional

Table 1 Test conditions

No.	n [rpm]	n_c	S	l_D/L
1	1500	3	2.5	0.12
2	1260	3	2.1	0.12
3	1020	3	1.7	0.12
4	900	3	1.5	0.12
5	1020	3	1.7	0.24
6	1020	3	1.7	0.48

Nomenclature

C = characteristic length
C_d = drag coefficient
d = diameter of cylinder
f = wake passing frequency
k = reduced frequency
L = length of the flat plate = 1 m
l_D = distance between the wake-generating cylinder and the leading edge of the flat plate
n = revolution number
n_c = number of cylinders
Re = Reynolds number = $U_\infty L/\nu$
Re_x = Reynolds number based on the length measured from the leading edge of the plate
Re_θ = momentum thickness Reynolds number
S = Strouhal number
S_w = wake passing Strouhal number = $L/(U_\infty T)$
T = wake passing period
t = time
Tu = ensemble-averaged turbulence intensity
U_∞ = free-stream velocity
x_S = turbulent spot initiation point
x_{tw} = start point of wake-induced transition
β_E, β_F = trailing edge and leading edge propagation velocity ratios of turbulent spot to the free-stream velocity
$\gamma_w(x)$ = local intermittency factor of wake-affected boundary layer
ν, ν_t = kinematic viscosity, eddy viscosity
τ_w = wake duration
ω = angular frequency

Downloaded 01 Jun 2010 to 171.66.16.53. Redistribution subject to ASME license or copyright; see http://www.asme.org/terms/Terms_Use.cfm

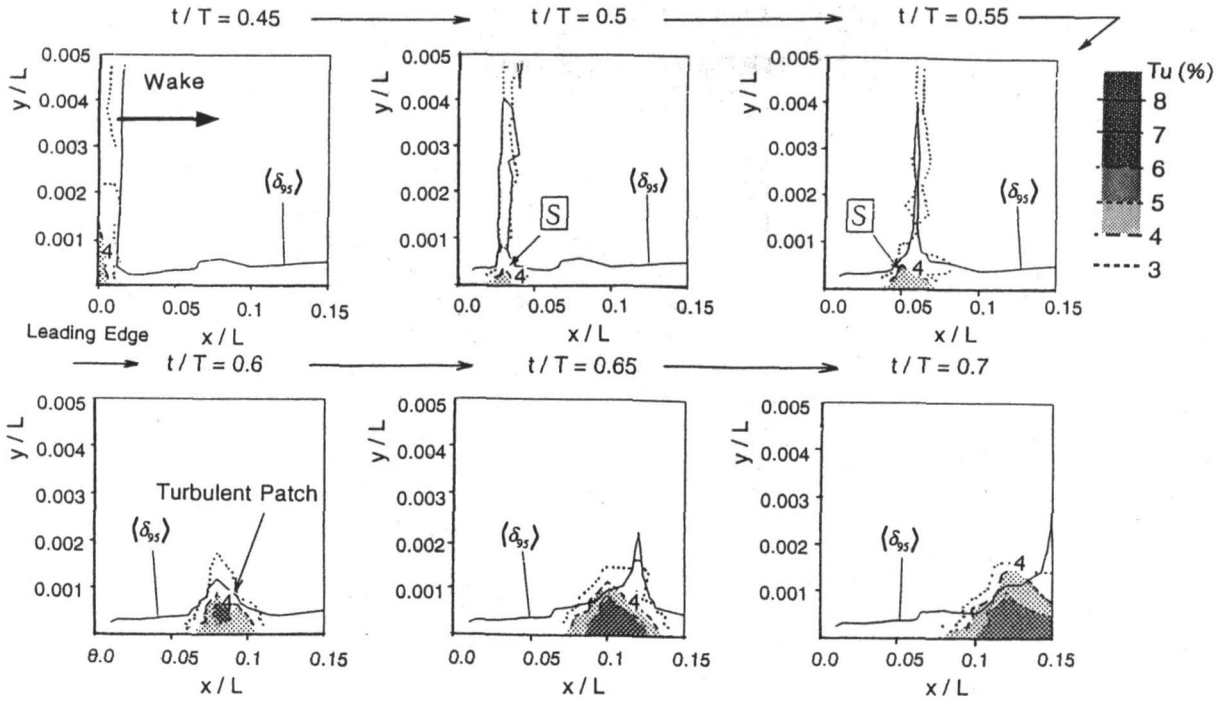


Fig. 2 Phase-locked-averaged contours of turbulence intensity within the $x-y$ plane for several instants during one wake-passing period (Case 5 in Table 1 and d = 2 mm)

wake from a circular cylinder, its eddy viscosity ν_t is given by Schlichting (1979):

$$\nu_t \sim C_D U d, \tag{2}$$

which means that the enlarged distance between the plate and the cylinder has little effect on the diffusive time scale. Accordingly, the difference in growth rate of turbulent patch can be attributed to the difference in magnitude of the wake turbulence intensity. It is again clear that the wake passage surely causes a turbulent patch inside the boundary layer in a direct manner even in this weak wake case.

Figure 5 shows a distance–time diagram of turbulence intensity obtained for case 5, which has same test condition as Fig. 3, except that the cylinder diameter d = 5 mm. It is difficult to identify the appearance of any wake-induced turbulent patches from this figure because of the wider and more intense wake, in contrast with the case 11, where a turbulent patch appeared at the foot of the wake center. Since the turbulent patches move downstream more slowly than the wake, they finally come out of the wake as seen around t/T = 0.65 through t/T = 0.70. It is also clear from the diagram that the highly turbulent state lasts for about one tenth of the wake passing period over the surface to $x/L \cong 0.04$, from which the duration of the turbulent state starts to expand.

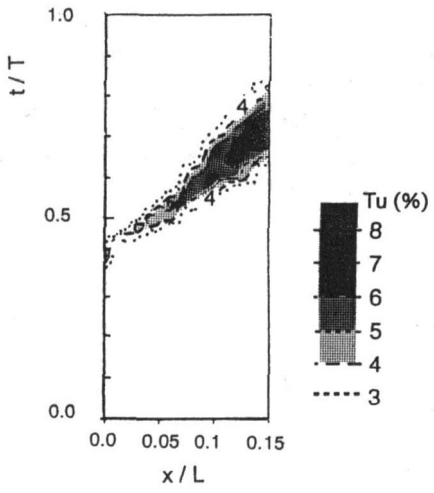


Fig. 3 Phase-locked-averaged contours of turbulence intensity measured at $y/L = 0.2 \times 10^{-3}$ (Case 5, d = 2 mm)

Measurements of Boundary Layers Near the End of the Wake-Induced Transition. Figure 6 is a sample diagram that illustrates movements of the wake-induced turbulent regions over the region from x/L = 0.30 to x/L = 0.60 for case 3. It is attached with the reproduction of Fig. 3 for better understanding of the entire evolution process of the turbulent patch. This figure shows that the turbulent patches appearing in a periodic manner continue to grow from their initiation until the end of the transition process. In this case another highly turbulent region appears around x/L = 0.5 before the two consecutive turbulent regions merge, which could be attributed to the effect of steady flow transition phenomena. As the Strouhal number increases, it is found that the merger points for S = 2.1 (case 2) and S = 2.5 (case 1) are located around at x/L = 0.55 and x/L = 0.45, respectively. Therefore, such a turbulent region tends to disappear due to the earlier merger of those wake-induced turbulent regions. This matches the observation in Figs. 19 and 20 of Part I.

Comparisons Between the Experimental Data and the Model

In this section, the present experimental data are examined from the viewpoint of the wake-induced transition model proposed in Part I.

One might recall that the transition model is developed on a basis of the presumed state of the wake-affected boundary layer in a distance–time diagram as shown in Fig. 14 of Part I. This presumption can be checked by comparing that figure with the contours of the turbulence intensity measured at y/L = 0.2 ×

Downloaded 01 Jun 2010 to 171.66.16.53. Redistribution subject to ASME license or copyright; see http://www.asme.org/terms/Terms_Use.cfm

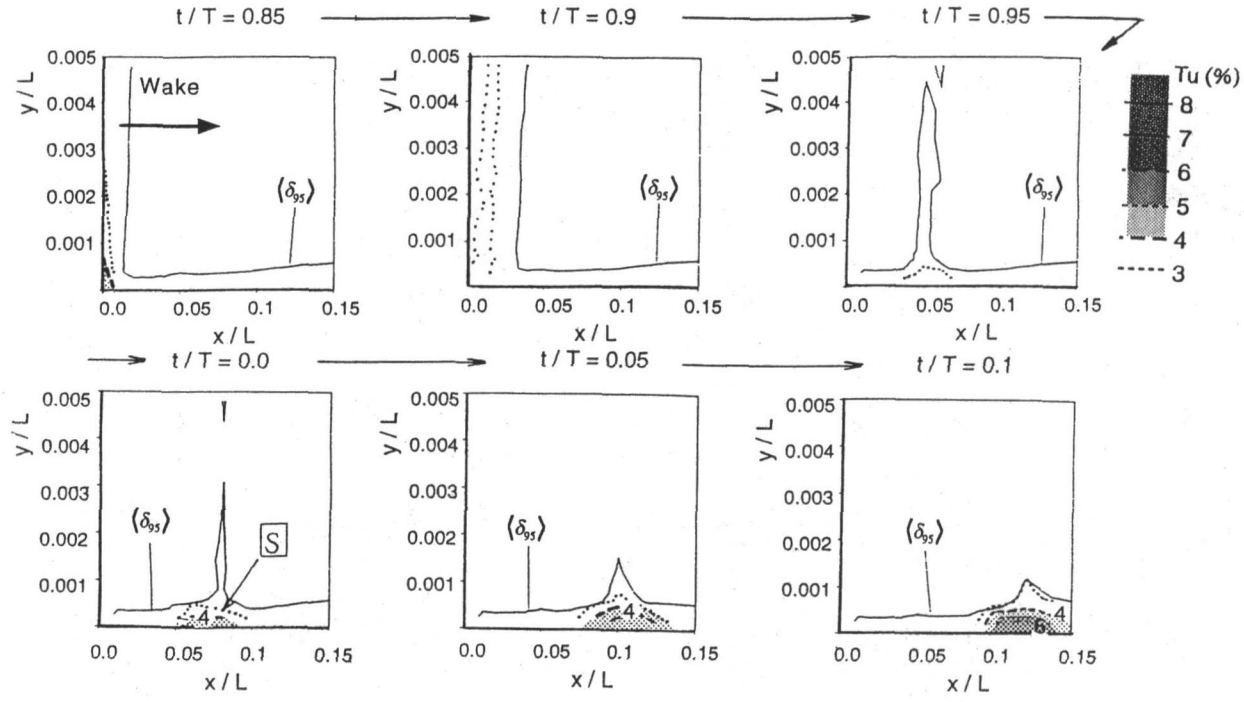


Fig. 4 Phase-locked-averaged contours of turbulence intensity for several instants during one wake-passing period (Case 6, d = 2 mm)

10^{-3} in Fig. 6. From such a comparison, it is seen that the measured growing patterns of turbulent regions are similar to the presumed one, supporting the standpoint upon which the proposed transition model is based. But quantitative evaluations are also necessary in order to check the validity of the values employed in the transition model, namely wake duration τ_w and a turbulence propagation velocity ratio β_E. In addition, the criterion for determining wake-induced transition point (Eq. (14) in Part I) should be checked. For that purpose, the experimental data obtained for all flow conditions of Table 1 with various configurations of the test section are compared with an idealized state of the wake-affected boundary layer as in Fig. 7 (note that Fig. 7 is actually a rough sketch of Fig. 6). In executing this task, however, one will be soon aware of the necessity to make a clear definition of the extent of the wake-induced turbulent region like the shaded region in Fig. 7. Hence we begin the following examination with a discussion of this problem.

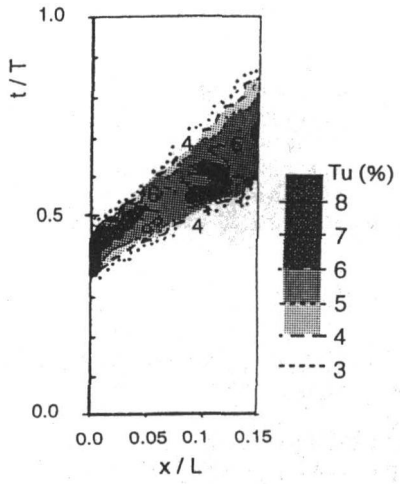


Fig. 5 Phase-locked-averaged contours of turbulence intensity (Case 5, d = 5 mm), with the same flow condition as Fig. 3 except for the cylinder diameter

Definition of Turbulent Region and Wake Duration. So far, there have been few arguments about a definition of the turbulent region in wake-induced transition problems. It seems difficult to give any rigorous definition for the turbulent region; hence a somewhat practical approach is employed in this study, that is, the present contours of the turbulence intensity are compared with the results of the heat transfer measurement of Part I in order to find out what level of the turbulence intensity gives almost the same result with the heat transfer measurement at the end of the wake-induced transition. From Fig. 17 in Part I, for example, the transition completes around at Re = 1.0×10^6, which corresponds to $x/L = 0.50$. Comparing this result with the corresponding turbulence contours shown in Fig. 8, it is seen that regions with more than 4 percent turbulence intensity exhibit almost the similar results to the heat transfer data because they merge around $x/L = 0.50$. After several inspections, we have confirmed that using 4 percent turbulence intensity as the threshold of the wake-induced turbulent region yields reasonable agreement with the heat transfer data.

Applying this definition to the turbulent region in Fig. 6 for example, we have tried to determine the extent of the turbulent region. Slopes of the edges of the turbulent region in the distance–time domain are then calculated for each of the test conditions with a curve-fitting technique, giving the edge-propagation velocities shown in Fig. 7. These results are listed in Table 2 in terms of the ratio of the trailing edge velocity to a free-stream velocity, β_E, where the ratio for the leading edge, β_F, was almost unity in all cases. Although small scattering appears in the data, its average becomes $\beta_E \cong 0.54$, which is very close to the presumed value ($\beta_E = 0.55$) in the transition model. This also gives somewhat favorable evidence for using the 4 percent intensity as the threshold for the turbulent region. Apart from this finding, Gostelow et al. (1993) have recently used 4 percent disturbance level as an indicator of turbulent spot edges. Despite different experimental situations in both studies, this supports our present approach.

Downloaded 01 Jun 2010 to 171.66.16.53. Redistribution subject to ASME license or copyright; see http://www.asme.org/terms/Terms_Use.cfm

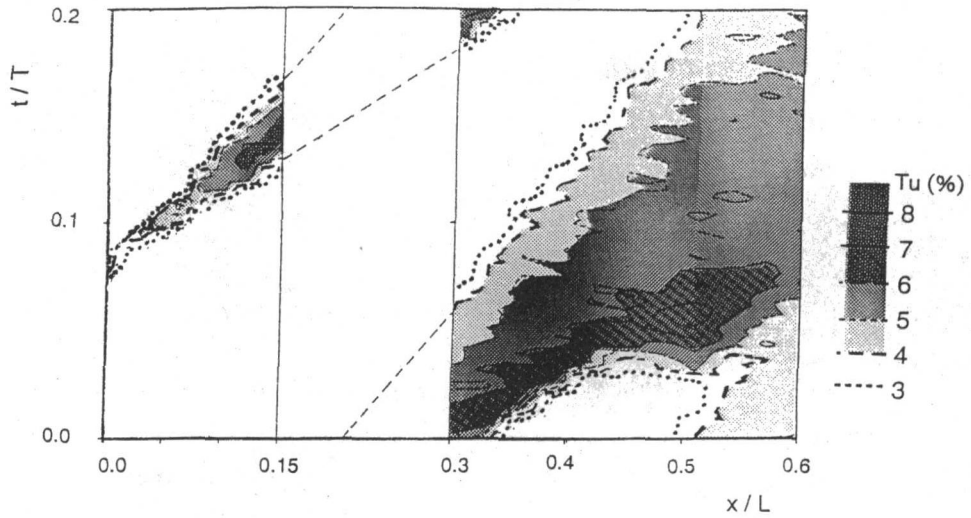


Fig. 6 The turbulent regions on the plane of $y/L = 0.2 \times 10^{-3}$ measured over the surface from to $x/L = 0.0$ to 0.15 and $x/L = 0.3$ to 0.6 (Case 5), show the evolution of the wake-induced turbulent patches

According to the present definition of wake duration τ_w as shown in Fig. 7, we can graphically determine values of the wake duration from the turbulence intensity contours obtained near the leading edge where the edges of the contours lie almost

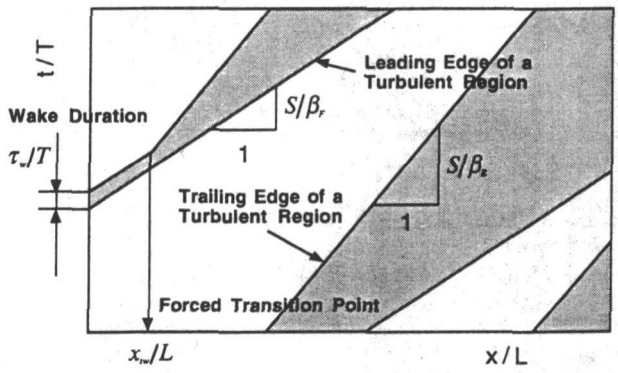


Fig. 7 An idealized state of the wake-affected boundary layer

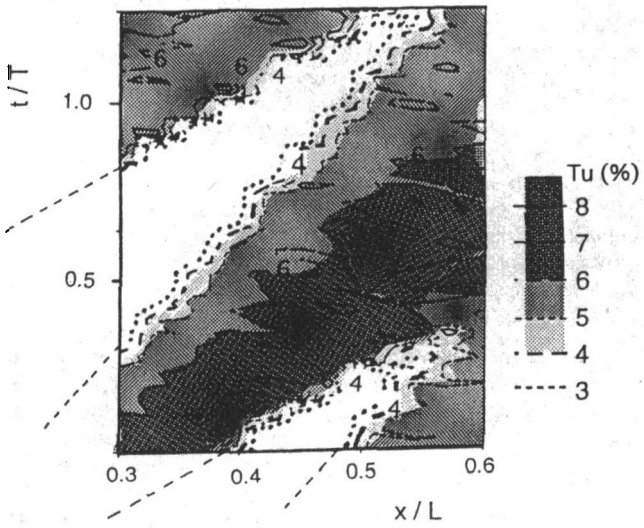


Fig. 8 The turbulent regions on the plane of $y/L = 0.2 \times 10^{-3}$ measured over the surface from $x/L = 0.3$ to 0.6 (case 6), showing the merger of the consecutive turbulent regions around $x/L = 0.5$

in parallel. In this case, the above-mentioned threshold for the wake-induced turbulent region is applied. Table 3 shows such values of the wake duration for three types of the wake-generating cylinders, in conjunction with the values presented in Part I. Although these values contain considerable uncertainty due to the somewhat rough estimation used here, the values agree with the experimental data. Relatively large discrepancy between the model and the experiment is seen for the 2 mm diameter case, probably because of the obscure edges of the turbulent region for that case. This comparison shows that the increasing trend of the wake duration for larger cylinder diameter, which has been incorporated in the transition model of Part I, is directly verified in this measurement.

Table 2 Trailing edge propagation velocity ratio for each of the test conditions

d	Flow Condition	x/L	β_E
2	Case 1	0.3 - 0.6	0.54
2	Case 2	0.3 - 0.6	0.54
2	Case 3	0.3 - 0.6	0.55
2	Case 4	0.3 - 0.6	0.54
5	Case 1	0.3 - 0.6	0.50
5	Case 2	0.3 - 0.6	0.59
5	Case 3	0.3 - 0.6	0.52
10	Case 3	0.3 - 0.6	0.54
2	Case 5	0.3 - 0.6	0.53
5	Case 5	0.3 - 0.6	0.57
2	Case 5	0.0 - 0.15	0.53
5	Case 5	0.0 - 0.15	0.51
10	Case 5	0.0 - 0.15	0.59
2	Case 6	0.0 - 0.15	0.53
5	Case 6	0.0 - 0.15	-

Table 3 Wake duration (Measured and model values) (unit is ms)

	Wake duration	Model value
d = 2	0.48	0.15
d = 5	2.13	1.77
d = 10	3.96	3.40

Downloaded 01 Jun 2010 to 171.66.16.53. Redistribution subject to ASME license or copyright; see http://www.asme.org/terms/Terms_Use.cfm

Onset of the Wake-Induced Transition

Direct and Indirect Effects of the Wake Passing. Before discussing where wake-induced transition will start, it should be noted that some controversy recently arose among several researchers about the mechanism of the wake-induced transition. Dong and Cumpsty (1990) and Addison and Hodson (1990a, b, 1991) concluded that the wake turbulence was mainly responsible for the transition and any effect of velocity fluctuations associated with the wake passage on the transition was minimal. A similar concept was presented by Mayle and Dullenkopf (1990), stating that the wake was a production source of turbulent spots. On the contrary, Walker (1993), citing the data of compressor blade measurements, claimed that velocity fluctuations in the wake-induced transition process were important and held that turbulent spots evolved from the growth of "instability wave pockets," which tended to lag the wake passage. Meanwhile, the present study concludes that turbulent patches arise due to the passage of the periodic wakes, while finding no evidence for the appearance of the turbulent patches induced by the velocity fluctuations. Nevertheless, because of the limited number of data in this study, it is impossible to deny any possible roles of the wake-associated velocity fluctuation in the transition process.

According to Obremski and Fejer (1964), the effect of the velocity fluctuations can be characterized by a nonsteady Reynolds number Re_{NS}, which is defined as

$$\mathrm{Re}_{NS} = \frac{U}{\nu}\frac{\Delta U}{\omega} = \frac{UC}{\nu}\frac{U}{\omega C}\frac{\Delta U}{U} = \mathrm{Re}\,\frac{1}{k}\frac{\Delta U}{U}, \qquad (3)$$

where Re is a plate-length Reynolds number, k is a reduced wake-passing frequency, and ΔU is an amplitude of velocity fluctuation. They claimed that when Re_{NS} was less than 26,000, no transition due to the fluctuation occurred. In a high-pressure turbine stage of a typical aeroengine, on which the flow conditions in this study are based, one may find that $\mathrm{Re} \cong 10^6$, $k \cong 10^1$, and $\Delta U/U \cong 10^{-1}$, then $\mathrm{Re}_{NS} \cong 10^4$. In this sense, the effect of the velocity fluctuations can be discounted in the present cases. Accordingly, we hereafter regard the wake turbulence, rather than the velocity fluctuations, as a main cause of wake-induced transition.

Walker cited the observations by Orth (1992) as evidence of an indirect mechanism of wake passage, which was regarded as the counterpart of the direct action of the wake turbulence to induce a boundary layer transition. Before further discussion, the author would like to draw the readers' attention to the difference between wake generators used in the present study and in the experiment by Orth. He used a wake generator like a squirrel cage, in which several bars were horizontally installed so as to generate two-dimensional wakes behind them. This type of wake generator has some drawbacks; for example, it cannot help generating two different kinds of wake that were referred to as "near wake" and "far wake," respectively, by Orth. The near wake was generated when a bar in the wake generator passed just ahead of the plate leading edge and the far wake was generated when a bar moved at the far distance from the leading edge. In fact, existence of the far wake makes the simulated flow field more complicated. In addition, due to the structure of the wake generator, relative motions of the wake-generating bars to the inlet flow at the near and far positions differ. As a result, both the near and the far wakes impinge on the test plate in considerably different ways. In other words, the directions of wake-associated negative jets, whose existence was pointed out by Meyer (1957), are different for the near and the far wake cases, which makes the situation more complex and sometimes confusing. Accordingly, careful attention should be paid when using a squirrel cage as the wake generator.

Figure 9, which is a reproduction of one of the figures in Orth's paper, depicts contours of turbulence intensity obtained

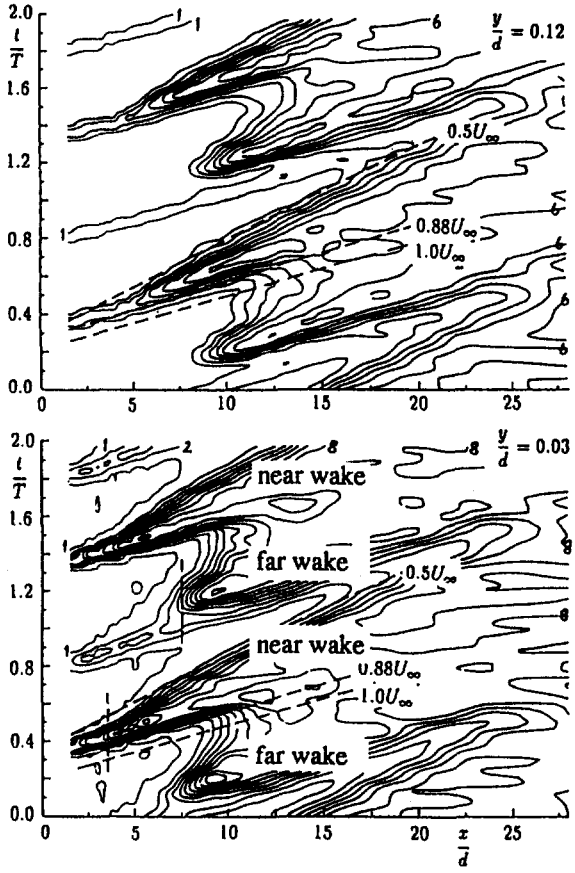


Fig. 9 Experimental data cited from Orth (1992), illustrating the evolution of the highly turbulent regions induced by the near and far wakes

on the plane nearest to the test surface as in the current Fig. 3. Note that the measurement location is at $y/L = 0.6 \times 10^{-3}$ according to this paper's notation. Orth stated in his paper that it is clear that the "near" wake affects the boundary layer so directly that it induces a turbulent patch immediately underneath. Walker pointed out, on the other hand, that the effect of the far wake appears to be somewhat restrictive and the wake seemingly has no direct connection with the turbulent patch appearing at $t/T \cong 1.2$ (see upper portion of Fig. 9). Considering the observed slow growth rate of the induced turbulent patch by the far wake ($l_D/L = 0.48$) as well as the fact that the measurement location of Fig. 9 is three times distanced from the test surface than that of the present case, however, it is quite likely that a turbulent patch is caused by a weak far wake but it is not detected while it grows under the measuring plane of $y/L = 0.6 \times 10^{-3}$. Consequently, the present author has come to believe the following story: The far wake in Orth's case affected the boundary layer directly and accordingly induced a turbulent patch underneath. However, its growth was slow compared to the near-wake case mainly because the low turbulence intensity involved and partly because of the direction of the far wake "negative" jet is opposite to that of the near wake.

Proposal of a New Model for Onset of the Transition. In the transition model proposed in Part I, the onset of the wake-induced transition was regarded as the point where the trailing edge of a wake-induced turbulent patch emerged from the preceding wake (x_{tw} in Fig. 14 of Part I), and the effect of the wake characteristics on that point was ignored. Through the present experiments, however, we have found that the situation is not so simple as in that model. For example, location of x_{tw} depends considerably on the wake characteristics as indicated in Table 4. These results show that some modification on the

Downloaded 01 Jun 2010 to 171.66.16.53. Redistribution subject to ASME license or copyright; see http://www.asme.org/terms/Terms_Use.cfm

Table 4 Comparison of the wake-induced transition point

	x_{tw}/L (Exp.)	x_{tw}/L (Model)
d = 2	0.052	0.045
d = 5	0.038	0.045
d = 10	0.032	0.045

model is necessary, especially about the onset of the wake-induced transition.

Based on the findings in this study, a slightly modified transition model shown in Fig. 10 is developed. This new model assumes that one or more turbulent patches appear somewhere beneath a wake, whose locations depend on the wake turbulence intensity. Because of the short diffusion time scale of the wake turbulence into the boundary layer, it is possible to adopt a quasi-steady approach by use of the well-known natural transition criterion of Abu-Ghannam and Shaw (1980)

$$\mathrm{Re}_\theta = 163 + \exp(6.91 - Tu), \tag{4}$$

in order to determine an onset location of the turbulence patch as Addison and Hodson (1990a, b) did. In this case, local turbulence intensity distribution within the wake is substituted into Tu of Eq. (4) for a free-stream turbulence intensity. Equation (4) implies that even in a highly turbulent wake case ($Tu \geq 6$ percent), no turbulent patch occurs before the position of Re = 163. This means $x_{tw}/L = 0.03$ in the present case. Note that this model does not guarantee any appearance of the wake-induced turbulent patch at the place that Eq. (4) specifies, but only provides a particularly possible position of the appearance of the turbulent patch beneath the wake. One might wonder if this method makes the estimation of the transition onset rather difficult because of its uncertainty about the position of the turbulent patch. As far as the growth of the turbulent region is concerned, however, it is not necessary to pay attention to all possible turbulent patches but only to those appearing after the peak of the turbulence intensity. When the wake is sufficiently intense, as shown schematically in the upper part of Fig. 10, it is quite likely that turbulent patches appear even at the rear portion of the wake center. It follows from this assumption that the wake-induced transition point in the "old" definition, x_{tw}, would be found near the limiting line of Re = 163 ($x_{tw}/L = 0.03$), which matches the situation for the 10 mm cylinder case in Table 4 ($x_{tw}/L = 0.032$). When the wake is weak, on the other hand, a limited number of turbulent patches arise around the wake center at the location marked with x_s. In that case, x_{tw} tends to be located a little downstream from x_s, which is determined by the following relationship:

$$x_{tw} = x_s + \frac{U_\infty \tau_w}{2\left(\frac{1}{\beta_E} - \frac{1}{\beta_F}\right)} = x_s + 0.61 U_\infty \tau_w. \tag{5}$$

Since a peak value of Tu for the 2 mm cylinder case was about 4 percent, combining Eq. (4) with Eq. (3) yields $x_{tw} = 0.046$, which is close to the corresponding value in Table 3 ($x_{tw} = 0.052$). Moreover, the peak value of Tu in the far wake case was 3 percent at most, which means that any turbulent patch initiates around $x/L \cong 0.05$, and is consistent with the result of Fig. 4.

Discussion

We have concentrated our attention on the wake turbulence intensity only, and no discussions are made about the effects of the other wake turbulence statistics, for instance the length scale of the wake turbulence or the Reynolds stress. O'Brien and Capp (1989), on the other hand, conducted unsteady flow measurements behind a spoke-wheel wake generator, which had the structure similar to that of the present study, and found that higher levels of Reynolds stress was obtained by the moving circular cylinders as compared to those measured behind an actual inlet guide vane. They concluded that the higher wake turbulence level could be responsible for the higher heat transfer measured in a cascade test case using the wake generator, as compared to the results of an actual rotating turbine stage. Their study accordingly indicates that further investigation is necessary about the effect of the wake turbulence characteristics on the transitional behavior of the wake-affected boundary layer.

As for a natural transition criterion, Mayle (1991) recently proposed another correlation as follows:

$$\mathrm{Re}_\theta = 400\, Tu^{-5/9}, \tag{5}$$

where Tu is in percent. He claimed that his correlation yielded better results than the correlation of Abu-Ghannam and Shaw did, especially at high free-stream turbulence case. Using Eq. (5) instead of Eq. (4) seems to be one of the possible options, but care should be paid to the fact that the natural transition point given by Eq. (5) goes upward monotonously according to the free-stream turbulence. This is quite a contrast to that of Eq. (4), which yields the asymptotic value of the transition point. Therefore, further studies remain to be done about which is more suitable for the wake-induced transition problem.

Conclusions

Behavior of the wake-affected boundary layer on the flat plate is investigated in detail by hot-wire anemometry. Comparisons are then made between the results obtained and the wake-induced transition model proposed in Part I. Findings in this study are summarized as follows:

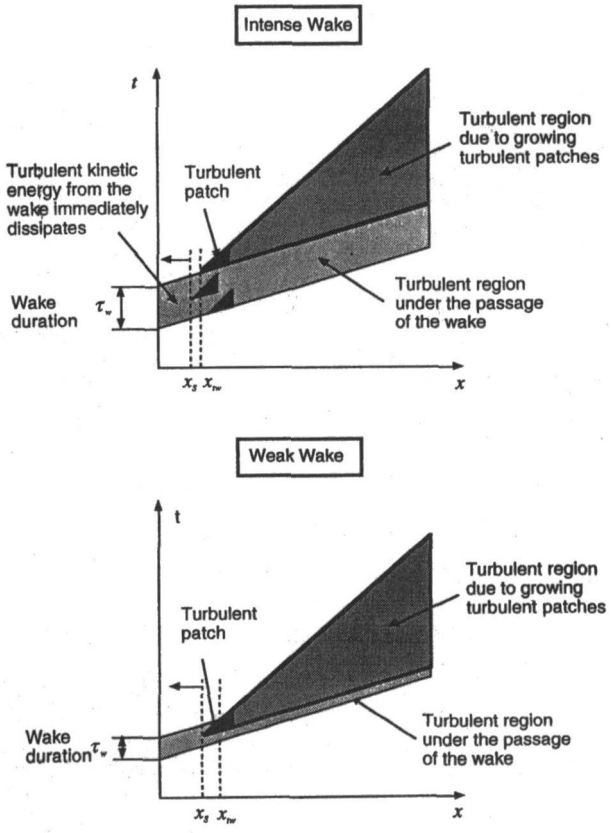


Fig. 10 A modified model for an onset of the wake-induced transition

Downloaded 01 Jun 2010 to 171.66.16.53. Redistribution subject to ASME license or copyright; see http://www.asme.org/terms/Terms_Use.cfm

1 Wake passing directly induces turbulent patches beneath the wake, but their onset locations and evolving behavior depend heavily on the incident wake turbulence intensity.

2 Measured states of wake-affected boundary layer in the distance–time diagrams are quite similar to the presumed ones in the transition model proposed in Part I, except for the wake-induced transition points, which was previously assumed to be independent of the wake properties.

3 A threshold for defining turbulent region is proposed for convenience in terms of the turbulence intensity, which yields somewhat plausible results when compared to the data in the heat transfer experiments.

4 Based on the observations in this study, a slight modification to the transition model is made with respect to the transition onset. A quasi-steady approach using the criterion of Abu-Ghannam and Shaw is adopted with great success predicting the onset location of the wake-induced turbulent patch.

Acknowledgments

This study is financially supported by IHI, Ishikawajima-Harima Heavy Industries, monitored by S. Yamawaki and R. Henk. Contributions from T. Meguro as well as Y. Yamashita are to be acknowledged.

References

Abu-Ghannam, B. J., and Shaw, R., 1980, "Natural Transition of Boundary Layers—The Effects of Turbulence, Pressure Gradients, and Flow History," *Journal of Mechanical Engineering Science,* Vol. 22, pp. 231–228.

Addison, J. S., and Hodson, H. P., 1990a, "Unsteady Transition in an Axial-Flow Turbine: Part I—Measurements on the Turbine Rotor," ASME JOURNAL OF TURBOMACHINERY, Vol. 112, pp. 206–214.

Addison, J. S., and Hodson, H. P., 1990b, "Unsteady Transition in an Axial-Flow Turbine: Part II—Cascade Measurements and Modeling," ASME JOURNAL OF TURBOMACHINERY, Vol. 112, pp. 215–222.

Addison, J. S., and Hodson, H. P., 1992, "Modeling of Unsteady Transition Boundary Layers," ASME JOURNAL OF TURBOMACHINERY, Vol. 114, pp. 580–589.

Dong, Y., and Cumpsty, N. A., 1990, "Compressor Blade Boundary Layers: Part 2—Measurements With Incident Wakes," ASME JOURNAL OF TURBOMACHINERY, Vol. 112, pp. 231–240.

Gostelow, J. P., Hong, G., Melwani, N., and Walker, G. J., 1993, "Turbulent Spot Development Under a Moderate Adverse Pressure Gradient," ASME 93-GT-377.

Kline, S. J., and McClintock, F. A., 1953, "Describing Uncertainties in Single Sample Experiments," *Mechanical Engineering,* Jan., pp. 3–8.

Mayle, R. E., and Dullenkopf, K., 1990, "A Theory for Wake-Induced Transition," ASME JOURNAL OF TURBOMACHINERY, Vol. 112, pp. 188–195.

Mayle, R. E., 1991, "The Role of Laminar–Turbulent Transition in Gas Turbine Engines," ASME JOURNAL OF TURBOMACHINERY, Vol. 113, pp. 509–537.

Meyer, R. X., 1957, "The Effect of Wakes on the Transient Pressure and Velocity Distributions in Turbomachines," ASME *Journal of Basic Engineering,* Vol. 80, pp. 1544–1552.

O'Brien, J. E., and Capp, S. P., 1989, "Two-Dimensional Phase-Averaged Turbulence Statistics Downstream of a Rotating Spoked-Wheel Wake Generator," ASME JOURNAL OF TURBOMACHINERY, Vol. 111, pp. 475–482.

Obremski, H. J., and Fejer, A. A., 1964, "Transition in Oscillating Boundary Layer Flows," *Journal of Fluid Mechanics,* Vol. 18, pp. 438–448.

Orth, U., 1993, "Unsteady Boundary-Layer Transition in Flow Periodically Disturbed by Wakes," ASME JOURNAL OF TURBOMACHINERY, Vol. 115, pp. 707–713.

Schlichting, H., 1979, *Boundary-Layer Theory,* McGraw-Hill, New York.

Walker, G. J., 1993, "The Role of Laminar–Turbulent Transition in Gas Turbine Engines: A Discussion," ASME JOURNAL OF TURBOMACHINERY, Vol. 115, pp. 207–217.

DISCUSSION

H. P. Hodson[1]

The author has produced an interesting series of experimental results and observations based on the use of simple models of wake-induced transition. I have had an interest in the impact of wake-induced transition on profile loss and proposed (Hodson, 1991) the first model used by the author in Part I to describe wake-induced transition. This model was applied to test cases with realistic pressure distributions operating with relatively strong incoming wakes using a more general form of Eq. (2) of the present paper (see Hodson et al., 1992, and Eq. (A) below). The model gave satisfactory predictions of loss. It is encouraging that the present author observes similar agreement in the case of heat transfer on a zero-pressure gradient flat plate.

All the simple models incorporate the assumption that wake-induced transition takes place via the formation of a turbulent zone, uniform in the spanwise direction, that grows in streamwise extent as it moves downstream. Many classical boundary layer transition studies lead us to expect that individual turbulent spots should form under the influence of incoming wakes. Following the work of Addison and Hodson, Hodson (1991) and Hodson et al. (1992) examined extensions of these simple models to include the unsteady production of turbulent spots in a similar manner to that outlined in Fig. 10 of Part II. These extensions revealed that in the case of very intense wakes, such as those investigated by Pfeil and his co-workers, by Orth, and by the present author, the rate of turbulent spot formation is such that the boundary layer under the wake very rapidly becomes fully turbulent. This explains the success of these simple models. Hodson et al. also examined cases in turbines and compressors where the wake intensity around the start of transition was much less than that investigated by the present author. Consequently, the rate of spot formation was much lower, and this is believed to explain why individual turbulent events (spots) can be observed some distance downstream of the origin of wake-induced transition, particularly in low Reynolds number experiments.

The studies of Hodson (1990, 1991) and Hodson et al. (1992) examined test cases where Re_θ at the start of wake-induced transition seemed to range from 93 to 153. In the present papers, a model is proposed (see Fig. 14 in Part I and Fig. 10 in Part II) whereby a turbulent strip forms underneath the wake at the leading edge. The present data and published correlations do not support the validity of this aspect of the model. Indeed, the hot-wire data presented in Part II show that the turbulent intensities within the boundary layer near the leading edge do not exceed 5 percent. Could the author provide additional data to support the adoption of his model?

Could the author comment on the values he has used for the factors β_E and β_F? Following an examination of the then available data, I chose to set the factors equivalent to β_E and β_F in Eq. (2) equal to 0.5 and 1.0, respectively (Hodson, 1990). The factor $\beta_E = 0.5$ was chosen because it means that the rear of the wake-affected zone propagates at a speed equal to that of most turbulent spots. The factor $\beta_F = 1.0$ was used since it equals the speed of propagation of the wake and was thought to represent the speed of the front of the wake-induced disturbance. This value in particular is open to question. Orth, for example, quotes a value of $\beta_F = 0.88$. Traditional values for speeds of propagation of the leading and trailing edges of turbulent spots are $\beta_F = 0.88$ and $\beta_E = 0.5$, respectively. In practice, the factors β_F and β_E only appear in that part of Eq. (2) which is enclosed by parentheses, and the value of this part of the equation directly affects the intermittency. My own values for β_F and β_E, those of the present author, and those for a typical turbulent spot produce values of 1.0, 0.82, and 0.86, respectively, for that part of Eq. (2) which is enclosed by parentheses.

Notwithstanding these reservations, simple models may still be used to assess the probable significance of wake-induced transition. If natural transition or separation occurs at a distance x_{ln} from the leading edge, while wake-induced transition occurs at x_{tw}, then the maximum value of the time-mean intermittency that can be reached prior to the start of natural transition or separation is given by the value of the reduced frequency parameter f, i.e.,

$$\bar{f} = \bar{\gamma}(x_{ln}) = \frac{1}{T}\int_{x_{tw}}^{x_{ln}} \left[\frac{1}{\beta_E} - \frac{1}{\beta_F}\right]\frac{dx}{U} = \frac{1}{T}\frac{x_{ln} - x_{tw}}{U} \quad \text{(A)}$$

Hodson (1990) used the parameter $\hat{f}$ to correlate the effects of

[1] Whittle Laboratory, University of Cambridge, Madingley Road, Cambridge, CB3 ODY United Kingdom; Mem. ASME.

Downloaded 01 Jun 2010 to 171.66.16.53. Redistribution subject to ASME license or copyright; see http://www.asme.org/terms/Terms_Use.cfm

1 Wake passing directly induces turbulent patches beneath the wake, but their onset locations and evolving behavior depend heavily on the incident wake turbulence intensity.

2 Measured states of wake-affected boundary layer in the distance–time diagrams are quite similar to the presumed ones in the transition model proposed in Part I, except for the wake-induced transition points, which was previously assumed to be independent of the wake properties.

3 A threshold for defining turbulent region is proposed for convenience in terms of the turbulence intensity, which yields somewhat plausible results when compared to the data in the heat transfer experiments.

4 Based on the observations in this study, a slight modification to the transition model is made with respect to the transition onset. A quasi-steady approach using the criterion of Abu-Ghannam and Shaw is adopted with great success predicting the onset location of the wake-induced turbulent patch.

Acknowledgments

This study is financially supported by IHI, Ishikawajima-Harima Heavy Industries, monitored by S. Yamawaki and R. Henk. Contributions from T. Meguro as well as Y. Yamashita are to be acknowledged.

References

Abu-Ghannam, B. J., and Shaw, R., 1980, "Natural Transition of Boundary Layers—The Effects of Turbulence, Pressure Gradients, and Flow History," *Journal of Mechanical Engineering Science,* Vol. 22, pp. 231–228.

Addison, J. S., and Hodson, H. P., 1990a, "Unsteady Transition in an Axial-Flow Turbine: Part I—Measurements on the Turbine Rotor," ASME JOURNAL OF TURBOMACHINERY, Vol. 112, pp. 206–214.

Addison, J. S., and Hodson, H. P., 1990b, "Unsteady Transition in an Axial-Flow Turbine: Part II—Cascade Measurements and Modeling," ASME JOURNAL OF TURBOMACHINERY, Vol. 112, pp. 215–222.

Addison, J. S., and Hodson, H. P., 1992, "Modeling of Unsteady Transition Boundary Layers," ASME JOURNAL OF TURBOMACHINERY, Vol. 114, pp. 580–589.

Dong, Y., and Cumpsty, N. A., 1990, "Compressor Blade Boundary Layers: Part 2—Measurements With Incident Wakes," ASME JOURNAL OF TURBOMACHINERY, Vol. 112, pp. 231–240.

Gostelow, J. P., Hong, G., Melwani, N., and Walker, G. J., 1993, "Turbulent Spot Development Under a Moderate Adverse Pressure Gradient," ASME 93-GT-377.

Kline, S. J., and McClintock, F. A., 1953, "Describing Uncertainties in Single Sample Experiments," *Mechanical Engineering,* Jan., pp. 3–8.

Mayle, R. E., and Dullenkopf, K., 1990, "A Theory for Wake-Induced Transition," ASME JOURNAL OF TURBOMACHINERY, Vol. 112, pp. 188–195.

Mayle, R. E., 1991, "The Role of Laminar–Turbulent Transition in Gas Turbine Engines," ASME JOURNAL OF TURBOMACHINERY, Vol. 113, pp. 509–537.

Meyer, R. X., 1957, "The Effect of Wakes on the Transient Pressure and Velocity Distributions in Turbomachines," ASME *Journal of Basic Engineering,* Vol. 80, pp. 1544–1552.

O'Brien, J. E., and Capp, S. P., 1989, "Two-Dimensional Phase-Averaged Turbulence Statistics Downstream of a Rotating Spoked-Wheel Wake Generator," ASME JOURNAL OF TURBOMACHINERY, Vol. 111, pp. 475–482.

Obremski, H. J., and Fejer, A. A., 1964, "Transition in Oscillating Boundary Layer Flows," *Journal of Fluid Mechanics,* Vol. 18, pp. 438–448.

Orth, U., 1993, "Unsteady Boundary-Layer Transition in Flow Periodically Disturbed by Wakes," ASME JOURNAL OF TURBOMACHINERY, Vol. 115, pp. 707–713.

Schlichting, H., 1979, *Boundary-Layer Theory,* McGraw-Hill, New York.

Walker, G. J., 1993, "The Role of Laminar–Turbulent Transition in Gas Turbine Engines: A Discussion," ASME JOURNAL OF TURBOMACHINERY, Vol. 115, pp. 207–217.

DISCUSSION

H. P. Hodson[1]

The author has produced an interesting series of experimental results and observations based on the use of simple models of wake-induced transition. I have had an interest in the impact of wake-induced transition on profile loss and proposed (Hodson, 1991) the first model used by the author in Part I to describe wake-induced transition. This model was applied to test cases with realistic pressure distributions operating with relatively strong incoming wakes using a more general form of Eq. (2) of the present paper (see Hodson et al., 1992, and Eq. (A) below). The model gave satisfactory predictions of loss. It is encouraging that the present author observes similar agreement in the case of heat transfer on a zero-pressure gradient flat plate.

All the simple models incorporate the assumption that wake-induced transition takes place via the formation of a turbulent zone, uniform in the spanwise direction, that grows in streamwise extent as it moves downstream. Many classical boundary layer transition studies lead us to expect that individual turbulent spots should form under the influence of incoming wakes. Following the work of Addison and Hodson, Hodson (1991) and Hodson et al. (1992) examined extensions of these simple models to include the unsteady production of turbulent spots in a similar manner to that outlined in Fig. 10 of Part II. These extensions revealed that in the case of very intense wakes, such as those investigated by Pfeil and his co-workers, by Orth, and by the present author, the rate of turbulent spot formation is such that the boundary layer under the wake very rapidly becomes fully turbulent. This explains the success of these simple models. Hodson et al. also examined cases in turbines and compressors where the wake intensity around the start of transition was much less than that investigated by the present author. Consequently, the rate of spot formation was much lower, and this is believed to explain why individual turbulent events (spots) can be observed some distance downstream of the origin of wake-induced transition, particularly in low Reynolds number experiments.

The studies of Hodson (1990, 1991) and Hodson et al. (1992) examined test cases where Re_θ at the start of wake-induced transition seemed to range from 93 to 153. In the present papers, a model is proposed (see Fig. 14 in Part I and Fig. 10 in Part II) whereby a turbulent strip forms underneath the wake at the leading edge. The present data and published correlations do not support the validity of this aspect of the model. Indeed, the hot-wire data presented in Part II show that the turbulent intensities within the boundary layer near the leading edge do not exceed 5 percent. Could the author provide additional data to support the adoption of his model?

Could the author comment on the values he has used for the factors β_E and β_F? Following an examination of the then available data, I chose to set the factors equivalent to β_E and β_F in Eq. (2) equal to 0.5 and 1.0, respectively (Hodson, 1990). The factor $\beta_E = 0.5$ was chosen because it means that the rear of the wake-affected zone propagates at a speed equal to that of most turbulent spots. The factor $\beta_F = 1.0$ was used since it equals the speed of propagation of the wake and was thought to represent the speed of the front of the wake-induced disturbance. This value in particular is open to question. Orth, for example, quotes a value of $\beta_F = 0.88$. Traditional values for speeds of propagation of the leading and trailing edges of turbulent spots are $\beta_F = 0.88$ and $\beta_E = 0.5$, respectively. In practice, the factors β_F and β_E only appear in that part of Eq. (2) which is enclosed by parentheses, and the value of this part of the equation directly affects the intermittency. My own values for β_F and β_E, those of the present author, and those for a typical turbulent spot produce values of 1.0, 0.82, and 0.86, respectively, for that part of Eq. (2) which is enclosed by parentheses.

Notwithstanding these reservations, simple models may still be used to assess the probable significance of wake-induced transition. If natural transition or separation occurs at a distance x_{ln} from the leading edge, while wake-induced transition occurs at x_{tw}, then the maximum value of the time-mean intermittency that can be reached prior to the start of natural transition or separation is given by the value of the reduced frequency parameter f, i.e.,

$$\bar{f} = \bar{\gamma}(x_{ln}) = \frac{1}{T}\int_{x_{tw}}^{x_{ln}} \left[\frac{1}{\beta_E} - \frac{1}{\beta_F}\right]\frac{dx}{U} = \frac{1}{T}\frac{x_{ln} - x_{tw}}{U} \quad \text{(A)}$$

Hodson (1990) used the parameter $\hat{f}$ to correlate the effects of

[1] Whittle Laboratory, University of Cambridge, Madingley Road, Cambridge, CB3 ODY United Kingdom; Mem. ASME.

Copyright © 1996 by ASME

Downloaded 01 Jun 2010 to 171.66.16.53. Redistribution subject to ASME license or copyright; see http://www.asme.org/terms/Terms_Use.cfm

wake-induced transition on profile loss. When $\hat{f}$ is less than unity, natural transition should occur between wake-passing events. In LP turbines, the values of $\hat{f}$ rarely exceed 0.3. It is for this reason that investigations have revealed the presence of laminar separation bubbles in some LP turbines (Hodson et al., 1994). For the same reason, the work reported by Dong and Cumpsty (1990) on the effect of wakes on compressor blades revealed that separation bubbles exist in compressors. It is rare for the reduced frequencies as defined by Eq. (A) to reach the values used in the present paper. Could the author comment on his use of relatively high reduced frequencies?

References

Dong, Y., and Cumpsty, N. A., 1990, "Compressor Blade Boundary Layers: Part I—Test Facility and Measurements With No Incident Wakes; Part II—Measurements With Incident Wakes," ASME JOURNAL OF TURBOMACHINERY, Vol. 112, pp. 222–240.

Hodson, H. P., 1991, "Aspects of Unsteady Blade-Surface Boundary Layers and Transition in Axial Turbomachines," in: VKI Lecture Series No. 9, *Boundary Layers in Turbomachines,* Von Karman Institute.

Hodson, H. P., Addison, J. S., and Shepherdson, C. A., 1992, "Models for Unsteady Wake-Induced Transition in Axial Turbomachines," *Jnl. de Physique,* Vol. 2, No. 4, Apr., pp. 545–574.

Hodson, H. P., Huntsman, I., and Steele, A. B., 1994, "An Investigation of Boundary Layer Development in a Multistage LP Turbine," ASME JOURNAL OF TURBOMACHINERY, Vol. 116, pp. 375–383.

R. E. Mayle[2] and K. Dullenkopf[3]

We have been unable to explain the discrepancy between your laminar heat transfer data and any laminar boundary layer calculation that accounts for an unheated starting length. The growth of the thermal boundary layer in your experiment does not appear to be correct. Can you explain? This of course would drastically affect the initial portion of the intermittency distribution, which you claim is significantly different than that predicted by the Mayle–Dullenkopf theory. In addition, there are two other points that must be considered in your measurements which you do not address: (1) If wake-induced transition begins before the end of the unheated length, which your results indicate, heat transfer measurements alone are not sufficient to determine the intermittency distribution, and (2) your analysis implies that the increase in heat transfer for a wake-affected laminar flow is the same as that obtained by a turbulent boundary layer flow. The latter point is not true. For further details regarding the effect of turbulent wakes on laminar boundary layers we refer you to the ideas presented by Dullenkopf and Mayle (1992), even though the analysis is for accelerating flows. In conclusion, you are confusing two separate wake effects in your analysis, which have already been addressed. The first, called wake-induced transition, is the effect of periodically passing wakes on boundary layer transition, which has been addressed by Mayle and Dullenkopf (1989, 1991) among others. The second, which might be called turbulent enhancement, is the effect of a periodic increase in the free-stream turbulence on the laminar boundary layer caused by the passing wake (Dullenkopf and Mayle, 1992). These are two distinctly different effects, which should not be lumped into the term "wake-induced transition."

U. Orth[4]

The present paper by K. Funazaki is a welcome and significant contribution toward improvement of our understanding of boundary layer transition induced by turbulent wakes, and presents valuable new measurements. Periodic turbulent wakes can influence boundary layer development due to (1) low-frequency periodic fluctuations of free-stream velocity and pressure gradient, and (2) superimposed high-frequency wake turbulence. The discussion about which of the two is the dominating mechanism of wake-induced transition is an ongoing one. Wake-turbulence-induced transition is often referred to as "direct," whereas transition resulting from periodic unsteadiness of the free stream, and lagging behind the outer wake, is called "indirect." I agree with Funazaki's view that wake turbulence is the main cause of wake-induced transition in his measurements and in those of most other authors.

Concerning Funazaki's reference to measurements of Orth (1993), there are two things I would like to point out:

1 In Fig. 9, Funazaki cites experimental data from Orth (1993) that show that in case of low-intensity wake turbulence ("far wake"), the onset of wake-induced transition occurs noticeably downstream of the point where wake turbulence is ingested into the boundary layer, and that the patch of turbulent fluid within the boundary layer, when it finally does cause transition, has separated from the wake passing over outside the boundary layer. Contrary to Orth's argument, Funazaki assumes that this apparent delay does not actually exist, and that the immediate growth of turbulent patches merely remains undetected due to this taking place nearer to the wall than the measuring plane ($y/d = 0.03$, $y/L = 0.0006$ in Funazaki's notation) in Fig. 9.

I do not agree with this interpretation, and there is further experimental evidence to support the view that the wake did not lead to immediate transition in this case. Orth (1993) took measurements at 18 wall distances down to $y/d = 0.01$ ($y/L = 0.0002$ in Funazaki's notation) and presented them in Figs. 5–8 of his paper. It is observed that the momentary onset of transition actually extends farthest upstream at around $y/d = 0.03$. Orth's Fig. 8 (temporal development of boundary layer momentum thickness and shape parameter) shows conclusively that the onset of transition does indeed occur significantly later in case of a weak disturbance than it does for a strong disturbance. Full details of these measurements were published by Orth (1991).

2 Although Orth's (1993) measurements for the "far wake" case show that turbulent breakdown in the boundary layer lags behind the outer wake, I believe, contrary to Walker (1993), that turbulence, and not periodic fluctuations, was responsible for wake-induced transition. The lag can be explained by the reduced velocity with which the patch of turbulent fluid convects within the boundary layer, as pointed out by N. A. Cumpsty in his discussion of Walker's paper. Wake turbulence is ingested into the laminar boundary layer as it is being formed near the leading edge. However, the thin laminar boundary layer is so stable that turbulent fluid with comparatively low turbulence intensity may convect downstream within it until, with increasing thickness (and Reynolds number), the boundary layer becomes unstable for disturbances of this magnitude, leading to turbulent breakdown.

Since turbulent breakdown in Orth's "far wake" case lags behind the passing wake outside the boundary layer, Walker (1993) characterizes the transition as "indirect," irrespective of which mechanism actually caused it. It may be preferable to avoid the terms "direct" or "indirect" in this context since they can cause confusion, but instead to differentiate between wake-turbulence-induced and periodic-unsteadiness-induced transition.

References

Orth, U., 1991, "Untersuchung des Umschlagvorganges von Platten- und Zylindergrenzschichten bei ungestörter und stationär oder periodisch gestörter Zuströmung," Doctoral Thesis, TH Darmstadt, Federal Republic of Germany.

Author's Closure

First, the author appreciates the discussions addressed to the present papers.

[2] Professor Emeritus of Mechanical Engineering, Rensselaer Polytechnic Institute, Troy, NY 12180.

[3] Dr.-Ingenieur, Institut für Thermische Strömungs Maschinen, Universität Karlsruhe, 76128 Karlsruhe, Federal Republic of Germany.

[4] MAN Gutehoffnungshütte AG, Bahnhofstr. 66, 46145 Oberhausen, Federal Republic of Germany.

Downloaded 01 Jun 2010 to 171.66.16.53. Redistribution subject to ASME license or copyright; see http://www.asme.org/terms/Terms_Use.cfm

wake-induced transition on profile loss. When $\hat{f}$ is less than unity, natural transition should occur between wake-passing events. In LP turbines, the values of $\hat{f}$ rarely exceed 0.3. It is for this reason that investigations have revealed the presence of laminar separation bubbles in some LP turbines (Hodson et al., 1994). For the same reason, the work reported by Dong and Cumpsty (1990) on the effect of wakes on compressor blades revealed that separation bubbles exist in compressors. It is rare for the reduced frequencies as defined by Eq. (A) to reach the values used in the present paper. Could the author comment on his use of relatively high reduced frequencies?

References

Dong, Y., and Cumpsty, N. A., 1990, "Compressor Blade Boundary Layers: Part I—Test Facility and Measurements With No Incident Wakes; Part II—Measurements With Incident Wakes," ASME JOURNAL OF TURBOMACHINERY, Vol. 112, pp. 222–240.

Hodson, H. P., 1991, "Aspects of Unsteady Blade-Surface Boundary Layers and Transition in Axial Turbomachines," in: VKI Lecture Series No. 9, *Boundary Layers in Turbomachines,* Von Karman Institute.

Hodson, H. P., Addison, J. S., and Shepherdson, C. A., 1992, "Models for Unsteady Wake-Induced Transition in Axial Turbomachines," *Jnl. de Physique,* Vol. 2, No. 4, Apr., pp. 545–574.

Hodson, H. P., Huntsman, I., and Steele, A. B., 1994, "An Investigation of Boundary Layer Development in a Multistage LP Turbine," ASME JOURNAL OF TURBOMACHINERY, Vol. 116, pp. 375–383.

R. E. Mayle[2] and K. Dullenkopf[3]

We have been unable to explain the discrepancy between your laminar heat transfer data and any laminar boundary layer calculation that accounts for an unheated starting length. The growth of the thermal boundary layer in your experiment does not appear to be correct. Can you explain? This of course would drastically affect the initial portion of the intermittency distribution, which you claim is significantly different than that predicted by the Mayle–Dullenkopf theory. In addition, there are two other points that must be considered in your measurements which you do not address: (1) If wake-induced transition begins before the end of the unheated length, which your results indicate, heat transfer measurements alone are not sufficient to determine the intermittency distribution, and (2) your analysis implies that the increase in heat transfer for a wake-affected laminar flow is the same as that obtained by a turbulent boundary layer flow. The latter point is not true. For further details regarding the effect of turbulent wakes on laminar boundary layers we refer you to the ideas presented by Dullenkopf and Mayle (1992), even though the analysis is for accelerating flows. In conclusion, you are confusing two separate wake effects in your analysis, which have already been addressed. The first, called wake-induced transition, is the effect of periodically passing wakes on boundary layer transition, which has been addressed by Mayle and Dullenkopf (1989, 1991) among others. The second, which might be called turbulent enhancement, is the effect of a periodic increase in the free-stream turbulence on the laminar boundary layer caused by the passing wake (Dullenkopf and Mayle, 1992). These are two distinctly different effects, which should not be lumped into the term "wake-induced transition."

U. Orth[4]

The present paper by K. Funazaki is a welcome and significant contribution toward improvement of our understanding of boundary layer transition induced by turbulent wakes, and presents valuable new measurements. Periodic turbulent wakes can influence boundary layer development due to (1) low-frequency periodic fluctuations of free-stream velocity and pressure gradient, and (2) superimposed high-frequency wake turbulence. The discussion about which of the two is the dominating mechanism of wake-induced transition is an ongoing one. Wake-turbulence-induced transition is often referred to as "direct," whereas transition resulting from periodic unsteadiness of the free stream, and lagging behind the outer wake, is called "indirect." I agree with Funazaki's view that wake turbulence is the main cause of wake-induced transition in his measurements and in those of most other authors.

Concerning Funazaki's reference to measurements of Orth (1993), there are two things I would like to point out:

1 In Fig. 9, Funazaki cites experimental data from Orth (1993) that show that in case of low-intensity wake turbulence ("far wake"), the onset of wake-induced transition occurs noticeably downstream of the point where wake turbulence is ingested into the boundary layer, and that the patch of turbulent fluid within the boundary layer, when it finally does cause transition, has separated from the wake passing over outside the boundary layer. Contrary to Orth's argument, Funazaki assumes that this apparent delay does not actually exist, and that the immediate growth of turbulent patches merely remains undetected due to this taking place nearer to the wall than the measuring plane (y/d = 0.03, y/L = 0.0006 in Funazaki's notation) in Fig. 9.

I do not agree with this interpretation, and there is further experimental evidence to support the view that the wake did not lead to immediate transition in this case. Orth (1993) took measurements at 18 wall distances down to y/d = 0.01 (y/L = 0.0002 in Funazaki's notation) and presented them in Figs. 5–8 of his paper. It is observed that the momentary onset of transition actually extends farthest upstream at around y/d = 0.03. Orth's Fig. 8 (temporal development of boundary layer momentum thickness and shape parameter) shows conclusively that the onset of transition does indeed occur significantly later in case of a weak disturbance than it does for a strong disturbance. Full details of these measurements were published by Orth (1991).

2 Although Orth's (1993) measurements for the "far wake" case show that turbulent breakdown in the boundary layer lags behind the outer wake, I believe, contrary to Walker (1993), that turbulence, and not periodic fluctuations, was responsible for wake-induced transition. The lag can be explained by the reduced velocity with which the patch of turbulent fluid convects within the boundary layer, as pointed out by N. A. Cumpsty in his discussion of Walker's paper. Wake turbulence is ingested into the laminar boundary layer as it is being formed near the leading edge. However, the thin laminar boundary layer is so stable that turbulent fluid with comparatively low turbulence intensity may convect downstream within it until, with increasing thickness (and Reynolds number), the boundary layer becomes unstable for disturbances of this magnitude, leading to turbulent breakdown.

Since turbulent breakdown in Orth's "far wake" case lags behind the passing wake outside the boundary layer, Walker (1993) characterizes the transition as "indirect," irrespective of which mechanism actually caused it. It may be preferable to avoid the terms "direct" or "indirect" in this context since they can cause confusion, but instead to differentiate between wake-turbulence-induced and periodic-unsteadiness-induced transition.

References

Orth, U., 1991, "Untersuchung des Umschlagvorganges von Platten- und Zylindergrenzschichten bei ungestörter und stationär oder periodisch gestörter Zuströmung," Doctoral Thesis, TH Darmstadt, Federal Republic of Germany.

Author's Closure

First, the author appreciates the discussions addressed to the present papers.

[2] Professor Emeritus of Mechanical Engineering, Rensselaer Polytechnic Institute, Troy, NY 12180.

[3] Dr.-Ingenieur, Institut für Thermische Strömungs Maschinen, Universität Karlsruhe, 76128 Karlsruhe, Federal Republic of Germany.

[4] MAN Gutehoffnungshütte AG, Bahnhofstr. 66, 46145 Oberhausen, Federal Republic of Germany.

Copyright © 1996 by ASME

Downloaded 01 Jun 2010 to 171.66.16.53. Redistribution subject to ASME license or copyright; see http://www.asme.org/terms/Terms_Use.cfm

The Influence of Blade Wakes on the Performance of Interturbine Diffusers

R. G. Dominy

D. A. Kirkham

School of Engineering,
University of Durham,
Durham, United Kingdom

Interturbine diffusers provide continuity between HP and LP turbines while diffusing the flow upstream of the LP turbine. Increasing the mean turbine diameter offers the potential advantage of reducing the flow factor in the following stages, leading to increased efficiency. The flows associated with these interturbine diffusers differ from those in simple annular diffusers both as a consequence of their high-curvature S-shaped geometry and of the presence of wakes created by the upstream turbine. It is shown that even the simplest two-dimensional wakes result in significantly modified flows through such ducts. These introduce strong secondary flows demonstrating that fully three-dimensional, viscous analysis methods are essential for correct performance modeling.

Introduction

Swan-necked ducts are used in the context of gas turbine design to provide continuity between the flow passages at exit from the HP or LP turbine and at entry to the usually larger diameter LP or power turbine. Diffusing the flow upstream of the LP turbine and thereby allowing an increase of the mean turbine diameter offers the potential advantage of reducing the flow factor in the following stages leading to increased efficiency. If unacceptable weight penalties are to be avoided, the diffusion must be achieved in the shortest possible length while avoiding flow separation in the regions of most rapid diffusion. The flows associated with these interturbine diffusers differ from those in well-documented annular diffuser flows (e.g., ESDU, 1976) as a result of the influence of both wakes and secondary flows generated by the upstream turbine.

The pressure distribution within an S-shaped or "Swan Neck" duct (Fig. 1) depends not only upon the area change along the length of the duct but also upon the curvature of the surfaces and hence of the flow streamlines. The effective local curvature will itself be modified by the growth of the surface boundary layers. Thus the initial transition from the parallel-walled, axial inlet passage into the diffuser gives rise to a pressure gradient from a high-pressure region at the hub to a lower pressure at the casing. The significance of this cross-passage pressure gradient relative to the diffusion that arises from the area increase along the length of the duct may be controlled by the design of the passage geometry, but in a realistically short duct both may be expected to be significant. At the downstream end of the duct the flow is turned back toward the axial direction, resulting in a second zone of curvature-induced pressure gradient, but in this instance from a high casing pressure to a lower hub pressure. Of particular importance to the performance of the duct is the boundary layer development along the hub and casing and the ability of those boundary layers to withstand the strong adverse pressure gradients that may occur, particularly in the flow regions most influenced by the wall curvature. If the flow at entry to the duct is swirling then the boundary layers will be further modified by the increased flow path through the duct which has the beneficial effect of reducing the pressure gradients along a streamline but which also increases the effective surface area of the duct with consequential boundary layer growth.

The presence of one or more upstream turbine stages may be expected to have a significant impact upon the nature of the flow through the duct. The influences may be broadly categorized into three types, although in practice the three are not independent. First, there is the pseudo-steady effect of the essentially two-dimensional blade wakes themselves extending from the hub to the casing in a radial or near radial direction. In the radial pressure fields within the duct the presence of upstream blades may be expected to give rise to exaggerated radial flows within the low-velocity, high-loss wakes. Second, there are the well-documented secondary flow vortices that are associated with the wakes from turbine and nozzle rows, which would be expected to have a significant influence upon the hub and casing boundary layers. Third, there are the unsteady effects that arise from the rotation of the turbine and hence of the wakes including the secondary flows giving rise to a periodic disturbance of the wall boundary layers at all points within the duct. In order to decouple these influences and therefore to approach the investigation of these highly complex flows in a systematic manner, the work presented here has focused upon the first and simplest of these phenomena, i.e., the influence of nonrotating wakes in the absence of strong, blade-induced secondary flows. These data approximate a swirl-free, nominal design case. The influence of swirl upon these flows is currently under investigation.

The performance of simple diffusers, both rectangular and annular, and the flow phenomena associated with them has been well documented (e.g., ESDU, 1976). In simple diffuser flows the factors influencing the efficiency of a diffuser are predominantly the area ratio (exit to inlet) of the diffuser and the length of the flow path over which the diffusion occurs. Typically minimum loss occurs when for a given area ratio the length is sufficient to limit separation losses but not so long as to allow friction losses to dominate. Losses resulting from separation are reflected in the static pressure recovery through the duct, which in its simplest form may be defined as a pressure rise coefficient where:

$$Cp = (p_n - p_i)/(P_{Oi} - p_i)$$

where the subscript n relates to the local position and i refers to the inlet plane. In flows where the pressures at a given plane are nonuniform, it is necessary to use an equivalent form of the equation based upon local integral parameters.

The modification of the local pressure gradients as a result of wall curvature and the consequent influence upon turbulent

Contributed by the International Gas Turbine Institute and presented at the 39th International Gas Turbine and Aeroengine Congress and Exposition, The Hague, The Netherlands, June 13–16, 1994. Manuscript received by the International Gas Turbine Institute February 18, 1994. Paper No. 94-GT-207. Associate Technical Editor: E. M. Greitzer.

Copyright © 1996 by ASME

Downloaded 01 Jun 2010 to 171.66.16.53. Redistribution subject to ASME license or copyright; see http://www.asme.org/terms/Terms_Use.cfm

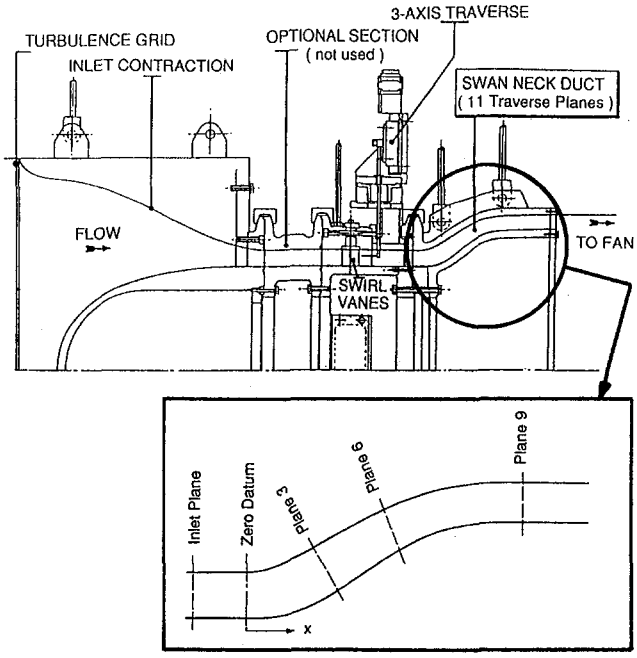


Fig. 1 Test rig and traverse plane positions

boundary layer behavior may substantially change the performance of the diffuser. Published data on S-shaped diffusers, though sparse, provide some information on both rectangular and annular ducts with wall curvature. The CFD test case of Fottner (1990) based upon the data of Taylor et al. (1982) and Towne (1984) describes the results from Laser-Doppler velocimetry measurements in a square-sectioned S-shaped duct of constant area with water as the working fluid. The test therefore relates most closely to S-shaped compressor ducts in which the pressure gradients arise solely from the influence of curvature with little or no overall diffusion. In this work flows with both laminar and turbulent inlet boundary layers were evaluated, although the conservative design of the duct did not induce flow separation at any point and the results therefore effectively differ from each other mostly as a consequence of different inlet boundary layer thicknesses in the two cases. The measurements clearly reveal pressure-driven secondary flows around the first bend, which are then opposed by streamwise vorticity of the opposite sign around the second bend. This is of some relevance to the work presented here as the secondary flows arising from the influence of the pressure field upon the side wall boundary layers may be expected to be qualitatively comparable to the generated flows in an annular S-shaped duct in the presence of blade wakes, since both wall and wake flows represent zones of velocity and pressure deficit. Data have also been widely reported relating to constant-area, internal blade cooling passages, although the extreme curvature in terms of both radius and arc length are of less direct relevance to the interturbine diffuser problem.

Information relating to the influence of wakes from an upstream blade row upon the performance of an annular diffuser is sparse. Quest and Scholz (1990) [see also Fottner (1990)] provide experimental data from a straight-core annular diffuser with a casing divergence angle of 7 deg and a diffuser area ratio of 3.52 situated downstream from a single stage, weakly loaded LP turbine. Measurements of the flowfield at the diffuser inlet and exit plane were made with and without swirl at entry to the diffuser. However, only circumferentially averaged values of the measured quantities were presented with no attempt to investigate the detailed structure of the flow or the propagation of the wake structures along the diffuser. Nor was any attempt made to record the radial flow components at any point in the diffuser. A strongly distorted radial inlet total pressure distribution, although typical of that from a turbine stage, makes analysis of the influence of the wakes upon the bulk flow difficult to interpret and the absence of any wall boundary layer information is a further limitation. The data does however provide an initial data set, which may prove of benefit for the development of two-dimensional axisymmetric, viscous flow calculations and to this end it has been adopted as an AGARD test case (Fottner, 1990). The work adds little to our understanding of the flow physics. The influence of wakes is considered more thoroughly by Pfeil and Going (1987) who observed that the character and development of the turbulent boundary layers in a straight-cored annular diffuser behind a single compressor stage were greatly influenced by the presence of wakes. In their experiment the flow at exit from the stator was essentially axial and the data presented from radial traverses within the stator wakes and at midpitch show a distinct contrast between the essentially two-dimensional boundary layers at midpitch and the strongly three-dimensional nature of the flow in the wake region. Significant differences in the turbulence structures in the two zones are also reported. Unfortunately no intermediate radial traverses were performed and the extent of the wake influence remains unknown. The authors not surprisingly concluded that the two-dimensional design of such diffusers in the presence of wakes from an upstream stage is questionable. Published data relating to the interturbine diffuser problem in which both diffusion and wall curvature are significant have been presented by Amman et al. (1971) but detailed information on flow development is lacking. However, published data are available for flows in curved annular ducts of constant area.

S-shaped annular ducts are commonly used between adjacent compressor stages of modern gas turbines. Britchford et al. (1993) examine the flows in such ducts. In this situation both wake propagation and wall curvature effects are present but the mean passage radius decreases along the length of the duct and although local diffusion occurs as a result of wall curvature there is no overall diffusion. They showed that in their typical duct a long diffusing zone along the hub surface around the first bend led to a peak boundary layer shape factor of 1.47, which rose to 1.65 in the absence of an upstream rotor. This is attributed to increased turbulent mixing introduced by the compressor stage. However, the authors do not specify the effect of the removal of the compressor stage upon the character of the boundary layer at the duct entry plane. The figures presented would seem to suggest a shape factor at the duct inlet of about 1.22 compared with the higher value of 1.26 with the compressor fitted. No corresponding values of δ^* or θ are available.

Nomenclature

A = local cross-sectional area
Cp = pressure rise coefficient
L = duct axial length
h = inlet passage height
H = boundary layer shape factor
p = static pressure
P_o = stagnation pressure
Re = Reynolds number
x = axial distance
δ^* = boundary layer displacement thickness
θ = boundary layer momentum thickness
ρ = density

Subscripts

e = exit plane
i = inlet plane
n = number of traverse plane

Downloaded 01 Jun 2010 to 171.66.16.53. Redistribution subject to ASME license or copyright; see http://www.asme.org/terms/Terms_Use.cfm

Total pressure coefficient measurements demonstrated the development of the wakes and in conjunction with secondary velocity vectors they provide some evidence of radially inward flow in the low-energy wakes, particularly around the first bend where the radial pressure gradient is greatest. However, the effect seems to be weak. Their measurements indicated that with a compressor stage at inlet, the tendency for the flow to separate from the inner wall was reduced as a result, in part, to a re-energizing of the inner wall boundary layer brought about by the inward radial pressure force driving the blade wake flow into the wall region.

Experimental Facility

The configuration of The University of Durham Swan Neck Duct Facility is shown in Fig. 1. A large, variable-speed centrifugal fan draws ambient air from the atmosphere through a turbulence grid and inlet contraction into a parallel section, which houses a row of 34 fixed swirl vanes and a traverse ring, which allows both radial and circumferential traversing of the inlet flow. From the parallel section the air is drawn through the annular diffusing duct into a plenum before being expelled through the fan back to the atmosphere. Both the hub and the casing of the diffusing duct are manufactured from aluminum alloy castings. Machined surfaces for the fixing of traverse equipment are located at 11 axial positions on the casing, which allow traversing perpendicular to the local meridianal direction. Data from only four of these traverse planes are presented here and their locations in terms of x/L are shown in Table 1. Static pressure tappings are located at each traverse plane on both the hub and the casing and additional tappings are positioned at the points of greatest change of surface pressure gradient. At entry to the diffuser the parallel passage has a hub diameter of 286 mm and a hub-to-casing radius ratio of 0.7. At exit from the duct the hub diameter has increased to 550 mm and the exit to entry area ratio $A_e/A_i = 1.5$. Inlet conditions are determined from pressure measurements at a plane 1.5 passage heights upstream from the start of curvature of the diffuser. Actual inlet conditions are derived from area traverse data at the same plane. For all of the data presented here a turbulence grid was fitted at entry to the inlet contraction, giving a mean turbulence level of 4 percent at the inlet plane. The operating Reynolds number at entry to the duct was 3.9×10^5 (based upon inlet passage height) which was close to the system maximum.

For the initial tests, which were carried out in the absence of the upstream swirl vanes, the boundary layer profiles at each traverse plane were measured by traversing a flattened pitot probe (0.12 mm thick) across the full passage height. The exact point at which the probe touches the surface was determined by electrical contact. For each measurement the tip of the pitot probe was aligned co-axially with a wall static pressure tapping but was separated circumferentially by about 30 mm to prevent interference as the probe tip approaches the surface.

With the swirl vanes installed, the flow through the duct is no longer circumferentially uniform and area traversing over one or more vane pitches has therefore been carried out at each traverse plane. These traverses were performed using 2-mm-dia, five-hole pressure probes for the bulk of the flow and 0.8-mm-thick, three-hole cobra-type probes close to the walls. The

Table 1 Traverse plane locations

Traverse Plane	x/L (Hub)	x/L (nominal)	x/L (casing)
inlet	-0.140	-0.14	-0.140
3	+0.221	+0.19	+0.159
6	+0.372	+0.35	+0.336
11	+0.676	+0.68	+0.676

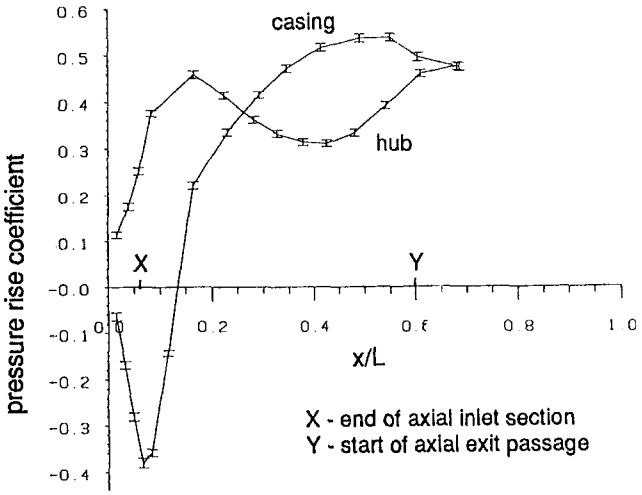


Fig. 2 Pressure rise coefficient (no vanes)

confines of the duct preclude the adoption of probe nulling so a calibration method was adopted allowing flow angles of up to ± 40 deg in yaw and pitch to be measured. The probes were calibrated at the operating Reynolds number to minimize potential Reynolds number induced calibration errors (Dominy and Hodson, 1993). Wall shear stress measurements were made using preston tubes.

Inlet swirl was created using a ring of 34 vanes. For simplicity a 32 mm chord, flat plate vane design of 1.5 mm thickness was adopted with a circular leading edge and 30 deg trailing edge. These generated wakes that were comparable both in area and intensity to those of HP or IP turbine blades. The vanes were located 2.5 passage heights upstream from the duct inlet.

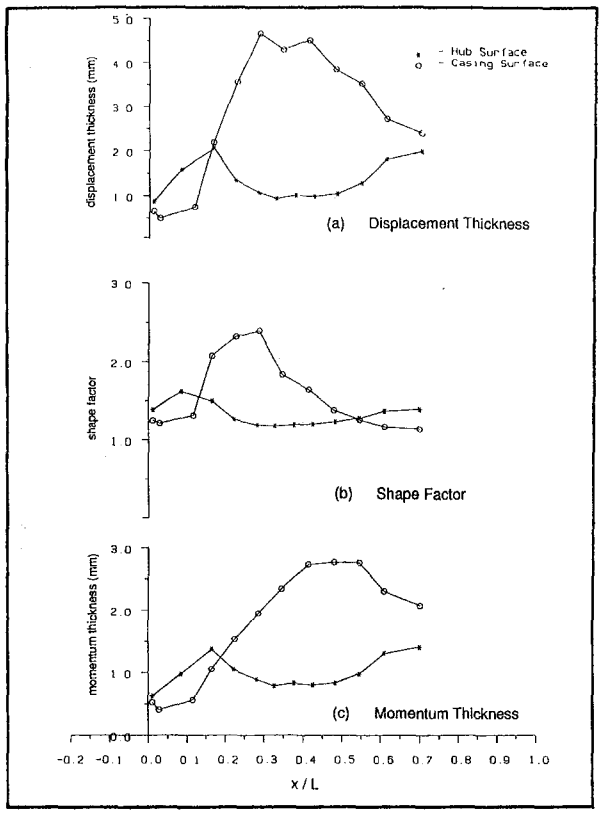


Fig. 3 Boundary layer growth (no wakes)

Downloaded 01 Jun 2010 to 171.66.16.53. Redistribution subject to ASME license or copyright; see http://www.asme.org/terms/Terms_Use.cfm

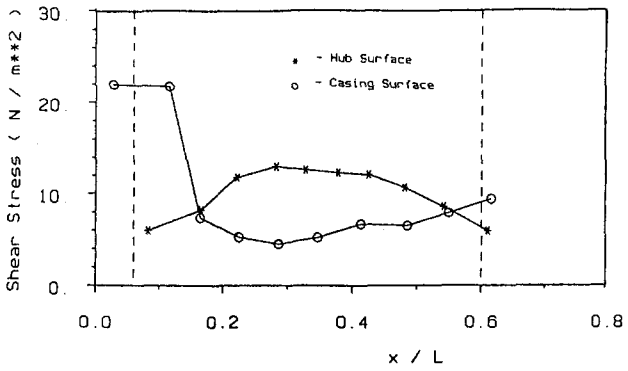


Fig. 4 Wall shear stress (no wakes)

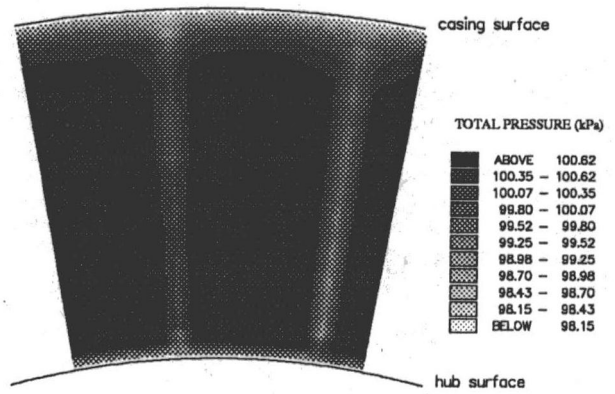


Fig. 5 Inlet total pressure contours

CFD

The presented CFD analysis of the flow was performed using the Moore Elliptic Flow Program (MEFP), which has been thoroughly described in numerous publications (e.g., Moore and Moore, 1985; Moore, (1985). This is a viscous three-dimensional CFD code that solves the Navier–Stokes equations. The elliptic nature of the equations allows reversed flows and hence flow separation to be indicated. The analysis was performed using a mixing length turbulence model. A grid of 71 axial, 41 radial, and 31 circumferential nodes was adopted with 10 radial grid nodes defining the inlet boundary layer on each surface.

Results and Discussion

Circumferentially Uniform Inlet Flow (No Wakes). The performance of the duct with a uniform inlet flow with neither swirl nor wakes present is described in Figs. 2–4. For this axisymmetric case the inlet wall boundary layer displacement thicknesses on the hub and casing were 0.87 mm and 0.66 mm, respectively. Full integral boundary layer parameters are given in Table 2. The pressure distribution along the duct at its design condition ($Re = 3.9 \times 10^5$) shown in Fig. 2 clearly demonstrates the zones of strongly adverse pressure gradient. The steepest gradient begins at the convex casing bend immediately downstream from the point of peak suction at $x/L = 0.08$. Here the diffusing influences of the wall curvature and the rapidly increasing duct cross-sectional area are additive. A comparable diffusion occurs a little further upstream on the hub as the bend is approached, although here the pressure rise is due almost entirely to curvature. The influence of these rapidly increasing pressures upon the development of the wall boundary layers is revealed by the measurements of Fig. 3 in which rapid boundary layer growth is observed in each of these regions. Whereas the initial hub diffusion is followed by a zone of re-acceleration, which results in a return of the boundary layer to a form that closely resembles that at the inlet in terms of both thickness (Fig. 3(a)) and shape factor (Fig. 3(b)) the casing diffusion is exaggerated by the influence of the second bend. Here δ^* rises from a minimum of 0.5 mm as the flow accelerates into the first bend to a peak of 4.8 mm. The maximum momentum thickness occurs further downstream at $x/L = 0.55$ (Fig. 3(c)) and the different locations of the maxima of the two parameters are explained by the dramatic changes in shape factor that occur as a result of the diffusion (Fig. 3(b)). However, at the design flow condition the growth of the casing boundary layer in the rapidly diffusing flow after the first bend does not reveal a sufficiently rapid fall in shear stress to cause separation (Fig. 4). As a basis for the evaluation of wake effects, the basic duct

Table 2 Inlet boundary layer parameters (without vanes)

	Hub	Casing
δ^* (mm)	0.87	0.66
δ^*/h	0.014	0.011
θ (mm)	0.63	0.52
H	1.40	1.26

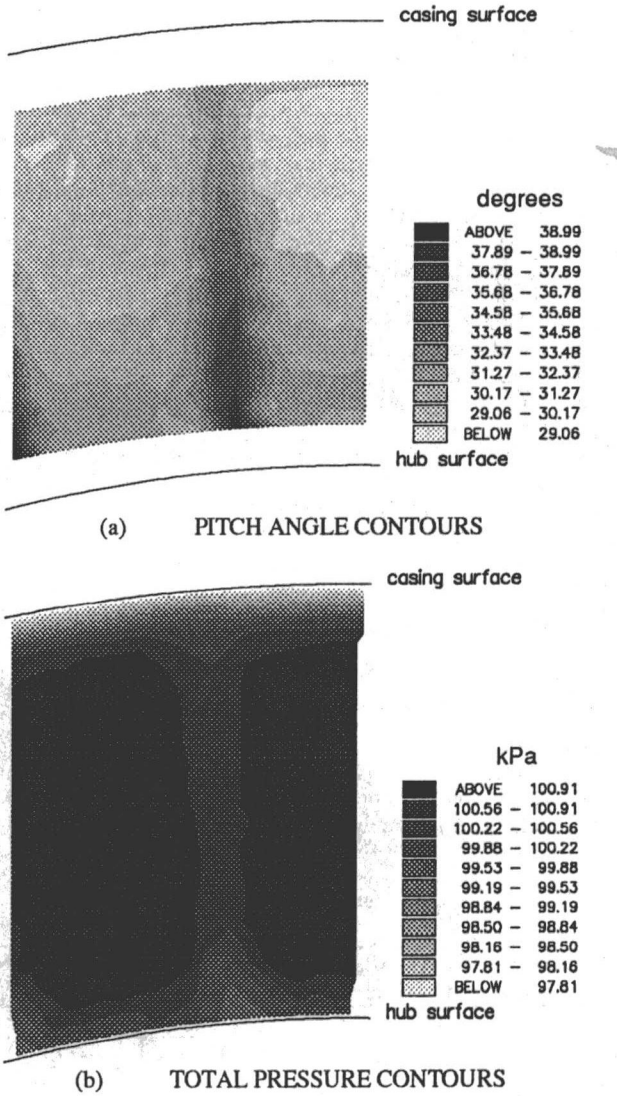


Fig. 6 Plane 3 ($x/L = 0.19$) pitch and Po contours

Downloaded 01 Jun 2010 to 171.66.16.53. Redistribution subject to ASME license or copyright; see http://www.asme.org/terms/Terms_Use.cfm

may therefore be seen to be a severe but nevertheless well-behaved test case.

Wake Influences. The influence of the propagation of wakes through the duct is revealed in Figs. 5–9. An indication of the nature of the wakes at the duct inlet plane is shown in the total pressure contours of Fig. 5. Here the wake structure and the loss distribution across the passage are seen to be essentially two dimensional with only very minor interaction between the wake and the wall boundary layers.

As the flow passes around the first bend, the pressure gradient between the hub and the casing leads to a radially outward flow component within the low-energy wake relative to the mean flow direction. At traverse plane 3 (nominal $x/L = 0.19$) the driving pressure gradient has fallen from a peak of almost 65 percent of the inlet dynamic head (Fig. 2) to about 20 percent. The cross-passage pressure gradient leads to a radial velocity within the wake which is greatest on the hub side of the flow field (Fig. 6(a)) giving rise to a pitch variation within the passage of 13 deg. Total pressure contours (Fig. 6(b)) show a slight broadening and weakening of the wake relative to the inlet flow and also a thickening of the casing boundary layer between the wakes, which is consistent with the observed boundary layer growth through the duct in the absence of swirl vanes (Fig. 3(a)). Across most of the passage the wakes remain essentially two dimensional and appear to influence the wall boundary layers only in the immediate vicinity of the wake–boundary layer interaction.

Farther downstream at traverse plane 6 (nominal $x/L = 0.35$) the strong adverse pressure gradient on the casing downstream from the first curvature results in further, rapid boundary layer growth (Fig. 7(a)). This is exaggerated by the radially outward flow that has occurred within the wakes. The cumulative influence of the flow within the wakes upstream from this point is clearly evident. The hub boundary layer remains relatively uniform circumferentially except in close proximity to the wake itself. Here the high loss fluid from the hub boundary layer is induced radially outward into the wake but its influence barely reaches midpassage. However, the casing boundary layer reveals strong evidence of the flow of high loss wake fluid into the boundary layer and also of the vorticity, which is demonstrated by the secondary velocity vectors either side of the wake (Fig. 7(b)). The vectors represent the deviation from the mean flow direction.

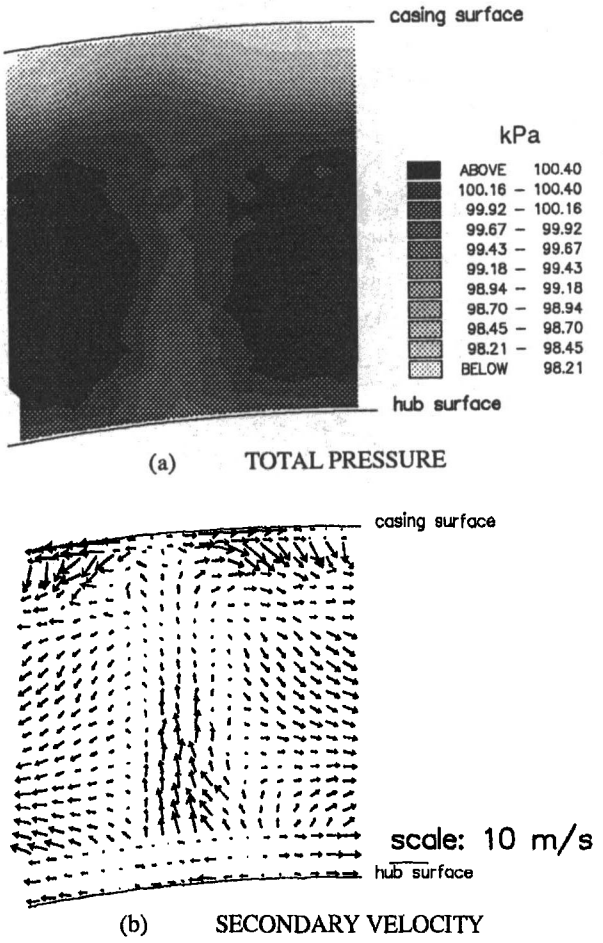


Fig. 7 Plane 6 ($x/L = 0.35$) total pressure contours and secondary velocity vectors

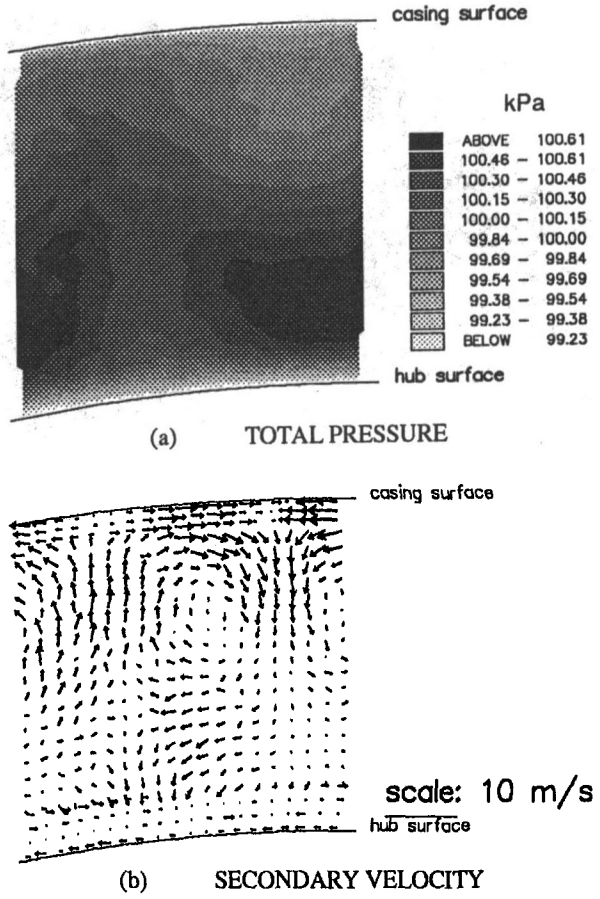


Fig. 8 Plane 11 ($x/L = 0.68$) total pressure contours and velocity vectors

As the flow is turned back toward the axial direction, the direction of the radial pressure gradient reverses at $x/L = 0.26$ (Fig. 2) and reaches a peak cross-passage pressure difference corresponding to 20 percent of the inlet dynamic head. Plane 11 ($x/L = 0.68$) lies in the parallel section of the duct downstream from the second bend and here the cross-passage pressure gradient is negligible. The cumulative influence of the zone of reversed pressure gradient appears not to be sufficient to have a major bearing upon the three-dimensional character of the flow that has developed within the upstream sections of the duct (Fig. 8(a)). Countervortices are observed either side of the wake at both the hub and the casing, which extend to midpassage (Fig. 8(b)). However, it is the casing vortices that are very much the stronger and the symmetric flows that were observed at the upstream planes have been severely distorted. This is shown most dramatically by the total pressure contours of Fig. 8(a)). At the casing the zone of greatest loss still lies close to the wall but is now sited beside the wake and not on the wake axis. At the hub the boundary layer at midpitch shows little evidence of three dimensionality in terms of total pressure

Downloaded 01 Jun 2010 to 171.66.16.53. Redistribution subject to ASME license or copyright; see http://www.asme.org/terms/Terms_Use.cfm

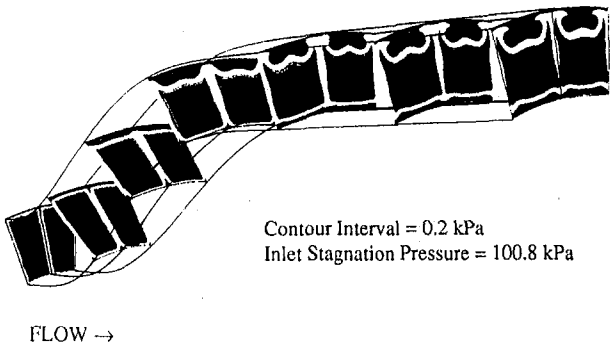


Fig. 9 Development of total pressure (CFD)

but the known existence of the hub countervortices, which at this plane are driving fluid radially inward along the wake, suggest the possibility of deviation from the "wake-free" flow case. The influence of the secondary vortices is to induce local flow angle variations of up to ±4 deg in both yaw and pitch.

The overall development of the flow field is perhaps demonstrated more clearly by the CFD total pressure predictions of Fig. 9. These use the measured inlet wake structure as the starting condition and throughout most of the duct both the character of the flow and the losses are reasonably predicted. The greatest difference lies in the flow downstream from the second bend where, as may be expected, there is no evidence of asymmetry. The origin of the asymmetry that is observed in the measurements at plane 11 is not clear since there is no clear evidence of asymmetry at any of the upstream measurement planes. The most likely cause would seem to be a small degree of swirl in the flow, which would be insufficient to create significant distortion of the wakes or of the overall flow field in the upstream sections of the duct, but which may result in minor differences in the strengths of the near-casing vortices, which in the rapidly developing flows near the second bend would create distortion. Close examination of the velocity vectors of Fig. 7(*b*) corresponding to plane 6 reveals some evidence of greater vortex strength to one side of the wake. This result would imply that such is the influence of the radially driven wake flows in diffusing S-shaped ducts that minor deviations from symmetry at inlet that are inevitable in real flows may have a disproportionately large influence upon the flow at entry to the first turbine stage downstream from the duct.

Despite the growth of the wake-induced secondary flows within the duct, their influence upon the overall performance of the diffuser is remarkably slight, there being no significant change in either the surface static pressure distribution or the overall pressure rise coefficient, which remains unchanged at $Cp = 0.47$. This implies that the three-dimensional flows that are observed result primarily in a redistribution of the inlet loss and not a creation of additional loss.

It must be noted that the wake influences reported here relate only to the simplest case of two-dimensional wakes in the absence of either secondary flows generated by the upstream turbine or swirl. Both of these influences may be expected to contribute significantly to the development of the flow through the duct and form the basis of current and further investigations.

Conclusions

It has been shown that the flow through a diffusing, interturbine S-shaped duct is strongly influenced by the presence of simple, axial wakes at inlet. The flow entering a following turbine stage sees not only hub and casing boundary layers that have been influenced by radial flows within the wakes but more significantly the strong secondary flows that lead to total pressure distortions and significant local yaw and pitch over much of the passage. Also shown has been the disproportionately large influence of minor inlet distortions upon the character of the exit flows.

Acknowledgments

The work described was supported by the Defence Research Agency and Rolls-Royce plc. The assistance of their representatives, in particular Mr. A. Smith for his flow predictions, and their permission to publish the work described in this paper is gratefully acknowledged.

References

Amman, C. A., Nordenson, G. E., and Razinskiy, E. H., 1971, "The Turbine Interstage Diffuser," GMR-1083 Report, General Motors Emissions Research Department.

Britchford, K. M., Manners, A. P., McGuirk, J. J., and Stevens, S. J., 1993, "Measurement and Prediction of Flow in Annular S-Shaped Ducts," *Engineering and Turbulence Measurements 2*.

Dominy, R. G., and Hodson, H. P., 1993, "An Investigation of Factors Influencing the Calibration of Five-Hole Probes for Three-Dimensional Flow Measurements," ASME JOURNAL OF TURBOMACHINERY, Vol. 115, pp. 513–519.

ESDU, 1976, "Introduction to Design and Performance Data for Diffusers," Engineering Science Data Unit, data item 66027.

Fottner, L., ed., 1990, "Test Cases for Computation of Internal Flows in Aero Engine Components," AGARD-AR-275, pp. 309–321.

Moore, J., and Moore, J. G., 1985, "Performance Evaluation of Linear Turbine Cascades Using Three-Dimensional Viscous Flow Calculations," ASME *Journal of Engineering for Gas Turbines and Power,* Vol. 107, pp. 969–975.

Moore, J. G., 1985, "An Elliptic Calculation Procedure for Three-Dimensional Viscous Flow," AGARD-LS-140 4.1–4.16.

Pfeil, H., and Going, M., 1987, "Measurements of the Turbulent Boundary Layer in the Diffuser Behind an Axial Compressor," ASME JOURNAL OF TURBOMACHINERY, Vol. 109, pp. 405–412.

Quest, J., and Scholtz, N., 1982, "Experimental Results of Annular Diffusers Behind a Turbine Stage," [in German], FVV-Heft 302.

Taylor, A. M. P. K., Whitelaw, J. H., and Yianneskis, M., 1982, "Developing Flows in S-Shaped Ducts. Part 1: Square Cross-Section Duct," NASA Contractor Report CR3550.

Towne, C. E., 1984, "Calculation of Viscous Flow in Curved Ducts and Comparison With Experimental Data," Paper No. AIAA-84-0531.

Downloaded 01 Jun 2010 to 171.66.16.53. Redistribution subject to ASME license or copyright; see http://www.asme.org/terms/Terms_Use.cfm

A Design Study of Radial Inflow Turbines With Splitter Blades in Three-Dimensional Flow

W. D. Tjokroaminata

C. S. Tan

W. R. Hawthorne

Gas Turbine Laboratory,
Massachusetts Institute of Technology,
Cambridge, MA 02139

An inverse design technique to design turbomachinery blading with splitter blades in three-dimensional flow is developed. It is based on the use of Clebsch transformation, which allows the velocity field to be written as a potential part and a rotational part. It is shown that the rotational part can be expressed in terms of the mean swirl schedule (the circumferential average of the product of radius and tangential velocity) and the blade geometry that includes the main blade as well as the splitter blade. This results in an inverse design approach, in which both the main and the splitter blade geometry are determined from a specification of the swirl schedule. Previous design study of a heavily loaded radial inflow turbine, without splitter blades, for a rather wide variety of specified mean swirl schedules results in a blade shape with unacceptable nonradial blade filament; the resulting reduced static pressure distribution yields an "inviscid reverse flow region"[1] covering almost the first half of the blade pressure surface. When the inverse design technique is applied to the design study of the turbine wheel with splitter blades, the results indicate that the use of splitter blades is an effective means for making the blade filament at an axial location more radial as well as a potential means for eliminating any "inviscid reverse flow" region that may exist on the pressure side of the blades.

1 Introduction

In the two papers on the "Theory of Blade Design for Large Deflections" published by Tan et al. (1984), a new technique was presented for designing the shape of turbomachinery blades in three-dimensional flow. Applications of this theory to the design of radial turbomachinery have been reported by Borges (1986), Ghaly (1986), Hawthorne and Tan (1987), Zangeneh (1988), Dang (1993), and Yang et al. (1993). The experimental data reported by Borges (1986) and Zangeneh (1988) showed that the radial inflow turbines designed by the new technique gave an improvement in efficiency over a rather wide operating range. Studies on the influence of the loading distribution, stacking position, etc., upon the resulting blade shape and pressure distribution were reported by Ghaly (1986). A concise but general exposition of the theoretical basis for the present design technique was presented by Hawthorne and Tan (1987). Dang (1933) applied the theory successfully to the design study of turbomachinery bladings in transonic flow regimes. In this paper, we describe: (1) the extension of the theory to include the design of turbomachinery blade-rows with main blades as well as splitter blades; and (2) the application of the method to the design study of a highly loaded radial inflow turbine wheel with splitter blades. The design study carried out in (2) above is built upon the works by Yang (1991) and Yang et al. (1993), which show that for a wide variety of specified mean swirl distributions the resulting inverse design calculations for a heavily loaded radial inflow turbines invariably yield a blade geometry with unacceptable nonradial blade filaments (i.e., unacceptably large blade lean angle). Furthermore, the resulting reduced static pressure distribution is always such that there exists a fairly large region of "inviscid reverse flow" on the pressure surface of the (designed) blade. A key objective of the present work is to assess whether the incorporation of splitter blades in the design of the radial turbine wheel would result in a blade geometry that has nearly radial blade filament as well as a negligibly small region of "inviscid reverse flow."

The paper is arranged as follows: In the next section we describe a concise theoretical development for inclusion of splitter blade in the inverse design technique presented by Tan et al. (1984), Hawthorne and Tan (1987), and Yang et al. (1993). We then discuss the design criteria and the manner in which the mean swirl distribution is prescribed for the situation where an impeller has main blades as well as splitter blades. This is followed by representative results from the design calculations. Finally we state the summary and the conclusions.

2 Theoretical Development

As the theoretical formulation and the key results have been presented (Tan et al., 1984; Hawthorne and Tan, 1987; Yang et al., 1993), we will confine the theoretical development to those aspects pertinent to the inclusion of splitter blades in the inverse design technique.

It has been proposed (Tan et al., 1984; Hawthorne and Tan, 1987; Yang et al., 1993) that a useful design specification for the inverse design of blading in three-dimensional flow is the mean swirl distribution $r\bar{V}_\theta$ (V_θ is the tangential velocity); it is given by:

$$r\bar{V}_\theta(r, z) = \frac{B}{2\pi}\int_0^{2\pi/B} rV_\theta(r, \theta, z)d\theta \qquad (1)$$

where the overbar defines a tangential mean, B is the number of blades, and (r, θ, z) is the usual right-handed cylindrical coordinate system. We will use the subscripts (r, θ, z) to denote vector components in the radial, tangential, and axial direction, respectively. As $2\pi r\bar{V}_\theta$ is the circulation around the axis, the swirl distribution is thus related to the bound circulation Γ on the blade. Thus it is natural to use surfaces of singularities to represent the blade surfaces (for the main blade as well as splitter blade):

[1] An inviscid reverse flow region refers to a region (on the blade surface) with negative meridional velocity.

Contributed by the International Gas Turbine Institute and presented at the 39th International Gas Turbine and Aeroengine Congress and Exposition, The Hague, The Netherlands, June 13–16, 1994. Manuscript received by the International Gas Turbine Institute February 4, 1994. Paper No. 94-GT-36. Associate Technical Editor: E. M. Greitzer.

Copyright © 1996 by ASME

Downloaded 01 Jun 2010 to 171.66.16.53. Redistribution subject to ASME license or copyright; see http://www.asme.org/terms/Terms_Use.cfm

$$\alpha_j(r, \theta, z) = \theta - f_j(r, z) = \pm \frac{n2\pi}{B}$$

$$\text{for } n = 0, 1, 2, 3, \ldots, (B-1) \quad (2)$$

where f is the angular coordinate of a point on the blade surface, B is the number of blades, and n is an integer. The subscript j can assume a value of 1 or 2; the value of 1 pertains to the main blade while the value 2 pertains to the splitter blade.

Assuming the flow is steady and that far upstream the approaching flow is axisymmetric, irrotational and reversible (i.e., a homenthalpic and homentropic flow), then the absolute vorticity $\vec{\Omega}$ bound to the blades can be written in the form

$$\vec{\Omega} = \sum_{j=1}^{2} (\nabla(r\bar{V}_\theta)_j \times \nabla\alpha_j)\delta_p(\alpha_j) \quad (3)$$

where $\delta_p(\alpha)$ is the periodic delta function (Lighthill, 1958) given as

$$\delta_p(\alpha) = \frac{2\pi}{B} \sum_{n=-\infty}^{\infty} \delta\left(\alpha - \frac{n2\pi}{B}\right) = \sum_{n=-\infty}^{\infty} e^{inB\alpha} \quad (4)$$

Use of Clebsch's transformation (Lamb, 1932) allows the (absolute) velocity $\vec{V}$ to be written as (Tan et al., 1984; Hawthorne and Tan, 1987; Yang et al., 1993)

$$\vec{V} = \nabla\Phi + \sum_{j=1}^{2} [r\bar{V}_{\theta j}\nabla\alpha_j - S(\alpha_j)\nabla r\bar{V}_{\theta j}] \quad (5)$$

where $S(\alpha)$ is the periodic sawtooth function (Lighthill, 1958), given as

$$S(\alpha) = \sum_{n=-\infty}^{\infty} \frac{e^{inB\alpha}}{inB} \quad (6)$$

We can decompose the velocity as a sum of a mean part $\bar{\vec{V}}$ and a periodic part $\tilde{\vec{V}}$ as

$$\bar{\vec{V}} = \nabla\bar{\Phi} + \sum_{j=1}^{2} r\bar{V}_{\theta j}\nabla\alpha_j \quad (7)$$

$$\tilde{\vec{V}} = \nabla\tilde{\Phi} - \sum_{j=1}^{2} S(\alpha_j)\nabla r\bar{V}_{\theta j} \quad (8)$$

The continuity equation can be written as

$$\nabla \cdot \vec{W} = -\vec{W} \cdot \nabla \ln \rho \quad (9)$$

where $\vec{W}$ denotes the relative velocity and ρ the density. Taking the pitch average of Eq. (9), we obtain

$$\nabla \cdot \bar{\vec{W}} = -\overline{\vec{W} \cdot \nabla \ln \rho} \quad (10)$$

We introduce an artificial density (Ghaly, 1986) $\rho_a(r, z)$ that satisfies

$$\nabla \cdot \rho_a\bar{\vec{W}} = 0 \quad (11)$$

to account for compressibility effects. Use of Eq. (10) in Eq. (11) yields

$$\bar{\vec{W}} \cdot \nabla \ln \rho_a = \overline{\vec{W} \cdot \nabla \ln \rho} \quad (12)$$

We use the Stokes stream function, ψ, to describe the mean flow. Thus the velocity components in the mean flow are given as

$$\rho_a\bar{W}_r = -\frac{1}{r}\frac{\partial\psi}{\partial z} \quad (13)$$

$$\bar{W}_\theta = \frac{\sum_{j=1}^{2} r\bar{V}_{\theta j}}{r} - r\omega \quad (14)$$

$$\rho_a\bar{W}_z = \frac{1}{r}\frac{\partial\psi}{\partial r} \quad (15)$$

The governing equation for ψ can be shown to be

$$\left[\frac{\partial^2}{\partial r^2} - \frac{1}{r}\frac{\partial}{\partial r} + \frac{\partial^2}{\partial z^2} - \frac{\partial(\ln \rho_a)}{\partial r}\frac{\partial}{\partial r} - \frac{\partial(\ln \rho_a)}{\partial z}\frac{\partial}{\partial z}\right]\psi = r\rho_a \sum_{j=1}^{2}\left[\frac{\partial r\bar{V}_{\theta j}}{\partial z}\frac{\partial f_j}{\partial r} - \frac{\partial r\bar{V}_{\theta j}}{\partial r}\frac{\partial f_j}{\partial z}\right] \quad (16)$$

A governing equation for the periodic velocity $\tilde{\vec{V}}$ is

$$\nabla \cdot \tilde{\vec{V}} = -\vec{W} \cdot \nabla \ln \rho + \overline{\vec{W} \cdot \nabla \ln \rho} \quad (17)$$

Use of Fourier Series for representing the θ dependence of the velocity (since the flow has inherent blade-to-blade periodicity) allows us to write

$$\tilde{\Phi} = \sum_{n=-\infty, \neq 0}^{+\infty} \tilde{\phi}_n(r, z)e^{inB\theta} \quad (18)$$

Substituting Eqs. (18) and (8) into Eq. (17), the result is

$$\nabla^2_{2D}\tilde{\phi}_n = \sum_{j=1}^{2}\left[\frac{e^{-inBf_j}}{inB}\nabla^2 r\bar{V}_{\theta j} - e^{-inBf_j}\left(\frac{\partial f_j}{\partial r}\frac{\partial r\bar{V}_{\theta j}}{\partial r} + \frac{\partial f_j}{\partial z}\frac{\partial r\bar{V}_{\theta j}}{\partial z}\right)\right] + [-\vec{W} \cdot \nabla \ln \rho + \overline{\vec{W} \cdot \nabla \ln \rho}]_{FT(n)} \quad (19)$$

where $\nabla^2_{2D} = (1/r)(\partial/\partial r)[r(\partial/\partial r)] + (\partial^2/\partial z^2) - (n^2B^2/r^2)$ and $FT(n)$ denotes the Fourier coefficients of the nth mode.

The condition of no normal velocity on the blade surface yields

$$\vec{W}_{bl,j} \cdot \nabla\alpha_j = 0 \quad (20)$$

where $\vec{W}_{bl} = \frac{1}{2}(\vec{W}^+ + \vec{W}^-)$ is the velocity at the blade (superscript $+/-$ denotes flow variables pertaining to the blade pressure/suction surface). Upon expanding Eq. (20) in cylindrical coordinates, we have

$$\bar{W}_r\frac{\partial f_j}{\partial r} + \bar{W}_z\frac{\partial f_j}{\partial z} = \sum_{k=1}^{2}\left[\frac{r\bar{V}_{\theta k}}{r^2}\right] - \omega + (\tilde{\vec{V}})_{bl,j} \cdot \nabla\alpha_j \quad (21)$$

In the absence of splitter blades, all these equations reduce to the equations for the situation with no splitter blades. The effect of blade thickness can be included in the formulation described by Yang et al. (1993); this is not repeated in the formulation here as the key objective is to explore the aerodynamic influence of the use of splitter blades in a highly loaded radial inflow turbine.

The procedure for determining the blade shape is an iterative one (Tan et al., 1984; Hawthorne and Tan, 1987; Yang et al., 1993). A first guess for the blade shape is used to compute the velocities, and the blade shape is updated by using the blade boundary condition in Eq. (21). The solution for Eq. (21) requires the specification of an integration constant for f_j, which implies that values of f have to be specified along a line on the surface stretching from the hub to the shroud for both the main blade and the splitter blade. This specification has been referred to as the "stacking condition" (Tan et al., 1984; Hawthorne and Tan, 1987; Yang et al., 1993).

When the relative flow is subsonic, both the governing equations for the mean and the periodic flow are of the elliptic type. Thus, their solution requires the specification of a boundary condition at: (*a*) an upstream boundary; (*b*) a downstream boundary; (*c*) the shroud and the hub surfaces; and (*d*) at the blade surface.

Downloaded 01 Jun 2010 to 171.66.16.53. Redistribution subject to ASME license or copyright; see http://www.asme.org/terms/Terms_Use.cfm

For practical implementation, we will have to truncate the Fourier series by taking a finite n in Eq. (18). Spatial discretization on (r, z) plane is based on a finite-element technique (Yang et al., 1993).

3 Design Criteria and Mean Swirl Distribution $r\bar{V}_\theta$

In this section we state the criteria used for assessing the aerodynamic goodness of results from design calculation for the main and splitter blades. Then we briefly review the technique for the specification of the $(r\bar{V}_\theta)$ distribution.

3.1 Design Criteria. The parametric influence of loading distribution, stacking position, lean in stacking angle, slip factor, number of blades, and hub and shroud profile geometry on the blade shape and the resulting flow field has been explored (Yang et al., 1991, 1993). However, those results show that for a rather wide choice of $r\bar{V}_\theta$ distributions, the resulting blade shapes are such that the blade filaments at constant z section are highly nonradial; this aspect of the blade shape is unacceptable from structural/stress consideration. Furthermore, there also exists a region of "inviscid reverse flow" on the pressure surface, which may imply flow separation for real fluids.

In the present investigation, the inclusion of splitter blades in the design is proposed as a mean to eliminate or reduce the "inviscid reverse flow regions" and to arrive at designs in which the blade filaments at constant z section is more radial. In view of these, we have adopted the following measures for assessing the goodness of the resulting design calculation:

- the curvature of the blade shapes at constant z sections
- the extent of the region of "inviscid reverse flow"

However, the extent of the reverse flow region can be considered as secondary as the reverse flow region may not necessarily result in an unacceptable loss level (Yang et al., 1991, 1993).

The inclusion of splitter blades in the design procedure results in several additional degrees of freedom. These are:

- the length of the splitter blades
- $r\bar{V}_\theta$ distribution on the splitter blades
- stacking position of the splitter blades
- lean in stacking angle of the splitter blades
- the relative angular distance between the main blades and the splitter blades at the stacking position (i.e., only the value at the stacking position; it does not apply to the entire splitter blade)

However, some of these degrees of freedom are constrained by the limitation that the relative angular distance between the main and splitter blades has to be within the values of 0 and $2\pi/B$. This implies that the resulting splitter blade shape cannot cross the main blade, which arises because of physical consideration. However, it is desirable to have relative angular distance that has a value between 0.4 and 0.6 when expressed as a fraction of the local pitch (which is equal to the angle between main blades, i.e., $2\pi/B$) so as to avoid flow choking.

3.2 Specification of $r\bar{V}_\theta$ Distribution. The various aspects pertaining to the specification of $r\bar{V}_\theta$ distribution have been presented in detail (Yang et al., 1991, 1993). We will simply summarize the key aspects here for ease of reference.

The swirl distribution $r\bar{V}_\theta$ cannot be specified arbitrarily (Tan et al., 1993; Hawthorne and Tan, 1987; Yang et al., 1993); it has to satisfy boundary conditions that involve its value and its normal derivative along the boundary of the blade region. Thus there are two conditions along each boundary so that the generation of a smooth $r\bar{V}_\theta$ distribution from a fourth-order equation such as the following biharmonic equation is an appropriate one:

$$\nabla^4(r\bar{V}_\theta) = R(r, z) \tag{22}$$

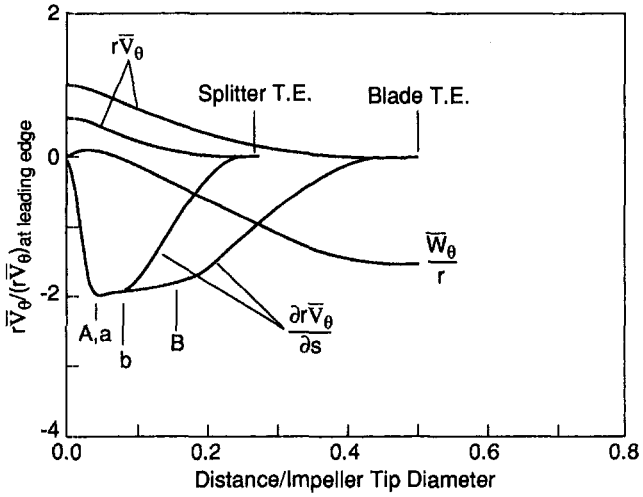


Fig. 1 Schematic plot of $r\bar{V}_\theta$ distribution along the hub of the main and splitter blades; A and B (a and b) demarcate region of different dependence of $\partial r\bar{V}_\theta/\partial s$ on s for main blades (for splitter blades)

where

$$\nabla^4 = \left(\frac{\partial^2}{\partial r^2} + \frac{1}{r}\frac{\partial}{\partial r} + \frac{\partial^2}{\partial z^2}\right)^2$$

The forcing function $R(r, z)$ can be used as a means to control the swirl distribution. However, by taking $R(r, z)$ to be identically zero (Yang et al., 1993) the swirl distribution is determined upon specifying the value of $r\bar{V}_\theta$ along the hub and the shroud, the leading edge, and the trailing edge. Thus the problem is reduced to specifying the swirl distribution along the boundary. A way to implement this is as follows:

The hub or the shroud region is divided into three sections (see Fig. 1) (Yang et al., 1993): from the leading edge ($L.E.$) to a point called A, from point A to a second point called B, and from point B to the trailing edge ($T.E.$). The maximum value of $(\partial r\bar{V}_\theta/\partial s)$ is specified at point A; s is used to denote the meridional distance along the quasi-streamline coordinate. To control the shape of the loading, we specify the magnitude of $\partial^2 r\bar{V}_\theta/\partial s^2$ along the second section (from point A to point B). The Kutta–Joukowski condition requires that $\partial r\bar{V}_\theta/\partial s = 0$ at the trailing edge, and $\partial r\bar{V}_\theta/\partial s$ at the leading edge is specified, which would be zero for zero incidence angle. A typical $r\bar{V}_\theta$ distribution along the hub of the main and the splitter blades is shown in Fig. 1, where lowercase a and b denote the points for the splitter blade and the uppercase A and B for the main blade. In general:

Section 1: $r\bar{V}_\theta(s)$ is cubic in s and we need to specify

$$r\bar{V}_\theta = (r\bar{V}_\theta)_{L.E.}, \quad (r\bar{V}_\theta)' = (r\bar{V}_\theta)'_{L.E.} \quad \text{at} \quad L.E.$$

$$(r\bar{V}_\theta)' = (r\bar{V}_\theta)'_{\max}, \quad (r\bar{V}_\theta)'' = (r\bar{V}_\theta)''_{A-B} \quad \text{at} \quad A$$

Section 2: $r\bar{V}_\theta(s)$ is quadratic in s and the dependence on s is chosen such that

$$r\bar{V}_\theta = (r\bar{V}_\theta)_A, \quad (r\bar{V}_\theta)' = (r\bar{V}_\theta)'_A, \quad (r\bar{V}_\theta)'' = (r\bar{V}_\theta)''_A \quad \text{at} \quad A$$

Section 3: $r\bar{V}_\theta(s)$ is quartic in s and the dependence on s is chosen such that

$$r\bar{V}_\theta = (r\bar{V}_\theta)_B, \quad (r\bar{V}_\theta)' = (r\bar{V}_\theta)'_B, \quad (r\bar{V}_\theta)'' = (r\bar{V}_\theta)''_B \quad \text{at} \quad B;$$

in addition we need to specify

$$r\bar{V}_\theta = (r\bar{V}_\theta)_{T.E.}, \quad (r\bar{V}_\theta)' = 0 \quad \text{at} \quad T.E.$$

where the subscripts A, B, $L.E$, and $T.E$ denote the respective values at location A, B, $L.E.$, and $T.E.$

Downloaded 01 Jun 2010 to 171.66.16.53. Redistribution subject to ASME license or copyright; see http://www.asme.org/terms/Terms_Use.cfm

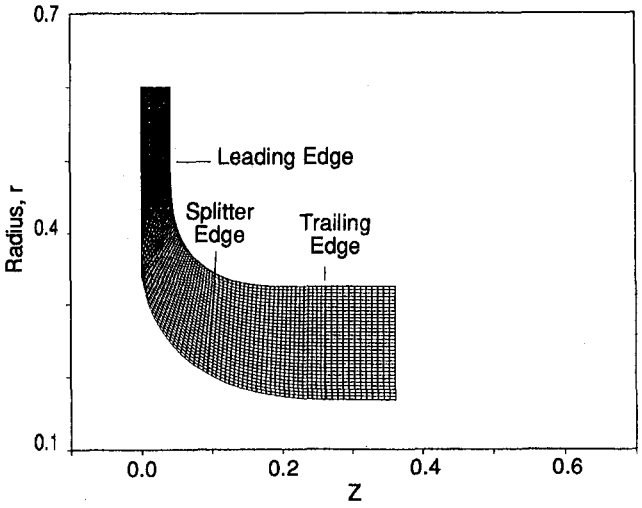


Fig. 2 Grid used for design calculation (splitter length of 0.61)

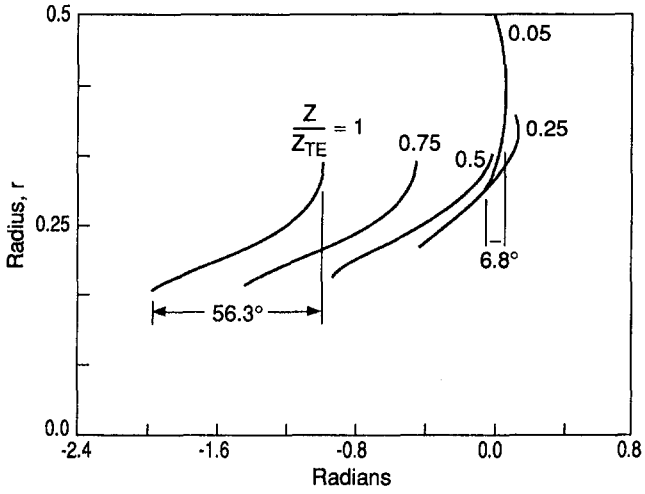


Fig. 3 Radial distribution of blade camber on z section at z/z_{TE} = 0.05, 0.25, 0.5, 0.75, 1.00 from design calculations (Yang et al., 1993); z_{TE} denotes value of z corresponding to blade trailing edge

The choice of the location of point A (the maximum loading position), the location of point B (the extent of finite loading), $(r\bar{V}_\theta)'_{\max}$ (the maximum loading), and $(r\bar{V}_\theta)''_{A-B}$ (the shape of the loading) allows one to produce a wide variety of swirl distributions.

3.3 Division of $(r\bar{V}_\theta)$ Between Main and Splitter Blades. The net specified $(r\bar{V}_\theta)$ has to be shared between the main and the splitter blades; in particular one needs to assign a priori a fraction of $(r\bar{V}_\theta)$ at the leading edge to the splitter. For the results presented here this fraction is the ratio of the mean length of the splitter blade to the sum of the mean length of the blade and the splitter (the mean length is taken to be the average of the meridional distances along the shroud and the hub of the blades). Such a simple linear division would yield a vanishing value of $(r\bar{V}_\theta)$ for a splitter blade of zero length and a value identical to that of the main blade for a splitter length equal to that of the main blade. In addition the division of $(r\bar{V}_\theta)$ at the leading edges and the manner in which $(r\bar{V}_\theta)$ is prescribed along the hub and the shroud would result in a loading distribution that is approximately the same for both the main and the splitter blade.

3.4 Stacking Conditions. As it is the net $(r\bar{V}_\theta)$, and not the individual $(r\bar{V}_\theta)$ on each blade, that appears on the right-hand side of Eq. (21), therefore both the main blade and the splitter would assume an identical blade shape if one were to neglect the blade-to-blade effects (last term on the right-hand side of Eq. (21)). Thus, if indeed the blade-to-blade variation is relatively small, the camber distribution of the main and the splitter blade would approximately be similar for identical stacking specifications. Based on this heuristic argument, the same stacking conditions for the main blade and the splitter have been chosen for the present study. However, the angular distance between the main and the splitter blades at the stacking positions need not be necessarily set to π/B (i.e., the splitter is exactly halfway between the main blades at the stacking position) so that it can be considered as an additional degree of freedom; its choice can influence the relative mass flow between the two different passages: one between the suction side of the main blade and the pressure side of the splitter blade and the other between the suction side of the splitter and the pressure side of the main blade. When the relative angular distance σ, expressed as fraction of the angle between the main blades, is less than or greater than 0.5, the splitter is closer to the suction side or the pressure side of the main blade respectively. Only the position of the splitter blade relative to the main blade is specified at the stacking position.

3.5 Distribution of $\bar{W}_\theta/r$ and the Wrap Factor. Upon neglecting the last term in Eq. (21), the blade boundary condition reduces to:

$$\frac{\partial f_j}{\partial s} = \frac{1}{\bar{V}_s}\frac{\bar{W}_\theta}{r} \tag{23}$$

This suggests that if we integrate the value of $\bar{W}_\theta/r$ with respect to the distance along the hub and the shroud from the stacking position to the trailing edge and take the difference between them, we would get some guidance on how to make the blade filament at constant z more radial. This integrated value will be referred to as the wrap factor, given as:

$$\text{Wrap factor} = \int_{\text{stacking axis}}^{\text{trailing edge}} \left(\frac{\bar{W}_\theta}{r}\,ds\right)_{\text{hub}} - \int_{\text{stacking axis}}^{\text{trailing edge}} \left(\frac{\bar{W}_\theta}{r}\,ds\right)_{\text{shroud}} \tag{24}$$

The values of $\bar{W}_\theta/r$ and the distances along the hub and the shroud are precisely known once we specify the geometry and the $r\bar{V}_\theta$ distributions along the hub and shroud. The wrap factor can be used as a measure of the degree of curvature in the blade

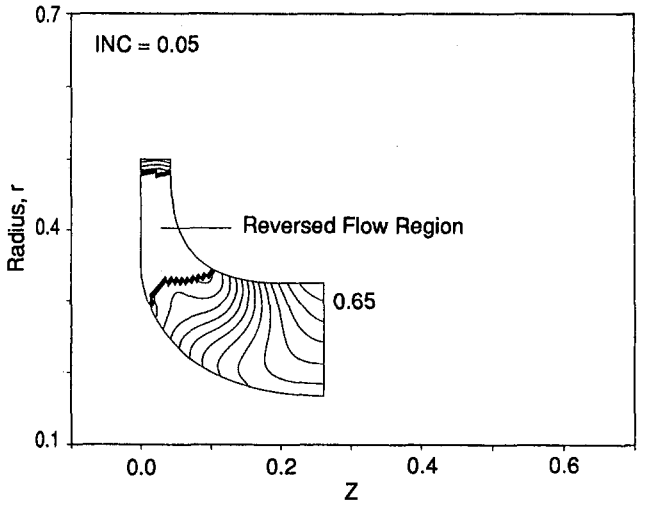


Fig. 4 The M_{rel} on the pressure side indicating the presence of inviscid reverse flow over nearly first half of blade from design calculations (Yang et al., 1993)

Downloaded 01 Jun 2010 to 171.66.16.53. Redistribution subject to ASME license or copyright; see http://www.asme.org/terms/Terms_Use.cfm

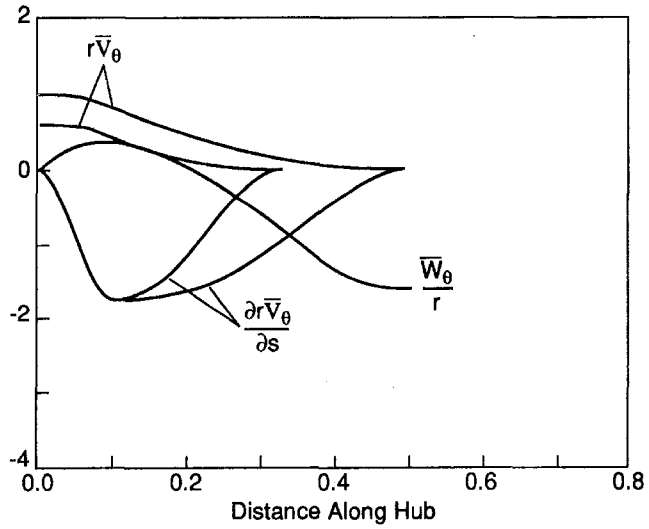


Fig. 5(*a*) The distribution of $r\bar{V}_\theta$, $\bar{W}_\theta/r$, and $\partial r\bar{V}_\theta/\partial s$ along the hub for Case A (stacking at 1/3 chord)

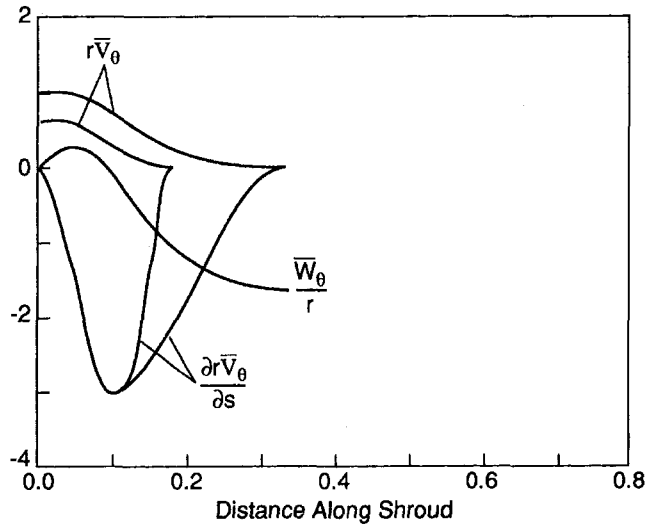


Fig. 5(*b*) The distribution of $r\bar{V}_\theta$, $\bar{W}_\theta/r$, and $\partial r\bar{V}_\theta/\partial s$ along the shroud for Case A (stacking at 1/3 chord)

filament; this can be done a priori without having to implement the design calculation.

If the values of the mean meridional velocity on the hub and the shroud are the same at the same axial location and if the last term in Eq. (21) is indeed small, then one would expect to have a wrap factor of value close to zero for highly radial blade on cross section at constant z. Otherwise, a value of the wrap factor different from zero would result in an optimally radial blade filament. This wrap factor will be used as a guide for specifying $r\bar{V}_\theta$ distributions along the hub and the shroud for the design examples presented in the next section.

4 Numerical Results From a Design Study

We now present a sample of results from a design study of a radial inflow turbine with splitter; this turbine has been proposed for application in a helicopter power plant (Civinskas and Povinelli, 1984). The design specifications for the turbine are: mass flow rate of 2.37 kg/s, power of 1105 kW, inlet stagnation pressure of 1.637×10^6 N/m^2, inlet stagnation temperature of 1607 K, wheel speed 64,000 rpm, rotor tip diameter of 0.2038 m. The absolute flow angle at the inlet is about 75 deg and the corresponding absolute Mach number was computed to be about 0.98. The radial inflow turbine wheel will be designed to yield a blade camber distribution that will result in the complete removal of swirl at the outlet. Thus, the flow will leave the turbine wheel axially at the exit.

For the results to be shown in the following, lengths are in units of impeller tip diameter and $r\bar{V}_\theta$ in units of its value at the blade leading edge unless indicated otherwise.

The calculation is implemented with a grid resolution of 49 elements spanning hub-to-shroud region, 33 Fourier collocation points between adjacent blades, and 145 elements extending from inflow to outflow boundary (Fig. 2). A four-node isoparametric elements for interpolation is used. For a blade number of 14 and a wide variety of specified $r\bar{V}_\theta$ distributions as well as stacking conditions (Yang et al., 1993), the three-dimensional inverse design method yields blade shapes with unacceptable nonradial blade filament (Fig. 3) and a relatively large region of "inviscid reverse flow" on the blade pressure surface (Fig. 4). Design calculations have been carried out (Tjokroaminata, 1992) to elucidate the influences of splitter length, $r\bar{V}_\theta$ distribution, stacking conditions, finite incidence angle, blockage, and slip factor on the blade shape as well as on the extent of "inviscid reverse flow" region on the pressure surface

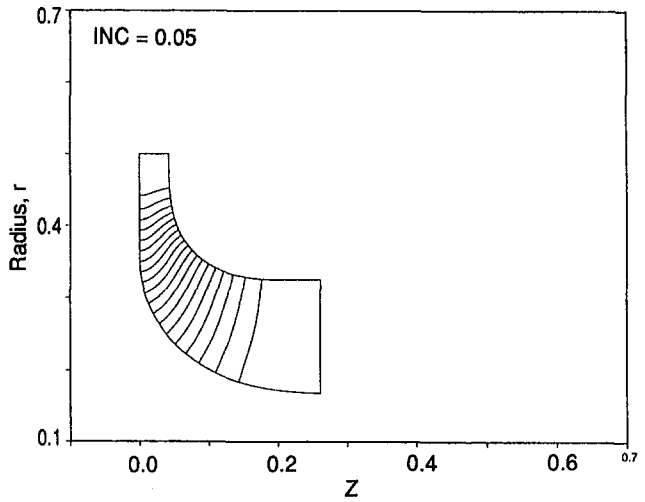


Fig. 6(*a*) The distribution of $r\bar{V}_\theta$ on main blade for Case A (stacking at 1/3 chord)

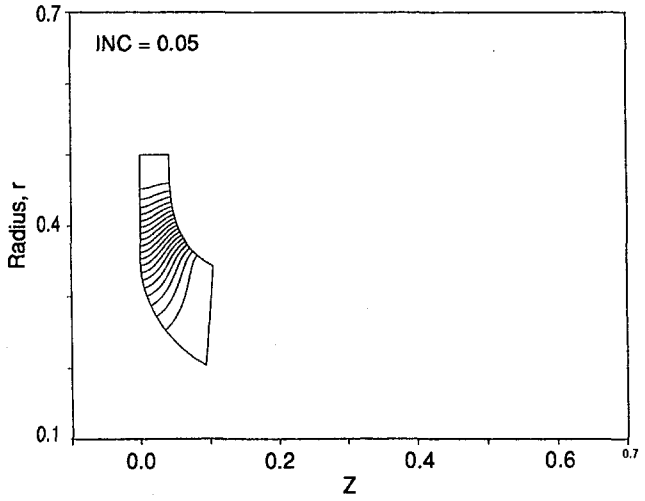


Fig. 6(*b*) The distribution of $r\bar{V}_\theta$ on splitter blade for Case A (stacking at 1/3 chord)

Downloaded 01 Jun 2010 to 171.66.16.53. Redistribution subject to ASME license or copyright; see http://www.asme.org/terms/Terms_Use.cfm

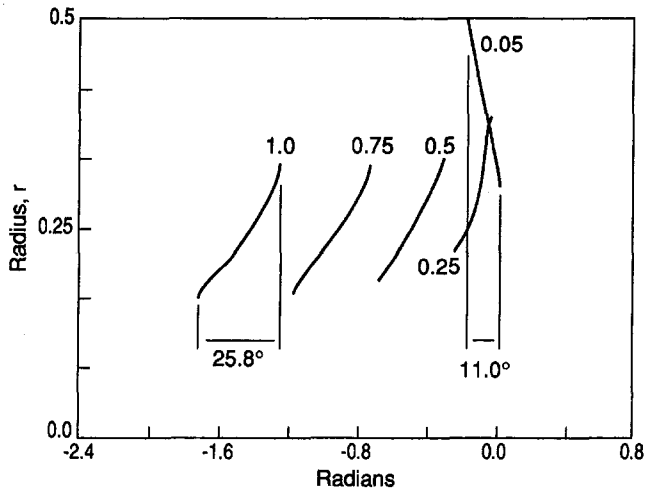


Fig. 7 Radial distribution of main blade camber on z section at z/z_{TE} = 0.05, 0.25, 0.5, 0.75, 1.00 for Case A (stacking at 1/3 chord)

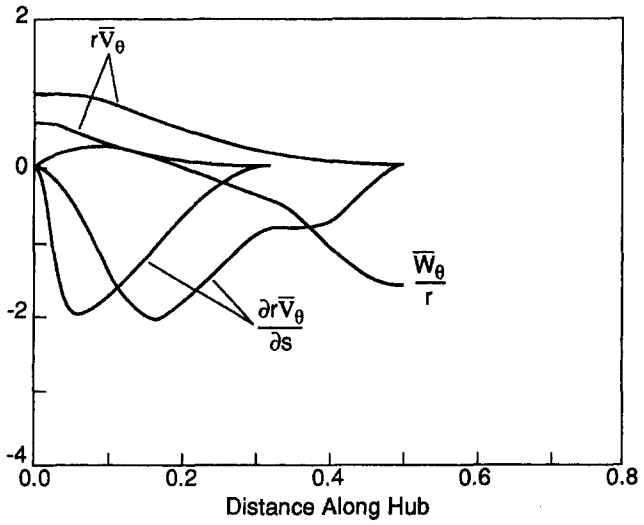


Fig. 9(*a*) The distribution of $r\bar{V}_\theta$, $\bar{W}_\theta/r$, and $\partial r\bar{V}_\theta/\partial s$ along the hub for Case C

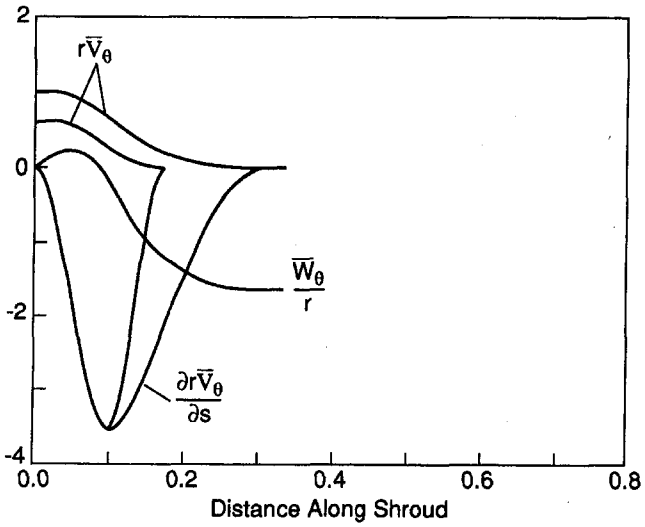


Fig. 8 The distribution of $r\bar{V}_\theta$, $\bar{W}_\theta/r$, and $\partial r\bar{V}_\theta/\partial s$ along the shroud for Case B

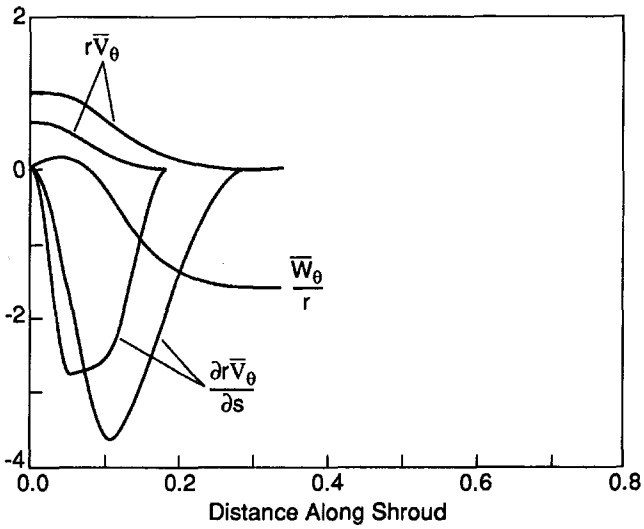


Fig. 9(*b*) The distribution of $r\bar{V}_\theta$, $\bar{W}_\theta/r$, and $\partial r\bar{V}_\theta/\partial s$ along the shroud for Case C

of the blades. Here we will present a sample of results to demonstrate the potential benefits of the use of splitters in radial inflow turbine design.

For the design examples reported here the splitter length has been taken to be 0.61 of the length of main blade. In the first case (which will be referred to as Case A) the $r\bar{V}_\theta$ along the hub and the shroud are as shown in Fig. 5(a) and 5(b), respectively. The maximum value of $\partial r\bar{V}_\theta/\partial s$ on the hub is chosen to be -1.75 while the maximum value of $\partial r\bar{V}_\theta/\partial s$ on the shroud is -3.0. The specified $r\bar{V}_\theta$ distribution along the hub and shroud is rather similar to that reported by Zangeneh (1988), which yields a blade shape with a lean angle of no more than 10 deg. Shown in Fig. 6(a) and 6(b) are the corresponding swirl distributions on the main and splitter blades.

Using the guideline (that the stacking position should be chosen to be near where the loading is maximum and preferably slightly downstream of it) reported by Yang et al. (1993) the stacking axis is selected to be at a location 1/3 chord downstream from the leading edge; this corresponds to the location of the maximum loading. The radial distribution of resulting main blade camber along constant z section is shown in Fig. 7. Indeed this new $r\bar{V}_\theta$ distribution gives a significant improvement in the blade camber distribution. The lean angle along constant z section has been reduced to 25.8 deg from a value of 56.3 deg (results of Fig. 3). These results appear to indicate that for designing a blade with more radial filament along constant z section, one should specify the maximum loading along the shroud to have a value more negative than that along the hub. Indeed, such a specification would tend to yield a more optimal value for the wrap factor alluded to above.

Two additional $r\bar{V}_\theta$ distributions are considered for evaluating the usefulness of the wrap factor; one of these corresponds to the determination of $r\bar{V}_\theta$ distributions subjected to the specified $r\bar{V}_\theta$ on the hub shown in Fig. 5(a) and on the shroud shown in Fig. 8 (this will be referred to as Case B); the other corresponds to those shown in Fig. 9(a) and 9(b) (Case C). For Case B, the maximum loading along the hub is taken to be the same as that for Case A (-1.75); however, the maximum loading along the shroud is specified to be 3.5, more negative than that of Case A. This increase in the value of $(\partial r\bar{V}_\theta/\partial s)_{\max}$ along the shroud yields a larger wrap factor. However, we cannot increase the maximum loading along the shroud further, nor can we decrease the maximum loading along the hub to obtain an even larger wrap factor (as this will result in negative mean velocity at the blade, which causes the inverse design procedure

Downloaded 01 Jun 2010 to 171.66.16.53. Redistribution subject to ASME license or copyright; see http://www.asme.org/terms/Terms_Use.cfm

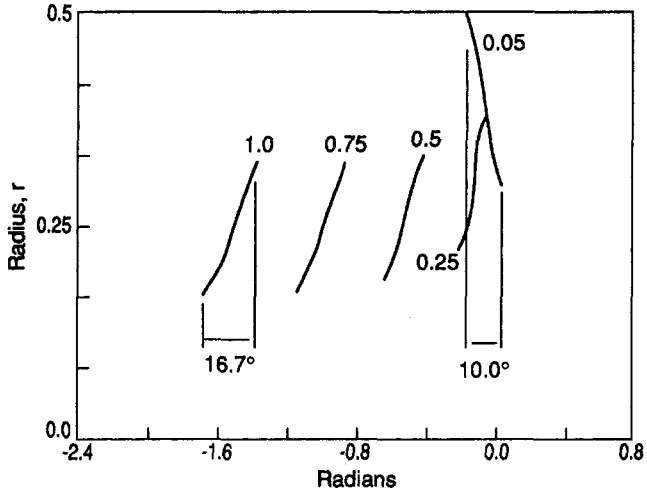


Fig. 10(*a*) Radial distribution of main blade camber on *z* section at z/z_{TE} = 0.05, 0.25, 0.5, 0.75, 1.00 for Case B

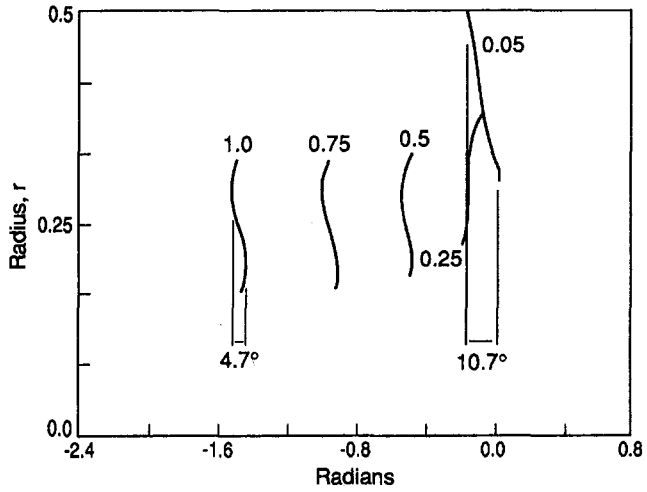


Fig. 10(*b*) Radial distribution of main blade camber on *z* section at z/z_{TE} = 0.05, 0.25, 0.5, 0.75, 1.00 for Case C

to fail to converge to a final blade shape). For Case C, the technique used is to move the position of point A (the point of maximum loading) so that a larger value of wrap factor is obtained.

The values of the wrap factor for Cases A, B, and C are shown in Table 1 with the corresponding wrap angle differences (or lean angles) at the trailing edge, which is denoted by $\Delta f_{T.E.}$, and at $z = 0.05z_{T.E.}$, which is denoted by $\Delta f_{0.05}$. The design case with no splitter (Yang et al., 1993) is also included for comparison. The resulting main blade shapes are shown in Fig. 10(*a*) for Case B and in Fig. 10(*b*) for Case C. From the results in Table 1, there appears to be a correlation between the wrap factor and the lean angle at the trailing edge. Thus the wrap factor may be used as an indicator of the curvature of the blade filaments.

Table 1 Wrap factor and wrap angle difference

Case	Wrap factor	$\Delta f_{T.E.}$ (deg)	$\Delta f_{0.05}$ (deg)
Yang (1993)	−0.75	56.3	6.8
A	−0.03	25.8	11.0
B	0.11	16.7	10.0
C	0.35	4.7	10.7

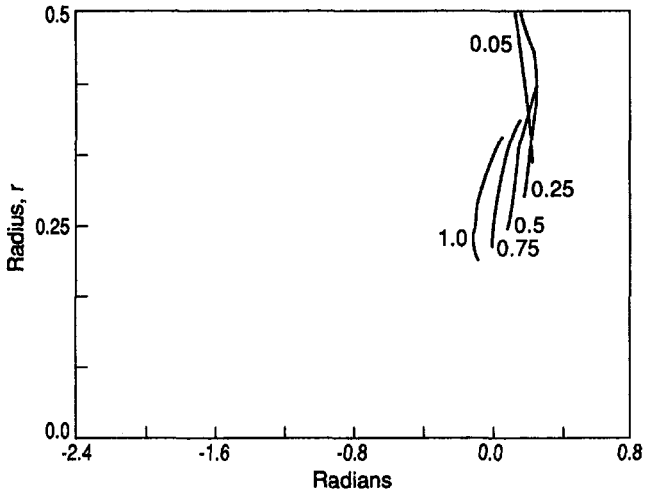


Fig. 11 Radial distribution of splitter blade camber on *z* section at z/z_{TE} = 0.05, 0.25, 0.5, 0.75, 1.00 for Case C

The corresponding splitter blade shapes at constant z section for Case C are shown in Fig. 11; those for cases A and B are quite similar. These figures show that the splitter blades themselves do not get more radial with an increase in the wrap factor. The main blade and the splitter blade should have approximately the same camber distribution if the term $(\vec{V})_{bl,j} \cdot \nabla\alpha_j$ in Eq. (21) is small; however the computed results imply that this is not the case. Ideally, without this term, the main and splitter blades would have exactly the same shapes, and the splitter blades will be exactly halfway between the main blades ($\sigma = 0.5$). Because of the influence of this term, the splitter blade shapes deviate from the middle of the passage between blades and can reach a value of σ as high as 0.8 (close to the pressure side of the main blade) and as low as 0.3 (close to the suction side of the main blade). This implies the significance of flow three dimensionality on blade design for the highly loaded radial inflow turbine wheel considered here.

The corresponding "inviscid reverse flow regions" for Case C are shown in Fig. 12 for the main blades (that for Case B is similar); those for the splitter blades are shown in Fig. 13(*a*) (Case B) and Fig. 13(*b*) (Case C). There still exist regions of "inviscid reverse flow" on the pressure surface, but they are now relatively small in extent.

We may now deduce that one has to specify $r\bar{V}_\theta$ on the hub and the shroud that results in an increase of the wrap factor in

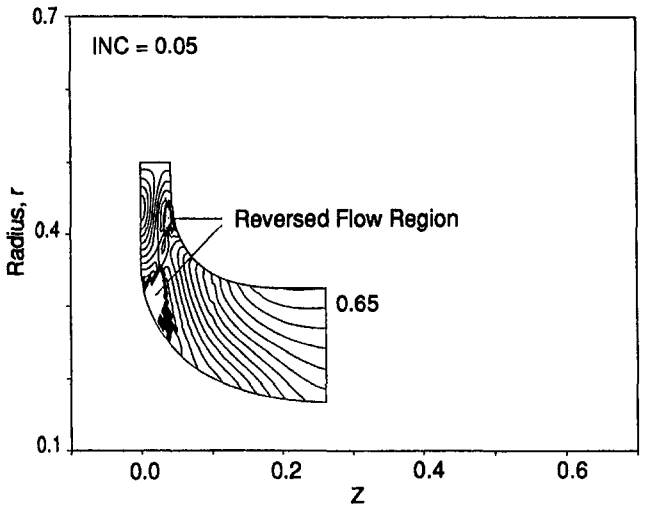


Fig. 12 The M_{rel} on the pressure side of main blade for Case C

Downloaded 01 Jun 2010 to 171.66.16.53. Redistribution subject to ASME license or copyright; see http://www.asme.org/terms/Terms_Use.cfm

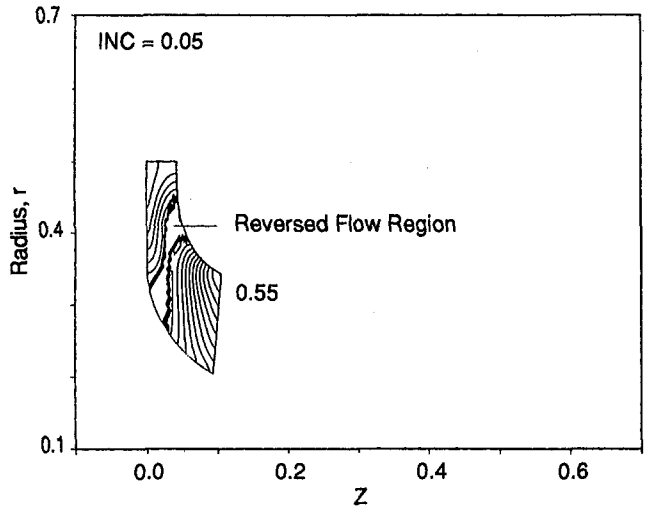


Fig. 13(*a*) The M_{rel} on the pressure side of splitter blade for Case B

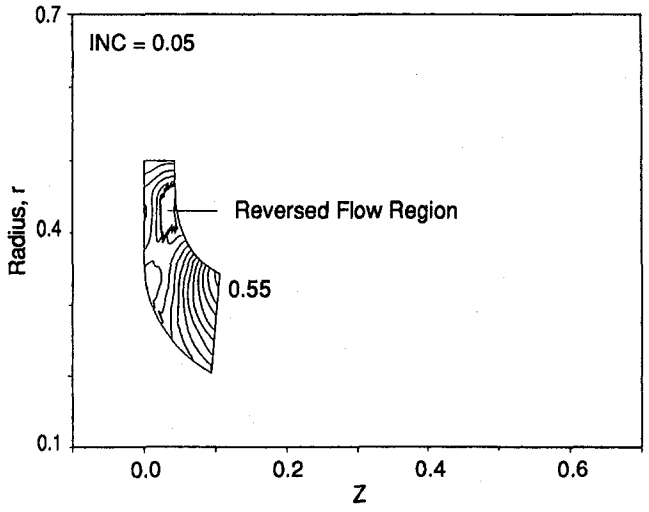


Fig. 13(*b*) The M_{rel} on the pressure side of splitter blade for Case C

order to make the blade filament at constant z section of the main blades more radial. A way is to increase the value of $(\partial r\bar{V}_\theta/\partial s)_{\max}$ on the shroud and reduce it on the hub. The value of $(\partial r\bar{V}_\theta/\partial s)_{\max}$ on the shroud for Case C is -3.6 and it is much higher than the value of $(\partial r\bar{V}_\theta/\partial s)_{\max}$ reported by Yang et al. (1993). Hence, the advantage of using splitter blades is that it gives more room for manipulating the $r\bar{V}_\theta$ distribution so as to alter the wrap factor without specifying too high a loading $(\partial r\bar{V}_\theta/\partial s)$ on either the main blade or the splitter blade; this would be difficult to do if we have main blades only.

In the design calculations reported by Yang et al. (1993) the values of $\partial r\bar{V}_\theta/\partial s$ at the leading edge are always set to zero. This corresponds to the condition of zero incidence angle at the leading edge. For the design cases considered here, a swirl distribution with nonvanishing $\partial r\bar{V}_\theta/\partial s$ at the leading edge (i.e., nonzero incident angle) can be shown to result in a more radial blade filament in the leading edge region. As an illustration consider the $r\bar{V}_\theta$ distributions determined from a specified $r\bar{V}_\theta$ along the hub and the shroud shown respectively in Figs. 14(a) and 14(b) (we will refer to this as Case D). The maximum loading along the shroud for the main blade is the same as that of Case A (-3), but on the splitter blade it is reduced to -2.5 because the distance along the shroud for the splitter is shorter than that for the main blade. Along the hub of the main blade, a region of finite loading is used to avoid the occurrence of

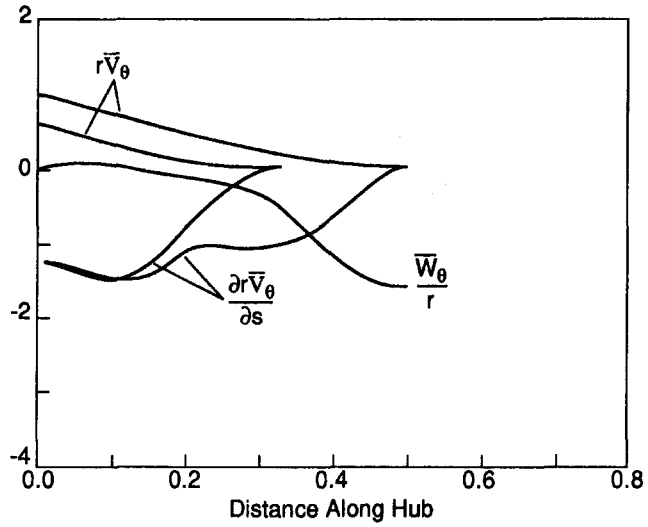


Fig. 14(*a*) The distribution of $r\bar{V}_\theta$, $\bar{W}_\theta/r$, and $\partial r\bar{V}_\theta/\partial s$ along the hub for Case D (nonzero $\partial r\bar{V}_\theta/\partial s$ at L. E.)

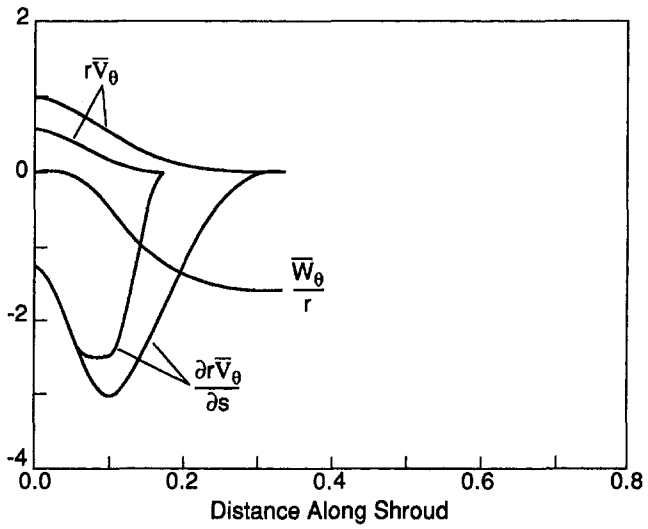


Fig. 14(*b*) The distribution of $r\bar{V}_\theta$, $\bar{W}_\theta/r$, and $\partial r\bar{V}_\theta/\partial s$ along the shroud for Case D (nonzero $\partial r\bar{V}_\theta/\partial s$ at L. E.)

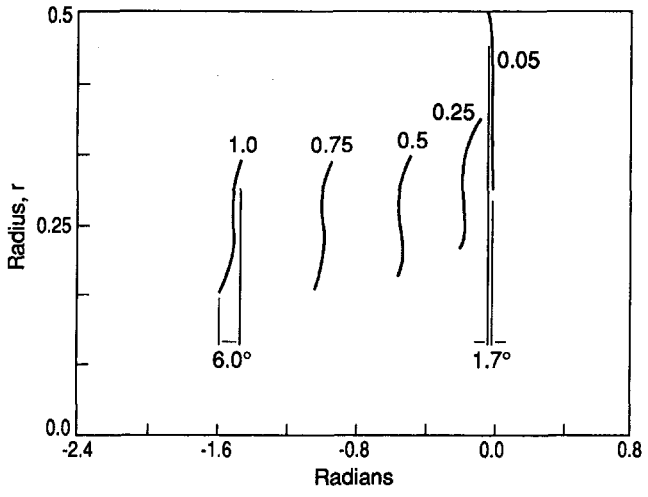


Fig. 15 Radial distribution of main blade camber on z section at z/z_{TE} = 0.05, 0.25, 0.5, 0.75, 1.00 for Case D (nonzero $\partial r\bar{V}_\theta/\partial s$ at L. E.)

Downloaded 01 Jun 2010 to 171.66.16.53. Redistribution subject to ASME license or copyright; see http://www.asme.org/terms/Terms_Use.cfm

small mean velocity. The value of $\partial r\bar{V}_\theta/\partial s$ at the leading edge is taken to be -1.25. This number is chosen so that the resulting $\bar{W}_\theta/r$ along the hub and shroud near the leading edge is close to zero. As expected, this vanishing value of $\bar{W}_\theta/r$ near the leading edge results in highly radial blade shape at location $z = 0.05z_{T.E.}$, a location near the leading edge (see Fig. 15). The wrap factor is calculated to be 0.27 for this case. It results in lean angle of 6.0 deg at the trailing edge. This again shows the correlation between the wrap factor and the lean angle and confirms to the trend shown in Table 1.

5 Summary and Conclusions

The inverse design theory and the accompanying computational procedure have been extended to include the design of splitter blades. In particular, the present study has focused on blade design that attempts to make the blade filament on constant z section more radial as well as to reduce the extent of region of "inviscid reverse flow" on the pressure side. Based on the results from these parametric design calculations, we deduce that:

1 The use of splitter blades gives more flexibility for tailoring the loading on the main blades and this has resulted in the reduction or elimination of "inviscid reverse flow" region on the pressure side of the blades. Its use has also resulted in blades with nearly radial blade filament.
2 The extent of the "inviscid reverse flow" region is more influenced by the specified loading than by the stacking position.
3 A number referred to as the wrap factor can be constructed to give an indication of the curvature of the blade shape at constant z section. The use of this number can reduce the number of design calculations aimed at obtaining more radial blade shape.
4 In general, the main blade filament near the trailing edge can be made more radial by increasing the wrap factor while that near the leading edge can be made more radial by imposing a nonzero incidence angle.

Acknowledgments

Support for this research work was provided by the Army Propulsion Directorate Grant NAG3-772, Mr. Pete Meitner, Technical Officer.

References

Borges, J. E., 1986, "Three-Dimensional Design of Turbomachinery," Ph.D. Dissertation, Cambridge Univ., Sept.

Civinskas, K. C., and Povinelli, L. A., 1984, "Application of a Quasi-Three-Dimensional Inviscid Flow and Boundary Layer Analysis to the Hub-Shroud Contouring of a Radial Turbine," AIAA-84-1297.

Dang, T. Q., 1993, "A Fully Three-Dimensional Inverse Method for Turbomachinery Blading in Transonic Flows," ASME JOURNAL OF TURBOMACHINERY, Vol. 115, pp. 354–361.

Ghaly, W. S., 1986, "A Study and Design of Radial Turbomachinery Blading in Three-Dimensional Flow," Ph.D. Thesis, Department of Aero. and Astro., MIT, Sept.

Hawthorne, W. R., and Tan, C. S., 1987, "Design of Turbomachinery Blading in 3-D Flow by the Circulation Method: A Progress Report," ICIDES-II, pp. 207–226.

Lamb, H., 1932, *Hydrodynamics,* 6th ed. Dover Publications, New York.

Lighthill, M. J., 1958, "Fourier Analysis and Generalized Functions," Cambridge University Press, United Kingdom.

Tan, C. S., Hawthorne, W. R., McCune, J. E., and Wang, C., 1984, "Theory of Blade Design for Large Deflections," ASME *Journal of Engineering for Gas Turbines and Power,* Vol. 106, pp. 354–365.

Tjokroaminata, W. D., 1992, "A Design Study of Radial Inflow Turbines With Splitter Blades in Three-Dimensional Flow," M. S. Thesis, Department of Aero. and Astro., MIT, Cambridge, MA.

Yang, Y. L., 1991, "A Design Study of Radial Inflow Turbines in Three-Dimensional Flow," PhD Thesis, Department of Aero. and Astro., MIT, Cambridge, MA.

Yang, Y. L., Tan, C. S., and Hawthorne, W. R., 1993, "Aerodynamic Design of Turbomachinery Blading in Three-Dimensional Flow: An Application to Radial Inflow Turbines," ASME JOURNAL OF TURBOMACHINERY, Vol. 115, pp. 602–613.

Zangeneh, M., 1988, "Three-Dimensional Design of Radial Inflow Turbines," PhD Thesis, Cambridge University, United Kingdom.

Downloaded 01 Jun 2010 to 171.66.16.53. Redistribution subject to ASME license or copyright; see http://www.asme.org/terms/Terms_Use.cfm

Design and Test of a Small, High Pressure Ratio Radial Turbine

A. C. Jones
Sundstrand Power Systems,
San Diego, CA 92138

This paper describes the aerodynamic design and rig test of a radial inflow turbine having a rotor tip diameter of 4.58 inches. The single-stage turbine was designed for use in the Sundstrand Power Systems (SPS) T-100 Multipurpose Small Power Unit (MPSPU). The T-100 is a small, single-shaft, simple-cycle gas turbine engine intended for airborne, vehicular, and ground-based auxiliary power application. Nominal power output of the engine is 50 hp, with growth capability to 100 hp with minimal modification. Aggressive specific fuel consumption goals for the engine led to a demanding turbine efficiency target of 87 percent total to static, referred to exhaust diffuser exit, at an expansion ratio of 5.7:1 and a flow rate of 0.73 lb/s. Details of the design approach are given, together with test results from the turbodrive rig. The results include overall stage mapping and rotor exit surveys.

Introduction

The Multi Purpose Small Power Unit program (AVSCOM 1986) was a technology demonstration effort funded by the U.S. Army Aviation Applied Technology Directorate (AATD). It was intended to improve the performance, reliability, maintainability, and life cycle cost of very small gas turbine auxiliary power units. SPS's engine design—the T-100—included the powerhead, reduction drive, and electronic fuel control unit. The powerhead (Fig. 1) was a single shaft, shaft power-only (no bleed) design with ratings of 50 hp, 75 hp, and 100 hp. The uprating was accomplished by increasing the turbine inlet temperature (75 hp) and speed (100 hp).

SPS (formerly Sundstrand Turbomach) teamed with Pratt and Whitney (P&W) to complete the design of the powerhead. P&W were primarily responsible for the compressor and integral inlet particle separator (IPS).

One of the most important goals of the program was to demonstrate significant power and specific fuel consumption (SFC) improvements over existing APUs of the same physical size. The benchmark in this regard is the Sundstrand T-20G Gemini engine, developed in the late 60's and early 70's. The Gemini is an eight-inch nominal diameter engine developing 43 hp (sea level standard day) at an SFC of 1.15 lb/h.hp. The objective for the T-100 was an SFC of 0.75 lb/h.hp at an output power of 50 hp, combined with growth to 100 hp, all within the same frame size as the Gemini. The design life was a minimum of 6500 hours and 19,000 cycles.

The thermodynamic cycles selected for the T-100 are summarized in Table 1.

Details of the philosophy behind the choice of these cycle parameters have been given previously (Thompson and Parker, 1988; Napier and Thompson, 1988). However, it is evident from the table that the selection of a relatively low turbine inlet temperature for the 50 hp engine placed a premium on high component efficiencies for the compressor and turbine. Furthermore, uprating to 75 hp became very straightforward, simply by increasing turbine inlet temperature to the level typically used in long-life, modern technology APUs today. To maintain compressor match point, this implied a slight increase in turbine flow function, easily accommodated by restaggering the nozzle vanes.

A single-stage, radial inflow turbine was the natural configuration choice for this duty, rather than a two-stage axial. The reasons were (*a*) higher efficiency potential due to lower tip clearance losses and reduced sensitivity to trailing edge thickness; (*b*) elimination of a hot end bearing in favor of the cold end/overhung rotor arrangement; and (*c*) lower cost due to fewer parts.

Design Point

The primary design point for the turbine stage was the 50 hp engine operating condition. However, a common rotor was desired for the 75 hp engine, the only physical change being to increase the nozzle throat area by 9.3 percent. The overall design parameters resulting from the cycle are summarized in Table 2.

The term "*sde*" is used to indicate static pressure at the turbine diffuser exit plane. Conventionally, APUs are rated in terms of uninstalled conditions with a short (about one diameter) engine tailpipe dumping to atmosphere. Hence ambient static pressure is imposed on the outer diameter of the exhaust jet. During testing of engines, this static pressure is measured and the performance measurements corrected to zero gage pressure. The same procedure was adopted for the turbine rig test.

No internal cooling of the nozzle or rotor was needed; however, there was to be modest (0.5 percent) external cooling flow applied to the rotor disk back face.

Mean-Line Design

Mean-line, or one-dimensional optimization of the nozzle, rotor, and exhaust diffuser (taken as a complete system) was performed at the 50 hp design condition using an empirical performance prediction code based on the methods of Rodgers (1966). The geometric parameters varied included:

- Rotor tip diameter
- Rotor tip width
- Exducer diameter
- Exducer blade angle
- Rotor blade number
- Tip clearances
- Diffuser exit diameter

Contributed by the International Gas Turbine Institute and presented at the 39th International Gas Turbine and Aeroengine Congress and Exposition, The Hague, The Netherlands, June 13–16, 1994. Manuscript received by the International Gas Turbine Institute February 15, 1994. Paper No. 94-GT-135. Associate Technical Editor: E. M. Greitzer.

Copyright © 1996 by ASME

Downloaded 01 Jun 2010 to 171.66.16.53. Redistribution subject to ASME license or copyright; see http://www.asme.org/terms/Terms_Use.cfm

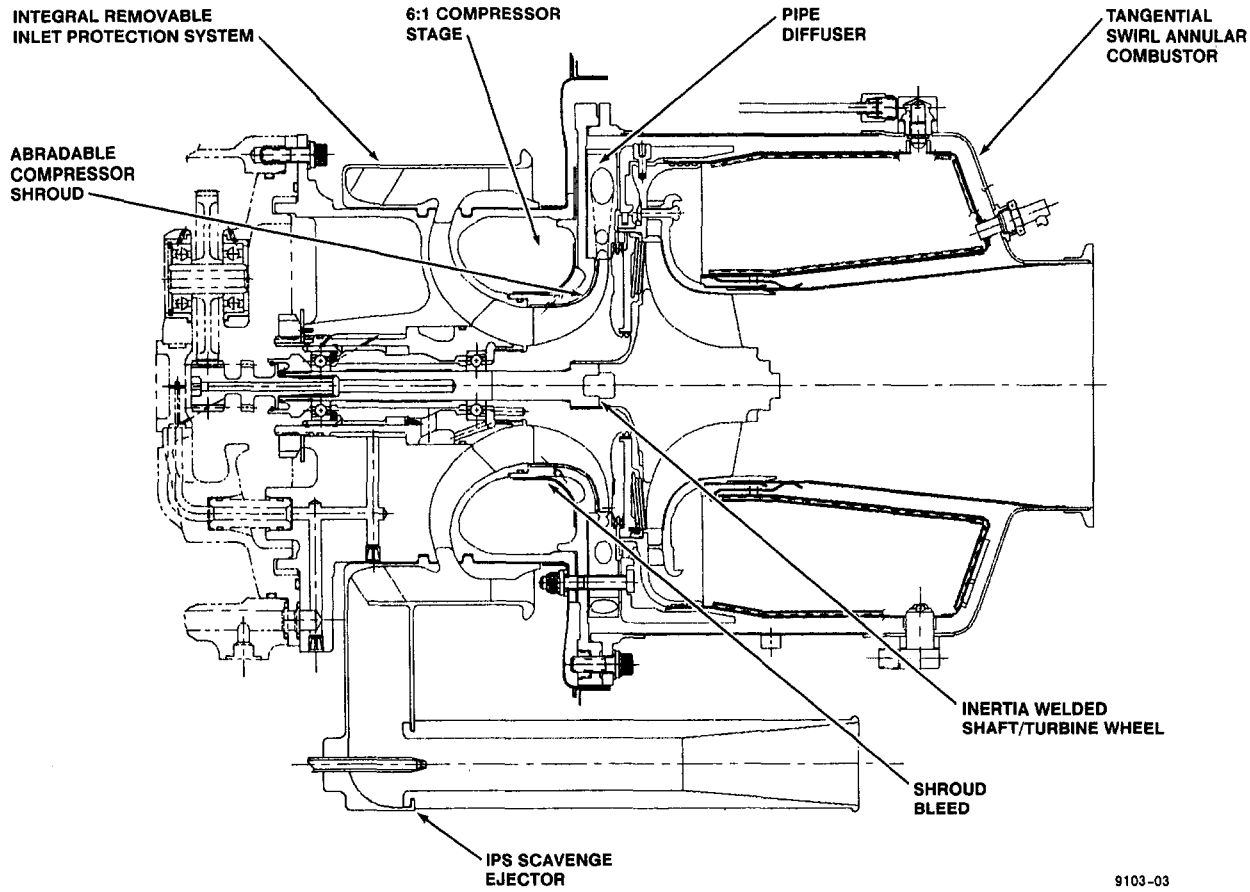


Fig. 1 T-100 MPSPU power module

Table 1 T-100 predicted performance sea level 59°F with IPS

Rating hp	*50*	*75*
Speed rpm	*106588*	*106588*
IPS loss %	*1.5*	*1.5*
Airflow lb/s	*0.73*	*0.73*
Pressure ratio t−s	*6.05*	*6.05*
Comp. efficiency % t−s	*78.0*	*78.0*
T.I.T °F	*1442*	*1789*
Burner ΔP/P %	*4.0*	*4.0*
Burner efficiency %	*99.5*	*99.5*
Turbine efficiency % t−sde	*87.0*	*85.1*
Leakage flow %	*1.5*	*2.0*
Gearbox loss hp	*3*	*4.5*
E.G.T °F	*856*	*1136*
S.F.C. lb/h.hp	*0.724*	*0.685*

Table 2 Turbine design parameters

Rating hp	*50*	*75*
Physical speed rpm	*106588*	*106588*
Pressure ratio t−sde	*5.73*	*5.73*
Inlet temperature °F	*1442*	*1789*
Inlet pressure psia	*84.2*	*84.2*
Flow rate lb/s	*.724*	*.726*
Goal efficiency t−sde %	*87.0*	*85.1*
Corrected speed rpm	*55666*	*51191*
Flow function lb/s √°R/psia	*.375*	*.410*
Corrected flow lb/s	*.242*	*.265*
Specific work BTU/lb	*43.9*	*42.8*
Specific speed non dim.	*.55*	*.53*

Examples of the sensitivity of predicted efficiency to some of these parameters are shown in Figs. 2(*a*) through 2(*e*). The single most important variable in radial turbines is rotor tip speed, followed closely by rotor exit kinetic energy and, especially in a small size, tip clearance.

Figure 2(*a*) shows the effect of rotor tip speed (i.e., tip diameter for a fixed rpm). The chosen tip speed of 2130 ft/s (tip diameter of 4.58 in.) was close to the theoretical optimum

Nomenclature

AN^2 = annulus area times speed squared
BETA = relative flow angle
Cp = static pressure coefficient
DP = design point
E.G.T. = exhaust gas temperature
ΔH = enthalpy drop
ΔHis = isentropic enthalpy drop
Mabs = absolute Mach number
Mrel = relative Mach number
PR = pressure ratio
ΔP = pressure drop
R = radius
S.F.C. = specific fuel consumption
THETA = wrap angle
T.I.T. = turbine inlet temperature
Tt = total temperature
t-s = total to static
t-sde = total to static at diffuser exit
t-t = total to total
U = rotor inlet tip speed
V_{merid} = meridional velocity
Va = axial velocity
$V\Theta$ = absolute tangential velocity
$V0$ = spouting velocity = $\sqrt{(2\Delta His)}$

Downloaded 01 Jun 2010 to 171.66.16.53. Redistribution subject to ASME license or copyright; see http://www.asme.org/terms/Terms_Use.cfm

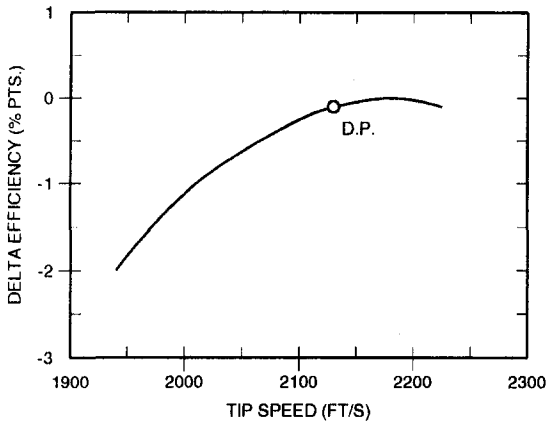


Fig. 2(*a*)

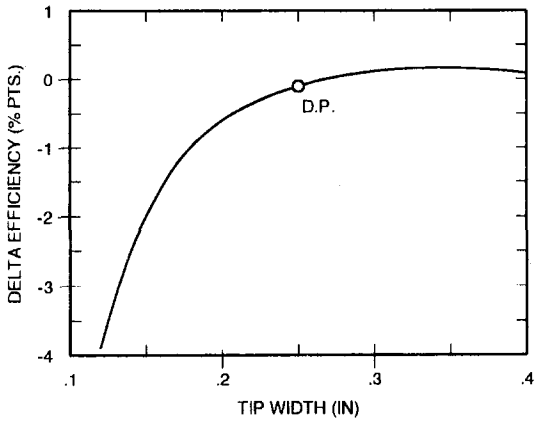


Fig. 2(*b*)

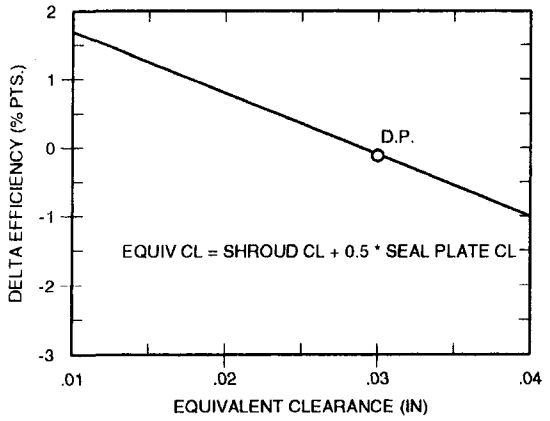


Fig. 2(*c*)

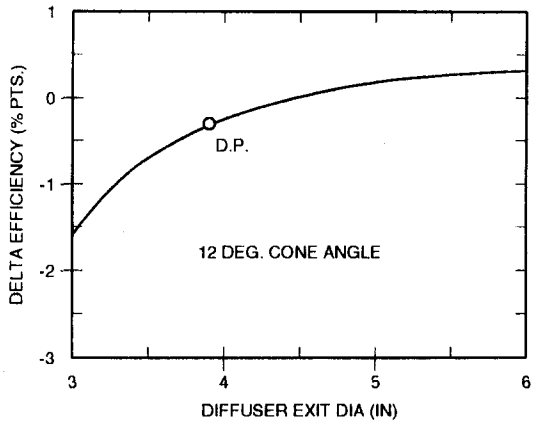


Fig. 2(*d*)

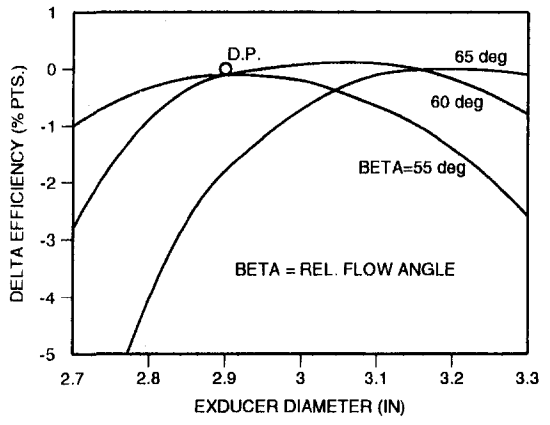


Fig. 2(*e*)

Fig. 2 One-dimensional optimization of geometry

of 2180 ft/s. Velocity ratio $U/V0$—the ratio of tip speed to isentropic spouting velocity—was 0.7 and the tip loading $\Delta H/U^2$ was 0.91. Subsequent finite element stress analysis showed that the 19,000 cycle life goal could be met at 2130 ft/s tip speed provided that deep scalloping of the disk rim was used.

Figure 2(*b*) shows that relatively wide tip width was needed. This has the effect of reducing tip clearance loss for a given physical clearance while increasing nozzle vaneless space loss from increased flow angle/path length. However, the tip clearance loss dominates until the flow angle becomes highly tangential. Blade stress considerations, on the other hand, make it desirable to keep tip width low.

Clearance sensitivity is shown in Fig. 2(*c*). The lowest practical design hot clearance for a production engine was initially considered to be on the order of 0.020 in. As it turned out, extensive transient thermal/deflection analyses of the structures showed that clearances of 0.010 to 0.015 in. were theoretically possible with the modest turbine inlet temperature chosen.

Figure 2(*d*) shows that, as expected, exhaust diffuser diameter should be as large as possible to minimize dump loss. The chosen diameter of 3.9 in. was a compromise based on accepted installation length constraints typical of existing APUs, together with a maximum diffuser cone angle of 12 deg. In addition, there was a desire to maximize combustor dome height (to improve pattern factor and altitude start capability) which limited the available size of the exhaust. It is very common in radial turbine designs of engines with reverse flow annular combustors for the combustor considerations to outweigh those of turbine performance.

The optimization of the exducer geometry is shown in Fig. 2(*e*). There are a series of combinations of exducer diameter and mean flow angle that result in maximum efficiency. As the flow angle is increased, however, the stress parameter AN^2 eventually becomes excessive because the optimum diameter also increases. Additionally the desire to maintain a large combustor dome height favors the use of a smaller diameter. Also, and again particularly at small size, trailing edge thickness to throat opening is an important parameter to consider. An exducer diameter of 2.9 in. at a mean flow angle of 58 deg was selected. Angles in the range 55 to 60 deg are typical of moderate to high specific speed turbines.

There is usually a strong desire to minimize rotor blade number for reasons of stress/life and manufacturing cost. Typically,

Downloaded 01 Jun 2010 to 171.66.16.53. Redistribution subject to ASME license or copyright; see http://www.asme.org/terms/Terms_Use.cfm

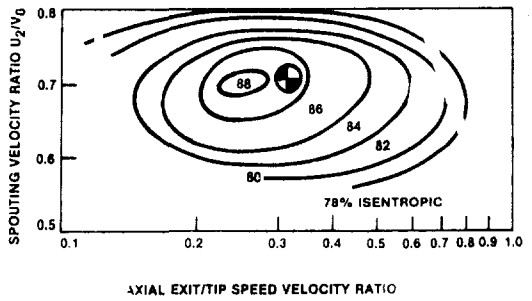


Fig. 3 Radial turbine efficiency correlation

in past APUs, blade numbers of 12 to 14 have been used. In this case, however, the analysis indicated an advantage to increased blade count; therefore a value of 16 was selected. Another advantage of a higher blade count is reduced exhaust noise signature—an increasingly important consideration in the modern aircraft APU.

Figure 3 shows an empirical correlation of the efficiencies of a large number of radial turbines in terms of velocity ratio and exit kinetic energy with the T-100 design point superimposed. This correlation provided an independent check on the mean-line design and verified that the tip speed and exducer geometry were near optimum.

The rotor inlet and exit velocity triangles, presented in Fig. 4, reveal a relatively high nozzle exit absolute angle and Mach number, 31 deg of rotor negative incidence, slightly positive (i.e., in the direction of rotation) rotor exit swirl and a low absolute exit Mach number consistent with the desire for best total–static efficiency (higher total–total efficiency could have been achieved with more rotor acceleration/reaction and negative exit swirl). The choice of near-zero exit swirl at the design point was influenced by the desire also to have good efficiency at the more highly loaded 75 hp operating point where the swirl would naturally become more negative.

Rotor Three-Dimensional Design

Rotor blading profiles were optimized using quasi-three-dimensional codes: streamline curvature for the hub-to-shroud solution and finite difference for the blade-to-blade velocity distributions.

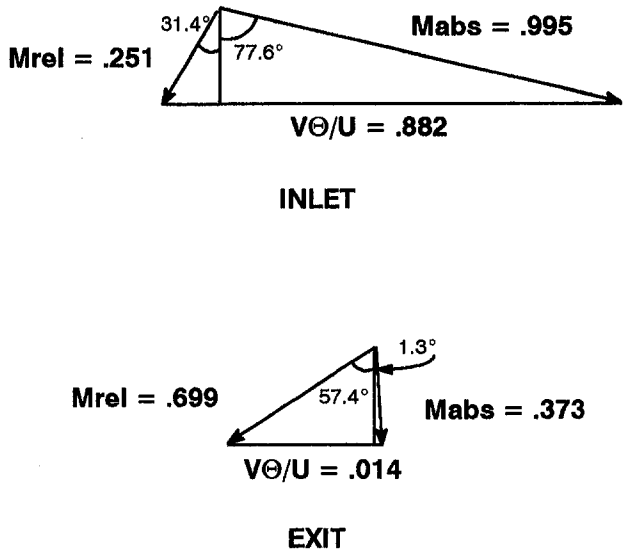


Fig. 4 Rotor mean velocity triangles

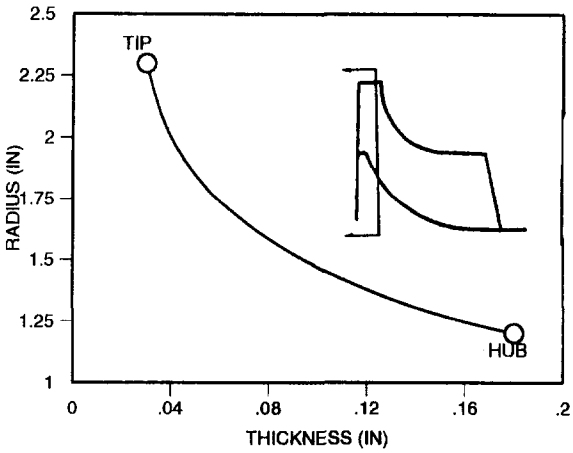


Fig. 5 Blade thickness distribution

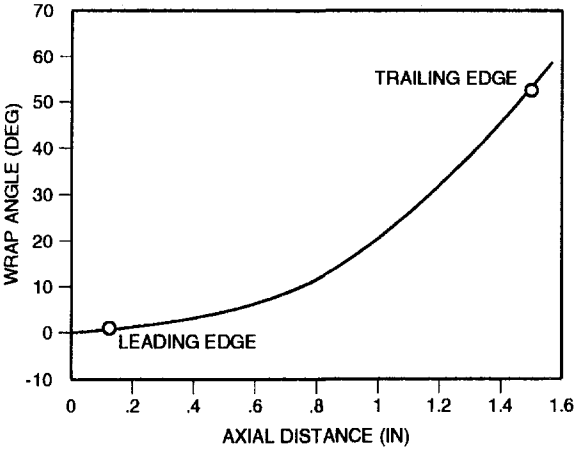


Fig. 6 Wrap angle distribution

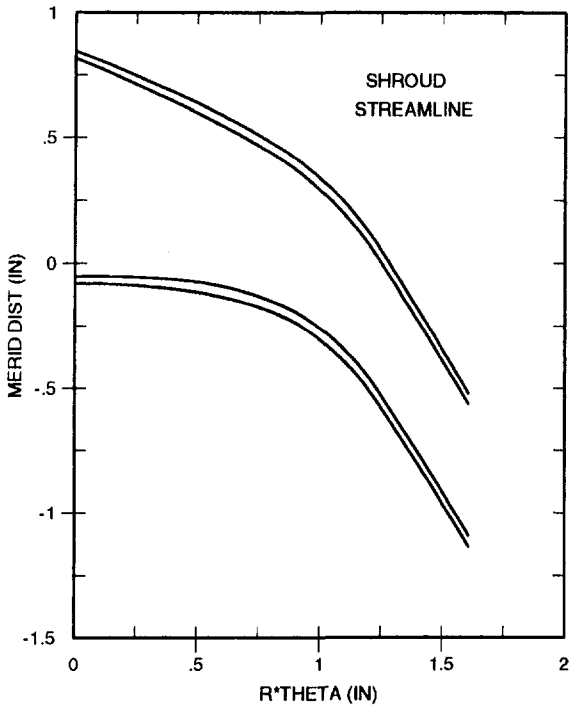


Fig. 7 Blade profile at shroud

Downloaded 01 Jun 2010 to 171.66.16.53. Redistribution subject to ASME license or copyright; see http://www.asme.org/terms/Terms_Use.cfm

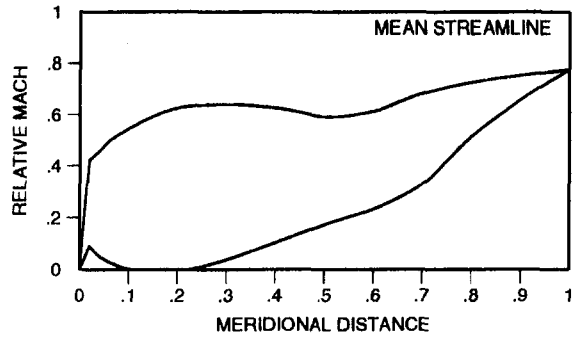


Fig. 8(*a*) Mean streamline

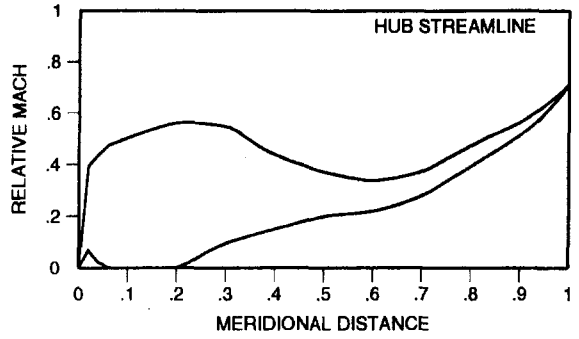


Fig. 8(*b*) Hub streamline

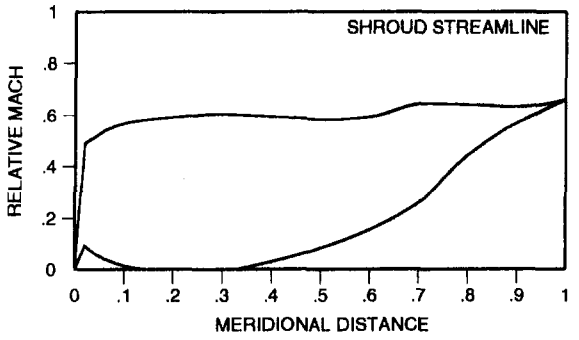


Fig. 8(*c*) Shroud streamline

Fig. 8 Blade surface velocities

Losses for the throughflow computations were distributed linearly in the streamwise direction and in accordance with previous test results in the spanwise direction. Different radial inflow turbines usually display similar characteristics with regard to efficiency distribution at the rotor exit, i.e., the apparent efficiency is much higher than the average at the hub and much lower at the shroud. This phenomenon is only partly due to high loss generation along the shroud streamline caused by tip clearance, curvature, and blade loading. Mainly it is the result of secondary flows of high loss fluid, which migrate toward the low static pressure at the shroud, this being generated by meridional turning. Similarly it has been found that the rotor flow deviation at the trailing edge is a strong function of radius. In this case a "typical" deviation distribution was applied. These distributions can be calculated from rotor exit surveys of existing designs available in the open literature. In general the deviation is low near the hub and peaks near the shroud. The mass-averaged rotor efficiency and deviation were adjusted to match the mean-line predictions.

The blade design was performed iteratively with finite element stress analysis to ensure that a viable mechanical solution was being produced. The thickness distribution used is shown in Fig. 5. It displays the normal characteristic of minimum tip thickness as governed by the limits of the investment casting process combined with generous hub thickness governed by centrifugal stress limits of the IN792 material. Natural frequencies were also calculated in an attempt to eliminate interference with known sources of excitation.

The radial turbine designer is quite limited in the variation of blade profile, which can be used since, conventionally, radial element blading must be chosen. Otherwise unacceptable bending stresses will be produced. Therefore the major variables are meridional profile, chord length, and blade wrap angle distribution. A long chord was used in this case to ensure good guidance of the exit flow through high overlap, i.e., low exducer loading. Some negative rake (15 deg) was introduced at the inlet since quasi-three-dimensional analysis showed that this was effective in reducing hub-to-shroud pressure gradients and tip blade-to-blade loading. The camber line wrap angle distribution is shown in Fig. 6 and the "unwrapped" blade-to-blade profiles along the shroud streamline in Fig. 7.

Blade loadings (velocity distributions) are shown in Figs. 8(*a*, *b*, *c*) and display the following characteristics:

- Velocity distributions typical of radial turbines
- Negligible shroud suction surface diffusion
- Relatively low hub suction surface diffusion
- Small areas of negative pressure surface velocity
- Subsonic velocities throughout

At the 75 hp rating the tip loading was increased by the higher incidence—7 deg negative—the velocity ratio being 0.64 (*t-sde*).

The final dimensions selected for the scantlings are shown in detail in Fig. 9.

Nozzle Design

Inlet flow to the nozzle was not radial due to the strongly swirling nature of the flow discharging from the engine's combustor. At the nozzle leading edge the flow angles varied from approximately 20 to 40 deg from radial, which reduced the amount of turning needed in the vanes. A two-dimensional vane profile was selected for ease of manufacture. Figure 10 shows a sector of the 19-vane ring.

The same quasi-three-dimensional methods as for the rotor were used to optimize the vane profile. The resulting velocity

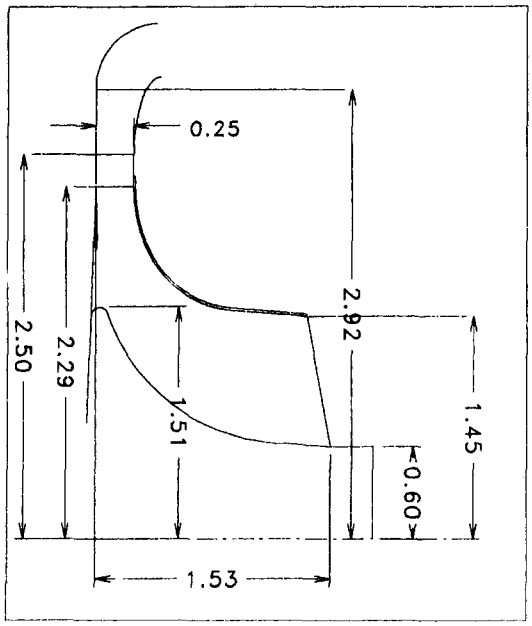


Fig. 9 Scantling dimensions

Downloaded 01 Jun 2010 to 171.66.16.53. Redistribution subject to ASME license or copyright; see http://www.asme.org/terms/Terms_Use.cfm

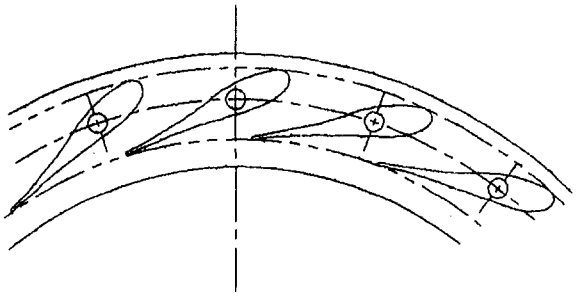


Fig. 10 Nozzle vane profile

distribution (Fig. 11) displays the desirable characteristic of continuous acceleration on both pressure and suction surfaces. Low inlet loading is created by the inlet swirl combined with modest meridional contraction. At both 50 and 75 hp conditions the nozzle throat was close to choke, the exit Mach number being just subsonic.

Test Facility and Instrumentation

A cross section of the rig is shown in Fig. 12. The drive air was supplied without preheat at a pressure ratio of 4:1 and a temperature of approximately 400°F. The inlet plenum was fed by a single tangential inlet duct sized to produce the correct inlet swirl angle at the nozzle leading edges. An exhaust ejector enabled the overall pressure ratio to be adjusted between 3:1 and 9:1. Power was absorbed by a load compressor having a vaneless diffuser. A throttle valve was used to adjust load and thus speed at a given test pressure ratio. Provision was made in the rig design to adjust axial build clearances on the shroud and seal-plate sides by means of shims. The nozzle vanes were made separately from the shrouds and could be restaggered to change their throat area.

Turbine flow was measured by an ASME standard inlet orifice accurate to ±2 percent. Efficiency was calculated from measured pressure ratio and temperature drop. The inlet pressure and temperature was measured immediately upstream of the nozzle ring by means of total pressure probes and half-shielded recovery thermocouples. The Keil probes were aligned to the flow experimentally until the pressure readings were maximized. At the exit, pressure was measured by means of wall static tappings and temperature by means of multiple recovery thermocouples several diameters downstream of the rig where the flow was fairly well mixed.

The rig exit temperature was close to ambient, which served to reduce conduction errors. Nevertheless, insulation was applied internally and externally to reduce heat conduction.

A check of the measured power was provided by measurement of the load compressor flow and temperature rise. This power was generally within 2 percent of the power calculated from the turbine side, the difference being attributable to bearing and windage losses as well as measurement errors. The rig employed relatively high loss hydrodynamic bearings.

At selected operating conditions, rotor exit surveys were made at a plane about one exducer blade height downstream of the trailing edge. Traversing probes allowed total temperature, total pressure, static pressure, and yaw angle to be measured. No attempt was made to measure the radial component of velocity.

A fixed wedge probe was installed at rotor exit, measuring total pressure and swirl angle. The probe radial position was chosen so that its readings closely represented mass average values as determined from a full survey. Since the optimum probe position was likely to change with velocity ratio, full survey data at two or three different operating conditions was used to correct readings from the fixed rotor probe at any given pressure ratio. In this manner the rotor exit efficiency and swirl angle could be calculated at every data point without performing a time-consuming full-up survey.

Figure 12(*a*) shows the test rotor machined from a titanium alloy forging.

Test Results

Measured efficiencies for the tightest build clearances are presented in Figs. 13 and 14. Peak overall total-to-static efficiency on the order of 87 percent and total-to-total efficiencies on the order of 89 percent were obtained. The hot running clearances, expressed in terms of percent of local blade height, were 4.0 percent axial at the inlet on the shroud side, 7.2 percent on the seal plate side, and 1 percent at the exducer. It is apparent that the efficiency peaked at a much higher velocity ratio than the design point of 0.7. At the design tip speed and pressure ratio the efficiency was 86.4 percent. Measured flow function was within 1 percent of design intent.

The efficiency was quite good at very high pressure ratio as shown in Fig. 15 for a velocity ratio of 0.7. Of course, in practice it would be quite impractical with today's materials and life requirements to operate at 0.7 velocity ratio at 9:1 pressure ratio in an APU since a tip speed on the order of 2500 ft/s is implied for 1800°F turbine inlet temperature. The estimated pressure ratio at rotor choke for this stage is 7.8:1. The good performance at high pressure ratio is due to the choice of near-zero exit swirl (i.e., low reaction) at the design point.

At the higher loading condition more typical of APU operation—a velocity ratio of 0.64—the overall total-to-static efficiency was 84.8 percent and the total-to-total 86.4 percent.

Table 3 presents a breakdown of test component performance at the design point. The split of losses was calculated from a combination of rotor exit survey data and rotor tip static pressure. The rotor exit mass average swirl, measured enthalpy drop, and Euler equation allowed the rotor inlet tangential velocity to be derived. The rotor tip velocity triangle could then be solved using the measured static pressure, derived absolute tangential velocity, and continuity. No blockage factors were used.

The most interesting aspect of the component performance was the remarkably high nozzle and vaneless space loss and correspondingly high rotor efficiency. This casts doubt on the accuracy of the rotor tip static pressure measurement on which this split is strongly dependent. The rotor inlet absolute flow angle, on the other hand, was in good agreement with predictions.

Figure 16 shows the overall efficiency as a function of rotor tip incidence. It is evident that this turbine thrives on negative incidence since peak efficiency occurs at around −45 deg. At the design velocity ratio the incidence was close to the design intent of −31 deg.

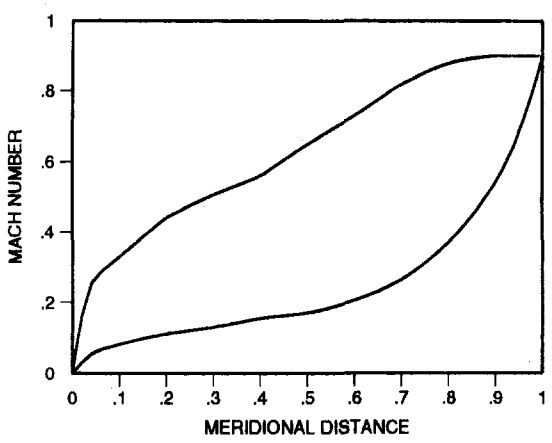


Fig. 11 Vane surface velocities

Downloaded 01 Jun 2010 to 171.66.16.53. Redistribution subject to ASME license or copyright; see http://www.asme.org/terms/Terms_Use.cfm

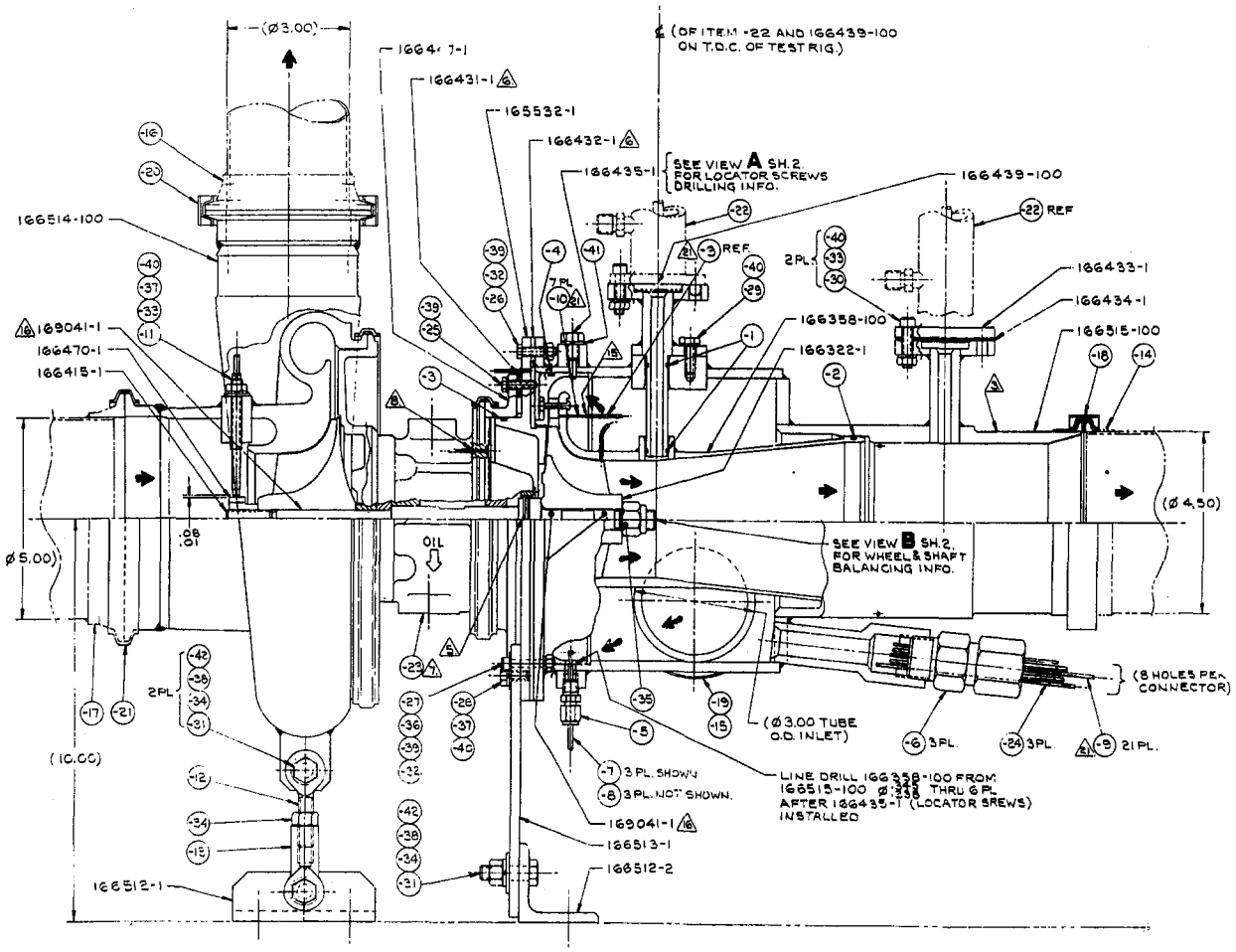


Fig. 12 Turbine test rig

Data were also obtained for increased shroud axial and seal plate clearances. The sensitivity of efficiency to these clearances at the design loading is shown in Fig. 17. Exducer radial clearance was held constant during these tests.

Results of the rotor exit survey (Fig. 18) displayed the expected trend of high apparent efficiency at the hub and low efficiency at the shroud. There was also an axial velocity deficit resulting from low-energy fluid being centrifuged to the exducer tip, together with a reduction in temperature drop in the mid to shroud streamtubes. The temperature drop and hence the efficiency displayed a curious inversion between the mean and outer streamtubes, suggesting perhaps that the secondary flow had not migrated completely to the shroud.

The absolute swirl angle varied from mildly antirotative at the hub to strongly corotative at the shroud. The variation was not as strong as was expected from the quasi-three-dimensional prediction made during rotor design. An attempt was made to match the three-dimensional analysis to the measured survey

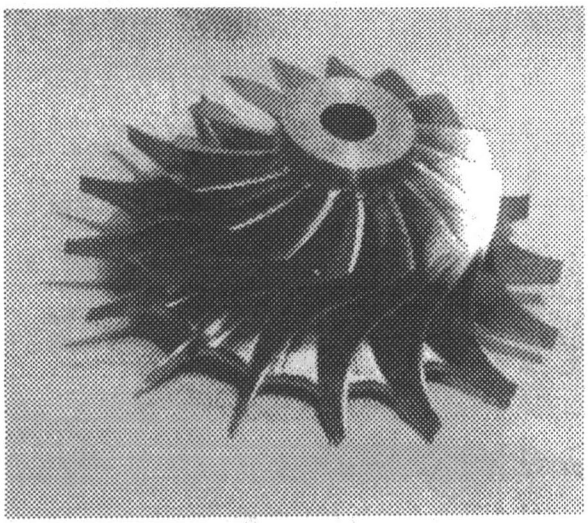


Fig. 12(*a*) Rig test rotor

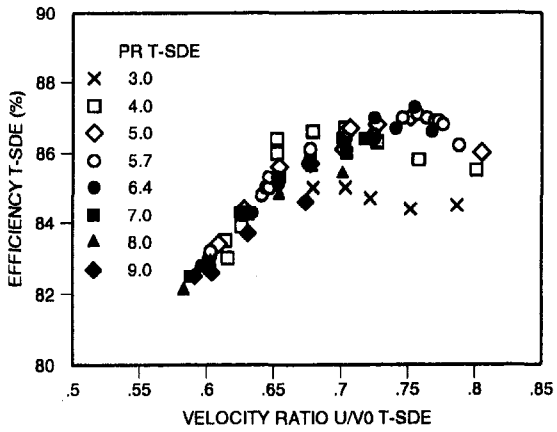


Fig. 13 Static efficiency results

Downloaded 01 Jun 2010 to 171.66.16.53. Redistribution subject to ASME license or copyright; see http://www.asme.org/terms/Terms_Use.cfm

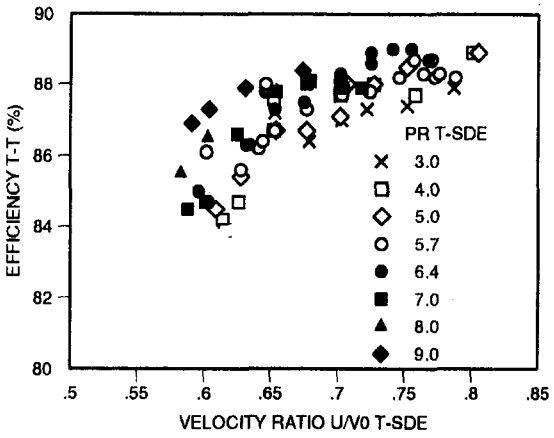


Fig. 14 Total efficiency results

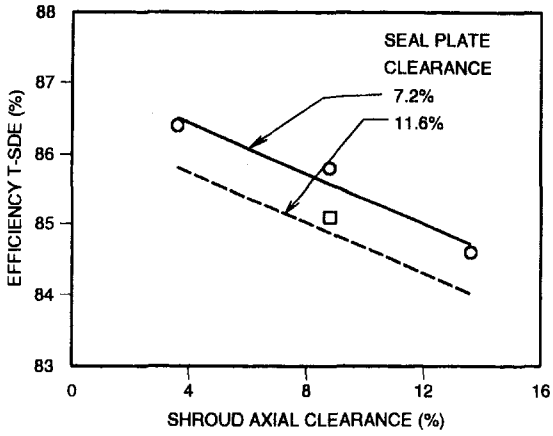


Fig. 17 Effect of tip clearances (PR = 5.7, U/VO = 0.7)

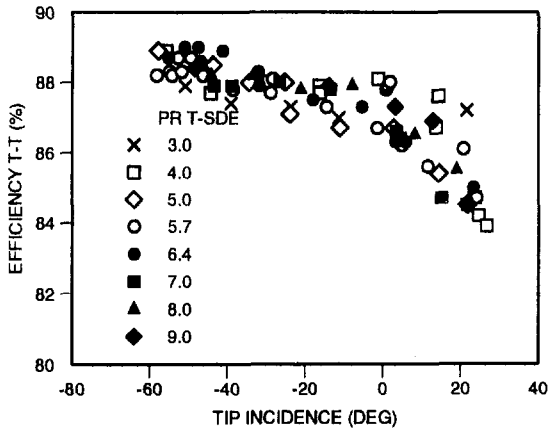


Fig. 15 Variation of static efficiency with incidence

Table 3 Component performance breakdown

Overall pressure ratio t−sde	*5.78*	*Rotor tip V/θ/U*	*.89*
Rotor exit pressure ratio t−t	*5.54*	*Rotor tip incidence*	*−28.3*
Overall efficiency t−sde %	*86.4*	*Rotor only efficiency t−t %*	*94.1*
Rotor exit efficiency t−t %	*88.1*	*Rotor exit Mach number*	*0.38*
Velocity ratio t−sde	*0.70*	*Exit relative flow angle*	*56.1°*
Flow function lb/s$\sqrt{°R}$*/psia*	*.373*	*Exit absolute swirl angle°*	*+5.0*
Nozzle exit angle°	*77.7*	*Rotor exit Va/U*	*.31*
Nozzle + vaneless space loss coeff.	*.32*	*Diffuser recovery coefficient Cp*	*0.55*
Rotor tip absolute Mach number	*.985*		

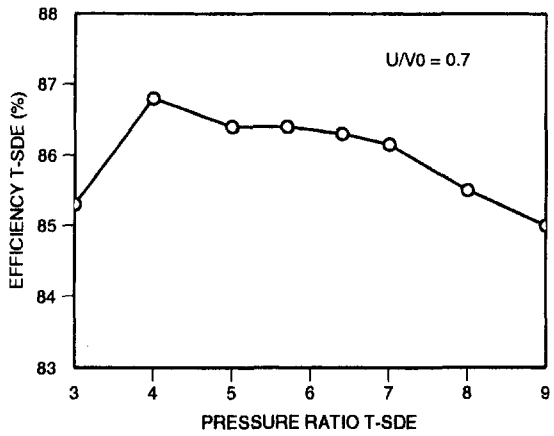


Fig. 16 Variation of total efficiency with pressure ratio

results by changing the assumed efficiency and deviation distributions at the trailing edge in accordance with test data. Although this improved the match of swirl angle significantly, there were still quite large differences. A fully three-dimensional viscous analysis using a computational fluid dynamics (c.f.d.) code such as that of Dawes (1988) would probably provide a better solution.

Engine Results. The results of the T-100 engine testing have been reported in the open literature at various times (Napier et al., 1989; Napier, 1991). In general, problems were encountered with internal leakage and excessive gearbox drag. Hot running clearances were larger than the tightest values used in the rig. At the 50 hp rating the estimated turbine efficiency

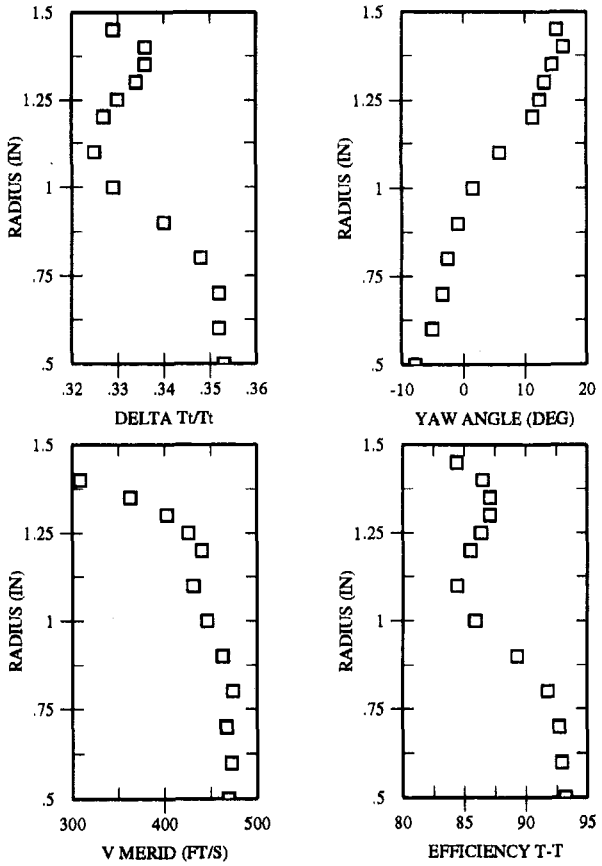


Fig. 18 Rotor exit survey at design point

Downloaded 01 Jun 2010 to 171.66.16.53. Redistribution subject to ASME license or copyright; see http://www.asme.org/terms/Terms_Use.cfm

was 84.5 percent *t-sde* at a velocity ratio of 0.68, some two percentage points lower than the rig. The results at the 75 hp rating were better, engine efficiency being 84.4 percent at a velocity ratio of 0.64 compared to 84.8 percent in the rig. The difference is attributable to tip clearance. After correcting for gearbox drag, the best S.F.C.'s obtained were on the order of 0.76 lb/h.hp at 57 hp and 0.71 lb/h.hp at 80 hp, IPS losses included in both cases.

Conclusions

This effort demonstrated that small radial inflow turbines are capable of producing good efficiencies at high stage pressure ratios. An efficiency level on the order of 86 percent total-to-static or 88 percent total-to-total was obtained in a rig test of the T-100/MPSPU design at pressure ratios up to 7:1. With further refinements such as an increase in tip speed, the original goal of 87 percent *t-s* at 5.7:1 could probably be achieved. This level is higher than could be obtained from multistage axial turbines at the same physical tip clearance and flow function.

The rotor exit surveys produced an unusual result regarding the radial distribution of losses. Investigation of the internal aerodynamics of the rotor using fully three-dimensional c.f.d. codes and in particular the development of secondary flows would make an interesting topic for future work. The c.f.d. might also shed some light on the reasons why the efficiency peaked at such a high negative incidence.

Acknowledgments

Thanks are given to the U.S. ARMY Aviation Applied Technology Directorate and to Sundstrand Power Systems for permission to publish this information. The author also recognizes the efforts of technical contributors at SPS and Pratt & Whitney.

References

Dawes, W., 1988, "Development of a 3D Navier–Stokes Solver for Application to All Types of Turbomachinery," ASME Paper No. 88-GT-70.

Napier, J. C., and Thompson, R. G., 1988, "T-100 Multipurpose Power Unit: Technology for the Next Generation Auxiliary Power Units," SAE Paper No. 881501.

Napier, J. C., Thompson, R. G., and Rodgers, C., 1989, "Development Test Status T-100 Multipurpose Small Power Unit," ASME Paper No. 89-GT-117.

Napier, J. C., 1991, "Development of T-100 Multipurpose Small Power Unit," ASME Paper No. 91-GT-327.

Rodgers, C., 1966, "Efficiency and Performance Characteristics of Radial Turbines," SAE Paper No. 660754.

Thompson, R. G., and Parker, S. D., 1988, "Technical Approach for a Multipurpose Small Power Unit," ASME Paper No. 88-GT-262.

USAARTA (AVSCOM), 1986, "T-100 Multipurpose Small Power Unit," Aviation Applied Technology Directorate, Contract No. DAAJ02-86-C-0007.

Downloaded 01 Jun 2010 to 171.66.16.53. Redistribution subject to ASME license or copyright; see http://www.asme.org/terms/Terms_Use.cfm

An Experimental and Computational Investigation of Flow in a Radial Inlet of an Industrial Pipeline Centrifugal Compressor

M. B. Flathers
Solar Turbines Inc.,
San Diego, CA 92123

G. E. Bache
Advanced Scientific Computing Corp.,
El Dorado Hills, CA

R. Rainsberger
XYZ Scientific Applications Inc.,
Livermore, CA

The flow field of a complex three-dimensional radial inlet for an industrial pipeline centrifugal compressor has been experimentally determined on a half-scale model. Based on the experimental results, inlet guide vanes have been designed to correct pressure and swirl angle distribution deficiencies. The unvaned and vaned inlets are analyzed with a commercially available fully three-dimensional viscous Navier–Stokes code. Since experimental results were available prior to the numerical study, the unvaned analysis is considered a postdiction while the vaned analysis is considered a prediction. The computational results of the unvaned inlet have been compared to the previously obtained experimental results. The experimental method utilized for the unvaned inlet is repeated for the vaned inlet and the data have been used to verify the computational results. The paper will discuss experimental, design, and computational procedures, grid generation, boundary conditions, and experimental versus computational methods. Agreement between experimental and computational results is very good, both in prediction and postdiction modes. The results of this investigation indicate that CFD offers a measurable advantage in design, schedule, and cost and can be applied to complex, three-dimensional radial inlets.

Introduction

Many pipeline and multistage industrial centrifugal compressors require complex radial inlets, which can significantly impact overall compressor performance. However, the inlet design is typically based on prior experience with little or no subsequent development. Analysis is usually limited to the axisymmetric section with assumed or experimentally derived gross boundary conditions upstream. Radial inlet guide vanes based on these boundary conditions may be employed to ensure a particular swirl condition and pressure profile entering the impeller, even if they might not be necessary. This may seem crude, but it has historically been the most practical method to specify radial inlets due to the time and cost of experimental studies and the complexity and uncertainties associated with fully three-dimensional computational studies. This process is further justified by the lack of both experimental and computational investigations in the open literature.

Computational Fluid Dynamics (CFD), verified by experimental data, has been used extensively for centrifugal compressor impellers and more recently, vaneless and vaned diffusers in the design process. This, however, is not the case for radial inlets of centrifugal compressors. Since these types of inlet are cast, final design decisions must be made from whatever data are available prior to hardware commitment. Initially, the radial inlet investigation presented herein was to be an experimental study only, even though a general purpose three-dimensional viscous code was available. The main concerns with a fully three-dimensional viscous study were grid generation, node count, solution convergence, and accuracy of results. The computational grid represented the largest challenge in that the physical passage area shape varies from circular to elliptical to arbitrary as the flow path changes from radial to axial. In addition, there are top and bottom splitters, which require special consideration. The node count is an issue because of the tradeoff between accuracy and CPU time requirements for a very large model of this kind. If a converged solution is obtained, it can be compared to the experimental results to verify accuracy. In order to determine the viability of CFD for radial inlets and because the fabrication, testing, and data reduction of a half-scale model is neither timely nor cost effective, a computational study was launched after the initial testing was completed.

The basis of the present work was the need for an efficient radial inlet for an industrial pipeline centrifugal compressor. The primary objectives of this investigation were to experimentally determine the performance of an experience based radial inlet design and modify as necessary; verify CFD findings with experimental data; and evaluate the usefulness of CFD as a design tool for complex, fully three-dimensional radial inlets.

Experimental Investigation

The half-scale model, shown in Fig. 1, was fabricated from a pattern developed from sections in a CADDS 4X layout. In the cylindrical to elliptical section up to the top splitter, the area reduction is small and nearly linear. Downstream, from $\theta = 0$ to 180 deg, the area is reduced to zero at the pinch point using a parabolic type distribution. The model body is vertically split and made from fiberglass. The entry flange, machined from aluminum, has eight instrumentation locations equally spaced 45 deg. The axisymmetric hub was machined from aluminum and attaches to an aluminum ring on the model side and to an aluminum base on the mounting side. The axisymmetric shroud was machined from aluminum with an integral discharge flange. The discharge flange had ten instrumentation locations, two

Contributed by the International Gas Turbine Institute and presented at the 39th International Gas Turbine and Aeroengine Congress and Exposition, The Hague, The Netherlands, June 13–16, 1994. Manuscript received by the International Gas Turbine Institute February 19, 1994. Paper No. 94-GT-134. Associate Technical Editor: E. M. Greitzer.

Copyright © 1996 by ASME

Downloaded 01 Jun 2010 to 171.66.16.53. Redistribution subject to ASME license or copyright; see http://www.asme.org/terms/Terms_Use.cfm

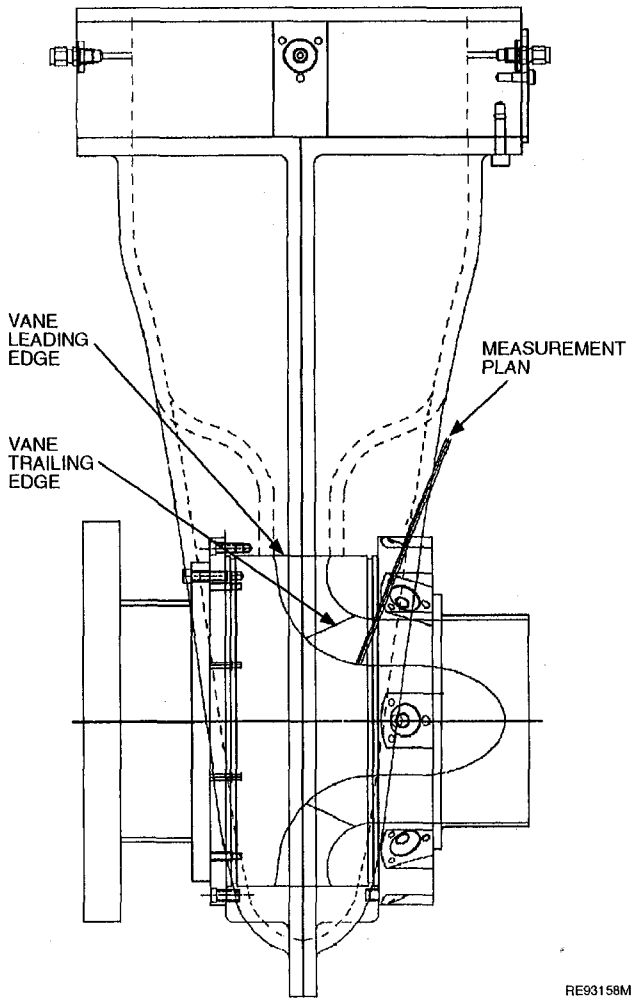


Fig. 1 Radial inlet scale model layout

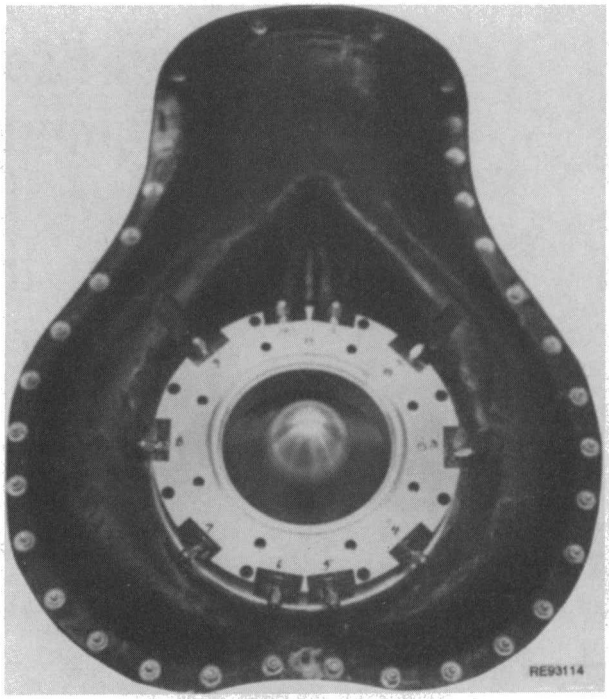


Fig. 2 Radial inlet scale model

placed ±10 deg of top splitter vane, two placed ±10 deg of bottom splitter, three equally spaced 45 deg on one side and the remaining three 180 deg opposite. For discussion purposes, the circumferential locations were numbered clockwise 1 to 10 looking upstream. The top and bottom splitters vanes were machined from aluminum and recessed in and bolted to the shroud. All fiberglass and aluminum interfaces were sealed and blended smooth with an epoxy. The finished model is pictured in Fig. 2.

Test Facility. The inlet model was tested in pressure rather than suction to simplify the test setup and to allow access to the measurement plane at the model discharge. The facility schematic is shown in Fig. 3. A 15 hp, 2200 cfm blower was used to supply air to the model through a 17 foot straight aluminum pipe. Between the blower and model, provision for a pitot tube was located about 50 percent of the axial distance while an additional pressure tap was located about 75 percent of the axial distance. Flow rate was adjusted by varying the blower motor speed with a variable frequency controller. The model was mounted to an adjustable height table with a rubber pad to isolate the model from the table. There was no provision made for a downstream impeller as this was a static test only. Flexible ducting from the model discharge to the cell roof was setup for easy on/off installation. This was important for high flow runs where noise generation was a concern.

Data Aquisition and Instrumentation. The data acquisition system used a Daytronics series 10 computer for the front end coupled with Realtime Engine Test System (RETS) software. Test data were stored on a MicroVAX II minicomputer for uploading to a VAX mainframe cluster via ethernet. A PSI 780B system with a 1 psi module was used for pressure scanning purposes. All pressure measurements were confirmed with either incline or U-tube water manometers simultaneously.

Air flow was measured with a Miriam Instrument pitot tube, which provided total, delta, and static pressure. These measurements were monitored with the PSI system and the flow was calculated using the RETS software with an equation provided by the pitot tube manufacturer. The pressure measurements were manually confirmed with a double incline manometer.

Total pressure was measured with miniature Kiel probes. These probes have a head diameter of 0.067 in. and allowed approximately ±52 deg yaw variation and +47/−40 deg pitch variation: ideal for relatively small channels with unknown swirl angles. Total and static pressure and swirl angle were measured with United Sensor three-hole, two-dimensional directional probes. Unlike the Kiel probes, these probes have a head size of 0.265 in. and need to be aligned with flow direction, but yield velocity and angle. Probe alignment was based on static pressure balancing with measurements scanned with the PSI system and confirmed with a U-tube manometer. A probe fixture was fabricated to record insertion depth and rotation. Both Kiel

Nomenclature

P = pressure, psia
Re = Reynolds number
α = swirl or flow angle, deg
θ = circumferential location

Subscripts

s = static conditions
t = total conditions
05 = inlet entry
1 = inlet discharge

Downloaded 01 Jun 2010 to 171.66.16.53. Redistribution subject to ASME license or copyright; see http://www.asme.org/terms/Terms_Use.cfm

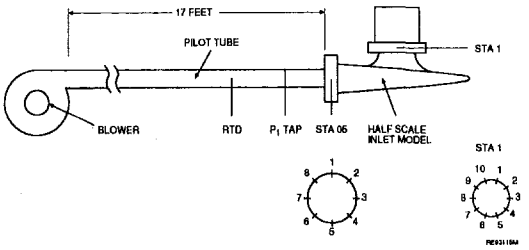


Fig. 3(*A*) Radial inlet blow down rig schematic

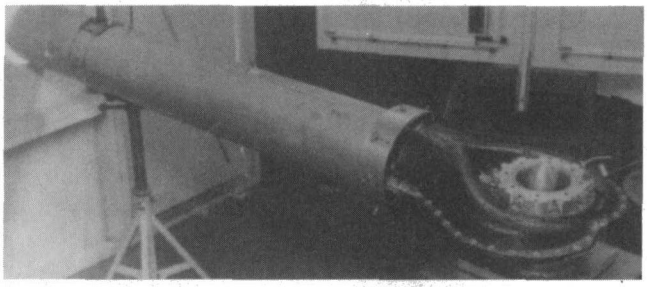


Fig. 3(*B*) Radial inlet blow down rig photo

probe and three-hole probe total pressure measurements were confirmed with incline manometers.

Test Procedure and Results. The total pressure distribution at the inlet to the model was measured with a Kiel probe to verify its uniformity. At each of the eight circumferential locations, nine spanwise measurements were taken at a flow rate 70 percent of design flow. The measurements were in 1 in. increments, starting at 0.034 in. from the outer diameter. The results indicated an extremely clean flow into the model with the only small deviation at the outer diameter.

Prior to detailed swirl angle and total pressure loss surveys, tuft tests were performed with a 4 in. string on a small rod to obtain an overall perspective of the flow field. Although no separations were noted at a flow rate 60 percent of design flow, the swirl angles on the bottom of the inlet, especially near the hub, seemed excessive. Tuft testing was repeated at flow rates of 74 and 95 percent of design flow with relatively the same qualitative results.

The swirl angle survey was completed with the three hole probes at a flow rate 60 percent of design flow. Measurements were taken at five spanwise positions, 25, 44, 62, 80, and 99 percent for each of the ten circumferential locations. The results, shown in Fig. 4, indicate high swirl angles between the top and bottom splitter vanes at 0 deg and 180 deg. The swirl angles are higher in the bottom half of the inlet and increase toward the hub, which is consistent with the tuft findings. The results also show a very symmetric flow side to side as intended.

The swirl angle survey was repeated at flow rates of 74, 87, and 100 percent of design flow to check sensitivity at higher flows. Locations 1, 6, and 7 (10, 190, and 225 deg) showed less than a ± 1 deg variation from the results at 60 percent of design flow. The corresponding static pressure results are also shown in Fig. 4 and indicate side-to-side symmetry.

The total pressure loss survey was completed with the Kiel probes at a flow rate 60 percent of design flow. Measurements were taken at six spanwise positions, 3, 21, 40, 58, 74, and 94 percent for each of the ten circumferential locations. The results, shown in Fig. 4, indicate very low total pressure loss from entry to discharge. Since the entry profile measured previously is very uniform, the entry total pressure is based on a fixed Kiel probe in the center of the flange. The entry static pressure was calculated based on the entry total pressure and the flow rate derived from the pitot tube measurements. The total pressure loss is quite symmetric, as was the swirl angle, and the loss generally increases toward the shroud, opposite of the swirl angle trend, which seems logical. The loss is higher in the bottom quarter of the inlet, approximately 135 to 225 deg, which is also sensible. Although an accurate mass-averaged total pressure loss is not possible with these limited data, the loss coefficient is estimated to be 45 percent of entry dynamic head, which is well below the design intent of nearly 120 percent. The total pressure loss survey was repeated at flow rates of 74, 87, and 100 percent of design flow. Based on the velocity measured with the three-hole probe, the total pressure loss increased with the square of the velocity as expected.

Inlet Modifications. The experimental investigation showed that although the inlet design was quite efficient, the swirl angles were excessively high for the downstream impeller. In order to remove the swirl, inlet guide vanes (IGV's) were designed and fabricated with the objective of minimizing additional losses. Since the test data show significant circumferential and spanwise variation, the specification of the upstream boundary conditions for the IGV's is not straightforward. Obviously, no one vane profile would be optimum for all circumferential locations or spanwise positions, and without more extensive test data, ideal profiles are less likely to be attained. However,

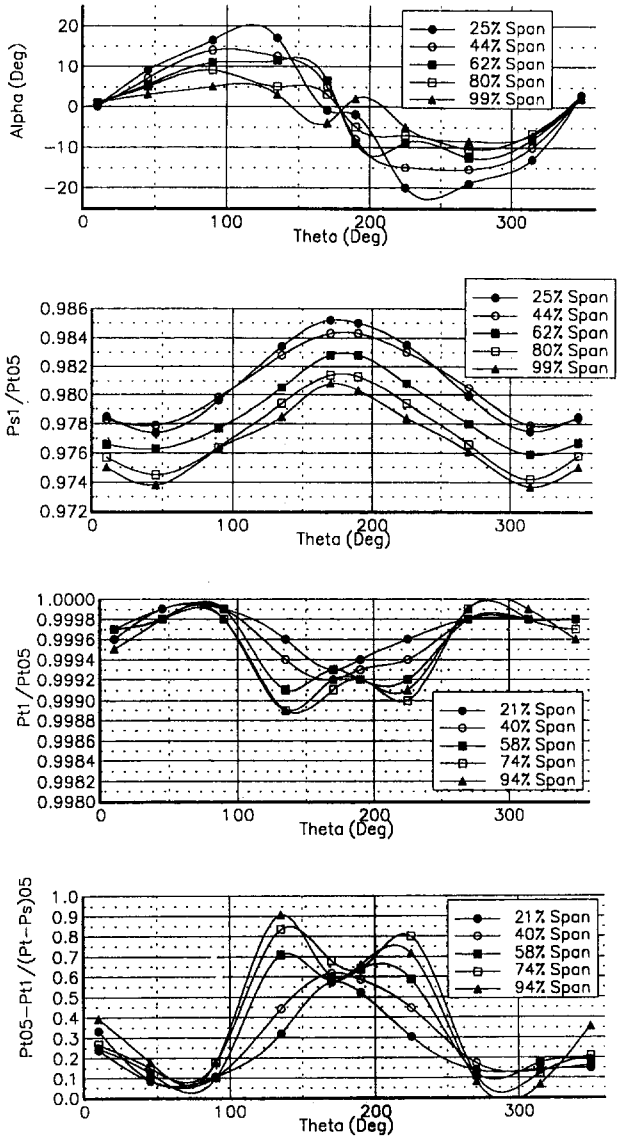


Fig. 4 Experimental results

Downloaded 01 Jun 2010 to 171.66.16.53. Redistribution subject to ASME license or copyright; see http://www.asme.org/terms/Terms_Use.cfm

the accelerating radial inflow tends to be somewhat forgiving to less than ideal vane shapes.

The approach taken here was to specify a vane profile based on the highest spanwise average of swirl angle at a given circumferential location. The resultant swirl velocity set the turning requirements of the "full turning" IGV. The vane was designed with a relatively large leading edge radius in order to accept significant incidence variations and with a fairly large trailing edge radius due to structural requirements. The vane shape was based on an internal loading criterion and was subsequently analyzed with Dawes' BTO3B (Dawes, 1988) using upstream boundary conditions derived from the experimental results. The Dawes analysis confirmed a sound IGV design for the specified boundary conditions. With this baseline IGV defined, less cambered versions were developed based on the "full turning" profile to accommodate reduced swirl conditions on the top half of the inlet. The complete 360 deg IGV, which is mirrored side to side, is shown in Fig. 5.

Computational Methods

The focus of this paper is application of numerical and experimental techniques in the design of a radial inflow compressor inlet. It is, however, important to understand, at least in an abbreviated way, the techniques employed during the numerical study, since these techniques make the investigation feasible and useful. A brief discussion of the computational methods is provided below. More details can be found in the references.

The Computational Fluid Dynamics (CFD) code TASCflow, which is commercially available, was used for the numerical investigation. TASCflow solves the Reynolds Stress Averaged Navier–Stokes equations in primitive variable form, and is applicable to incompressible and compressible (subsonic, transonic, and supersonic) flows. The effects of turbulence are modeled by the standard k–e turbulence model.

The code allows for modeling of extremely complex geometries, as is evident from the examples presented in this paper. A general nonorthogonal, boundary fitted, structured grid is utilized. Often the domain of interest does not lend itself to subdivision by a single structured mesh. For these situations, the code allows the user to connect simple blocks into a multiblock assembly. A convenient feature is that the grids are not required to match at the connection interface, and they need not even be contiguous. The preprocessor will make the necessary adjustments to ensure a "leak-proof" connection. Further modeling flexibility is possible through the ability to handle internal objects, pinched grids, and local grid refinement (also known as "grid embedding"). With the exception of grid embedding, each of these capabilities was exercised by this numerical investigation and will be discussed in more detail in later sections.

The method employs an element-based finite volume method. Pressure/velocity coupling is handled using a fourth-order pressure redistribution method that is standard for pressure based (as opposed to density based, time marching) codes. The domain is subdivided into hexahedral elements, which are the building blocks of the discretization. Volumes are constructed by the appropriate subdivision of the elements. The discretization scheme employed is second-order accurate. Its two key components are a directionally sensitive upwind discretization scheme known as Linear Profile Skew upwinding (LPS), combined with a physically based correction term known as Physical Advection Correction (PAC) (Galpin et al., 1986; Schneider and Raw, 1986; and Van Doormaal et al., 1987). Together these schemes reduce solution errors that would naturally arise due to flow directionality and streamwise gradients. The result is a discretization scheme that exhibits very low levels of false total pressure loss, a property that is very important to the present investigation.

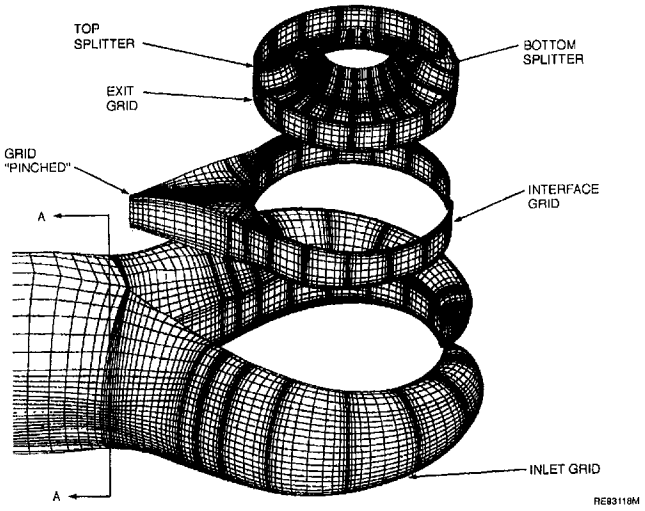


Fig. 6 Computational model

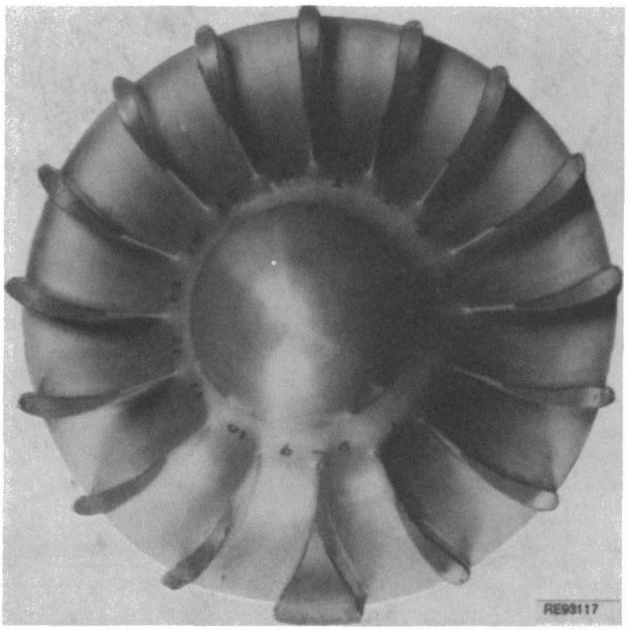


Fig. 5 Half-scale inlet guide vanes

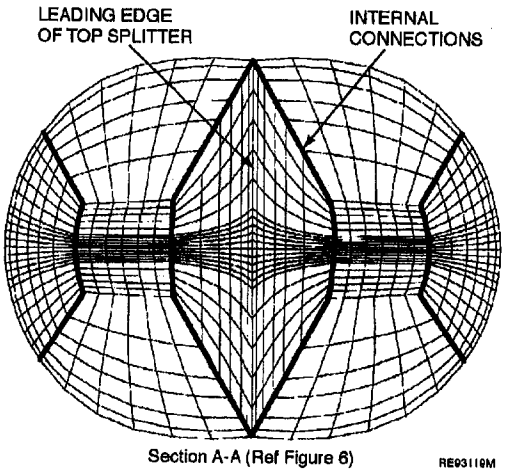


Fig. 7 "Butterfly grid" cross section

Downloaded 01 Jun 2010 to 171.66.16.53. Redistribution subject to ASME license or copyright; see http://www.asme.org/terms/Terms_Use.cfm

The previous paragraph discusses discretization accuracy. Another factor that is key to the feasibility of the scheme is the method used to solve the linearized algebraic equations. TASCflow uses an implicit, coupled iterative solution method, which is accelerated by a multigrid method known as Additive Correction Multigrid (Van Doormaal et al., 1986; Hutchinson and Raithby, 1986; Hutchinson et al., 1988). The strengths of this method, from the point of view of the user, are that it is very efficient and robust over a wide range of problems, it requires little user intervention, solution cost increases only linearly with increase in the number of nodes, and it can handle the wide range of control volume sizes and shapes commonly encountered in turbomachinery applications.

Numerical Investigation

Initially, four grid sizes, roughly 32,000, 90,000, 112,000, and 120,000, were investigated to determine grid sensitivity. The effect of grid density was most apparent for the total pressure loss, where the mass-averaged loss was significantly reduced with finer meshes. However, the total pressure loss difference diminished with each increase in grid size. The total pressure loss decreased by approximately 50 percent from 32,000 to 90,000 nodes and by approximately 10 percent from 90,000 to 112,000 nodes. The loss level using 120,000 nodes was essentially the same as for 112,000 nodes. Although more nodes would most likely improve modeling accuracy, it was felt that 120,000 nodes would provide sufficient engineering resolution. In addition, more nodes becomes unattractive for practical solution turnaround, even with state-of-the-art desktop workstations.

The computational model used during the numerical investigation is shown in Fig. 6. Symmetry exists through the center of the component; thus the computation was only performed on half the inlet. The domain was modeled using three structured computational blocks: an inlet grid ($7 \times 77 \times 129$), an interface grid ($11 \times 11 \times 108$), and an exit grid ($35 \times 95 \times 11$). Each of the three domains were connected together through grid attaching to form the complete model. Summing the nodes in each block yields an overall node count of 119,174. The interface grid was "pinched" at one end to accommodate modeling of the upstream portion of the inlet splitter vane. To facilitate the top and bottom splitter vanes in the exit grid, internal objects were used. Figure 7 shows how arbitrary grid connectivity was utilized to improve mesh quality in the inlet section. Shown is a view of the inlet grid along section A-A in Fig. 6. A single structured grid has been constructed by blocking out along two grid lines and performing six internal grid connection. Precise grid control in the near-wall region and improved overall grid orthogonality was achieved by using this "butterfly" mesh arrangement instead of the simpler "H" type grid.

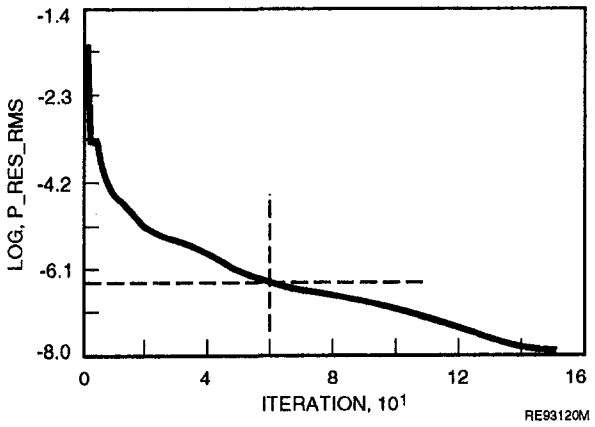


Fig. 8 Convergence history

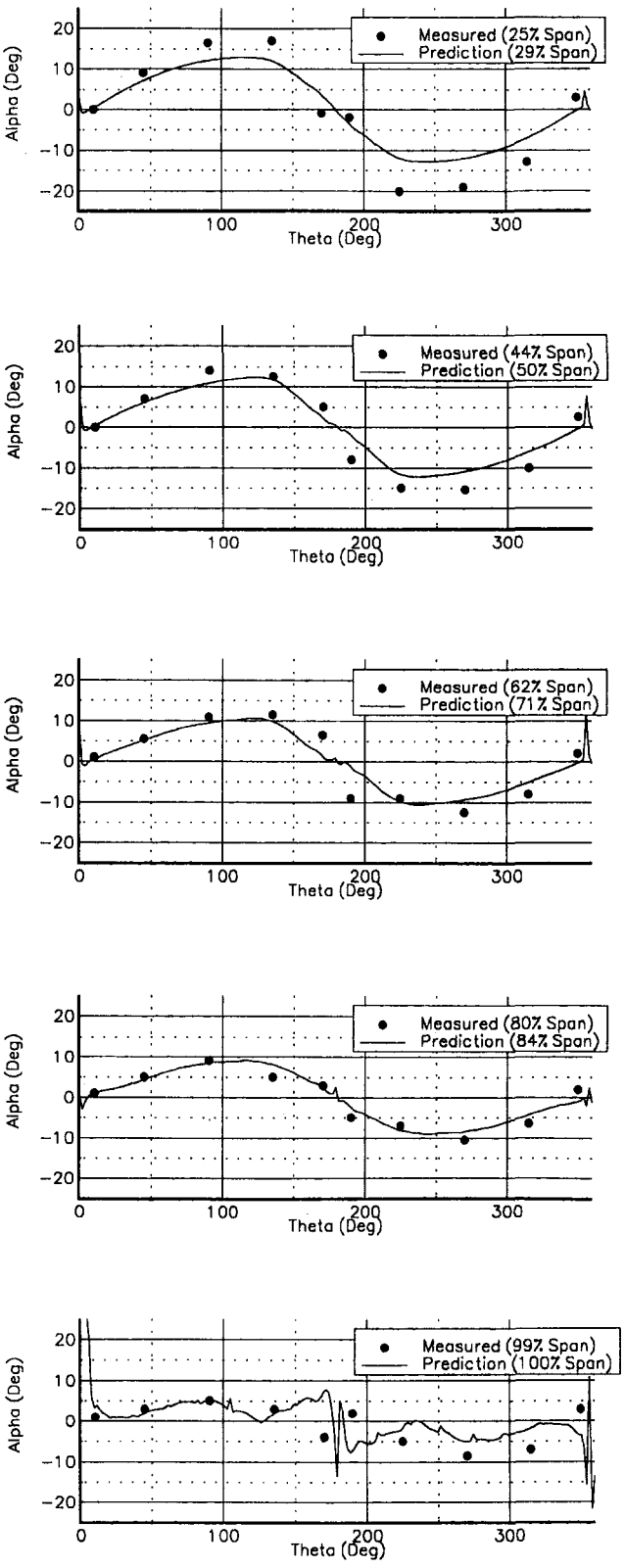


Fig. 9(A) Computational versus experimental results: flow angle

The TrueGrid mesh generator was used to generate the grids for this calculation interactively. It is capable of building multiple block structured parts and is designed to import CAD geometry. TrueGrid employs the projection method to mold a block mesh to the desired shape. The first step in this process is to define a rectangular block structured mesh. The corners of the

Downloaded 01 Jun 2010 to 171.66.16.53. Redistribution subject to ASME license or copyright; see http://www.asme.org/terms/Terms_Use.cfm

blocks are then moved close to their final positions. They only need to be close since the projection onto the surfaces will position them exactly. This initial position of a corner is required for the same reason one must supply an initial estimate to a nonlinear solver to find a local minimum. In the next step, faces of the mesh are assigned to surfaces, invoking the projection algorithm. This projection method first moves each corner of the grid to the intersection of the required surfaces. The projection method automatically interpolates the edges of the grid and projects them to the required surfaces. Similarly, faces are interpolated and projected.

There are numerous advantages to the projection technique. The geometry and the topology are independent. The geometry

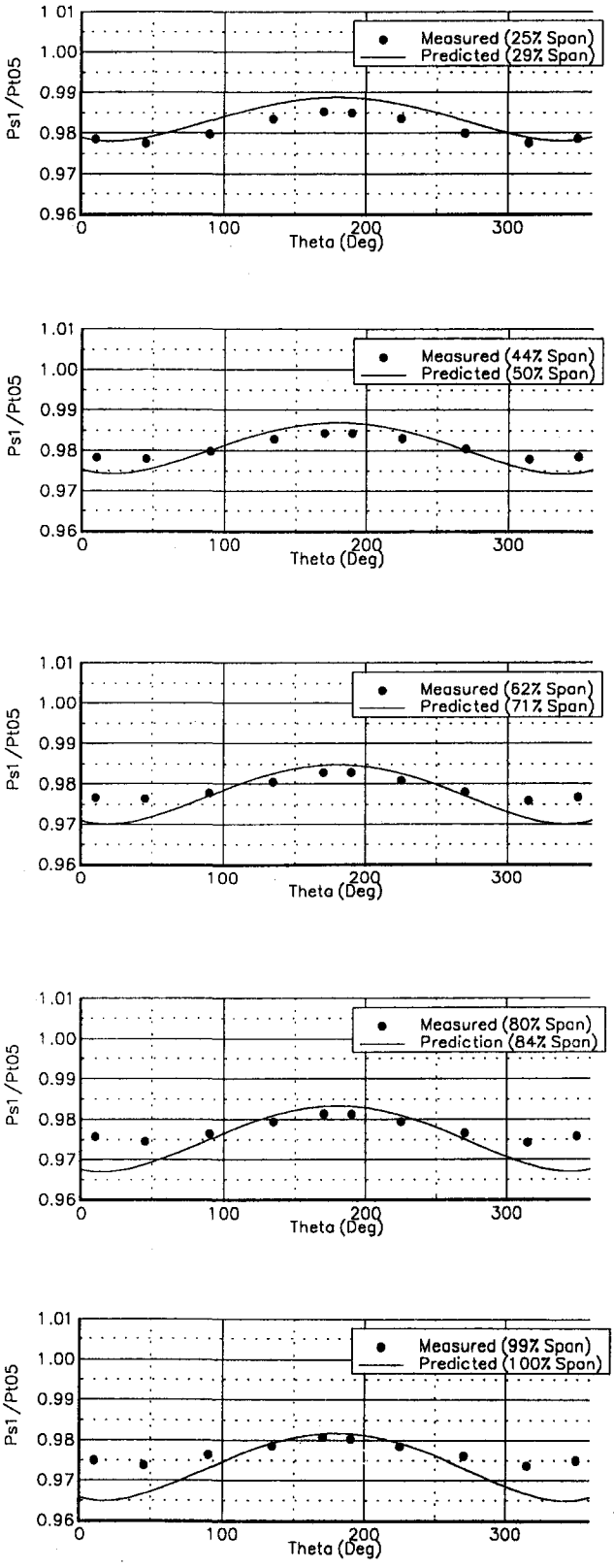


Fig. 9(B) Computational versus experimental results: static pressure

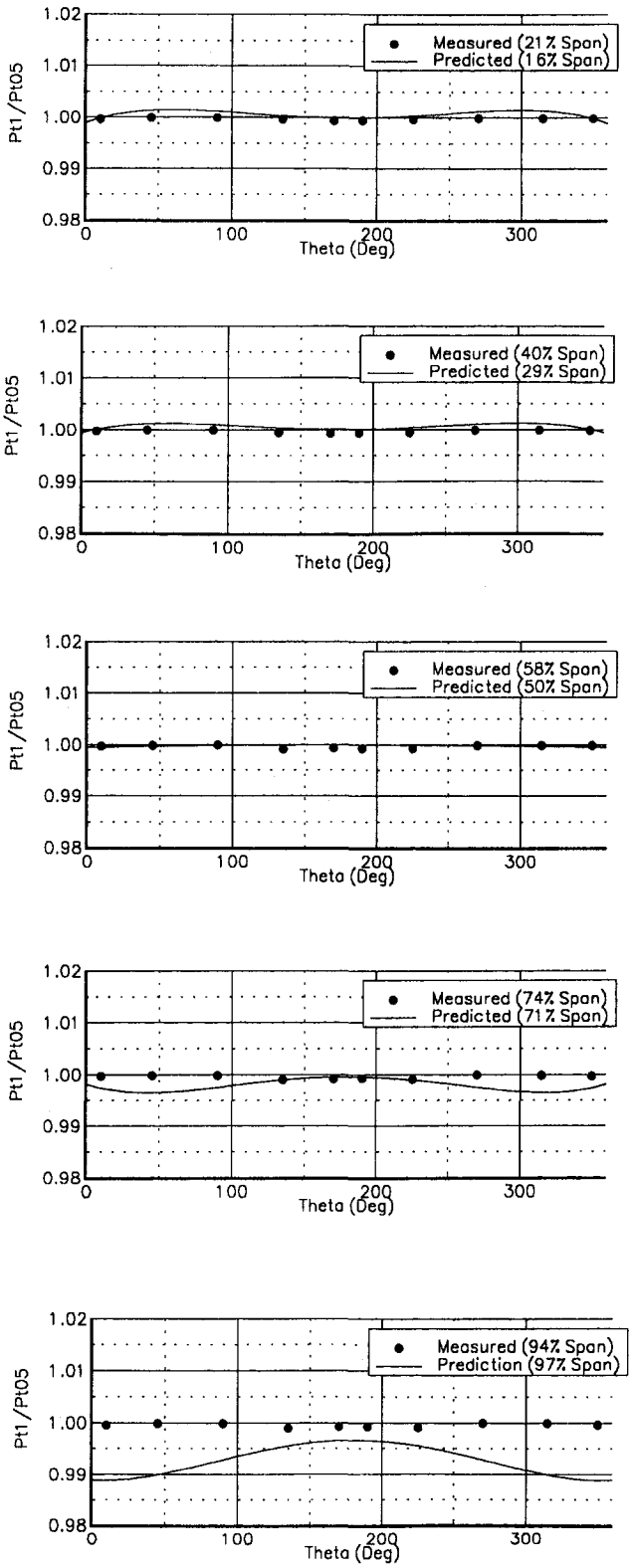


Fig. 9(C) Computational versus experimental results: total pressure ratio

Downloaded 01 Jun 2010 to 171.66.16.53. Redistribution subject to ASME license or copyright; see http://www.asme.org/terms/Terms_Use.cfm

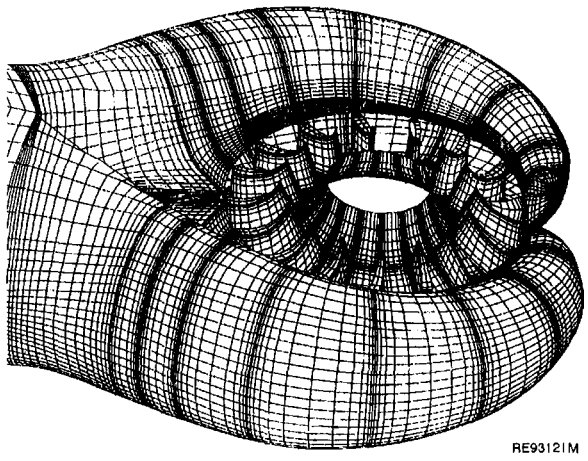


Fig. 10 Computational model: vaned

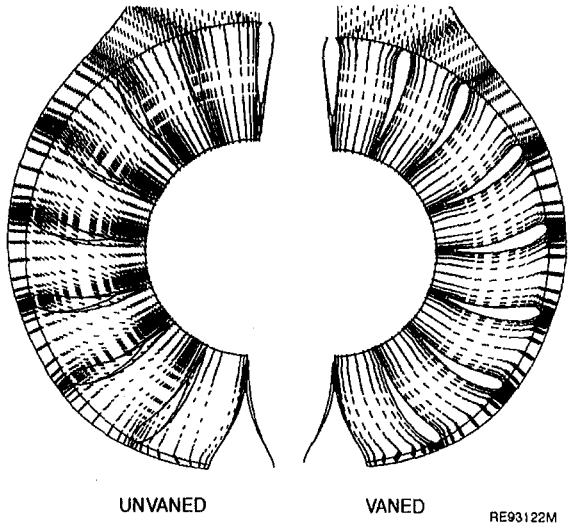


Fig. 11 Velocity vectors vaned versus unvaned

or the topology can be modified without affecting the other. This means the geometry can be built without regard to the topology of the grid. It is possible to have small gaps between surfaces or for surfaces to overlap without consequence. When surfaces are combined and have a gap between them, a node of the mesh is simply projected to the closest point of both surfaces, disregarding the gap. If a node is projected to the intersection of two surfaces that do not meet, the surfaces are automatically extended tangentially and intersected. Thus no intersecting curves are required for the grid. These features reduced the preparation needed in the geometry to create a grid.

The surface and curve geometry for the inlet model was imported from the ComputerVision CADDS 4X data base via several IGES files. Some of the surfaces were combined in TrueGrid, forming composite surfaces, so that faces of the grid could transition smoothly from one surface to another. The top and bottom splitter vanes were defined by curves. Several additional curves were needed to place the edges of the grid along smooth contours crossing composite surfaces. These curves were also useful in aligning the initial grid before the faces of the grid were projected to the composite surfaces. Four additional curves were needed to position the interior edges of the butterfly structure of the grid. Particular care was taken to position the butterfly grid at the end of the torus-shaped portion of the inlet. No curves were needed to trim the surfaces or to locate the intersection of the surfaces since TrueGrid automatically calculates the intersection. The pinched region of the grid was easily obtained by initially placing two corners of the grid at the same location and then projecting both corners to the same surface. The block boundary feature in TrueGrid was used to guarantee that the interface between the grids matched.

Many features were added to this basic grid. The distributions of the nodes with clustering near boundaries and vanes were carefully selected by interactive experimentation. The Thomas–Middlecoff (1980) elliptic solver was used extensively to position the surface nodes between edges, across composite surfaces, and throughout the interior of the grid. This method produced nearly orthogonal grid lines near the boundaries and produced an ideal grid in the area where the grid transitioned from the pinched region to the neighboring regions. A short session file was automatically saved and run later in batch mode. This made it easy to experiment with different node clustering, number of relaxation iterations, and the number of nodes used in the grid. Interactive diagnostics in TrueGrid detected problem areas in the grid design, which were then corrected by interrupting the session file. The multiblock design of TrueGrid allowed generation of each of the three blocks within the same TrueGrid session. Grid output was in a form compatible with the TASCflow solver. Development took approximately three days.

Half-scale predictions were made at test conditions, 60 percent of design flow and ambient exit pressure (Re = 2.0e5), for direct comparison with data. All half-scale predictions were made using hydraulically smooth walls. Boundary conditions specified were consistent with the conditions given above. The inlet condition specified was mass flow and direction. The exit condition was static pressure at a single point.

Figure 8 presents the convergence characteristic typical of inlet calculations performed during this study. All cases were started from a uniform initial guess. As shown, the rms continuity residual was brought to machine roundoff in approximately 150 iterations. This took 32 hours CPU on an IBM 560 (RS/6000) workstation. Convergence is normally taken after a residual reduction of approximately 6-7 orders of magnitude. This level of convergence was reached after just 60 iterations, which took only 13 hours CPU time. From a design perspective, this rate of solution turnaround is rapid enough to make CFD a productive tool within the overall design process.

Comparisons to Experimental Results—Postdiction. Computational results are compared to experimental results in Fig. 9. A plane of nodes was located along the exact same plane that the measurements were taken; thus no axial interpolation was required. Nodes in the computational model, however, were not located at precisely the same spanwise position as the survey

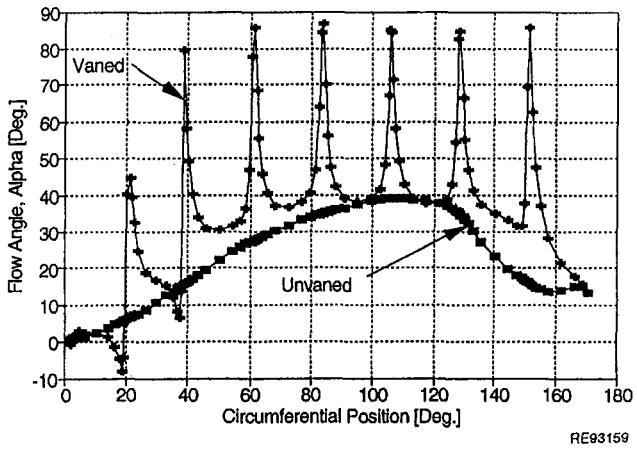


Fig. 12 Flow angle distribution, vaned versus unvaned

Downloaded 01 Jun 2010 to 171.66.16.53. Redistribution subject to ASME license or copyright; see http://www.asme.org/terms/Terms_Use.cfm

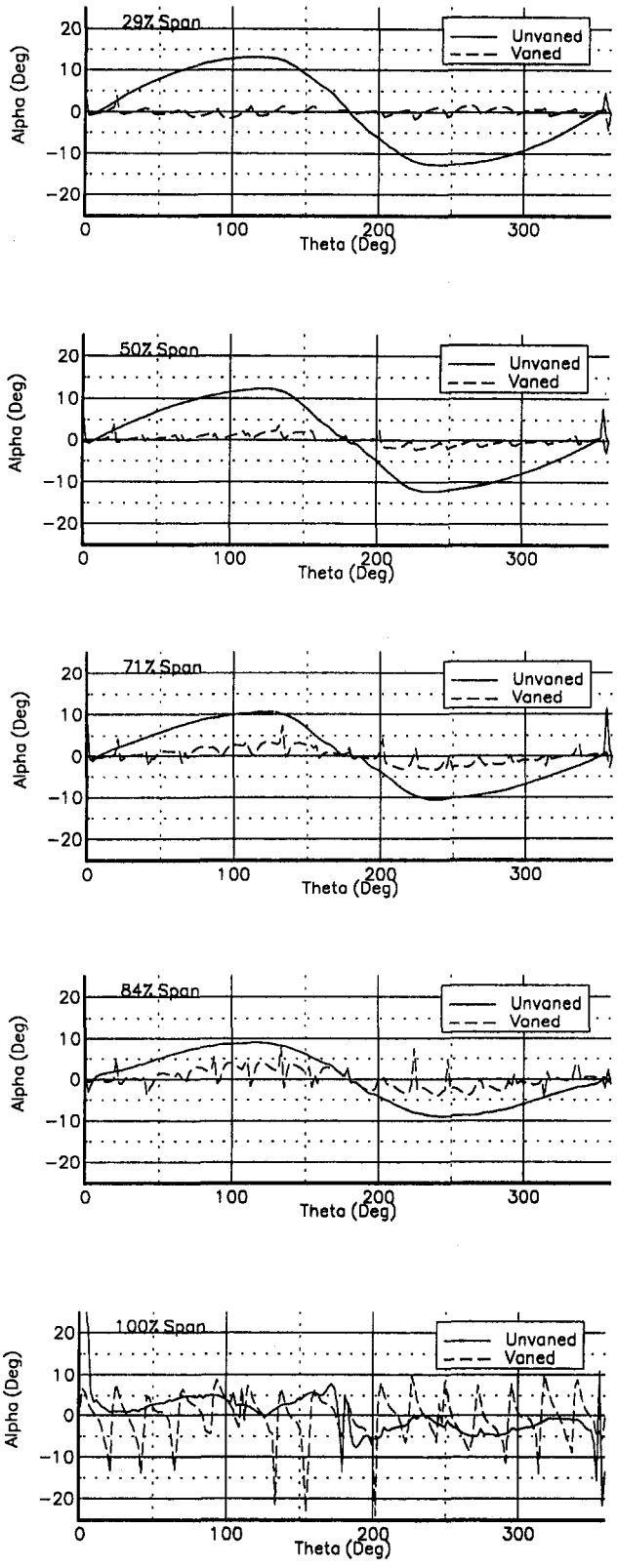


Fig. 13(*A*) Computational vaned versus unvaned, flow angle

probe in the experiment. Comparison, therefore, is made at the nearest span position, as indicated in the figure. Three parameters are compared: flow angle, static pressure ratio, and total pressure ratio. Static and total pressure have been normalized by the inlet total pressure at a position equivalent to experimental station 05. All quantities are plotted against circumferential position. The top splitter is located at 0 deg, the bottom at 180 deg. The experimental survey encompassed the full 360 deg. The numerical investigation assumed symmetry; therefore the results were mirrored for comparative purposes.

Flow angle predictions compared well with the experimentally measured distributions. The circumferential nonuniformities discovered experimentally have been predicted nicely

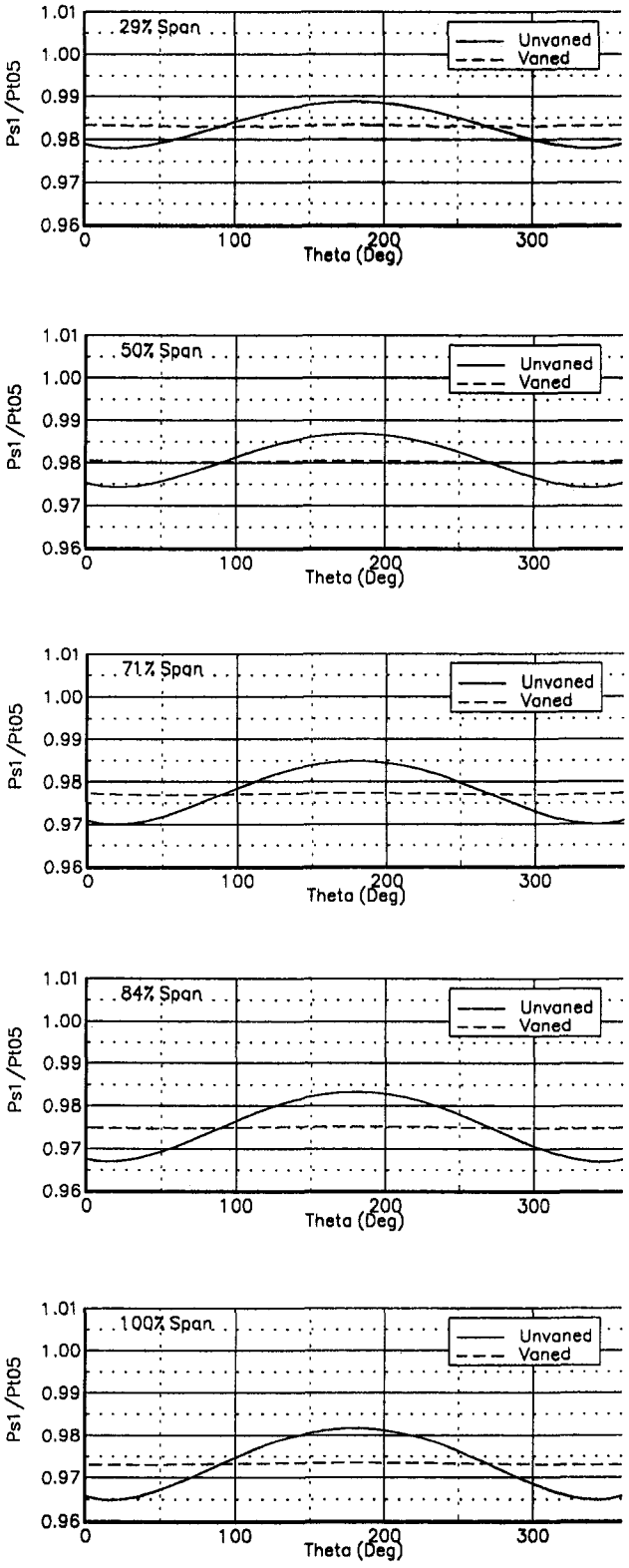


Fig. 13(*B*) Computational vaned versus unvaned, static pressure ratio

Downloaded 01 Jun 2010 to 171.66.16.53. Redistribution subject to ASME license or copyright; see http://www.asme.org/terms/Terms_Use.cfm

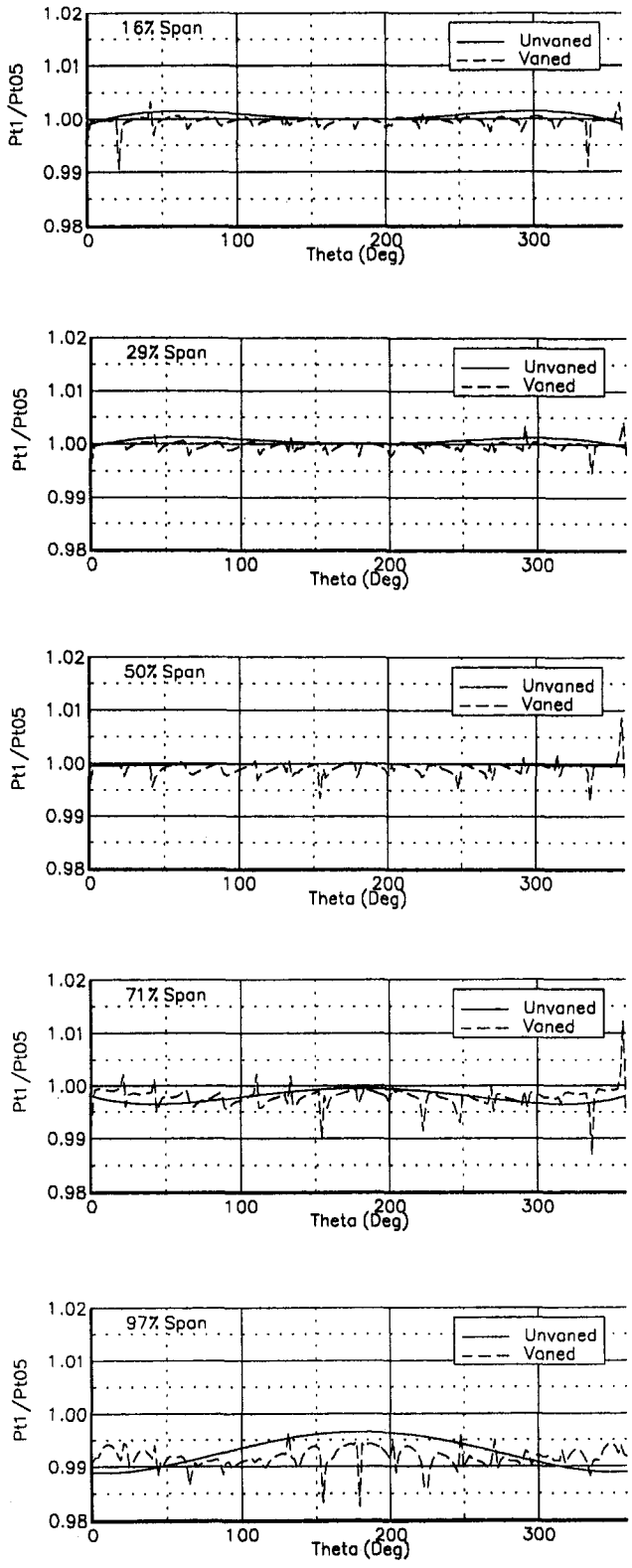


Fig. 13(C) Computational vaned versus unvaned, total pressure ratio

through numerical investigation. At 29 percent span, the predicted flow angle has a maximum variation of approximately ±13 deg from radial. If confidence in the CFD methodology had been established and the inlet computation been performed prior to the experiment, the design would have been modified and this configuration might not have been tested. Static pressure distributions also exhibit good overall agreement. In the shroud region, the calculation predicts a larger circumferential pressure gradient than experimentally measured. At the shroud (100 percent span), where the deviation is the largest, the pressure difference is only 1 percent of inlet total pressure. Similarly with total pressure, agreement is good in near the hub but begins

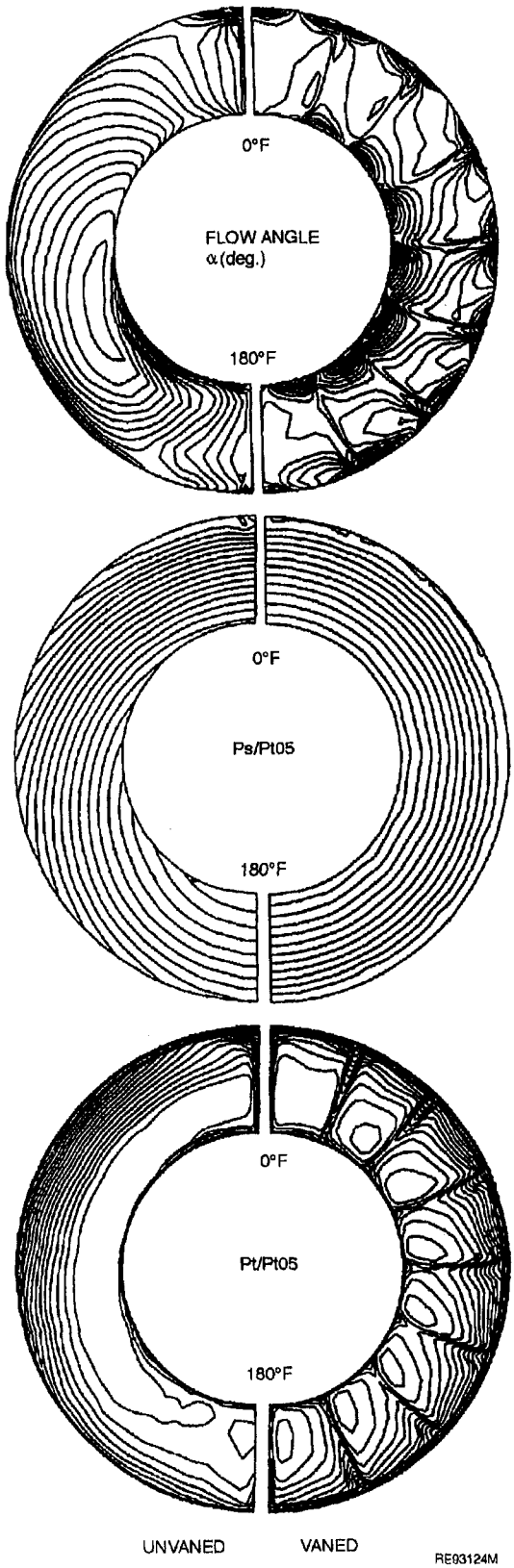


Fig. 14 Vaned versus unvaned discharge contours

Downloaded 01 Jun 2010 to 171.66.16.53. Redistribution subject to ASME license or copyright; see http://www.asme.org/terms/Terms_Use.cfm

to deviate toward the shroud. The computation appears to overpredict total pressure near the hub between splitters and underpredict total pressure near the shroud, especially in the top half of the inlet.

In fact, it is important to note that the circumferential differences in total pressure are extremely small (maximum of 1 percent of inlet total pressure). The loss from station 05 to the measurement plane is also extremely low. Computed mass average total pressure loss is only 0.25 percent of inlet total pressure. These low levels of loss and circumferential pressure gradients make the job of experimentalist and analyst extremely challenging.

Vaned Inlet

The model used to compute flow in the vaned inlet is shown in Fig. 10. It has been mirrored graphically to show both sides of the inlet. Exactly the same topology and node count was used for this case as was used during the previous calculation. Three structured grids were again connected together to form the complete model. Inlet and interface grids for this case are identical to the previous case in both node count, and node distribution. Only the exit grid has been altered to include the additional vanes.

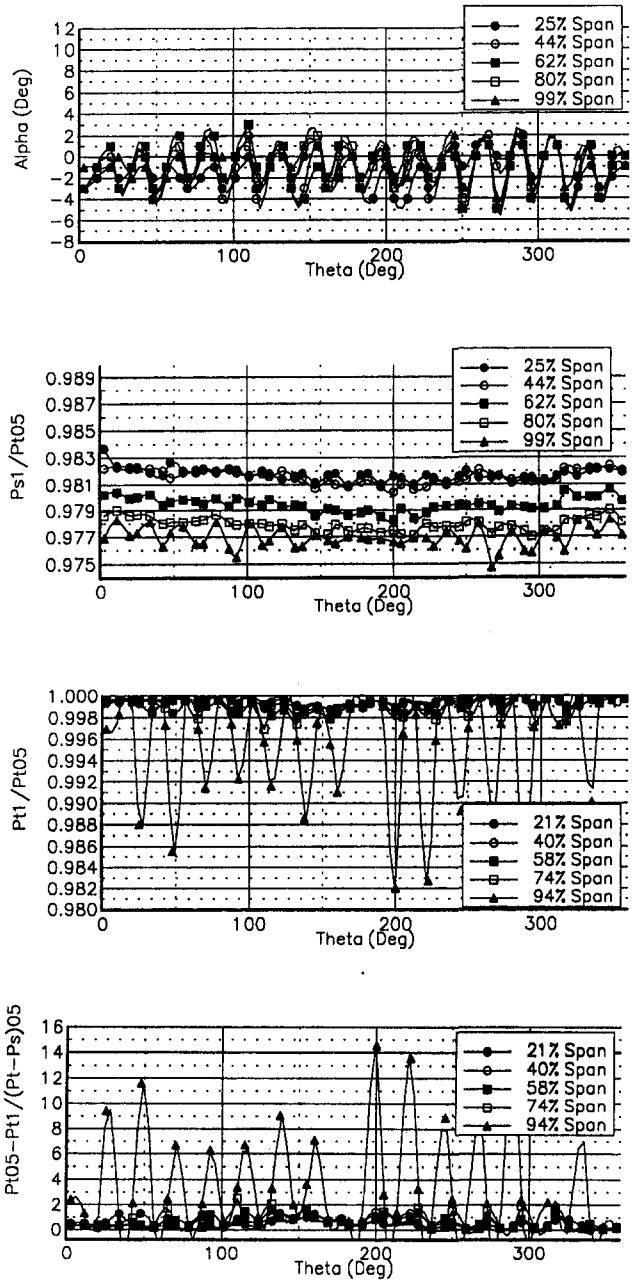


Fig. 15 Vaned experimental results

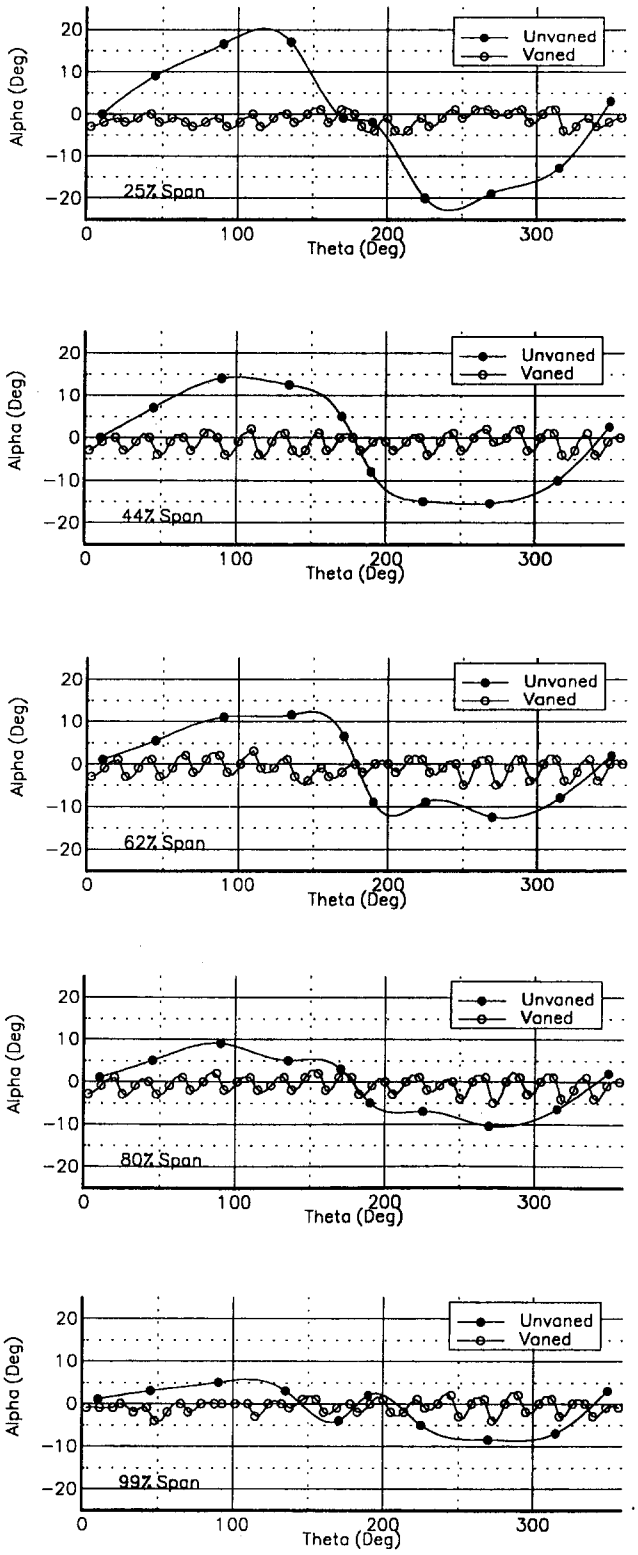


Fig. 16(A) Experimental vaned versus unvaned, flow angle

Comparisons to Unvaned Case—Numerical. Figure 11 shows the resultant velocity vectors for both the unvaned and

Downloaded 01 Jun 2010 to 171.66.16.53. Redistribution subject to ASME license or copyright; see http://www.asme.org/terms/Terms_Use.cfm

vaned inlets. Recalling that the IGV's were specified based on the unvaned experimental results, the vaned velocity vector plot indicates reasonable incidence levels and no major flow field anomalies. However, superimposing the IGV's on the unvaned velocity vector plot indicates that an improved turning schedule would have been selected based on the CFD results rather than the experimental results. This is more easily seen in Fig. 12, which shows the swirl angle distribution just upstream of the

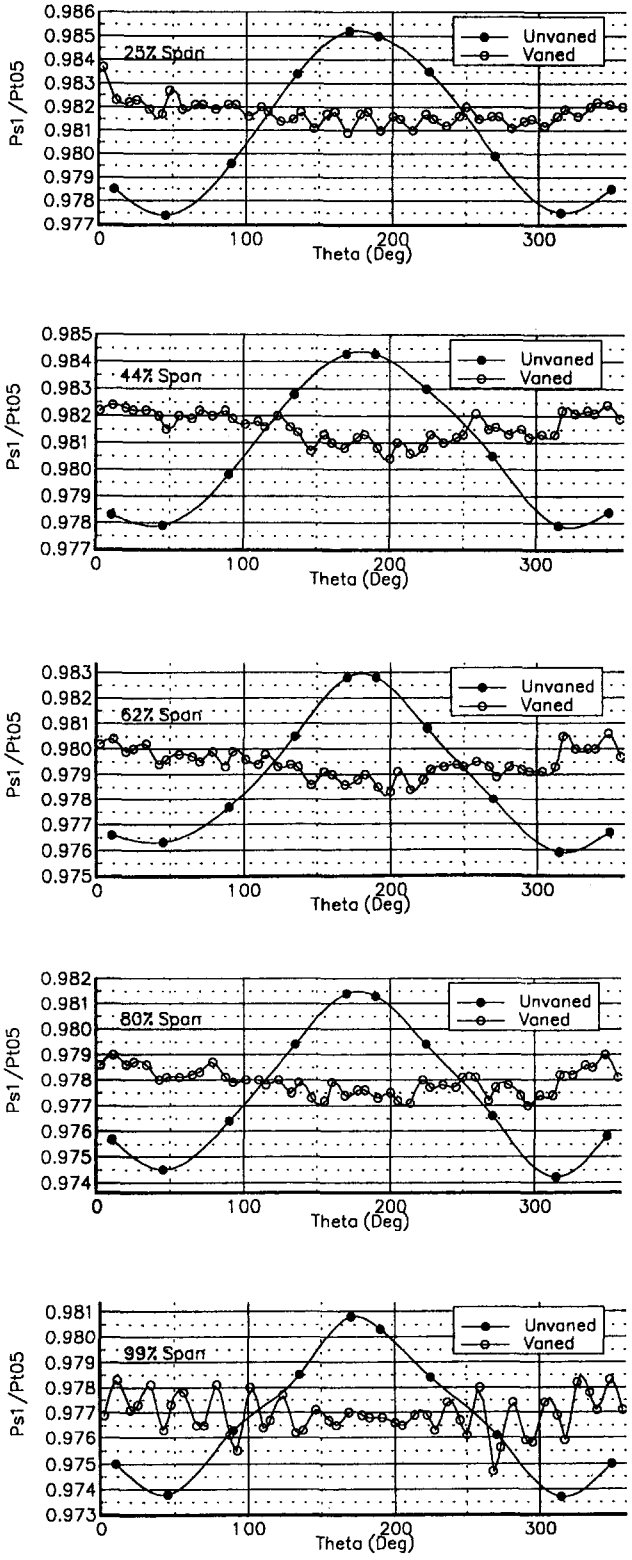


Fig. 16(B) Experimental vaned versus unvaned, static pressure ratio

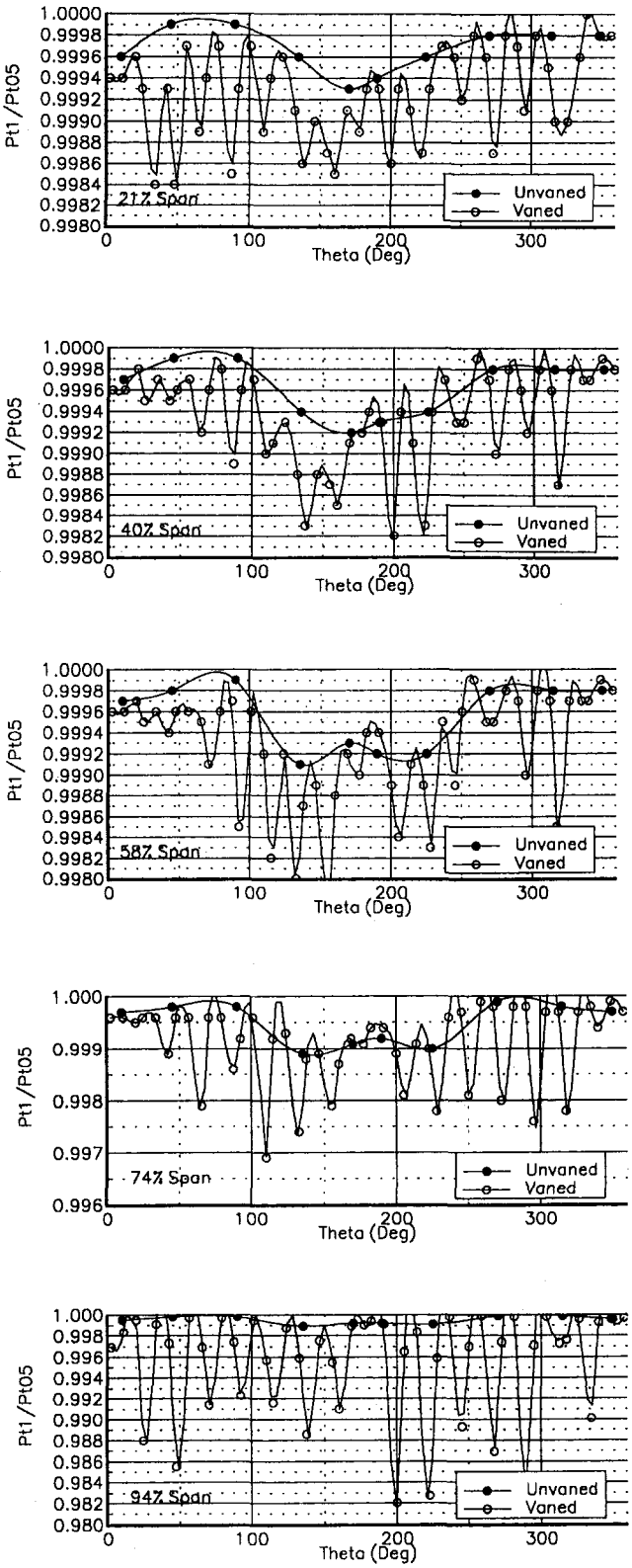


Fig. 16(C) Experimental vaned versus unvaned, total pressure ratio

IGV leading edge. Although fewer cambered vanes would be superior, the accelerating flow field and large radius leading edge result in acceptable performance.

Numerical predictions for the previous unvaned inlet geometry are compared to those of the vaned inlet in Fig. 13. The primary goal of incorporating additional vanes in the axisymmetric section of the inlet was to straighten out the flow nonunifor-

Downloaded 01 Jun 2010 to 171.66.16.53. Redistribution subject to ASME license or copyright; see http://www.asme.org/terms/Terms_Use.cfm

mity discovered both experimentally and numerically without increasing total pressure loss significantly. The calculation indicates that both goals have been achieved. Figure 14 shows discharge contours of flow angle, static, and total pressure ratio contours for both vaned and unvaned configurations. Static pressure distribution in the circumferential direction is flat and maximum flow angle has been reduced from 13 deg to approximately 2 deg, excluding wakes. Over the majority of the passage the flow angle is essentially axial. Total pressure distribution indicates only a moderate decrease in total pressure at discharge. Numerically, a mass-averaged loss calculation for the vaned and unvaned inlets indicates that total pressure loss has only been increased by 11 percent as a result of the additional vanes.

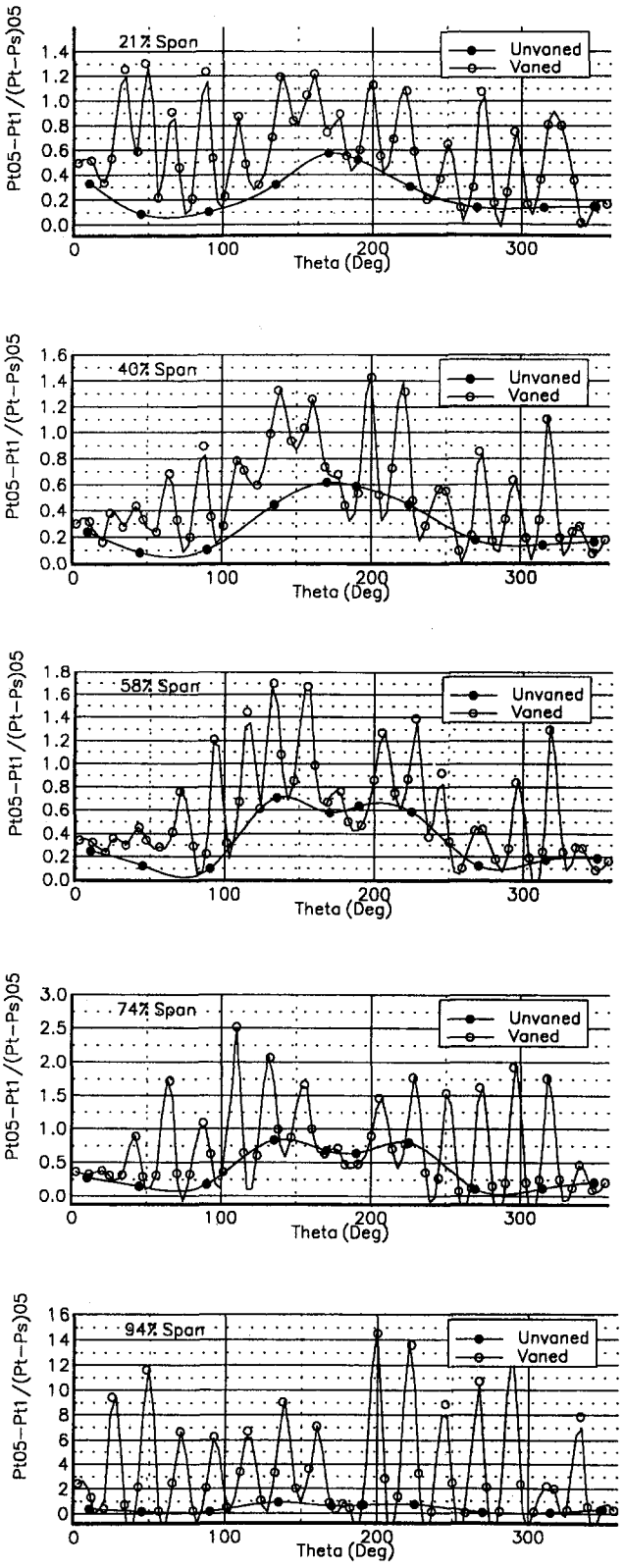


Fig. 16(*D*) Experimental vaned versus unvaned, loss coefficient

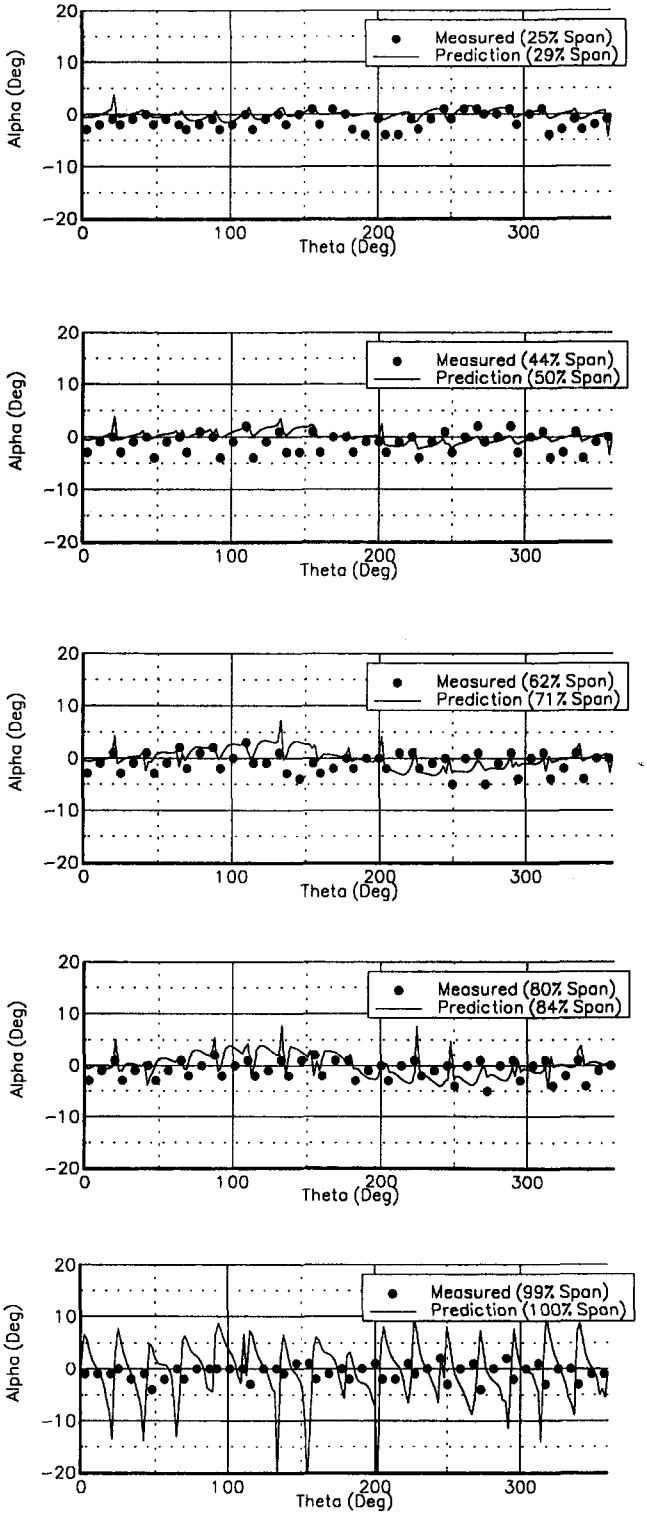


Fig. 17(*A*) Experimental versus computational vaned, flow angle

Comparisons to Unvaned Case—Experimental. The same experimental procedure was used for the vaned inlet case except that more circumferential locations were measured.

Downloaded 01 Jun 2010 to 171.66.16.53. Redistribution subject to ASME license or copyright; see http://www.asme.org/terms/Terms_Use.cfm

Three circumferential measurements for each vane-to-vane passage were taken and no measurements were made behind the vane trailing edge. The measurements were taken at 2.5, 11.25, and 20 deg over the 22.5 deg span between the pressure-to-suction side. Figure 15 shows the swirl angle, static pressure, total pressure, and loss coefficient results for the vaned inlet. Comparisons to the unvaned inlet for these parameters are shown in Fig. 16. The removal of unwanted swirl is evident in the swirl angle comparisons. The static pressure comparisons indicate a more uniform profile while the total pressure and loss comparisons show only modest increases in losses. As with the unvaned case, an accurate mass-averaged loss coefficient is not possible with a small experimental database, but is estimated to be 140 percent of entry dynamic head, which is slightly above design intent. The experimental results confirm that the addition of the IGV's yields a nearly swirl-free, uniform flow at the discharge with only a moderate penalty in total pressure loss.

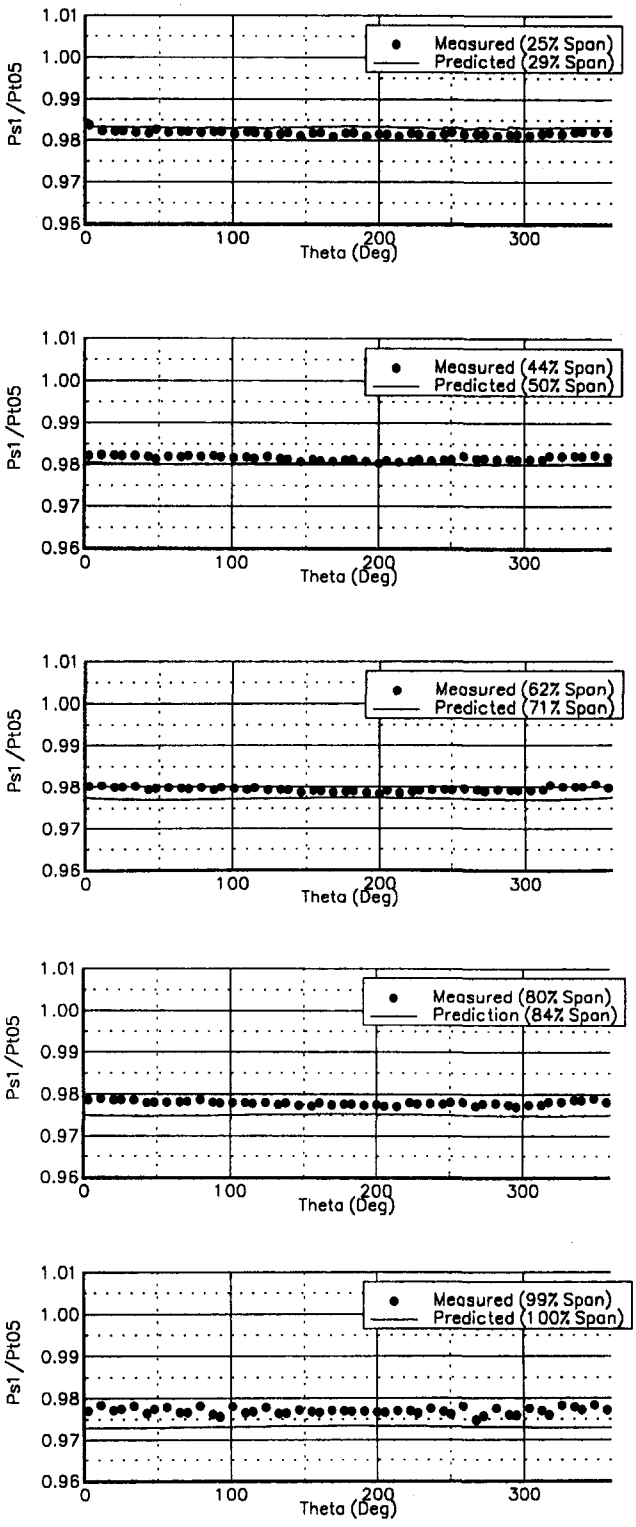


Fig. 17(B) Experimental versus computational vaned, static pressure ratio

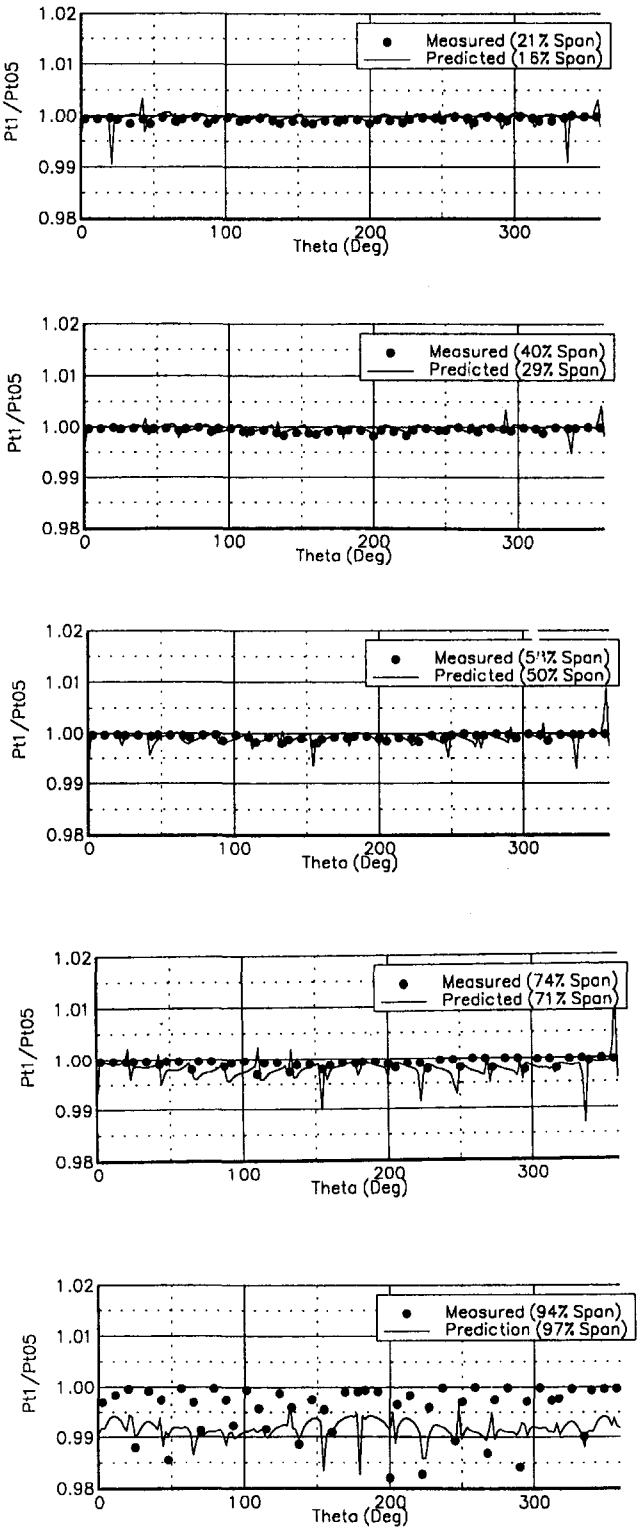


Fig. 17(C) Experimental versus computational vaned, total pressure ratio

Downloaded 01 Jun 2010 to 171.66.16.53. Redistribution subject to ASME license or copyright; see http://www.asme.org/terms/Terms_Use.cfm

Comparisons to Numerical Results—Prediction. The same comparisons between experimental and computational results for the unvaned configuration (Fig. 9) is made for the vaned configuration in Fig. 17. The calculations were made prior to testing, thus this represents a true prediction. Flow angle, static pressure distribution, and total pressure distribution are all compared. Agreement with data is very encouraging. As with the unvaned case, flow angle is reasonably well predicted, even though the effect of the vane wakes is evident. Static pressure ratio shows good agreement while total pressure ratio is slightly underpredicted (i.e., more total pressure loss) toward the shroud. The overall agreement is quite satisfactory considering the static and total pressure ratios, as with the unvaned configuration, are very small. Although the loss level is small, it is higher than the unvaned case, and subsequently the numerical prediction for the vaned case is more accurate.

Conclusions

The present work, to the best of our knowledge, is the first time that a fully three-dimensional viscous code has been applied to a complex three-dimensional radial inlet for an industrial centrifugal compressor and its results compared to experimental data. The major conclusions are as follows.

The computational results agree well with the experimental findings for both the unvaned (postdiction) and vaned (prediction) configurations, especially considering the complex geometry, modest node count, and lack of extensive measurements. Swirl angle and static pressure ratio are well predicted while total pressure ratio is underpredicted toward the shroud. The total pressure ratio prediction is superior for the vaned case due to the generally higher total pressure loss level. Since the actual level of total pressure loss is so low, agreement might be improved with more nodes or more experimental data. However, from a designer's viewpoint, this would not lead to a different design direction.

Both experimental and computational findings indicated design deficiencies with the unvaned configuration. CFD might have led the designer to a superior IGV turning schedule for circumferential swirl variations rather than the schedule derived from the experimental results. However, the addition of inlet guide vanes removed swirl with only a modest increase in total pressure losses. This was confirmed with both computational and experimental investigations.

The results of this investigation clearly demonstrate the usefulness of CFD as a design tool. CFD, coupled with advanced grid generation techniques, offers a cost and schedule effective alternative to pure experimental methods. Although experimental verification is critical to product development, applied CFD can significantly reduce design iterations and therefore reduce time to market. Based on this work, future radial inlet geometries can be screened with CFD and the final configuration can be experimentally confirmed.

Acknowledgments

We would like to acknowledge the efforts of Bert Edlebeck, who developed the conceptual design, Tibby Tibiatowski for completing the CAD layout work, and Joel Otsuka for coordinating all of the experimental activities. Last, we would like to thank Solar Turbines Incorporated for permission to publish this paper.

References

Dawes, W. N., 1988, "Development of a 3D Navier–Stokes Solver for Application to All Types of Turbomachinery," ASME Paper No. 88-GT-70.

Galpin, P. F., Huget, R. G., and Raithby, G. D., 1986, "Fluid Flow Simulations in Complex Geometries," presented at the CNS/ANS Conference on Simulation Methods in Nuclear Engineering, Montreal, Canada.

Hutchinson, B. R., and Raithby, G. D., 1986, "A Multigrid Method Based on the Additive Correction Strategy," *Numerical Heat Transfer,* Vol. 9, pp. 511–537.

Hutchinson, B. R., Galpin, P. F., and Raithby, G. D., 1988, "Application of Additive Correction Multigrid to the Coupled Fluid Flow Equations," *Numerical Heat Transfer,* Vol. 13, pp. 133–147.

Schneider, G. E., and Raw, M. J., 1986, "A Skewed, Positive Influence Coefficient Upwind Procedure for Control Volume-Based Element Convection-Diffusion Computations," *Numerical Heat Transfer,* Vol. 8, pp. 1–26.

Thomas, P. D., and Middlecoff, J. F., 1980, "Direct Control of the Grid Point Distribution in Meshes Generated by Elliptic Equations," *AIAA Journal,* Vol. 18, No. 6, pp. 652–656.

Van Doormaal, J. P., Hutchinson, B. R., and Turan, A., 1986, "An Evaluation of Techniques Used to Accelerate Segregated Methods for Predicting Viscous Fluid Flow," AIAA Paper No. 86-1653.

Van Doormaal, J. P., Turan, A., and Raithby, G. D., 1987, "Evaluation of New Techniques for the Calculation of Internal Recirculating Flows," AIAA Paper No. 87-0059.

Downloaded 01 Jun 2010 to 171.66.16.53. Redistribution subject to ASME license or copyright; see http://www.asme.org/terms/Terms_Use.cfm

Inverse Design of Centrifugal Compressor Vaned Diffusers in Inlet Shear Flows

M. Zangeneh
Department of Mechanical Engineering,
University College London,
London, United Kingdom

A three-dimensional inverse design method in which the blade (or vane) geometry is designed for specified distributions of circulation and blade thickness is applied to the design of centrifugal compressor vaned diffusers. Two generic diffusers are designed, one with uniform inlet flow (equivalent to a conventional design) and the other with a sheared inlet flow. The inlet shear flow effects are modeled in the design method by using the so-called "Secondary Flow Approximation" in which the Bernoulli surfaces are convected by the tangentially mean inviscid flow field. The difference between the vane geometry of the uniform inlet flow and nonuniform inlet flow diffusers is found to be most significant from 50 percent chord to the trailing edge region. The flows through both diffusers are computed by using Denton's three-dimensional inviscid Euler solver and Dawes' three-dimensional Navier–Stokes solver under sheared in-flow conditions. The predictions indicate improved pressure recovery and internal flow field for the diffuser designed for shear inlet flow conditions.

Introduction

The requirement for high efficiency and compact size has led to a widespread use of vaned diffusers in centrifugal compressors. Despite this, there is as yet no systematic technique for the design of this important turbomachinery component. Part of the difficulty in designing vaned diffusers is the exit flow field from the impeller, which is highly nonuniform in both the axial and circumferential directions, as a result of the accumulation of low-momentum fluids on the shroud suction corner by the action of the secondary flows in the impeller. Although in the future it may be possible to design impellers with uniform exit flow (see, for example, Zangeneh et al., 1994), for most conventionally designed impellers the exit flow nonuniformity is present. In order to design efficient vaned diffusers with high pressure recovery, it is important to account for this nonuniform flow entering the diffuser.

Considerable detailed experimental work has been done in the previous decade (for example Senoo (1984), Inoue and Cumpsty (1984), and Dalbert et al. (1993), among others) to investigate the mixing of the impeller exit flow nonuniformity in a vaned and vaneless diffuser. One important conclusion from these studies is that the circumferential variation in the exit flow mixes out very rapidly and seems to have very little effect on the performance of the diffuser, while the axial variation in the exit flow field from the impeller persists well into the diffuser and has an appreciable adverse effect on the pressure recovery of the vaned diffuser.

To design diffusers with high pressure recovery it is therefore essential to account for the axisymmetric shear flow entering the diffuser. In the past there has been some attempt to account for the shear flow, by making appropriate changes to the diffuser geometry near the leading edge. One approach reported by Yoshinaga et al. (1980) was to cut a section (rectangular or triangular) from the vane leading edge. They found that the vane with the rectangular cut showed lower stage efficiency, while the vane with the triangular cut showed a slight improvement in stage efficiency. However, it was not clear why the vane shape used in the latter case resulted in improved stage efficiency. In another approach reported by Bammert et al. (1983), the vane inlet blade angle was adapted to the axial distribution of the impeller exit flow angle, resulting in a twisted vane geometry. The results show slightly improved stage efficiency as compared to a corresponding conventional cambered vane diffuser, but at lower rotational speed. There are some improvements in the flow range at low speed, although the range at high speed was reduced.

The problem with both of the above-mentioned approaches is that they attempt to account for the inlet shear flow by changing the vane leading edge geometry. This is far from ideal, especially as the shear flow generates strong secondary flows, which will have very significant effects on the flow field throughout the diffuser particularly near the trailing edge region; see for example Gregory-Smith et al. (1988) who investigated the effects of inlet shear flows on the flow field in an axial turbine cascade. Currently there are no methods available that can account for the effect of the inlet shear flow on the vane geometry.

In this paper a three-dimensional inverse design method is presented in which the geometry is designed for a specified circulation distribution in presence of inlet shear flows. The method is based on the approach of Hawthorne et al. (1984) to the design problem in which the blades are represented by sheets of vorticity whose strength is determined by a specified distribution of circumferentially averaged swirl velocity, or $r\bar{V}_\theta$ (directly related to the bound circulation $2\pi r\bar{V}_\theta$ and the blade loading) defined as:

$$r\bar{V}_\theta = \frac{B}{2\pi}\int_0^{2\pi/B} rV_\theta \, d\theta,$$

where B is the number of blades.

The original application of the method was confined to the design of two-dimensional cascades of infinitely thin blades in incompressible flow. The method has since been extended to the three-dimensional design of incompressible rectilinear cascades in irrotational flow by Tan et al. (1984). It was later applied to design of incompressible radial-inflow turbines by Borges (1990) using a finite difference approach and Ghaly (1990) using the finite element approach. The first extension

Contributed by the International Gas Turbine Institute and presented at the 39th International Gas Turbine and Aeroengine Congress and Exposition, The Hague, The Netherlands, June 13–16, 1994. Manuscript received by the International Gas Turbine Institute February 15, 1994. Paper No. 94-GT-144. Associate Technical Editor: E. M. Greitzer.

Copyright © 1996 by ASME

Downloaded 01 Jun 2010 to 171.66.16.53. Redistribution subject to ASME license or copyright; see http://www.asme.org/terms/Terms_Use.cfm

of this method to the design of mixed and radial flow turbomachines in compressible flow was reported by Zangeneh (1991). The method was applied to the design of a high (subsonic) speed radial-inflow turbine and appreciable improvements in efficiency over conventional impellers of identical size and design point were obtained (Zangeneh, 1990). This method has recently been applied to the design of centrifugal compressors using a viscous/inviscid interaction approach to account for entropy generation by viscous effects in the impeller; see Zangeneh (1994). An implementation of the compressible design approach based on the use of the direct potential flow solver of Jameson and Caughey (1977) has been recently reported by Dang (1993).

As a first stage in the development of a fully three-dimensional rotational (i.e., nonhomenthalpic) version of the inverse design method, in this paper we present an approximate approach for modeling the effect of the inlet shear flows. For this purpose we adopt the so-called "secondary flow approximation" (see Hawthorne, 1967) in which Bernoulli surfaces (or surfaces of constant stagnation enthalpy) are convected by the tangentially mean velocity field. The method is applied to the design of a generic diffuser in an inlet shear flow. The flow through this diffuser is computed (by using three-dimensional Euler and Navier–Stokes solvers) and is compared to the computed flow field through a corresponding diffuser designed for uniform inflow conditions, in order to establish the advantages and disadvantages of this approximate approach.

Inverse Design Method

In this section a brief description of the three-dimensional inverse design method is presented. The basic theory has been described in detail in most of the references given above (e.g., Tan et al., 1984; Zangeneh, 1991) and the reader should refer to these references for a more detailed description of the method.

In this design method, for simplicity, the blades are represented by a single sheet of vorticity, representing the mean camber line of the blades. The blade blockage effects are then accounted for by using a mean streamsurface thickness parameter in the continuity equation of the mean flow. Assuming that the flow is irrotational (and steady), the absolute bound vorticity can be expressed as:

$$\Omega_b = \nabla \times V = (\nabla r \bar{V}_\theta \times \nabla \alpha)\, \delta_p(\alpha), \tag{2}$$

where

$$\alpha = \theta - f(r, z) = n \frac{2\pi}{B}, \tag{3}$$

represents the blade surfaces, θ is the tangential coordinate of a cylindrical polar coordinate system and $f(r, z)$ is the angular coordinate of the point on the thin blade surface, or the mean camber angle. $\delta_p(\alpha)$ is the periodic delta function, whose pitchwise mean is unity, so that the tangentially mean bound vorticity is given by

$$\bar{\Omega} = \nabla \times \bar{V} = (\nabla r \bar{V}_\theta \times \nabla \alpha). \tag{4}$$

For a homentropic rotational (i.e., a nonhomenthalpic) upstream flow, Hawthorne and Tan (1987) state that the vorticity can be expressed by using the following expression:

$$\Omega = (\nabla r \bar{V}_\theta \times \nabla \alpha)\, \delta_p(\alpha) + (\nabla h_o \times \nabla \tau) \tag{5}$$

where h_o is the stagnation enthalpy (or stagnation pressure in incompressible flow) and τ is the drift function. However, closer inspection will indicate that this expression is inconsistent (refer to the appendix for more information), if used in a fully three-dimensional rotational flow. If we assume, however, that the shear flow is convected by the tangentially mean inviscid flow field, we obtain the following mathematically consistent expression for the vorticity field:

$$\Omega = (\nabla r \bar{V}_\theta \times \nabla \alpha)\, \delta_p(\alpha) + (\nabla \bar{h}_o \times \nabla \bar{\tau}) \tag{6}$$

This equation accounts for the stretching and twisting of the vortex filaments by the mean flow field, which results in a streamwise component of vorticity and therefore secondary flows. However, the effect of secondary velocities on the convection of Bernoulli surfaces and their resulting distortion is neglected in this case. This is equivalent to the approach used by Squire and Winter (1951) to account for secondary flows, which Hawthorne (1967) has labeled as the "secondary flow" or "small shear large disturbance approximation."

The method starts by using one-dimensional estimates of the meridional velocity obtained from the specified mass flow rate and meridional geometry together with the specified mean tangential velocity to compute an initial blade shape. The blade shape is computed by using the inviscid slip condition, which implies that the flow must be aligned to the blade surfaces. This condition can be expressed mathematically as:

$$\mathbf{V}_{bl} \cdot \nabla \alpha = 0. \tag{7}$$

where $\nabla\alpha$ is a vector normal to the blade surface and $\mathbf{V}_{bl}$ is the relative velocity at the blade surface ($\mathbf{V}_{bl} = (\mathbf{V}^+ + \mathbf{V}^-)/2$, where $\mathbf{V}^+$ and $\mathbf{V}^-$ are the velocities on the upper and lower surface of the blades). Expanding Eq. (7) we obtain

$$V_{zbl} \frac{\partial f}{\partial z} + V_{rbl} \frac{\partial f}{\partial r} = \frac{V_{\theta bl}}{r} \tag{8}$$

where f is the wrap angle. Equation (8) is a first-order hyperbolic partial differential equation, which has to be integrated along the meridional projections of streamlines on the blade surface in order to find the blade shape. The integration, as in the case of other initial value problems, cannot be completed without some initial condition on f. This initial value will be called the *stacking condition of the blade.* In this method the stacking condition is implemented by giving as input the values of blade wrap angle f along a quasi-orthogonal, for example at the leading edge.

Nomenclature

B = number of blades
f = blade camber angle (θ value at the blade)
h_o = stagnation enthalpy
r = radius
(r, θ, z) = cylindrical-polar coordinate system
U = blade speed
V = velocity
α = angular coordinate of blade surfaces (Eq. (3))
β = blade angle = $\tan^{-1}(-r\,\partial f/\partial m)$
$\delta_p(\alpha)$ = periodic delta function
τ = drift function
ω = rotational speed
Ω = vorticity

Subscripts

bl = at the blade
i = upstream boundary of the computational grid
m = meridional distance
r = radial component
z = axial component
θ = tangential component
2 = impeller exit

Superscripts

$\overline{(\ )}$ = pitchwise mean value
$+$ = relative to upper blade surface
$-$ = relative to lower blade surface

Downloaded 01 Jun 2010 to 171.66.16.53. Redistribution subject to ASME license or copyright; see http://www.asme.org/terms/Terms_Use.cfm

Once a value for the blade shape has been obtained, it is then possible to use Eq. (6) to determine the vorticity throughout the blade region, if values of $\bar{h}_o$ and $\bar{\tau}$ are known. These are computed by solving Eqs. (A7) and (A8) of the appendix, which are one-dimensional hyperbolic equations similar to Eq. (8). The initial conditions for $\bar{h}_o$ are given by the known stagnation temperature at the far upstream boundary while $\bar{\theta}$ is set to zero there. Equation (6) can then be used to compute the velocity field throughout the flow; see Hawthorne and Tan (1987) and Zangeneh (1991). The flow field is decomposed into tangentially mean and periodic components. A governing equation for the mean flow is obtained by using a Stokes streamfunction together with the tangential component of Eq. (6). The governing equation of the periodic flow is obtained by applying the continuity equation of the periodic flow to the Clebsch formulation for the velocity.

The flow field is computed by solving the governing equations of the mean and periodic flow (two-dimensional and three-dimensional Possion partial differential equations, respectively). For the solution of the governing equation of the periodic flow it is possible to express all three-dimensional flow variables in terms of a Fourier series in the tangential direction. As a result the three-dimensional Possion equation is reduced to a two-dimensional Helmholtz equation, which is then solved for each hamonic of the Fourier coefficients in the frequency domain. The use of a Fourier expansion in the tangential direction results in substantial savings in computational time and memory as the three-dimensional flow field is solved without the need for a grid in the tangential direction.

In computing the flow field for an inviscid flow, it is important to correctly satisfy the Kutta condition at the blade trailing edges. Now the enthalpy jump across the blades, in an irrotational flow or a rotational flow in which h_o is convected by the tangentially mean flow field (as in this case), can be shown (see Zangeneh, 1991) to be given by:

$$h^+ - h^- = \mathbf{V}_{bl} \cdot \nabla r\bar{V}_\theta \tag{9}$$

so the Kutta is satisfied by solving:

$$\mathbf{V}_{bl} \cdot \nabla r\bar{V}_\theta = 0 \tag{10}$$

at the trailing edge. The density is computed from the stagnation enthalpy using the appropriate perfect gas relations.

The partial differential equations for the flow field are solved numerically by using a finite difference approximation on a body-fitted coordinate system; see Zangeneh (1991) for more detail. Equations (6), (A7), and (A8) are also solved numerically by using a Crank–Nicholson type finite difference discretization.

Once a new estimate for the velocity field has been obtained, it is then possible to compute the new blade shape by using Eq. (8). This iterative process is then repeated until changes in blade shapes between two iterations fall below a certain given tolerance, usually taken as 10^{-5} rad.

In the method described above the flow was assumed to be homentropic. To account for the presence of entropy gradients in the flow as a results of viscous losses or shock waves, it is possible to use the method described by Zangeneh (1994).

Results

In this section, the application of the method to the design of a generic vaned diffuser is described.

Design Specification. The conditions used for this design were based on Eckardt's (1980) backswept impeller with a mass flow rate of 4.54 kg/s, a spanwise uniform inlet tangential velocity of 211.7 m/s and an inlet diffuser width of 26 mm. The leading edge of the diffuser was placed at $r/r_2 = 1.09$ and the trailing edge was placed at $r/r_2 = 1.466$. The design was carried out with 25 diffuser vanes.

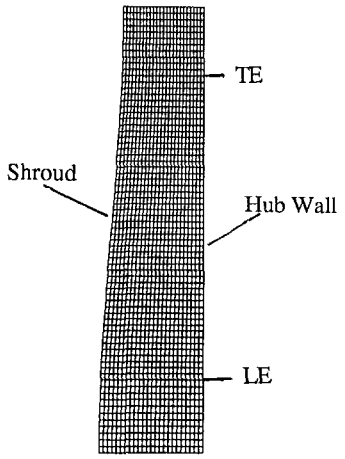


Fig. 1 Computational mesh (73 × 25)

In order to establish the effect of the inlet shear flow on the geometry of the diffuser vanes, two different designs were considered. In the first design (to be denoted as diffuser A) the vanes were designed for a uniform inlet flow angle of 66.9 deg. In the second diffuser design (to be designated diffuser B) a sheared inlet flow was assumed. For simplicity the radial velocity (nondimensionalized by the tip speed) at inlet was set to vary linearly from 0.2 at the shroud wall to 0.416 at the hub side. This distribution corresponds to a linear variation in inlet flow angle from 60 deg at the hub to 74.5 deg at the shroud. This distribution is fairly typical of the exit flow field from relatively high specific speed impellers in which secondary flows accumulate low-momentum fluids on the shroud wall, resulting in a radial velocity deficit there and an increase in velocity near the hub.

Apart from the inlet velocity (or flow angle) distribution, the design method requires four other important inputs: the meridional geometry, the rV_θ (or circulation) distribution, the stacking condition, and the thickness distribution. All these four inputs were kept the same for both designs in order to investigate the effect of the inlet flow field. For the thickness distribution, a constant tangential thickness (normalized by impeller tip radius r_2) of 0.02 was used. An axial stacking condition (constant f along the quasi-orthogonal) was applied at the trailing edge. The choice of meridional geometry and loading distribution, however, was to some extent interrelated.

It is a well-known fact that in most conventional designs the flow at exit is not turned to radial and the diffuser is designed for some amount of exit swirl (between 10–20 percent of inlet swirl). In this case, however, in order to maximize the pressure recovery, it was decided to design the diffuser for zero exit swirl and then compensate for the high loading and therefore diffusion (which may cause severe flow separation) by narrowing the diffuser width toward the trailing edge. For this purpose the meridional geometry shown in Fig. 1 was used. In this case the diffuser width at the leading edge was 26 mm, while the diffuser width at the trailing edge was reduced to 20 mm. The diffuser width between leading and trailing edges varied with radius according to a cubic distribution. The computational mesh used for the design consisted of 73 quasi-orthogonals (with 51 quasi-orthogonals inside the blade region) and 25 quasi-streamlines. As the variations in flow variables in the tangential direction are represented by a Fourier series no mesh is generated in the tangential direction.

Although the design method requires the $r\bar{V}_\theta$ (or circulation distribution) as input, it is in fact more convenient to specify the loading distribution or the meridional derivatives of $r\bar{V}_\theta$; see Zangeneh (1992) or Zangeneh et al. (1994) for more details. In this case a parabolic loading distribution was assumed at the

Downloaded 01 Jun 2010 to 171.66.16.53. Redistribution subject to ASME license or copyright; see http://www.asme.org/terms/Terms_Use.cfm

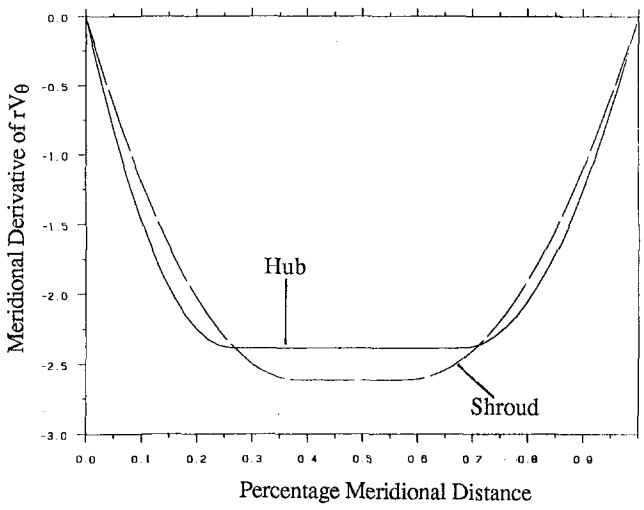
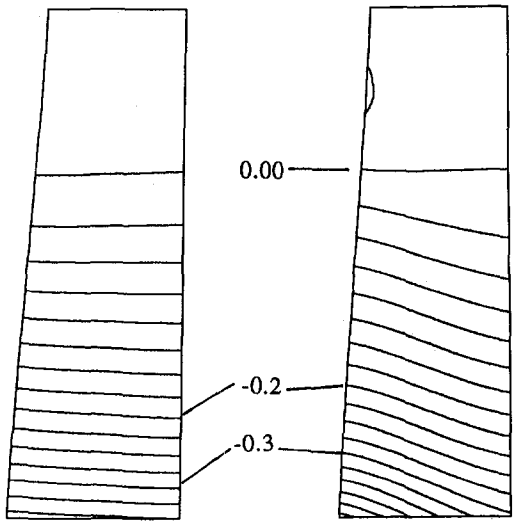


Fig. 2 Specified loading distribution

hub and shroud walls, shown in Fig. 2. The main reason for selecting this distribution was that it provides a fairly neutral loading distribution and does not place the point of maximum loading near the leading edge, as it seems to be common in conventional designs. The overall $r\bar{V}_\theta$ distribution was obtained by assuming a linear distribution between hub and shroud. The resulting $r\bar{V}_\theta$ distribution is presented in Fig. 6(a).

Designed Diffusers. Using these specifications, the two diffusers A and B were designed. The computed vane camber angle (f) distributions for the two designed diffusers are compared in Fig. 3, while the absolute differences in blade angles (i.e., $|\beta_B - \beta_A|$) of the two diffusers at a number of locations along the chord are presented in Table 1. From Fig. 3(a) it is possible to see that there is little variation of camber angle in the axial direction and the vane geometry is almost two dimensional, which is typical of most conventional diffuser designs. On the other hand the vane camber angle distribution for diffuser B (Fig. 3(b)) shows considerable variation in the axial direction. The largest difference in blade angles between the two diffusers (Table 1) occurs near the trailing edge, where secondary flow effects are more significant. The difference in blade angles near



(a) Diffuser A **(b) Diffuser B**

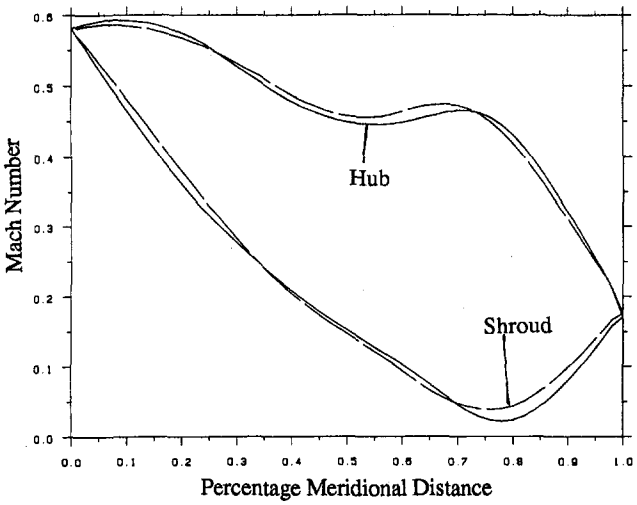
Fig. 3 Comparison of blade camber angle distribution f (contour interval = 0.025 rad)

Table 1 Absolute blade angle difference between diffuser A and diffuser B ($|\beta_B - \beta_A|$) (deg)

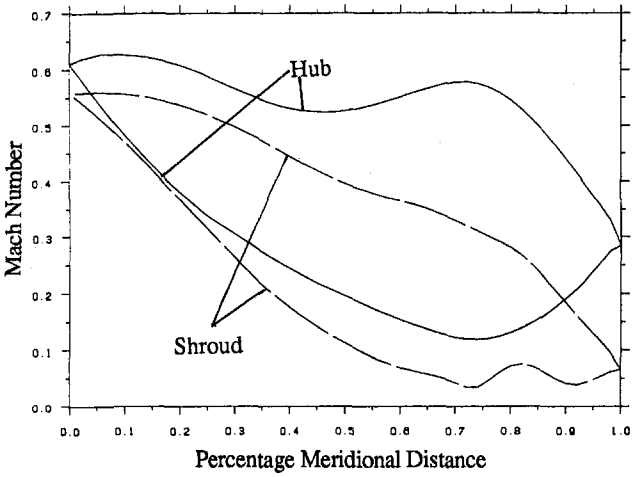
	L.E.	r/r2=1.19	r/r2=1.28	r/r2=1.38	T.E.
Hub	5.6	1.38	5.1	5.6	6.8
Shroud	6.9	2.0	2.77	22.9	26.42

the leading edge, although significant, is only about a quarter of that observed near the trailing edge.

The resulting Mach number distributions on the hub and shroud are presented in Fig. 4. The Mach number distributions on the hub and shroud of diffuser A (Fig. 4(a)) are almost identical. Figure 4(b) shows the considerable effect of inlet shear flow on the Mach number distribution particularly on the shroud wall as a result of the action of secondary flows. The resulting contours of mean stagnation enthalpy $\bar{h}_o$ (Fig. 5(a) and drift function $\bar{\tau}$ (Fig. 5(b)) as computed for diffuser B are presented in Fig. 5. As the stagnation enthalpy is computed from Eq. (A7), lines of constant enthalpy correspond to streamlines of the mean flow. Also shown in Fig. 5(c) are contours of drift function as computed for diffuser A, which had a uni-



(a) Diffuser A



(b) Diffuser B

Fig. 4 Mach number distributions

Downloaded 01 Jun 2010 to 171.66.16.53. Redistribution subject to ASME license or copyright; see http://www.asme.org/terms/Terms_Use.cfm

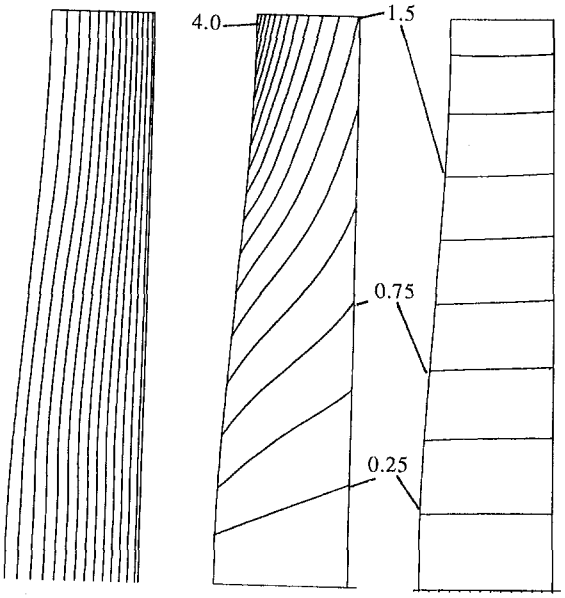


Fig. 5 Distribution of h_O and τ (τ normalized by impeller rotational speed, Interval = 0.25)

form inflow. The drift function represents the time taken by a fluid particle to move from a reference plane (i.e., the upstream boundary) to reach a particular point a given distance (along the streamline of the mean flow) away from the reference plane. It is, therefore, possible to see from Fig. 5 that as a result of the inlet rotational flow, a fluid particle starting at the shroud wall at inlet will take considerably longer than a particle starting at the hub wall to reach the outlet boundary.

Three-Dimensional Euler Solver Predictions. It was explained earlier that Diffuser B was designed by using the so-called "secondary flow approximation" in which the Bernoulli surfaces are assumed to be convected by the tangentially mean flow field and as a result all distortions in Bernoulli surfaces are ignored. In order to establish the limitations of this approximation, the flow through the designed diffusers was computed by using Denton's (1983) fully three-dimensional Euler solver. For these inviscid computations a grid consisting of 73 streamwise, 17 bladewise, and 17 spanwise stations was used. The bladewise and spanwise stations were uniformly spaced. For calculation of the flow through both diffusers the inlet boundary conditions were specified by fixing the inlet stagnation pressure, inlet stagnation temperature, and inlet flow angles used to design diffuser B (i.e., sheared inflow conditions).

The flow field computed by the Euler solver was processed to calculate the pitchwise-averaged rV_θ distribution. The resulting $r\bar{V}_\theta$ distributions for diffusers A and B are presented in Figs. 6(b) and 6(c). By comparing Fig. 6(b) with the specified $r\bar{V}_\theta$ distribution presented in Fig. 6(a), it is possible to conclude that the shear inlet flow has an appreciable effect on the diffuser blade circulation distribution, resulting in considerable distortion of the specified $r\bar{V}_\theta$ distribution. In the case of diffuser B (Fig. 6(c)), however, the computed $r\bar{V}_\theta$ distribution is very similar to that specified, in the region from leading edge up to about 50 percent chord. After 50 percent chord, appreciable distortion of the specified $r\bar{V}_\theta$ distribution can be observed.

The main reason for the discrepancy between the specified and computed circulation distribution for diffuser B can be attributed to the distortion of Bernoulli surfaces by secondary flows. This can be seen clearly by considering the contours of pitchwise-averaged stagnation temperature for diffuser B com-

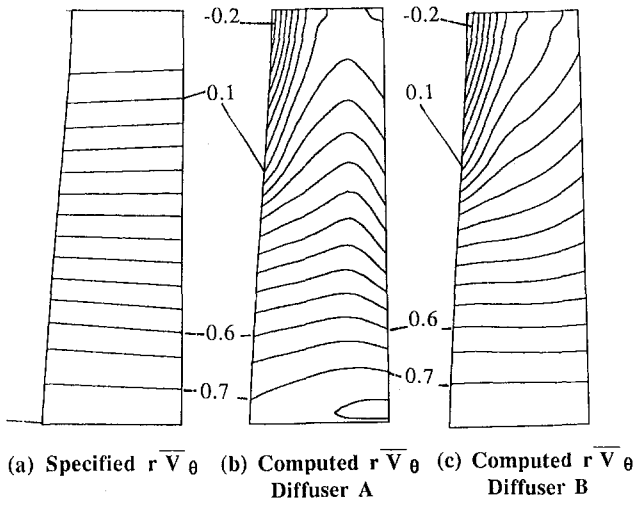


Fig. 6 Comparison of specified and computed $r\bar{V}_\theta$: three-dimensional Euler solver predictions (normalized by r_2U_2, contour interval = 0.05)

puted by the three-dimensional Euler solver, presented in Fig. 7(a). The results show clearly that the Bernoulli surfaces (i.e., surfaces of constant stagnation temperature, T_o) are not distorted in the first half of the diffuser, but distortions in T_o surfaces can be seen from 50 percent chord to the trailing edge, particularly near the shroud. This correlates well with the discrepency between the specified and computed circulation distribution for diffuser B. Contours of T_o on the suction and pressure surfaces, presented in Figs. 7(b) and 7(c), respectively, indicate a strong distortion of Bernoulli surfaces near the shroud, particularly on the pressure surface. As expected, this region of high distortion on the shroud pressure surface corresponds with the location of very strong blade-to-blade secondary flows. The velocity vec-

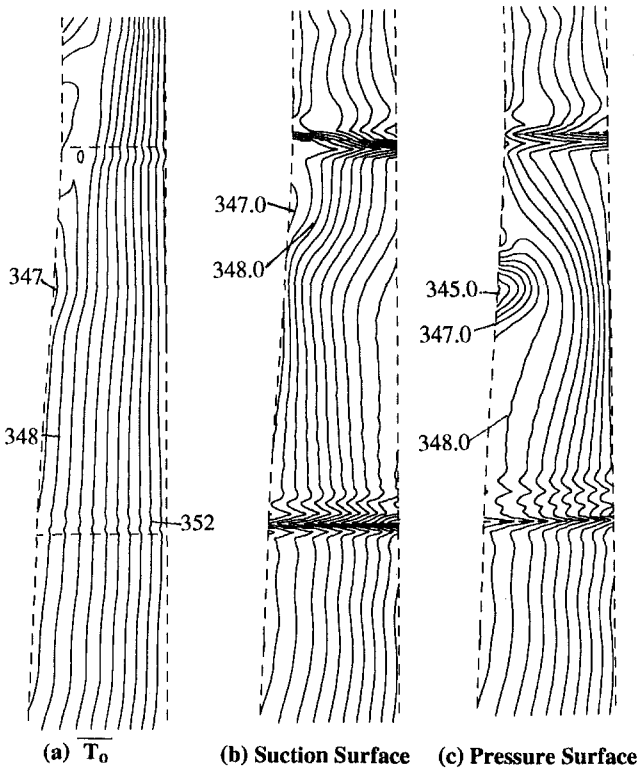


Fig. 7 Contours of stagnation temperature: Diffuser B Euler solver predictions (contour interval = 0.5 K)

Downloaded 01 Jun 2010 to 171.66.16.53. Redistribution subject to ASME license or copyright; see http://www.asme.org/terms/Terms_Use.cfm

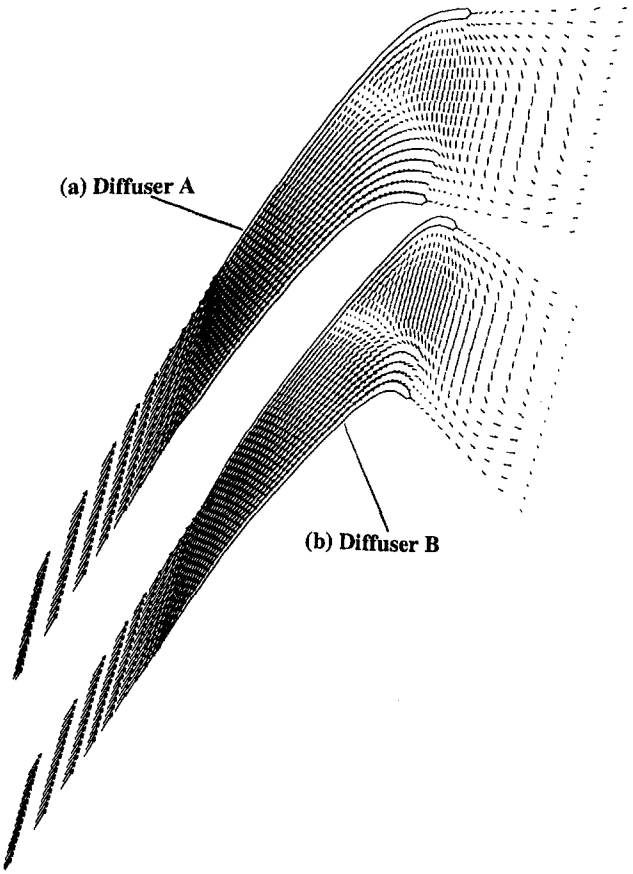
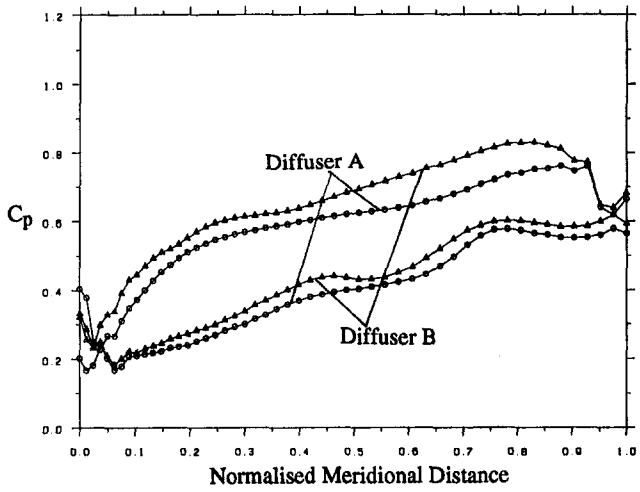


Fig. 8 Velocity vectors on the shroud endwall Euler solver predictions

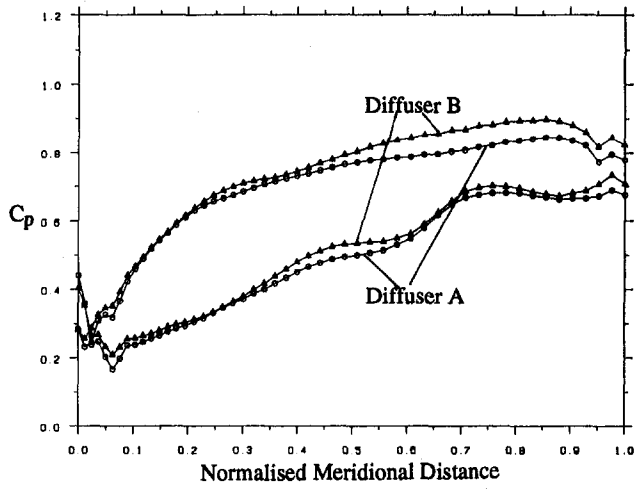
tors, computed by the Euler solver, on the shroud endwall of diffuser B are presented in Fig. 8(b). The velocity vectors show strong secondary flows moving low-momentum fluids from the pressure surface to the suction surface as well as secondary flows moving exactly in the opposite direction to the primary flow. When this latter secondary flow meets the primary flow, a stagnation point is created. The location of the stagnation point correlates closely with the region of high distortion in Bernoulli surfaces. The predicted secondary flow on the shroud endwall of diffuser A, presented in Fig. 8(a), is very similar to that of diffuser B.

Three-Dimensional Navier–Stokes Predictions. In the previous section the limitations of the approximate approach used to account for shear flow effects were considered with reference to three-dimensional Euler solver predictions. The purpose of this section is to establish whether this method provides any advantages over conventional methods in which the diffuser has a two-dimensional geometry. For this purpose the flow through both diffusers A and B will be computed by Dawes' (1988) three-dimensional Navier–Stokes solver. For the viscous computations a mesh consisting of 73 streamwise, 17 bladewise, and 17 spanwise stations was used. The grid points were clustered near the blade surfaces and the endwalls, in order to resolve the shear layers there. Again, both computations (for diffusers A and B) were performed under inlet shear boundary conditions used to design diffuser B. The exit pressure was varied until the design mass flow rate was obtained.

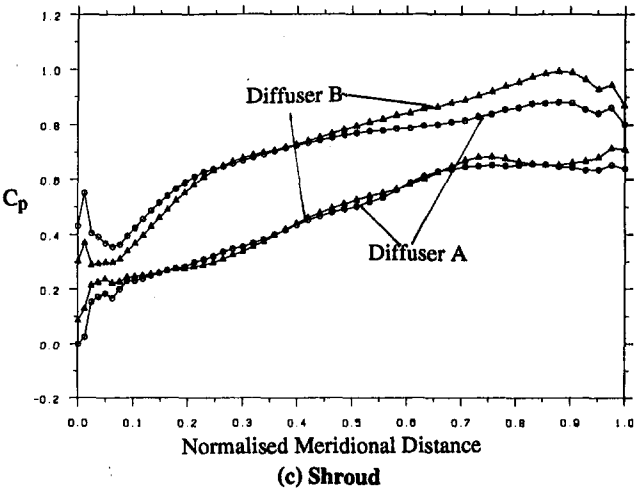
The predicted mixed-out losses (calculated from the mass-averaged entropy) for diffuser A was found to be 3.1 percent while the corresponding losses for diffuser B was only 2.1 percent. A better measure of diffuser performance, however, is the pressure recovery. To compare the overall pressure recovery of the two diffusers, a pressure recovery coefficient was defined as $C_{pr} = (p - p_i)/(P_{oi} - p_i)$ where P_{oi} and p_i are the reference stagnation and static pressures, respectively. In this case the reference values were taken at the midspan position at the far upstream boundary. A comparison of pressure recovery coefficients for the two diffusers at the hub, midspan and shroud is presented in Fig. 9. The results indicate clearly that the pressure recovery of diffuser B is significantly higher than that of diffuser



(a) Hub



(b) Mid-Span



(c) Shroud

Fig. 9 Comparison of predicted pressure recovery coefficient: viscous predictions

Downloaded 01 Jun 2010 to 171.66.16.53. Redistribution subject to ASME license or copyright; see http://www.asme.org/terms/Terms_Use.cfm

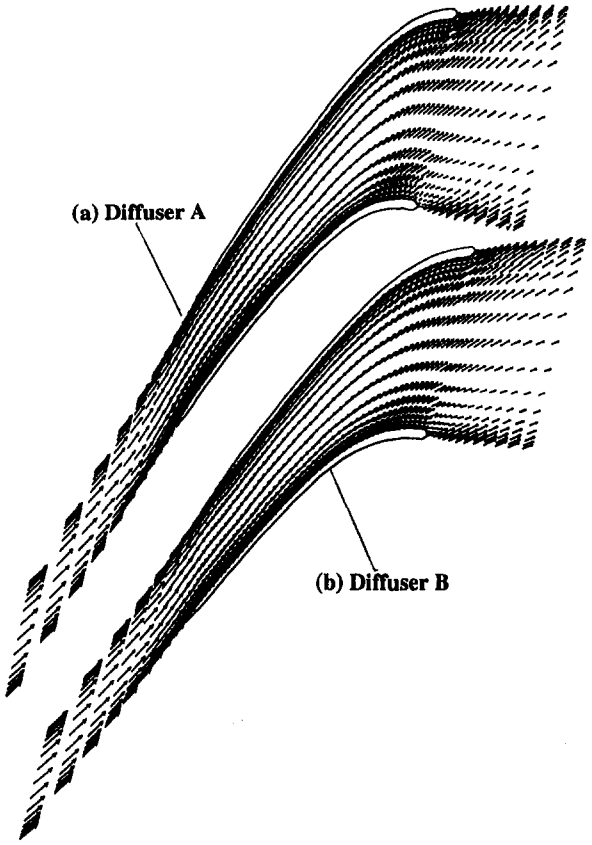


Fig. 10 Predicted velocity vectors near hub: viscous predictions

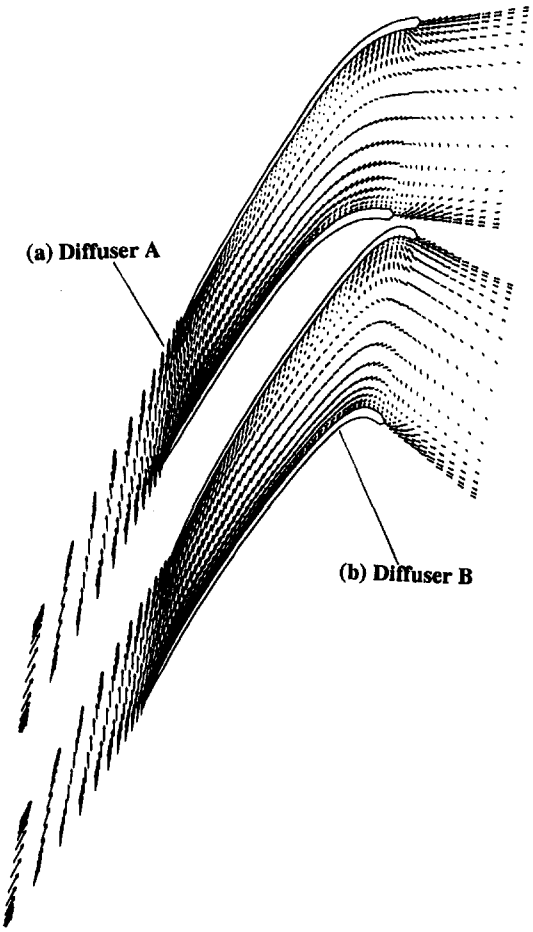


Fig. 11 Predicted velocity vectors near shroud: viscous predictions

A, which was designed for uniform inflow conditions. The improvement in the pressure recovery of diffuser B seems to be more significant in the region from 50 percent chord to the trailing edge, where the blade geometry of diffuser B is appreciably different from that of diffuser A (see Table 1). The results show a negative incidence at hub leading edge of diffuser A, while no significant incidence can be observed at the leading edge of diffuser B. At the shroud there is a large positive incidence at the leading edge of diffuser A, while the incidence has been reduced substantially in the case of diffuser B.

The main reasons for the higher pressure recovery and lower loss in diffuser B can be explained with reference to the velocity vector plots near the hub and shroud endwalls, presented in Figs. 10 and 11, respectively. The velocity vectors on the hub indicate a secondary flow near the trailing edge moving low-momentum fluid from the suction surface to pressure surface in the case of both diffusers. The velocity vectors on the shroud (Fig. 11) show secondary flow patterns very similar to that predicted by the Euler solver in the region near the trailing edge. The main difference between the viscous predictions for the two diffusers is in the extent of the almost stagnant region on the pressure surface of shroud endwall.

Finally the predicted mass-averaged exit tangential and radial velocities for diffusers A and B are compared in Fig. 12. The result indicates clearly that the exit velocity in the case of diffuser B is substantially lower than that predicted for diffuser A, thereby providing further evidence for the higher pressure recovery in diffuser B. The results also indicate that in both cases the specified zero exit swirl velocity has not been achieved. This is partly due to the high blade loading used for the designs, which results in strong secondary flows and sever reverse flow regions as shown in Fig. 11. Obviously the narrowing of the diffuser width has not provided sufficient compensation for the high blade loading to suppress reverse flow in the diffuser.

Conclusion

The three-dimensional inverse design method of Zangeneh (1991), in which the blade shapes are designed for a prescribed distribution of circulation, blade thickness, and meridional geometry, has been applied to the design of radial vaned diffusers for centrifugal compressors. The inverse design method has been extended to account for inlet shear flows entering the diffuser by using the so-called "secondary flow approximation"

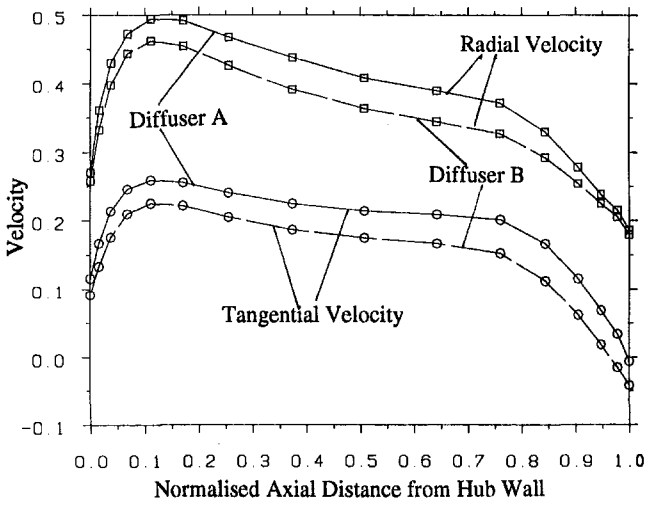


Fig. 12 Comparison of exit velocity distribution: viscous predictions, normalized by U_2

Downloaded 01 Jun 2010 to 171.66.16.53. Redistribution subject to ASME license or copyright; see http://www.asme.org/terms/Terms_Use.cfm

in which Bernoulli surfaces are convected by the tangentially mean inviscid flow field.

Two diffusers were designed using the inverse method, both with the same circulation distribution, thickness distribution, meridional geometry, and number of blades. Diffuser A was designed for uniform inflow, while diffuser B was designed for an inlet shear flow. The flow through both diffusers was analyzed by using an inviscid three-dimensional Euler solver and a three-dimensional Navier–Stokes solver under inlet shear flow conditions. From the results we can conclude that:

- The shear flow and the resulting secondary flows alter the specified circulation distribution on the blades. In the case of diffuser B the specified circulation distribution is altered only in regions of significant Bernoulli surface distortion, as a result of using the "secondary flow approximation" in the design method.
- There is a substantial difference in the vane geometry of diffuser B as compared to diffuser A, indicating that the effect of inlet shear flow is most significant away from the leading edge region. This is in contrast to previous work by many investigators in which they attempted to account for the inlet shear effects by changes to the vane geometry at the leading edge region.
- The predicted (from the N–S method) losses and pressure recovery of diffuser B show significant improvement over those of diffuser A, particularly in the region from 50 percent chord to trailing edge where there is an appreciable difference in vane geometry. The predictions also show improved incidence at the leading edge region of diffuser B.
- Despite narrowing the diffuser width toward the trailing edge, the diffuser performance was adversely affected by the high blade loading as a result of using zero exit swirl in the design.

The method presented in this paper provides an efficient and systematic means for the design of centrifugal compressor vaned diffusers. However, to account fully for the shear flow effects, it is essential to model the effect of distortion of Bernoulli surfaces by the secondary velocities. An incompressible version of the design method that accounts for Bernoulli surface distortion has already been developed and work is now in progress to extend the method to compressible flow.

Acknowledgments

The author would like to thank Professor J. D. Denton and Dr. W. N. Dawes of Whittle laboratory at Cambridge University (UK) for making their computer programs available for the present study.

References

Bammert, K., Jansen, M., and Rauternberg, M., 1983, "On the Influence of the Diffuser Inlet Shape on the Performance of a Centrifugal Compressor Stage," ASME Paper No. 83-GT-9.

Borges, J. E., 1990, "A Three-Dimensional Inverse Design Method in Turbomachinery: Part I—Theory," ASME JOURNAL OF TURBOMACHINERY, Vol. 112, pp. 346–354.

Dalbert, P., Gyarmathy, G., and Sebestyen, A., 1993, "Flow Phenomena in a Vaned Diffuser of a Centrifugal Stage," ASME Paper No. 93-GT-53.

Dang, T. Q., 1993, "A Fully Three-Dimensional Inverse Method for Turbomachinery Blading in Transonic Flows," ASME JOURNAL OF TURBOMACHINERY, Vol. 115, pp. 354–364.

Dawes, W. N., 1988, "The Development of a 3D Navier–Stokes Solver for Application to All Types of Turbomachinery," ASME Paper No. 88-GT-70.

Denton, J. D., 1983, "An Improved Time Marching Method for Turbomachinary Flow Calculations," ASME *Journal of Engineering for Power,* Vol. 105, p. 514.

Eckardt, D., 1980, "Flow Field Analysis of Radial and Backswept Centrifugal Compressor Impellers—Part I. Flow Measurements Using a Laser Velocimeter," *Performance Prediction of Centrifugal Pumps and Compressors,* Gopalakrishnan, ed, ASME, pp. 77–86.

Ghaly, W. S., 1990, "A Parametric Study of Radial Turbomachinery Blade Design in Three-Dimensional Subsonic Flow," ASME JOURNAL OF TURBOMACHINERY, Vol. 112, pp. 338–345.

Gregory-Smith, D. G., Graves, C. P., and Walsh, J. A., 1988, "Growth of Secondary Losses and Vorticity in an Axial Turbine Cascade," ASME JOURNAL OF TURBOMACHINERY, Vol. 110, pp. 1–8.

Hawthorne, W. R., 1954, "Rotational Flow Through Cascades," *Quarterly J. of Mech. and Applied Math.,* Vol. 8, pp. 266–292.

Hawthorne, W. R.,'1967, "The Applicability of Secondary Flow Analyses to the Solution of Internal Flow Problems," *Fluid Mechanics of Internal Flow,* Elsevier.

Hawthorne, W. R., Tan, C. S., Wang, C., and McCune, J. E., 1984, "Theory of Blade Design for Large Deflections: Part I—Two Dimensional Cascades," ASME *Journal of Engineering for Gas Turbines and Power,* Vol. 106, pp. 346–353.

Hawthorne, W. R., and Tan, C. S., 1987, "Design of Turbomachinery Blading in 3D Flow by the Circulation Method: A Progress Report," *ICIDES-II,* pp. 207–226.

Inoue, M., and Cumpsty, N. A., 1984, "Experimental Study of Centrifugal Compressor Impeller Discharge Flow in Vaneless and Vaned Diffusers," ASME *Journal of Engineering for Gas Turbines and Power,* Vol. 106, pp. 455–467.

Jameson, A., and Caughey, D. A., 1977, "A Finite-Volume Method for Transonic Potential Flow Calculations," *Proc. AIAA 3rd Computational Fluid Dynamic Conference,* pp. 35–44.

Senoo, Y., 1984, "Vaneless Diffusers and Vaned Diffusers," in: *Flow in Centrifugal Compressors,* VKI lecture series 1984-07.

Squire, H. B., and Winter, K. G., 1951, "The Secondary Flow in a Cascade of Aerofoils," *Journal of Aero Sciences,* Vol. 18, p. 271.

Tan, C. S., Hawthorne, W. R., Wang, C., and McCune, J. E., 1984, "Theory of Blade Design for Large Deflections: Part II—Annular Cascades," ASME *Journal of Engineering for Gas Turbine and Power,* Vol. 106, pp. 354–365.

Yoshinaga, Y., Gyobu, I., Mishina, H., Koseki, F., and Nishida, H., 1980, "Aerodynamic Performance of a Centrifugal Compressor With Vaned Diffusers," ASME *Journal of Fluids Engineering,* Vol. 102, pp. 486–493.

Zangeneh, M., 1990, "Three Dimensional Design of a High Speed Radial-Inflow Turbine by a Novel Design Method," ASME Paper No. 90-GT-235.

Zangeneh, M., 1991, "A Compressible Three Dimensional Blade Design Method for Radial and Mixed Flow Turbomachinery Blades," *Int. J. Numerical Methods in Fluids,* Vol. 13, pp. 599–624.

Zangeneh, M., 1992, "An Inverse Design Method for Radial Turbomachines," VKI Lecture Series, Radial Turbines, 1992-5.

Zangeneh, M., 1994, "Inviscid/Viscous Interaction Method for Three-Dimensional Inverse Design of Centrifugal Impellers," ASME JOURNAL OF TURBOMACHINERY, Vol. 116, pp. 280–290.

Zangeneh, M., Goto, A., and Takemura, T., 1994, "Suppression of Secondary Flows in a Mixed Flow Pump Impeller by Application of 3D Inverse Design Method. Part 1 Design and Numerical Validation," Paper No. 94-GT-44.

APPENDIX

Assume that the vorticity for a nonhomenthalpic (i.e., rotational upstream) flow is given by the following expression as suggested by Hawthorne and Tan (1987):

$$\Omega = \nabla \times \mathbf{V} = (\nabla r\bar{V}_\theta \times \alpha)\, \delta_p(\alpha) + (\nabla h_o \times \nabla \tau) \quad \text{(A1)}$$

where h_o is the stagnation enthalpy, which is known on the upstream boundary and can be calculated throughout the flow field by applying the energy equation, which in the absence of viscous effects can be expressed as:

$$\mathbf{V} \cdot \nabla h_o = o \quad \text{(A2)}$$

In the Eq. (A2) τ is the drift function (see Hawthorne, 1967), which represent the time taken for a fluid particle to move from a reference plane (usually taken as the upstream boundary) to reach a particular point in the flow a distance s along the streamline away from the reference plane

$$\tau = \int_o^s \frac{ds}{v}$$

$$\mathbf{V} \cdot \nabla \tau = 1 \quad \text{(A3)}$$

However, Eq. (A1) can be shown to be inconsistent on closer inspection. To show this, ho and τ are decomposed into circumferentially mean and periodic components, viz.,

$$h_o = \overline{h_o} + \tilde{h}_o$$

$$\tau = \bar{\tau} + \tilde{\tau}$$

Now taking the circumferential mean of both sides of Eq. (A1) we can see that the right-hand side takes the following form:

Downloaded 01 Jun 2010 to 171.66.16.53. Redistribution subject to ASME license or copyright; see http://www.asme.org/terms/Terms_Use.cfm

$$\bar{\Omega} = (\nabla r\bar{V}_\theta \times \nabla\alpha) + (\nabla\bar{h}_o \times \nabla\bar{\tau}) + (\overline{\nabla\tilde{h}_o \times \nabla\tilde{\tau}o}) \quad \text{(A4)}$$

The tangential component of Eq. (A4) is used to obtain the governing equation of the mean flow (see Zangeneh, 1991). So for Eq. (A1) to be consistent the r and z components of Eq. (A4) should equal the r and z components of $\nabla \times \bar{V}$. But:

$$e\hat{r} \cdot (\nabla \times \bar{\mathbf{V}}) = -\frac{1}{r}\frac{\partial r\bar{V}_\theta}{\partial z} \quad \text{(A5)}$$

while

$$\hat{e}r \cdot \bar{\Omega} = \frac{1}{r}\frac{\partial r\bar{V}_\theta}{\partial z} + \frac{1}{r}\left[\overline{\frac{\partial\tilde{\tau}}{\partial z}\frac{\partial\tilde{h}_o}{\partial\theta}} - \overline{\frac{\partial\tilde{\tau}}{\partial\theta}\frac{\partial\tilde{h}_o}{\partial z}}\right] \quad \text{(A6)}$$

Obviously the term in brackets on the right-hand side of Eq. (A6) is *not* zero and therefore Eq. (A1) is *inconsistent,* i.e., the clebsch scalar representing the bound vorticity in presence of fully three-dimensional shear flow is no longer $r\bar{V}_\theta$.

However, if we assume that the Bernouli surfaces (or surfaces of constant stagnation enthalpy) are convected by the tangentially mean flow then we can see that Eq. (A2) reduces to:

$$\mathbf{V} \cdot \nabla\bar{h}_o = o \quad \text{(A7)}$$

and similarly the drift function can be found from:

$$\bar{\mathbf{V}} \cdot \nabla\bar{\tau} = 1 \quad \text{(A8)}$$

and the expression for vorticity is reduced to:

$$\Omega = (\nabla r\bar{V}_\theta \times \nabla\alpha)\,\delta_p(\alpha) + (\nabla\bar{h}_o \times \nabla\bar{\tau}) \quad \text{(A9)}$$

This expression, which represents a "secondary flow approximation" to the shear flow problem, is *consistent.*

Downloaded 01 Jun 2010 to 171.66.16.53. Redistribution subject to ASME license or copyright; see http://www.asme.org/terms/Terms_Use.cfm

Detailed Stress Tensor Measurements in a Centrifugal Compressor Vaneless Diffuser

A. Pinarbasi

M. W. Johnson

Department of Mechanical Engineering,
University of Liverpool,
Liverpool, United Kingdom

Detailed flow measurements have been made in the vaneless diffuser of a large low-speed centrifugal compressor using hot-wire anemometry. The three time mean velocity components and full stress tensor distributions have been determined on eight measurement planes within the diffuser. High levels of Reynolds stress result in the rapid mixing out of the blade wake. Although high levels of turbulent kinetic energy are found in the passage wake, they are not associated with strong Reynolds stresses and hence the passage wake mixes out only slowly. Low-frequency meandering of the wake position is therefore likely to be responsible for the high kinetic energy levels. The anisotropic nature of the turbulence suggests that Reynolds stress turbulence models are required for CFD modeling of diffuser flows.

Introduction

Although the geometry of a vaneless diffuser is simple, the flow is complex due to the highly nonuniform three-dimensional flow, which is inherited from the centrifugal impeller. The features of the impeller outlet flow are well documented (e.g., Johnson and Moore, 1980; Eckardt, 1975; Inoue and Cumpsty, 1984). The flow, whether from a radial discharge or backswept impeller, invariably consists of a jet and a passage wake, although the position and size of the wake are dependent on flow rate and impeller geometry (Johnson and Moore, 1983; Farge and Johnson, 1992). The wake is usually located on the shroud, however, and is of sufficient size to have a strong influence on the diffuser flow. Strong secondary flows that develop in the impeller also persist in the diffuser. This is particularly true in backswept impellers where a strong passage vortex is induced (Krain 1988; Farge and Johnson, 1990). Wakes from the impeller blade trailing edges add to the complexity of the highly nonuniform three-dimensional flow that enters the diffuser.

In the vaneless diffuser, the nonuniformities mix out such that the flow closely resembles a Couette flow between the diffuser walls at the diffuser exit. The blade wakes are observed to mix out very rapidly while the passage wake only mixes out slowly (Inoue and Cumpsty, 1984; Maksoud and Johnson, 1987; Mounts and Brasz, 1992; Pinarbasi and Johnson, 1994). Mixing out is also more pronounced in the circumferential direction than in the axial direction. The Reynolds stresses play a dominant role in the mixing out process in the diffuser. The objective of the current work was to measure the Reynolds stresses in a vaneless diffuser with a view to improving the understanding and hence the modeling of the flow.

Experimental Procedure

A schematic of the low-speed centrifugal compressor rig used in the study is shown in Fig. 1. The impeller was a De Havilland Ghost impeller, the geometry of which is given by Johnson and Moore (1980). In the current study, the original radial outlet section was replaced to provide a 30 deg backswept outlet angle as shown in Fig. 2. The vaneless diffuser has straight walls and a constant cross sectional area. The geometry operating conditions and measurement stations are summarized in Table 1.

Contributed by the International Gas Turbine Institute and presented at the 39th International Gas Turbine and Aeroengine Congress and Exposition, The Hague, The Netherlands, June 13–16, 1994. Manuscript received by the International Gas Turbine Institute February 15, 1995. Paper No. 94-GT-227. Associate Technical Editor: E. M. Greitzer.

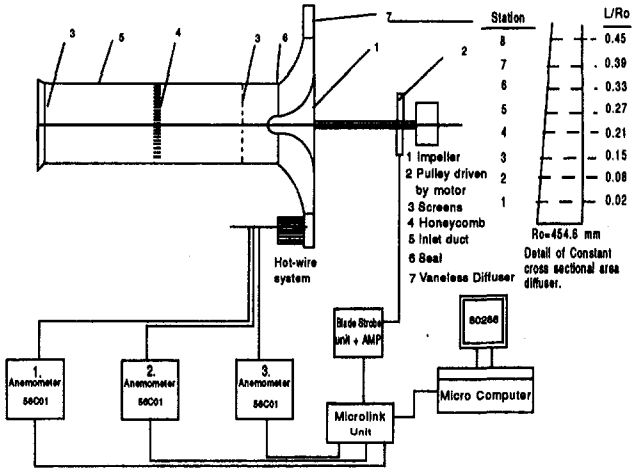


Fig. 1 Schematic of centrifugal compressor test rig

Instrumentation and Measurement Technique

Triple hot wires, which were utilized to measure the velocities within the diffuser, were arranged in a measurement volume of size 5 × 5 × 5 mm. A single wire probe (Dantec 55P11) was aligned circumferentially with a double wire probe (Dantec 55P61) arranged with each wire in the axial radial plane and at 45 deg to both the radial and axial directions. This mutually perpendicular arrangement of wires was therefore capable of

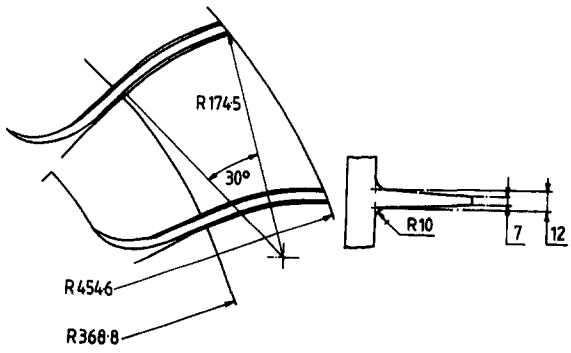


Fig. 2 Backswept impeller blade geometry

Copyright © 1996 by ASME

Downloaded 01 Jun 2010 to 171.66.16.53. Redistribution subject to ASME license or copyright; see http://www.asme.org/terms/Terms_Use.cfm

Table 1 Geometry, operating condition, and measurement locations

Impeller Geometry and Operating Condition:

Inlet blade radius at the hub	R_h = 88.75 mm
Inlet blade radius at the shroud	R_s = 283.75 mm
Outlet radius	R_o = 454.6 mm
Backswept blade angle	β = 30°
Number of the blades	N = 19
Outlet blade span	b = 72.3 mm
Mass flow rate	$\dot{m}$ = 0.142 kg/s
Mean absolute flow angle at diffuser inlet	α = 45°
Rotating speed	n = 500 rpm

Measurement Locations:

Sta.	1	2	3	4	5	6	7	8
L/R_o	0.02	0.08	0.15	0.21	0.27	0.33	0.39	0.45

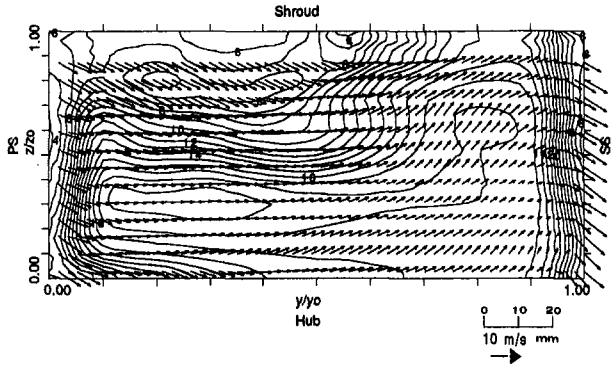


Fig. 3 Mean velocities at Station 1 (L/R_o = 0.02)

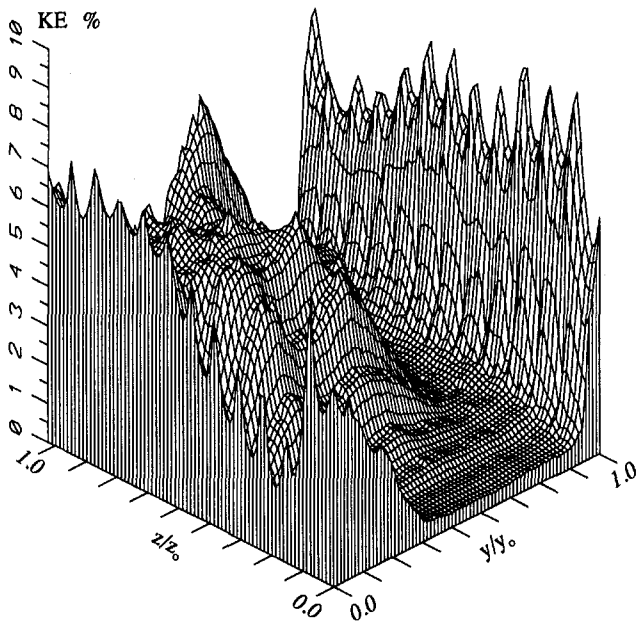


Fig. 4 Turbulent kinetic energy at Station 1 (L/R_o = 0.02)

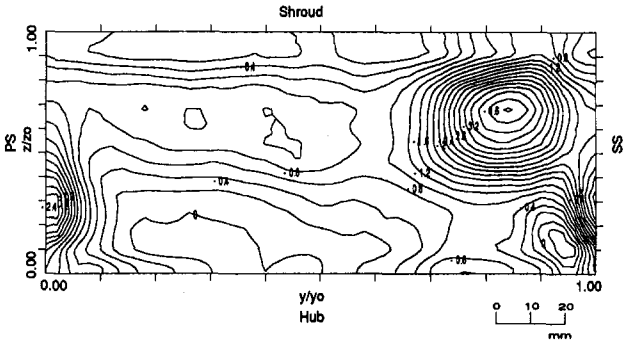


Fig. 5 Reynolds stress $\overline{u_r' u_\theta'}/U_T^2$ (percent): Station 1 (L/R_o = 0.02)

resolving the axial, circumferential, and radial velocity components and the directional sign of the axial component. It was assumed that the radial and circumferential components remained positive throughout the flow. There was no evidence in the results of either of these components reducing to zero and hence this assumption was justified.

The hot wires were connected to three constant-temperature hot-wire anemometer bridges. The wires were then calibrated in two stages in a wind tunnel following the procedure of Jørgensen (1971). In the first stage, the velocity/voltage relationship was established with the wire perpendicular to the flow direction. King's law

$$E^2 = A + B \cdot U_e^c \qquad (1)$$

was then fitted to the data for each wire using a least rms error technique to establish the calibration coefficients A, B, and C. The second stage of calibration was achieved by varying the wire orientation at fixed wind tunnel velocity to establish the directional coefficients K and H where

$$U_e^2 = U_n^2 + K \cdot U_t^2 + H \cdot U_b^2 \qquad (2)$$

U_n, U_t, and U_b are the normal, tangential, and binormal velocity components relative to the wire. K and H are also obtained by a least rms error curve fitting procedure.

An optical shaft encoder provided a pulse for every $\frac{1}{3}$ deg of impeller rotation. This was used to trigger the simultaneous sampling of the three anemometer voltages through a Microlink data acquisition unit. Readings from 57 measurement points spanning one of the 19 impeller passages were logged on each

Nomenclature

A, B, C = King's law calibration coefficients
E = hot-wire anemometer voltage
H, K = directional coefficients for hot wire
L = radial distance from impeller outlet
R_o = impeller outlet radius
U_T = peripheral blade velocity
U_e = effective cooling velocity
u_θ, u_r, u_z = tangential, radial, and axial mean velocity components
u_θ', u_r', u_z' = tangential, radial, and axial rms fluctuating velocity components
y = tangential coordinate in measurement plane
y_o = tangential distance between consecutive blade wakes
z = axial coordinate in measurement plane
z_o = axial diffuser width in measurement plane

Downloaded 01 Jun 2010 to 171.66.16.53. Redistribution subject to ASME license or copyright; see http://www.asme.org/terms/Terms_Use.cfm

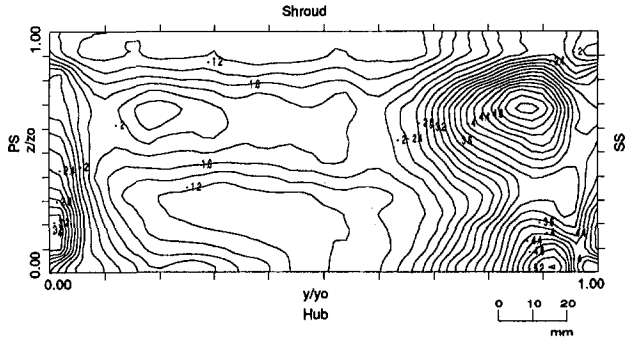


Fig. 6 Reynolds stress $\overline{u_\theta' u_z'}/U_T^2$ (percent): Station 1 (L/R_o = 0.02)

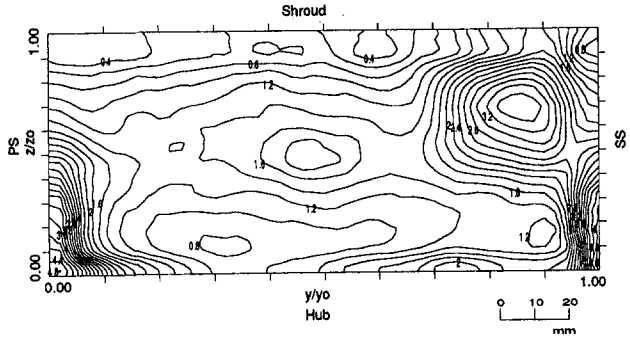


Fig. 7 Reynolds stress $\overline{u_r' u_z'}/U_T^2$ (percent): Station 1 (L/R_o = 0.02)

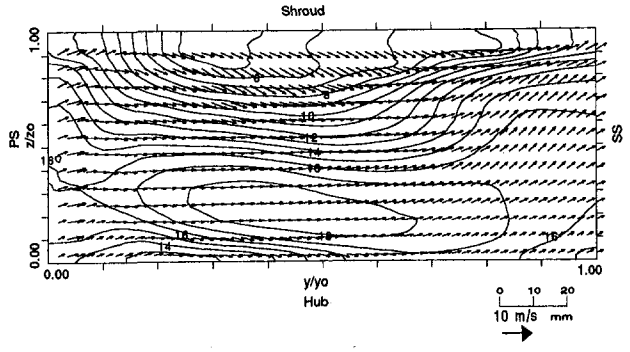


Fig. 8 Mean velocities at Station 2 (L/R_o = 0.08)

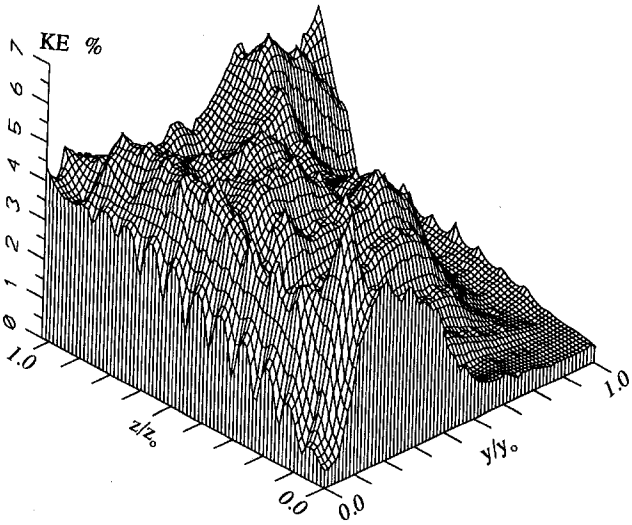


Fig. 9 Turbulent kinetic energy at Station 2 (L/R_o = 0.08)

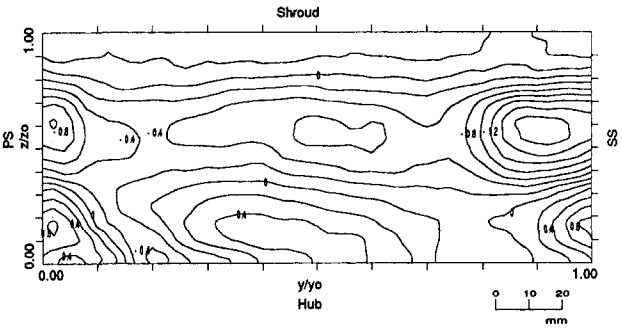


Fig. 10 Reynolds stress $\overline{u_r' u_\theta'}/U_T^2$ (percent): Station 2 (L/R_o = 0.08)

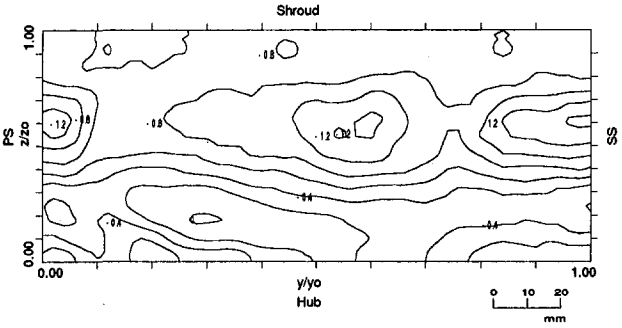


Fig. 11 Reynolds stress $\overline{u_\theta' u_z'}/U_T^2$ (percent): Station 2 (L/R_o = 0.08)

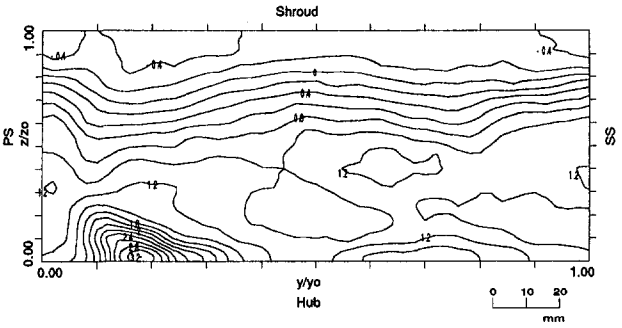


Fig. 12 Reynolds stress $\overline{u_r' u_z'}/U_T^2$ (percent): Station 2 (L/R_o = 0.08)

of 230 consecutive impeller revolutions. The triple wire sensor was traversed in the axial direction in order to provide a mesh of data points for each measurement plane.

Analysis of Results

The 230 readings obtained at each measurement point for each of the three anemometers were used to compute the mean

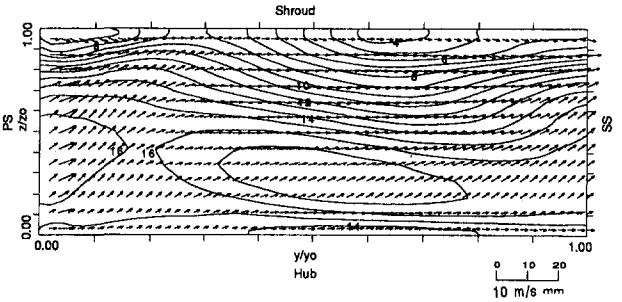


Fig. 13 Mean velocities at Station 3 (L/R_o = 0.15)

Downloaded 01 Jun 2010 to 171.66.16.53. Redistribution subject to ASME license or copyright; see http://www.asme.org/terms/Terms_Use.cfm

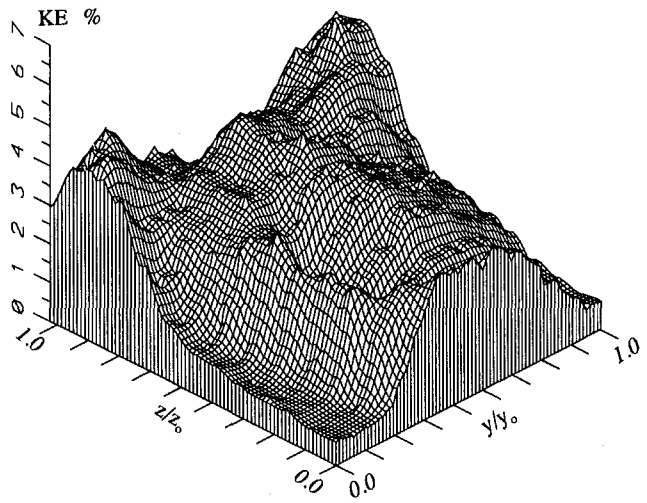


Fig. 14 Turbulent kinetic energy at Station 3 (L/R_o = 0.15)

velocity components and Reynolds stress tensor using the calibration coefficients. The flow rate was also computed by numerical integration of the radial velocity component over each of the measurement planes. The maximum deviation of this flow rate from the mean for all stations was 4.8 percent, which gives an indication of the overall experimental accuracy.

Experimental Results

Station 1. The mean velocities at station 1 are shown in Fig. 3. The radial velocity component is presented as a contour and the remaining velocity in the measurement plane is shown as an arrow. This figure clearly shows the passage wake on the shroud close to the pressure side and the blade wake on the suction side.

Figure 4 shows the turbulent kinetic energy levels at station 1:

$$\frac{\sqrt{(u_r'^2 + u_\theta'^2 + u_z'^2)}}{U_T}$$

The highest levels of around 10 percent are observed in the blade wake, with slightly lower values in the passage wake. It might therefore be expected that the rate of mixing out of the blade and passage wakes would be similar. However, this is not the case as the Reynolds stresses in the passage wake are very much lower than in the blade wake as shown by Figs. 5, 6, and 7. In fact the level of Reynolds stress in the passage wake is similar to that in the majority of the passage where the turbulent kinetic energy is only 1 or 2 percent. It therefore seems likely, as suggested by Hathaway et al. (1993), that the

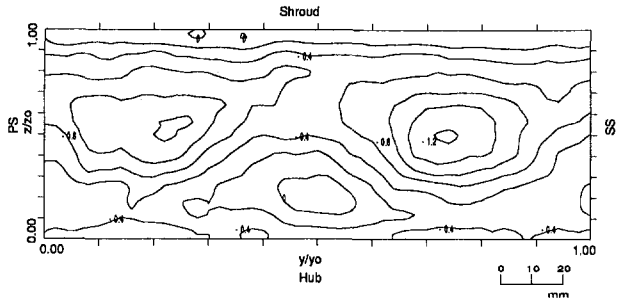


Fig. 16 Reynolds stress $\overline{u_\theta' u_z'}/U_T^2$ (percent): Station 3 (L/R_o = 0.15)

high turbulent kinetic energy level in the wake is due to variations in the position of the wake between impeller revolutions rather than high-frequency turbulent dissipation. The exact position of the wake at the impeller exit is dependent on the opposing secondary flows induced by the impeller axial to radial bend and induced toward the exit of the impeller by Coriolis forces. Quite small changes in the strengths of the secondary flows will therefore lead to variations in the wake position.

The peak levels of Reynolds stress do not in fact occur at the center of the blade wake, but on the suction side of it at $y/y_0 = 0.85$, $z/z_0 = 0.65$. In order to understand the reasons for this, it is necessary to consider the stability of the shear layers within the blade wake, which is governed by the streamline curvature. It has been observed by Bradshaw (1973) that where the shear velocity increases toward the center of curvature, the flow is destabilized as it is in a boundary layer on a concave surface. Conversely, a boundary layer on a convex surface or in a shear layer where the velocity decreases toward the center of curvature is stabilised. In the diffuser, the tangential velocity decreases while the radial velocity is approximately constant, thus the streamline curvature is such that the shear layer on the suction side of the blade is destabilized and that on the pressure side is stabilized. This is consistent with the observation of high levels of Reynolds stress on the suction side of the blade wake with much lower levels of Reynolds stress on the pressure side. Ubaldi et al. (1993) also observed a similar effect on the Reynolds stresses at the exit of their centrifugal pump turbine impeller operated as a pump. In their case however the streamline curvature was in the opposite sense because of the diffuser design.

The relatively different levels of the three components of Reynolds stress indicate that the turbulence is anisotropic. This is particularly true in the hub suction side corner where high levels of $\overline{u_\theta' u_z'}$ stress and low levels of $\overline{u_r' u_\theta'}$ and $\overline{u_r' u_z'}$ stress coexist. This suggests that turbulent eddies (with their axes in the radial direction) exist, which probably originate due to mixing processes within the impeller. However, these eddies are not now associated with large u_r' fluctuations and hence do not lead to significant mixing.

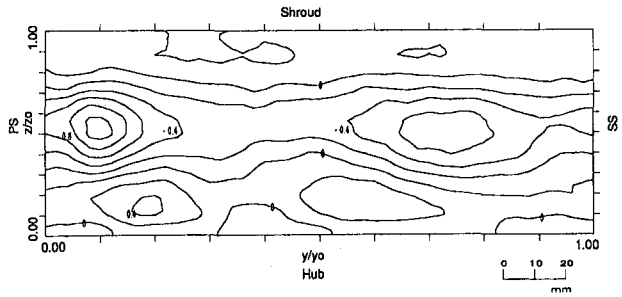


Fig. 15 Reynolds stress $\overline{u_r' u_\theta'}/U_T^2$ (percent): Station 3 (L/R_o = 0.15)

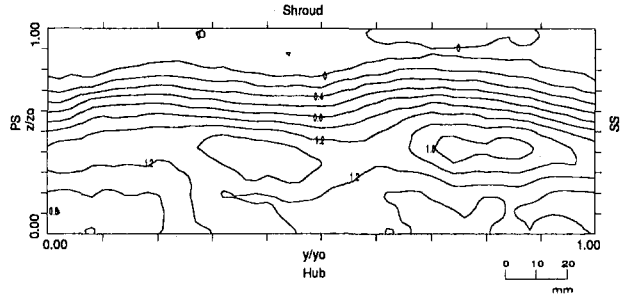


Fig. 17 Reynolds stress $\overline{u_r' u_z'}/U_T^2$ (percent): Station 3 (L/R_o = 0.15)

Downloaded 01 Jun 2010 to 171.66.16.53. Redistribution subject to ASME license or copyright; see http://www.asme.org/terms/Terms_Use.cfm

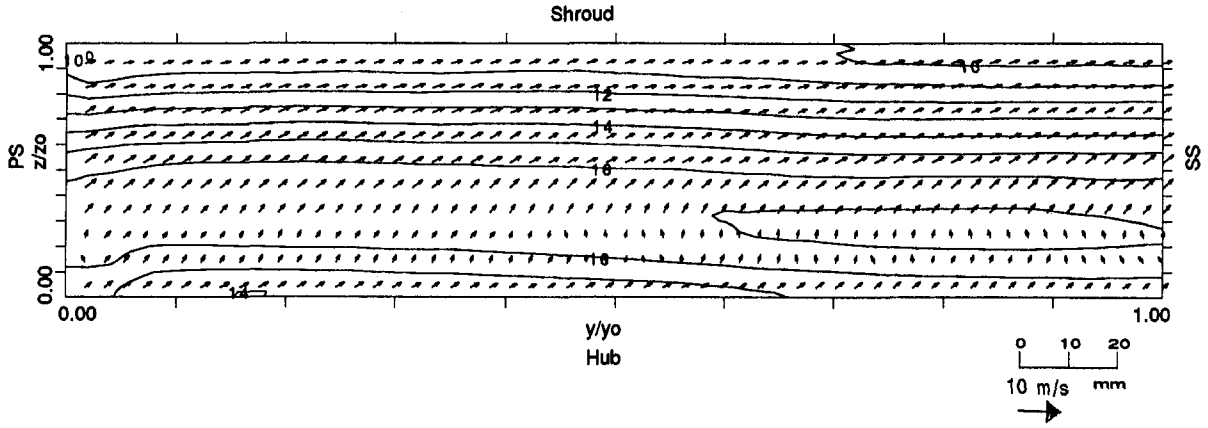


Fig. 18 Mean velocities at Station 8 (L/R_o = 0.45)

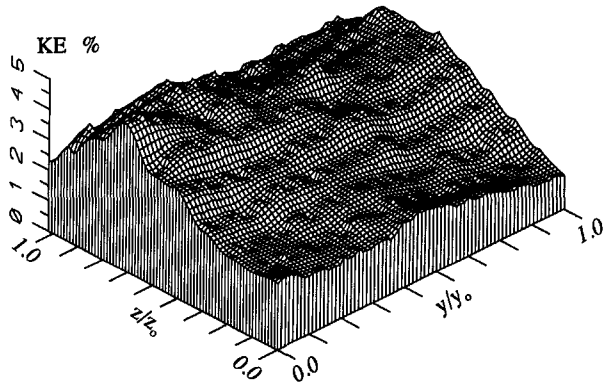


Fig. 19 Turbulent kinetic energy at Station 8 (L/R_o = 0.45)

A further region of mixing occurs near the hub pressure side corner. This appears to be due to destabilizing of the boundary layer on the concave hub surface.

The anisotropic nature of the turbulence suggests that Reynolds stress turbulence models are required for CFD codes used to compute vaneless diffuser flows.

Station 2. Figure 8 shows how the blade wake has largely mixed out and has moved to $y/y_o \approx 0.1$. The kinetic energy and Reynolds stress levels (Figs. 9–12) have all decreased substantially in this region.

The peak level of Reynolds stress occurs in $\overline{u_r' u_z'}$ (Fig. 12) within the blade wake on the hub surface at $y/y_o = 0.2$. This stress is associated with mixing in the boundary layer on the concave hub surface, which is thickened in this region by the blade wake (see Fig. 8). The high level of kinetic energy (Fig. 9) at $y/y_o = 0.9$, $z/z_o = 0.9$ is again due to the meandering of the passage wake across the shroud surface. Even infrequent movement of the wake toward the suction side will result in high levels of kinetic energy due to the large difference in mean velocity between the passage wake (3 m/s) and the main flow (10 m/s). The high level of kinetic energy is not, however, associated with any significant Reynolds stress (Figs. 10, 11, and 12).

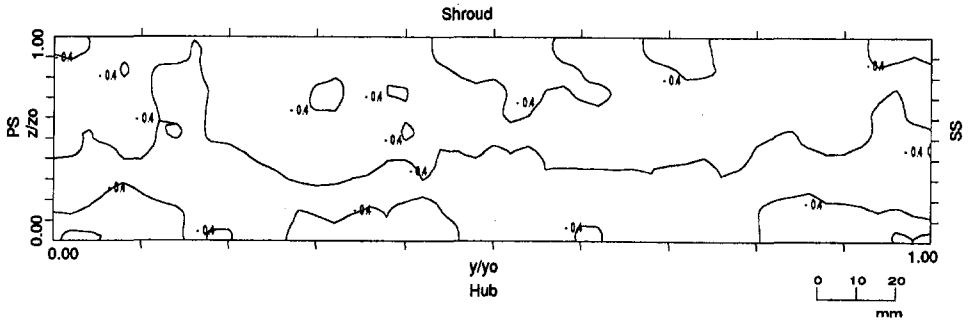


Fig. 20 Reynolds stress $\overline{u_r' u_\theta'}/U_T^2$ (percent): Station 8 (L/R_o = 0.45)

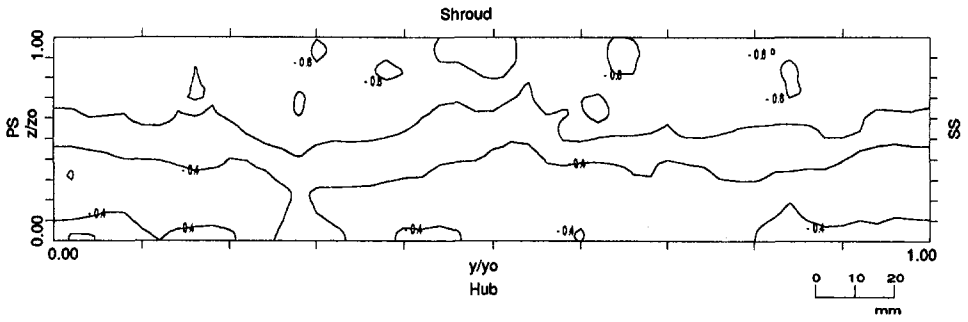


Fig. 21 Reynolds stress $\overline{u_\theta' u_z'}/U_T^2$ (percent): Station 8 (L/R_o = 0.45)

Downloaded 01 Jun 2010 to 171.66.16.53. Redistribution subject to ASME license or copyright; see http://www.asme.org/terms/Terms_Use.cfm

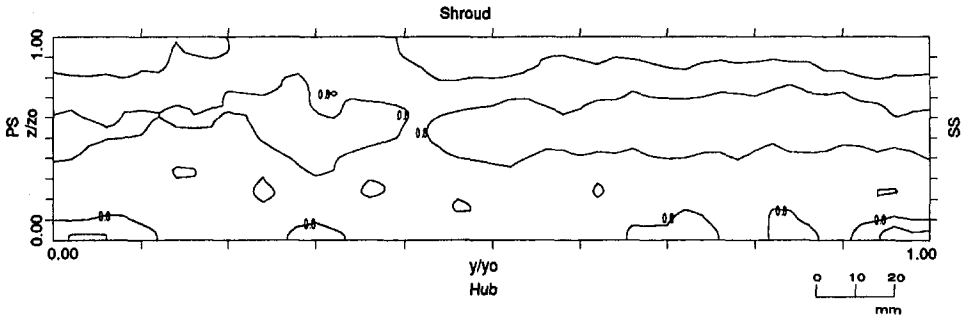


Fig. 22 Reynolds stress $\overline{u_r' u_z'}/U_T^2$ (percent): Station 8 (L/R_o = 0.45)

Station 3. At Station 3 the mean flow (Fig. 13) is beginning to resemble a Couette flow between the hub and shroud walls of the diffuser. The blade wake is still discernible near the hub at $y/y_o \approx 0.3$. The kinetic energy (Fig. 14) also shows a slight increase in this region, however the maximum kinetic energy values are still found on the shroud and are due to meandering of the passage wake. The $\overline{u_r' u_\theta'}$ and $\overline{u_\theta' u_z'}$ Reynolds stress components (Figs. 15 and 16) are now less than the $\overline{u_r' u_z'}$ component (Fig. 17). This would be expected in a Couette flow where mixing is dominated by the hub and shroud wall boundary layers.

Stations 4 to 8. Beyond Station 3, the flow continues to tend toward a Couette flow between the two diffuser walls as shown by the mean velocities at Station 8 (Fig. 18). The passage wake is no longer discernible, although the boundary layer on the shroud surface remains much thicker than that on the hub. The axial velocity from hub to shroud is evidence of the continuing leveling in the two boundary layer flow rates. The peak in turbulent kinetic energy (Fig. 19) is also still located closer to the shroud wall. The levels of all three components of Reynolds stress (Figs. 20, 21, and 22) are now very low, indicating that mixing out of the flow is complete.

Conclusions

1 Turbulent kinetic energy levels and strong Reynolds stresses rapidly mix out the blade wake downstream of the impeller discharge. The Reynolds stresses on the suction side of the blade wake are much larger than those on the pressure side, which is probably due to the effects of streamline curvature on shear layer stability.

2 Although the turbulent kinetic energy levels in the passage wake are as high as those in the blade wake, the Reynolds stresses are very much weaker and hence the passage wake mixes out only slowly. This is consistent with low-frequency turbulent meandering of the passage wake rather than high-frequency turbulent mixing.

3 The diffuser flow eventually develops into a Couette flow between the diffuser walls. The turbulent kinetic energy and Reynolds stress levels at Station 8 suggest that the mixing out of the flow is essentially complete.

4 The Reynolds stress measurements demonstrate that the turbulence is anisotropic. Thus accurate prediction of vaneless diffuser flows will only be possible using Reynolds stress turbulence models in CFD codes.

References

Bradshaw, P., 1973, "Effects of Streamline Curvature on Turbulent Flow," AGARDograph 169.

Eckardt, D., 1975, "Instantaneous Measurements in the Jet-Wake Discharge Flow of a Centrifugal Compressor Impeller," ASME JOURNAL OF ENGINEERING FOR POWER, Vol. 97, pp. 337–346.

Farge, T. Z., and Johnson, M. W., 1990, "The Effect of Backswept Blading on the Flow in a Centrifugal Compressor Impeller," ASME Paper No. 90-GT-231.

Farge, T. Z., and Johnson, M. W., 1992, "Effect of Flow Rate on Loss Mechanisms in a Backswept Centrifugal Impeller," *Int J. Heat Fluid Flow,* Vol. 13, No. 2, pp. 189–196.

Hathaway, M. D., Chriss, R. M., Wood, J. R., and Strazisar, A. J., 1993, "Experimental and Computational Investigation of the NASA Low Speed Centrifugal Compressor Field," ASME JOURNAL OF TURBOMACHINERY, Vol. 115, pp. 527–542.

Inoue, M., and Cumpsty, N. A., 1984, "Experimental Study of the Centrifugal Impeller Discharge Flow in Vaneless Diffusers," ASME *Journal of Engineering for Gas Turbines and Power,* Vol. 106, pp. 455–467.

Johnson, M. W., and Moore, J., 1980, "The Development of Wake Flow in a Centrifugal Compressor," ASME *Journal of Engineering for Power,* Vol. 102, pp. 383–390.

Johnson, M. W., and Moore, J., 1983, "Influence of Flow Rate on the Wake in a Centrifugal Impeller," ASME *Journal of Engineering for Power,* Vol. 105, pp. 33–39.

Jørgensen, F. E., 1971, "Directional Sensitivity of Wire and Fibre Film Probes," DISA information No. 11, pp. 31–37.

Krain, M., 1988, "Swirling Impeller Flow," ASME JOURNAL OF TURBOMACHINERY, Vol. 110, pp. 122–128.

Maksoud, T. M. A., and Johnson, M. W., 1987, "Mean and Turbulent Flow Measurements Within the Vaneless Diffuser of a Centrifugal Compressor," *Proc. IMechE Conf.,* C263/87.

Mounts, J. S., and Brasz, J. J., 1992, "Analysis of the Jet/Wake Mixing in a Vaneless Diffuser," ASME Paper No. 92-GT-418.

Pinarbasi, A., and Johnson, M. W., 1994, "Detailed Flow Measurements in a Centrifugal Compressor Vaneless Diffuser," ASME JOURNAL OF TURBOMACHINERY, Vol. 116, pp. 453–461.

Ubaldi, M., Zunino, P., and Cattanei, A., 1993, "Relative Flow and Turbulence Measurements Downstream of a Backward Centrifugal Impeller," ASME JOURNAL OF TURBOMACHINERY, Vol. 115, pp. 543–551.

Downloaded 01 Jun 2010 to 171.66.16.53. Redistribution subject to ASME license or copyright; see http://www.asme.org/terms/Terms_Use.cfm

Experimental and Numerical Study of Orifice Discharge Coefficients in High-Speed Rotating Disks

S. Wittig

S. Kim

R. Jakoby

I. Weißert

Lehrstuhl und Institut für Thermische Strömungsmaschinen, Universität Karlsruhe (T.H.), Karlsruhe, Federal Republic of Germany

Experimental and numerical results of the flow through orifices in rotating disks are presented, with emphasis on basic physical phenomena. It is shown that rotational effects strongly influence the massflow discharged, a phenomenon that cannot be modeled by a stationary setup. The study includes the determination of discharge coefficients under variation of the length-to-diameter ratio, pressure ratio, and rotational speed. The pressure ratio covers low as well as critical values, the maximum rotational speed is 10,000 rpm, which is equivalent to a tangential velocity of 110 m/s. In order to understand the flow structure, local flow velocities were measured by means of a two-dimensional Laser-Doppler Velocimeter. Phase-resolved measurements have been carried out in front of and behind the orifices. A three-dimensional Finite-Volume Code with body-fitted coordinates in a rotating frame of reference is employed for the numerical analysis and the verification of its possibilities and limitations. The results reveal a very complex flow field, which is dominated by high velocity gradients in close vicinity to the orifices. The comparison of the computational solutions with the experimental data shows good agreement. Based on the measurements in combination with the numerical solution, a detailed insight into the physical properties of the flow is achieved.

Introduction

In order to improve the thermal efficiency of the basic cycle of gas turbine engines, an increase of the turbine inlet temperature is a well-known necessity. These temperature levels exceed the critical temperature of the blade material. Consequently, an efficient cooling system, which combines the demand of safe operation of the engine with a minimized internal air mass flow, is required. In addition, a large variety of other tasks, such as preventing the ingestion of hot gas into the turbine disk cavities, balancing axial loads and many others, have to be fulfilled. To meet this demand, the discharge characteristics of the various components like disks and annular gaps with or without orifices, labyrinth seals, etc., have to be known.

Concerning the discharge characteristics of orifices in disks, numerous investigations have been published in the past. Nevertheless, most of them are based on a static setup. Herning (1962) and Benedict et al. (1975) for example, determined the effect of edge sharpness. Orifices with radiused or chamfered inlet corners have been studied by Hay and Spencer (1992) and Rhode et al. (1969), who also determined the influence of an inclined orifice axis. Similar studies are presented by Hay et al. (1994). Lichtarowicz et al. (1965) published measurements under variation of the orifice length, Jobson (1955) and Bragg (1960) on the influence of compressibility and Callaghan and Bowden (1949) were interested in the discharge of orifices with square, elliptic, and circular shape. Based on experimental results of previous investigations, McGreehan and Schotsch (1988) derived correlations considering a variety of geometric parameters.

The discharge behavior of rotating orifices as an element of the internal air system has been studied by Meyfarth and Shine (1965), who varied the orifice number, diameter, and arrangement. Wiles (1976) also had a rotating setup, where he determined discharge coefficients for disks with conical orifices of different number and diameter. Becker et al. (1977) investigated the discharge of radial orifices in rotating shafts.

As there are few data available on the influence of rotation, the subject of this paper is to study the basic properties of the flow through orifices in rotating disk systems. The discharge behavior is analyzed by means of local flow velocities as well as discharge coefficients with variation of the most important parameters, such as the pressure ratio, the rotational speed, and the length-to-diameter ratio.

2 Experimental Setup

2.1 Test Rig. For the determination of the discharge properties of orifices in high-speed rotating disks, a test facility was built at the Institut für Thermische Strömungsmaschinen (ITS). Compressor air is discharged from a settling chamber through the flange of the rig on the left-hand side as shown in Fig. 1. To minimize perturbations caused by the flange, the edges of the struts are rounded. Additionally, a turbulence mesh is mounted to homogenize the flow.

A high degree of flexibility considering geometric variations is obtained by using cylindrical shells. The orifices are bored into the shells, which provides easy modification of the geometry. The length of the orifices can be varied by mounting disks of different thickness. The disks are fixed to the shaft using a flexible junction element, clamped by a nut.

To meet the demand of high rotational speeds, precision bearings are used. Thus, a maximum rotational speed of 10,000 rpm could be achieved. Due to the high circumferential velocity of the disk, a labyrinth seal has been chosen for the sealing of rotor and stator. The unavoidable leakage loss of the seal was determined by extensive calibration measurements with closed orifices to ensure a high accuracy level.

Contributed by the International Gas Turbine Institute and presented at the 39th International Gas Turbine and Aeroengine Congress and Exposition, The Hague, The Netherlands, June 13–16, 1994. Manuscript received by the International Gas Turbine Institute February 4, 1994. Paper No. 94-GT-142. Associate Technical Editor: E. M. Greitzer.

Copyright © 1996 by ASME

Downloaded 01 Jun 2010 to 171.66.16.53. Redistribution subject to ASME license or copyright; see http://www.asme.org/terms/Terms_Use.cfm

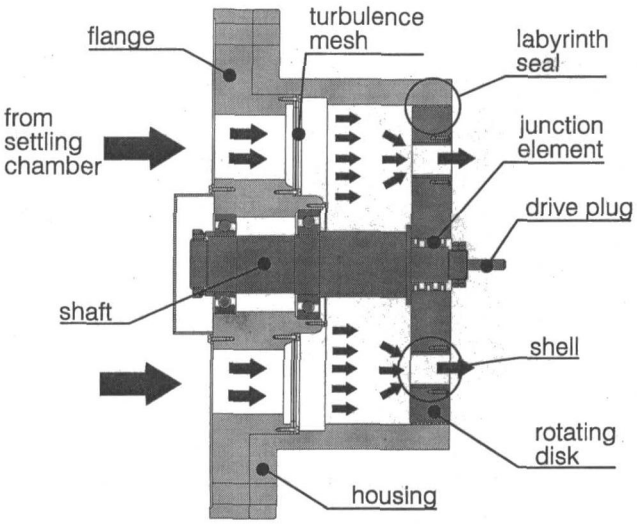


Fig. 1 Test rig rotating disks

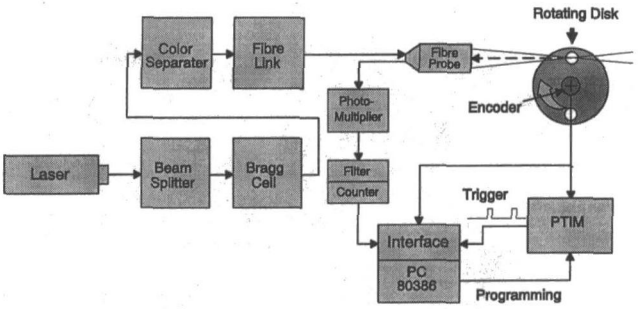


Fig. 2 LDV setup

The disk drive is located on the righthand side of the test section, where a DC motor is connected to the drive plug on the shaft by a flexible clutch.

The optical access to the upstream side of the disk is realized by a window in the housing (Fig. 3). Downstream of the disk, the air is discharged into the surroundings to avoid the influence of a housing geometry.

The mass flow discharged through the test section was measured by one of three orifice flow meters, applicable to the appropriate measurement range and connected to a calibrated differential pressure gage. The temperature of the gas flow in the orifice meter, in the settling chamber, and in the test section as well as the ambient temperature is measured with NiCr–Ni thermocouples. The corresponding static pressure is obtained from pressure taps connected to a scanivalve and an absolute pressure gage. The pressure ratio across the orifice is defined as $\pi = p_0/p_\infty$, which is the ratio of the static pressure in the settling chamber to the ambient pressure. The pressure drop from the settling chamber to the test section housing turned out to be negligible. The consistency of the measured discharge coefficients was checked by a complete dismantling of the test section, followed by a reassembly and a recalibration of the leakage losses of the labyrinth seal. The uncertainties were always smaller than 2.5 percent.

2.2 LDV Setup. For the measurement of the flow velocities, a two-component fiber-optic LDV system provided by Dantec was used. The LDV system comprises a 4 W argon-ion laser in multimode operation, a standard optics with 40 MHz Bragg-cell, color and beam separators, and a two-dimensional-fiber probe (Fig. 2). The signals are detected by a two-component photomultiplier setup in combination with counterprocessors. In order to determine the angular position of the disk, an angular encoder and a Zech 1400A interface card are used. The interface is equipped with an internal clock, which operates with an internal oscillator or an external trigger. The encoder is generating one trigger signal per revolution to reset the clock and 8192 impulses to be summarized within one cycle. Depending on the mode chosen, the position of the clock is a measure for the arrival time of the signals or the respective position of the rotor. Working as a data link between the counterprocessors and the computer (PC 80386), the interface card writes all data into the computer memory.

Additionally, a Programmable-Trigger-Inhibit-Module (PTIM), which was developed at our institute, provides selective data acquisition within predefined angular segments to save computer storage and processing capacity for measurements in rotating systems.

For the seeding, a Pallas RGB 1000 particle generator is used in combination with $CaCO_3$ particles with a mean size of 1 μm. The probe volume had a length of approximately 1 mm; its diameter was 0.3 mm. For reasons of a high degree of flexibility, backscatter mode for the measurements was chosen. The arrangement of the fiber probe for measurements near and in the orifices is illustrated by Fig. 3. If the probe is located at position 1, the tangential and axial component of the flow field before and behind the disk will be measured. Placing it into position 2, the flow inside the orifices can be detected by measuring the radial and tangential component. A detailed error analysis of the measurement technique is carried out by Jakoby et al. (1994).

3 Numerical Procedure

Corresponding to the experimental setup (section 2.1) the grid for the numerical simulation is divided into three sections (Fig. 4). The inflow region consists of a cylindrical housing with a central rotating shaft, followed by the disk with orifices. As there is an extremely high ratio of housing area to orifice

Nomenclature

A = area, m^2
c = velocity, m/s
c_D = discharge coefficient
d = orifice diameter, mm
D = pitch circle diameter of orifices, mm
k = turbulent kinetic energy, m^2/s^2
l = orifice length, mm
$\dot{m}$ = mass flow, kg/s
n = rotational, speed, min^{-1}
p = pressure, N/m^2
pdf = probability density function
Q = ideal flow function = $\sqrt{kgK/J}$
r = coordinate, mm
R = specific gas constant, J/kgK
T = temperature, K
U = circumferential velocity of orifices, m/s
x = coordinate, mm
ϵ = dissipation rate, m^2/s^3
κ = isentropic coefficient
π = pressure ratio
Φ = coordinate, deg
ω = angular velocity, s^{-1}

Subscripts

ax = axial
in = inlet
out = outlet
t = tangential
t = total
0 = settling chamber
∞ = behind disk

Downloaded 01 Jun 2010 to 171.66.16.53. Redistribution subject to ASME license or copyright; see http://www.asme.org/terms/Terms_Use.cfm

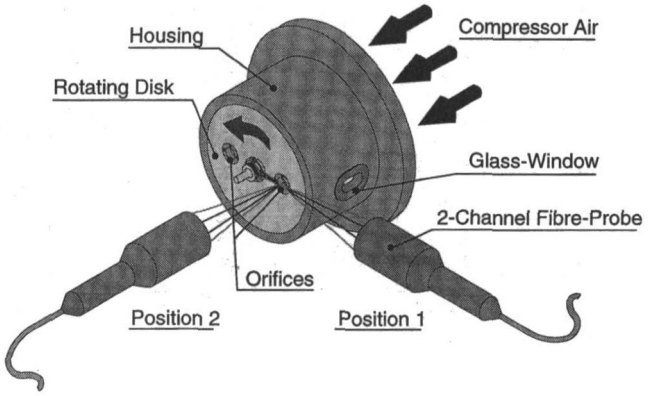


Fig. 3 Probe arrangement

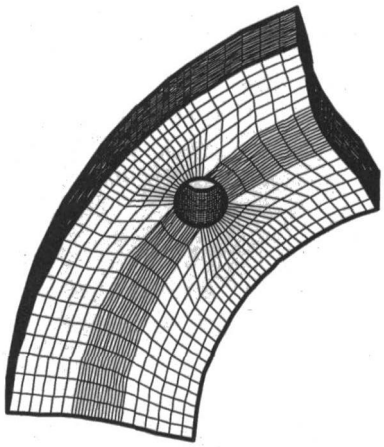


Fig. 5 Detailed geometry modeling using an embedded, refined grid

area, high-velocity gradients in the vicinity of the orifices occur. These gradients are resolved by an embedded, refined mesh (Fig. 5). Behind the disk, reasonable boundary conditions have to be defined in order to simulate the free jet condition of the experimental setup. Therefore, the flow is discharged into a large housing, whose influence on the discharge behavior is assumed to be negligible.

The computational results were obtained by using a commercial finite-volume code (TASCflow3D), where the time-averaged Navier–Stokes equations are solved on a nonorthogonal, body-fitted grid. This code uses a second-order discretization scheme, the so-called Linear Profile Scheme (LPS) combined with Physical Advection Correction (PAC) terms (TASCflow User Documentation (1993)). Due to the rotation of the disk, the flow through the orifices is of unsteady, three-dimensional type. Choosing a rotating coordinate system, a reduction to a steady three-dimensional type of flow is possible. The turbulence characteristics of the flow are described by the well-known standard $k-\epsilon$ model (Launder and Spalding, 1974). For the determination of the near-wall velocity, the logarithmic wall function was used. Due to the occurrence of high Mach numbers, compressibility effects were considered. More details of the numerical code are described in the TASCflow User Documentation (1993).

3.1 Grid Generation. The basic configuration consists of a rotating disk with two orifices as shown in Fig. 4. Due to the symmetry of the setup, a reduction of the grid to a 180 deg segment is possible. In the static case, a further reduction of the grid to a 90 deg segment could be carried out due to the symmetry of the flow through the orifice. However, the investigation of rotational effects requires the choice of a 180 deg segment.

The resolution of pressure and velocity gradients is achieved by a local grid refinement as shown in Fig. 5. Consequently, the approximation of the circular geometry of the orifice is improved. In order to resolve recirculation zones in front of and behind the orifice, the embedded grid is extended into the tangential direction. The total number of nodes of the main and embedded grid is 60,000. The grid independence of the calculated discharge coefficients and the velocities in front of and behind the disk was tested by use of refined grids.

3.2 Boundary Conditions. In the rotating frame of reference, the disk is a stationary wall and the housing rotates with negative angular velocity. Downstream of the disk, the influence of the outer wall on the discharge characteristics can be neglected due to the extremely small ratio of orifice to outflow area of 0.0005. At the inlet boundary, a pressure specified opening with presupposed axial inflow direction is used. In the downstream section, recirculation zones in the outlet cross section may occur. Therefore, the outlet boundary condition is a pressure specified opening where, according to the experimental setup, the static pressure is equal to the ambient pressure, allowing the appearance of small recirculation flows in the outlet area. In the plane of geometric symmetry, periodic boundary conditions are set. The axis of rotation, corresponding to a collapsed plane with degenerated cells, is preset with symmetric boundary conditions.

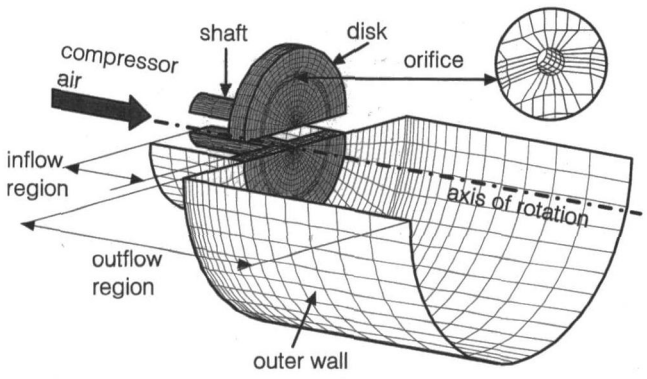


Fig. 4 Numerical grid

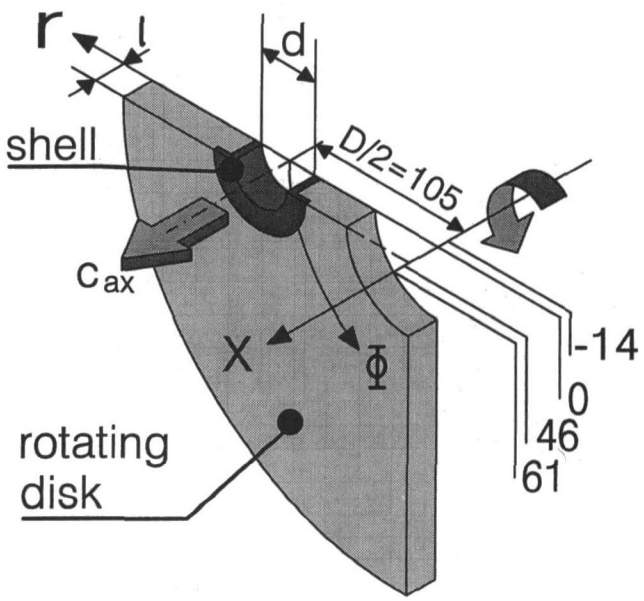


Fig. 6 Frame of reference

Downloaded 01 Jun 2010 to 171.66.16.53. Redistribution subject to ASME license or copyright; see http://www.asme.org/terms/Terms_Use.cfm

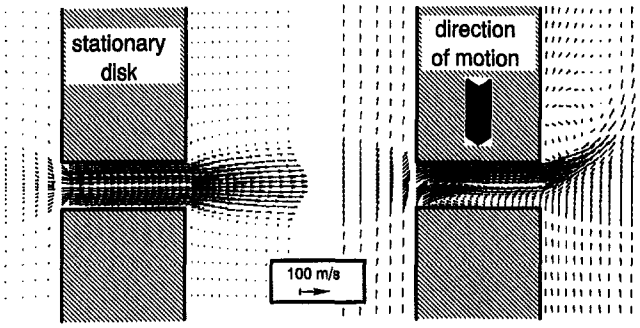


Fig. 7 Influence of rotation: computation (π = 1.1, l = 40 mm, d = 15 mm)

4 Results

In the following chapter, an overview on the influence of rotation on the flow field and the discharge behaviour is given. With the exception of Fig. 12, all the results presented refer to a rotating frame of reference, introduced by Fig. 6.

4.1 Flow Field in the Vicinity of Rotating Orifices. The difference between the rotating and the nonrotating case is shown by Fig. 7, where the numerical solution for a stationary and a rotating orifice is presented for a circumferential intersection (r = const). The thickness of the disk is l = 40 mm with the orifice diameter d = 15 mm and the radial position of the orifice axes r = 105 mm.

In the nonrotating case, the well-known flow structure with convergent afflux, separation at the inlet corner, vena contracta, and dissipating core on the downstream side of the disk is obtained. Considering a rotational speed of 4500 rpm (U/c_{ax} = 0.38) and a pressure ratio of π = 1.1, there is a tangential afflux due to the rotating frame of reference. Consequently, the velocity vectors at the inlet plane show an inclination angle toward the orifice axis, which leads to separation and a large recirculation zone on the "suction side," filling almost the whole length of the orifice. The velocity vectors in the exit cross section turn out to be almost perpendicular to the disk, due to the relatively large ratio of orifice length-to-diameter, which is causing a tangential acceleration of the flow. In the exit plane, the tangential flow velocity is almost equal to the disk speed. The jet discharged is deflected into the tangential direction, due to the crossflow of the stationary air (rotating frame of reference).

The velocity profiles of the outflow region measured in a cross section at x = 61 mm are shown by Figs. 8 and 9, presenting the axial and the tangential component for a clockwise rotating disk. The two orifices of the disk are mirrored in the two peaks of the axial velocity distribution. The "wake flow" of the jets discharged is expressed by a "tail" extending into the circumferential direction. Toward the center of the disk, a recirculation zone is indicated by negative axial velocities, being detected for small radial coordinates. With the exception of the peaks, the general velocity profile has a concave shape like a soup plate. On the outside of the measuring plane, the jets are dragging ambient air. Therefore, there are no negative velocities. In the center, the swirl flow causes a recirculation zone.

The tangential velocity distribution in the vicinity of each orifice is characterized by a small, local maximum followed by a minimum and a large maximum. Since in the rotating frame of reference, the flow is discharged into a crossflow of ambient air, there is a three-dimensional flow around the jets with rotating stagnation points, which are represented by the small, local maxima. The small peaks are below the disk speed, because the stagnation point is not located in this measuring plane. The wake regions are also rotating with the speed of the disk, causing the two large maxima. As shown by Figs. 10 and 7(b), the flow in the exit plane of the orifices is perpendicular to the disk. With increasing axial distance, the jets are deflected into the circumferential direction, which is expressed in a reduction of the tangential velocity component. Accordingly, the minima mentioned above represent the core of the jets.

The vector plot in Fig. 10 gives a superposition of the measured axial and tangential component along the trajectory of

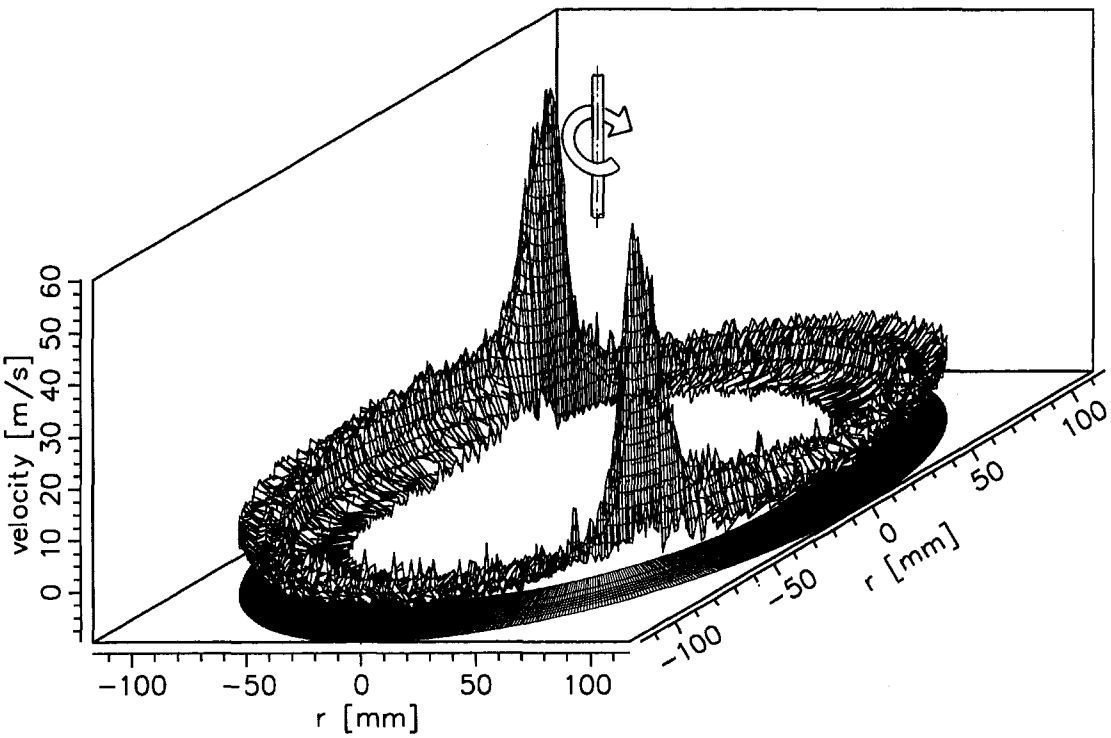


Fig. 8 Axial velocity distribution: measurement (π = 1.1, U/c_{ax} = 0.38, n = 4500 rpm, l = 40 mm, d = 15 mm, x = 61 mm)

Downloaded 01 Jun 2010 to 171.66.16.53. Redistribution subject to ASME license or copyright; see http://www.asme.org/terms/Terms_Use.cfm

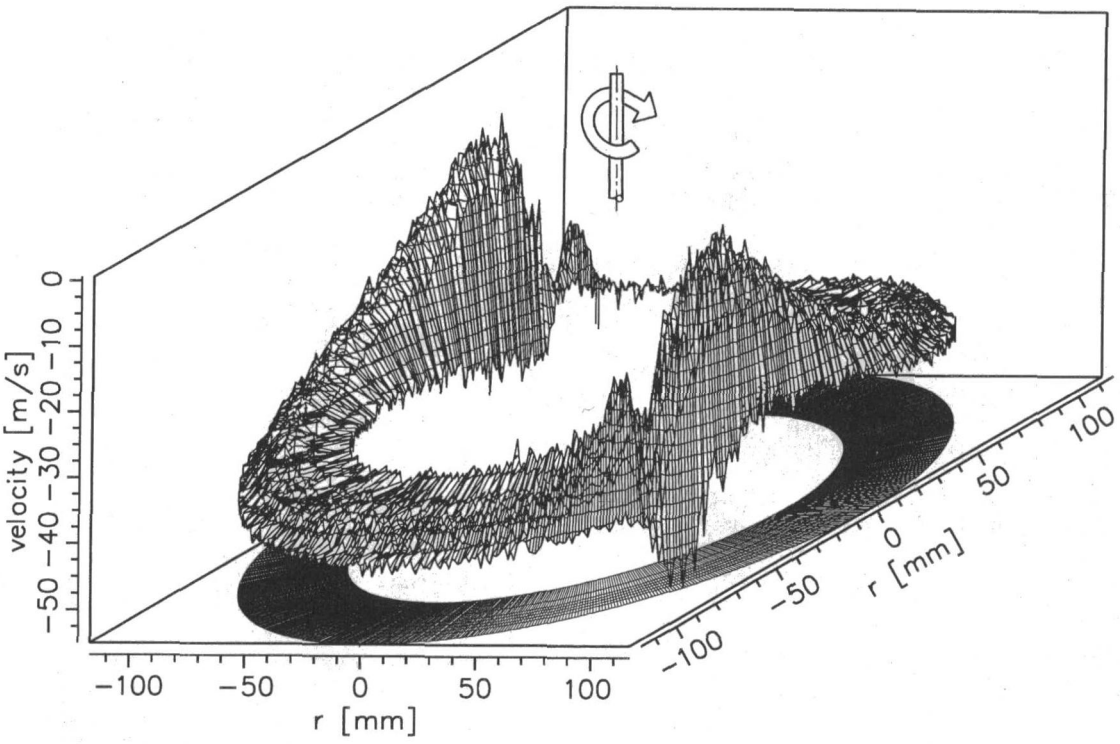


Fig. 9 Tangential velocity distribution: measurement (π = 1.1, U/c_{ax} = 0.38, n = 4500 rpm, l = 40 mm, d = 15 mm, x = 61 mm)

the orifice axes. As outlined in the plot, the angular extension of the orifice is 8 deg. On the other hand, the extension of the core of the jet is approximately 4 deg at $x = 46$ mm. This is a consequence of the separation bubble on the suction side of the orifice (Fig. 7), blocking parts of the flow area. The reattachment of the flow takes place in the rear part of the orifice, but the core of the jet is confined to the pressure side. Figure 10 also shows an expansion of the jet into the downstream direction, due to secondary motions and the wake of the crossflow.

A comparison between the experimental and numerical results is presented in Fig. 11, where the axial velocity distribution according to Fig. 10 ($x = 61$ mm) is shown. The experimental determination of mean velocities has been carried out by an ensemble averaging of the single counts within an angular range of 0.5 deg (Jakoby et al., 1994). Along the whole line of constant radius, 40,000 valid counts have been attempted, which is a good compromise between acceptable statistics and measurement duration.

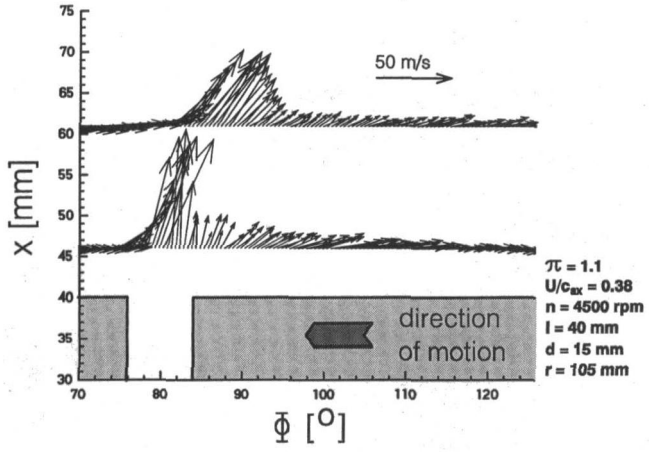


Fig. 10 Downstream side of the disk: measurement

Comparing the LDV data and the computational results, the predicted velocity distribution is characterized by sharper and higher peaks. In general however, good agreement was obtained.

Changing into a stationary frame of reference for a better illustration of the measured data, the flow field on the upstream side of the disk is presented by Fig. 12. There is a convergent type of flow, which is characterized by a very low velocity level. Even at a distance of −14 mm to the inlet corner, the axial velocity does not exceed 10 m/s. The averaged tangential velocity in this measuring plane is approximately 2.5 m/s. Consequently, an extreme acceleration of the flow occurs within the entrance region of the orifices. Changing back into the rotating frame of reference, Fig. 13 shows the predicted velocity distribution along the orifice axis. The acceleration of the flow takes place within a very small range from -10 mm $\leq x \leq +$ 5 mm. In the orifice, the axial velocity in the center is decreasing into the downstream direction, because there is an eccentric shift of the velocity maximum. On the outside, the velocity is sinking rapidly, due to the tangential deflection of the jet. The behavior of the tangential component is similar to the axial one.

4.2 Influence of Rotation on the Discharge Behavior. In addition to the general influence of rotation on the flow field of orifices in disks, the discharge behavior is of major interest. Therefore, the well-known discharge coefficient c_D, which is defined in the context of labyrinth seal analysis (e.g., Waschka et al., 1992) as the ratio of the real and the ideal massflow, is used.

$$c_D = \frac{\dot{m}}{\dot{m}_{\text{ideal}}} = \frac{\dot{m}\sqrt{T_0}}{Q_{\text{ideal}} p_0 A} \tag{1}$$

$$Q_{\text{ideal}} = \sqrt{\frac{2\kappa}{R(\kappa-1)}\left[\left(\frac{p_\infty}{p_0}\right)^{2/\kappa} - \left(\frac{p_\infty}{p_0}\right)^{(\kappa+1)/\kappa}\right]} \tag{2}$$

The influence of rotation is characterized by the ratio of the tangential velocity of the orifices to the ideal axial velocity of the flow:

Downloaded 01 Jun 2010 to 171.66.16.53. Redistribution subject to ASME license or copyright; see http://www.asme.org/terms/Terms_Use.cfm

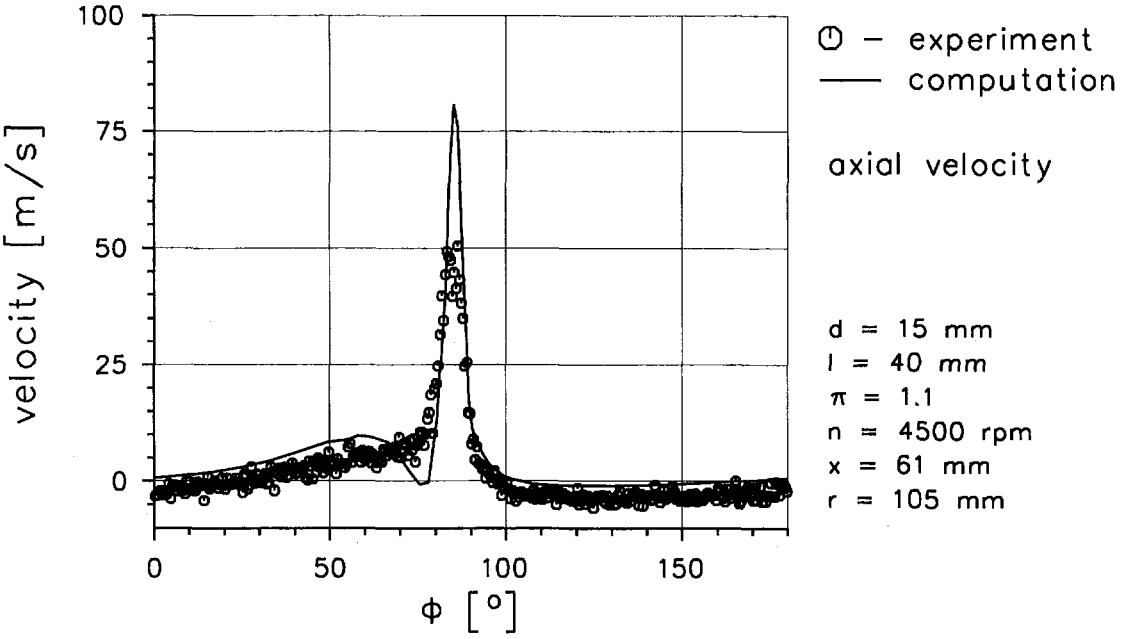


Fig. 11 Comparison of experimental and numerical results

$$U = \frac{\omega \cdot D}{2}, \quad c_{ax} = \frac{\dot{m}_{\text{ideal}}}{\rho_\infty \cdot A} \tag{3}$$

In this definition, D is the pitch circle diameter, ω the angular velocity of the disk, and A the orifice area.

Figure 14 shows the discharge behavior of our basic orifice geometry discussed. With increasing ratio of U/c_{ax}, there is a reduction of the discharge coefficient, because the growing inclination angle of the afflux is leading to enlarged separation at the orifice inlet corner. When the pressure ratio rises, the influence of compressibility causes an enlargement of the vena contracta (see, e.g., Bragg 1960) leading to an increase of c_D. The maximum rotational speed of the rotor was 10,000 rpm, which is equivalent to $U = 110$ m/s. Due to the increase of c_{ax} for rising pressure ratio, U/c_{ax} is diminishing, if the angular velocity remains constant. Therefore, there are different maximum values of U/c_{ax} for each line of constant pressure ratio. A qualitative comparison of our experimental and numerical results shows fairly good agreement. There is a representation of the physical tendencies. In the course of our present studies, the reasons for the quantitative differences of approximately 10 percent are analyzed in detail.

4.3 Influence of the Length to Diameter Ratio. The influence of the length-to-diameter ratio is illustrated by Fig. 15, showing the measured discharge coefficients versus l/d for three ratios of U/c_{ax}. The continuous lines represent functional approximations. For the nonrotating case, the well-known development of c_D (e.g., Hay and Spencer, 1992; McGreehan and Schotsch, 1988) has been obtained. Considering very small l/d values, the separation at the inlet corner, and the contraction of the jet is dominating the discharge behavior, the discharge coefficient is rather small. If the length of the orifice is increased, c_D is growing until the maximum is reached within a range of $1.5 \leq l/d \leq 3$. If l/d is increased even further, the friction losses are dominating the development of c_D, which is expressed in a steady decrease.

The appearance of different discharge coefficients for constant l/d is explained by the large variety of geometries which have been considered. Orifices with constant l/d but different length and diameter are causing a scatter of c_D.

As the disk is rotating, the lower curves of Fig. 15 are obtained, showing the discharge coefficients for $U/c_{ax} = 0.27$ and $U/c_{ax} = 0.60$, which is corresponding to a rotational speed of 4500 rpm and 10,000 rpm, respectively. First of all, orifices with $l/d \approx 1$ are influenced by rotational effects, which is expressed by a dramatic decrease of c_D. For such geometries, the influence of the pressure side wall causes a compression of

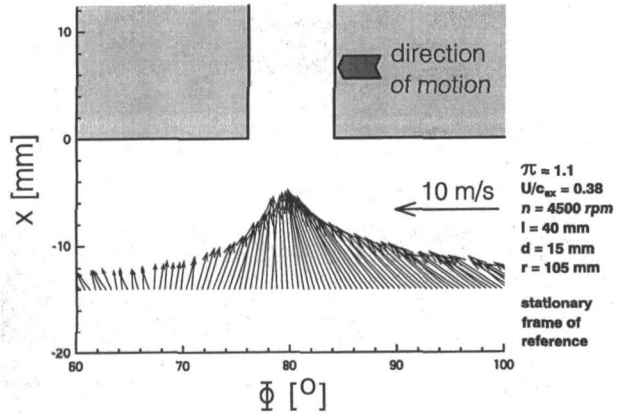


Fig. 12 Velocity distribution on the upstream side: measurement

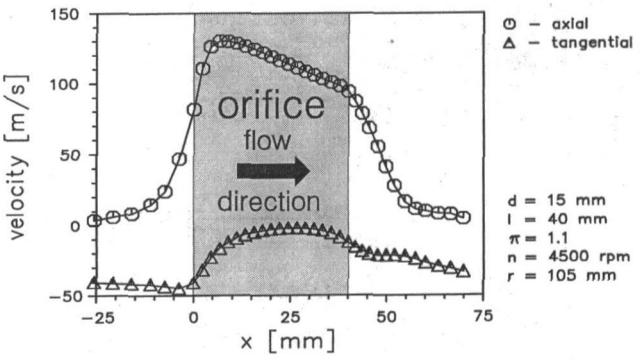


Fig. 13 Velocity distribution along the orifice axis: computation

Downloaded 01 Jun 2010 to 171.66.16.53. Redistribution subject to ASME license or copyright; see http://www.asme.org/terms/Terms_Use.cfm

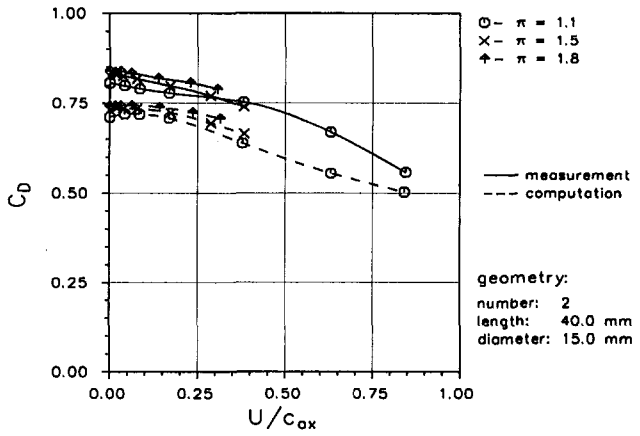


Fig. 14 Discharge behavior of rotating orifices

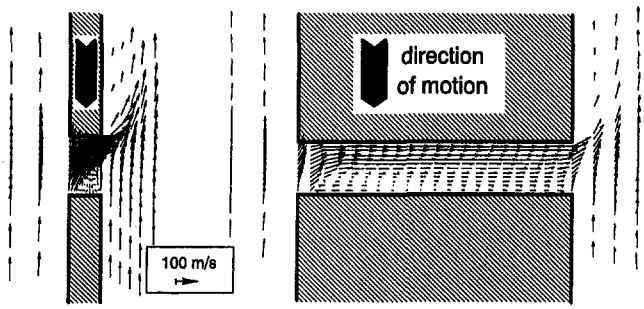


Fig. 16 Influence of l/d on the flow field: computation (π = 1.1, n = 10,000 rpm, d = 15 mm)

the vena contracta (see Fig. 16). Additionally, strong separation on the suction side leads to a further reduction of the flow area, reducing the massflow discharged. There is only little deflection of the flow through the orifice. Increasing the orifice length, there is reattachment of the flow on the suction side wall. The enclosed low pressure separation bubble causes an expansion of the vena contracta, leading to increased discharge coefficients. Consequently, the lines of constant U/c_{ax} in Fig. 15 are converging for increasing length.

5 Summary

A study on the basic properties of the flow through rotating orifices and a discussion of discharge coefficients was presented. The flow has been analyzed by experimental and numerical methods. The experimental activities covered the determination of local flow velocities in a rotating frame of reference, using a two-dimensional Laser-Doppler Velocimeter. The measurements had been carried out in front of and behind high-speed rotating orifices, where an angular resolution of 0.5 deg could be obtained. Furthermore, discharge coefficients had been determined, varying the most important parameters. For the numerical predictions, a three-dimensional Finite-Volume Code with body-fitted coordinates and local grid embedding had been used. The experimental and numerical data about the flow conveyed a revealing insight into the physical phenomena.

The parameters investigated consisted of the pressure ratio, the rotational speed, and the ratio of length to diameter. Considering long, sharp-edged orifices, the influence of rotation causes a separation bubble on the suction side of the orifice, which is almost filling the whole length. The maximum of the axial velocity is shifted toward the pressure side. In a rotating frame of reference, there is an inclined inflow and an axial outflow.

Regarding the influence of the length-to-diameter ratio, orifices with $l/d \approx 1$ are mostly affected by rotation. Due to the influence of the pressure side wall, causing a compression of the vena contracta and a strong separation on the suction side, there will be a maximum reduction of the massflow discharged, if the disk rotates. Increasing the orifice length, there is a reattachment of the flow on the suction side wall, leading to an enclosed low-pressure separation bubble. Consequently, an expansion of the vena contracta is causing increased discharge coefficients for constant rotational speeds.

The results and conclusions presented in this paper show that rotational effects strongly influence the flow through orifices. Presently, extensive studies are under way on the influence of radiused inlet corners, which was found to be of significant importance.

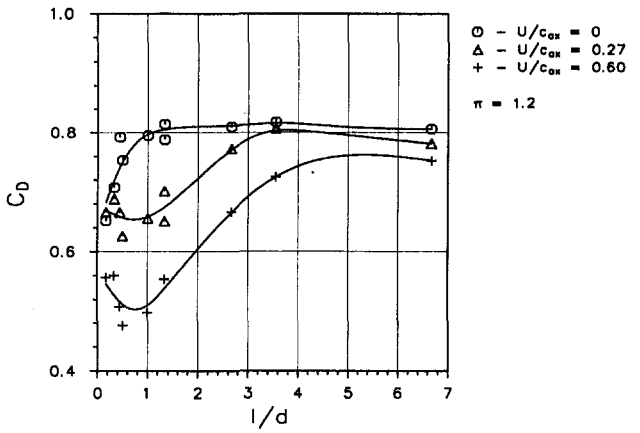


Fig. 15 Influence of l/d: measurement

Acknowledgments

Thanks are due to M. Heldner and H. Güntner for their assistance in carrying out the measurements, M. Hlilou for his cooperation in producing the numerical data, and H. Zimmerman of "Motoren- und Turbinen-Union," München, for helpful discussions. This work was supported by the Forschungsvereinigung Verbrennungskraftmaschinen e. V.

References

Becker, B., Schwerdtner, O., and Hosenfeld, H.-G., 1977, "Investigation of the Cooling Air Flow From Stationary to Rotating Components," presented at the 12th International Congress on Combustion Engines, CIMAG.

Benedict, R. F., Wyler, J. S., and Brandt, G. B., 1975, "The Effect of Edge Sharpness on the Discharge Coefficients of an Orifice," ASME *Journal of Engineering for Power,* Vol. 97, No. 4.

Bragg, S. L., 1960, "Effect of Compressibility on the Discharge Coefficient of Orifices and Convergent Nozzles," *Journal of Mechanical Engineering Science,* Vol. 2, No. 1.

Callaghan, E. E., and Bowden, D. T., 1949, "Investigation of Flow Coefficient of Circular, Square and Elliptical Orifices at High Pressure Ratios," NACA Technical Note 1947.

Hay, N., Henshall, S. E., and Manning, A., 1994, "Discharge Coefficients of Holes Angled to the Flow Direction," ASME JOURNAL OF TURBOMACHINERY, Vol. 116, pp. 92–96.

Hay, N., Khaldi, A., and Lampard, D., 1987, "Effect of Crossflows on the Discharge Coefficients of Film Cooling Holes With Rounded Entries or Exits," *Proc. 2nd ASME–JSME Thermal Engineering Joint Conference,* Honolulu, HI, Vol. 3, pp. 369–374.

Hay, N., and Spencer, A., 1992, "Discharge Coefficients of Cooling Holes With Radiused and Chamfered Inlets," ASME JOURNAL OF TURBOMACHINERY, Vol. 114, pp. 701–706.

Herning, F., 1962, "Untersuchungen zum Problem der Kantenunschärfe bei Normblenden und bei Segmentblenden," *BWK,* Vol. 14, No. 3.

Jakoby, R., Benz, E., Willmann, M., and Wittig, S., 1994, "Phase Resolved LDV-Measurements in High-Speed Rotating Disk Systems With Orifices," *Proc. Fifth International Symposium on Transport Phenomena and Dynamics of Rotating Machinery (ISROMAC-5),* Maui, HI, May 8–11.

Jobson, D. A., 1955, "On the Flow of a Compressible Fluid Through Orifices," *Proc. Inst. Mech. Engrs.,* London, Vol. 169, p. 767.

Downloaded 01 Jun 2010 to 171.66.16.53. Redistribution subject to ASME license or copyright; see http://www.asme.org/terms/Terms_Use.cfm

Launder, B. E., and Spalding, D. E., 1974, "The Numerical Computation of Turbulent Flows," *Computer Methods in Applied Mechanics and Engineering,* Vol. 3, pp. 269–289.

Lichtarowicz, A., Duggins, R. K., and Markland, E., 1965, "Discharge Coefficients for Incompressible Non-cavitating Flow Through Long Orifices," *Journal Mechanical Engineering Science,* Vol. 7, No. 2.

McGreehan, W. F., and Schotsch, M. J., 1988, "Flow Characteristics of Long Orifices With Rotation and Corner Radiusing," ASME JOURNAL OF TURBOMACHINERY, Vol. 110, pp. 213–217.

Meyfarth, P. F., and Shine, A. J., 1965, "Experimental Study of Flow Through Moving Orifices," ASME *Journal of Basic Engineering,* Vol. 87, pp. 1082–1083.

Rhode, J. E., Richards, H. T., and Metger, G. W., 1969, "Discharge Coefficients for Thick Plate Orifices With Approach Flow Perpendicular and Inclined to the Orifice Axis," NASA-TN-D-5467.

TASCflow User Documentation, 1993, Advanced Scientific Computing Ltd.

Waschka, W., Scherer, T., Kim, S., and Wittig, S., 1992, "Study of Heat Transfer and Leakage in High Rotating Stepped Labyrinth Seals," *Fourth Int. Symp. on Transport Phenomena and Dynamics of Rotating Machinery (ISROMAC-4),* Honolulu, HI, Apr. 5–8.

Wiles, W. F., 1976, "Flow Through Holes in Rotating Discs," presented at the Thermofluids Conference, Hobart, Dec. 1–3.

Wittig, S., Schelling, U., Kim, S., and Jacobsen, K., 1987, "Numerical Predictions and Measurements of Discharge Coefficients in Labyrinth Seals," ASME Paper No. 87-GT-188.

Downloaded 01 Jun 2010 to 171.66.16.53. Redistribution subject to ASME license or copyright; see http://www.asme.org/terms/Terms_Use.cfm

Turbulent Flow Between Two Disks Contrarotating at Different Speeds

M. Kilic

X. Gan

J. M. Owen

School of Mechanical Engineering,
University of Bath,
Claverton Down, Bath, United Kingdom

This paper describes a combined computational and experimental study of the turbulent flow between two contrarotating disks for $-1 \leq \Gamma \leq 0$ and $Re_\phi \approx 1.2 \times 10^6$, where Γ is the ratio of the speed of the slower disk to that of the faster one and Re_ϕ is the rotational Reynolds number. The computations were conducted using an axisymmetric elliptic multigrid solver and a low-Reynolds-number $k-\epsilon$ turbulence model. Velocity measurements were made using LDA at nondimensional radius ratios of $0.6 \leq x \leq 0.85$. For $\Gamma = 0$, the rotor–stator case, Batchelor-type flow occurs: There is radial outflow and inflow in boundary layers on the rotor and stator, respectively, between which is an inviscid rotating core of fluid where the radial component of velocity is zero and there is an axial flow from stator to rotor. For $\Gamma = -1$, antisymmetric contrarotating disks, Stewartson-type flow occurs with radial outflow in boundary layers on both disks and inflow in the viscid nonrotating core. At intermediate values of Γ, two cells separated by a streamline that stagnates on the slower disk are formed: Batchelor-type flow and Stewartson-type flow occur radially outward and inward, respectively, of the stagnation streamline. Agreement between the computed and measured velocities is mainly very good, and no evidence was found of nonaxisymmetric or unsteady flow.

1 Introduction

In gas turbines, the turbine disk usually rotates close to either a stationary casing or another rotating disk. The essential features of the flow and heat transfer can be modeled using rotating-disk systems in which plane disks represent the more complex turbine disks in an engine. The rotor–stator system, which is used to model the flow between a turbine disk and an adjacent casing, has been and still is studied extensively (see Owen and Rogers, 1989), and the rotating cavity, which is used to model the flow between corotating disks, has also received considerable attention (see Gan et al., 1993, for a recent review). Contrarotating disks are not so widely used as the other configurations and, as a consequence, have received less attention. They may be used in future generations of ultra-high-bypass-ratio engines, in which contrarotating fans are employed, and a consequential advantage is that contrarotating turbines require one fewer row of stator nozzles, thereby reducing the weight and size of the engine.

The turbulent flow structure for contrarotating disks is quite different from that for a rotor–stator system, as shown schematically in Fig. 1. (Here and elsewhere in the paper, the rotation ratio Γ, where $\Gamma = \Omega_2/\Omega_1$, will be used to define the system: $\Gamma = 0$ refers to the rotor–stator system, and $\Gamma = -1$ to disks rotating at equal and opposite speeds.) Referring to Fig. 1(a), fluid moves radially outward in a thin boundary layer on the rotating disk (disk 1) and radially inward in a boundary layer on the stationary one (disk 2). Fluid flows from disk 1 to 2 in a thin boundary layer on the shrouds, and returns from disk 2 to 1 as a weak axial flow in the inviscid core between the boundary layers. This core rotates in quasi-solid-body rotation (with $V_\phi/\Omega r \approx 0.4$); as a consequence of the Taylor–Proudman theorem (see, for example, Batchelor, 1967), $V_r = 0$ and both V_ϕ and V_z are invariant with z in the core.

At this point, it is convenient to comment on the so-called Batchelor–Stewartson paradox. Batchelor (1951), from consideration of laminar flow between infinite rotating disks, predicted that for the rotor–stator system ($\Gamma = 0$) there would be an inviscid rotating core between the two boundary layers; Stewartson (1953) concluded that, for $\Gamma = 0$, there would be no such core and rotation would fall to zero outside the boundary layer on the rotor. For $\Gamma = -1$, Batchelor forecast that there would be radial outflow in boundary layers on both disks and radial inflow would be confined to a thin shear layer in the midplane, on either side of which was a rotating core of fluid; again Stewartson concluded that there would be no such cores, and radial inflow would occur in the (nonrotating) region between the two boundary layers. Gan et al. (1995) showed, from computations for laminar flow in a finite contrarotating-disk system, that Batchelor's predictions were correct: for $\Gamma = -1$, there was indeed a thin shear layer with contrarotating cores of fluid. However, computations for turbulent flow, and experimental measurements, showed that Batchelor-type flows are intrinsically unstable and are unlikely to occur in practice. For turbulent flow, therefore, Stewartson-type flow occurs for $\Gamma = -1$, as illustrated schematically in Fig. 1(b).

In an engine, it is possible for the ratio of the speeds of contrarotating turbine disks to be in the range $-1 < \Gamma < 0$. The question then arises: How does the flow structure change from Batchelor-type flow at $\Gamma = 0$ to Stewartson-type flow at $\Gamma = -1$? In other rotating-disk systems ($\Gamma = 0$, $\Gamma = +1$), laminar computations provide good insight into the flow structure that occurs in both the laminar and the turbulent cases; for contrarotating disks, however, this is not necessarily the case, and studies of laminar flow must be treated with caution.

The most comprehensive study for laminar flow was conducted by Dijkstra and van Heijst (1983) who carried out computations and measurements for $-0.825 \leq \Gamma \leq 0$ for rotational Reynolds numbers up to $Re_\phi \approx 2 \times 10^5$. For $\Gamma = 0$, there is a single-cell axisymmetric flow structure where, as can be seen from Fig. 1(a), the fluid circulates up the rotor and down the stator in a clockwise sense. For $-0.825 \leq \Gamma \leq -0.15$, a two-cell axisymmetric structure was computed and observed: Circulation

Contributed by the International Gas Turbine Institute and presented at the 39th International Gas Turbine and Aeroengine Congress and Exposition, The Hague, The Netherlands, June 13–16, 1994. Manuscript received by the International Gas Turbine Institute February 9, 1994. Paper No. 94-GT-54. Associate Technical Editor: E. M. Greitzer.

Copyright © 1996 by ASME

Downloaded 01 Jun 2010 to 171.66.16.53. Redistribution subject to ASME license or copyright; see http://www.asme.org/terms/Terms_Use.cfm

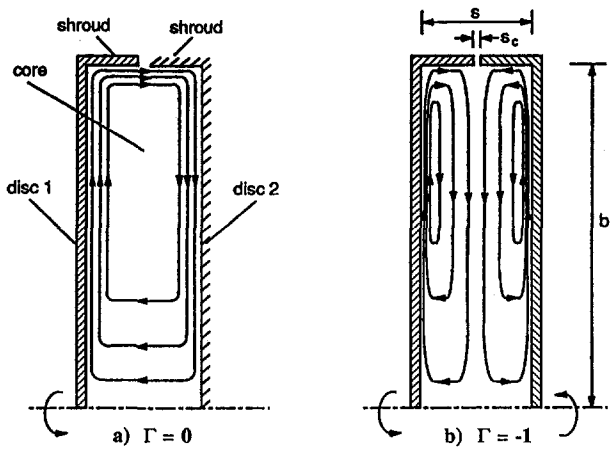


Fig. 1 Schematic diagram of flow structure

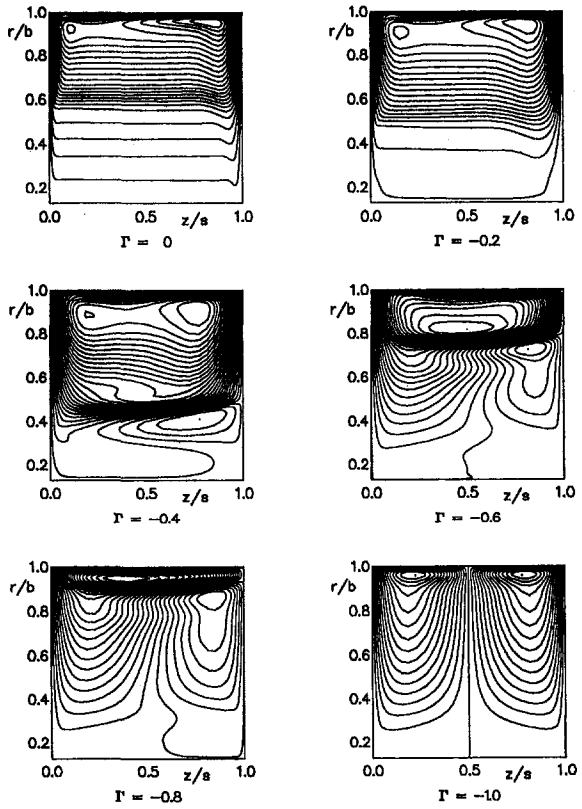


Fig. 2 Computed streamlines for $Re_\phi = 1.25 \times 10^6$

near the faster disk is clockwise, and that near the slower one anticlockwise. A stagnation streamline, separating the two cells, forms a stagnation ring on the slower disk at a nondimensional radius of $x = x_{st}$, and x_{st} increases as Γ decreases. For $-1 \le \Gamma \le -0.825$, no reliable experimental or computational results were obtained and "wavy instabilities" were observed.

The purpose of this paper is to study the structure of turbulent flow in the range $-1 \le \Gamma \le 0$, and in particular to look at the transition from Batchelor-type flow to Stewartson-type flow. By limiting the study to rotational Reynolds numbers where turbulent flow occurs, the additional complication of transition from laminar to turbulent flow can be avoided: The "double transitional" flow will be discussed elsewhere. Section 2 of this paper outlines the computational method and presents some computations of the flow structure. In Section 3, the experimental apparatus is briefly described, and comparisons are made between the computations and the experiments. Conclusions are presented in Section 4.

2 Computed Flow

2.1 Computational Method. The code used was a modified version of a finite-volume, multigrid, elliptic solver developed at Sussex University. Simplec pressure-correction smoothing was carried out with a V-cycle, full-approximation-storage multigrid scheme as employed by Lonsdale (1988) and extended by Vaughan et al. (1989). The axisymmetric, Reynolds-averaged, steady-state Navier–Stokes equations were solved in conjunction with a low-Reynolds-number (LR) $k-\epsilon$ turbulence model.

The code was used by Gan et al. (1995) for the case of contrarotating disks with $\Gamma = -1$. In that paper, a variant of the LR $k-\epsilon$ model of Morse (1991a, b) was used; in this paper, the (original) LR $k-\epsilon$ model of Launder and Sharma (1974) is used. Kilic (1993) has used both turbulence models for rotating-disk systems and, although neither was ideal for all flows, both were satisfactory for most of the cases considered. Both models were found to handle transition from laminar to turbulent without the need to specify transitional criteria, or to "trip the flow" artificially, but the Launder–Sharma and Morse models predicted transition to occur later and earlier, respectively, than that shown by the experimental data. The main advantage of the Launder–Sharma model is that it is more "robust"; that is, it is easier to achieve converged solutions of the multigrid elliptic solver at high rotational Reynolds numbers.

For $\Gamma = -1$ and $C_w = 0$, Gan et al. (1995) took advantage of the symmetry about the midplane ($z/s = \frac{1}{2}$) to halve the size of the computational domain to $a \le r \le b$, $0 \le z \le \frac{1}{2}s$; the computed velocity profiles provide "mirror images" for $\frac{1}{2}s \le z \le s$. For $-1 < \Gamma \le 0$, no such symmetry exists. For the solid boundaries ($r = a$, $r = b$, $z = 0$, $z = s$), no-slip conditions were used. For the small clearance, s_c, between the two contrarotating shrouds, it was assumed that V_r and V_z were zero and V_ϕ varied linearly with z.

The dimensions of the computational domain were the same as those of the experimental rig: $G = 0.12$, $G_c = 0.016$, $a/b = 0.128$. Grid-dependency tests were conducted for nonuniform grids with up to 91 × 115 (axial × radial) nodes, and it was found that a grid with 67 × 67 nodes (contracted to the bound-

Nomenclature

a = inner radius of disk
b = outer radius of disk
C_w = nondimensional mass flow rate = $\dot{m}/\mu b$
G = gap ratio = s/b
G_c = shroud-clearance ratio = s_c/b
r = radial coordinate
Re_ϕ = rotational Reynolds number = $\rho\Omega b^2/\mu$
s = axial gap between disks
s_c = shroud clearance
V_r, V_ϕ, V_z = velocity components referred to stationary cylindrical coordinates
x = nondimensional radius = r/b
x_{st} = nondimensional radius of stagnation ring
z = axial coordinate
Γ = ratio of speed of slower disk to that of faster one
μ = dynamic viscosity
ρ = density
Ω = angular speed of disk

Downloaded 01 Jun 2010 to 171.66.16.53. Redistribution subject to ASME license or copyright; see http://www.asme.org/terms/Terms_Use.cfm

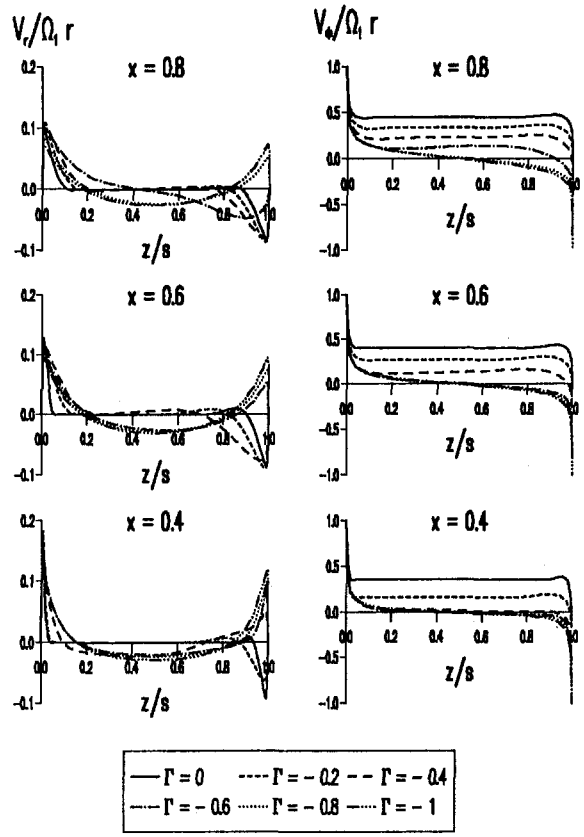


Fig. 3 Computed velocity profiles for $Re_\phi = 1.25 \times 10^6$

aries) gave sensibly grid-independent results. Morse (1991b) recommended that the grid point closest to the wall should be located to ensure that $y+ < 0.5$, where $y+$ is the wall-distance Reynolds number, and this condition was achieved for the computations presented here. The computations were conducted on one of the 16 i860 nodes of a Meiko parallel computing facility. The time for a converged solution depended on the rotational Reynolds numbers and on Γ, and typical times ranged from 1 to 2 hours for 91 × 115 nodes.

Further details of the computational methods are given by Kilic (1993).

2.2 Computed Flow Structure. Figure 2 shows the computed streamlines in the r–z plane for $Re_\phi = 1.25 \times 10^6$ and $-1 \le \Gamma \le 0$. The computations were conducted for $G = 0.12$, but the aspect ratio of the figures has been distorted to clarify the details of the flow. The left-hand boundary corresponds to disk 1, the faster disk.

For $\Gamma = 0$, the rotor–stator flow structure described above can be seen: There are thin boundary layers on the disks and shrouds, and the streamlines in the core, which are parallel to the axis of rotation, signify axial flow from the stator (disk 2) to the rotor (disk 1). This Batchelor-type flow structure is basically the same at $\Gamma = -0.2$.

For $\Gamma = -0.4$, the two-cell structure observed by Dijkstra and van Heijst for laminar flow is clearly visible, with a stagnation ring on disk 2 at $x \approx 0.45$. Radially outward of the stagnation streamline, the circulation is clockwise; radially inward, it is anticlockwise. In fact, as shown below, Batchelor-type flow and Stewartson-type flow occur radially outward and inward, respectively, of this stagnation streamline.

As Γ changes from −0.4 to −0.6 to −0.8, the stagnation ring on disk 2 moves radially outward from $x \approx 0.45$ to 0.75 to 0.94, and Stewartson-type flow occupies an increasingly large part of the domain. For $\Gamma = -1$, the streamlines are symmetric about the midplane, and Stewartson-type flow occurs throughout the domain with radial outflow in boundary layers on both disks and inflow between them.

An alternative way of viewing this transition from Batchelor-type flow to Stewartson-type flow is shown in Fig. 3 where the computed radial and tangential components of velocity, corresponding to the conditions in Fig. 2, are shown. Referring to $x = 0.8$, the following observations can be made:

(*i*) For $-0.4 \le \Gamma \le 0$, there are separate boundary layers on both disks with radial outflow on disk 1 and inflow on disk 2. In the core between the boundary layers, $V_r \approx 0$ and V_ϕ is virtually invariant with z. This corresponds to Batchelor-type flow.

(*ii*) For $-1 \le \Gamma \le -0.8$, there are separate boundary layers with radial outflow on both disks. Between the boundary layers, $V_r < 0$ and V_ϕ is sheared continuously from a positive value near disk 1 to a negative value near disk 2. This corresponds to Stewartson-type flow.

(*iii*) For $\Gamma = -0.6$, V_r is sheared continuously from a positive value near disk 1 to a negative value near disk 2, whereas V_ϕ shows the existence of separate boundary layers and core rotation. This indicates transition between Batchelor-type flow and Stewartson-type flow.

For $x = 0.6$, transition occurs between $\Gamma = -0.4$ and $\Gamma = -0.6$; for $x = 0.4$, transition occurs at $\Gamma \approx -0.4$. These velocity profiles are consistent with the flow structure shown by the streamlines in Fig. 2: Transition from complete Batchelor-type flow at $\Gamma = 0$ to complete Stewartson-type flow at $\Gamma = -1$ takes place by the development of a two-cell structure in which Batchelor-type flow occurs in the outer cell and Stewartson-type flow in the inner one.

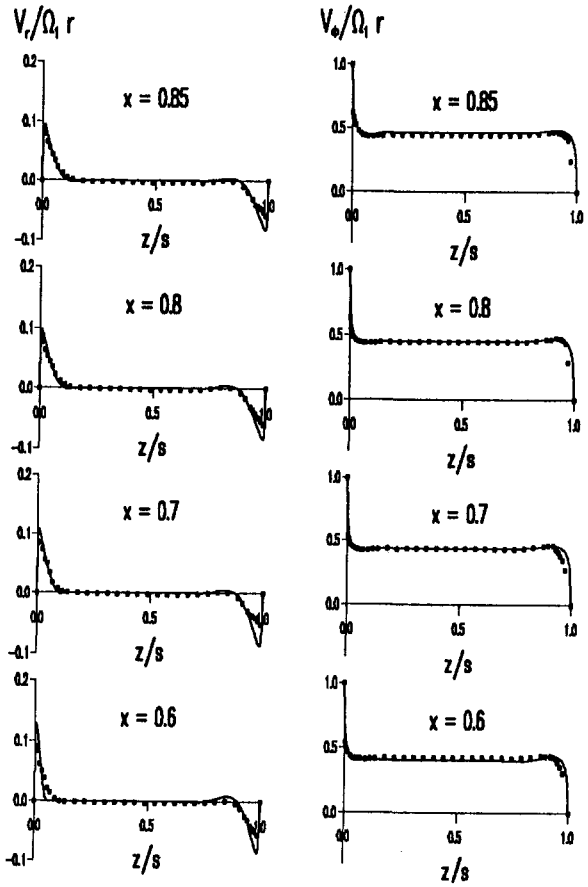


Fig. 4 Computed and measured velocity profiles for $Re_\phi = 1.25 \times 10^6$, $\Gamma = 0$: ○ experimental data; - - - - computed profile

Downloaded 01 Jun 2010 to 171.66.16.53. Redistribution subject to ASME license or copyright; see http://www.asme.org/terms/Terms_Use.cfm

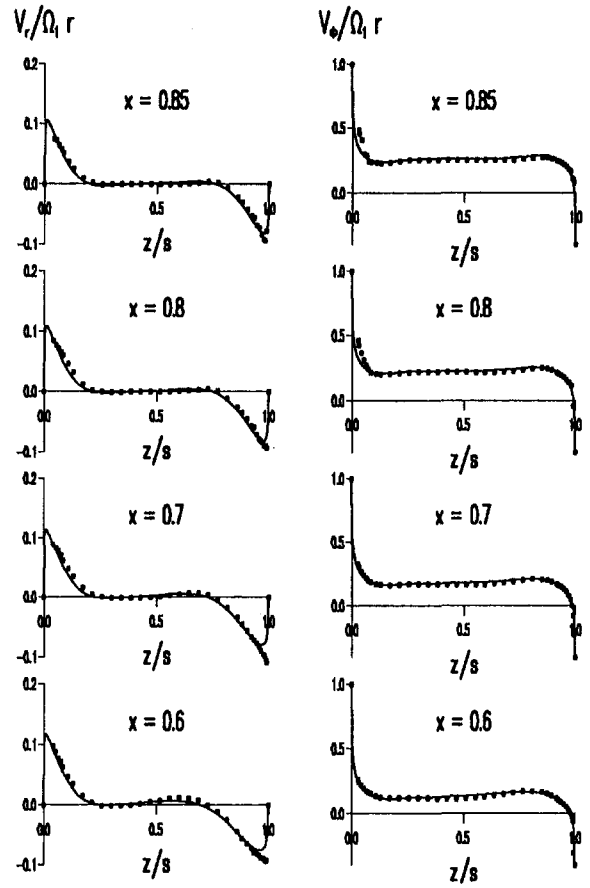


Fig. 5 Computed and measured velocity profiles for $Re_\phi = 1.25 \times 10^6$, $\Gamma = -0.4$: ○ experimental data; - - - - computed profile

These solutions were obtained for axisymmetric, steady flow using the Launder–Sharma turbulence model. There is, of course, no guarantee that the real flow will be either steady or axisymmetric, and, even if it were, the real flow is not constrained to follow the solutions obtained with the turbulence model. Having found a possible solution for the transition process, it is now convenient to test it on the experimental data.

3 Comparison Between Computations and Measurements

3.1 Experimental Apparatus. The apparatus is identical to that described by Gan et al. (1995), and the salient details are given below for convenience.

The rotating-disk rig comprised two disks of 762 mm diameter, which were independently rotated at up to 1500 rpm in either direction. A peripheral shroud was attached to each disk, and the axial clearance between the two shrouds was less than 4 mm; the axial gap ratio for the disks was $G = 0.12$. A radial outflow of air could be supplied through rotating gauze tubes, of 100 mm diameter, attached to the center of the disks; for the experiments described below, no superposed air was supplied and the tubes acted as rotating solid surfaces with $a/b \approx 0.13$.

One disk was made from transparent polycarbonate, and a single-component TSI laser-Doppler anemometer, with an IFA 750 burst correlator, was used to measure the radial and tangential components of velocity. Micron-sized oil particles were used to "seed" the air in the immediate vicinity of the disks, and enough particles were ingested into the "wheel-space" between the two disks to produce acceptable Doppler signals. With the optical "probe-volume" of the LDA system inside the polycarbonate disk, the tangential component of velocity could be compared with the independently measured angular speed of the disk: The difference was typically less than 0.5 percent of the speed.

3.2 Computed and Measured Velocity Profiles. Figure 4 shows the comparison between the velocity profiles, computed using the method described in Section 2 and measured using the apparatus outlined above, for $\Gamma = 0$, $Re_\phi = 1.25 \times 10^6$, and $0.6 \leq x \leq 0.85$: the rotor–stator case. Apart from some differences near the stationary disk, the agreement between the computed and measured velocities is mainly very good. The expected Batchelor-type flow structure is clearly visible: $V_r \approx 0$ and V_ϕ is invariant with z.

Figure 5 shows the equivalent results for $\Gamma = -0.4$, and again the agreement between computations and experiments is mainly very good. The computations shown in Figs. 2 and 3 indicate that, for $\Gamma = -0.4$, Batchelor-type flow occurs for $x \geq 0.4$, and the experimental results for $x \geq 0.6$ support this. No measurements were made for $x < 0.6$, and so the existence of Stewartson-type flow at the smaller radii could not be confirmed.

The co-existence of Batchelor-type flow and Stewartson-type flow can be seen in Fig. 6 for $\Gamma = -0.6$: Batchelor-type flow occurs at $x = 0.85$, Stewartson-type flow at $x = 0.6$ and 0.7, and transitional flow at $x = 0.8$. Agreement between computation and experiment is again mainly very good. It is interesting to see that radial inflow between the boundary layers is associated with $V_\phi/\Omega r < 0.1$ in the core: For $V_\phi/\Omega r > 0.1$, the Taylor–Proudman theorem appears to hold such that there is no radial flow in the (inviscid) core. For $x \leq 0.7$, where Stewartson-type flow occurs, both the radial and tangential components of velocity are sheared across the (viscid) core between the boundary layers.

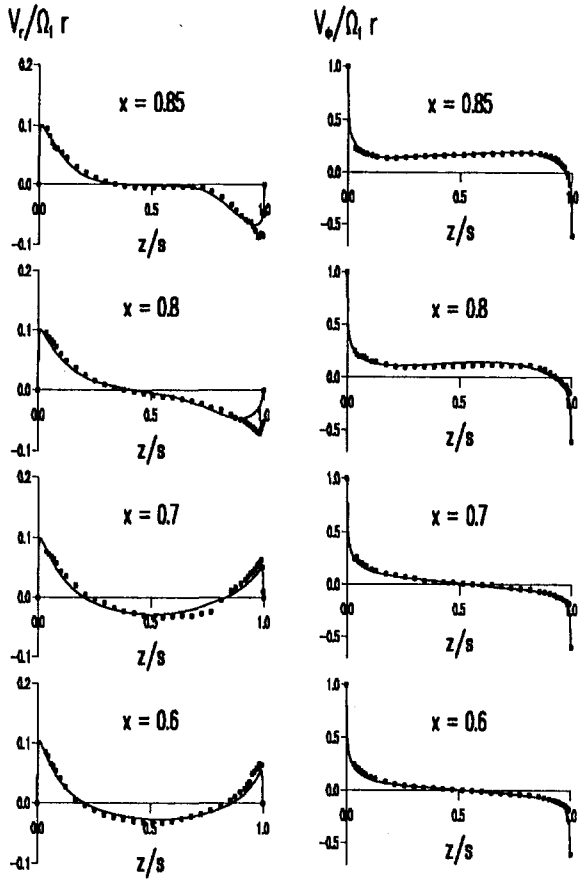


Fig. 6 Computed and measured velocity profiles for $Re_\phi = 1.25 \times 10^6$, $\Gamma = -0.6$: ○ experimental data; - - - - computed profile

Downloaded 01 Jun 2010 to 171.66.16.53. Redistribution subject to ASME license or copyright; see http://www.asme.org/terms/Terms_Use.cfm

Figure 7, for $\Gamma = -0.8$, shows that Stewartson-type flow exists for $x \leq 0.85$; Fig. 8, for $\Gamma = -1$, shows the final stage of the transition.

In conclusion, it can be seen that the experimental data have confirmed the two-cell transition from Batchelor-type flow to Stewartson-type flow predicted in Section 3. Although no LDA measurements were made for $x > 0.85$ or $x < 0.6$, measurements were made at other values of Γ and Re_ϕ in addition to those shown here. Although the agreement between computations and experiment was not as good at lower values of Re_ϕ, where transition from laminar to turbulent flow complicates the picture, the basic mechanism remains the same. Also, apart from regions of laminar-to-turbulent transition, both the Launder–Sharma and the Morse turbulence models yield similar results for the flow structure. While it would be unsafe to conclude that the turbulent axisymmetric flow *never* becomes three dimensional or unsteady, the authors have seen no evidence to suggest that it does: Transition from Batchelor-type flow to Stewartson-type flow appears to be a continuous steady process.

4 Conclusions

A combined computational and experimental study of the turbulent flow between contrarotating disks has been conducted for $G = 0.12$, $Re_\phi \approx 1.2 \times 10^6$, and $-1 \leq \Gamma \leq 0$.

The axisymmetric computations show that Batchelor-type flow occurs for $\Gamma = 0$, the rotor–stator case, with radial outflow and inflow in boundary layers on the rotor and stator, respectively, and axial flow from the stator to the rotor in the inviscid rotating core. For $\Gamma = -1$, antisymmetric contrarotating disks, Stewartson-type flow occurs with radial outflow in boundary layers on both disks and inflow between the boundary layers in the viscid nonrotating core. For intermediate values of Γ, the computations show a two-cell structure separated by a streamline that stagnates on the slower disk: Batchelor-type flow occurs radially outward of the stagnation streamline, and Stewartson-type flow occurs radially inward.

Velocity measurements, using LDA for $0.6 \leq x \leq 0.85$, provide evidence to support the computations, and agreement between computations and measurements is mainly very good. No evidence of unsteady or nonaxisymmetric flow was found for the range of variables considered, and measurements and computations carried out at other values of Re_ϕ show similar results.

This study was conducted without a superposed flow. The effect of a radial outflow of air on both the flow structure and heat transfer will be reported elsewhere.

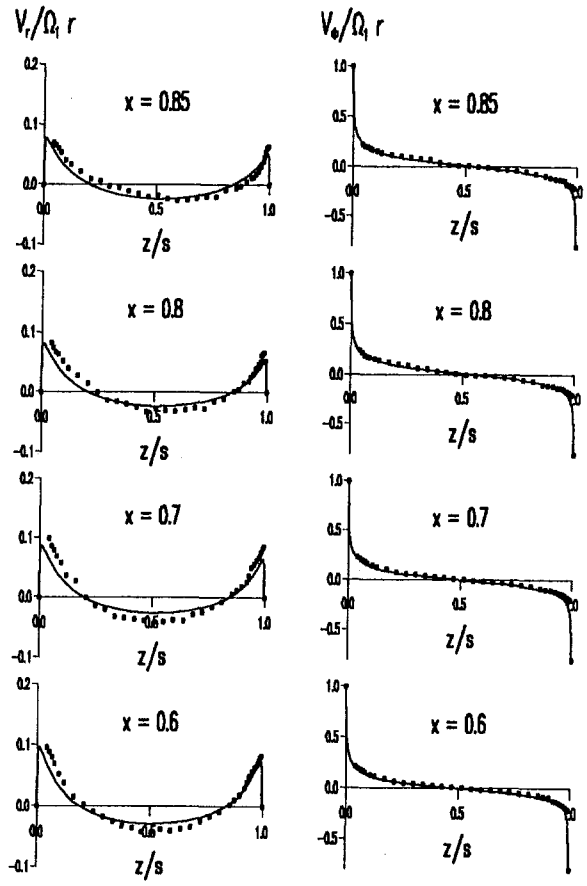


Fig. 7 Computed and measured velocity profiles for $Re_\phi = 1.25 \times 10^6$, $\Gamma = -0.8$; ○ experimental data; - - - - computed profile

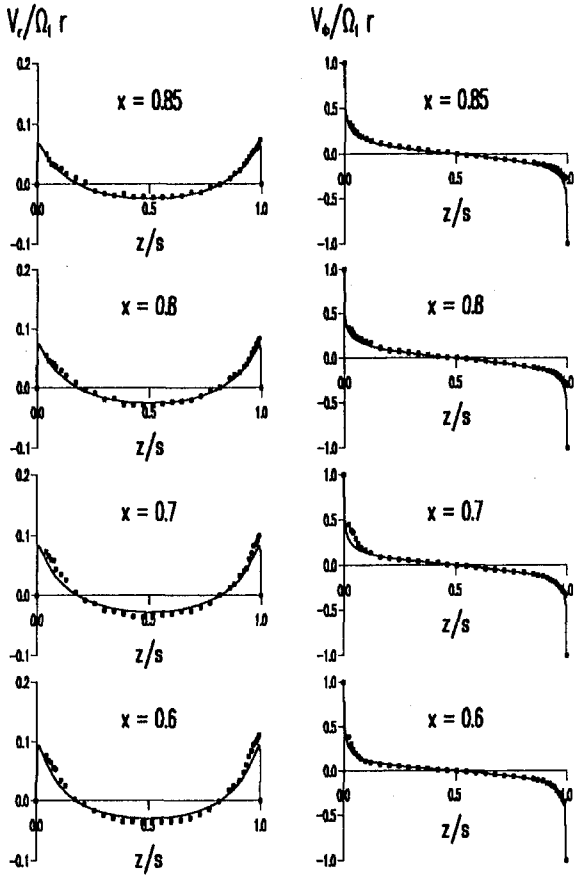


Fig. 8 Computed and measured velocity profiles for $Re_\phi = 1.25 \times 10^6$, $\Gamma = -1$: ○ experimental data; - - - - computed profile

Acknowledgments

The authors wish to thank the Ministry of Defence and the Science and Engineering Research Council (SERC) for supporting the work described in this paper; in particular, the Meiko parallel computer and much of the TSI LDA system was provided by SERC. We also wish to thank the Turkish Government and the University of Uludag, Bursa, for providing financial support for Dr. Kilic.

References

Batchelor, G. K., 1951, "Note on a Class of Solutions of the Navier–Stokes Equations Representing Steady Rotationally-Symmetric Flow," *Quart. J Mech. Appl. Maths.*, Vol. 4, pp. 29–41.

Batchelor, G. K., 1967, *An Introduction to Fluid Dynamics*, Cambridge University Press, London.

Downloaded 01 Jun 2010 to 171.66.16.53. Redistribution subject to ASME license or copyright; see http://www.asme.org/terms/Terms_Use.cfm

Dijkstra, D., and van Heijst, G. J. F., 1983, "The Flow Between Two Finite Rotating Disks Enclosed by a Cylinder," *J. Fluid. Mech.,* Vol. 128, pp. 123–154.

Gan, X., Kilic, M., and Owen, J. M., 1993, "Flow and Heat Transfer Between Gas Turbine Discs," AGARD-CP-527, pp. 25.1 to 25.11.

Gan, X., Kilic, M., and Owen, J. M., 1995, "Flow Between Contrarotating Discs," ASME JOURNAL OF TURBOMACHINERY, Vol. 117, pp. 298–305.

Kilic, M., 1993, "Flow Between Contrarotating Discs," PhD thesis, University of Bath, United Kingdom.

Launder, B. E., and Sharma, B. I., 1974, "Application of the Energy Dissipation Model of Turbulence to the Calculation of Flow Near a Spinning Disc," *Letters in Heat and Mass Transfer,* Vol. 1, pp. 131–138.

Lonsdale, G., 1988, "Solution of a Rotating Navier–Stokes Problem by a Nonlinear Multigrid Algorithm," *J. Comp. Phys.,* Vol. 74, pp. 177–190.

Morse, A. P., 1991a, "Assessment of Laminar–Turbulent Transition in Closed Disc Geometries," ASME JOURNAL OF TURBOMACHINERY, Vol. 113, pp. 131–138.

Morse, A. P., 1991b, "Application of a Low Reynolds $k-\epsilon$ Turbulence Model to High-Speed Rotating Cavity Flows," ASME JOURNAL OF TURBOMACHINERY, Vol. 113, pp. 98–105.

Owen, J. M., and Rogers, R. H., 1989, *Flow and Heat Transfer in Rotating Disc Systems, Vol. 1: Rotor–Stator Systems,* Research Studies Press, Taunton; Wiley, New York.

Stewartson, K., 1953, "On the Flow Between Two Rotating Coaxial Disks," *Proc. Camb. Phil. Soc.,* Vol. 49, pp. 333–341.

Vaughan, C. M., Gilham, S., and Chew, J. W., 1989, "Numerical Solutions of Rotating Disc Flows Using a Non-linear Multigrid Algorithm," *Proc. 6th Int. Conf. Num. Meth. Lam. Turb. Flow.,* Pineridge Press, Swansea, pp. 66–73.

Downloaded 01 Jun 2010 to 171.66.16.53. Redistribution subject to ASME license or copyright; see http://www.asme.org/terms/Terms_Use.cfm

Windage Heating of Air Passing Through Labyrinth Seals

J. A. Millward

M. F. Edwards

Rolls-Royce Plc,
Derby, United Kingdom

The viscous drag on rotating components in gas turbine engines represents both a direct loss of power from the cycle and an input of heat into the secondary (cooling) air system. Hotter cooling air in turn means increased flow requirements. The effects of windage on performance are therefore compounded. To facilitate accurate temperature predictions of highly stressed components, information is needed on windage characteristics of all elements in the secondary cooling system. Much information is available in the literature for disks, cones, cylinders, bolts, etc., but little has been published on windage heating in high-speed seals. Results are presented for experiments carried out (at representative nondimensional conditions) on different designs of labyrinth seals. The results are compared with values calculated from the simple momentum balance theory suggested by McGreeham and Ko [13] and with several values determined from CFD analysis.

1 Introduction

With improvements in efficiency of main gas path components of gas turbines (i.e., compressors and turbines) becoming ever more difficult and costly to achieve, attention continues to be directed toward reductions in secondary losses. Since the internal air system, though vital to satisfactory functioning of the engine, is entirely parasitic on the main cycle, increased effort is being put into its understanding and optimization.

The internal air system of a gas turbine engine performs many complex, interrelated functions. The system extracts cooling air from the main gas path and distributes it so as to provide a thermal environment that will maintain engine structural integrity and running clearance goals under steady-state and transient conditions. At the same time it also pressurizes (i.e., seals), cools, and thrust balances the rotor.

The viscous drag on rotating components, the so-called windage effect, represents both a direct loss of power from the cycle *and* an input of energy in the form of heat into the internal cooling system. The degraded quality of the cooling air in turn necessitates increased quantities of cooling flow (for such components as disks and blades) to be bled from the main annulus. The effects of windage on performance are therefore compounded.

Much information has been published on the windage of disks (e.g., Refs. [2–8]) and some, though much less information is available on the windage of cylinders, cones and protrusions (e.g. Refs [9, 10, 11, 12]). At the time of starting the work described in this paper, no published information was available on the windage heating of air passing through labyrinth seals.

Subsequently McGreeham and Ko [13] presented results of seal windage tests and compared experimental data with a simple friction factor model. Due to high heat transfer caused to some extent by the design of the experiment, the experimental results at low leakage could not be adequately predicted by the simple friction factor model. Since the experiments reported in the present paper were all for flow levels much higher than for [13], it was hoped that the simple friction factor model proposed in that reference would be able to match the measured data without the same problem of high heat loss at low flows being apparent.

The model of McGreeham and Ko, using the expressions for surface friction coefficients proposed in that paper, has been compared with the newly published experimental data for a range of leakage flows, rotor speeds, and seal fin numbers. Results of some limited test cases using a full CFD analysis of the "straight through" test seal are also compared with the experimental data.

The objectives of the experiments reported in this paper were to establish the effect of leakage flow on seal windage power (the effect of flow on seal windage had previously not been allowed for in systems calculations) and to carry out a parametric study of the effect of fin geometry and seal lining materials on seals windage.

2.0 Description of Facility and Rig

The Rolls-Royce Internal Air Systems Research facility is installed on the Hucknall Thermal Site and has access to airflows up to 1.474 kg/s at temperatures up to 650°C and pressures up to 4136 kPa. The particular test rig used for this program of work (see Fig. 1) is essentially a test box, which houses cantilevered rotor assemblies of diameters up to 0.47 m. The rotor on test is driven by a 74.5 kW electric motor via a 10:1 ratio gearbox, which allows speeds up to 13,500 rpm to be achieved. The test unit is designed for maximum conditions of 345 kPa and 250°C.

The relevant operating nondimensionals for the rig are very close to engine values as shown in Table 1.

For the labyrinth seal tests reported in this paper, the test air was fed via a control valve and an airflow measuring section into the entry chamber. The flow then splits to pass through the test seal and also the front balance seal, thereby cooling the pocket between those two seals. On leaving the test seal, the air splits again. Some of the air flows directly out of the exit chamber and the remainder flows through the rear balance seal, thereby ventilating the rear pocket and the rear of the disk before exiting from the cooling air rear compartment. The outlets from the exit chamber and cooling air rear compartment are both fitted with airflow measuring sections. The front cooling air compartment has a direct airfeed to supplement the air leakage over the front balance seal. The mixed air then exits directly from the front cooling air compartment without the mass flow being measured.

3.0 Description of Test Seals; Determination of Running Clearance

The test seals were basically of four types:

(*a*) Straight through, radial fins
(*b*) Straight through, inclined fins

Contributed by the International Gas Turbine Institute and presented at the 39th International Gas Turbine and Aeroengine Congress and Exposition, The Hague, The Netherlands, June 13–16, 1994. Manuscript received by the International Gas Turbine Institute February 4, 1994. Paper No. 94-GT-56. Associate Technical Editor: E. M. Greitzer.

Copyright © 1996 by ASME

Downloaded 01 Jun 2010 to 171.66.16.53. Redistribution subject to ASME license or copyright; see http://www.asme.org/terms/Terms_Use.cfm

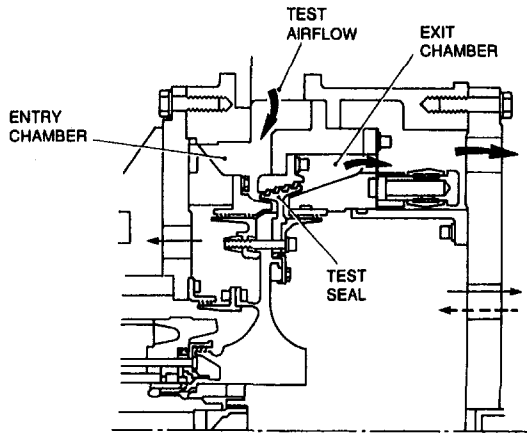


Fig. 1 Test rig arrangement

(*c*) Stepped, radial fins
(*d*) Two-stage brush

The important dimensions of the finned seals are shown in Fig. 2.

All the finned seals were tested against plain stators. The stepped seal was also tested against a Feltmetal lining, and some of the straight through seals were tested against honeycomb linings.

Table 2 shows the specification for each of the builds tested.

With the end cover off the rig, the actual cold build radial clearances were measured by means of feeler gages. Rotor growth checks had been carried out on previous runs of this rig using capacitance clearance probes and a high level of confidence had been established in prediction of both centrifugal and thermal growths. From the measured air temperatures within the running rig at any given rotor speed, the mean running clearance was calculated from the mean cold build clearance.

4.0 Experimental Technique

The objective of the experimental work was to establish the effects of various geometric parameters and environmental conditions on the *overall* heat pickup of air passing through labyrinth seals. The experiment was kept as simple as possible and so all instrumentation was static (see 5.0 below) and intermediate parameters (e.g., in each seal cell) were not measured.

Table 1

	Engine	Rig Max
$\frac{Nr_R}{\sqrt{T}_R}$	370	600
$\frac{\dot{m}}{\mu r_R}$ (ie.Cw)	4.0×10^4	8.0×10^4
$\frac{\rho \omega r_R^2}{\mu}$ (ie.Re)	3.0×10^7	1.7×10^7

For an adiabatic system, all windage power absorbed in a rotor/stator system must be dissipated into the cooling air as heat. The experiments described in this paper were aimed at being adiabatic so that windage power absorbed by the air passing through the seal could be obtained very simply by means of measurement of enthalpy change in the main test cooling air i.e.,

$$\text{Windage Power absorbed} = \dot{m}\, Cp \Delta T$$

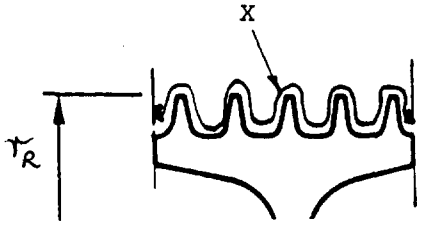
Within the labyrinth seal itself the flow can be considered as a series of throttling processes, which in classical theory are normally assumed to be adiabatic because each throttling takes place in such a short length that the surface area across which heat can flow is very small. In the particular series of tests reported in this paper the temperature differences between the seal and its immediate environment were kept as low as possible to further reduce the potential heat loss.

The temperature rise of the air passing through the seal was obtained by measuring inlet and outlet temperatures immediately as the air entered and left the seal. Windage heat generated by the mounting disk rim section and the inlet and outlet balance seals was isolated from the test seal and main airflow by bleeding air into the front and rear seal cooling air compartments and thereby ventilating the section of the disk rim radially spaced between the test seal and balance seals.

Any heat conducted from the hot side of the disk rim to the cold side would not affect the results since the upstream ventilation air

Nomenclature

A = leakage area, m^2
c = seal radial clearance ($r_s - r_R$), m
Cp = specific heat at constant pressure, J/kg · K
Cms = seal moment coefficient = $W/\pi\rho X \omega^3 r_R^4$
Cw = flow number = $\dot{m}/\mu r_R$
C_{fR} = rotor surface friction coefficient (see Eq. (7.3))
C_{fS} = stator surface friction coefficient (see Eq. (7.3))
h = seal fin height, m
H = calculated windage heating for seals with plain linings (power), kW
HHC = calculated windage heating for seals with honeycomb liners (power), kW
l = fin pitch, m
m = leakage mass flow rate, kg/s
N = rotor speed, rpm
n = number of seal fins
P = total pressure, kPa
p = static pressure, kPa
r = radius, m
Re* = modified rotational Reynolds number = $\rho \omega r_R h/\mu$
Re = rotational Reynolds number = $\rho \omega r_R^2/\mu$
T = air total temperature, K
t = air static temperature, K
V_{CORE} = fluid core tangential velocity, m/s
W = measured windage heating (power), kW
X = length of seal surface (rotor), m



β = fluid core velocity ratio = $V_{core}/\omega r_R$
Δ = difference
μ = dynamic viscosity, N · s/m^2
ρ = air density, kg/m^3
ω = rotor angular velocity, rad/s

Subscripts

in = inlet
out = outlet
R = rotor
S = stator

Note: FELTMETAL is a seal lining material in sheet form made from randomly oriented fibers, which are sintered to provide strength. It is produced by the Brunswick Corporation of the USA. The standard used in these tests was FM-515B.

Downloaded 01 Jun 2010 to 171.66.16.53. Redistribution subject to ASME license or copyright; see http://www.asme.org/terms/Terms_Use.cfm

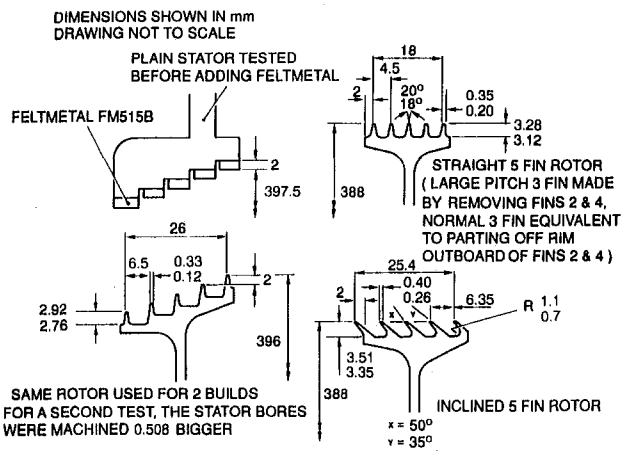


Fig. 2

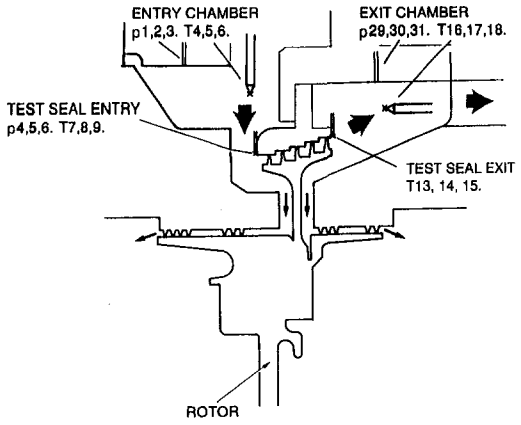


Fig. 3 Location of rig instrumentation

carries this heat away from the inlet air thermocouples. Any heat conducted from the hot side of the seal stator to the cold side would not affect the results since this heat is dissipated into the main inlet air upstream of the inlet air thermocouples.

The outside of the rig was lagged and measurements were taken when the particular test setup had reached steady state.

5.0 Instrumentation

The location of the pressure and temperature tappings within the working section of the rig are shown in fig. 3.

Table 2 Test seal details

			RADIAL CLEARANCE (mm)	
BUILD	TYPE	NO OF FINS	BUILD	13,000 RPM
1	Stepped	5	.610	.330
2	Stepped + Feltmetal Lining	5	.660	.381
3	"	5	.889	.610
4	Straight	5	1.105	.826
5	"	5	.533	.254
6	Straight + .062" Cell Honeycomb	5	.584	.305
7	"	5	1.079	.800
8	Straight	3	1.067	.787
9	Inclined Fins	5	1.143	.864
10	Straight + Filled Honeycomb	5	1.105	.826
11	Straight	1	1.041	.762
12	Brush	-	0	0
13	Straight	3 Large Pitch	1.092	.813
14	Straight + .020" Cell Honeycomb	3 Large Pitch	.546	.267
15	Straight + .062" Cell Honeycomb	3 Large Pitch	.584	.305

In order to improve accuracy, all main test parameter measuring points (pressures and temperatures) were triplicated and thermocouples used were of the exposed junction type. All thermocouples used were individually calibrated prior to fitment and so could be relied upon to read to an accuracy of $\pm\frac{1}{2}$°C.

The pitot/static measuring sections used were all calibrated prior to fitment against air standard meters and could be relied upon to facilitate flow measurement to an accuracy of ±1 percent.

6.0 Test Conditions

Nominal inlet air temperature 25°C
Test seal inlet pressure level: 30, 40, 50 psia (i.e., ≃ 207, 276, 345, kPa)
Rotor speed: 0, 7, 9, 11, 13, rpm × 10^{-3}
Test seal pressure ratio 1.05 to 1.90 (i.e., P_{in}/p_{out})

Normally three pressure ratios per build were tested. Wide clearance seals were tested toward the bottom end of the pressure ratio range and tight clearances toward the top end of the range. Where one seal configuration was tested at two clearances, the range of mass flow overlapped.

To limit the amount of testing some of the seals were tested at one inlet pressure only.

7 Discussion of Results

The results from each test were plotted in the following forms:

(*i*) Flow function versus pressure ratio

$$\frac{\dot{m}\sqrt{T_{in}}}{AP_{in}} \text{ versus } \frac{P_{in}}{p_{out}}$$

(*ii*) Windage heating versus Rotor speed

$$\dot{m}\ Cp\Delta T \text{ versus } N$$

7.1 Seal Leakage. A typical set of flow characteristics is shown in Fig. 4. Since the flow results are not the main purpose of this paper, nothing more detailed is said of the results other than to say that no surprises were evident from the experiments. The order of merit was as expected from both previous two-dimensional static tests and other rotating tests. The most efficient "labyrinth" seal tested in terms of limiting leakage at a pressure ratio was the five-finned stepped seal.

By plotting $(\dot{m}\sqrt{T_{in}})/(2r_R P_{in})$ against pressure ratio, the result of the (zero clearance) brush seal could be compared with the positive clearance labyrinths. This result is shown in Fig. 5 and it can be seen that the sealing performance of the brush is best of all the seals tested with a leakage of only approximately 60

Downloaded 01 Jun 2010 to 171.66.16.53. Redistribution subject to ASME license or copyright; see http://www.asme.org/terms/Terms_Use.cfm

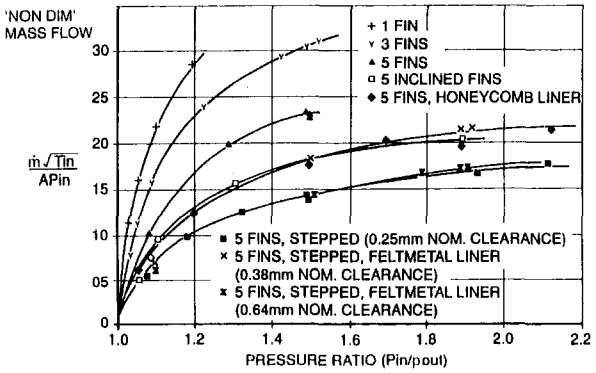


Fig. 4 Comparison of different seal configurations 13,000 rpm, 0.75 mm *nominal running clearance unless otherwise stated*

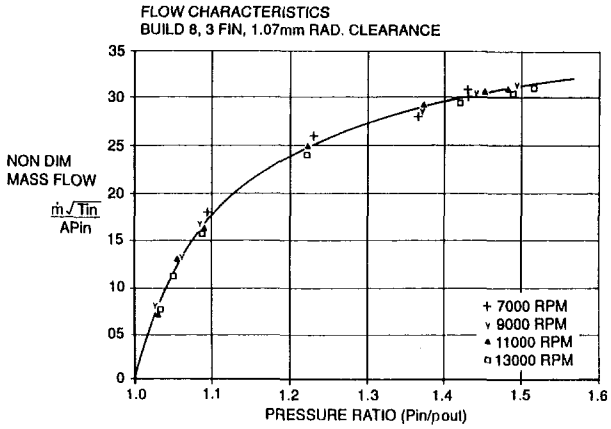


Fig. 6

percent of the five finned stepped labyrinth running at 0.25 mm radial clearance.

It is also worth nothing that for all unlined seals, rotation was found to have no effect on sealing effectiveness over the range tested. This is clearly illustrated by the typical plot in Fig. 6 below. The honeycomb and feltmetal linings did display the expected "small clearance" effect (seen in previous unpublished static tests) of *slightly* degrading sealing performance at the smallest running clearances (i.e., in this case at the highest speeds with the tightest build clearances where centrifugal loading results in the smallest running clearances $\simeq$ 0.3 mm). This is due to the fact that, approaching the limit of zero clearance honeycomb and porous lined seals can still pass some flow. The one honeycomb build tested at relatively large clearance ($\simeq$ 1.0 mm) showed no significant effect of rotation, which tends to confirm the effect mentioned above as being the small absolute clearance rather than rotation.

7.2 Windage Heating Measurements. A typical plot of measured windage heating versus rotor speed obtained from the experiments is shown in Fig. 7 below. The plot also includes curves of an early RR model for labyrinth seal windage based on simple free disk and free cylinder windage. Since the free disk and cylinder moment coefficients only vary with rotational Reynolds number, the model did not allow for variation in seal leakage flow (which is a function of pressure ratio). It can also be seen from the plot that, while the model adequately predicted the variation of windage with pressure level (and hence density), the predicted variation with rpm is distinctly different from that observed. It was in fact due to the known inadequacies of this model in allowing for seal flow that the experimental program had been initiated.

By plotting measured windage heating against leakage flow for all test builds at a speed and a pressure level, it is possible to make certain observations directly. A typical plot for the 13,000 rpm speed and an inlet pressure of 344.7 kPa is shown in Fig. 8 below.

The observations which are possible from plotting in this form are:

- (*a*) A clear relationship exists between windage heating and leakage flow largely independent of clearance over the range tested. Where the same seal was tested at more than one clearance, the results fall close to a common line.
- (*b*) Both inclined fin seals and stepped seals generate similar levels of heat to the straight through seal *at the same airflow* (but the flows through the inclined fin seal and stepped seal are of course less than the straight through seal *at the same pressure ratio*).
- (*c*) As might have been anticipated, the brush seal results fall on the extrapolated single fin seal line but, at any pressure ratio, the flow through the brush was obviously very small by comparison.
- (*d*) At a given *flow* level, honeycomb linings result in an increase in measured windage of approximately 15 percent.
- (*e*) For the only direct "back to back" tests carried out on the two sizes of honeycomb lining (tested against a large pitch three fin seal), the measured windage was the same for each at a given level of seal leakage flow.

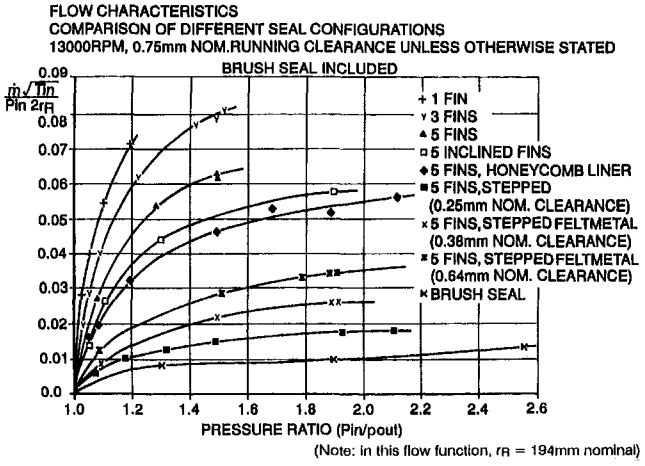


Fig. 5

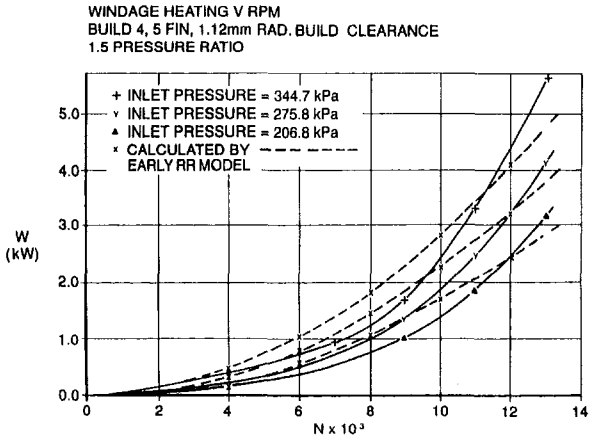


Fig. 7

Downloaded 01 Jun 2010 to 171.66.16.53. Redistribution subject to ASME license or copyright; see http://www.asme.org/terms/Terms_Use.cfm

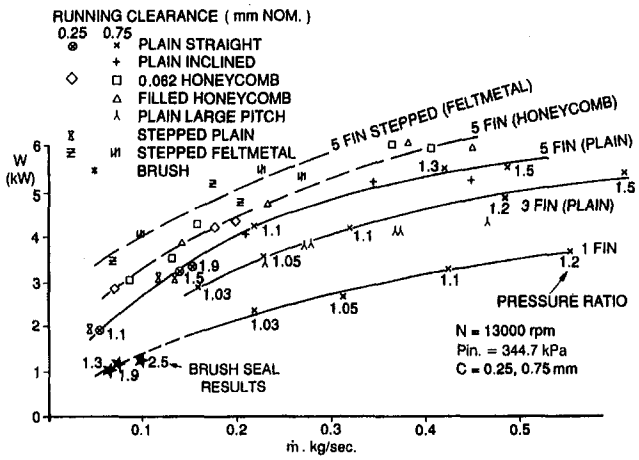


Fig. 8 Typical experimental results

From all the windage measurements made on the various seals with plain linings, the simple correlation for seal windage given below was determined with no great difficulty:

$$H = Cms\,\pi X \rho \omega^3 r_R^4$$

where *Cms* is a seal moment coefficient given by

$$6 \times 10^{-5}\left[\frac{Cw}{\mathrm{Re}}\right]^{0.55} n^{-0.65}$$

It is found that the correlation predicts the measured seal windage data for the plain liners to within ±25 percent at all levels of flow. The few points that fall outside these limits all overestimate windage (the single worst value being + 40 percent). Windage heat for the honeycomb lined seals can be predicted to similar levels of accuracy using

$$\mathrm{HHC} = 1.15\,H$$

7.3 Comparison Between Measured Seal Windage and Values Computed Using the McGreeham and Ko model. The attraction of this model over the given above correlation is the fact that it is based on a relatively simple but plausible assumption about the actual physics of seal windage heating. This method of predicting seal windage, if sufficiently accurate, is a much quicker means for use in air system analysis than a full CFD analysis of the flow within the seal.

Results are presented for the model using the same surface friction coefficients used by McGreeham and Ko [13].

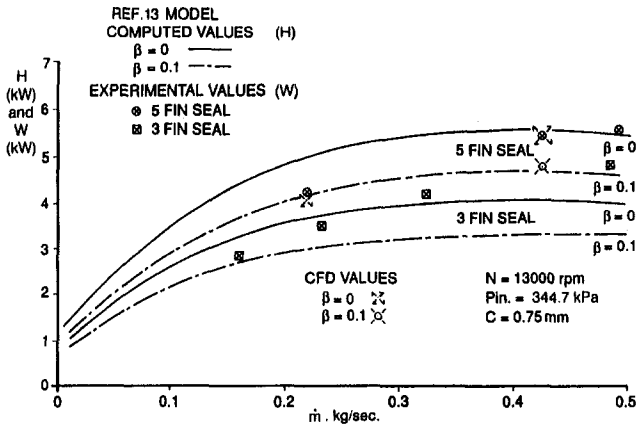


Fig. 9 Straight seals: plain liners

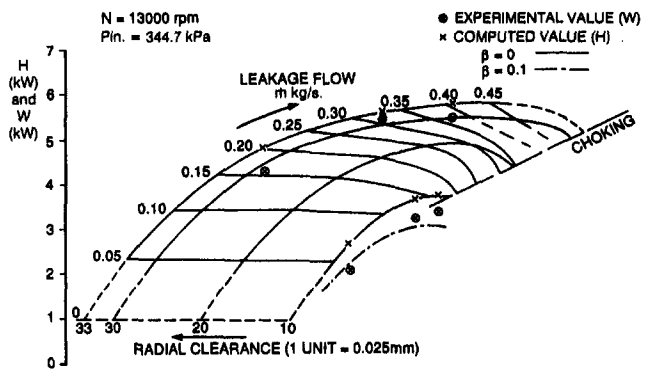


Fig. 10 Carpet plot of *H* (and *W*) versus *ṁ* and *c* (Five fin straight seal, plain liners, *N* = 13,000 rpm)

$$C_{fR} = 0.042\,(1-\beta)^{1.35}\mathrm{Re}^{*-0.2}$$

and

$$C_{fS} = 0.063\,\beta^{1.87}\,\mathrm{Re}^{*-0.2}$$

As can be seen from Fig. 9, the curves produced by the model are of the same form as seen for the experimental results in Fig. 8. Windage is seen to fall to low levels at low leakage flows and to approach a maximum at high flows as the seal becomes choked (Note: Upstream pressure is constant). Computed curves are shown for three and five fin seals for inlet swirl fractions of 0 and 0.1. The experimental values for the five fin seal are well predicted by the model between the set limits of inlet swirl fraction. The results for the three fin seal are not as well predicted but are only significantly underpredicted at the highest flows.

Typical carpet plots for the five fin straight seal generated using the model are given in Figs. 10 and 11 for rotor speeds of 13,000 and 10,000 rpm, respectively. The main carpets are generated assuming an inlet swirl fraction of zero and a half seal cell at inlet and exit. It can be seen that the model predicts the observed effect that actual clearance has little effect on windage until the seal approaches choking (for constant upstream pressure). The major effect of clearance change at a pressure ratio is a change of flow, which does have a direct and significant effect on seal windage. The model, run with zero inlet swirl, is seen slightly to overpredict the measured data. However it can be seen that application of even a small amount of inlet swirl (in this case to 0.1) encompasses most of the test points shown. It is quite possible that while every effort was made to run an adiabatic experiment with zero inlet swirl, a small level of swirl could have been generated in the entry chamber or some small heat loss could have occurred. Either effect could result in the small discrepancy between the model and the experimental results.

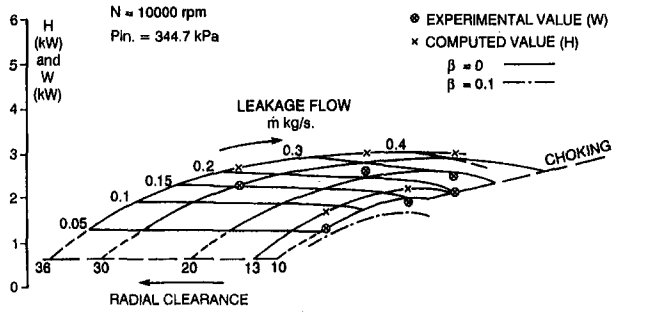


Fig. 11 Carpet plot of *H* (and *W*) versus *ṁ* and *c* (Five fin straight seal, plain liners, *N* = 10,000 rpm)

Downloaded 01 Jun 2010 to 171.66.16.53. Redistribution subject to ASME license or copyright; see http://www.asme.org/terms/Terms_Use.cfm

Table 3

Case	RPM	P.R.	$\dot{m}$ (kg/sec)	FINS	Pin(kPa)	SEAL WINDAGE measured W(kW)	SEAL WINDAGE Computed H(kW)
1	13000	1.1	0.217	5	344.7	4.178	4.047
2	13000	1.3	0.421	5	344.7	5.412	5.448

7.4 Comparison Between Measured Seal Windage and Values Computed Using the RR-CFD code "PACE." A very limited investigation was carried out to see how well the experimental results could be matched using an existing RR CFD code ("PACE"). The CFD method used is a finite volume Navier–Stokes solver, which employs boundary-fitted coordinates and uses the $k-\epsilon$ turbulence model with alternative near wall treatments. In this case the $k-\epsilon$ region was coupled to the near-wall regions using a near-wall low Reynolds number one-equation $k-l$ model. A full description of the method is given in [14].

Since the method is strictly for incompressible flow, the experimental points chosen for comparison were at the two lowest pressure ratios tested on the five fin straight seal operating at the largest clearance. An inlet swirl fraction of 0 was used and adiabatic conditions were assumed. The results of the CFD computation for the two different flows (both for rotor speeds of 13,000 rpm) are given in Table 3. It can be seen that the agreement with the experimental results is very good.

It is encouraging to note that accurate predictions of seals windage for seals operating "incompressibly" are possible using CFD techniques if a particular case justifies the effort. A further extension of the work would be to use CFD to further calibrate the simple friction factor method.

8 Conclusions

The main conclusions from the work presented can be summarized as follows:

8.1 The power absorbed due to frictional drag in labyrinth seals is strongly affected by the airflow ($\dot{m}$).

8.2 Different designs of labyrinth seals with the same nominal radii and surface areas (which may have different sealing efficiences) will result in similar levels of windage heating at a given *flow level.*

8.3 Labyrinth seal windage heating *for a given inlet pressure* will reach a maximum before the seal is choked. This is due to falling pressure levels in the seal cells outweighing the less rapid increase in flow as choking is approached.

8.4 Honeycomb linings of two different cell sizes were both found to increase windage by approximately 15 percent.

8.5 Feltmetal-lined seals resulted in even higher windage heating than honeycomb lined seals. (The "step gaps" present on the feltmetal seal but absent on the honeycomb seal in the present tests could possibly have been the cause of this effect due to recirculation of flow.)

8.6 Windage heating for the brush seal was of a very low level, due no doubt to the very low leakage flows.

8.7 A simple correlation can be used to predict windage heating in plain lined labyrinth seals to approximately ±25 percent.

8.8 A better, more accurate and still simple method of predicting seal windage is that proposed by McGreeham and Ko [13].

8.9 The most accurate method for predicting labyrinth seals windage was found to be by the use of the RR "PACE" finite volume Navier–Stokes solver. This method however requires much more effort to execute and may not be justified for normal "systems" calculations.

Acknowledgments

The authors would like to thank the UK Ministry of Defence Procurement Executive for providing part funding for the work presented in this paper and would also like to thank Rolls-Royce plc for allowing publication of the work. Thanks also goes to G. P. Virr who carried out the CFD calculations referred to in section 7.4.

References

1 Graber, D. J., Daniels, W. A., and Johnson, B. V., 1987, "Disc Pumping Test," (US) Air Force Wright Aeronautical Laboratories, TR-2050.

2 Dorfman, L. A., 1963, *Hydrodynamic Resistance and Heat Loss of Rotating Solids* Oliver & Boyd publishers.

3 Nece, R. E., and Daily, J. W., 1960, "Roughness Effects on Frictional Resistance of Enclosed Rotating Discs," ASME *Journal of Basic Engineering,* Vol. 82, p. 553.

4 Daily, J. W., and Nece, R. E., 1960, "Chamber Dimension Effects on Induced Flow and Frictional Resistance of Enclosed Rotating Discs," ASME *Journal of Basic Engineering,* Vol. 82, p. 217.

5 Daily, J. W., Ernst, W. D., and Asbedian, V. V., 1964, "Enclosed Rotating Discs With Superimposed Throughflow, Mean Steady and Periodic Unsteady Characteristics of Induced Flow," Massachusetts Institute of Technology Lab Report No. 64.

6 Owen, J. M., and Haynes, C. M., 1961, "Design Formulae for Heat Loss and Frictional Resistance of Air Cooled Rotating Discs," University of Sussex Report No. 75/Me/61.

7 Haynes, C. M., and Owen, J. M., 1974, "Heat Transfer From a Shrouded Disc System With a Radial Outflow of Coolant," ASME Paper No. 74-GT-4.

8 Bayley, F. J., and Owen, J. M., 1970, "The Fluid Dynamics of a Shrouded Disk System With a Radial Outflow of Coolant," ASME *Journal of Engineering for Power,* Vol. 92, p. 335.

9 Yamada, Y., Watanabe, S., 1993, "Frictional Moment and Pressure Drop of the Flow through Co-axial Cylinders With an Outer Rotating Cylinder," *Bulletin of the JSME,* Vol. 16, No. 93, p. 551.

10 Yamada, Y., and Ito, M., 1979, "Frictional Resistance of Enclosed Rotating Cones with Superimposed Throughflow," ASME *Journal of Fluids Engineering*, Vol. 101, p. 259.

11 Zimmerman, H., Firsching, A., Dibelius, G. H., and Ziemann, M., "Friction Losses and Flow Distribution for Rotating Disks With Shielded and Protruding Bolts," ASME *Journal of Engineering for Gas Turbines and Power,* Vol. 108, pp. 547–552.

12 Millward, J. A., and Robinson, P. H., 1989, "Experimental Investigation Into the Effects of Rotating and Static Bolts on Both Windage Heating and Local Heat Transfer Coefficients in a Rotor/Stator Cavity," ASME Paper No. 89-GT-196.

13 McGreeham, W. F., and Ko, S. H., 1989, "Power Dissipation in Smooth and Honeycomb Labyrinth Seals" ASME Paper No. 89-GT-220.

14 Virr, G. P., Chew, J. W., and Coupland, J., 1993, "Application of Computational Fluid Dynamics to Turbine Disk Cavities," ASME JOURNAL OF TURBOMACHINERY, Vol. 116, pp. 701–708.

15 Waschka, W., Wittig, S., and Kim, S., 1990, "Influence of High Rotational Speeds on the Heat Transfer and Discharge Coefficients in Labyrinth Seals," ASME JOURNAL OF TURBOMACHINERY, Vol. 114, pp. 462–468.

16 Kuznetsov, A. L., and Zhuravlev, O. A., 1972, "Heat Transfer in Labyrinth Glands in Gas Turbines," *Energomashinostroenie,*

Downloaded 01 Jun 2010 to 171.66.16.53. Redistribution subject to ASME license or copyright; see http://www.asme.org/terms/Terms_Use.cfm